Interactions of Plutonium and Lanthanides with Ordered Mesoporous Materials

By

Tashi Parsons-Moss

A dissertation submitted in partial satisfaction of the

requirements for the degree of

Doctor of Philosophy

in

Chemistry

in the

Graduate Division

of the

University of California, Berkeley

Committee in charge:

Professor Heino Nitsche, Chair
Professor Darleane Hoffman
Professor Joseph Cerny
Professor Joonhong Ahn

Spring 2014

Interactions of Plutonium and Lanthanides with Ordered Mesoporous Materials

By Tashi Parsons-Moss

Abstract

Interactions of Plutonium and Lanthanides with Ordered Mesoporous Materials

by

Tashi Parsons-Moss

Doctor of Philosophy in Chemistry

University of California, Berkeley

Professor Heino Nitsche, Chair

Ordered mesoporous materials are porous solids with a regular, patterned structure composed of pores between 2 and 50 nm wide. Such materials have attracted much attention in the past twenty years because the chemistry of their synthesis allows control of their unique physicochemical properties, which can be tuned for a variety of applications. Generally, ordered mesoporous materials have very high specific surface areas and pore volumes, and offer unique structures that are neither crystalline nor amorphous. The large tunable interface provided by ordered mesoporous solids may be advantageous in applications involving sequestration, separation, or detection of actinides and lanthanides in solution. However, the fundamental chemical interactions of actinides and lanthanides must be understood before applications can be implemented. This dissertation focuses primarily on the fundamental interactions of plutonium with organically modified mesoporous silica, as well as several different porous carbon materials, both untreated and chemically oxidized. The interactions were studied by batch contact, Pu L_{III} edge X-ray absorption spectroscopy, and electron microscopy techniques. Some batch sorption experiments were also performed with europium, and to a lesser extent, cerium and zirconium, to complement the plutonium studies. The extensive efforts that were required in the synthesis and characterization of the materials are also discussed.

A method for functionalizing mesoporous silica by self assembly and molecular grafting of functional organosilane ligands was optimized for the 2D-hexagonal ordered mesoporous silica known as SBA-15 (**S**anta **B**arbara **a**morphous silica). Four different organically-modified silica materials were synthesized and characterized with several techniques. To confirm that covalent bonds were formed between the silane anchor of the ligand and the silica substrate, functionalized silica samples were analyzed with ^{29}Si nuclear magnetic resonance spectroscopy. Infrared spectroscopy was used in combination with ^{13}C and ^{31}P nuclear magnetic resonance spectroscopy to verify the molecular structures of the ligands after they were synthesized and grafted to the silica. The densities of the functional silane ligands on the silica surface were estimated using thermogravimetric analysis. Batch sorption experiments were conducted with solutions of Pu(IV), Pu(VI), Eu(III), Ce(III), and Zr(IV). The acetamide phosphonate functionalized silica called Ac-Phos-SBA-15 required more extensive synthesis than the other three functionalized silica materials. Development of functionalized mesoporous silica extractants for actinides is contingent on their synthesis and hydrolytic stability, and these two aspects of the Ac-Phos-SBA-15 material are discussed. This material showed the highest binding affinity for all of the target ions, and the sorption and desorption of Pu(VI) to Ac-Phos-SBA-15

was extensively investigated. An experimental Pu uptake capacity of 30 ± 3 mg Pu per g Ac-Phos-SBA-15 was determined in pH 1.8 solutions. A combination of density functional theory modeling and experimental X-ray absorption spectroscopy data indicated that a strong 2:1 bidentate octahedral complex of PuO_2^{2+} is formed with the acetamide phosphonate ligands at the silica surface.

Ordered mesoporous carbons are attractive as sorbents because of their extremely high surface areas and large pore volumes, and could be suitable substrates for the development of actinide sensors based on their electrochemical properties. Three different mesoporous carbon materials were synthesized by collaborators to test their application as radionuclide sorbent materials. The first is called CMK (**c**arbons **m**esostructured by **K**orea Advanced Institute of Science and Technology), and was synthesized using a hard silica template with 3D-bicontinuous ordered mesostructure. Highly ordered body-centered cubic mesoporous carbon was synthesized by self-assembly of a phenol resin around a soft polymer template, and this material is known as FDU-16 (**F**u**d**an **U**niversity). Etching of the silica portion of mesoporous carbon-silica composites created the 2D-hexagonal mesoporous carbon called C-CS (**c**arbon from **c**arbon-**s**ilica nanocomposites) with a bimodal pore size distribution. The as-synthesized nanocast mesoporous carbon in this work is called UN CMK, and the same material after oxidation treatment with nitric acid is called OX CMK. A portion of both FDU-16-type and C-CS-type ordered mesoporous carbons were oxidized with acidic ammonium persulfate, which created the oxidized carbon materials called FDU-16-COOH and C-CS-COOH, respectively. The mesoporous carbons were characterized by scanning electron microscopy to view their particle sizes and morphologies. Their porosities and structures on the meso-scale were analyzed using transmission electron microscopy, nitrogen adsorption isotherms, and small-angle X-ray scattering. The identity and density of functional groups on the different carbon surfaces were investigated using infrared spectroscopy, elemental analysis, thermogravimetric analysis, and determination of the point-of-zero-charge with the powder addition technique. The porous carbon materials studied present a wide range of particle morphologies, mesostructures, surface areas, pore volumes, and surface chemistries.

Batch Pu(VI) sorption and desorption tests in 0.1 M $NaClO_4$ solutions ranging from pH 1 to 10 were performed with all six mesoporous carbons, and a commercial amorphous activated carbon powder for comparison. More extensive batch sorption studies were completed with the different carbon samples, mostly in pH 4 $NaClO_4$ solutions. Plutonium sorption kinetics, uptake capacities, competition with ethylenediaminetetraacetic acid in solution, Pu desorption, and effects of ionic strength were examined. Batch Eu(III) sorption studies with C-CS-type carbon and its oxidized counterpart C-CS-COOH were performed to complement the Pu studies, by demonstrating how pristine and highly oxidized ordered mesoporous carbons interact with lanthanide cations. The oxidation state and coordination environment of plutonium sorbed to pristine and oxidized ordered mesoporous carbon surfaces were probed using X-ray absorption spectroscopy and transmission electron microscopy. Both untreated and oxidized mesoporous carbons demonstrated high affinity for Pu over a wide range of solution pH conditions, and proved to be superior to activated carbon in terms of Pu sorption kinetics and capacities. The 23-hour Pu uptake capacity of mesoporous carbon materials was measured to be at least 60 ± 5 mg ^{239}Pu per g carbon, compared to 12 ± 5 mg ^{239}Pu per g activated carbon. The batch and spectroscopic studies with four different mesoporous carbons showed two main Pu sorption mechanisms, depending on the concentration of oxygen-containing functional groups on the

surface. Analysis of the X-ray absorption near-edge spectra determined that both untreated and oxidized carbons reduce Pu(VI) and Pu(V) to Pu(IV) in solutions with pH 2-7. The preferred binding mechanism is complexation by surface groups, which controls the sorption kinetics on a time scale of 0 to 40 minutes. After surface sites are saturated, the uptake is controlled by the formation of PuO_2 colloids, which exhibit a high affinity for mesoporous carbon surfaces. The colloids form when Pu is reduced to Pu(IV) by carbon materials with low concentrations of surface functional groups. Although Pu(V) and (VI) are also reduced at oxidized carbon surfaces, colloid formation is inhibited by surface complexation of Pu. Based on Eu sorption studies, highly oxidized ordered mesoporous carbon is a very effective general scavenger for actinide and lanthanide cations. Pu and Eu uptake by highly oxidized ordered mesoporous carbon appears to be dictated by chemisorption, and the Eu uptake capacity (138 mg/g from pH 4 solution) is higher than those previously reported for several other carbon materials. Pristine ordered mesoporous carbon exhibits a low affinity for Eu(III), but is an excellent sorbent of PuO_2 nanocrystals due to its high surface area, as well as its large pore size relative to activated carbon. The high affinity of mesoporous carbon for Pu, and the spontaneous reduction of Pu(VI) or Pu(V) to Pu(IV) at these carbon surfaces could be valuable for a variety of applications.

The plutonium sorbed to mesoporous carbon surfaces could be removed with 1 M $HClO_4$ or 1 M HCl, yielding solutions of Pu(III). The redox interaction between porous carbons and aqueous Pu was further investigated in batch experiments with acidic solutions. These experiments showed that porous carbons reduce Pu(VI) to Pu(III) in 1-1.5 M HCl or 1-1.5 M $HClO_4$, and reduce Pu(VI) to Pu(IV) in 1.3 M HNO_3. The contact time required for complete reduction of Pu generally decreases with higher surface areas, and increases with carbon surface oxidation. The pore size and ordered structure of the carbon had little or no effect on the redox reaction, provided the carbon had a high surface area. As expected, no redox activity was observed with mesoporous silica. It was demonstrated with activated carbon powder that acidic solutions of oxidized Pu can easily be reduced to Pu(III) by being passed through a column packed with porous carbon particles. This is a fast (~16 min per mL solution with the column size used in this work) and convenient way to reduce oxidized forms of Pu and dissolve Pu(IV) colloids without changing the solution matrix, adding chemical reagents, or using a potentiostat. This may be useful in a variety of settings, as manipulation and control of the oxidation state of plutonium is applicable to almost all processes involving remediation, separation and chemical purification of plutonium.

For Sachi and Halona, who bring me great joy.

Contents

List of Figures

List of Tables

List of Abbreviations and Sample Names

Δ	change in
Ω	Ohm
2D	2 dimentional
3D	3 dimentional
A	mass number of a nucleus
AAPS	acidic ammonium persulfate
AC	activated carbon
Ac-Phos	acetamide phosphonic ester silane molecule
Ac-Phos-SBA-15	SBA-15-type ordered mesoporous silica functionalized with the acetamide phosphonic ester silane molecule
AGAPS	N-(acetylglycyl)-3-aminopropyltriethoxysilane
AGAPS-SBA-15	SBA-15 mesoporous silica functionalized with N-(acetylglycyl)-3-aminopropyltriethoxysilane
AMT	Advanced Microscopy Techniques (company name)
An	actinide
APS	aminopropyltriethoxysilane
APS-SBA-15	SBA-15-type ordered mesoporous silica functionalized with aminopropyltriethoxysilane
aq	aqueous
ATR	attenuated total reflection
a.u.	arbitrary units
B_0	external magnetic field
bcc	body centered cubic
BET	Brunauer-Emmett-Teller
BJH	Barret-Joyner-Halenda
CCD	charge-coupled device
C-CS	carbon from carbon-silica nanocomposites: refers to ordered mesoporous carbon that was synthesized by etching the silica component of nanocomposites, which

	were formed by evaporation-induced co-assembly of triblock copolymers, phenol resin, and silicate oligomers
C-CS-COOH	C-CS that was chemically oxidized by treatment with acidic ammonium persulfate
C-CS-COOH-D	C-CS-COOH samples after undergoing dialysis
CDI	carbonyl diimidazole
Ci	Curie
CMK-n	carbons mesostructured by The Korea Advanced Institute of Science and Technology: refers mesoporous carbons that were synthesized by nanocasting against a hard silica template. The number n describes the ordered mesostructure, and was omitted for the CMK materials used in this work because the mesostructure was not confirmed
CMK-8	refers to CMK with 3D-bicontinuous ordered cubic array of carbon nanorods
CMK-9	refers to CMK with 3D-bicontinuous ordered cubic array of carbon nanotubes, which gives a bimodal pore size distribution
CMPEI	carboxymethylated polyethyleneimine
CNT	carbon nanotube
CP	cross polarization
cpm	counts per minute
cps	counts per second
CSA	chemical shift anisotropy
DFT	density functional theory
Diphos-SAMMS	MCM-41 mesoporous silica functionalized with a diphosphonic acid silane
DMA	dimethylacetamide
DP	depth of penetration
DRC	dynamic reaction chamber
DSC	differential scanning calorimetry
DTA	differential thermal analysis
EDS	X-ray energy disperse spectroscopy
EDTA	ethylenediaminetetraacetic acid

EISA	evaporation-induced self assembly
EO	ethylene oxide
EpHL	equilibrium pH at high loading
eV	electron Volt
EXAFS	extended X-ray absorption fine structure
FA	furfuryl alcohol
fcc	face centered cubic
FDU-n	ordered mesoporous silica or carbon synthesized in the method of Fudan University
FDU-16	Fudan University number 16: refers to ordered mesoporous carbon that was synthesized by evaporation-induced self assembly of phenol resins with a soft triblock copolymer template, and has body-centered cubic ordered mesostructure
FDU-16-COOH	FDU-16 that was chemically oxidized by treatment with acidic ammonium persulfate
FFT	Fourier transform
FID	free-induction decay
FTIR	Fourier transform infrared spectroscopy
g	gram
Gly-UR-SAMMS	MCM-41 mesoporous silica functionalized with a glycinyl-urea silane
GO	graphene oxide
GONS	graphene oxide nanosheets
h	hours
HOPO-SAMMS	a series of hydroxypyridinine functionalized MCM-41-type mesoporous silicas
HPGe	high-purity germanium
HR-SEM	high resolution scanning electron microscopy
HR-TEM	high resolution transmission electron microscopy
Hz	Hertz
I	spin quantum number of a nucleus

I	ionic strength
ICP-MS	inductively coupled plasma mass spectrometry
IDA-amide-SAMMS	MCM-41-type mesoporous silica functionalized with an aminodiacetic amide
IEP	isoelectric point
IR	infrared
IUPAC	The International Union of Pure and Applied Chemistry
J	coupling constant in NMR spectroscopy
K	Kelvin
KE	kinetic energy
KIT-n	ordered mesoporous silicas synthesized in the method of the Korea Advanced Institute of Science and Technology (KIT-6 refers specifically to an ordered mesoporous silica with 3D-bicontinuous ordered cubic mesostructure)
L	liter
LCA	linear combination analysis
LLNL	Lawrence Livermore National Laboratory
Ln	lanthanide
LSC	liquid scintillation
M	molar
m	meter
MAS	magic angle spinning
MCA	multichannel analyzer
MCM-41	Mobile Composition of Matter number 41: refers to ordered mesoporous silica or alumino-silicate with a 2D hexagonal mesostructure that was synthesized in a basic medium using micelles formed from cationic surfactants as a structural template
MHAPS	N-(3-methacryloxy-2-hydroxypropyl)-3-aminopropyl-triethoxysilane
MHAPS-SBA-15	SBA-15 mesoporous silica functionalized with N-(3-methacryloxy-2-hydroxypropyl)-3-aminopropyl-triethoxysilane
min	minutes

MWCNT	multi-walled carbon nanotube
MWCO	molecular weight cut off
NHE	normal hydrogen electrode
NMR	nuclear magnetic resonance
OEt	ethoxy
OMC	ordered mesoporous carbon
OMe	methoxy
ox.	oxidation
OX CMK	CMK mesoporous carbon that was oxidized with nitric acid
OX CMK'	Refers to the first batch of nitric-acid oxidized CMK synthesized for this work, which showed different structural properties from the second batch
P123	the triblock copolymer $(oxyethylene)_{20}(oxypropylene)_{70}(oxyethylene)_{20}$
PAA	phosphonoacetic acid
PEO	poly(ethylene oxide)
pH_f	final pH
pH_i	initial pH
PMT	photomultiplier tube
PNNL	Pacific Northwest National Laboratory
PO	propylene oxide
ppb	parts per billion
ppm	parts per million
PPO	poly(propylene oxide)
ppt	parts per trillion
Prop-Phos-SAMMS	MCM-41 mesoporous silica functionalized with a propionamidephosphonate silane
PUREX	Plutonium Uranium Redox EXtraction
PZC	point-of-zero charge (pH)
PZNPC	point of zero net proton charge

PZSE	point of zero salt effect
R	in a chemical formula, refers to an alkyl group
RF	radiofrequency
RPM	revolutions per minute
Sal-SAMMS	MCM-41 mesoporous silica functionalized with a salicylamide silane
SAMMS	self-assembled monolayers on mesoporous supports
SAXS	small-angle X-ray scattering
SBA-15	Santa Barbara Amorphous number 15: refers to ordered mesoporous silca that was synthesized in acidic conditions using a non-ionic triblock copolymer template, and has a 2D hexagonal mesostructure
SEM	scanning electron microscopy
SHE	standard hydrogen electrode
soln.	solution
SSRL	Stanford Synchrotron Radiation Laboratory
STEM	scanning transmission electron microscopy
SWCNT	single-walled carbon nanotube
T	Tesla
TEM	transmission electron microscopy
TEOS	triethoxyorthosilicate
TES	tetraethoxysilane
TESPMA	triethoxysilylpropylmaleamic acid
TESPMA-SBA-15	SBA-15-type ordered mesoporous silica functionalized with triethoxysilylpropylmaleamic acid
TGA	thermogravimetric analysis
TMB	trimethylbenzene
TMOS	tetramethoxysilane
TMS	tetramethylsilane
TPD	temperature-programmed desorption

TPOS	tetrapropoxysilane
UC	University of California
UN CMK	Untreated CMK mesoporous carbon used in this work
US DOE	United States Department of Energy
UV	ultraviolet
V	Volt
Vis-NIR	Visible and near-infrared
XANES	X-ray absorption near edge structure
XAS	X-ray absorption spectroscopy
XPS	X-ray photoelectron spectroscopy
XRD	X-ray diffraction
YAG	yttrium aluminum garnet
Z	number of protons in a nucleus

Acknowledgements

The work presented in this dissertation includes many direct contributions from my esteemed colleagues and collaborators, and also would never have been possible without the many indirect contributions from mentors, colleagues, family and friends.

First, I want to thank God, and my mother, for giving me life, for guiding me towards opportunities, and for giving me the strength to persevere through life's challenges. I would like to thank my entire family for their love and support throughout my academic journey. I especially need to thank Juan, for the many late nights and long work weekends that were required to complete this work would never have been possible had he not been such a wonderful father to our children. I would like to thank Sachi and Halona for their laughter and unconditional love, which has helped me stay positive and maintain perspective when work was difficult. I thank my brother and sisters for their support, for loving me through all of life's changes, and helping me stay grounded. I thank my grandmother, NanAnn, and Auntie Rosalind for their help with childcare, without which I never would have proceeded with this program. I also want to thank my Uncle Dave and Aunt Micheline for helping and convincing me to come to California for college, which marked the beginning of my academic career.

I would like to thank my research advisor, Professor Heino Nitsche, for accepting me into his group, for everything he taught me, and for his academic guidance and support. Heino, I thank you not only for the scientific advice that you gave, but also for the times that you opted to withhold advice. By allowing me to struggle through my "Valley of Tears", you helped me to become a more confident and independent scientist. Most of all I thank you for your commitment to providing opportunities for women in science, and your support and understanding of my needs as a graduate student who is also a mother. You have far exceeded the standards set by the University in this regard, and your kindness paved a road toward a better life for me and my daughters. I thank you for trusting me to always work hard, even when my family duties required that the work be done at unconventional hours. I hope I have proven that your trust is deserved, and I am motivated to continue earning your respect.

I would also like to thank the other members of my dissertation committee, Professor Darleane Hoffman, Professor Joe Cerny, and Professor Joonhong Ahn for their valuable input. I thank Professor Cerny also for a wonderful teaching experience in the spring 2011 semester of Chemistry 146. Darleane, I am humbled and inspired to be in your presence at group meetings over these past years, and I thank you for your scientific discussions and kind words of encouragement.

There are several mentors who were instrumental in helping me get in to graduate school at UC Berkeley, and I would like to thank them here. I thank my undergraduate advisor, Dr. Elizabeth Wade for her endless patience and help in General Chemistry, and for seeing potential in me when it was not obvious. I want to thank Dr. Wade also for her academic guidance, and particularly for directing me to the American Chemical Society Nuclear Chemistry Summer School program. I also thank my undergraduate research mentor Eric Hoppe at Pacific Northwest

National Laboratory, and Dr. David Keeports of Mills College, for all they taught me, and their letters of recommendation.

I would like to thank all of the Nitsche group members, past and present, for their help, advice and camaraderie over the years. We have a wonderful group dynamic, and I am glad to call you all colleagues and friends. I have learned so much from all of you, especially those who became doctors before me: Dr. Mitch Garcia, Dr. Zuzana Dvorakova, Dr. Yung-Jin Hu, Dr. Paul Ellison, Dr. Anthony Bruchet, Dr. Daniel Olive, Dr. Thomas Wall and Dr. Kestrel Brogan. I especially would like to thank Kestrel for being my co-pioneer in the early months of this project, and for her friendship and helpful discussions during our time as office-mates. I also want to thank those who are soon to follow me for great scientific discussions, general help and support in lab, and friendship: Mazar Ali, Deborah Wang, Oliver Gothe, Jennifer Shusterman, Erin May, Nick Esker, Eva Uribe, Phillip Mudder, Carolina Fineman-Sotomayor and Stephen Jones. If I left anybody out, it was not intentional. I am particularly grateful to Deborah Wang and Erin May for their help proofreading this manuscript.

I want to thank all of the scientific staff, radiation control technicians, and health physicists with whom I have interacted at Lawrence Berkeley National Laboratory. I am grateful to the College of Chemistry staff, and especially to Michele Pixa for all of their administrative support. I would like to thank the U.S. Department of Homeland Security Academic Research Initiatives (ARI) program for funding my research.

Now there are many acknowledgements to be made of specific scientific contributions to this work from my collaborators and colleagues, to whom I am extremely grateful. The SBA-15 mesoporous silica was synthesized by Professor Peidong Yang's group at UC Berkeley. I also want to thank Dr. Yang for his assistance in establishing our collaboration with the Zhao group at Fudan University, and for allowing my colleagues and I the use of his group's scanning electron microscope. I want to thank Aude Hubaud, a former Junior Specialist in the Nitsche group, for all of her work on the synthesis and characterization of organically modified SBA-15, and for teaching me techniques used in organic synthesis. Aude performed the synthesis of MHAPS-SBA-15, AGAPS-SBA-15, and several of the reactions to make APS-SBA-15 and Ac-Phos-SBA-15, and did the TGA analysis on the APS-SBA-15 samples. I would also like to thank Aude for her valuable input in the interpretation of NMR spectra. I want to thank Chris Canlas of the UC Berkeley Department of Chemistry NMR facility for running all of our solid NMR samples. I am very grateful for the TGA analysis of functionalized SBA-15 samples presented in Section 5.3.3, which was completed by Dr. Jing-Jen Wanglee of the Katz group at UC Berkeley. I want to thank the Long group of UC Berkeley for allowing my colleagues and I to use their infrared interferometer and thermogravimetric analysis instrument. I would like to thank Dr. Kestrel Brogan for teaching me how to analyze samples with ICP-MS, and for her contributions to the batch sorption experiments presented in Section 5.4.1. I also thank Kestrel for joining me in the extensive testing of centrifugal filters for plutonium work. The SBA-15-type silica monoliths and the CMK synthesis and oxidation were performed by Dr. Harun Tüysüz while he was a postdoctoral associate of the Yang group at UC-Berkeley. I also want to thank Dr. Tüysüz for collecting TEM micrographs on the silica monoliths, the CMK samples, and Ac-Phos-SBA-15 samples. I want to thank the Tilley group of UC Berkeley for use of their nitrogen adsorption instrument. I am extremely grateful to Dr. Daniel Olive for his analysis of XANES data collected on the functionalized SBA-15 and C-CS samples, and analysis of the EXAFS data from all

functionalized SBA-15 and carbon samples. This dissertation would not be nearly as interesting without Dan's contributions. I would like to thank Professor Krishnan Balasubramanian and his group for the molecular modeling of Ac-Phos-SBA-15 and TESPMA-SBA-15. The analysis of XANES data collected on CMK samples was performed by Deborah Wang. I also want to thank Deborah for doing all of the administrative chores associated with the XAS measurements, and for her help with the Np(V) batch contact experiment presented in Section 6.5.4. For the initial analysis of XANES data collected on the first Ac-Phos-SBA-15 sample I thank Dr. Yung-Jin Hu. I want to thank Dr. Olive, Dr. Hu, Deborah Wang, Dr. Brogan, Stephen Jones, Erin May, and Eva Uribe for their help with XAS experiments at the beamline.

The synthesis, oxidation, and most of the characterization of FDU-16 and C-CS mesoporous carbons were performed by Dr. Jinxiu Wang of the Zhao group at Fudan University. I am very grateful for the collaboration of Dr. Wang and Professor Dongyuan Zhao, and particularly for their great idea to include C-CS carbon in this study. The point-of-zero charge characterization, batch experiments, and XAS experiments done with the Fudan carbons could not have been completed within the timeframe that they were, without a tremendous amount of help from my former undergraduate assistant, Stephen Jones. Stephen completed potentiometric titration, powder addition, and ATR-FTIR analysis of the Fudan carbons. He also performed several duplicates batch experiments presented in Sections 6.3.1, 6.3.6, 6.5.2, and 6.5.3. Stephen measured the Vis-NIR spectra of Pu control samples presented in Section 3.4.4, and prepared the batch C-CS samples for XAS, two vital experiments that had to be done while the author was away for child birth. Stephen, thank you for all of your hard work, and for the pleasure of serving as your mentor. I look forward to seeing what awesome science has yet to come out of your career. I want to also thank Dr. Anthony Bruchet for taking SEM images of the Fudan carbons, which are shown in Sections 6.24 and 6.25. All of the batch sorption experiments with ^{152}Eu and C-CS carbons were performed by Erin May. These experiments were a lot of work, including extensive data analysis, and I am very grateful to Erin for her contributions. For collaboration in the TEM analysis of C-CS samples loaded with Pu, presented in Section 6.4.2, I thank Dr. Zurong Dai, Dr. Mavrik Zavarin, and Dr. Annie B. Kersting of Lawrence Livermore National Laboratory. I want to thank Eva Uribe, for attempting the batch contact experiment with C-CS and uranium, mentioned in Section 6.5.4. Finally, I thank Carolina Fineman-Sotomayor for her help with the patent application associated with the work presented in Section 6.5.

1 Introduction

Mesoscale science involves materials and chemical processes on a scale that lies in-between the molecular and continuum approaches. This is a strongly emerging field of interest in the past 20 years, as insights into physicochemical processes on this scale offer potential for new discoveries and innovations. Since the first reports of ordered mesoporous silica synthesis in 1992[1, 2], there has been an explosion of research involving the synthesis of ordered mesoporous materials, as well as their application for catalysis, environmental remediation, chemical detection, chromatography[3], electronics, and medical applications. Several unique and appealing features of mesoporous solids have invoked interest, including the chemistry of their synthesis and their physical properties. The many synthetic routes for mesoporous materials allow hierarchal control of ordered structures, which can be designed and tuned to suit desired applications, and offer structures in between and beyond crystalline or glass-like phases.[4] The chemistry of mesoporous materials often involves molecular self-assembly, and therefore synthetic procedures are typically undemanding and tolerant of human error.[4, 5] Mesoporous materials offer access to very complex structures and strong curvatures in solid-state chemistry.[5] Besides the obvious advantage of very high surface areas, mesoporous materials often have very large pore volumes, giving them interesting mass transport properties. The interfacial behavior of mesoporous solids is of great interest, as fluids contained within mesopores show different physical properties and behaviors than bulk fluids.[5, 6]

The exploration of mesoscale actinide chemistry can potentially lead to new insights of fundamental and practical significance in the field of actinide science. The advantages of ordered mesoporous solids may be applied toward sequestration, vitrification, separations, or detection of actinides and other radionuclides in aqueous solutions. The high surface areas of mesoporous materials provide a large and tunable interface, which should translate to high actinide uptake capacities and fast sorption kinetics for remediation efforts, as well as a means for efficient and low-waste separations. Solid-liquid extractions may be advantageous over current liquid-liquid extractions used in nuclear fuel reprocessing because the latter produce large volumes of mixed hazardous-organic and radioactive wastes, and also suffer kinetic hindrances associated with phase changes, and third-phase formation. Another potential application of mesoporous materials is in nuclear forensics, where the development of chemical sensors for *in situ* actinide detection would save valuable time and resources by pre-screening suspicious samples before they are sent to a forensic laboratory for extensive analysis. The ultimate goal of this project is to develop powerful identification and complexation techniques for fast characterization and detection of actinides and fission products in unknown radioactive solutions. Completion of this goal would contribute to national security, as one of the concerns in nuclear forensics is theft of radioactive materials from sources such as nuclear power plants. However, there is much to learn about the fundamental chemistry of actinides at mesoporous interfaces before such a sensor can be effectively developed. The work presented in this dissertation is a small but significant contribution to the still expanding body of knowledge regarding how mesoporous materials interact with the actinide elements.

At the time this work began, there were just a handful of publications dealing with actinide and lanthanide sorption to functionalized mesoporous materials [7-22], but many more have appeared since [23-51]. Most of these papers are concerned with the application of functionalized

mesoporous materials for environmental remediation, and recovery of uranium from seawater. Just a few of those reports include plutonium experiments,[13, 15-17, 40, 47] which describe batch sorption tests with low concentrations of tetravalent Pu. There are good reasons for inorganic and materials chemists to shy away from plutonium studies. Pu chemistry is notoriously complex with respect to solubility and oxidation state. Because it is fissile and radioactive, there are relatively few laboratories where experimentation with Pu is permitted. On the other hand, Pu is one of the most fascinating elements of the Periodic Table, and still provides much opportunity for new discoveries. Thus the interactions of Pu with mesoporous materials became the main focus of the work presented here. The chemistry of plutonium is very complex, with four different stable oxidation states available under various environmental conditions.[52, 53] The higher oxidation states (V and VI), exist in solution as PuO_2^+ and PuO_2^{2+}, and are generally much more soluble than the lower oxidation states, and thus more mobile in oxic environments. Therefore, the investigation of high-capacity sorbent materials for oxidized Pu is important. Although PuO_2^{2+} is often considered analogous to the uranyl ion, there are fundamental differences in the redox behavior and coordination chemistry of the actinyl ions.[53] The lanthanides were chosen for comparison, as their behavior is more predictable and well understood. The lanthanides also serve as models for the chemical behavior of the trivalent actinides americium and curium.

The Nitsche group has traditionally studied the environmental behavior of oxidized Pu and its sorption to environmentally relevant minerals.[54-62] The work presented in this dissertation represents a break from this tradition, and the beginning of a new interdisciplinary project that the Nitsche group will continue, in pursuit of novel actinide separations and sensors. Admittedly, this break from tradition started out quite tentatively, with only two novice graduate students, and little of the expertise and infrastructure required for this interdisciplinary approach. Nonetheless, these efforts ultimately yielded some very interesting results, including the discovery of new plutonium chemistry and high-capacity Eu and Pu sorbent materials.

It is the author's hope that the work presented in this dissertation may be viewed as a pioneering effort, laying the groundwork for more refined studies of actinides with mesoporous materials that are ongoing in the Nitsche group. Chapter two presents an introduction to ordered mesoporous materials, and a brief description of the methods used to characterize them. These descriptions are not intended to give complete theoretical overviews of the methods, but simply a short introduction to how they work, and how they were used in this project. Chapters three and four give some background information about the chemistries of plutonium, and the lanthanides, respectively. These chapters are far from exhaustive, but provide some relevant discussion of the literature, as well as descriptions of solution preparation and characterization in the present work. Chapter five illustrates work that was done with organically-functionalized SBA-15-type mesoporous silica, which was the first phase of this author's endeavors related to this project. The ambition to develop actinide sensors led the project to include electron-conducting carbon substrates, and these efforts are summarized in chapter six. Oxidized plutonium sorption to nanocast mesoporous carbon, both untreated and chemically oxidized, was compared with sorption to a commercial activated carbon powder. The nanocast carbons greatly outperformed the activated carbon in terms of Pu sorption kinetics and uptake capacities, and the work became the first published study of plutonium interactions with a mesoporous carbon.[63] Due to some ambiguity regarding the Pu sorption mechanism and role of surface oxidation, plutonium sorption studies continued with more pristine and robust soft-template ordered mesoporous

carbons (OMCs), and their highly oxidized counterparts. The batch sorption, X-ray absorption spectroscopy (XAS), and transmission electron microscopy (TEM) studies painted a clearer picture of how oxidized Pu interacts with OMCs, and Eu sorption experiments added further insight by demonstrating the OMCs behavior toward simple hard cations. Desorption studies led to the discovery of interesting redox chemistry in acidic conditions between plutonium and carbon materials with high surface area, and these results are the last to be presented in this dissertation. Further analysis of this serendipitous breakthrough may lead to the future development of carbon-based plutonium sensors.

2 Ordered Mesoporous Materials

2.1 Definition and history

The International Union of Pure and Applied Chemistry (IUPAC) has designated length scales by which to define porous materials, which divide materials into groups based only on pore length.[4] Microporous materials are those with pores < 2 nm, mesoporous materials have pore lengths 2-50 nm, and materials with pores >50 nm are called macroporous materials. In the 1970s and 1980s, there was little mention of mesoporous materials in scientific literature, but a few examples included partially mesoporous activated carbons, and porous glass.[5] These early mesoporous materials were amorphous structures with wide and variable pore size distributions. The idea of ordered mesoporous materials was born in 1992 when Beck and coworkers at Mobil Research and Development Corporation reported the micelle-templated hydrothermal synthesis of ordered mesoporous alumino-silicates.[1, 64] The synthesis involves the formation of micelles from cationic surfactants in basic medium, to create a "liquid-crystal" structural template around which the aluminate and silicate precursors polymerize and condense at 100-120° C, and subsequent calcination above 500° C removes the organic template. The pore dimensions and symmetry are determined by the liquid-crystal scaffold, which depends on many factors including the nature of the surfactant, surfactant/precursor ratio, water concentration, and drying time and temperature. Figure 2.1 is the schematic of the liquid-crystal template mechanism proposed by Beck *et al.* [1] for the formation of 2D-hexagonal MCM-41 (**M**obil **C**omposition of **M**atter).

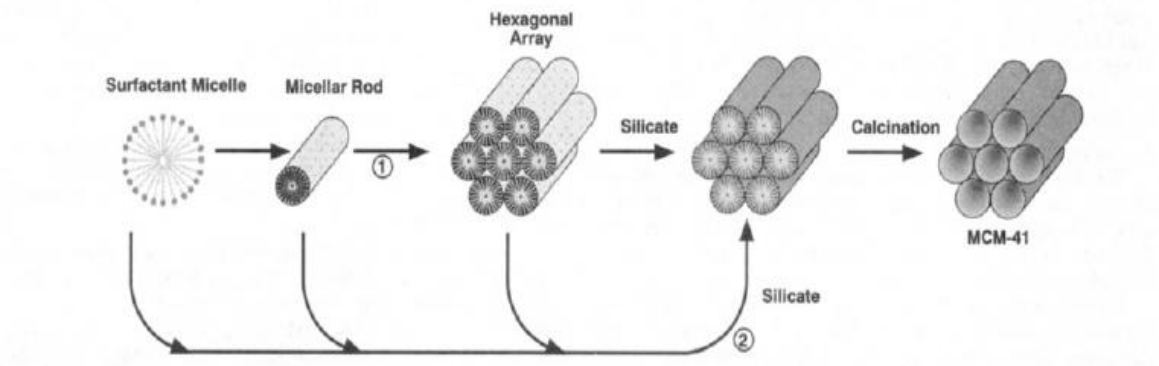

Figure 2.1. Proposed mechanism for liquid-crystal template formation of MCM-41[1].

An alternate mechanism known as cooperative self-assembly was soon proposed by the Stucky group,[65] who suggested the synthesis should be generalized to include all metal oxides. In the cooperative self-assembly mechanism, the mesostructure is formed mainly by coulombic attractions between the surfactant and the inorganic precursor, and thus different combinations of charged surfactants, precursors and counter ions, as well as control of the solution pH, allow versatile control of the formed structures. Another important development in the history of ordered mesoporous materials came from Zhao and coworkers in the Stucky group with the synthesis of the SBA (**S**anta **B**arbara **A**morphous) series of ordered mesoporous silica.[66, 67] This synthesis uses non-ionic triblock copolymers as a structure-directing agent under acidic conditions. Triblock copolymers have a hydrophobic block and two hydrophilic blocks (as in P123, shown in Figure 2.2, or vice versa. Selection of the polymer with regard to the hydrophobic/hydrophilic ratio, pH and concentration of solution, and reaction time and temperature are critical factors for control of the mesoporous structure. The SBA synthesis is more practical than the MCM-14 synthesis since it does not require an autoclave. Furthermore, much larger pore sizes can be achieved (5-30 nm) without the use of a swelling agent. The SBA silicas are also more thermally and hydrothermally stable than the MCMs due to thicker pore walls.

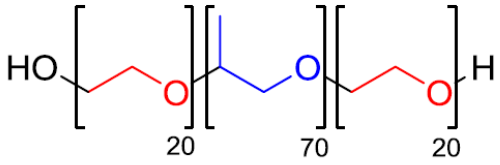

Figure 2.2. Structure of tri-block copolymer P123.

Both MCM-14 and SBA-15 are famous examples of ordered mesoporous silicas with 2D-hexagonal mesostructure (*26mm* symmetry), like the model shown in Figure 2.3A. Figure 2.3 also shows unit cell models of other common 2D and 3D ordered mesostructures, including bicontinuous cubic (*Ia*3*d*, figure 3B) and body-centered cubic (*Im3m*, figure 3D). Famous examples of 3D ordered mesoporous silicas are the KIT-n series (**K**orea Advanced **I**nstitute of Science and **T**echnology),[68] and the FDU-n series (**Fu**d**a**n **U**niversity).[69] Many different non-silicous ordered mesoporous materials have also been synthesized using various methods since 1994.[70] Figure 2.4 shows a schematic representation of the general synthetic pathways used. A significant example of the nano-casting or "hard-template" approach was the first synthesis of ordered mesoporous carbons,[71, 72] known as CMK-n (**C**arbons **M**esostructured by **K**orean Advanced Institute of Science and Technology). The success of the nanocasting synthetic approach demonstrated that mesoporous silicas such as SBA-15 have a secondary network of micropores that interconnect the mesopores. Today, over 18,000 publications are returned in an ISI Web of Science search for "mesoporous" as a topic, and ordered mesoporous structures have been prepared of hundreds of different materials. Ordered mesoporous silicas such as MCM-41 and SBA-15 are now commercially available, or can be easily synthesized by students or technicians in any materials laboratory. Although powders are the most common morphology, ordered mesoporous materials can be made in the form of monoliths[73, 74] and thin films,[75, 76] which may be much more useful for many applications.

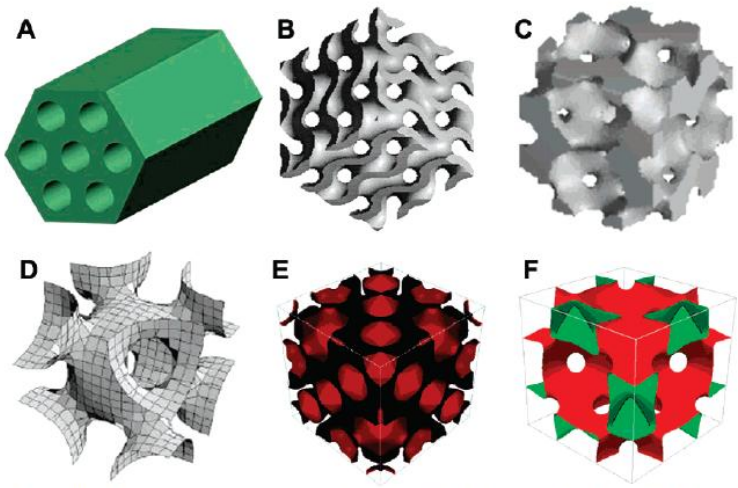

Figure 2.3. Pore models of mesostructures with symmetries (A) *p6mm* (B) *Ia3d* (C) *Pm3n* (D) *Im3m* (E) *Fd3m*, and (F) *Fm3m*.[77]

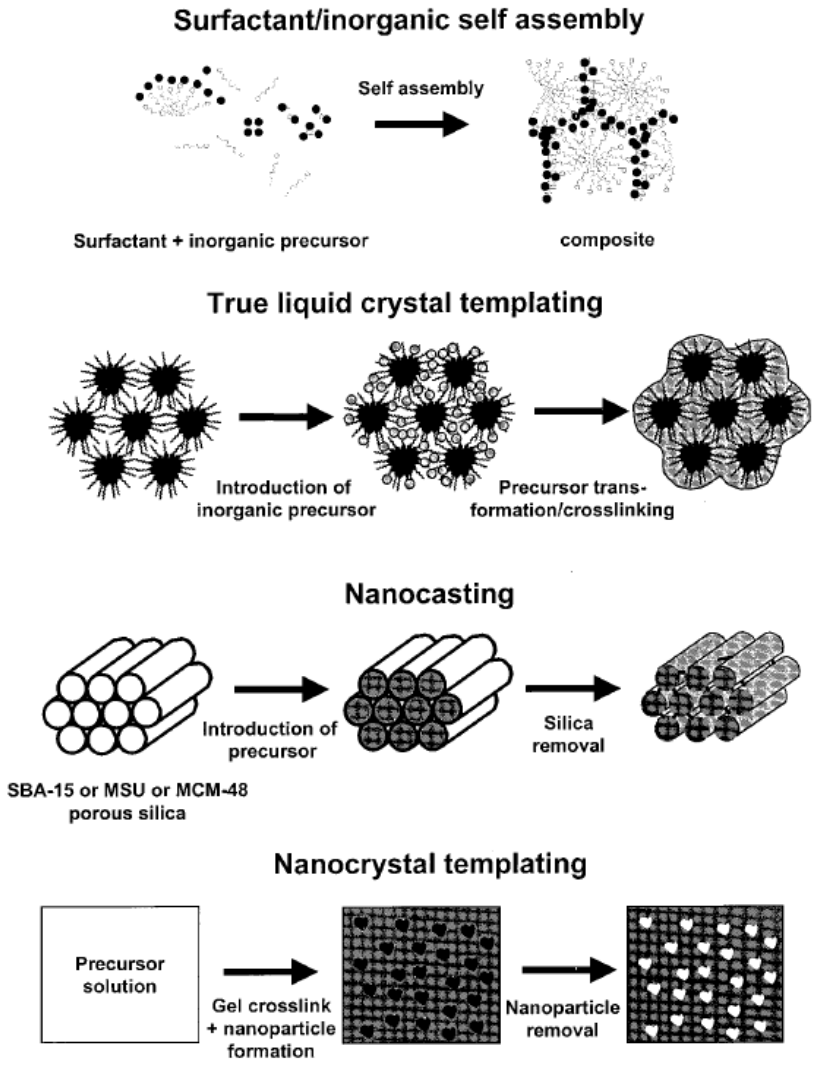

Figure 2.4. General synthetic pathways used for synthesis of non-silicous mesoporous materials[70].

There are many ways to functionalize ordered mesoporous materials for desired applications.[5, 78] Figure 2.5 shows a schematic of three popular ways to functionalize mesoporous materials for metal extraction. In the one-step method, the functional groups or nanoparticles are doped into the mixture at the beginning of the synthesis of the mesoporous solid. For organic modification, this is known as co-condensation, and the functional organosilane is incorporated into the silica pore walls.[78] Advantages to this method are simplicity and the ability to prepare functionalized mesoporous materials with complex morphologies. However, the extent of functionalization is limited, as many of the functional groups will be buried in the pore walls and high loading compromises structural integrity. Another method is surfactant displacement, where the organic mesoporous template is replaced by a functional organosilane, and the mesoporous support is left uncalcined. This method is also simple, and allows greater functionalization than co-condensation, but the uncalcined structure could be subject to long-term degradation. Therefore the most popular method of organic modification is the multi-step process, including silanation of the fully calcined mesoporous silica. Figure 2.6 shows a schematic view of two subtly different ways of post-calcination silanation.[78] Without water, the silanes can only react

with silanols that are already available on the surface. The silica is often boiled beforehand to increase the density of silanols for capping. If interfacial amounts of water are included in the reaction mixture, organosilanes are hydrolyzed and tris(hydroxysilanes) undergo self-assembly into a dense, crosslinked functional monolayer. Fryxell and coworkers at Pacific Northwest National Laboratory (PNNL) have dubbed this method "SAMMS" (**S**elf-**A**ssembled **M**onolayers on **M**esoporous **S**upports), and successfully employed it to create a variety of metal-extracting mesoporous materials.[15, 16, 19, 21, 78-81] Further discussion of the functionalization reaction can be found in sections 5.3.1 and 5.3.2, as this method was chosen and optimized for the SBA-15 substrate in the present work.

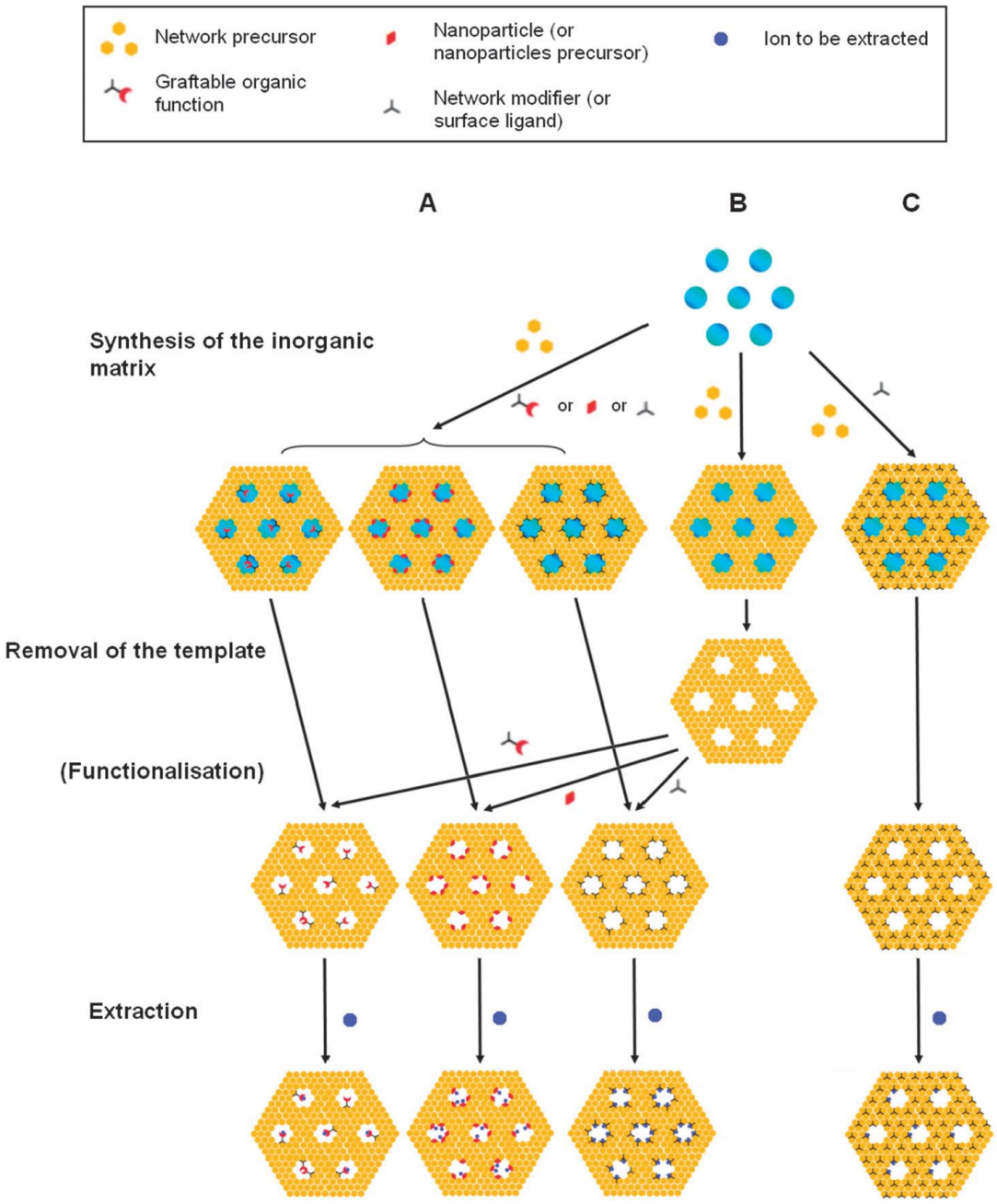

Figure 2.5. Schematic view of three ways to obtain functional mesoporous materials.[5] In the "one-step" method (A), the functional groups are included in the original synthetic mixture with the inorganic precursor. Way (C) shows another variation of this, where the functional modifier is included throughout the mesoporous framework. More commonly, the inorganic mesoporous material is formed first, and then functionalized after removal of the template (B).

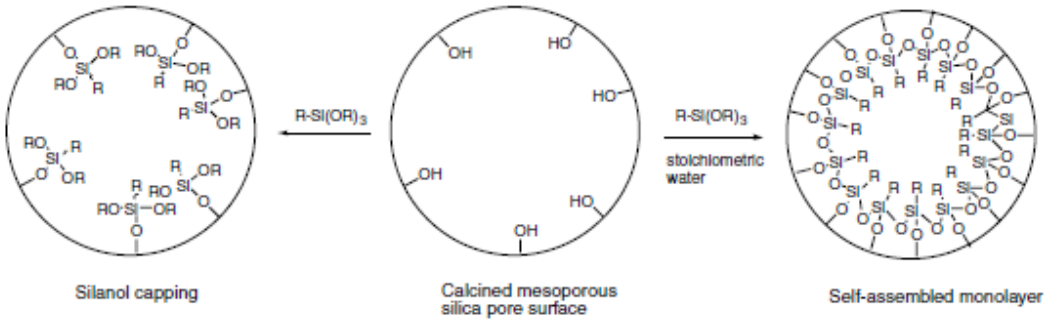

Figure 2.6. Schematic representation of two different ways of introducing functional silanes to calcined mesoporous silica.[78]

2.2 Characterization

All materials must be properly characterized to better understand the chemistry occurring at their interface, and to understand which properties are most important for applications. The particle size and morphology, as well as domains of ordered pore structure, can be visualized using electron microscopy. If the mesoporous structure is truly ordered, this will be reflected in the X-ray diffraction or scattering patterns. Extensive analysis of gas adsorption isotherms, usually N_2 adsorption, can yield information regarding specific surface areas, pore volumes, and pore size distributions. The chemical properties of mesoporous materials and functionalized mesoporous materials may be analyzed by thermogravimetric analysis, nuclear magnetic resonance, infrared spectroscopy, and by determination of the point-of-zero charge (PZC). All of these techniques were utilized during the course of the project, although these techniques were not always available when needed. Some of the characterizations were performed by this author, while others were kindly provided by colleagues and collaborators, who are described on the acknowledgements page. This chapter provides brief descriptions of the characterization methods, and how they were used in the present work.

Many different spectroscopic methods were used throughout this work, both for characterizing the materials as described in this chapter, as well as for characterizing plutonium species as described in Chapter 3. Therefore, it is helpful to keep in mind an overview of the electromagnetic spectrum, and the different atomic and molecular excitations that can be initiated by radiation of the various energy ranges. Figure 2.7 provides a graphical representation of the electromagnetic spectrum, with labels underneath indicating common processes probed with each energy range. This project used methods over the entire range, from nuclear magnetic resonance spectroscopy at the low energy to X-ray absorption spectroscopy at the high energy end.

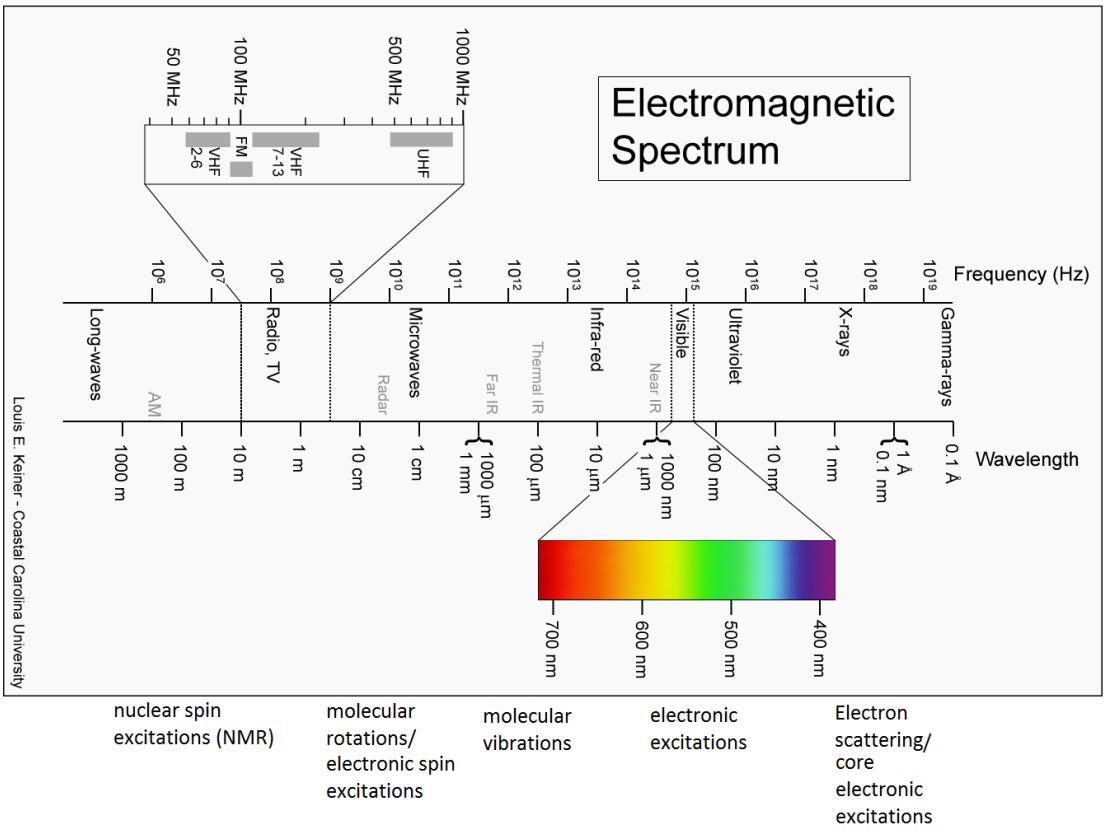

Figure 2.7. Graphical representation of the electromagnetic spectrum (from http://www.unwittingvictim.com/Electromagnetic-Spectrum-3H.PNG) with general atomic and molecular processes that are probed in spectroscopy labeled underneath.

2.2.1 Electron microscopy

Electron microscopy is a powerful tool for studying the morphology, topology and crystallography of materials. Several books are available to explain electron microscopy, but the main source used for this section was a book by Goodhew, Humphreys and Beanland[82]. When electrons are accelerated to a high energy and focused onto a material, they interact electrostatically with the nuclei and electrons of atoms within the material. Elastic or inelastic scattering and backscattering occur, and a variety of signals may be produced such as X-rays, secondary electrons, Auger electrons, and photons, and each carries information about the structure of the material. An electron microscope uses a high-voltage electron beam to create a magnified image of a sample. The resolution of a microscope ρ is defined as the distance between two details that are just discernible, and can be described for image formation from a light or electron beam by equation 2.1, where λ is the wavelength of the incident light, μ is the refractive index, and α is the maximum angle between incident and deflected beam in the limit of the lens aberrations.

$$\rho = \frac{0.61\lambda}{\mu sin\alpha} \qquad (2.1)$$

The resolution of an electron microscope is far greater than that of an optical microscope because the wavelength of high energy electrons is five orders of magnitude smaller than the wavelength of light. The resolution is limited, however, by the convergence angle afforded by the electromagnetic lens, which is limited to about 0.5° instead of 70° for the glass lens used in optics. Nonetheless, resolutions on the order of angstroms can be achieved, and the smaller convergence angle actually gives electron microscopes a greater field of depth than optical microscopes. All electron microscopes need an electron gun, a system of condenser lenses, a sample chamber, and some sort of signal detector. Different combinations of these elements and additional detectors result in a variety of analytical techniques associated with electron microscopy. In almost all electron microscopy the samples must be held under vacuum because of the strong scattering between electrons and matter (including air). The two most common electron microscopy techniques are transmission electron microscopy (TEM) and scanning electron microscopy (SEM). Some TEM microscopes have the ability to do both, resulting in a technique known as scanning transmission electron microscopy (STEM). In general, SEM can provide images of external morphology similar to, though more magnified than, those formed by the human eye. On the other hand TEM probes the internal structure of samples, and provides microstructural or ultrastructural details not visible to the eye.

In TEM a beam of electrons is emitted by a cathode (usually a tungsten filament), accelerated under high voltage to high energy (100-300 keV), and is transmitted through an ultra thin specimen. The electron beam interacts with the sample as it passes through it, carrying information about the inner structure of the specimen to the imaging system of the microscope. A series of electromagnetic lenses magnify the spacial variation until it is recorded with a fluorescent screen, photographic plate, or a CCD (charge-coupled device) camera. CCDs are most commonly used for detection because the image detected by the CCD may be displayed in real time on a monitor or computer. A CCD is a pixilated silicon surface that creates a digital copy of light patterns via detection of photons. CCD cameras are optimized for TEM applications by coupling with high-resolution phosphors such that the electron energy is transferred to photons for detection by the CCD. One of the challenges of TEM is preparing a sample thin enough to be imaged without changing or disturbing the sample. Common sample preparation methods include mechanical grinding, cleaving, sputtering, and electrical or chemical polishing.

The focus mode of a TEM projection system can be changed to obtain either an image or a diffraction pattern on the screen or film. In imaging mode, either a bright field image or a dark field image may be generated depending on the position of the microscope's objective aperture (contrast aperture). The aperture is located behind the objective lens and will stop electrons that have been scattered by too large an angle from passing down the column and contributing to the image. In bright field imaging, the aperture is centered around the optical axis, and in the absence of a specimen, a bright background is seen. Thicker or higher density regions of the sample will scatter electrons more strongly, and appear darker in the bright field image. However, interpretation of the contrast is not always straightforward, as it depends on specimen thickness, focus, the resolution of the microscope and phase contrast. If the sample is crystalline, diffraction of the electron beam occurs and the intensity of electron scattering is greatly increased at particular orientations of the specimen. The objective aperture can then be used to allow undeflected or defracted beams to form an image, giving higher contrast to regions that defract strongly. The aperture can be moved to select only a particular defracted beam, and thus

only a selective reflection *hkl* will contribute to the image formation. This is known as dark field imaging because in the absence of a specimen a dark background image is seen, and areas where the Bragg condition is met appear bright. Dark field imaging allows working in diffraction mode with the formation of an electron diffraction pattern when a selected area aperture is used instead of an objective aperture.

In SEM, the electron beam of about 1 to 30 keV is focused onto the sample and scanned across a rectangular area in a raster pattern. Signals from the interaction of the incident electrons with the sample's surface are detected to create an image. Usually secondary electrons and backscattered electrons are detected to create the image, while X-rays are used for chemical analysis. Auger electrons are much lower in energy and are only used on specialized instruments with ultra high vacuum. There is usually a semiconductor or scintillator detector for backscattered electrons, and a separate scintillator-based detector for secondary electrons, which are most commonly used for imaging the topography of surfaces. The intensity of backscattered electrons is proportional to the atomic number Z of the material, so it is possible to create composition-contrast images using the backscattered electrons. A huge advantage of SEM is the large depth of field, which allows a large amount of the sample to be in focus at one time. Preparation of the samples is relatively easy, as the only requirement for the sample is electrical conductivity. Because of this, SEM is often preferable to TEM for imaging and studying surfaces. One of the limitations of this technique is low resolution due to the samples becoming negatively charged during operation. Semiconductor or non-conducting samples are usually sputter coated with a thin layer of gold or carbon prior to imaging. The probe size and current running through the probe are very important factors for optimizing image resolution, and the probe size should be adjusted whenever the magnification is changed. Some modern microscopes have the ability for the high resolution-SEM (HR-SEM) technique, working at very low currents and voltages.

Some TEM instruments have scanning coils added to combine the benefits of SEM and TEM with STEM, and there are also dedicated STEM instruments. In STEM the electrons pass through the thinned specimen, but, as in scanning electron microscopy, the electron optics focus the beam into a narrow spot which is scanned over the sample in a raster. A useful feature of STEM is the ability for high resolution Z-contrast imaging using an annular detector to detect electrons that were scattered by relatively large angles.

Both TEM and SEM can be combined with other techniques to study structure of materials. For example, energy disperse X-ray spectroscopy (EDS) can provide elemental analysis and even elemental mapping of samples. The technique involves detection of X-rays emitted from the sample after electron scattering occurs, and the X-rays have energies that are quantized and element specific. EDS systems include computer software that contains a large library of X-ray energies and gives real-time analysis. The technique in SEM is sometimes called EDAX, which is the name of one of the more popular software programs. EDS is more reliable as a qualitative rather than quantitative technique, because although percent compositions are given, they only represent the composition at the surface of a small sample. The resolution of X-ray produced elemental maps is limited by the long range of X-rays.

For the characterization of mesoporous materials, SEM is generally used to view the particle morphology, and TEM is used to image and confirm the ordered mesostructure. In this work most of the particles were imaged by SEM using a JEOL field emission SEM (JEOL PC-

SEM 6340 software) set to 5.0 kV and a 6.0 mm working distance. EDS was used to analyze some functionalized silica particles. Powder samples were sonicated for 10 minutes in isopropanol, then drop cast onto a smooth Si wafer for SEM imaging. TEM micrographs were provided by collaborators, some with a Hitachi H-7650 TEM set at 120 kV, in imaging mode with an AMT (Advanced Microscopy Techniques) camera, and others using a JEOL JEM2011F microscope operating at 200 kV. Additionally, TEM and EDS were used for analysis of plutonium sorbed to C-CS and oxidized C-CS-COOH mesoporous carbon as described in Section 6.4.2. Electron microscopy is a wonderful tool for visualizing mesoscale samples, but it is important to remember the limitations. Most notably, because the sample size is so small, there is no way to guarantee that the observed properties are representative of the bulk sample. Many particles should be imaged to examine the variation, and obtaining quality images can take extended periods of time even for experts. It can be very difficult to get all of the correct focusing conditions and sample orientations.

2.2.2 X-ray techniques for confirming ordered structure

X-ray diffraction (XRD) is a versatile, non-destructive technique for determining the crystal structure of materials. A crystal lattice is a regular three-dimensional distribution of atoms in space, arranged so that they form a series of parallel planes separated from one another by a distance *d*. Planes of various orientations exist in any crystal, each with its own specific *d*-spacing. When a monochromatic X-ray beam with wavelength λ is projected onto a crystalline material at an angle θ, diffraction occurs only when the distance traveled by the rays reflected from successive planes differs by an integer number *n* of wavelengths. The diffracted beam contains a large number of X-rays that were scattered in the direction of θ to travel in phase with the incident beam. The condition for diffraction is summarized by Bragg's Law, Equation 2.2, and Figure 2.8 gives a simple schematic of X-ray diffraction by a crystal.

$$n\lambda = 2dsin\theta \qquad (2.2)$$

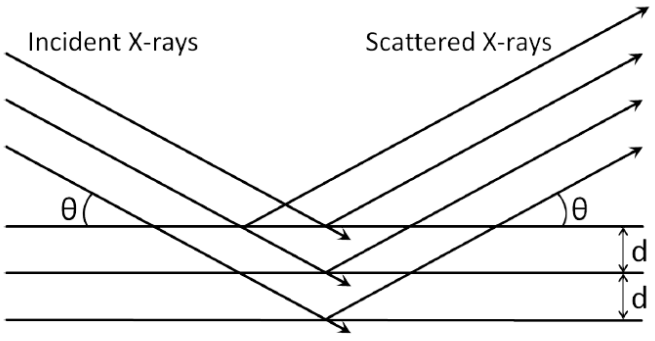

Figure 2.8. Schematic of X-ray diffraction by a crystal.[83]

An X-ray diffractometer (XRD) instrument typically varies the angle θ so that the Bragg's Law conditions are satisfied by different *d*-spacings in polycrystalline materials. The detected intensity of defracted X-rays is plotted against degrees 2θ, since 2θ is the angle between the incident and diffracted beam. The plots will include peaks of larger intensity associated with

different *d*-spacings in the crystal. The instrument's software contains an extensive library of diffractograms of different materials, so XRD is often used as a fingerprint method to identify crystalline phases. Where a mixture of different phases is present, the resultant diffractogram is formed by addition of the individual patterns, and a wealth of structural, physical and chemical information about the material investigated can be obtained.

X-ray diffraction work is usually classified as being single crystal or polycrystalline powder XRD. The single crystal sample is a perfect crystal (all unit cells aligned in a perfect extended pattern), with a cross section of about 0.3 mm. The single crystal diffractometer and associated computer package is used mainly to elucidate the molecular structure of novel compounds. Powder diffraction is mainly used for identification of solid materials. In powder XRD, it is important to have a sample with a smooth plane surface, therefore samples are pressed flat on a sample holder. If possible, the sample should be ground to particles of about 0.002 mm to 0.005 mm cross section. The ideal sample is homogeneous with randomly distributed crystallites.

Using powder XRD for identification of materials' crystal structures usually requires scans of 2θ from ~10° to 70°. Many mesoporous materials like silica and carbon are amorphous on the angstrom scale, but have ordered mesostructures and thus *d*-spacing on the order of 10 nm. Because the wavelength is fixed and determined by the type of X-ray tube in the instrument, it is easy to see in Equation 2.2 that in order for diffraction peaks to be observed, very low angles (2θ ~ 1°- 6°) must be scanned. This can be tricky, as not all XRD instruments are set-up to scan low angles. The author attempted to analyze the CMK-type mesoporous powders by low-angle XRD multiple times on two different available instruments, without success. It is likely that the sample stage and sample holders were not the appropriate geometry, but it is also possible that the samples were not thin enough. Because the CMK materials were not as highly ordered as the SBA-15, no diffraction patterns were obtained. For SBA-15, a diffraction pattern was obtained over a 2θ range of 0° to 6° on a PANanalytical X'Pert Pro powder X-ray diffractometer using Co K_α X-rays, but the background was peculiar due to the system not being properly set up for low angles.

The ordered mesoporous carbon materials that came from Fudan University were analyzed by small-angle X-ray scattering (SAXS) to confirm the ordered mesostructure. SAXS operates on the same principle as XRD, but all of the scattered X-rays are detected rather than just the diffracted beam. Therefore SAXS can be used to study the structure of non-crystalline partially ordered materials, which show diffuse peaks at scattering angles that meet the Bragg condition. The detector is typically a 2-dimensional flat X-ray detector located behind the sample, perpendicular to the direction of the primary beam. The scattering pattern contains information about the structure of the sample, and can also be matched with known scattering patterns. Compared to XRD, a SAXS measurement is faster, but has a lower signal-to-noise ratio. The scattering patterns of the ordered mesoporous carbons showed the expected Bragg peaks, which confirmed their ordered structure.

2.2.3 N_2 physisorption

Nitrogen adsorption is commonly used for the identification of the specific surface area, pore volume, and pore size distribution of porous materials. Other probe gases including Ar and

CO_2 may be used as adsorptives, depending on the nature of the material (adsorbent) and the information required. Porous solid samples are precisely weighed into a clean and dry glass tube, then held under vacuum at a warm temperature (usually 120° C) for several hours to evacuate the physisorbed water or other species from pores. The mass of the sample after degassing is taken and used for all calculations. When the sample is held in a closed system with a measurable pressure of gas, the gas molecules will adsorb to the solid powder. Most of the analysis assumes physisorption, which involves only weak intermolecular forces such as Van der Waals interactions and hydrogen bonding. The amount of gas adsorbed is usually measured by the difference in pressure after adsorption, provided the volume is known, but gravimetric methods may be used on some instruments. By slowly increasing the gas pressure, physisorption measurements are usually carried out at constant temperature, and thus involve the determination of an adsorption isotherm where the amount of gas adsorbed (n^a) is expressed as a function of the equilibrium relative pressure (p/p_0) as expressed in Equation 2.3.[84]

$$n^a = f\,(p/p_0)\,T,_{\text{gas, solid}} \qquad (2.3)$$

The porisometer's software plots the adsorption and desorption isotherms, and does a multitude of calculations based on the data and the sample mass entered by the user. The first step in the interpretation of a nitrogen isotherm is the identification of the physisorption mechanism, which could be monolayer-multilayer adsorption, capillary condensation, or micropore (pore size < 2 nm) filling. Capillary condensation is involved as a secondary process in the filling of mesopores, and results in a hysteresis loop, a range of relative pressures where the desorption and adsorption isotherms do not match up.[84]

According to the IUPAC, adsorption isotherms are classified into six groups, with features that are associated with the nature of the gas-solid interactions and the surface area and porosity of the solid.[85] Figure 2.9 displays the general shapes of the six isotherm types. Isotherms of real samples often look a bit different than these, and may contain features of more than one isotherm type.

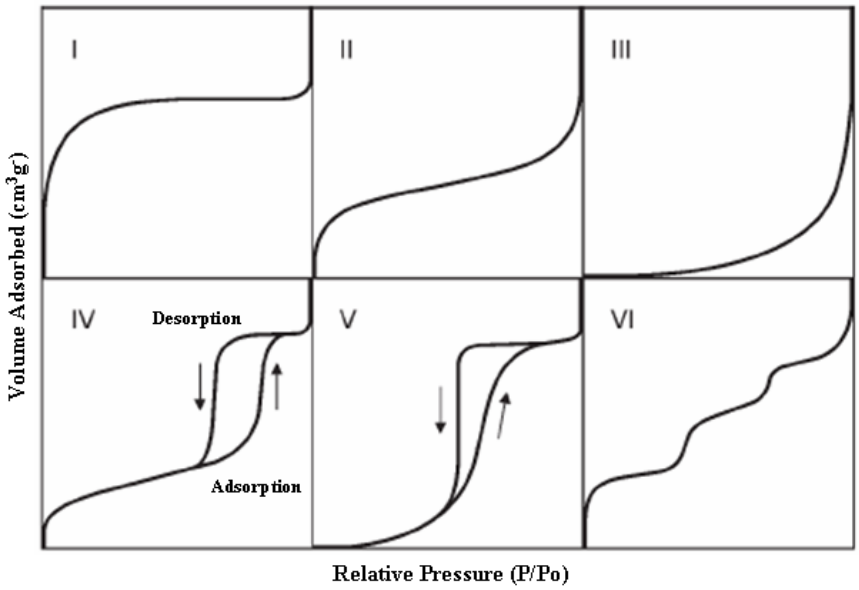

Figure 2.9. Types of physisorption isotherms.[85]

Type I isotherms are observed for microporous solids with relatively small external surfaces, where the limiting uptake is governed by the accessible micropore volume rather than by the internal surface area.

Type II isotherms represent unrestricted monolayer-multilayer adsorption, and are normally obtained with non-porous or macroporous (> 50 nm) adsorbents.

Type III isotherms are convex to the p/p_0 axis over its entire range, and are not common. There are a number of systems (*e.g*. nitrogen on polyethylene) which exhibit isotherms with gradual curvature, in which the adsorbate-adsorbate interactions play an important role.

Type IV isotherms are distinguished a hysteresis loop, which is associated with capillary condensation taking place in mesopores, and also have a limiting uptake over a range of high p/p_0. The initial part of the Type IV isotherm is attributed to a monolayer-multilayer adsorption to the external surface. Type IV isotherms are characteristic of many mesoporous adsorbents, including SBA-15, KIT-6, FDU-16, and C-CS.

Type V isotherms are uncommon. They are related to the Type III isotherm in that the adsorbent-adsorbate interaction is weak, and they also exhibit hysteresis as in Type IV.

Type VI isotherm exhibits stepwise multilayer adsorption on a uniform nonporous surface. The sharpness of the steps depends on the system and the temperature, and the step-height represents the monolayer capacity for each adsorbed layer.

The Type IV isotherm deserves some further discussion, because it is the most relevant to mesoporous materials. The hysteresis loop in the multilayer portion of a Type IV isotherm may assume a wide variety of shapes, which are categorized as shown in Figure 2.10. Types H1 and H4 are two extremes, and H2 and H3 shapes are intermediate. The steep region of the desorption

branch leading to the lower closure is generally almost independent of the porous sorbent, and depends on the nature of the adsorptive. Other features of hysteresis loops are not fully understood, but the shapes have been identified with specific pore structures. H1 hysteresis loops are associated with narrow pore size distributions, while H2 loops are difficult to interpret and are often associated with materials that have poorly defined pore-shape and size. The H3-type loop does not show a limiting adsorption at high p/p^0, and is observed with aggregates of plate-like particles that make slit-like pores. H4 hysteresis loops are associated with microporous materials having slit-like pores.[85] Ideally the nitrogen adsorption isotherms of ordered mesoporous materials have H1 hysteresis loops, as the pore size distribution should be well defined.

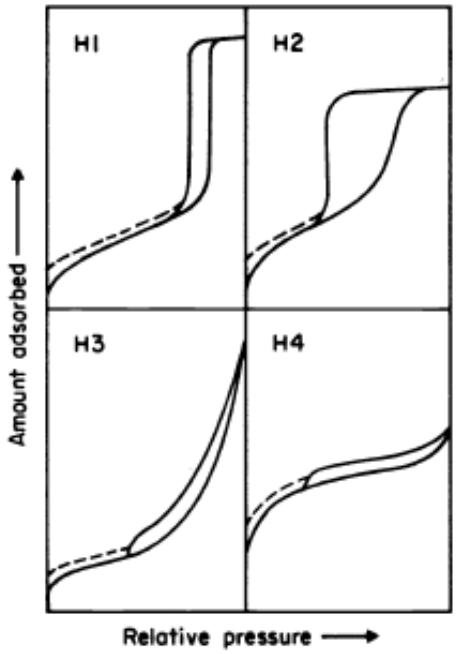

Figure 2.10. Types of hysteresis loops observed in gas adsorption isotherms [85].

The Brunauer-Emmett-Teller (BET) method[86] is widely used for calculating the specific surface area of porous solids from the nitrogen adsorption isotherm, despite the oversimplifications made in BET theory. The linear form of the BET equation is given in Equation 2.4, where n^a is the amount adsorbed at the relative pressure p/p_0, n_m is the monolayer capacity, and C is a constant that is dependent on the isotherm shape, and associated with the magnitude of adsorbent-adsorbate interaction energy.

$$\frac{p}{n^a.(p^\circ - p)} = \frac{1}{n_m^a.C} + \frac{(C-1)p}{n_m^a.Cp^\circ} \qquad (2.4)$$

According to the BET equation, a linear relation is given if p / n^a $(p_0 - p)$ is plotted against p/p_0, known as the BET plot. In this manner, it is possible to obtain n_m, and the surface area is then calculated using Avogadro's number and the assumed area occupied by the N_2 molecule in a densely packed layer. The range of linearity of the BET plot is always restricted to a limited part of the isotherm, usually not above $p/p_0 \approx 0.3$.

BET theory is based on an oversimplified extension of the Langmuir mechanism to multilayer adsorption. To obtain a reliable value of n_m it is necessary that the knee of the isotherm be fairly sharp (*i.e.* the BET constant *C* is not less than ~100). A very low value of *C* (< 20) is associated with an appreciable overlap of monolayer and multilayer adsorption, and the application of the BET analysis not valuable in that case.

Nitrogen adsorption isotherms are also commonly used to estimate the pore volumes and pore size distributions of porous materials. Pore size analysis is based on an adopted interpretation of the mechanism of capillary condensation and associated hysteresis phenomena. If applied over a wide range of relative pressures (p/p_0), N_2 adsorption isotherms provide information on size distributions in a wide range (approximately 0.5–200 nm)[87] using various models. For mesopore evaluation, usually the classical pore size model developed by Barret, Joyner and Halenda (BJH)[88] is applied, which is based on the Kelvin equation (Equation 2.5) and includes corrections for multilayer adsorption.

$$r_K = \frac{2\sigma^{1g}v^1}{RTln(p^\circ/p)} \qquad (2.5)$$

In Equation 2.5, r_K is the Kelvin radius based on the curvature of a liquid meniscus in a pore, which is related to the relative pressure p/p° at which condensation occurs, σ^{1g} is the surface tension of the liquid condensate, and v^1 is its molar volume. In application of the Kelvin equation, the pores are assumed to be cylindrical or slit-like, and it is assumed that the curvature of the condensate meniscus is directly related to the pore width. Other assumptions in calculating pore size distributions include (a) that the pores are rigid and regularly shaped, (b) there are no micropores (other methods are used for micropore analysis), and (c) the size distribution does not continuously extend from the mesopore range into macropores. Plots are generated of cumulative pore volume vs. pore radius, and well ordered mesoporous materials will show a peak centered around the average pore radius. The result will vary slightly depending on whether the adsorption or desorption branch of the isotherm is used. The adsorption branch seems to be most common.

The *t*-plot method is commonly used for analysis of microporosity (surface area and volume from pores < 2 nm) in carbons and other porous powders. The method involves comparison of the sample's gas adsorption isotherm to that of a standard planar, nonporous surface, and requires gas adsorption measurements to high relative pressures where multilayer adsorption occurs.[89] The thickness *t* of an adsorbed layer of nitrogen is given by Equation 2.6, where the thickness of one layer is 3.54 Å, *V* is the volume of adsorbed nitrogen, and V_m is the volume of a monolayer.

$$t = 3.54(V/V_m) \qquad 2.6$$

The *t* plot is the volume *V* at relative pressure p/p_0 plotted against *t*, and the slope is related by a constant value to the specific surface area of the powder. If the t plot is linear and passes through the origin, the solid is considered to be non-porous. If the *t* plot is linear with an extrapolated y-intercept that is positive, the adsorbent is porous. Information about the micropore widths can be extracted from changes in the slope of the *t* plot.[89]

Although physisorption is widely accepted as a standard characterization procedure for porous materials, there are many assumptions, simplifications and limitations in the data

interpretation. Values obtained such as BET surface areas and average pore size should not be considered absolute, true values, but may be used for comparison of materials in some cases. The classical methods, especially BJH, often greatly underestimate the pore size distribution[87] and should only be applied to a portion of the isotherm. In materials with significant volumes of both mesopores and micropores (such as activated carbon and some mesoporous carbons), the classic models are often insufficient. Surface areas may also be underestimated, because the samples have to be held under high vacuum, which could collapse some of the micropores, and nitrogen diffusion into micropores could be kinetically hindered at low temperatures. Furthermore, the extreme temperature changes that the sample is subject to during outgassing and adsorption measurements can cause structural changes. For example, outgas temperatures around 250° C are often recommended to fully evacuate the micropores in carbon materials, but will damage the sample by removing functional groups from the surface.

All of the mesoporous materials in this work were subject to nitrogen adsorption for surface area and pore analysis. The SBA-15 silica substrates were sent to the company Quantachrome, which manufactures many gas adsorption instruments, for analysis at 77 K using their Autosorb iQ model. Nitrogen Adsorption isotherms of activated carbon and CMK materials were measured (by the author) at 77 K using a Quantachrome Autosorb 1 analyzer. Samples were held under vacuum at 120 °C for at least 20 hours prior to analysis. The BET surface areas were in the expected range, but meaningful pore size distributions were not obtained. The BET plots were linear, and the total pore volumes were estimated from the isotherm at p/p_0 of 0.978. The values extracted from the t-plot data were also verified to be reliable, but there was a problem with the BJH algorithm in the program, so BJH analysis was omitted. Those measurements were done at least in duplicate, and average values used. Nitrogen adsorption/desorption isotherms of the FDU-type and C-CS-type mesoporous carbons were measured by Dr. Jinxiu Wang of the Zhao group of Fudan University (Shanghai, China) with a Micromeritics Tristar 3020 analyzer at 77 K. Before the measurements, samples were degassed in vacuum at 180 °C for at least 6 hours. The surface areas were calculated using the BET method, and pore size distributions were obtained with the BJH method based on the adsorption branch of the isotherm. The total pore volume was estimated from the adsorbed amount at p/p_0 of 0.995. The micropore volume and micropore surface area were calculated using the t-plot method.

2.2.4 Thermogravimetric analysis

Thermogravimetric analysis (TGA) is a simple analytical technique used to determine the thermal stability and fraction of volatile components of materials. Solid samples are heated at a constant rate in an inert atmosphere, and the weight is recorded as a function of increasing temperature. Alternatively, the specimen may be held at a constant temperature, and the weight recorded as a function of time. The important components of TGA instruments are a high precision balance and an accurate, programmable oven. Some instruments also record the temperature difference between the sample and one or more reference pans, which is called differential thermal analysis (DTA), or the heat flow into the specimen pan compared to that of the reference pan, known as differential scanning calorimetry (DSC). Many TGA instruments are coupled with a mass spectrometer for further analysis of the volatile components.

TGA is a very convenient way to estimate the concentration of functional groups on the surface of mesoporous materials. The analysis requires some prior knowledge and/or assumptions about the kinds of functional groups on the surface and their decomposition. It is especially convenient for comparison of materials that have the same functional groups on the surface, but may differ in surface coverage. In our effort to optimize the functionalization of SBA-15 using aminopropyltriethoxysilane (APS), former Nitsche group researcher Aude Hubaud analyzed the APS-SBA-15 samples with a TG Instruments Q5000 TGA. The thermogravimetric measurements of several of the functionalized SBA-15 samples were later kindly provided by Dr. Ying-Jen Wanglee of the Katz group at UC Berkeley. The samples were held at 120° C to remove physisorbed water, and then ramped to 800° C at the rate of 10° per minute. The sample weight at 120° C was normalized, and the total mass percentage lost between 120° and 800° C was used to estimate the specific surface coverage of the functional silane. The major assumptions made were that the material contained only the desired silane, and that the entire silane disintegrated. Thus, the calculated densities of functional groups are only rough estimates. TGA measurements of FDU-type and C-CS-type OMCs were conducted by Dr. Jinxiu Wang on a Mettler Toledo TGA/SDTA851 analyzer from 25 to 900° C under N_2 with a ramp rate of 5 °C per minute. The concentrations of carboxyl and hydroxyl groups were estimated by attributing mass lost between 100° C and 280° C to the decomposition of carboxyl groups, and the mass lost between 280° C and 350° C to the decomposition of phenolic groups.[90] The mass lost from 350° C and 650° C can be assigned to the decomposition of lactone, quinine, and anhydride groups.

2.2.5 Solid-state nuclear magnetic resonance spectroscopy

Solid state nuclear magnetic resonance (NMR) spectroscopy is a very powerful tool for studying the structure and dynamics of a wide variety of materials. A great many sophisticated techniques have been developed to study exchange processes, molecular dynamics, spin diffusion, atomic orientations, torsion angles, anisotropy and internuclear distances.[91] In this work, NMR was simply used as an analytical tool to confirm that covalent grafting of silanes to ordered mesoporous silica occurred, and to provide evidence that the silane ligands remained intact during functionalization. Multiple large books have been written about solid state NMR, and one example used here was edited by Melinda Duer [92] and another good source was a review by Laws *et al.* [91]. A complete description of the theory of NMR is far beyond the scope of this thesis, so only a cursory introduction is presented.

All nuclei have a spin quantum number I, which is the sum of all the nucleons' intrinsic spin and orbital angular momenta. Nuclei with an even mass number (A) have whole-integer values for I, while odd-A nuclei have half-integer values for I. The spinning charge of the nucleus generates a magnetic field, and the magnetic moment describes the distribution of current in the nucleus. There are 2I+1 possible spin states, which are degenerate in the absence of an external magnetic field. When an external magnetic field B_0 is applied, it becomes slightly energetically favorable for the spin to be aligned with B_0, and the states split with an energy difference ΔE that is proportional to B_0 and the magnetic moment of the nucleus (called Zeeman splitting). Resonance occurs when electromagnetic radiation is applied in the plane perpendicular to B_0, with a frequency precisely tuned to the rotational frequency of the nuclear spin vector of the nuclei in the lower energy states (called the Larmor frequency). The nucleus absorbs energy and "flips" to the higher energy spin state in the direction opposing B_0. Deexcitation of the

nucleus releases quantized energy that is detected as the NMR signal. Different nuclei will give signals at different frequencies based on their structural environments. Usually a broad radiofrequency pulse is applied to excite all nuclei in the sample simultaneously, and a time-domain signal is produced as excited nuclei decay back to a stable Boltzmann distribution. The oscillating and continually decaying sine curve is called free-induction decay (FID), and is converted to the frequency domain by Fourier transform to produce familiar NMR spectra.

The energy difference ΔE is very small, so very strong magnets (1 to 20 T) are needed, with stronger magnets giving higher resonance frequencies and better signal-to-noise. Typical NMR instruments operate at 300 to 500 MHz. The lifetimes of the nuclear excited spin states are on the order of seconds to minutes, which is much longer than typical electronic excited states. This makes multi-pulse NMR experiments possible, but can also mean long recycle times between scans are often needed if stoichiometric information is desired. Some important properties of the NMR-active nucleus are relative abundance, spin, magnetic moment, and magnetogyric ratio γ, which is the ratio of the magnetic moment to the angular momentum. Table 2.1 summarizes these properties for the three nuclei that were subject to NMR in this work: ^{29}Si, ^{13}C, and ^{31}P, and ^{1}H as it is the most common nucleus studied by liquid NMR.

Table 2.1. Properties of some NMR active nuclei.

Nucleus	Natural Abundance (%)	Spin	Magnetic moment (μ)	Magnetogyric ratio (10^7 rad/TSec)
^{1}H	99.9844	1/2	2.7927	26.753
^{13}C	1.108	1/2	0.7022	6,728
^{29}Si	4.700	1/2	-0.5555	-5,319
^{31}P	100.0	1/2	1.1305	10,840

The frequency of the NMR signal caused by relaxation of an excited nucleus depends upon the electron density surrounding that nucleus. The electrons surrounding the nucleus are always in motion and generate a small local magnetic field opposing B_0. Thus the total field strength is reduced around the nucleus, which is "shielded" from the magnetic field. Increased electron density around a nucleus leads to greater shielding and displaces the signal peak to the right on the NMR spectrum (lower frequency), and removing electron density gives a higher frequency signal and shifts the peak to the left. The deshielding effect is caused by electromagnetic neighboring atoms, and thus the peak position contains information about the chemical environment of the nucleus. NMR spectra are plotted on an X-axis with a frequency scale called chemical shift (δ) in units of ppm (parts per million), with peak integrations that are proportional to the number of nuclei in the sample with that same chemical environment. Chemical shift, δ in Equation 2.7, depends on the selection of a reference material. For proton and ^{29}Si NMR, tetramethylsilane (TMS) is generally used, and adamantane is often used for ^{13}C NMR. Proton NMR spectra generally span about 10 ppm, while ^{13}C spectra cover about 200 ppm.

$$\delta\ (ppm) = \frac{Frequency\ difference\ of\ peak\ from\ reference\ (Hz)}{spectrometer\ frequency\ (MHz)} \qquad (2.7)$$

The other feature that is commonly used in liquid proton NMR for elucidation of organic structures is the so-called J coupling that arises from spin-spin interactions. A nucleus with a near neighbor of different chemical shift that is aligned with B_0 will experience greater total field strength and requires less external field to achieve resonance. If there are N equivalent neighbors,

the signal will be split into a multiplet of N+1 peaks, because each neighbor can be aligned with or against B_0. The coupling constant, J, is the distance between the individual peaks, and the integrations will follow Pascal's triangle. In rare-spin NMR like ^{13}C, the probability of two ^{13}C neighboring each other is low, and J coupling is not observed. However, protons split ^{13}C very strongly, with coupling constants between about 125 and 200 Hz with directly bonded protons, and fine splitting patterns for protons on neighboring carbons. Because this greatly complicates the ^{13}C spectrum, decoupling techniques have to be used. The simplest case is broad-band hydrogen decoupling, where a broad RF signal covering all the proton resonance frequencies is applied simultaneously with the lower frequency RF pulse required for ^{13}C resonance. This causes the protons to undergo rapid spin flips so that the local field contributions average out to zero. Fine splitting caused by J coupling normally cannot be discerned in solid-state NMR because the peaks are too broad.

The largest difference between liquid and solid state NMR is that the peaks in solid state NMR spectra are characteristically broad due to various interactions affecting nuclear spins, such as dipole-dipole coupling between magnetic nuclear dipoles, and anisotropic chemical shielding. In most liquid samples, these types of interactions are averaged away to zero due to rapid molecular motions. There are various sophisticated techniques in solid state NMR designed to extract information out of these interactions, but more often it is desirable to gain spectral resolution by removing their contributions. The common technique used in this work is called magic angle spinning (MAS), in which powder samples are spun rapidly on an axis that is 54.74° with respect to B_0. The spinning speed should be greater than the splitting width caused by the interactions that are being removed, and faster speeds usually reduce the broadening effect better. The specialized sample holder is called a rotor, and is usually made of zirconia, which does not affect the magnetic behavior of the sample. When preparing the sample it is important to pack the powder well into the rotor, and avoid contact of the rotor with metal tools.

Dipole-dipole coupling is an interaction through space (unlike spin-spin coupling, which occurs through chemical bonds) in which the magnetic dipole moments of nuclei can alter the Zeeman interaction of other nuclei within about 10 Å. Heteronuclear dipolar coupling can often be removed along with spin-spin coupling by broad band decoupling, but will also be averaged out by MAS. Consider a sample containing an abundant spin I and rare spin S. Both I and S have magnetic dipole moments, which produce small local magnetic fields, which will be felt by other spins within reasonable proximity. Depending on the orientation of the I spin, its local field will either add or subtract from the external field felt by the S spin, and changes its resonance frequency. Since surrounding I spins will have a variety of orientations, resonance for the S spin occurs over a range of frequencies and broadens the NMR signal. The degree to which the I spin effects the magnetic field of the S spin is characterized by the strength of heteronuclear dipole coupling, which is described by the Hamiltonian in equation 2.8.

$$H_{IS} = -d(3cos^2\theta - 1)I_zS_z \qquad (2.8)$$

In Equation 2.8, d is the dipolar coupling constant, proportional to the magnetogyric ratios of I and S, and inversely proportional to the cube of the internuclear distance. I_z and S_z are the z components of the nuclear spin angular momentum operators I and S, and θ describes the orientation of the internuclear vector with respect to B_0. By spinning the sample rapidly at the magic-angle of 54.74°, the constant tumbling and reorientation of crystallites averages all other

values of θ such that they cancel out, and the $(3\cos^2\theta-1)$ term goes to zero, therefore the heteronuclear dipole coupling is not observed. However, homonuclear dipole coupling also contains a term related to the energy-conserving exchange of spin angular momentum "flip-flop" interaction that occurs between coupled spins whose resonance frequencies overlap. The homonuclear dipolar coupling for low-γ nuclei such as ^{13}C can often be removed by MAS. On the other hand, the strength of homonuclear dipole coupling between two protons can approach 100 kHz, which along with their high abundance makes decoupling very difficult. Even with very high MAS speeds, solid state proton NMR spectra usually consist of a single peak that is too broad to be useful.

Chemical shift anisotropy (CSA) occurs because molecules rarely have a spherical distribution of electron density, and the degree to which the electron density affects the resonance frequencies of neighboring nuclei depends on the orientation of the electron cloud with respect to B_0. Larger chemical shifts (deshielded nuclei) occur when the narrowest part of the electron cloud is aligned with B_0, and the smallest shifts occur when the widest part of the electron cloud (the long axis of the ellipsoidal cloud) is in line with B_0. Since the broad CSA signal is the result of an interaction between the external field and the detected spins, there is no way to remove the interaction by RF pulses without affecting the free precession of the spins required to obtain a signal. However, the orientation-dependent term in the chemical shift Hamiltonian can be removed by MAS, as it also contains the expression $(3\cos^2\theta-1)$. In this case θ represents the angle between B_0 and the long axis of an ellipsoid describing the electron cloud. By rapidly spinning the powder sample, the average CSA is made to look like an ellipsoid whose long axis is aligned with the spinning axis.

Another NMR technique that deserves description is cross polarization (CP), as it was used for the ^{13}C spectra in this work. CP is a technique used to enhance signals from rare nuclei by transferring polarization from abundant nuclei (usually protons). CP occurs when dipolar contact between two nuclei is established, because magnetization tends to flow from the more highly polarized nucleus to the nucleus with lower polarization. The Hartmann-Hahn method involves simultaneous application of two RF fields, one at the resonance frequency of the abundant I spin, and the other at the resonance frequency of the rare S spin. This causes both I and S spins to rotate independently at rates determined by the amplitude of the applied fields. When the nutation (nodding or rocking motion in the axis of rotation) frequencies of I and S are equal, energy conserving dipolar contact allows polarization to be transferred. Then the S spins are detected while the I spins are decoupled. Multiple CP sequences can further enhance sensitivity. Another benefit to CP techniques is that the sampling time depends on the relaxation time of I nuclei, which is faster than that of S nuclei, so more scans can be acquired. However, there are many parameters involved with CP experiments, and the result is that the peak integrations are no longer stoichiometric.

^{13}C CP-MAS-NMR, ^{31}P MAS-NMR, and ^{29}Si MAS-NMR spectra were collected on the functionalized SBA-15 materials by Chris Canlas at the UC Berkeley College of Chemistry NMR facility using a 500 MHz Bruker AV-500 spectrometer. Most of the spectra were collected with an MAS spinning speed of 10 kHz-13 kHz. The ^{13}C spectra took approximately two hours to collect, and were used to confirm the structure of silane ligands after grafting to the SBA-15 surface. All spectra were plotted and analyzed using the MNova NMR program. In solid-state ^{13}C NMR, one peak is expected for every carbon in the molecule. The peak integrations are not

meaningful because of the CP process. The fact that many of the peaks have shoulders is not surprising, because in practice MAS does not completely eliminate the broadening interactions, and also because there are probably some slight structural variations. It is unlikely that the silanes form a perfect monolayer on the surface, and a carbon that is in very close proximity to neighboring ligands in an oligomer chain would be slightly more shielded than an equivalent carbon on an isolated silane. The peak assignments were made as the author's best guess, based on the electronegativity of neighboring atoms in the structure, and on previous literature, as cited within the discussion. Although there is some uncertainty in the peak assignments, in most cases the ^{13}C NMR spectra assisted with determining whether or not the ligand structure withstood the grafting process. Either a reasonable spectrum was obtained for the expected structure, or the spectrum did not have the expected number of peaks and/or peak positions, indicative that a problem occurred in the synthesis. For an example of a reasonable NMR spectrum, Figure 2.11 shows the ^{13}C CP-MAS-NMR spectrum of SBA-15 that was believed to be successfully functionalized with triethoxysilylpropylmaleamic acid (TESPMA), along with the structure and tentative peak assignments. This spectrum is shown here as an example, but further explanation of the synthesis, characterization, and batch experiments involving TESPMA-SBA-15 can be found in Chapter 5.

^{31}P MAS-NMR was used with Ac-Phos-SBA-15 before and after contact with acid in an attempt to quantify the amount of ligand lost to acid hydrolysis (because TGA was not available at the time), as described in section 5.3.5.

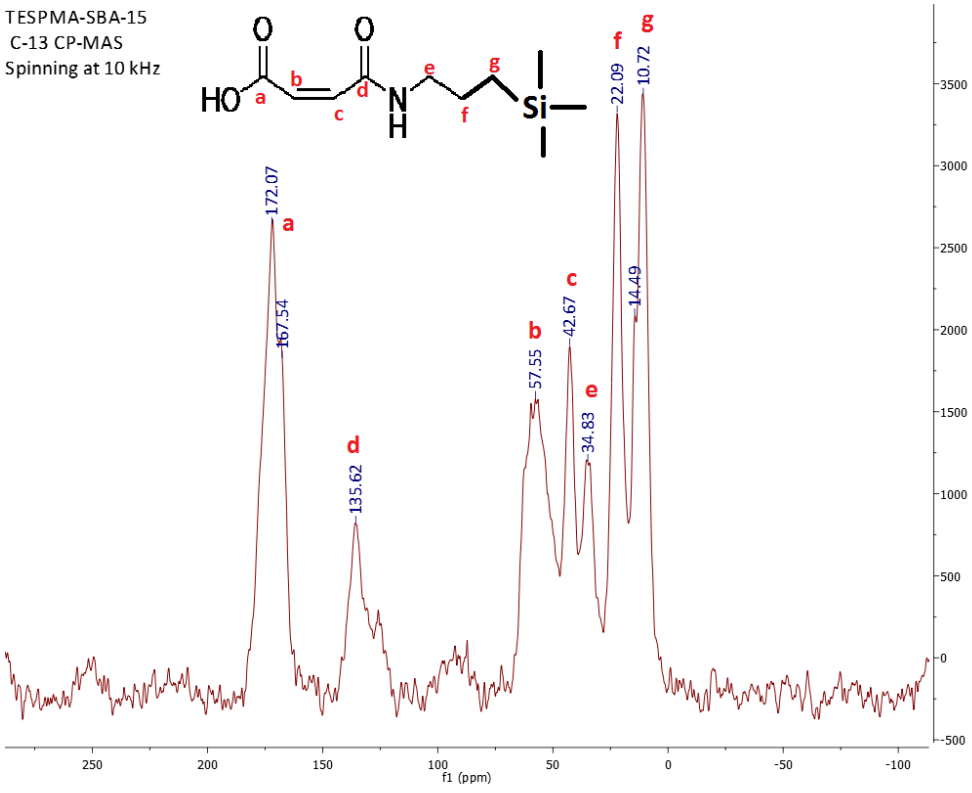

Figure 2.11. ^{13}C CP-MAS-NMR spectrum of TESPMA-SBA-15.

Cross polarization was not used for ^{29}Si NMR on silica because while the peak integrations in the spectra can theoretically quantify the relative amounts of silane grafted to the silica surface, CP spectra are not quantitative due to different relaxation behavior. Because of this, the spectra were collected overnight, and would need even longer collection times for improved resolution. If long recycle times are used to allow complete relaxation of nuclei between scans, then high resolution ^{29}Si NMR spectra can be used to quantify cross-linked, terminal, and solitary silanes grafted to a silica surface.[79] The silicon nuclei within the solid silica framework are the most shielded, and will always be seen to the right of the silane peak in a ^{29}Si NMR spectrum. Figure 2.12 shows which silicon atoms in a functionalized silica layer correspond to peaks on the spectrum, although better resolution would be needed to quantify these groups. In a high resolution spectrum, another peak to the left of the T2 peak would be observed if solitary silanes were also grafted to the sample. The obtainable resolution for this work was limited by the time available for acquisition, and was not sufficient to resolve cross-linked, terminal, and solitary silanes. The spectra could confirm that covalent ligand grafting occurred, because the bulk silane peak was in the chemical shift range expected for a grafted silane. By integrating the silica and silane peaks, the concentration of surface groups can be estimated. Figure 2.13 shows an example ^{29}Si spectrum of the TESPMA-SBA-15 sample whose ^{13}C spectrum is shown in Figure 2.11. According to the peak integrations, the sample contains 0.54 moles silane for every 1 mole SiO_2, which converts to approximately 9 mmol silane grafted per gram SBA-15. From TGA of the same sample, it was calculated that 4.13 mmol grafted per gram SBA-15. The TGA method may underestimate the surface coverage if only a portion of the silane grafted, because the mass lost would correlate to more moles of silane than that calculated using the entire molecular weight of the silane ligand. However, the ^{29}Si NMR method seemed to consistently overestimate the silane density of the functionalized SBA-15. Indeed, some of the samples showed larger silane peaks than silica peaks in their NMR spectra, as shown by the spectrum in Figure 2.12. This overestimation may be an artifact of the relaxation behavior of the Si nuclei in the samples. Excited nuclear spins within a solid lattice often take longer to return to the ground state than those in a more conformationally free setting. If the RF pulse is applied before the spin has returned to the lower-energy state, then resonance will not occur, and thus no NMR signal would be recorded for that pulse. The resulting spectrum has a systematically underestimated Q4 peak. Chris generally used a 60 second recycle time for ^{29}Si NMR collection, which is relatively long, but perhaps still not long enough for complete relaxation of the Si nuclei within the SBA-15 framework.

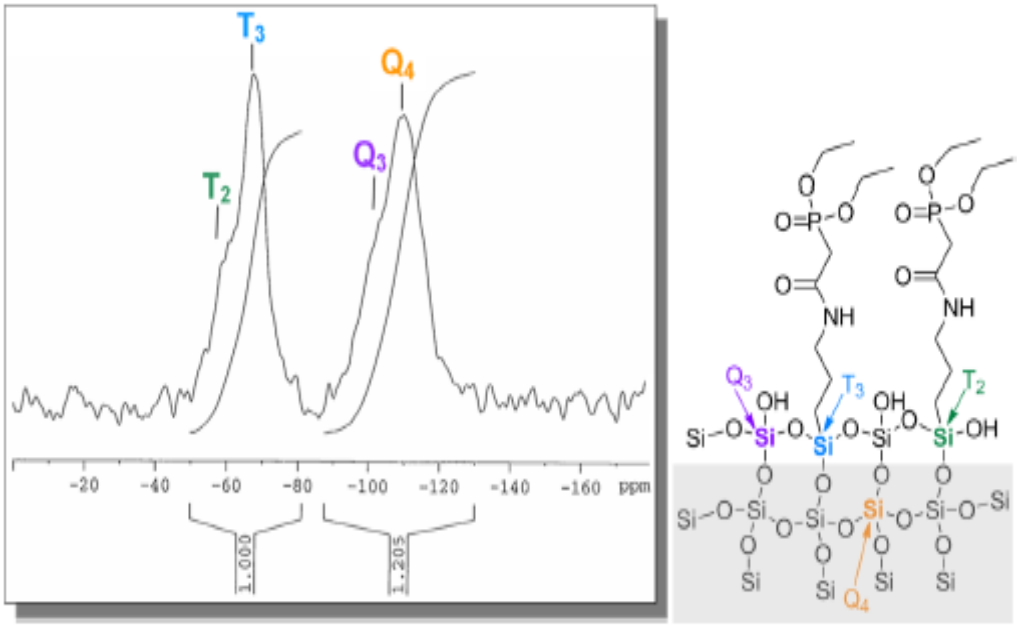

Figure 2.12. Schematic of solid state ^{29}Si NMR spectral peaks (left) and the species they represent (right). Although Si species are outlined, a better spectral resolution would be needed to resolve the peaks. The image was created by Aude Hubaud.

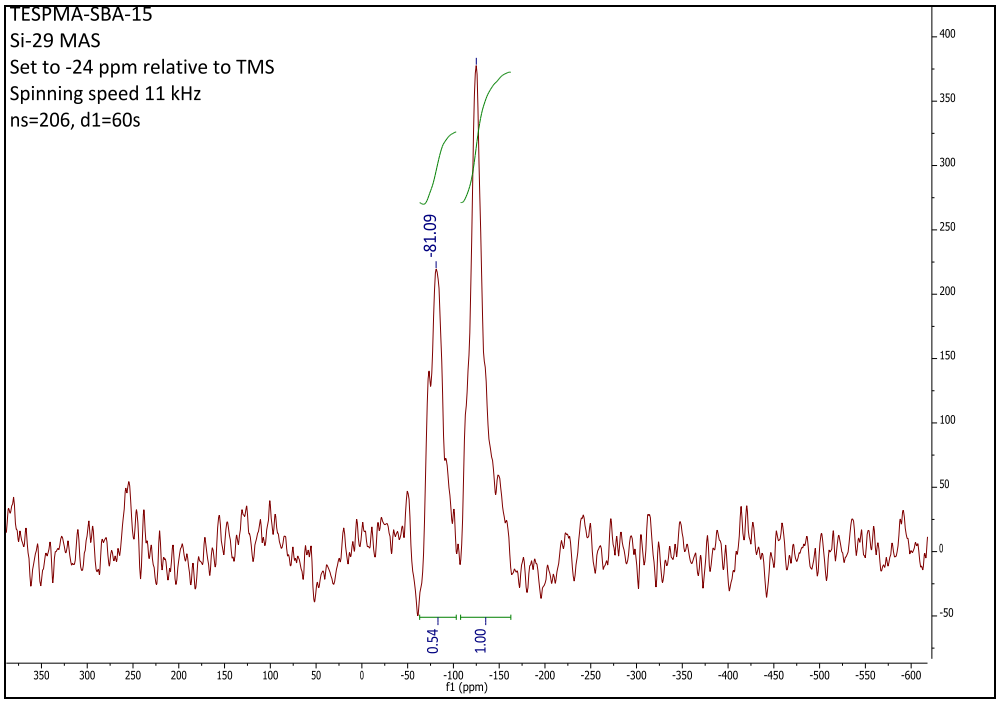

Figure 2.13. ^{29}Si MAS-NMR spectrum of TESPMA-SBA-15 sample.

2.2.6 Infrared spectroscopy

Infrared spectroscopy is an analytical technique used to identify the functional groups present in samples by measuring the ability of molecules to absorb infrared radiation. Atoms in

molecules are not static, but vibrate about their equilibrium positions at a frequency that depends on the mass of the atom and the length and strength of the bonds. Molecular bonds absorb radiation of the same frequency as their natural vibrational frequency, causing excitation of electrons into higher vibrational energy levels. Different functional groups have characteristic absorbance frequencies that can be used to identify their presence in samples, but complete determination of the structure cannot be accomplished using IR alone. As in UV-visible spectroscopy, IR spectroscopy can be quantitative with careful control of parameters using Beer's law, given in Equation 2.9, where A is the absorbance, T is transmittance, c is the concentration of the analyte, b is the path length that light travels through the sample, and ε is the molar extinction coefficient of the analyte, which is often determined empirically.

$$A = \epsilon bc = -logT \tag{2.9}$$

The main component of all IR instruments is an interferometer, which is diagrammed in Figure 2.14.[93] The collimating mirror collects light from the infrared source (usually an air-cooled nichrome wire) and makes the light rays parallel. The rays then travel to the beamsplitter, which is a thin film of Ge sandwiched between two infrared transparent windows, designed to transmit some of the incident light and reflect some of it. The transmitted light goes to a mirror that is stationary, and the reflected light is directed to a mirror that moves left to right. The rays reflected from the two mirrors travel back to the beamsplitter where they interfere with each other, combining their amplitudes to form a single wave that travels through and interacts with the sample before reaching the detector. As the moving mirror is gradually moved away from the beamsplitter, the two beams grow in and out of phase, resulting in cosinusoidal variations in the detected light intensity. One "scan" corresponds to the instrument moving the mirror back and forth once. An interferogram is created by the instrument's software, which plots the intensity of light detected (a voltage signal) against the optical path difference (2 times the mirror displacement). A Fourier transform of the interferogram yields a spectrum, where intensity is plotted against the frequency of light, hence the term Fourier transform infrared spectroscopy (FTIR) is used. Because each frequency of light in the beam has a corresponding Fourier frequency in the interferogram, the different frequencies of light need not be separated by space or time in order to be discerned. The amplitude of the corresponding Fourier frequency in the interferogram is proportional to the intensity of light of a given frequency (or wavenumber) hitting the detector. Light that is absorbed by the sample will not be detected, and the amplitude of the corresponding Fourier frequency is diminished. The user chooses the number of scans, and the resulting interferograms are averaged to one that is sent to the computer for Fourier transform. FTIR spectra are usually plotted as percent transmission versus wavenumber (1/cm). The signal-to-noise ratio in the spectrum is proportional to the square-root of the number of averaged scans. Since each scan takes about four seconds, suitable FTIR spectra of most samples can be acquired within a few minutes.

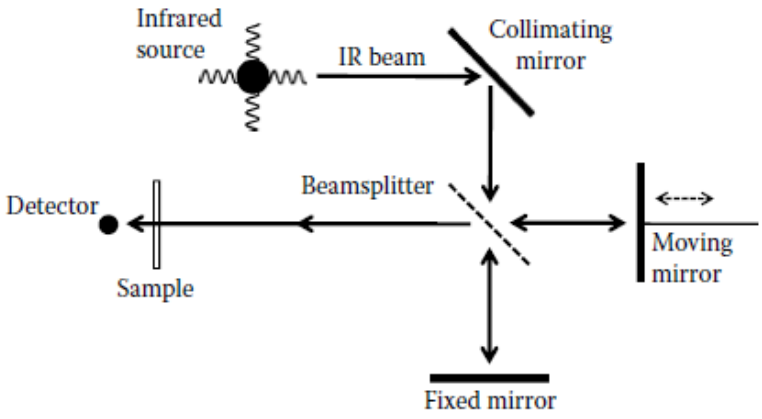

Figure 2.14. Diagram of a Michelson interferometer.[93]

The user can choose the spectral resolution, since it is limited by and inversely proportional to the optical path difference. Higher resolution spectra contain more information, but lower resolution spectra have better signal-to-noise ratios. Because the absorbances of most functional groups are at least 10 wavenumbers apart, resolution of 4 to 8 cm^{-1} is often used. The quality of FTIR spectra can also depend on the sample, and how it is introduced to the instrument. Samples that are too thin, too dilute, or scatter infrared light may have poor signal-to-noise ratio even with a large number of scans. Water and carbon dioxide have strong absorbances in the IR region, so background scans must be subtracted. Some instruments have inert gas sample chambers and built in desiccants. Gas samples can be measured in a special cell that is normally around 10 cm long. Liquids can be introduced in a number of ways, the most common is as a thin film between two potassium bromide discs. Solids are ground up in nujol (a long chain hydrocarbon) or are made into a KBr disc with pressure. Alternatively, attenuated total reflection infrared (ATR-FTIR) spectroscopy is very convenient for analysis of any non-gas material.

In ATR-FTIR, the sample is placed on top of a crystal with a high refractive index (commonly used materials are diamond, ZnSe, Si, and Ge). When the IR beam goes through the crystal and meets the interface of the crystal and the lower refractive index sample, total internal reflection occurs if the angle of incidence is above a critical angle θ_c, which depends on the refractive indices of the sample (n_s) and the crystal (n_c) according to Equation 2.10.

$$\theta_c = sin^{-1}(n_s/n_c) \quad (2.10)$$

Figure 2.15 shows an illustration of this phenomenon.[93]

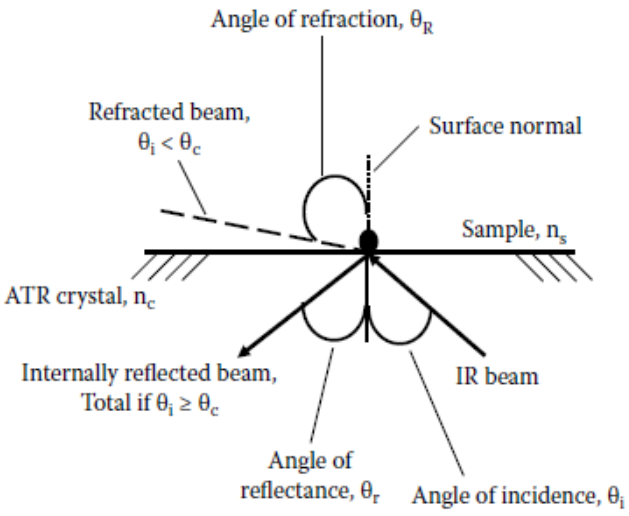

Figure 2.15. Illustration of the optical processes that occur when an infrared beam in a crystal with high refractive index meets a sample with lower refractive index. Total internal reflection occurs when the angle of incidence θ_i is greater than the critical angle θ_c. [93]

Under certain conditions the infrared amplitude at the point of reflectance is enhanced by constructive interference of the incident and reflected beams. This creates a so-called evanescent wave or "hot spot" of infrared light that sticks up above the crystal by less than a micron to about 10 microns, depending on the experiment. When the sample is in close contact with the hot spot, it can absorb some of the beam, thus attenuating some of the totally reflected beam before it reaches the detector. The background spectrum is taken with the crystal exposed only to air. Depending on the type of ATR element used, the beam may be reflected once or multiple times. Because of the limited path length of IR light within the sample, ATR-FTIR is much less sensitive than transmission FTIR, but also does not suffer so much from sample opacity. This makes it ideal for analysis of the surfaces of samples like carbon that significantly scatter IR light. As ATR-FTIR is inherently a surface technique, it cannot be used for analysis of bulk samples. Using ATR-FTIR quantitatively can be tricky since the path length b in Equation 2.9 is often unknown. An important parameter of an ATR experiment is the depth of penetration (DP) of the infrared beam into the sample, which is defined as the depth at which the evanescent wave intensity decreases to 36.8%. The DP depends on the wavenumber (W) of the IR light, the refractive index of the ATR crystal (n_c), the angle of incidence (θ), and the ratio $n_{sc} = n_{sample}/n_{crystal}$ according to Equation 2.11.

$$DP = 1/\left[2\pi W n_c (sin^2\theta - n_{sc}^2)^{1/2}\right] \quad (2.11)$$

Typical DPs using a diamond crystal with an organic sample are on the order of 1-2 microns. Depth profiling experiments can sometimes be performed using several crystals with different indices of refraction. A very important consequence of the relationship described in Equation 2.11 is that as the wavenumber increases, the DP decreases, resulting in lower intensity peaks on the left side of the spectrum. Thus ATR-FTIR spectra are qualitatively different from transmission FTIR spectra, and can only be compared with other ATR-FTIR spectra and spectral libraries. Note also that the DP dependence on n_{sc} means that the DP will vary from sample to sample, so only spectra of materials with similar refractive indices are comparable. Another

potential disadvantage of ATR is that the spectral range can be limited by the crystal. For example, diamond absorbs strongly between 2000 and 2200 cm^{-1}, making sample peaks in this region difficult to see. ATR-FTIR is versatile for many different liquid, semi-solid and solid samples, but powders may have to be ground into fine particles for good optical contact. The ATR accessory includes a clamp that presses down on the powder sample. Compared to the grinding, mulling and pressing that is often necessary to prepare transmission FTIR samples, ATR-FTIR is less tedious. However, it is important that the ATR element remains clean and free of cracks or scratches.

The absorbance peaks in FTIR spectra, often called "bands", correspond to excitation of electrons to higher energy vibrational states upon stretching or bending of chemical bonds within the molecule. Stretching usually requires higher energy light than bending, and the stretching modes are most commonly used for structure determination. In general, higher bond order corresponds to higher frequency absorption, and more polar bonds give more intense peaks. Common organic functional groups show characteristic absorbances and the stretching modes may be categorized into four distinct regions:

a) bonds to H (C-H, N-H, O-H), 4000-2200 cm^{-1}
b) triple bonds (C≡C, C≡N), 2200-2000 cm^{-1}
c) double bonds (C=C, C=N, C=O), 1800-1550 cm^{-1}
d) other single bonds, 1550-650 cm^{-1}

FTIR can help with structural determination by identifying the functional groups within a sample. Variations in the local environment of the functional groups can lead to slight changes in the frequencies absorbed, and FTIR is often most useful for comparison with known samples. Sometimes the characteristic peaks are redshifted or blueshifted when the functional group coordinates a metal, and this can provide some insight into which groups are involved with coordination.

FTIR was used only qualitatively in this project. ATR-FTIR spectra were measured for all functionalized silica and carbon samples, by the author and/or Stephen Jones, using a Nicolet Avatar 360 FTIR spectrometer with a diamond ATR accessory. When possible, the IR spectrum of functionalized silica was compared with that of the liquid silane solution used for functionalization, in order to verify that the functional groups remained intact. An example is shown in Figure 2.16 where the ATR-FTIR spectrum of TESPMA-SBA-15 is overlaid with that of the 90% TESPMA solution in ethanol. The ATR-FTIR spectra of carbon powders were collected to show evidence of the surface groups before and after chemical oxidation. Those spectra were collected with 2-3 hours of scans to improve signal-to-noise, and baseline-corrected due to the large amount of scattering that occurs by carbon samples. Transmission FTIR spectra were collected by Jinxiu Wang on a Nicolet Fourier spectrophotometer from 4000 to 400 cm^{-1} using KBr pellets of the Fudan carbon samples. Figure 2.17 shows the unprocessed transmission FTIR with the unprocessed ATR-FTIR spectra of the Fudan carbon samples, for comparison. Note that the limited sensitivity of ATR-FTIR only allowed detection of distinct peaks in the C-CS-COOH sample, because it has a high concentration of carboxyl and phenol groups at the surface. In the ATR-FTIR spectrum, the –OH stretch from the phenol groups is not seen because of the low DP at higher wavenumbers according to Equation 2.11. Overall the transmission FTIR is more informative. Some efforts were made by the author and Stephen Jones to analyze KBr

pellets made of C-CS and C-CS-COOH that had Pu bound to it, to observe any changes in peak positions. Overall the spectra were too noisy for any interpretations to be made.

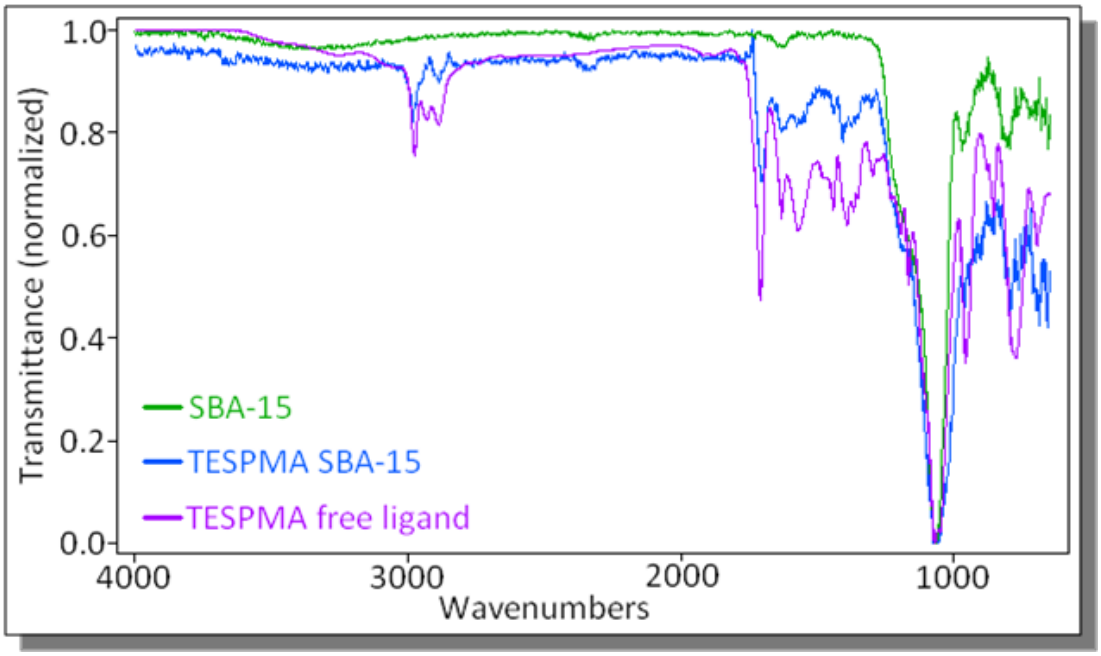

Figure 2.16. Normalized ATR-FTIR spectra of SBA-15 (green), 90% TESPMA in ethanol (purple), and TESPMA-SBA-15 (blue).

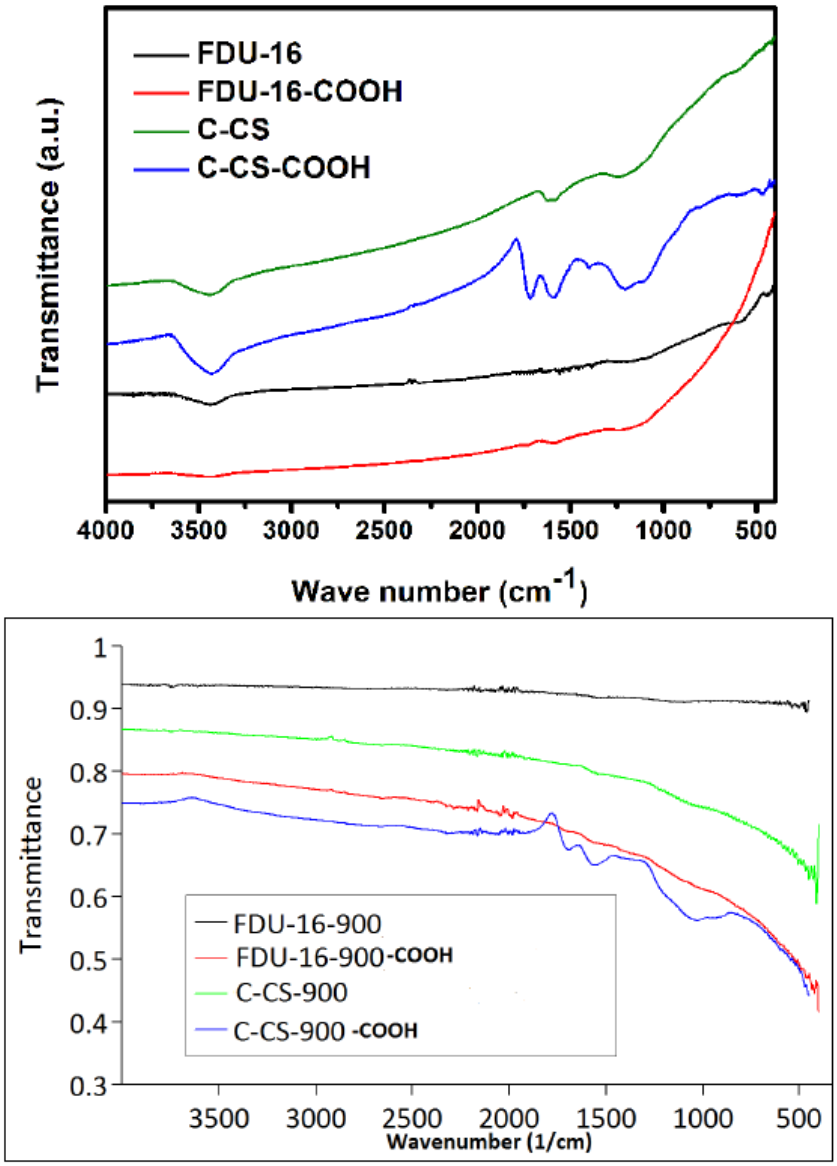

Figure 2.17. Transmission FTIR spectra (top) and ATR-FTIR spectra (bottom) of the same mesoporous carbon samples: FDU-16 (black), FDU-16-COOH (red), C-CS (green), and C-CS-COOH (blue).

2.2.7 Determination of point-of-zero charge

In this work, adsorption of plutonium and lanthanide species to ordered mesoporous materials is investigated by the batch method. Adsorption is any chemical reaction that occurs at a phase boundary, and adsorption of aqueous species at a solid-liquid interface is known as surface complexation. Surface complexation may be categorized as inner-sphere (specific adsorption), where the adsorbate is bound directly to the surface, or outer-sphere (non-specific adsorption), where there are one or more solvent molecules between the surface and the adsorbed species. In both cases, much of the adsorption interaction can be electrostatic, and thus is heavily influenced by the distribution of charges at the solid surface. The point-of-zero charge (PZC) of a solid material generally describes the solution pH at which the total positive surface charge

equals the total negative surface charge, and thus the net surface charge is neutral. The PZC has a large impact on surface complexation of ions from aqueous solutions, especially for minerals and simple metal oxides. Small changes in solution pH can sometimes change the electrostatic interactions between the ionizable surface sites and solution ions dramatically. There are several different types of PZCs defined depending upon how they are measured. One approximation of the PZC is the measurement of the isoelectric point (IEP), which can be determined with an electrophoresis measurement of the pH where the solid particles do not move in an electric field, or by measurement of the pH of aqueous solution in which the particles do not coagulate. If the PZC is determined by measuring the pH where equal moles of H^+ and OH^- are adsorbed on the solid surface, it is called the point of zero net proton charge (PZNPC). The PZNPC can be determined using potentiometric titration, mass titration, and powder addition methods. The PZNPC and IEP coincide only if no adsorption of other ions besides H^+ and OH^- occurs.[61, 83, 94]

The potentiometric titration method involves titrating a suspension of the solid, which acts as a weak diprotic acid or base, with a strong acid or base in the presence of a background electrolyte. Blank and suspension titrations are performed in a minimum of three different concentrations of the background electrolyte. After the blank curves are subtracted from the sample titration curves, the pH at the common intersection point among all curves from the different ionic strength suspensions is considered the PZC. This pH is called the point of zero salt effect (PZSE), and actually only coincides with the PZC for pure mineral phases where no inner-sphere adsorption occurs. The mass titration technique may be used to estimate the PZC of pure, simple oxides. The dry oxide is assumed to be uncharged before it is placed into pure water, and the pH of the final suspension depends on the oxide concentration. The pH of suspension reaches a constant value after the addition of an excess of solid, which is taken as the PZC. Of course this technique requires that the solid be insoluble, and that the constant pH can be reached before the suspension becomes too saturated to properly measure the pH. The powder addition technique is performed by adding identical amounts of solid powder to a set of solutions of the same ionic strength but different pH values. The presence of the powder changes the pH of each solution according to the adsorption and desorption of protons. If the initial pH (pH_i) is lower than the PZC of the solid, the surface adsorbs protons and the final pH (pH_f) will be higher. The reverse is true if the initial pH is higher than the PZC. The final pH values are usually measured about 24 hours after addition of the solid. The final pH minus the initial pH ($pH_f - pH_i = \Delta pH$) is plotted against pH_i and, provided the plot is linear, the PZC is taken as the x-intercept, where $\Delta pH = 0$. The range of pH values that will give valid, linear data with the powder addition method depends on the PZC, surface area, and amount of solid used, but often lies between 4 and 10. This method is similar to potentiometric titration at a single ionic strength. It is faster and simpler than potentiometric titration, and often yields similar results. These methods may not work accurately for solids with low surface areas or small micropores that hinder the diffusion of ions. In all three methods, the aqueous solutions must be kept free of carbon dioxide CO_2, which acidifies the solutions when it dissolves to make carbonic acid H_2CO_3. The carbonate-free solutions are prepared by bubbling argon through doubly distilled Milli-Q water, while boiling for about a half hour. After that the solutions must be stored under argon and experiments carefully executed under argon. This requirement is difficult when weighing the solid powders and measuring pH of solutions, and thus introduces some experimental error.[61, 83, 94]

The PZC of functionalized silica is a cumulative effect of the silica surface and the pK_a of the functional ligand, where applicable. The PZCs of the functionalized SBA-15 materials were not measured, because they are not homogenous surfaces, and some of the ligands do not follow simple surface complexation models. Marjorie Guillermo, a former undergraduate assistant to the Nitsche group, attempted unsuccessfully to measure the PZC of the unfunctionalized SBA-15 substrate. Besides the ongoing problem of carbonate contamination, she was not able to obtain a common intersection point among the curves from different ionic strength solutions. Other researchers have reported a PZC of 5.2 ± 0.2 for SBA-15 by the powder addition method.[95] This is consistent with our findings that the sorption of lanthanides to unfunctionalized SBA-15 becomes significant only in solutions with a pH greater than 5.

A modified powder addition method was used to estimate the PZCs of the carbon materials studied in this work. Carbon materials exhibit a variety of surface functional groups including carboxyl, carboxylic anhydrides, carbonyl groups, lactones, lactols, phenols, quinines, ethers, and γ-pyrone-like structures.[96, 97] Therefore, the PZC does not have as stark an importance for the ion-exchange properties of carbon materials as it does for those of simple oxide minerals. Particularly with such high-surface-area carbons, there can still be sufficient negatively charged sites to bind cations from solutions with a pH below the PZC. Nevertheless, carbon materials do demonstrate an overall bulk amphoteric behavior in aqueous suspension, and the surface ionization model that is used to describe simple oxides is often applied to carbons.[98] The PZC of carbon materials can be determined by mass titration,[98-101] but this method was not used because only limited amounts of the mesoporous carbons were available. Potentiometric titration has also been used to determine the PZC of activated carbons, but often the three curves at different ionic strengths intersect at three points instead of a single point.[98] Another problem with direct potentiometric titration is that equilibration tends to be very slow, which could be caused by slow diffusion into narrow pores, and by slow hydrolytic ring opening of carboxylic anhydrides and lactones.[102] Boehm titration is a method sometimes used to estimate the concentrations of acidic surface groups on carbon materials,[96-98, 101, 102] and involves treating the sample with excess base, then the supernatant is back-titrated with HCl. Different bases are used as approximate probes of the various acidic surface groups as follows: $NaHCO_3$ (carboxyl), Na_2CO_3 (carboxyl and f-lactonic), and NaOH (carboxyl, f-lactonic, and phenolic). Another common technique that has been applied to describe the PZC of carbon materials is the measurement of the "equilibrium pH at high oxide loading" (EpHL).[103-105] In this method solutions with pH 1-12 are prepared, the solid is added to incipient wetness, and the equilibrium pH after 12 hours is measured with a spear-tip semisolid electrode. In a plot of final pH vs. initial pH, a plateau is observed at the EpHL, taken to be the PZC. This is described as an extension of the mass titration method, that can be used even when the PZC lies in the extreme. Essentially, the EpHL method is the same as the powder addition method, only with much higher loading of solid, which extends the linear portion when the change in pH is plotted against initial pH. None of the above techniques were suitable because they require that large amounts of solid material be used for the characterization.

The relative points of zero charge of the seven carbon powders were measured using a modified powder addition method,[54, 94, 106] which was chosen for convenience and to minimize the amount of carbon powder used. Sets of carbonate-free 0.1 M $NaClO_4$ solutions were adjusted to pH 3-10 with NaOH and $HClO_4$ in polypropylene tubes under argon. The initial pH (pH_i) values were measured with a pH electrode (Thermo Scientific Orion 8103BNUWP) before the

carbon powders were added (1.4 g/L for AC, CMK, and OX-CMK; 1 g/L for FDU-16, FDU-16-COOH, C-CS, and C-CS-COOH) and the tubes backfilled with argon. The samples were placed on a rocker and the pH (pH_f) was measured after 22 hours. Plots of ΔpH (pH_f - pH_i) vs. pH_i were linear within the initial pH range 4 to 10, and the x-intercept was taken as the PZC. The experiment was duplicated and average PZC values reported. The solid-to-liquid ratio was lower than that used in many of the previous powder addition experiments with minerals,[61, 83, 94] due to the limited availability of the mesoporous carbon powders. This effect may be partially offset by the larger specific surface area of the carbon materials. However, powder addition experiments with activated carbon powder were performed with 1 g/L and 4 g/L ratios, and the PZCs obtained differed by about one pH unit. The PZC values in all of the carbon samples also changed over time, generally to lower values after one week compared with the values derived when pH_f was measured after one day. It could be that carbonate contamination is inevitable in aqueous samples containing solid carbon, and the PZC measurement experiments for carbons referenced above generally were not done in CO_2-free solutions or under inert gases. Also, pH measurements are generally made within 24 hours and are not monitored over extended time periods. Even though the PZC values obtained in this work may not represent the true PZCs as fundamental thermodynamic quantities, the values reflect the differences in surface acidity between the carbon samples. No matter which method of PZC determination is employed, there is consistent evidence throughout the literature that the more oxidized a carbon surface, the more acidic it is, and the lower the PZC.[96, 98, 99, 101, 103, 105, 107]

Stephen Jones measured the PZC of C-CS type ordered mesoporous carbon using the potentiometric titration method, to see how the powder addition and potentiometric titration methods compare for porous carbon materials. He averaged the pH at each point of five titrations of each type (5 titrations of 0.1M $NaClO_4$ blank, 5 titrations of 0.1M $NaClO_4$ with 1 g/L C-CS, 5 of 0.01M $NaClO_4$ blank, etc.). All of the volumes were the same because steps of 0.1 μL were used in each titration. The volumes were interpolated as a function of pH for each averaged curve, using the program Origin. The blank curves were then subtracted from the C-CS titration curves, and plotted as surface charge σ_0 times surface area *S*, calculated with Equation 2.12 vs. pH (Figure 2.18). In Equation 2.12, Δ*n* is the difference in the number of moles of base added to the solid and the number of moles added to the blank, *F* is Faraday's constant, and *m* is the mass of the mineral added, which was an average for each set of titrations.

$$\sigma_0 S = \frac{F\Delta n}{m} \qquad (2.12)$$

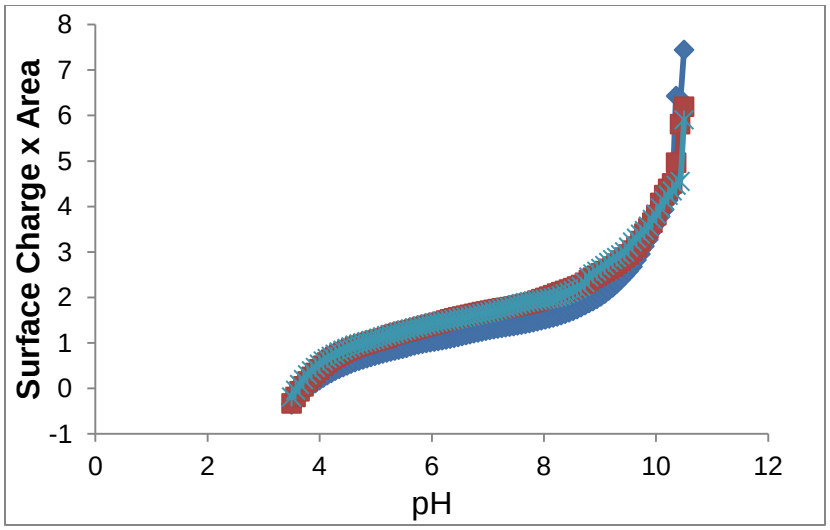

Figure 2.18. σ_0 × Area vs. pH for titrations of C-CS in 3 $NaClO_4$ solutions of different ionic strengths.

Using quadratic fits of the data plotted in figure 2.18, the PZC of C-CS was calculated to be 3.7 ± 0.2, where the error bar represents 95% confidence. This result is comparable to the value obtained using the powder addition method described above, which was 3.9 ± 0.1. Figure 2.19 shows the powder addition plots from samples of C-CS as an example. The PZC was lower than expected, so the C-CS powder underwent dialysis to ensure that all traces of HF and silica left from the synthesis were removed, and the PZC was much higher after dialysis. However, the initial agreement between the values obtained using the two methods showed that the PZC of mesoporous carbons can be estimated using potentiometric titration or powder addition methods. Ultimately it was decided that potentiometric titration was too consuming of time and material, so powder addition was adopted as standard.

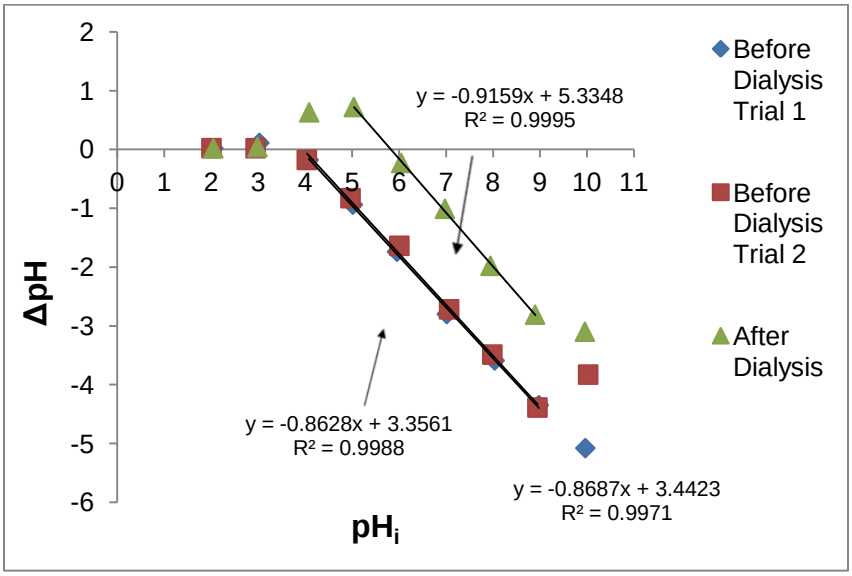

Figure 2.19. Change in pH vs. initial pH in powder addition experiments using 1 g C-CS mesoporous carbon per L 0.1 M $NaClO_4$, before and after dialysis of the carbon.

3 The Chemistry of Plutonium

The primary focus of this dissertation is the investigation of the interactions between solid mesoporous materials and aqueous plutonium species. Plutonium, element 94, is a fascinating element that has had a tremendous impact on human political history. Soon after its discovery and isolation at UC Berkeley by Seaborg, Kennedy and Wahl, plutonium was implemented in nuclear weapons that became a deciding factor in World War II. The fissile nature of ^{239}Pu can also be used peacefully as a fuel source in nuclear power reactors, and the high decay heat of ^{238}Pu make it useful as a primary fuel source for robotic space missions. Plutonium is of great environmental concern because it is a component of spent nuclear fuel, and thus could be a major contaminant in the event of a storage tank leak or natural disaster. The long half-life of 24,100 years, along with its toxicity and abundance in nuclear weapons stockpiles, render ^{239}Pu of particular interest. Some ^{239}Pu has already been released into the environment via nuclear weapons production and testing, nuclear reactor accidents, and accidents during the transport of nuclear weapons.[108, 109] For example, at The United States Department of Energy (US DOE) Hanford Operations Site, the first industrial-scale plutonium production site, approximately 220,000 m^3 of liquid reprocessing waste totaling 320 MCi are stored in steel tanks, and up to 3800 m^3 were released into the environment.[109] At the US DOE Oak Ridge Operations site, 160,000 m^3 of liquid waste containing fission products and transuranium elements were directly discharged into the ground. In the whole U.S. weapons complex there are 5700 contaminated underground plumes. The 1986 reactor explosion in Chernobyl released 23 kg of Pu isotopes totaling 0.18 MCi into the surrounding area. Other examples of major Pu releases occurred at the MAYAK Pu production complex in the former Soviet Union, and the Sellafield nuclear fuel reprocessing plant in Great Britain.[109]

Plutonium lies in the actinide series between the so-called light actinides (Th-Pu), which behave chemically more like transition metals, and the heavy actinides (Am-Lr), which have simpler chemistry similar to the lanthanide elements. Plutonium is one of the most chemically complex elements in the Periodic Table, which makes it very interesting to study but also difficult to control in laboratory experiments. Plutonium is an incredibly reactive element with a ground state electron configuration of $[Rn]5f^6 7s^2$. In solid form, the pure element exhibits at least seven different crystal phases and forms alloys and compounds with a variety of other elements.[53] In aqueous solutions, there are five different oxidation states of plutonium available, which leads to a rich myriad of coordination chemistry. One of the unique and intriguing things about plutonium is that the redox potentials of the different oxidation states are relatively close together, thus up to four different oxidation states can coexist in solution. The different oxidation states all have different hydrolytic and complexation behavior, and also disproportionate and react with one another to create a dynamic steady-state mixture. The chemistry of plutonium is even further complicated by the fact that it is invariably a radioactive element, and the alpha decay energy induces other chemical reactions. All of these factors lead to Pu being highly reactive and sensitive to the local environment.

3.1 Pu-239 production and decay

The isotope of plutonium used in this work was ^{239}Pu, which is the most abundant isotope of plutonium, as about 1000 metric tons have been manufactured since World War II.[61] This isotope is convenient to work with, because the half life is long enough that decay corrections are

not necessary on the experimental time scale, but short enough to render it traceable over a wide range of concentrations (≥10^{-9}M). The isotope ^{239}Pu is a byproduct in nuclear reactors that use uranium fuel, as it is produced by the neutron capture of ^{238}U, and subsequent decay according to reactions 3-1 through 3-3.

$$^{238}_{92}U + {}^{1}_{0}n \rightarrow {}^{239}_{92}U \quad (3.1)$$

$$^{239}_{92}U \rightarrow {}^{239}_{93}Np + \beta^- \quad (3.2)$$

$$^{239}_{93}Np \rightarrow {}^{239}_{94}Pu + \beta^- \quad (3.3)$$

Because the half-lives of decay reactions 3.2 and 3.3 are 23.5 minutes and 2.35 days, respectively, the longer lived ^{239}Pu is the dominant product, and decays by alpha emission according to reaction 3.4.

$$^{239}_{94}Pu \rightarrow {}^{4}_{2}He + {}^{235}_{92}U \quad (3.4)$$

Besides the alpha decays (5.105 MeV α with branching ratio γ=11.5%, 5.144 MeV α with γ=15.1%, and 5.157 MeV α with γ=73.3%), there is a very small spontaneous fission branch (γ=3*10^{-10}). What makes ^{239}Pu potentially dangerous as a weapon is that the thermal neutron (0.025 eV) induced fission cross section is about 50% larger than that of ^{235}U, and under certain conditions a chain reaction can be sustained with the neutrons released during fission. Most of the radioactive fission products undergo beta decay with short half-lives.

3.2 Complexation chemistry

The coordination chemistry of Pu is as variable as the available oxidation states. All of the f-elements are generally considered hard Lewis acids, so most of the bonding with ligands is ionic in nature. However, the actinides are capable of interacting slightly more covalently because of a relativistic effect, where in higher Z elements, the s and p orbitals contract, and the d and f orbitals expand. The relativistic Dirac model predicts comparable energies of 5f, 6d, 7s, and 7p orbitals, with energy gaps similar to chemical bond energies, such that bonding may occur with any of them depending on the chemical environment. Nevertheless, the inclination of actinide ions to form complexes with inorganic and organic ligands is dependent on the effective charge of the ion. The oxidation states higher than IV immediately hydrolyze to form linear trans-dioxo, "actinyl" cations in aqueous solutions. Thus, the different oxidation states of actinides are generally written as An^{3+}, An^{4+}, AnO_2^{+}, AnO_2^{2+} (An = U, Np, Pu, Am, and Cm) representing the oxidation states (III), (IV), (V), and (VI), and their respective effective charges are 3, 4, 2.2 ± 0.2, and 3.3 ± 0.1.[110] The relative tendency to form complexes, as well as the strength of the bonds formed with ligand donor atoms is thus in the following order: An(IV) > An(III) ≈ An(VI) > An(V). In general, plutonium forms complexes more readily than neptunium or uranium in the same oxidation state, although this can depend upon solution conditions.[111] Additionally, the order of complex forming ability for an actinide in a single oxidation state with selected inorganic ligand anions is: $CO_3^{2-} > SO_3^{2-} > C_2O_4^{2-} > SO_4^{2-} \geq F^- > NO_3^- > Cl^- > ClO_4^-$. A

notable exception to the rule is that PuO_2^{2+} complexes better with the chloride anion than nitrate, possibly because of electrostatic repulsions between the axial plutonyl oxygens and the nitrate oxygens.[111] Plutonium in any oxidation state can be complexed by ethylenediaminetetraacetate (EDTA), although the complex involving higher oxidation states degrades within a couple of days to the Pu(IV) complex.[112] Complexes of Pu(III), (IV) and (VI) with organic ligands such as acetate, citrate, and tartrate have been studied. Hexavalent PuO_2^{2+} forms stronger complexes with α-hydroxycarboxylic acids than with acetate, apparently because of the chelation effect.[111] Like other actinides, a wide variety of coordination numbers are possible, between 6 and 12 for Pu^{3+} and Pu^{4+}, and between 2 and 6 for PuO_2^{+} and PuO_2^{2+}.[52] The coordination number is often determined by steric and electrostatic considerations. The coordination chemistry of the PuO_2^{2+} cation resembles that of uranyl, where ligands always bind in the equatorial plane to form complexes with 6 (octahedral, large monodentate ligands), 7 (pentagonal bipyramidal, small monodentate ligands) or 8 (hexagonal bipyramidal, bidentate ligands) coordinate geometry.

There are several possible complexing ligand classes: solvate or adduct complex formers (alcohols, ketones, ethers, and trialkyl phosphates), chelating complex formers (hydroxyquinolines and diketonates), metal salt formers (amines, ammonium salts, acidic phosphoric esters, phosphoric acid, and acidic phosphonic esters), cation exchangers (sulfonic acids or carboxylic acids), anion exchangers (quaternary or less substituted amines), or novel multifunctional complexing ligands with multiple functional groups that vary in binding capabilities as a function of pH.

With adduct complex formers, the solvent or inorganic ligand from solution is a necessary part of the complex. Plutonium is separated from uranium and fission products by solvent extraction, and organophosphorous compounds with a phosphoryl group (P=O) are among the most common extractants. Plutonium is usually kept in the tetravalent oxidation state for extraction, and the extracting power may be arranged as follows: phosphine oxides > phosphinates > phosphonates > trialkyl phosphates. The most widely used industrial separation procedure is the PUREX process, which extracts plutonium(IV) nitrate and uranyl nitrate complexes from nitric acid into the organic phase using tri-n-butylphosphate (TBP), thus separating them from fission products. The extraction of Pu(IV) with TBP is most effective when extractin from solutions of 4 M HNO_3. Plutonium is subsequently back-extracted by reducing Pu(IV) to Pu(III), which does not form TBP complexes. There are other extractants such as methylisobutylketone that work simply by solvating the neutral nitrate complex, without actually forming any complex. Metal salt formers are a different class of compounds that remove ions from aqueous solution by forming an insoluble salt. For example, high-molecular weight amines are protonated in highly acidic solutions and form insoluble salts with anionic complexes such as $Pu(NO_3)_6^{2-}$, bringing the plutonium to the organic phase where the salt is more soluble. This is essentially the same principle used for anion exchange, where polymer beads are functionalized with quaternary amines to create the stationary phase of an anion exchange column. Anion exchange is widely used for purification and separation of plutonium because tetravalent plutonium forms anionic complexes so effectively, and Pu can be eluted from the column by reduction to Pu(III) or by controlling the acid concentration. Trivalent actinides do not form anionic complexes in 10-12 M HCl or 7-8 M HNO_3, making their separation from Pu(IV) by anion exchange convenient. In practice, elution of Pu by reduction to the trivalent state works well in any concentration of HCl, but HNO_3 is too oxidizing. Tetravalent Pu can be eluted in dilute (< 0.5 M) HNO_3 because only neutral complexes are formed at low nitrate concentrations.

Plutonium of all oxidation states is readily adsorbed to cation exchange resins, which often consist of polymer beads with sulfonate groups. The retention of plutonium by the cation exchange resin decreases with increasing acid concentration, and because there is less variability in metal speciation at low acidities, cation exchange is not used as much as anion exchange.

Chelate complex formers are bi- or multi-dentate ligands that form exceptionally strong complexes with metal cations. These also tend to be most effective at low acidities. An example is solvent extraction by 1,3-diketones, which complex Pu(IV) to a greater extent than uranyl, so careful control of acid and extractant concentration can separate the two. One of the things that makes plutonium so biologically toxic is the striking similarity of Pu(IV) to Fe(III), meaning it can be taken up into the biological iron transport and storage systems of mammals. The chemical similarity of Pu(IV) and Fe(III) stems from their similar ionic radii. Thus, another family of multidentate chelating ligands used for plutonium decorporation and remediation are the biomimetic siderophores like the desferrioxamines and synthetic ligands with catecholate or hydroxypyridinonate binding groups inspired by siderophores.[113] Additionally, several organometallic plutonium(IV) complexes have been prepared, such as plutonocene $Pu(\eta\text{-}C_8H_8)_2$ and complexes with the cyclopentyldienyl ligand $\eta\text{-}C_5H_5$.[53]

3.3 Measurement and characterization

In the study of plutonium interactions with solid materials, it is imperative to assess the purity and oxidation state of the plutonium solutions before proceeding with experiments. After preparation of the plutonium stock solutions as described in Section 3.4.3, the purity was qualitatively evaluated using alpha and gamma spectroscopy. All quantitative measurements of plutonium involved liquid scintillation counting (LSC) of solution aliquots. The oxidation state of plutonium in solutions was characterized using optical absorbance spectroscopy in the visible and near-infrared (Vis-NIR) range. Several samples of plutonium adsorbed to functionalized SBA-15 or mesoporous carbon were subject to X-ray absorption spectroscopy (XAS) for characterization of the Pu oxidation state and local coordination environment. The following sections briefly explain how these techniques work and how they were used for plutonium characterization.

3.3.1 Gamma spectroscopy

Gamma spectroscopy was performed with high-purity germanium (HPGe) detectors, both for characterization of purified plutonium stock solutions, and for the Eu-152 radiotracer batch experiments described in Section 4.4.2. This is the same type of detector that was used to measure X-ray fluorescence in the X-ray absorption spectroscopy experiments. Germanium is a semiconductor with a band-gap of around 0.75 eV, and is the most commonly used material for gamma spectroscopy because of the high-resolution spectra obtained. Solid-state semiconductors are either p-type (doped with an excess of positive charges, or “holes”) or n-type (doped with an excess of negative charges). At a junction between a p-type and an n-type crystal, a small electric field naturally occurs. When high voltage is applied across the junction, the electric field is increased, creating a depleted region that is the active region of the detector. When ionizing radiation passes through the depleted region it interacts with the detector material to form electron-hole pairs. The holes are attracted to the n-type side of the junction, and electrons are attracted to the p-type side. The charges are collected to give an electrical signal, which is

amplified and registered as one count. The amplitude of the pulse is proportional to the charge collected, which is proportional to the energy deposited into the depleted region of the detector. With careful energy and efficiency calibration, the resulting spectrum of counts vs. energy can be used to identify and quantify X-ray or gamma emitting nuclides. Figure 3.1 shows a schematic diagram of a p-n junction semiconductor detector.[114]

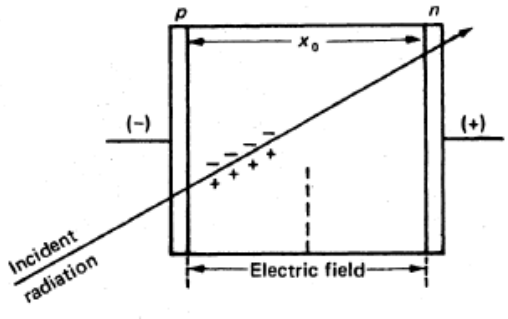

Figure 3.1. A diagram of a p-n junction in a semiconductor detector, where x_0 shows the depleted, active region of the detector.[114]

High energy photons have a much larger range through matter than charged particles, so a large depleted detector area is needed to detect them. The efficiency of the HPGe detector of course increases with crystal size, but large crystals of the required purity are difficult to grow and very expensive. Thus HPGe detectors have relatively low efficiency, and the efficiency decreases non-linearly with photon energy. Efficiency curves should be created for quantitative work, but if one wishes to quantify only one species, it is easiest to make an efficiency calibration with standard activities based on the photopeak of interest. The resolution of a semiconductor detector is related to the number of charges collected, and so the small band gap of Ge results in better resolution because there are more ionizations per interaction. Also due to the small band gap, the detector must be cooled with liquid nitrogen to suppress detector noise caused by thermal fluctuations. HPGe detectors can become easily damaged if they are allowed to warm up to room temperature while high voltage is applied. The resolution also increases with photon energy, but is superior to that of solid scintillator detectors at all gamma energies.

Despite the high resolution, interpretation of gamma spectra is often not straightforward because of the many possible interactions of photons with the detector material. The photopeak is a result of the full gamma energy being deposited into the detector, and is used for identification and quantification of the gamma emitter. When the photon ejects an electron to ionize an atom, known as the photoelectric effect, the kinetic energy (KE) of the ejected elecron is described by Equation 3.5, where E_γ is the photon energy and B_e is the binding energy of the electron.

$$KE = E_\gamma - B_e \tag{3.5}$$

In this case both KE and E_γ are usually recovered because electrons do not travel very far through matter, and when an electron from a higher orbital decays to fill the vacancy, a photon with energy B_e is emitted. However, when the incoming photon gives only a portion of its energy

to an electron (called Compton scattering), the scattered photon or electron (if near the surface) could escape the detector, which gives rise to the Compton continuum and backscatter peak. These features appear on all gamma spectra, and increase with photon energy. If the photon has energy greater than 1.022 MeV, it can disappear to create an electron-positron pair, and then either or both could escape. Considering the fact that most nuclides emit multiple gamma rays, and samples may have multiple nuclides, gamma spectra can become very complex.

Trace ^{241}Am is produced in the Pu stock via beta decay of ^{241}Pu, and must be removed by anion exchange (see Section 3.4.3). Gamma spectroscopy was performed qualitatively on purified ^{239}Pu stock solutions to confirm that the stock was free of ^{241}Am, which has a strong gamma line at 59.54 keV (γ = 35.9 %). Therefore the amplifier and multichannel analyzer (MCA) of the detector system were optimized for collecting low-energy (< 100 keV) gamma spectra. Figure 3.2 shows an example gamma spectrum of a ^{239}Pu stock solution. The photopeaks of gammas emitted by ^{239}Pu can be seen, the most prominent are at 38.66 keV (0.0105 %) and 51.62 keV (0.0271 %). The lower energy peaks are plutonium X-rays, and some small peaks can be seen from gamma emission of other plutonium isotopes. The spectrum does not show a peak at 59.5 keV, indicating that the ^{241}Am was effectively removed by the anion exchange column.

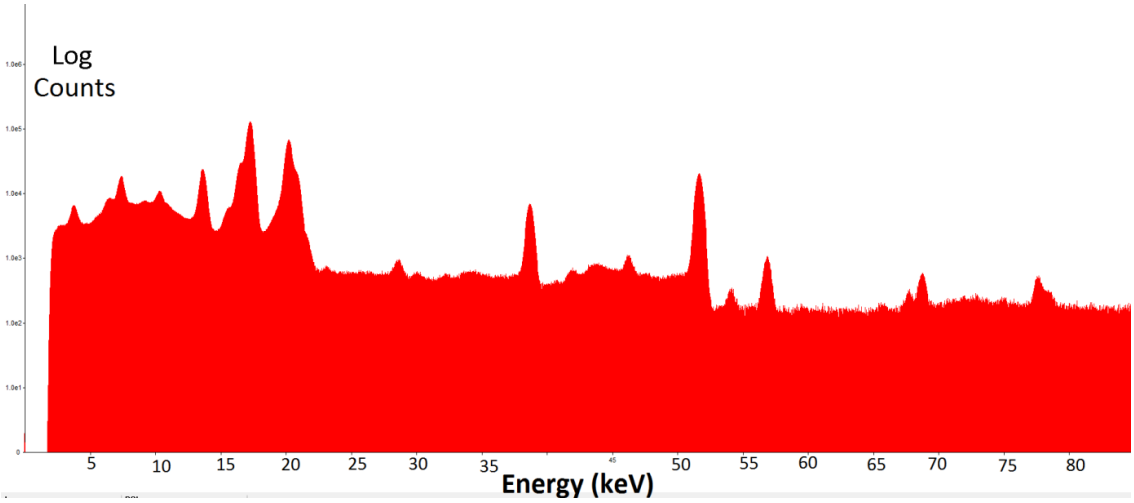

Figure 3.2. Example gamma spectrum (plotted on a log scale) of ^{239}Pu stock solution collected with a HPGe detector. The ^{241}Am peak at 59.54 keV is not observed, while the ^{239}Pu peaks at 38.66 keV and 51.62 keV are prominent, confirming that the anion exchange column was successful.

3.3.2 Alpha spectroscopy

Alpha spectroscopy was performed on ^{239}Pu stock solutions when the detector system was available. The detector commonly used for alpha spectroscopy is a surface barrier silicon diode detector. Silicon is a semiconductor with a band gap of approximately 1.1 eV, and functions in a similar way to the Ge detector described in Section 3.3.1. It is called a silicon diode detector because the p-n junction acts as a diode, conducting current readily if high voltage is applied in the forward direction, and little if applied in the reverse direction. The “reverse bias” high voltage is what creates the depleted region. Because of the larger band gap, silicon detectors don’t require cryogenic cooling. The resolution is not as good as HPGe detectors, but

still better than most scintillators. In surface barrier detectors, a thin layer of gold is coated on an n-type crystal, providing a high density of electron traps and assuming the role of the p-type material. This is ideal for detection of charged particles, which do not travel far through any medium, because the depleted region is right at the surface of the detector, and the non-depleted "dead layer" is thinner. The thickness of the depleted region in the silicon is about a few millimeters.

The surface barrier detector must be enclosed in a well sealed chamber and held under vacuum because it is sensitive to light. The vacuum is also necessary to detect alpha particles more efficiently, and improves the resolution. Resolution is also limited by electronic noise, charge collection efficiency, and dead layer activity, which are affected by the applied voltage and radiation damage in the detector. Very energetic alpha particles and fission fragments create plasma, which slows the pulse rise time and creates a pulse height defect. The energy resolution is also influenced by the method of sample preparation. The preferred method for the preparation of alpha plates is electrodeposition. In this work, for convenience, small aliquots were dropcast onto an aluminum or stainless steel planchette and dried on a hot plate. Platinum planchettes are often used and will yield a nicer spectrum, but for the purpose of this work there was no need to waste platinum. The drop cast method does not work well with solutions of high salt (or acid) concentration, so the stock solutions should be diluted first. Incomplete vacuum, loss of alpha energy in the sample medium or dead layer, and incomplete charge collection all result in detection of a lower energy than the actual alpha energy, which explains why the peaks are not Guassian but have a tail on the low energy side. Figure 3.3 shows the alpha spectrum with counts plotted on a log scale of the same example ^{239}Pu stock solution whose gamma spectrum is shown in Figure 3.2. The large peak corresponds to the 5.157 MeV α with γ=73.3%, with shoulders corresponding to the 5.105 MeV α with branching ratio γ=11.5% and 5.144 MeV α with γ=15.1%. The small higher energy peak could correspond to an alpha energy arount 5.4-5.5 MeV, where peaks from ^{241}Am (5442.80 MeV α, γ = 13.1 %; 5485.56 α, γ = 84.8 %) overlap with those from ^{238}Pu(5456.3 MeV α, γ = 28.98 %; 5499.03α, γ = 70.91 %). This overlap highlights the reason for using multiple spectroscopic methods for assessment of the chemical purity of stock solutions. Even the smallest trace of ^{238}Pu in the sample creates a measurable signal because of the much shorter half-life (t1/2 = 87.7 y) of this isotope compared to ^{239}Pu.The smaller peak accounts for 0.02% of the entire activity in the alpha spectrum, which corresponds to 0.0004% of the atoms if the entire peak is assumed to be from Am, which is unlikely.

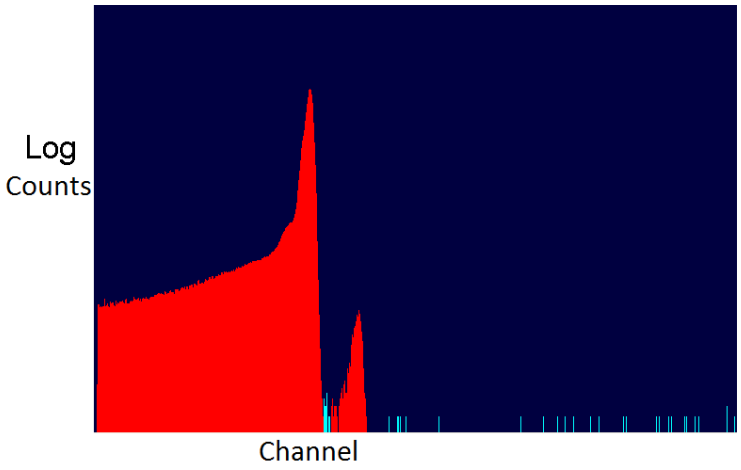

Figure 3.3. Uncalibrated alpha spectrum (plotted on a log scale) of ^{239}Pu stock solution, collected with a surface barrier silicon detector. The large peak corresponds to the 5.157 MeV α (γ=73.3%) from ^{239}Pu, with shoulders corresponding to the 5.105 MeV α (γ=11.5%) and 5.144 MeV α (γ=15.1%) from ^{239}Pu. The low-energy tail comes from incomplete charge collection or alpha energy loss in the sample medium, dead layer, or imperfect vacuum. The small higher energy peak may correspond to an alpha energy around 5.4-5.5 MeV, where peaks from ^{241}Am (5442.80 MeV α, γ = 13.1 %; 5485.56 α, γ = 84.8 %) overlap with those from ^{238}Pu(5456.3 MeV α, γ = 28.98 %; 5499.03α, γ = 70.91 %).

3.3.3 Liquid scintillation counting

All quantitative measurements of plutonium in solution were done by liquid scintillation counting (LSC), which is a convenient method for quantifying both alpha and beta emitters. Information about LSC was gathered from a book[114] and from laboratory experience. In LSC, an aliquot of radioactive solution is added to a translucent vial containing a larger volume of scintillation cocktail. The cocktail contains a proprietary mixture of solvent and phosphor molecules that absorb the alpha or beta decay energy and convert it into light that is detected by an array of photomultiplier tubes (PMTs). The biggest advantages of LSC are the high efficiency and ease of sample preparation. The main disadvantage is the relatively poor resolution, which is why it is excellent for quantification of known nuclides, but other spectroscopic methods are necessary to verify the radio-purity of solutions.

The solvents used in LSC are planar aromatic molecules such as toluene and anthracene that can easily absorb the energy of the alpha particle as it travels a very short distance through the cocktail. The energy is transferred to neighboring scintillator molecules, which undergo electronic excitations and release photons as they deexcite. The photon energy is always slightly lower than the incident energy because of molecular vibrations in the excited state, but is still usually too high for the spectral range of the PMT's photocathode. Therefore cocktails generally contain secondary phosphor molecules called waveshifters, which emit photons of a more suitable energy for detection. Each scintillator only emits photons of one specific quantized energy that is characteristic of the molecule. The alpha particle loses all of its energy within a

very small area, exciting many solvent and phosphor molecules along the way. Because of the short mean path of the particle (≤ 1 mm), the group of photons emitted from the molecules excited by a single alpha particle are registered as a single burst of light, yielding a single pulse, or "count". Because the number of excitations caused by the alpha particle is proportional to its energy, so is the number of photons emitted to create a single pulse. The pulses are sent to a preamplifier, amplifier, and MCA to create a spectrum of counts versus channel (which can be converted to energy units with calibration against known sources).

Because the alpha particles are completely surrounded by scintillators, the efficiency is essentially 100%, unless other substances exist within the sample that will absorb the energy without emitting light. This process is known as "quenching" and can reduce the efficiency (no pulse is registered for a decay) and/or reduce the intensity of photons detected for a single pulse. Quenching is usually not a problem for alpha samples, but for lower energy beta emitters a quenching (efficiency) curve should be measured with standards of known activity. Even when counting alpha decays, not every photon makes it to the PMTs, and there can be some overlap in signals produced by two alpha particles physically near each other, hence the poor energy resolution. The peak from a single energy alpha-emitter appears closer to a Gaussian peak than what is obtained with solid state alpha detectors. The differences in alpha and beta particles' ranges through the cocktail medium create different electrical pulse shapes that are used for discrimination between alpha and beta counts, even if the energies are similar. Additionally the user can select a window over a particular energy range to quantify counts from an individual nuclide of interest. Since precise volumetric aliquots are counted, the counts per unit time are easily converted to concentration using the decay constant.

LSC is suitable for measuring solutions over a wide range of radionuclide concentrations. The detection limit is determined by the background count rate. In this work a background sample was counted, which was an LSC vial that had no plutonium added to it, but had an aliquot of pure water pipetted into it in the same glovebox where samples were prepared. The background usually varied between 1 and 10 cpm, so the limit of detection for ^{239}Pu was in the nanomolar range if a 100 μL aliquot were measured. The upper limit for the amount of activity that can be counted is determined by the response time of the electronics. The timescale of the scintillation process is on the order of 10^{-8} seconds, and the PMTs work in nanoseconds, but the amplifier and MCA may slow the process to the order of microseconds. Therefore LSC may not be completely efficient at counting samples containing more than about 10^5 Bq (a few microcuries).

All plutonium solutions in this work were quantified using a Wallac 1414 liquid scintillation counter operating in *α/β* discrimination mode. Solution aliquots were carefully pipetted with Eppendorf™ micropipettors into LSC vials containing 5 mL Ecolume™ LSC cocktail. Most aliquots were 10 μL, but 5 μL was sometimes used for more concentrated samples, or 100 μL for the most dilute samples. The smaller LSC vials were passed out of the glovebox into 20 mL LSC vials, which were capped and shaken vigorously for at least 60 seconds before counting. The samples were counted for 5 to 30 minutes each. Duplicate LSC samples were counted of all solutions, and average concentrations calculated from the duplicates. More samples were taken in cases where the duplicates differed by more than about 5%, if possible. The counting efficiency was assumed to be 100%, which could give a slight systematic error, since the efficiency could actually be ~98-99 %. However, because the same LSC protocol

was used for quantification of plutonium in all stocks and samples, and usually relative concentrations were desired (i.e. percent sorption), this possible error is of no great consequence, and is far overshadowed by pipetting uncertainty.

The Ecolume™ cocktail is rated for "high salt content", and plutonium in several different media were measured without any problems. The author did notice, however, that count rates of solutions measured in 2-3 M perchloric acid were lower than expected, and it was unclear whether it was an experimental result, or an artifact caused by acid-damaged scintillation cocktail. When LSC vials that contained aliquots of 1 M or more acid were recounted several months after preparation, the spectra appeared different than those taken on the day the samples were prepared. The familiar plutonium peak was smaller, and a lower-energy shoulder had appeared. It is not surprising that the scintillation cocktail has limited tolerance for acid, but is just something to keep in mind. Small (5-10 μL) aliquots of 1-2 M acid solutions seemed to give reliable results when they were counted right away. Figure 3.4 shows an example LSC spectrum collected on a solution of approximately 1.5 nM ^{239}Pu.

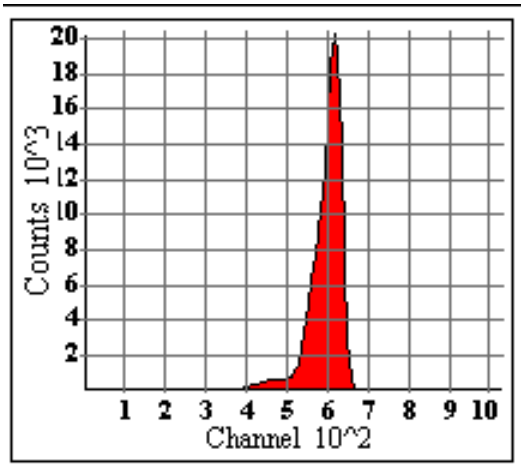

Figure 3.4. LSC spectrum of an approximately 1.5 mM ^{239}Pu solution. The broad peak has contributions from the 5.157 MeV α (γ=73.3%), the 5.105 MeV α (γ=11.5%) and the 5.144 MeV α (γ=15.1%) from ^{239}Pu.

3.3.4 Optical absorbance spectroscopy

Optical absorbance spectroscopy in the visible and near-infrared (Vis-NIR) energy range was used to determine oxidation states of plutonium in solution. In optical absorbance spectroscopy, light of many wavelengths travels through the sample, and some of the light of the correct energy is absorbed to cause electronic excitations in the sample. Measurement of the light after passing through the sample produces a spectrum of absorbance verses wavelength, which contains information about the electronic structure of the sample. For samples of species with known absorbance properties, the spectrum can be used for fingerprint identification, and quantification using Beer's law, Equation 2.8. The principles of absorbance spectroscopy are the same for UV-Vis-NIR and IR spectroscopy described in Section 2.2.6, but due to the higher energy, light in the UV-Vis-NIR range causes excitations of electrons from the highest occupied orbital to an unoccupied orbital, where IR transitions are only to vibrational levels of the highest occupied orbital. Also, the way the instrument works is different, as optical spectrometers are not based on the interferometer like FTIR.

Figure 3.5 shows a schematic of the OceanOptics S2000 fiber-optic spectrometer as it was used in this work. The "LS-1" is a Tungsten Halogen Light Source, which is a versatile white-light source optimized for the Visible-NIR range. The lamp was always turned on at least 30 minutes before collecting spectra to avoid any artifacts caused by temperature fluctuations. Light travels through a fiber optic cable (shown in blue) through a filter (when applicable), then through the sample and to the spectrometer. The filter was used to attenuate some light so that the intensity going through the sample was appropriate to be able to measure absorbance. There is also a light/dark switch that blocks all of the light when switched to the dark position. For every sample, reference light and dark spectra must be collected, where the reference cell contains the same solution but without the analyte of interest. The instrument's software subtracts the reference spectra from the sample spectra. The samples were placed into quartz cuvettes with a 1 cm path length, and the holder has an opaque black cover to shield the sample from ambient light.

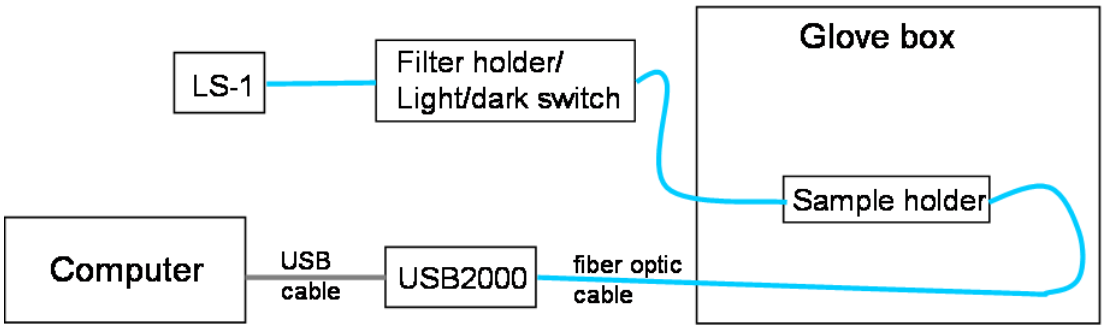

Figure 3.5. Schematic diagram of optical spectrometer setup. Image created by Paul Ellison.

In the spectrometer, light from the input optical fiber enters the optical bench through the connector, and then the slit, a dark piece of material with a rectangular aperture that regulates the amount of light that enters the optical bench and controls the spectral resolution. Light passes through a filter before entering the optical bench, and the filter only allows light of certain wavelength regions through. After passing through the filter, light reflects off of the collimating mirror toward the grating. The diffraction grating has a periodic structure that splits and defracts the incident beam of light into multiple beams of different wavelength. Gratings of different groove densities allow the selection of different regions of the electromagnetic spectrum, and also influence the spectral resolution. The diffracted light reflects off of the focusing mirror towards the collection lens, where it is further focused before finally reaching the CCD detector. Each pixel on the CCD array creates a digital response to the specific wavelength of light that strikes it, thus the pixel resolution of the detector also determines spectral resolution. The spectrometer used in this work was configured for the Vis-NIR range, with a grating of 600 lines blazed at 500 nm, a 25 μM slit, and a Sony ILX511 2048 pixel linear silicon CCD array. Based on the aperture, grating groove density, and pixel resolution, the spectral resolution obtained was 1.34 nm. The absorbance resolution is determined by the signal-to-noise ratio of the spectrum. [115] The spectrometer used was designed to cover a spectral range of 350 nm to 1000 nm, but in practice there was a large amount of noise below approximately 450 nm, making that region unreliable.

The characteristic ultraviolet, visible and infrared absorbance spectra of Pu^{3+}, Pu^{4+}, PuO_2^{+}, and PuO_2^{2+} in non-complexing $HClO_4$ were well characterized by Cohen.[116] The

relatively low extinction coefficients for plutonium and other actinide ions may be explained by considering the electronic transitions that occur upon absorbance of light. For all actinide ions, both the highest occupied orbital and the lowest unoccupied orbital are f-orbitals, and f-f transitions are forbidden by the azimuthal quantum number ($\Delta l = \pm 1$) and Laporte ($g \rightarrow u$) electric dipole selection rules. However, the extinction coefficients observed for spin-allowed, Laporte forbidden f-f transitions are higher than those typical for similar d-d transitions in d-block metal complexes. The selection rules are slightly relaxed due to increased spin-orbit coupling, which is a relativistic effect as the electrons' radial velocity increases with Z. It is the absorbance in the visible region that gives concentrated plutonium solutions their distinctive colors. Hexavalent plutonium has the lowest detection limit with a peak at around 830 nm that has an extinction coefficient which exceeds the others by an order of magnitude. In order to obtain quality spectra of the other oxidation states with a normal 1 cm cuvette, solutions of approximately millimolar Pu are required. In this work, absorbance spectroscopy was used only qualitatively, to identify oxidation states of Pu. Quantitative analysis requires proper calibration, as the extinction coefficients will vary slightly depending upon the solution conditions and the spectrometer. For semiquantitative estimates, the peaks and extinction coefficients used come from Cohen[117] and Silva and Nitsche[109] are tabulated in Table 3.1. Pu(IV) colloids are indicated by a large background absorbance of light with wavelength below around 500 nm caused by scattering, as well as a sharper peak around 613 nm.[118] Figures 3.6-3.9 show characteristic Vis-NIR absorbance spectra collected in the Nitsche lab on stock solutions of Pu(III), Pu(IV), Pu(V), and Pu(VI), respectively. All solutions except for the Pu(V) solution shown in Figure 3.8 were in approximately 1 M $HClO_4$, and all except Pu(VI) were prepared electrochemically according to Table 3.2. The Pu(VI) solution was prepared by boiling Pu in concentrated $HClO_4$ for several hours. Its spectrum, shown in Figure 3.9, has a characteristic peak of high absorbance at 830 nm. The y-axis in Figure 3.9 is scaled down so that the other spectral features can also be observed, but this cuts off the 830 nm peak, which has a maximum absorbance of 0.56.

Table 3.1. Optical spectroscopic parameters of Pu ions.[109, 117]

Ion	**Wavelength nm**	**Molar Abs. $M^{-1}cm^{-1}$**
Pu^{3+}	600	38
Pu^{4+}	470	55
PuO_2^{+}	568	19
PuO_2^{2+}	830	550

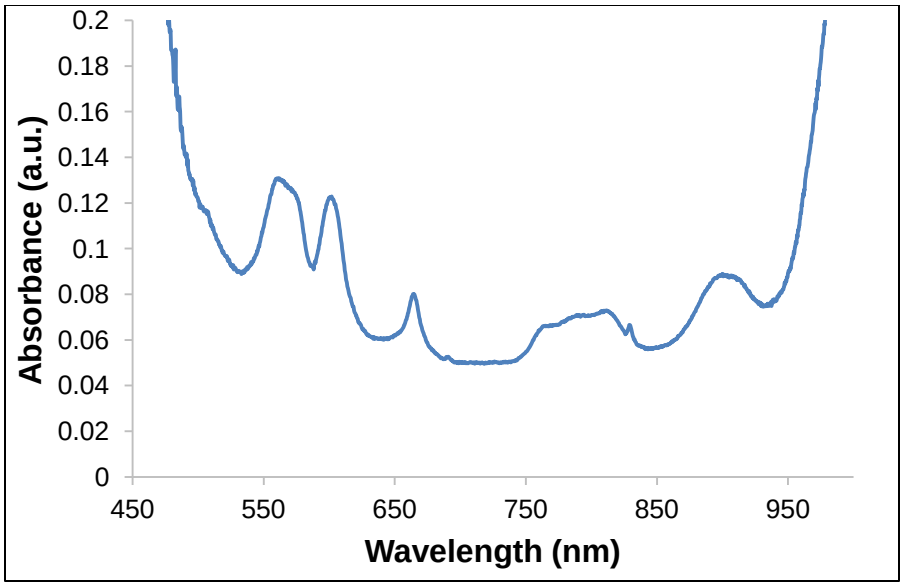

Figure 3.6. Vis-NIR absorbance spectrum of a Pu(III) stock solution in approximately 1 M $HClO_4$, which was prepared electrochemically from a Pu(VI) stock solution by Professor Heino Nitsche with graduate students Eva Uribe and Deborah Wang.

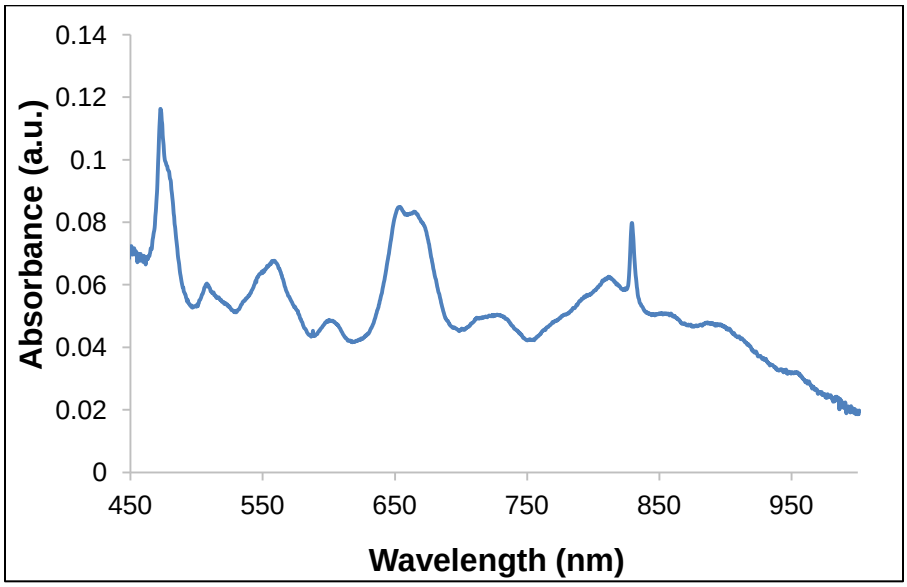

Figure 3.7. Vis-NIR absorbance spectrum of a Pu(IV) stock solution in approximately 1 M $HClO_4$, which was prepared electrochemically from a Pu(III) stock solution by Professor Heino Nitsche with graduate students Eva Uribe and Deborah Wang.

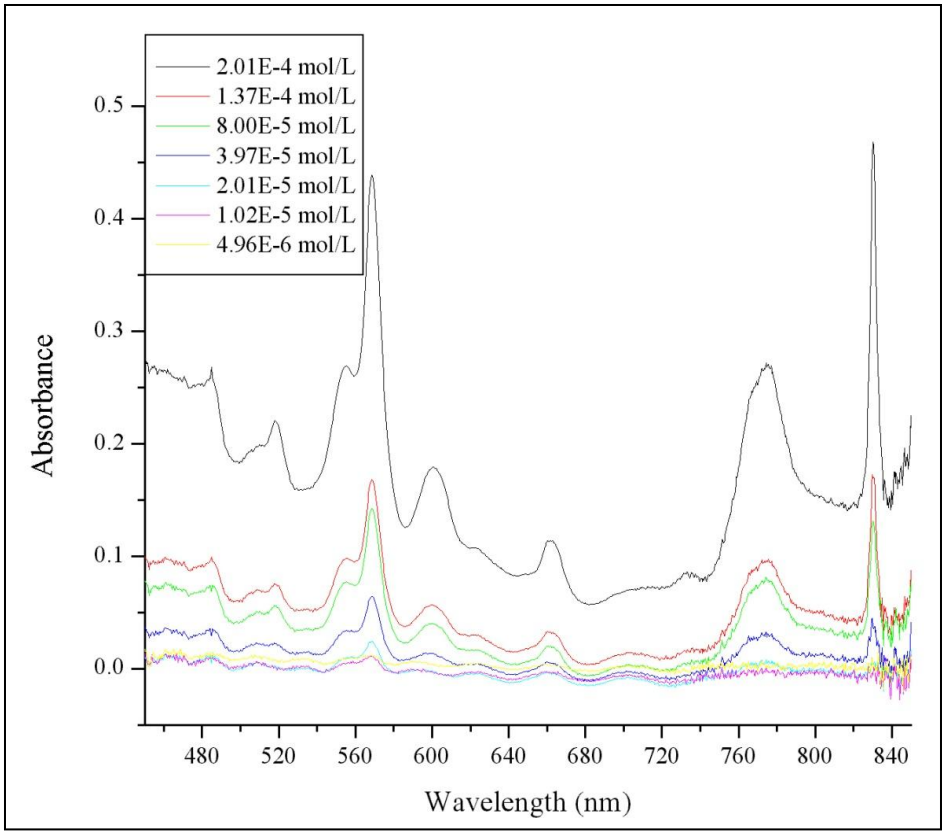

Figure 3.8. Vis-NIR absorbance spectra of Pu(V) solutions with various concentrations, which were prepared electrochemically from Pu(VI) stock solutions in a pH 3 perchlorate matrix, by former Nitsche graduate student Richard Wilson[62].

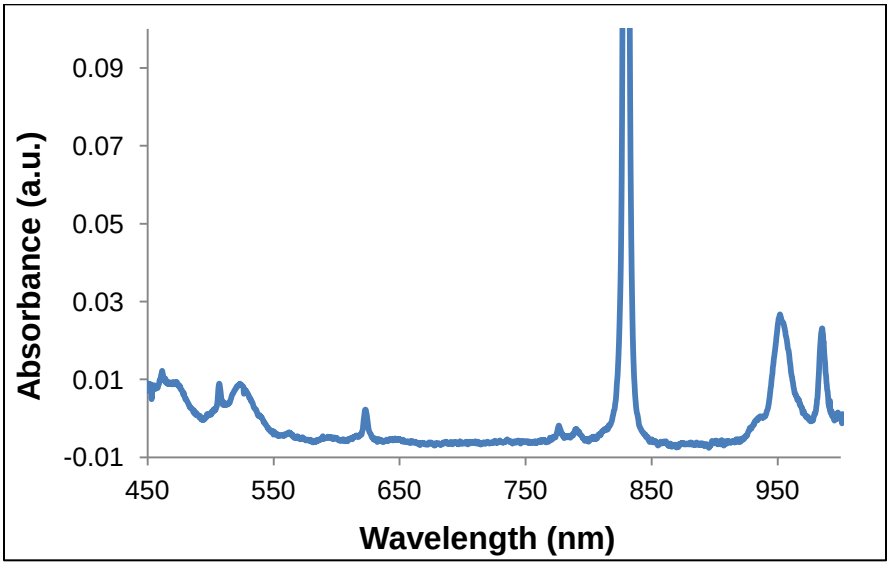

Figure 3.9. Vis-NIR absorbance spectrum of 1.25 mM Pu(VI) in 1.2 M perchloric acid.

3.3.5 X-ray absorption spectroscopy

X-ray absorption spectroscopy was used to probe the oxidation state of plutonium after it was bound to mesoporous materials, as well as extract some information about the local coordination environment. XAS uses X-rays to probe the core electronic structure and coordination environment of atomic species. These experiments are generally carried out at a synchrotron facility, which is capable of producing the high-intensity X-ray beams required to collect quality spectra in a timely manner. The incoming X-ray of sufficient energy ejects a core electron from the target species that will interact with surrounding electrons from neighboring atoms. The absorbance spectrum shows a sharp increase in absorbance at the binding energy of the electron, called the absorption edge, followed by higher energy oscillations caused by scattering with neighboring atoms. For plutonium, the L_{III} edge at 18.0623 keV is used, which corresponds to ejection of the $2p^{(3/2)}$ electron. The XAS spectrum can be divided into two regions, as shown in Figure 3.10, which are used for two different analytical techniques. The region from before the absorption edge to about 50 keV above the edge is used for analysis of X-ray absorption near edge structure (XANES), and the higher energy portion of the spectrum is used for extended X-ray absorption fine structure (EXAFS) analysis. XANES spectra are a direct probe of the electronic structure of the atom, while EXAFS spectra come from interference of the ejected photoelectron with neighboring atoms, and thus probe the local coordination environment.

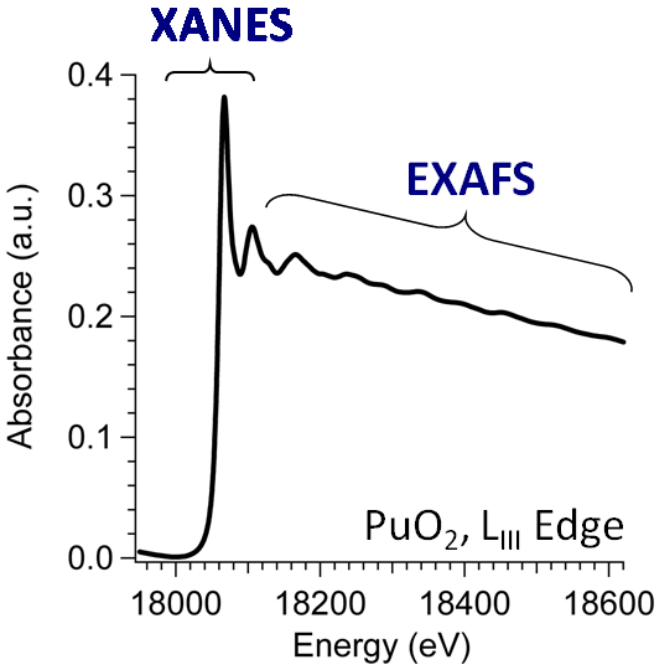

Figure 3.10. Example Pu L_{III} XAS spectrum with XANES and EXAFS regions depicted.[83]

The ways in which Pu L_{III} XAS experiments were conducted at Stanford Synchrotron Radiation Laboratory (SSRL) for this work were already established in the Nitsche group,[54, 55, 61, 62, 83] and a detailed introduction to the theory and data analysis of these techniques can be found in the thesis of Yung-Jin Hu.[61] The XANES technique provides measurements of the changes in

X-ray absorption cross section with incident X-ray energy. There are several fine structures near and above the edge that may be resolved for low-X materials, where the core-holes left by photoelectrons have a relatively long lifetime. Spectral broadening caused by the short core-hole lifetimes in high Z materials means the loss of sharp structure, but the exact position and shape of the edge varies with oxidation state, independent of the local molecular structure.[61] This allows XANES to be used for in-situ identification of Pu oxidation states in a wet paste sample. The XANES spectra are calibrated against a known standard, background subtracted, and the edge step normalized, since different oxidation states have different white-line (the largest peak at the absorption edge) heights. Then, theoretically the edge position (exact energy of the absorption edge) can be used to determine the oxidation state. However the single inflection point is sensitive to artifacts of background subtraction, so the entire XANES spectrum is fit with a least-squares analysis to a set of pure oxidation state standards. Samples may contain a mixture of oxidation states, and the composition can be estimated by the least squares fitting. The XANES spectrum can be somewhat sensitive to the coordination environment, as aqueous Pu(IV) and Pu(IV)O_2 have slightly different edge positions and white-line heights. Figure 3.11 shows example XANES spectra, including four known standards and samples of plutonium loaded onto C-CS-type mesoporous carbons. These spectra are only shown here as an example, but explanation of the synthesis and properties of these materials can be found in Section 6.2.5, and discussion of the XAS results can be found in Section 6.4.2. A notable feature about the XANES spectra of oxidized Pu(V) and Pu(VI) is the shoulder on the white line caused by scattering with the axial plutonyl oxygens.

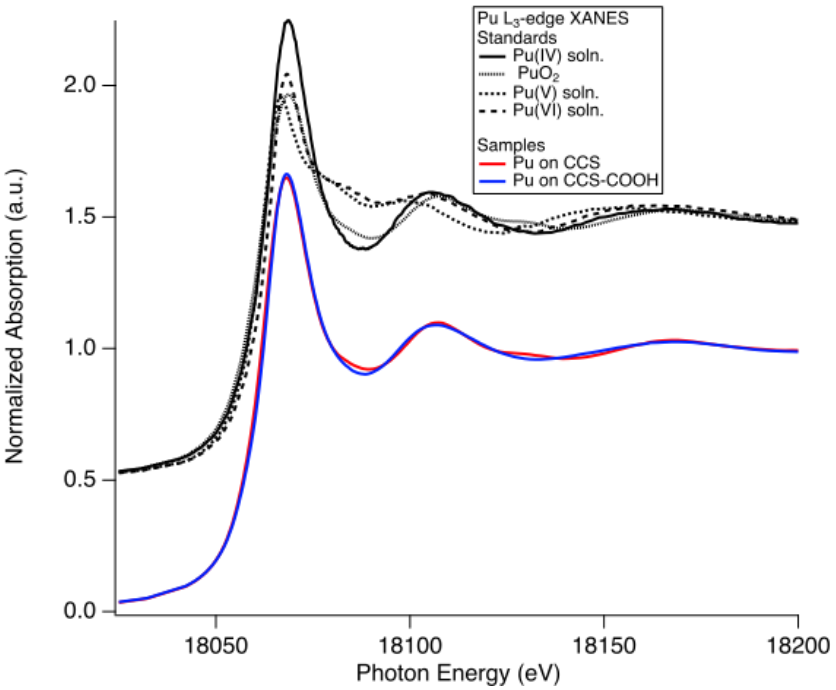

Figure 3.11. XANES spectra of the Pu on CCS samples, and associated Pu reference spectra (offset for clarity) used in XANES fitting.[119]

The XAS spectra in this work were measured in fluorescence mode. The fluorescence photons measured by HPGe detectors are emitted when higher energy electrons decay to fill the core holes left by the ejected photoelectrons. The use of fluorescence is helpful and necessary

when the element of interest only makes up a small percentage of the sample, as it improves signal-to-noise ratio. The counts from detected fluorescence X-rays are directly related to X-ray absorption in the sample, because fluorescence only occurs when core holes were created. Dead time corrections are very important since there may be other fluorescence X-rays coming from the sample, and the high flux can overload the detector. EXAFS spectra provide the oscillations in absorption cross section that occur due to scattering of the photoelectron with neighboring atom, and thus contain information about the molecular coordination environment. Most of the EXAFS oscillation spectrum is accounted for by the photoejected electrons being backscattered by a single neighboring atom back towards the central atom, which is called a single-scattering path. However, the spectra also contain significant contributions from multiple scattering paths, especially for the actinyl ions. The data is converted from energy-space to k-space, and usually Fourier transformed into R-space, to yield a spectrum with an X-axis related to bond lengths in the coordination environment, and Y-axis related to the number of neighboring atoms at that bond distance. The k-space range is directly related to the energy range of incident radiation, and collecting data out to higher k-space values gives better resolution in R-space. The k-space range is limited, however, by data collection time and interferences from higher energy absorption edges. The interpretation of EXAFS spectra is never straightforward, as it requires careful comparison with a reasonable model that may describe the coordination environment around the atom of interest. In samples with no long-range order, building the model is achieved using known pieces of information about the chemical structure of the surface where sorption is occurring. The model is deconstructed into different parts, and the scattering paths in standards must be measured or calculated for each part. It is important to consider the number of independent variables being fit compared to the number of independent data points in the spectra, for the fit is not unique if there are too many variables. Eventually information about the molecular coordination environment of the plutonium in the sample can be inferred according to how well the proposed model fits the sample EXAFS spectra. Figure 3.12 shows example Fourier transformed EXAFS spectra of the C-CS samples whose XANES spectra are shown in Figure 3.11, along with the EXAFS spectrum of a PuO_2 standard.

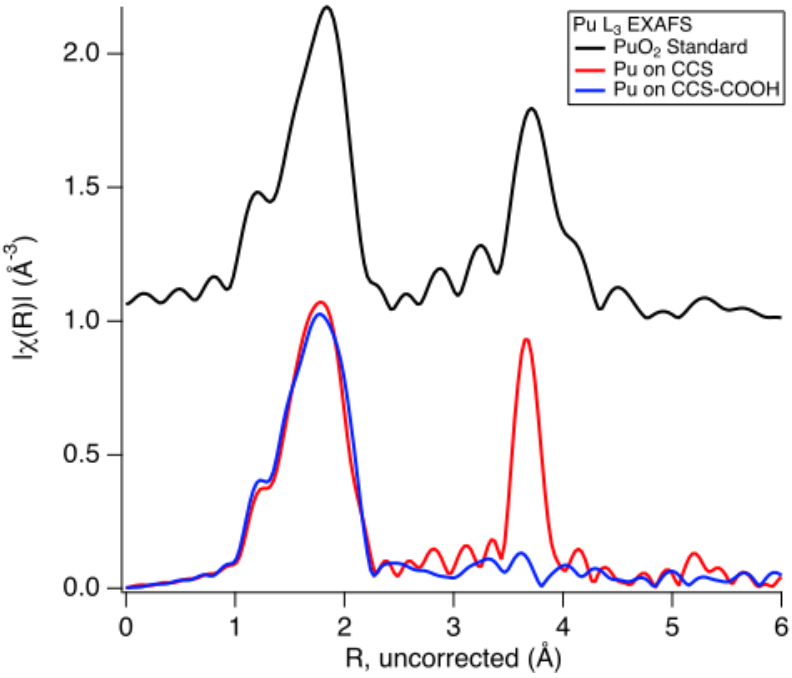

Figure 3.12. Fourier transform magnitude of the EXAFS from C-CS samples, and PuO_2 (offset) for comparison. The difference in widths of the Pu-Pu scattering peak between the PuO_2 and the untreated CCS sample is an artifact of the shorter k-space range available for the Fourier transform of the PuO_2 standard.

Pu L_{III} XAS spectra were measured for samples of Ac-Phos-SBA-15, TESPMA-SBA-15, CMK, OX CMK, C-CS, and C-CS-COOH loaded with Pu(VI) in a perchlorate medium, as well as Ac-Phos-SBA-15 loaded with Pu(IV) in a nitrate solution. The XAS samples were prepared in a similar manner to the batch sorption samples. Packaging and measurement of XAS samples was performed in the method of Hu et al.[54, 61] The carbons were loaded as wet pastes into Kapton tubes and triply contained in specialized sample holders before shipment to SSRL. XAS spectra were collected at SSRL on beamline 11-2 using a 30% detuned Si(220) φ-0° double-crystal monochromator. All spectra were collected at 30 ± 2 K, using a specially engineered liquid helium cryostat (Janis) to mitigate beam-induced reduction of Pu in the samples. Data were collected in fluorescence mode using a 32-element germanium detector (functionalized silica and CMK samples) and later a 100-element germanium detector (C-CS samples). To avoid overloading the detector, the vertical aperture of the beam was adjusted between approximately 0.25 mm to 0.50 mm. Energy calibration was performed by measuring the inflection point in the plutonium L_{III}-edge of a $^{242}PuO_2$ powder, 18062.3 eV,[120] in transmission mode between samples. At least 10 scans per carbon sample were acquired, using 1 second per point in the pre-edge and edge regions, increasing to 8 seconds per point at k = 14. The fluorescence spectra were dead time corrected using the method of Webb.[121]

The first sample from this work to be examined by XAS was Pu(VI) loaded onto Ac-Phos-SBA-15. The analysis of the XANES spectra was performed by Yung-Jin Hu, who carefully analyzed the beam-induced reduction of the sample. While cryogenic temperatures of 30-50 K have sufficiently suppressed beam reduction in Pu-containing iron oxide samples, this was not the case for organically modified silica, where slow beam-induced reduction slowly occurred even at 30 K.[61] The sample's composition changed over the course of 20 scans from

approximately 70% Pu(VI), 30% Pu(V), to 20% Pu(VI), 70% Pu(V), and ≤ 10 % Pu(IV) (see Figure 5.44 in Section 5.5.1). Therefore, data collection was limited to 5 scans on subsequent functionalized SBA-15 samples, and duplicate samples were prepared in order to improve statistics. XANES analysis on CMK-type mesoporous carbon samples was performed by Deborah Wang. Dr. Daniel Olive completed EXAFS analysis of all carbon and silica samples, as well as XANES analysis on the C-CS, Ac-Phos-SBA-15, and TESPMA-SBA-15 samples. The Nitsche group has successfully used EXAFS to measure Pu-Fe bond lengths in samples of plutonium sorbed to iron-oxide minerals, and thus determine whether sorption occurred via inner-sphere or outer-sphere coordination.[54, 55, 61, 62] The fact that the mineral systems were crystalline phases was very helpful for building the appropriate models. In this work, EXAFS analysis was limited both by the heterogeneity of the surfaces and sorbed plutonium species, as well as the fact that there were no heavy atoms in the immediate vicinity of the plutonium atoms to create distinctive scattering oscillations. The EXAFS spectra are not sensitive to the differences between scattering from oxygen, nitrogen, and carbon, so a great deal of hand waving is involved in the analysis of this type of sample. For the functionalized silica samples, molecular modeling was performed by Professor Krishnan Balasubramanian and his group at California State University East Bay. Molecular structures of the complexes were calculated at Lawrence Livermore National Laboratory supercomputing facility using *ab initio* relativistic density functional theory (DFT) geometry optimization techniques, and the calculated bond lengths were compared to experimental EXAFS data. The EXAFS region in spectra from the carbon samples were used to estimate the amount of crystalline PuO_2 in the samples, because XANES analysis showed that Pu was reduced to the tetravalent state.

Linear combination analysis (LCA) fitting of the XANES spectra was accomplished using the program RSXAP[122] (CMK samples) or ATHENA[123] (Functionalized silica and C-CS samples). The production and measurement of Pu(IV), Pu(V), and Pu(VI) solution spectra that were used for XANES analysis was published previously[124]. EXAFS analysis utilized the programs ATHENA and ARTEMIS [123] for data reduction and modeling, respectively. To determine the amount of PuO_2 present in the samples, as opposed to Pu(IV) sorbed to the surface with no long range Pu-Pu order, the EXAFS data were fit using paths generated by FEFF6.[125-128] Fitting of the PuO_2 standard used the first and second shell oxygen and plutonium single scattering paths, and eight associated multiple scattering paths. Using variables from the single scattering paths to account for changes in the multiple scattering paths minimized the number of fitting variables used. In the end, a total of 7 variables were used for the entire fit consisting of 11 paths. An 8th variable was added, representing the contribution of PuO_2 to the sample's spectrum, which was fit simultaneously with the PuO_2 standard. The number of independent points using the adjusted Nyquist formula[129] was 38.

3.4 Aqueous solution chemistry of plutonium

Mindful consideration of the chemical behavior of plutonium in solution is imperative to understanding the adsorption processes at liquid-solid interfaces. The solution chemistry of plutonium is heavily dependent upon oxidation state. The lower oxidation states Pu(III) and Pu(IV) exist in solution as bare cations with ionic radius 1.123 Å and 0.962 Å for an eight coordinate system, respectively, although these ions may accommodate up to 10 or 12 oxygen atoms in the first coordination shell.[130, 131] Pu(V) and Pu(VI) ions exist as linear dioxo-cations with Pu=O bond lengths of 1.81 and 1.74 Å, respectively.[124] The next two sections provide a

brief review of well known processes in plutonium solution chemistry, as described in the book by Cleveland[111] except where other citations are specified. In Section 3.4.3, the specific procedures for Pu stock preparation used in this work are briefly described, and Section 3.4.4 discusses the instability of Pu(VI) in solution, as it relates to this work.

3.4.1 Reduction-oxidation chemistry

The speciation and chemical reactivity of plutonium in solution is greatly complicated by its rich redox chemistry. Figure 3.13 shows a Latimer diagram for Pu in 1 M $HClO_4$ at 25° C. The reduction potential is a measure, in volts, of how easily a species collects electrons to become reduced. The more positive the reduction potential, the more easily the species is reduced, and these numbers are in comparison with the reduction of aqueous H^+, which is arbitrarily set to zero. The formal reduction potentials between the four common oxidation states of Pu are very similar, approximately 1 volt. This similarity results in the coexistence of several oxidation states in many solutions, with the exact composition being rather sensitive to the solution matrix.

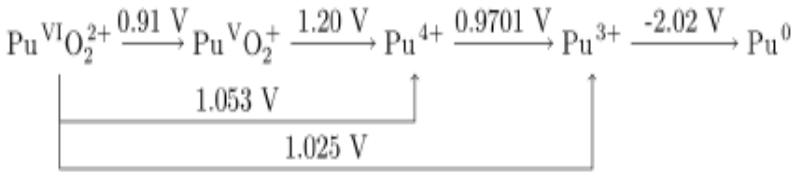

Figure 3.13. Latimer diagram showing formal reduction potentials among common oxidation states of plutonium in 1 M $HClO_4$ at 25° C. [61]

Both Pu(IV) and Pu(V) are unstable with respect to disproportionation in aqueous solution. The disproportionation of Pu(IV) occurs in two steps, shown in Reaction 3.6, which is slow due to the formation of the actinyl bonds, and Reaction 3.7, which is rapid. The overall net reaction for Pu(IV) disproportionation is shown in Reaction 3.8.

$$Pu(IV) + Pu(IV) \leftrightarrow Pu(III) + Pu(V) \quad (3.6)$$

$$Pu(V) + Pu(IV) \leftrightarrow Pu(III) + Pu(VI) \quad (3.7)$$

$$3Pu^{4+} + 2H_2O \leftrightarrow 2Pu^{3+} + PuO_2^{2+} + 4H^+ \quad (3.8)$$

Pu(V) undergoes disproportionation two different ways. If Pu(III) is present with Pu(V) in solution, Reactions 3.6 and 3.7 will proceed, but if there is only Pu(V) in solution, it can disproportionate by the much slower Reaction 3.9. The overall net reaction for Pu(V) disproportionation is given in Reaction 3.10. Notice the H^+ dependence of Reactions 3.8 and 3.10 indicate that Pu(V) is favored in high pH solutions and Pu(IV) should be favored in low pH solutions. The reason Pu(V) can dominate the oxidation state distribution of plutonium in many environmental settings, such as seawater, is that the concentration is so low, thus Reactions 3.9 and 3.10 are kinetically hindered.

$$Pu(V) + Pu(V) \leftrightarrow Pu(IV) + Pu(VI) \quad (3.9)$$

$$3PuO_2^{+} + 4H^{+} \leftrightarrow Pu^{3+} + 2PuO_2^{2+} + 2H_2O \quad (3.10)$$

Reaction 3.7 describes the equilibrium between all four common oxidation states of Pu, with equilibrium constant defined by Equation 3.11.

$$K = \frac{[Pu^{3+}][PuO_2^{2+}]}{[Pu^{4+}][PuO_2^{+}]} \quad (3.11)$$

The equilibrium constant K was determined in perchlorate solution of unit ionic strength to be independent of H^+ concentration in the range 0.1 to 1 M, and the value at 25° C is 13.1 ± 0.08. Keep in mind that these reactions only describe the equilibrium of plutonium as the sole solute in aqueous solution. The actual distribution of oxidation states is greatly influenced by any complexing ligands or redox active reagents present in solution, including those produced by radiolysis. The alpha particles emitted from ^{239}Pu deposit a lot of energy into the surrounding solution (~1.8 x 10^{14} eV/min in a 1 mM solution[111]), ionizing nearby molecules. Many of the ionized products can undergo redox reactions with Pu. Some examples are shown in Reactions 3.12 and 3.13.

$$Pu(III) \xrightarrow{OH,H,HO_2} Pu(IV) \xrightarrow{OH} Pu(V) \xrightarrow{OH} Pu(VI) \quad (3.12)$$

$$Pu(VI) \xrightarrow{e^-_{aq},H,HO_2} Pu(V) \quad (3.13)$$

Reactions such as 3.13 are so common the terms auto-reduction or self-reduction is used to describe the instability of Pu(VI) solutions. ^{239}Pu(VI) solutions in 1 M $HClO_4$ have been found to undergo reduction to Pu(V) by alpha-induced radiolysis products at a rate of about 1.5 % of the total Pu concentration per day.[132] Our observations in monitoring the stock solutions over time by Vis-NIR spectroscopy were consistent with this reported value. Once appreciable amounts of Pu(V) are formed, Pu(IV) grows in by the disproportionation Reaction 3.9. The oxidation state instability of the plutonium solutions used for this work is discussed more specifically in Section 3.4.4. In certain kinds of solutions, the radiolysis products are oxidizing and actually stabilize Pu(VI). It should also be noted that the presence of complexing ligands or surfaces can alter the redox potentials of the plutonium oxidation states. Generally strong complexing ligands stabilize the tetravalent oxidation state because it forms such strong complexes.

The rich redox chemistry of plutonium sets it apart from its oxidation state analogs in the actinide series (Th(IV), Am(III), Np(V), U(VI)) and can be a curse or a blessing to the plutonium chemist. These properties are often exploited for separations, and many reducing and oxidizing agents are commonly used in the laboratory. Pure or almost pure oxidation state solutions can also be prepared electrochemically using a potentiostat. Table 3.2 describes how the different oxidation states of plutonium can be prepared in the laboratory.[62, 117] Notice that a large overvoltage is necessary for reduction of Pu(VI) to Pu(III) because of the slow step of breaking the plutonyl bonds.

Table 3.2. Summary of potentials used on a potentiostat for electrochemical reactions of plutonium.[62]

Reaction	Potential vs. Ag/AgCl

Pu(VI) to Pu(V)	0.70 V at pH 3.0
Pu(III) to Pu(IV)	1.00 to 1.10 V in 1 M $HClO_4$
Pu(VI) to Pu(III)	0.00 V at 1 M $HClO_4$
Any oxidation state to Pu(VI)	Boiling perchloric acid

3.4.2 Solubility and speciation

The speciation and corresponding solubility of plutonium in aqueous solution depends on oxidation state, hydrolysis, and presence of carbonate and other complexing ligands in the solution. All metal ions in solution can be considered Brønsted acids, and may undergo pH dependent hydrolysis as described in Reaction 3.14.

$$M^{+n} + mH_2O \leftrightarrow M(OH)_m^{+(n-m)} + mH^+ \quad (3.14)$$

At neutral to high pH values, the fully hydrolyzed metal hydroxide species will precipitate out of solution. The tendency for aqueous plutonium ions to hydrolyze follows the general trend of complex formation Pu(IV) > Pu(III) ≈ PuO_2^{2+} > PuO_2^{+}. Tetravalent plutonium begins to hydrolyze in solutions below pH 1, and is the least soluble plutonium oxidation state in the absence of complexing ligands. Hydrolysis is known to create oligomers of plutonium and other actinides. The solubility of plutonium is dependent upon the redox conditions in the solution, as the solubility controlling phase changes in the presence of reducing agents. Under reducing conditions, the solubility controlling phase is PuO_2(am, hyd) in equilibrium with aqueous Pu(III) and Pu(IV); but if any oxygen is present then a mixed valent PuO_{2+x}(s, hyd) phase will control solubility in equilibrium with Pu(V) and much lower concentrations of Pu(IV).[133] These redox and solubility processes are diagrammed in Figure 3.14. The solubility of the mixed valence phase is increased by Pu(VI), which increases at higher redox potentials caused by carbonate or radiolysis in brines.[133] In solutions that are open to air, carbon dioxide dissolves to give carbonate in neutral to basic solutions, and complexation by carbonate generally increases the solubility of plutonium in higher pH solutions, where negatively charged carbonate species are formed. The formation constants for carbonate complexes of PuO_2^{2+} are greater than the hydrolysis formation constants, and thus the carbonate species dominate and control solubility. In neutral and slightly basic solutions, Pu(VI) solubility is decreased, as the K_{sp} for PuO_2CO_3 is lower than that for $PuO_2(OH)_2$. Further discussion of carbonate equilibria in aqueous solutions can be found in the dissertation of Yung-Jin Hu.[61]

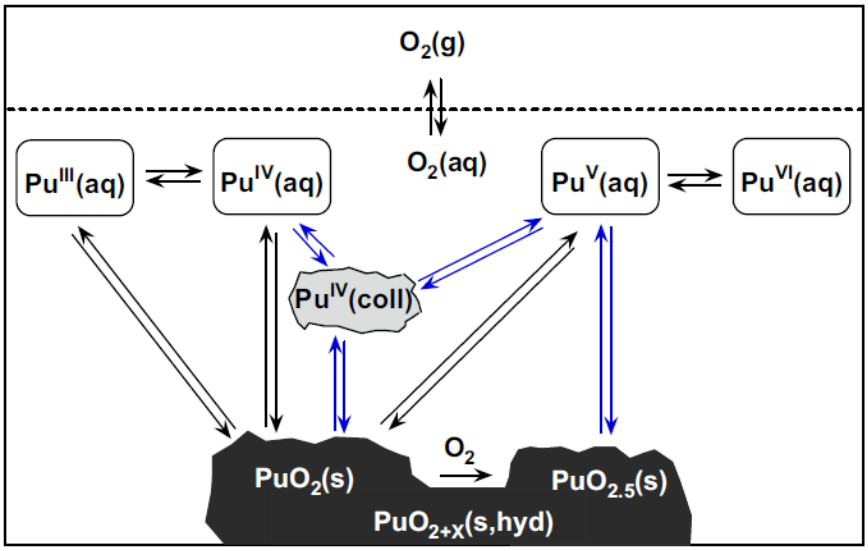

Figure 3.14. Schematic of solid-liquid and redox equilibria of plutonium under reducing conditions, redox-neutral conditions, and in the presence of oxygen.[133]

Besides hydroxide and oxide solids, another consideration in regards to plutonium solubility is the formation of Pu(IV) colloids. The concentration of Pu nanocolloids in near neutral solutions can far exceed the solubility of Pu(IV) hydroxide and oxide solids. Unlike U(IV) and Th(IV) colloids, the formation of Pu(IV) colloids or "polymer" is considered to be an irreversible reaction. This species is always formed in Pu(IV) solutions with dilute acid concentrations, and can also be formed in highly acidic solutions when the plutonium concentration is very high. Elevated temperatures also increase the rate of polymer formation. The structure and composition of the Pu(IV) colloid has been debated in the literature. Traditionally this species has been thought of as an amorphous polymer of hydrous Pu(IV) oxide.[134] However, some studies have suggested through the use of X-ray scattering techniques[135] and TEM[136] that the structure and composition of the polymer is actually nano-crystalline PuO_2.

The oxidation state speciation of plutonium in aqueous solutions depends on the redox conditions and pH of the solution.[137] There are several published Pourbaix diagrams that describe the expected thermodynamically stable oxidation state of plutonium in solutions over a range of pH and reduction potentials (E_h). These diagrams are calculated based on empirical data, and placement of lines of stability depends on which other species are in solution, whether the system is under air or an inert atmosphere, and how well colloidal Pu species are considered. It is also worth noting that Pourbaix diagrams describe systems at equilibrium, and cannot consider kinetic effects. An example Pourbaix diagram is shown in Figure 3.15, which considers only aqueous Pu species in a solution of low ionic strength and low plutonium concentration, in equilibrium with air.[137]

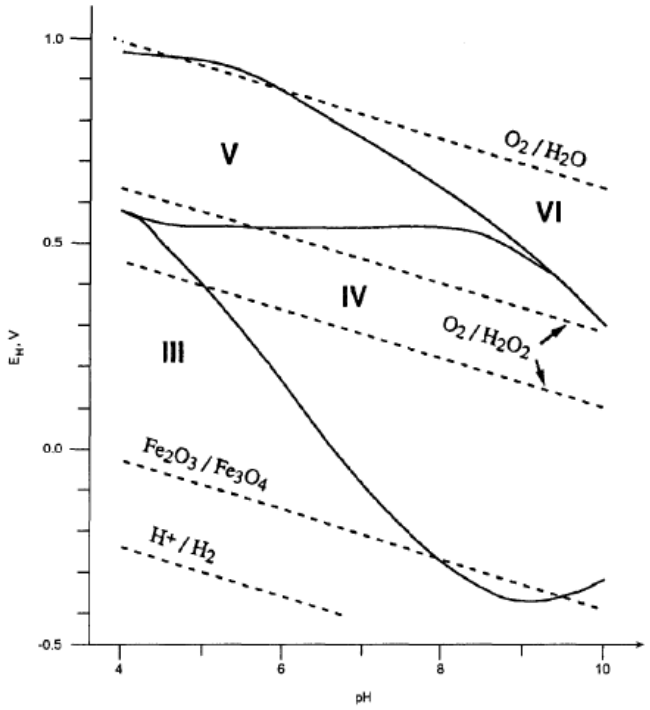

Figure 3.15. Pourbaix diagram for plutonium in a system with low ionic strength and low total Pu concentration, in equilibrium with atmospheric CO_2.[137]

A speciation diagram of Pu(VI) in solution exposed to normal atmospheric conditions was calculated by Yung-Jin Hu using the homemade program SPECIATE and previously measured thermodynamic data, and is shown in Figure 3.16.[61] The dotted lines represent 1σ uncertainty, so although these data give a general idea of species that will be present in solution, there is a great deal of uncertainty in neutral and high pH solutions. In addition, the Pu(VI) state is not stable in this pH range except under oxidizing conditions, such as those created by radiolysis products in brines.[133] Hexavalent Pu can also be stabilized against auto-reduction by carbonate complexation because Pu(VI) has a higher complex formation constant than Pu(V).[137] However, there will usually be some amount of lower oxidation states in solution as well.

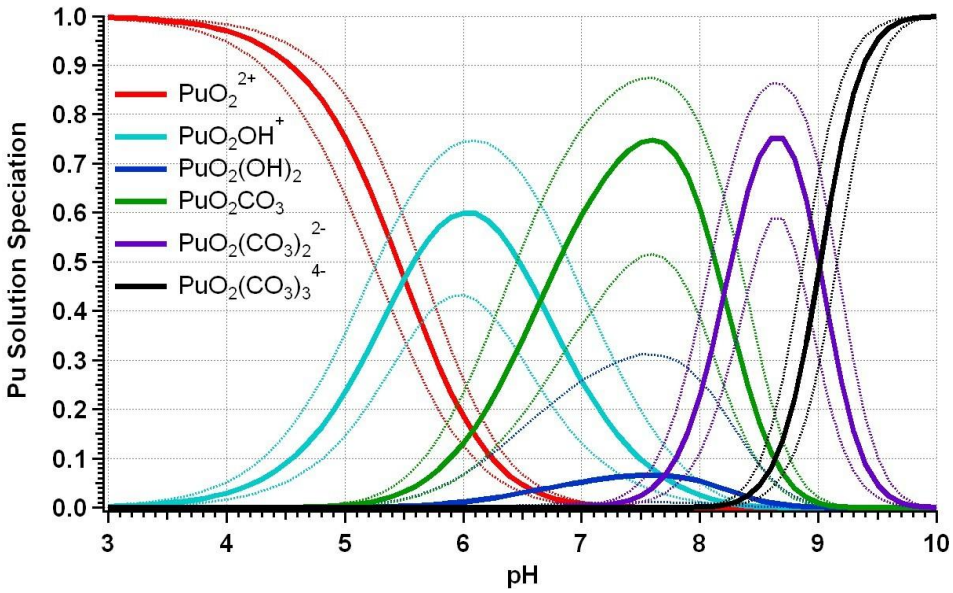

Figure 3.16. Speciation diagram calculated for Pu(VI) in aqueous solution in equilibrium with air [54, 61]. The dotted lines represent the region of 1σ uncertainty.

3.4.3 Preparation of stock solutions

All manipulation of plutonium was performed in a negative pressure glovebox, in air. A custom-made boiling flask was used when heating Pu solutions, with a long arm that connects to a bubbler system. A gentle flow of high-purity argon or nitrogen enters at the top of the flask, and then bubbles through H_2O, 7 M NaOH, and H_2O again. This was used to prevent the accumulation of hot acid vapors inside the glovebox and to contain perchlorate. *Warning: perchloric acid must be handled with extreme caution! Many perchlorate salts and compounds are shock-sensitive and explosive when dry at elevated temperatures. Hot perchloric acid is a very strong oxidizer, and any trace organic material in contact with perchloric acid at elevated temperatures can cause explosions. All acids and bases, and particularly hydrofluoric acid (HF) are corrosive and should be handled only after proper training.*

The ^{239}Pu stock solution was prepared by boiling PuO_2 powder in concentrated HNO_3 and approximately 0.09 M HF, under argon for 4 hours. HF concentrations between 0.05 M and 0.2 M will greatly increase the rate of dissolution of PuO_2 in HNO_3, but higher concentrations of HF will cause precipitation of PuF_4. The dark green solution was verified by Vis-NIR spectroscopy to be Pu(IV), and excess $NaNO_2$ was added to ensure that the Pu was completely tetravalent. The PuO_2 powder used was "weapons grade", which generally means that it is at least 93% ^{239}Pu, but small amounts of other plutonium isotopes are also present. The largest chemical impurity is ^{241}Am, which is introduced via beta decay of ^{241}Pu with a 14.35 year half-life. The Pu was separated from ^{241}Am and other impurities via an anion exchange column with Bio-Rad AG 1-X8 100-200 mesh capacity 1.2 mmol/mL resin, reformed in nitrate. The Pu solution was loaded onto the column in 8 M HNO_3, then the column was washed with several free column volumes of 10 M HCl before the Pu was eluted from the column with a 9:1 mixture of concentrated HCl and freshly distilled HI. A flow chart of the anion exchange procedure used is shown in Figure 3.17, with the four fractions color coded and described in Table 3.3.

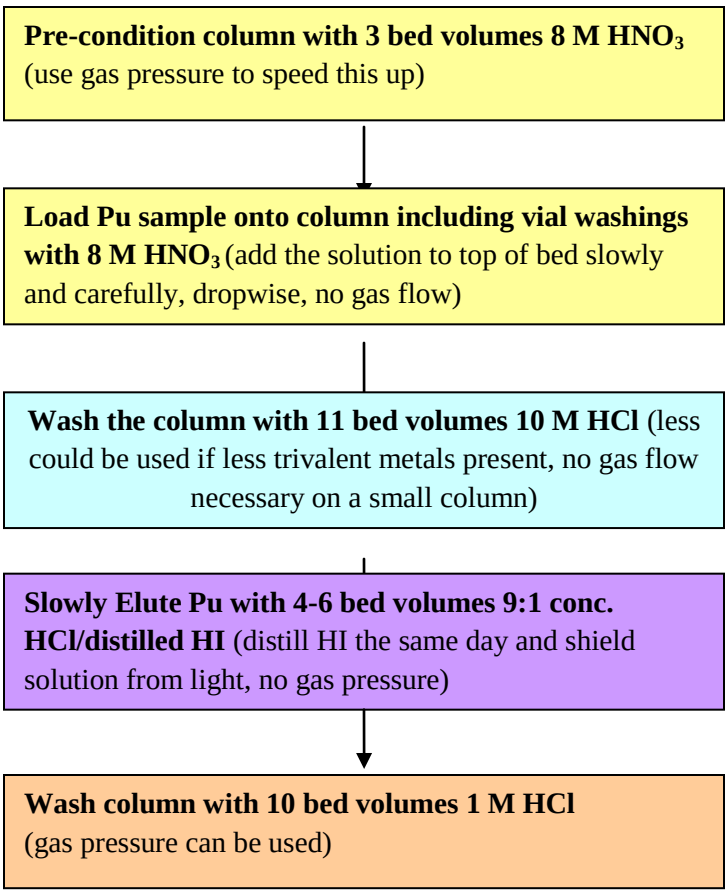

Figure 3.17. Flow chart of anion exchange procedure used for purification of plutonium purification.

Table 3.3. Descriptions of the four fractions collected in the anion exchange procedure.

Fraction 1: 8 M HNO_3 containing most of the ^{241}Am and other metals in oxidation states other than +4, which don't form anionic complexes in 8 M HNO_3. If any of the loaded Pu was in a different oxidation state it will come out here also. Fraction 1 solution is slightly yellow.
Fraction 2: Contains everything non-tetravalent that did not come out in fraction 1, in 10 M HCl. Many bed volumes are used if the amounts of non-Pu species in the solution are unknown, or known to be high (eg. A LaF_3 co-precipitation before column), but 3-4 bed volumes can be used if solution was relatively pure. It is important to flush out the nitric acid before eluting the Pu. Fraction 2 solution is clear.
Fraction 3: Contains Pu(III)Cl_3 in the HCl/HI mixture. The HI reduces the Pu(IV) to Pu(III), and quickly becomes I_2 and HI_3^-, which turns the solution dark reddish-brown. When concentrated Pu(III)Cl_3 elutes, the drops appear blue as they exit the column.
Fraction 4: Contains U(IV), Np(IV), and any other tetravalent constituent that can't be reduced by I^- in 1 M HCl. Also contains tailings from the Pu band. Fraction 4 solution is usually brown or yellow from trace HI left on the column.

The anion exchange procedure described in Figure 3.17 and Table 3.3 relies on the stronger complexation of An^{4+} by NO_3^- and Cl^- than any other oxidation state, as well as the fact that the chloride anion can displace the nitrate anion in the Pu(IV) complex. The advantage is the

high separation factors achieved, but the disadvantage is that it is rather complicated and messy. The resin is destroyed by the HI and cannot be reused. The procedure has been applied successfully on small and medium sized columns, but does not scale up well because NO_3^- can be involved in many reactions that create gas, and gas bubbles and pockets in the resin bed can destroy the column before the separation is complete. For example, HNO_3 can react with HCl according to Reactions 3.15 and 3.16.

$$HNO_3\ (aq) + 3\ HCl\ (aq) \rightarrow NOCl\ (g) + Cl_2\ (g) + 2\ H_2O\ (l) \quad (3.15)$$

$$2\ NOCl\ (g) \rightarrow 2\ NO\ (g) + Cl_2\ (g) \quad (3.16)$$

The flow of the column must be faster than the above reactions, and when this procedure was attempted with a large column (~3 mL bed volume), it slowed to a halt and the resin had to be removed and the plutonium recovered by batch extraction. An alternative method would be to use the same procedure except to load the Pu in concentrated HCl, thus avoiding the HNO_3 altogether. The problem is that PuO_2 is more difficult to dissolve in HCl. Anion exchange without a reducing agent can also be done with HCl or HNO_3, where the Pu(IV) is eluted with a low acid concentration. Those procedures are much simpler but have the disadvantage of possibly forming Pu(IV) colloids.

After ion exchange the HI was boiled away by refluxing with concentrated HCl or HNO_3. Refluxing with HNO_3 several times destroys organic material, and is an important safety precaution because trace organic materials can cause explosions when put in contact with hot perchloric acid. To make Pu(VI) stock solutions, the Pu was refluxed several times with 70% $HClO_4$ (double distilled from VYCOR, G. F. Smith) over at least three hours. Vis-NIR absorbance spectra of the final solution indicated the presence of only PuO_2^{2+}. Due to the slow self-reduction of ^{239}Pu that occurs in aqueous solutions,[111, 132] fresh diluted ^{239}Pu(VI) stock solutions were prepared in 1-2 M $HClO_4$ each week for batch experiments. The auto-reduction is slower in concentrated $HClO_4$, and these solutions were normally only re-boiled after a couple months, but were always boiled before loading Pu stock onto XAS samples.

3.4.4 Oxidation state instability

Pu(VI) was chosen as the initial Pu oxidation state for most of this work to minimize the formation of Pu(IV) precipitates and colloids in solution. Relatively high Pu concentrations were needed to observe differences in uptake by materials with such high surface areas, so Pu(IV) could not be used due to low solubility. Starting with Pu(V) would introduce Pu(IV) faster than starting with Pu(VI) at high concentrations because of the disproportionation Reaction 3.9. Therefore, Pu(VI) was chosen even though it is also unstable, and the behavior of the solution without the presence of any solid must be considered in order to properly understand the results with the mesoporous sorbents in place. Because new stock solutions were prepared each week for batch experiments, the Pu added to the samples was always at least 89% Pu(VI), and generally greater than 95% Pu(VI) initially. Once the Pu was added to the samples, the rate of auto reduction is expected to have increased slightly in the higher pH environments. The reduction of Pu depends not only on alpha radiation, but also on the redox potential of the solution,[137] which was not measured. Although the E_h were not measured, it may be approximated by the modified E_h upper limit pH relation given by Equation 3.17, which is based

on an assumed O_2 fugacity of 0.2 bars for systems open to air, along with an empirical correction.[138]

$$E_h\ (V) = 1.10 - 0.0592pH \qquad (3.17)$$

For example, the pH 4 solutions under study are likely $E_h \sim 0.86$, which would place them in the meta-stability field of aqueous Pu(V).[139] Although there is some disagreement in the literature about where the stability fields fall in Pourbaix diagrams, there is considerable evidence [111, 133, 137, 138, 140] that Pu(V) is the dominant oxidation state in solutions of pH between 3 and 9 when oxygen is present. Richard Wilson used a solvent extraction method adapted from Nitsche *et. al*[141] to determine the oxidation state of 1 μM Pu solutions in 0.1 M $NaClO_4$ of various pH, 24 hours after Pu(VI) stock was added.[62] He found that without a solid sorbent there was no Pu(IV) present at any pH, and the composition of Pu(VI) and Pu(V)/Pu(III) varied with pH. The method did not allow distinction between Pu(V) and Pu(III), but given the complete lack of Pu(IV), Pu(V) is the most likely result. For example, 65% Pu(VI) remained in pH 4 solution after 24 hours, and 34% had been reduced to Pu(V)/Pu(III). Romanchuk et al.[142] studied similar solutions to ours (2 μM Pu, added as Pu(VI) to 0.1 M $NaClO_4$), and found by solvent extraction that Pu(V) was the kinetically stable and dominant oxidation state for up to 236 days, even though the measured E_h and pH values placed the solutions in the stability fields of Pu(III) or Pu(IV). Once appreciable concentrations of Pu(V) are formed, it slowly disproportionates into Pu(VI) and Pu(IV) colloids.[111, 132, 143] Therefore it is expected that by the time of LSC measurement the solution would be a mixture of Pu(VI), Pu(V), and a very small fraction of Pu(IV) colloid. Because the time frame of most of the batch experiments was under one day, a significant portion of Pu(VI) would be expected to remain in the more acidic solutions if not for reduction by the sorbent, and the amount of Pu(IV) would be relatively small.[143] The behavior and redox speciation of Pu in some of the samples described in this work could be a little different than in the solvent extractions of Wilson[62] and Romanchuk[142] because significantly higher concentrations were used. Many of the carbon-Pu experiments were done at pH 4 in sufficient Pu concentration to measure the Pu(VI) absorption peak near 830 nm, and so control samples were monitored by Vis-NIR spectroscopy to estimate how much Pu(VI) would remain in solution after various amounts of time, without contact with the carbon solid.

Two types of control samples were prepared to test the stability and solubility of Pu(VI) at pH 4 with high concentrations: one without any solid material, and one in which SBA-15 mesoporous silica replaced carbon as the solid sorbent material. Silica was chosen as a control solid because it is not expected to participate in redox reactions, and we have observed no significant sorption of Pu(VI) to mesoporous silica from solutions with pH below 5.5 (see Figure 5.33), while sorption of tetravalent species would be expected.[144-147] The control samples were monitored by optical spectroscopy and LSC at various time intervals up to one week. Figure 3.18 shows the Pu(VI) absorbance peak in the pH 4, 0.1 M $NaClO_4$ solution without a solid sorbent, measured at various times. The solution pH was adjusted after each measurement and maintained between 3.84 and 4.14 throughout 7 days. After one day, the Pu(VI) peak near 830 nm in the spectra of these control samples showed approximately 80 percent of their original intensity, and this was further reduced to about 40 percent after one week. The peak height ratios cannot precisely quantify the remaining Pu(VI) due to limiting resolution in the spectrometer, and small absorbance of light at this wavelength by other oxidation states, but the peak height is certainly correlated with [Pu(VI)]. This test confirmed that Pu(VI) is unstable in the present solution

conditions, as might be expected. However, it also shows that the extent of Pu reduction in the absence of any solid is limited on the time scale of the sorption experiments. LSC monitoring showed that approximately 95% of Pu in the control samples remained in the solution phase after 4 days. This result in the silica samples suggests that Pu(IV) is not the dominant reduced Pu species in the control samples, so it is likely Pu(V). The LSC result clearly indicates that the observed sorption is due to the presence of the solid sorbent rather than precipitation or some other artifact of the experimental method.

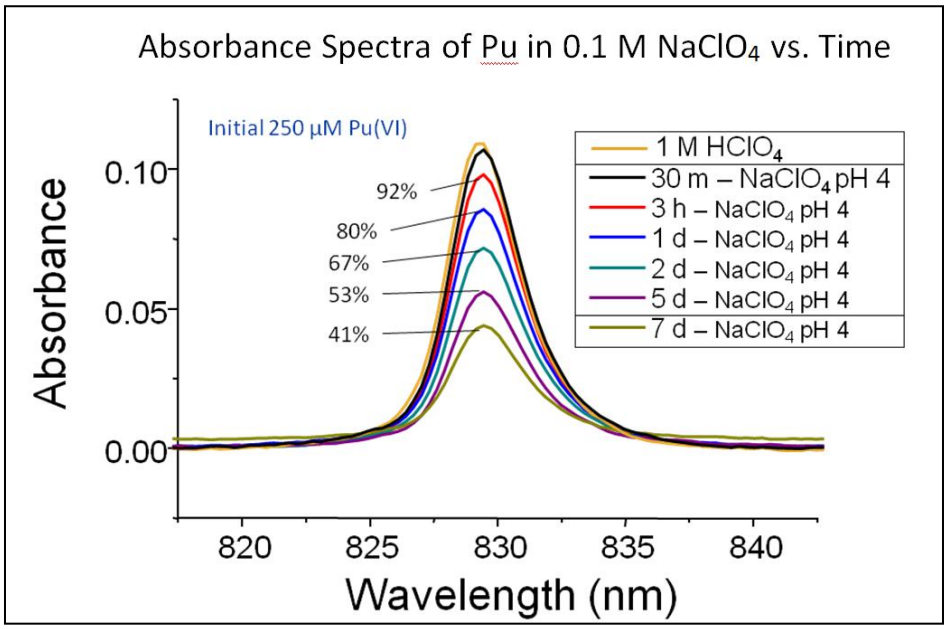

Figure 3.18 Baseline-corrected absorbance of light around 830 nm by 250 ± 17 µM Pu, 0.1 M $NaClO_4$, pH 4 solution, monitored over time. Percentages refer to the peak height relative to the peak height measured 30 minutes after solution preparation.

Based on the control test, and the data from the literature discussed above, it is clear that the batch sorption experiments, in lieu of any redox chemistry with the surface, are measuring the total Pu adsorption of a mixture between Pu(VI) and Pu(V). In this dissertation, the term "oxidized Pu" will be used to describe any mixture of Pu(V) and Pu(VI). The XANES analysis discussed in Sections 5.5 and 6.4 estimates the oxidation state distribution of Pu adsorbed to the mesoporous solid surfaces, *in situ*. When interpreting these results, it is important to remember that the reduction of Pu(VI) to Pu(V) is expected without any solid sorbent, and thus does not indicate redox activity of the surface. The presence of significant (> 10%) fractions of Pu(IV) in the samples indicates that the surface acted as a reducing agent toward Pu.

4 The Chemistry of the Lanthanides

In the early phase of this project, some batch experiments with aqueous solutions of Ce and Eu were performed with functionalized SBA-15, and later the batch sorption of Eu to C-CS-type OMCs was tested. Although the work with these elements was limited compared to what was done with plutonium, a brief introduction to the chemistry of the 4f series is warranted.

Sections 4.1-4.3 give some fundamental background of the lanthanide chemistry, mostly taken from books by Moeller[148], and Kaltsoyannis and Scott[149]. The methods used for quantification of the lanthanide ions in this work are briefly explained in Section 4.4.

The historically used term "rare earth elements" for the lanthanides comes from their discovery as oxides, which involved a great deal of confusion regarding elemental composition. In fact, most of these elements are rather abundant within the igneous rocks of the earth's crust, and compared with the actinides they are very common (except promethium, which occurs only as a fission product). Lanthanide chemistry began with the discovery of the minerals called gadolinite (C. A. Arrhenius, 1787, in Ytterby, Sweden) and cerite (A.F. Cronstedt, 1771, in Bastnäs, Sweden). From these minerals two previously unknown oxides, or "earths" as they were called then, were isolated: yttria from gadolinite (J. Gadolin, 1794) and ceria from cerite (M.H. Klaproth, J.J. Berzelius, and W. Hisinger, 1803). These oxides turned out to be complex mixtures, and through the painstaking efforts of countless researchers over the next century, the individual lanthanide elements were isolated and identified from yttria and ceria. The remarkable similarity of the compounds of the fourteen new elements led to much confusion, and meant that a fractional approach was required for complete separation using hundreds of steps and employing crystallization, precipitation, thermal decomposition, and extraction procedures. The challenges associated with the simplification of yttria and ceria, and characterization of their fractions, inspired the development of many important laboratory techniques and analytical methods, especially of emission and absorption spectroscopy. Today the only two commercially-important lanthanide minerals are monazite ($LnPO_4$) and bastnaesite ($LnCO_3F$).

The lanthanides have found a wide variety of applications. Alloys of cerium and other lighter lanthanides (known as mischmetals) have sufficiently strong reducing power for metallurgical applications. Lanthanide compounds, especially cerium oxide, have been used extensively in ceramic applications in glasses and enamels. Lanthanide oxides and chlorides have been used for catalysis of various organic reactions. The paramagnetic and ferromagnetic properties of lanthanides and their compounds have proved useful for several industrial applications, and for development of lanthanide shift reagents in NMR spectroscopy and contrast agents for magnetic resonance imaging. Several lanthanide compounds have gained interest as semiconductors and capacitors, but the property most widely used by electronics industries is the fluorescence arising from f-f transitions in Ln^{3+} ions. For example, color television sets use the green light emitted by Tb^{3+} and the red light emitted by Eu^{3+}. The near-IR emission of Nd^{3+} is commonly employed in Nd:YAG (yttrium aluminum garnet) lasers. Several of the lanthanides have high neutron capture cross sections, and their alloys and compounds have been used for control, shielding, and flux-suppressing devices in the nuclear industry. Also, lanthanides are a significant fraction of the high-activity fission products in spent nuclear fuel, which is of interest to actinide chemists and inspired their incorporation into this project. As described in the following sections, the +3 oxidation state is most common for all lanthanides, and these cations are often used in chemistry laboratories as analogs for trivalent actinides.

4.1 Electronic configurations

The generally accepted electron configurations for the elemental lanthanide series and their most common oxidation state, +3 cations, are tabulated in Table 4.1. The 4f orbitals are close in energy to the 5d, making them difficult to distinguish, but the observed emission spectroscopic and magnetic properties are consistent with the f orbitals generally being filled

preferentially across the series. The reason for the trivalent oxidation state being so dominant for all the lanthanides is not obvious from their electron configurations. For the entire series, the fourth ionization energy is greater than the sum of the first three ionization energies, although only marginally so for Ce, which exhibits tetravalent chemistry under some oxidizing conditions. The energetics involved with solvation or compound formation, compared with the ionization energies, render elemental lanthanides powerful reducing agents, and the other oxidation states widely inaccessible. The most notable exceptions to this may be explained by the electron configuration. Tetravalent Ce has the noble gas configuration of [Xe], and tetravalent Tb has the half-filled 4f orbital ($4f^7$). Likewise, compounds and solutions of dipositive Eu and Yb can be obtained due to stability of the $4f^7$ and $4f^{14}$ configurations.

Table 4.1. Electron configurations and radii of lanthanide atoms and trivalent cations.

symbol	configuration	+3 configuration	atomic radius (Å)	+3 ionic radius (Å)
La	$[Xe]5d^16s^2$	$[Xe]4f^0$	1.877	1.061
Ce	$[Xe]4f^15d^16s^2$	$[Xe]4f^1$	1.82	1.034
Pr	$[Xe]4f^36s^2$	$[Xe]4f^2$	1.828	1.013
Nd	$[Xe]4f^46s^2$	$[Xe]4f^3$	1.821	0.995
Pm	$[Xe]4f^56s^2$	$[Xe]4f^4$		0.979
Sm	$[Xe]4f^66s^2$	$[Xe]4f^5$	1.802	0.964
Eu	$[Xe]4f^76s^2$	$[Xe]4f^6$	2.042	0.950
Gd	$[Xe]4f^75d^16s^2$	$[Xe]4f^7$	1.802	0.938
Tb	$[Xe]4f^85d^16s^2$ or $[Xe]4f^96s^2$	$[Xe]4f^8$	1.782	0.923
Dy	$[Xe]4f^{10}6s^2$	$[Xe]4f^9$	1.773	0.908
Ho	$[Xe]4f^{11}6s^2$	$[Xe]4f^{10}$	1.766	0.894
Er	$[Xe]4f^{12}6s^2$	$[Xe]4f^{11}$	1.757	0.881
Tm	$[Xe]4f^{13}6s^2$	$[Xe]4f^{12}$	1.746	0.869
Yb	$[Xe]4f^{14}6s^2$	$[Xe]4f^{13}$	1.940	0.858
Lu	$[Xe]4f^{14}5d^16s^2$	$[Xe]4f^{14}$	1.734	0.848

Table 4.1 also shows the atomic and trivalent cationic radii of the lanthanides. One of the indirect consequences of the lanthanides' electron configurations is the steady decrease in ionic radii with increasing atomic number across the series, known as the lanthanide contraction. The contraction occurs because the electrons in 4f orbitals do not shield each other well from the nuclear charge. Although the addition of protons across the series is formally balanced by the addition of f-electrons, the effective nuclear charge felt by the valence electrons increases due to poor shielding, and the electrons become more tightly bound giving a smaller ionic radius. As a result, the Lewis acidity of these cations increases across the series with atomic number, and these differences are reflected in hydrolysis of ions, solubilities of salts, thermal decomposition of oxy salts, and complexation by ligands. Given the overall chemical similarity of the 4f elements, the lanthanide contraction is the main phenomenon that makes their chemical separation possible.

Direct consequences of the lanthanides' electron configurations include the magnetic and spectroscopic properties that arise from unpaired electrons. Hund's rule indicates that all seven f orbitals must be singly occupied before any pairing can occur, so all of the lanthanide ions

except Y^{3+}, La^{3+}, Lu^{3+}, Yb^{2+}, and Ce^{4+} are paramagnetic. The permanent magnetic moments of the lanthanides depend on spin and orbital effects, except Gd^{3+}, which only depends directly on electron spin. The ions Dy^{3+} and Ho^{3+} have the largest magnetic moments of the series, over 10 Bohr magnetons. Unlike the cations of d-transition elements, the magnetic properties of the lanthanides are unaffected by complexing ligands or anions. The 4f electrons are so tightly bound that they are not available for chemical bonding, and maintain their orbital structure even when complexed. This is also observed in the optical absorption spectra of the lanthanides (and colors of their crystalline salts) which seem to be independent of any anions or complexing groups present. The visible light absorption bands of the actinides are much very well defined because the 4f orbitals are shielded from the ligand by the 5d and 6s orbitals, and this yield sharp peaks in their absorption spectra. Also because of the unavailability of the 4f electrons, there is much less vibronic coupling in lanthanide complexes than d-transition metal complexes. Since it is the vibronic coupling (crystal field effects) that allow the formally forbidden d-d or f-f transitions to occur, the absorption peaks are much less intense for lanthanides. A few lanthanide ions including Ce^{3+} and Tb^{3+} have broader and more intense absorption bands in the UV region as a result of f-d transitions, which are allowed by electric dipole selection rules.

4.2 Complexation chemistry

The 4f valance electrons of the lanthanide cations are so closely bound that they are unavailable for chemical bonding, and to an incoming ligand the lanthanide cation appears as a noble gas atom, but with a positive charge. Thus the lanthanides are hard Lewis acids, which interact electrostatically with hard Lewis bases like oxygen donors and F^-. In aqueous solution, there are very few monodentate ligands that can compete with H_2O for lanthanide coordination. The Ln^{3+} cations are thought to coordinate 8 to 9 water molecules in aqueous solution, but coordination numbers up to 12 can be found. The study of substitution reaction mechanisms for lanthanide complexes with monodentate ligands is very difficult because they are so labile, with water exchange lifetimes on the order of 10^{-9} seconds. The coordination geometries are difficult to measure because of the lack of covalent bonding. However, X-ray crystallography has been used to examine many hydrated lanthanide ions in the solid state, and they generally form tricapped trigonal prismatic complexes. The most effective ligands for lanthanide complexation are oxygen-containing chelators and macrocyclic ligands. In non-aqueous solvents, the lanthanides can form linear alkoxide fragments (R-O-Ln) and planar complexes with dialkylamides (R_2N-Ln). The unique properties of lanthanides are exploited in organic chemistry for functional group transformations and catalysis. Their organometallic chemistry has also been studied, but is rather complicated compared to d-block organometallics, with complexes that are extremely sensitive to oxygen and water.

Separation of the lanthanides is difficult because they all generally exist as hydrated +3 cations and are similar chemically. The chemist must take advantage of the lanthanide contraction, as the decrease in ionic radius across the series means an increase in charge density, which creates a steady increase in the stability constants of chelate complexes. This is exploited for separation using cation exchange columns.[150] The Ln^{3+} cations sorb strongly to the stationary cation exchange resin, and then an aqueous mobile phase containing an anionic chelating ligand such as citrate or α-hydroxyisobutyrate is used to elute the lanthanide cations. The ions with the most stable chelate complexes (the smaller ones) elute first, and careful pH control increases the separation. This technique was also very important for the discovery of transcurium actinides.

Other methods for separating lanthanides may involve fractional crystallization, fractional precipitation, fractional thermal decomposition of salts, selective reduction/oxidation, and solvent extraction.

4.3 Solution chemistry

All of the lanthanide chemistry discussed in this dissertation occurred at the interface of mesoporous solids with aqueous solutions. Section 4.3.1 briefly describes some general trends of aqueous lanthanide chemistry, and Section 4.4.2 describes the specific solutions that were studied by batch methods.

4.3.1 General considerations

As mentioned in Sections 4.1 and 4.2, the lanthanides exist in aqueous solutions as 8 or 9-coordinate hydrated trivalent cations. The estimated standard reduction potentials for the Ln^{3+}-Ln^{0}couple in reaction 4.1 vary from -2.25 to -2.52 volts. Divalent Eu, Sm, and Yb can be formed under an inert atmosphere, but they are unstable and reduce water to hydrogen according to Reaction 4.2. Divalent Eu is the most stable of the three, but still the standard reduction potential for the Eu^{3+}-Eu^{2+}couple is -0.43 V.[148] Tetravalent lanthanides oxidize water to oxygen according to Reaction 4.3, and only Ce^{4+} is sufficiently kinetically stable to form aqueous coordination compounds (the standard reduction potential of Ce^{IV}-Ce^{III} couple is 1.74 V [148]).

$$Ln(s) \leftrightarrow Ln^{3+}(aq) + 3e- \quad (4.1)$$

$$2Ln^{2+}(aq) + 2H^{+}(aq) \rightarrow 2Ln^{3+}(aq) + H_2(g) \quad (4.2)$$

$$4Ln^{4+}(aq) + 2H_2O(l) \rightarrow 4Ln^{3+}(aq) + 4H^{+}(aq) + O_2(g) \quad (4.3)$$

The lanthanide salts of Cl^-, Br^-, I^-, NO_3^-, ClO_4^-, BrO_3^-, and $C_2H_3O_2^-$ are soluble in water, and these ligands are mostly displaced by water molecules in the coordination sphere of the Ln^{3+} cation in solution. On the other hand, the salts of F^-, OH^-, $C_2O_4^{2-}$, CO_3^{2-}, and PO_4^{3-} are insoluble in water. There are some slight differences in the solubilities of HCO_3^- and basic NO_3^- salts among the early (Z = 57-62) and late lanthanides (Z = 63-71), and a stark difference in the solubilities of salts formed with double sodium potassium or thallium(I) sulfates, $Ln_2(SO_4)_3.M^I_2SO_4.nH_2O$. Although the lanthanide oxides and hydroxides are insoluble in water, they are soluble in acidic solutions. The Ln^{3+} cations undergo hydrolysis described in Reaction 3.14, which leads to precipitation of $LnOH_3$ solid from high-pH solutions. The tendency of the Ln^{3+} cations to hydrolyze increases with atomic number due to the increased charge density via the lanthanide contraction. Figure 4.1 shows an example speciation diagram for Eu in aqueous solution.[30] The first hydrolysis product $Eu(OH)^{2+}$ begins to form around pH 5.5, and $Eu(OH)_3$ will precipitate out of solutions with pH $\geq$ 7.

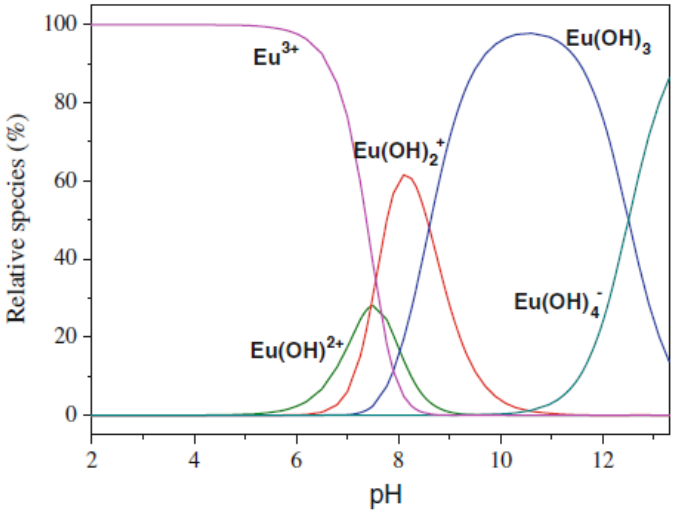

Figure 4.1. Distribution of Eu(III) species as a function of solution pH in aqeous 0.01 M $NaClO_4$ solution.[30]

The lanthanide batch experiments in our work were limited to solutions with pH ≤ 6 in order to avoid insoluble hydrolysis products. The early experiments with Ce and Zr were in a 0.1 M $NaNO_3$ matrix, and the later Eu-carbon experiments were in 0.1 M NaCl. Thus the complexation by Cl^- and NO_3^- must be considered in the speciation. The formation of metal ion complexes with simple inorganic ligands can be written in a general form as in Reaction 4.4, with the overall formation constant, β_q given by Equation 4.5.

$$M + qL \leftrightarrow ML_q \quad (4.4)$$

$$\beta_q = \frac{[ML_q]}{[M][L]^q} \quad (4.5)$$

Alternatively, the reaction may be written stepwise as in Reaction 4.6, with the stepwise stability constant K given by Equation 4.7.

$$ML_{q-1} + L \leftrightarrow ML_q \quad (4.6)$$

$$K_q = \frac{[ML_q]}{[ML_{q-1}][L]} \quad (4.7)$$

Thermodynamic stability constants are measured using a variety of techniques, including solvent extraction and spectroscopic techniques. The values will vary depending on the experimental method and solution conditions, but give a general idea of the favorability of complex formation in a given system, and can be used to estimate speciation. Based on thermodynamic data tabulated by Smith and Martell,[151] the compositions of Eu in 0.1 M NaCl, as well as Ce and Zr in 0.1 M $NaNO_3$ were estimated and tabulated in Table 4.2. These speciations are approximate, as the tabulated stability constants used were measured at higher ionic strengths than our experimental conditions, and the [L] term in Equation 4.5 was approximated at 0.1 before and after complexation. Furthermore, it has been evidenced by NMR and EXAFS studies that only outer-sphere chloride complexes of Eu are formed in chloride concentrations below ~5 M.[152]

Table 4.2. Estimated Eu speciation in 0.1 M chloride or nitrate matrices.

M/L	% M^{n+}	% $ML^{(n-1)+}$	% $ML_2^{(n-2)+}$
Eu^{3+}/0.1 M Cl^-	92.5	7.3	0.2
Ce^{3+}/0.1 M NO_3^-	86.1	13.7	0.2
Zr^{4+}/0.1 M NO_3^-	81.2	17.8	1.0

4.3.2 Preparation of lanthanide solutions for batch experiments

The first set of batch sorption experiments in this project examined the sorption of Eu(III), Ce(III), and Zr(IV) by functionalized mesoporous silica. Zirconium was examined as a model tetravalent fission product, which could also hint at the behavior of the materials toward tetravalent actinides. The analytes were measured by inductively coupled plasma mass spectrometry (ICP-MS) as described in Section 4.4.1, and so the concentrations of the solutions were calculated and measured by weight instead of volumetrically. A high precision Mettler Toledo balance was used along with a lower precision, higher capacity balance. The europium solutions were prepared by diluting a 50% $Eu(ClO_4)_3.6H_2O$ aqueous solution from Alfa Aesar with 0.1 M $NaClO_4$ that was prepared using the salt from Sigma Aldrich and water that was doubly distilled and sent through a Milli-Q (Milli-pore) filtration system. Solutions of 1 part per million (ppm) (6.6 μM) and 2 ppm (13 μM) Eu were prepared. In a similar manner, 2 ppm (22 μM) Zr solution was prepared in a 0.1 M $NaNO_3$ (Aldrich) solution by diluting a 35% wt. $ZrO(NO_3)_2$ 0.1 M HNO_3 solution from Alfa Aesar. The 2 ppm (14 μM) Ce solution was prepared by weighing the $Ce(NO_3)_3.6H_2O$ salt (supplier unknown) and dissolving in 0.1 M $NaNO_3$ solution.

The batch sorption studies of Eu(III) with ordered mesoporous carbon were performed using the ^{152}Eu radiotracer method described in Section 4.4.2. Europium stock solutions (1.25 ± 0.08 mM Eu, and higher concentrations) were prepared by weighing $EuCl_3.6H_2O$ (Aldrich, 99.99%) and dissolving in 0.1 M HCl (Fluka analytical grade HCl, diluted in 18.2 MΩcm doubly distilled water). The ^{152}Eu solution in 0.1 M HCl was purchased from Eckert & Ziegler and used to spike the stock solutions to reach a total specific activity of 1002 ± 100 Bq/μL. The stock solutions were added volumetrically to pre-prepared samples of mesoporous carbon with 0.1 < NaCl (Aldrich).

4.4 Measurement and detection

The measurement of lanthanide analytes was done in two different ways, by inductively coupled plasma mass spectrometry (ICP-MS) in the early experiments, and by using a radiotracer in more recent experiments. Although both methods have their advantages and disadvantages, your author has the bias of a radiochemist and prefers the radiotracer technique. The best thing about ICP-MS compared to radiochemistry is that sample analysis with the autosampler is much faster than gamma counting, so results of a series of batch experiments can be obtained within one day. However, ICP-MS is more labor intensive on the front-end with extensive sample preparation which relies on the precision and accuracy of a balance. Also, the data analysis is slightly more complicated, with more room for misinterpretation. Both methods are briefly described in the following sections.

4.4.1 Inductively coupled plasma mass spectrometry

Measurements of the Zr, Ce and Eu concentrations of solutions in batch experiments with functionalized mesoporous silica was achieved with a Perkin Elmer ELAN DRC II ICP-MS. Some of the measurements and analysis were done by Kestrel Brogan, and others were completed by the author using the methods of Kestrel Brogan, which are well described in appendix A of her thesis.[83] Here only a brief overview is presented.

ICP-MS is an analytical instrument designed for trace metal analysis, which has a wide analytical range covering around 9 orders of magnitude, with detection limits of some elements as low as a few parts per trillion (ppt). Another advantage is rapid sample analysis, and the autosampler makes it convenient to analyze many samples in a single run. Also a wide range of sample compositions can be analyzed, and there is no need to handle radioactivity.

Figure 4.2 shows a diagram of the Perkin Elmer Elan DRC II ICP-MS system. The acidic sample is injected into a nebulizer by a peristaltic pump, which can maintain a consistent flow rate regardless of viscosity differences. The nebulizer uses mechanical forces of argon gas to create the sample aerosol, which is sent to the spray chamber. The spray chamber allows only small droplets to enter the plasma torch, and also smooths out pulses that occur in the nebulization process. The plasma torch is a set of concentric quartz tubes wrapped at the end by an RF coil. The torch creates a plasma with temperature around 6000 K out of argon using seed electrons from an electron gun, and RF energy. When the aerosols enter the plasma they dry immediately, any molecules are dissociated, and each atom is ionized to form a singly-charged cation. The ionized sample is sent through a set of cones where it is put under vacuum by a set of roughing and then turbomolecular pumps. The autolens and shadow stop are the ion optics for this particular instrument, which removes phonons and neutral species, and directs ions of the appropriate masses to the quadrupole.

The dynamic reaction chamber (DRC) is an optional feature that is used when there are known interferences from other ions in the sample that have the same mass-to-charge ratio as the analyte. The DRC has a quadrupole inside a reaction chamber that is filled with a reaction gas specifically selected for the matrix and interference problem. The reaction gas will change the mass of the interfering ion through collisional dissociation, electron or proton transfer, or oxidation. The quadrupole is tuned to define a mass bandpass window that removes other ions prior to entering the DRC to avoid secondary interferences.

The quadrupole mass spectrometer changes voltages and frequencies among its four rods to allow only ions of one mass-to-charge ratio to pass through. During a single measurement, a range of mass-to-charge ratios is scanned, and each analyte is assayed multiple times per sample to obtain better statistics. The detector is an electron multiplier where the analyte ions hit the first dynode and the electrons released are multiplied at subsequent dynodes to create a measurable pulse. The pulse amplitude is related to the sample concentration, which is determined via calibration with a series of carefully prepared standards. The detector can operate in the more sensitive analog mode with samples up to about 500 parts per billion (ppb), and higher concentrations must be measured in digital mode with a lower detection limit.

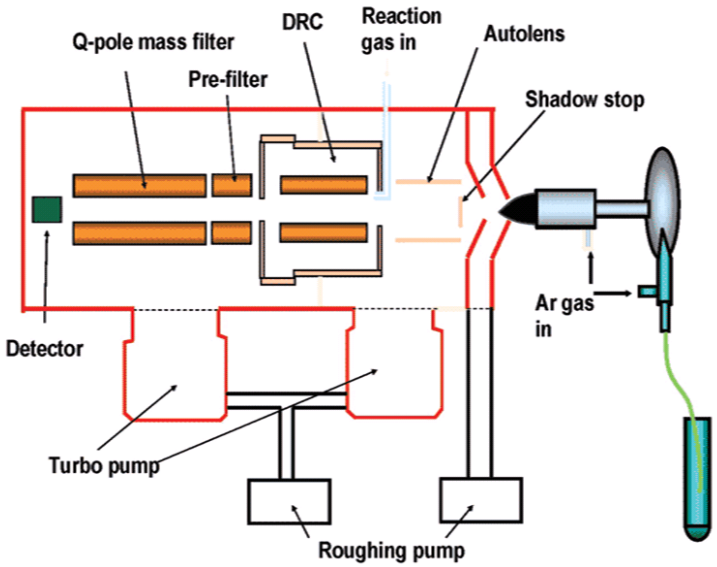

Figure 4.2. Schematic of Perkin Elmer ELAN DRC II ICP-MS system.[83]

The proper preparation of the standards and samples for ICP-MS can be rather extensive. Everything is acidified to 2% nitric acid, and ultrapure chemicals and vessels should be used to avoid interferences and high backgrounds. In order to maintain a low detection limit the analog mode was used on the detector, and thus the standard series generally ranged from 100 ppt to 500 ppb. The solution matrix of the standards should be matched to the samples in order to prevent differences in nebulizing efficiency or elemental interactions. Certified standards can be purchased and diluted gravimetrically. The samples themselves are diluted gravimetrically with ultrapure 2% nitric acid, which is also used to prepare blank samples. In batch sorption studies, the analyte concentration may be anything from zero up to the initial concentration. Therefore, for each sample a dilute and a concentrated version was prepared so that one of them would be within the appropriate range for detection. All samples and standards need an internal standard to account for instrumental drift. Every sample contains the same concentration (usually 20 ppb) of an element that is near to but at least one atomic unit away from the analyte of interest in the periodic table. For the lanthanides, Ho was used, and Sc was used for Zr.

The instrument's software averages replicates, subtracts the blank, and rounds to the nearest whole count. Then, the software multiplies the intensities in the data by the ratio of the intensity of the internal standard in the first standard to that measured in the sample. It calculates a concentration based on the calibration curve, and gives uncertainty equal to the standard deviation for the measured replicates. Most users take the concentrations directly from the software to be multiplied by the dilution factors from sample preparation. Analysis of the raw data was also performed outside of the software package in order to account for human errors and differences in internal standard concentrations. For the lanthanides, the measured concentrations were a mysterious factor of 2 greater than they should have been. However, the systematic error seemed to be consistent, and since the percent sorption was calculated relative to control samples with no solid sorbent, the results should still hold.

Overall ICP-MS is the preferred method of analysis for non-radioactive samples. It has a low detection limit of about 10 ppt, which is ~7×10^{-11} M Eu, and sample analysis is fast and

automated. The user must be aware of possible interferences, and very patient and careful during preparation of samples and standards for analysis. The enemy of the ICP-MS user is static electricity and humidity changes that can cause drifts in the high-precision balances used for preparations.

4.4.2 Detection with a ^{152}Eu radiotracer

Batch experiments with ordered mesoporous carbon and europium were performed by Erin May, using a ^{152}Eu radiotracer for measurement by gamma spectroscopy. The natural Eu stock solutions were prepared and spiked with ^{152}Eu as described in Section 4.3.2. This isotope of europium is produced by fast and thermal neutron activation, and decays 72.1% of the time by electron capture as in Reaction 4.8, and 27.9 % of the time by β^- decay, shown in Reaction 4.9.

$$^{152}_{63}Eu + e^- \rightarrow {}^{152}_{62}Sm + \nu_e \quad (4.8)$$

$$^{152}_{63}Eu \rightarrow {}^{152}_{64}Gd + \bar{\upsilon}_e \quad (4.9)$$

The decays in Reactions 4.8 and 4.9 give an overall half-life of 13.537 years, and give rise to many gamma rays. For convenience, the gamma line at 344 keV with intensity of 26.5% was chosen for quantification of Eu in solutions. Aqueous aliquots (100 µL) from the Eu samples were pipetted into 1.5 mL conical vials, which were placed into 20 mL vials and counted for at least 2 hours each with a high purity germanium detector (Ortec). Activities counted in duplicate aliquots were averaged. The principles behind gamma detection with HPGe detectors are described in Section 3.3.1. Figure 4.3 shows an example gamma spectrum on a log scale of a solution spiked with ^{152}Eu, with the 344 keV peak highlighted in red.

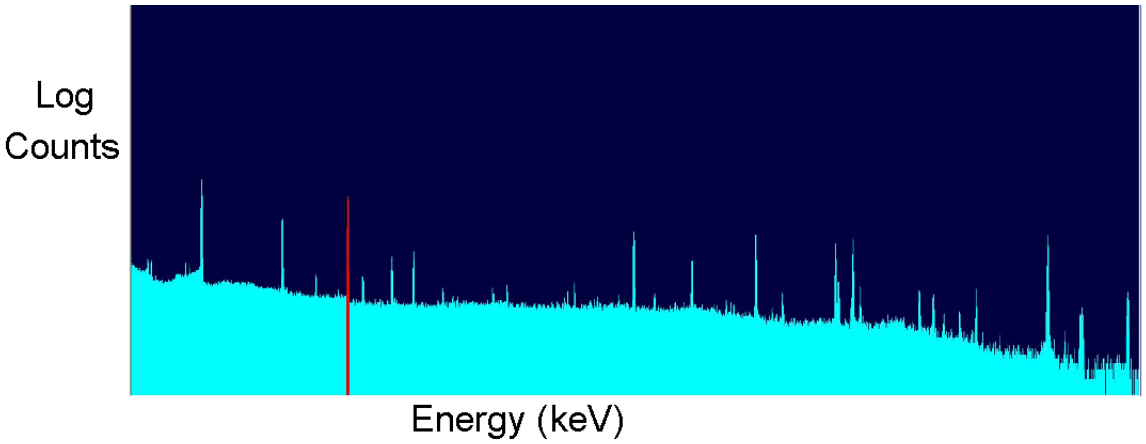

Figure 4.3. Gamma spectrum of ^{152}Eu spiked solution on a log scale. The 344 keV peak used for quantification is highlighted in red.

The advantages to using a radiotracer instead of ICP-MS are that sample preparation is very simple, and data analysis is relatively straightforward. Unlike ICP-MS, there are no matrix effects or sample phase transformations before counting. The biggest disadvantage is that it takes so long to count the samples, which are switched manually. Two hours was the minimum count time, but samples with low concentrations (high sorption) were counted for longer in order to obtain better counting statistics. Because duplicate aliquots were taken from duplicate samples, it

can take weeks to complete the counting from one set of batch sorption experiments. It was determined that no decay correction was needed on this timescale for ^{152}Eu.

The uncertainty of the Eu concentration includes propagation of the uncertainty in the concentration of carrier Eu in the stock, pipetting uncertainty (estimated at 5% based on the pippettors used), the standard variance between duplicate aliquots, variations in detection geometry, and nuclear counting statistics. The largest possible sources of random error in these experiments are from pipetting and detection geometry variations. Great care was taken to ensure consistent counting geometry. Changing the size and shape of the sample aliquot actually affects the geometric efficiency, so 100 μL was always used. For a given set of batch experiments, the same spiked Eu stock was used, and the amount of stock added was counted for reference. However, the geometric efficiency difference due to different volumes of stock and sample aliquots introduced systematic errors, so the initial count rates for percent sorption calculations were determined by counting 100 μL aliquots from control samples for every set of experiments, which had the same solution and no solid sorbent material. By counting a 100 μL aliquot of a standard solution, the overall detection efficiency at 344 keV was determined to be 5.6 %, and the maximum background was 0.1 counts per second (cps). The detection limit of two times background count rate is 3.6 Bq, which is 3.7 X 10^{-11} M ^{152}Eu in a 100 μL aliquot if no carrier is used. In this work, the lowest concentrations studied were 10 μM Eu, and a carrier was always used.

5 Organically Modified Silica

Separation or selective sequestration of actinides invariably relies on differences in the chemistry of the elements, thus the ability to manipulate surface chemistry is imperative to the design of solid extractants. Silica was naturally the first ordered mesoporous material to undergo extensive functionalization, because its surface chemistry is well known and can undergo several kinds of reactions. Macroporous silica gels and beads have long been tested as ion exchangers and used as solid supports for actinide extractions,[144, 153-162] thus the methods for chemical grafting and impregnation of silica for such applications had been established. Ordered mesoporous silica offers several advantages including larger surface areas and the greater control that comes with a highly ordered system. Five years after the first reports of the synthesis of MCM-41 mesoporous silica,[1, 64] the materials chemistry group at Pacific Northwest National Laboratory (PNNL) reported an efficient method for chemical functionalization,[79] and before long they applied the functionalized mesoporous materials for sorption of lanthanides and actinides.[15-17, 19, 21, 22] The early work in this project took a similar approach but used SBA-15 mesoporous silica as the standard substrate. Our collaborators in the Yang group at UC Berkeley were very familiar with the synthesis of SBA-15, and the synthesis is generally easier than that of MCM-41. Other advantages include the larger pore-size range than MCM-41, and the increased thermal and chemical stability that comes with thicker pore walls and a pure silica matrix instead of aluminosilicate.

This chapter describes the work that was done to synthesize functionalized SBA-15 materials and test their affinity for Pu, and (to a limited extent) Zr, Ce and Eu. Section 5.1 provides a brief literature review to summarize some work from other groups in the areas of lanthanide or actinide sequestration and extraction using functionalized mesoporous silica and similar materials. The synthesis (performed by members of the Yang group) and properties of the

SBA-15 silica substrate used in this work are presented in Section 5.2, and Section 5.3 includes important results regarding the functionalization of SBA-15. The functionalization step was done by the author, with help from former Junior Specialist Aude Hubaud. The grafting reaction used to create self-assembled monolayers was optimized for the SBA-15 substrate using the simple amine, aminopropyltriethoxysilane (APS) (Section 5.3.2). Several functionalized SBA-15 materials (Section 5.3.3), were prepared with organosilanes that were commercially available from the Gelest company, along with one based on the carbamoylphosphonate "Ac-Phos" ligand that was first reported by the PNNL group,[163] and had to be synthesized in-house (described in Section 5.3.4). Resistance or instability of functionalized silica toward acid hydrolysis is a key issue defining the scope of their application as actinide extractants, and a quick test of this is presented for Ac-Phos-SBA-15 in Section 5.3.5.

Section 5.4 describes the results of batch sorption experiments done with Pu, Zr, Eu and Ce and functionalized mesoporous materials. Initial experiments were done by the author and Kestrel Brogan, and more extensive work of the author involved Pu(VI) complexation by Ac-Phos-SBA-15. Samples of Ac-Phos-SBA-15 with Pu(IV) and Pu(VI), as well as TESPMA-SBA-15 with Pu(VI) were measured with Pu L_{III} XAS, and the results of data analysis done by Yung-Jin Hu and Dr. Dan Olive are shown in Section 5.5. A great deal was learned from all of these experiments regarding the appropriate experimental conditions, potential benefits and limitations of actinide sorption and extraction with functionalized mesoporous silica. The realization of novel functionalized mesoporous silicas with successful application toward actinide extraction was found to be very limited without extensive endeavors in organic synthesis. The most effective ligand tested in the batch sorption experiments was the Ac-Phos, which seemed to show little to no selectivity among different cations. Currently other students in the Nitsche group are extensively testing the acid resistance of functionalized mesoporous silica, and collaborating with synthetic organic chemists and specialized companies to create novel functionalized mesoporous silicas for extraction chromatography.

5.1 Background and previous work

Silica materials were the first synthesized and the most extensively researched ordered mesoporous solids. They were first synthesized for applications in catalysis, but the sudden increase in interest in their synthesis and chemistry led to a variety of new properties and applications. With high surface area, ordered structure, and large pore size, it was inevitable that mesoporous silica would be functionalized for the purpose of removing toxic contaminants from aqueous solutions. The silica matrix is also compatible with vitrification, which can condense and immobilize radioactive waste for storage in a geological repository. However, not all organic ligands are compatible with this process, as the toxicity and volatility of the incineration products must be considered. Table 5.1 summarizes some of the work that has been done by other research groups with functionalized mesoporous silica and similar materials for actinide sorption or extraction. The name given in the first column may or may not be the principal investigator, but was a common author in the cited literature. An exhaustive literature review will not be attempted here, but some of the work that is most similar to this project will be discussed.

Table 5.1. Summary of work involving organically functionalized silica for actinide sorption of extraction.

Group	Type of Substrate	Ligand types	Target Species	References
Pacific Northwest National Laboratory, USA, Fryxell, *et al.*	MCM-41	HOPOs, amide-phosphonates, carboxylamides, diamides, diphosphonic acids	U(VI), Pu(IV), Am(III), Np(V), Ln(III)	9, 12, 15-19, 21-23, 37-40, 81, 163, 164
Institut De Chemie Séparative de Marcoule, France, Meyer, *et al.*	Silica gel	polyamines, polyethers, pyridine diamides	Pu(IV), Am(III), Ln(III)	5, 165-170
Ecole Natl Super Chim Montpellier, France, Trens, *et al.*	MCM-41	diamides	Am(III), Eu(III)	20
University of Chicago, USA, Lin, *et. al.*	Commercial mesoporous silica and carbon	oximes, amide phosphonates, carboxylamides	U(VI)	33, 45, 46
Nucl. Sci. & Tech. Res. Inst, Iran, Jamali, *et al.*	Mesoporous silica	furals, salicycaldehydes	U(VI), Th(IV)	14, 24
Univ. Laval, Canada, Lebed *et al.*	SBA-15, KIT-6	phosphonate	U(VI)	26
Argonne National Laboratory, USA, Shkrob, *et. al.*	Macroporous glass beads	DOTA, DTPA, imide-phosphonates	Ln(III)	171
Dongguk University-Seoul Campus, Korea, Jin Kwon, *et. al.*	SBA-15, MCM-41, Si nanoparticles	CMPO	N/A	51

Group	Type of Substrate	Ligand types	Target Species	References
Institute of Materials Research, UK, Laboratory of Radiochemistry, Finland, Dyer *et al*.	MCM-41	doped with Al, Zn, B oxides	^{241}Am and ^{236}Pu + fission products	47
Chinese Academy of Science, Yuan *et. al.*	MCM-48	phosphonate	U(VI)	28
Zhejiang University, China, Zhang *et al.*	Macroporous silica gel	Calyx[4]arene, crown ethers, TODGA, CMPO and BTP polymer composites	Am(III), Cm(III), Ln(III) + other fission products	172-186
Bhabha Atomic Research Centre, India, Bhanushali, *et al*., Naik *et al.*	Macroporous silica gel	Aliquat-336 TBP, CMPO, Cyanex-923	Pu(IV) Am(III), Eu(III)	187, 188
Dokuz Eylul University, Turkey: Ayata *et al*.	Macroporous silica gel	benzoylthiourea	U(VI)	189
Tsinghua University, Beijing, China, Chen *et al.*	SBA-15	alkyl phosphine oxides	U(VI)	44

Feng, Fryxell and coworkers at PNNL first functionalized MCM-41 mesoporous silica with a high density of thiol-terminated silanes for the adsorption of mercury from aqueous solution.[79] The functionalization method used a small amount of water in a toluene reflux of functional silane with the solid mesoporous silica to create a cross-linked covalently grafted oligomer of the functional silane. They later dubbed materials functionalized by this method "Self-Assembled Monolayer on Mesoporous Supports (SAMMS)", and soon created SAMMS designed for the sequestration of lanthanides and actinides.[15-19, 21-23, 37, 38, 40, 81] The batch sorption experiments performed in these works highlighted the merits of SAMMS for actinide and lanthanide sequestration, and the results are summarized in the following paragraphs. Even though much was done by the PNNL group, there was still room for further investigation, and the work described in the remainder of chapter 5 differs from the literature in several ways. In

this work SBA-15 was used as the substrate instead of MCM-41, and several different silane ligands were tested with actinides for the first time. The PNNL group did exploratory batch experiments with many radionuclides in low, variable concentrations, with a low liquid-to-solid ratio. They did not investigate the complexation of Pu(VI), or attempt to measure the binding capacity of their materials. The work of this dissertation explored the complexation of Pu(VI), including higher Pu concentrations and liquid-to-solid ratios for investigation of the Pu uptake capacity. Furthermore, the acid stability of the Ac-Phos silane had not previously been tested, nor had its complexes been investigated with XAS.

In the PNNL work, various experimental parameters were varied, and the affinities of the mesoporous solids for the target species were characterized by their mass-weighted partition coefficients, K_d, which is defined by Equation 5.1. This group chose a standard liquid-to-solid ratio of 200 mL/g.

$$K_d = \frac{(C_0 - C_f)}{C_f} . \frac{L}{S} \qquad (5.1)$$

In Equation 5.1, C_0 and C_f are initial and final concentrations of the target species, L is the solution volume in mL, and S is the mass of solid sorbent in grams. In collaboration with Ken Raymond's group at UC Berkeley, they grafted monolayers of three isomers of hydroxypyridinones to MCM-41, creating "HOPO-SAMMS", which were applied toward sequestration of lanthanides[22] and actinides[15, 21]. Molecular structures of the HOPO-SAMMS monomers are shown in Figure 5.1, and the ligand densities of the SAMMS surface was estimated via ^{29}Si NMR to be about 0.5-1.0 silanes/nm^2.

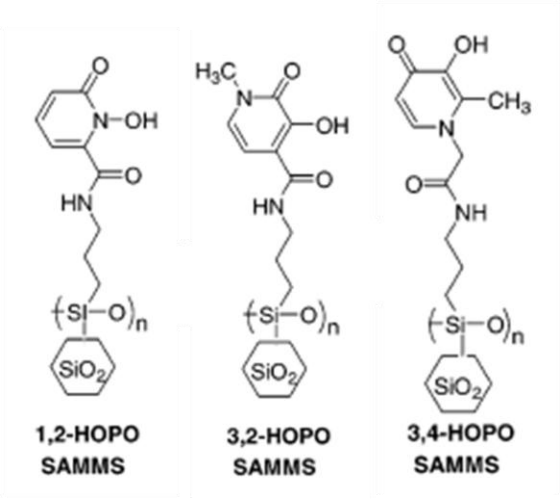

Figure 5.1 Structures of HOPO functionalized mesoporous silica previously applied to actinide sequestration.[15]

Their initial tests in 0.1 M $NaNO_3$ of pH 0.88 to 6.80 gave high K_d values on the order of 10^5 mL/g for Am(III), Np(V), Pu(IV), Th(IV) and U(VI).[21] Later the kinetics and selectivity of these materials were further investigated with U(VI), Np(V) and Pu(IV) at various pH values and in the presence of competing ions and ligands.[15] The Pu(IV) solutions were 0.06 μM Pu in 0.1 M HNO_3 and 0.1 M $NaNO_3$ at pH 2, while the U(VI) solutions were 4.2 μM in 0.2 M HNO_3, and 0.1 M $NaNO_3$ at pH 2, 4 and 6, with 0.05 M sodium acetate added to the higher pH solutions.

The 1,2-HOPO has the lowest protonation constant of the three, and showed the highest K_d values for Pu(IV) (Kd ~ 3.5 * 10^5) and U(VI) (Kd ~ 2.0 * 10^6 in solutions pH ≥2). A variety of competing cations and complexing agents were individually added in excess with Pu(IV), and they reduced the K_d values by an order of magnitude of less, except Zr(IV), which drastically reduced the Pu(IV) binding by HOPO-SAMMS. The removal of Pu(IV) from solution occurred within one minute. The NpO_2^+ sorption was tested from a pH 7.8 mock groundwater solution, and the best complexation was by 3,2-HOPO-SAMMS (K_d ~ 1.9 * 10^5).[15] The effective complexation of NpO_2^+ is noteworthy and highlight's the importance of ligand density on the surface, and ligand posture with respect to the surface. Molecular modeling suggested a 3:1 hexagonal bipyramidal complex with two bidentate and one monodendate ligand that also hydrogen bonds with the neighboring ligand for increased stability (Figure 5.2a). This could not be achieved with a rigid vertical ligand posture, as it is defined by Figure 5.2b, but is easily accommodated by a flexible horizontal posture.[164] Obviously it is also important to have a high enough density of ligands that 2:1, 3:1, and 4:1 complexes can be formed. 1,2-HOPO-SAMMS also achieved rapid sorption of La(III) (K_d ~ 3.5 * 10^5), Nd(III) (K_d ~ 3.4 * 10^5), Eu(III) (K_d ~ 2.1 * 10^5), and Lu(III) (K_d ~ 4.2 * 10^5) from pH 4-5.9 solutions.[22]

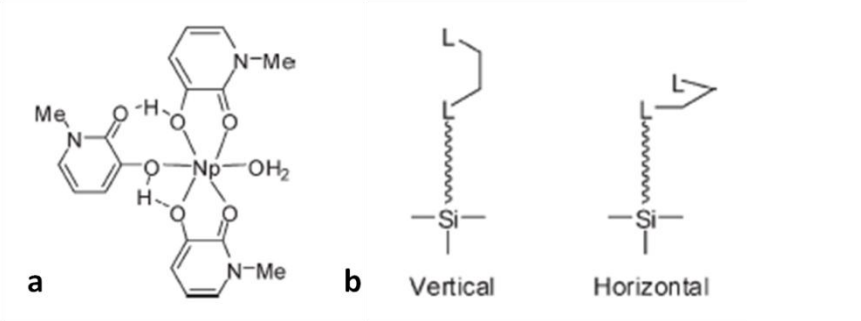

Figure 5.2. Proposed structure of 3,2-HOPO-NpO_2 complex looking down the axial neptunyl bond axis (a), and representations of possible vertical and horizontal ligand postures of a bidentate chelating ligand grafted to a mesoporous silica surface (b).[164]

Another set of ligands that was tested around the same time by Fryxell and coworkers in the form of SAMMS for lanthanide[19] and actinide[16] sorption is shown in Figure 5.3. The Ac-Phos and Prop-Phos ligands were tested for lanthanide and actinide sorption both in their ester form shown in Figure 5.3, and in their acid form (Figure 5.4). The surface ligand densities of these SAMMS were estimated by ^{29}Si NMR to be 0.88 silanes/nm^2 for Sal-SAMMS, 5.6 silanes/nm^2 for Gly-UR-SAMMS, 1.6 silanes/nm^2 for Ac-Phos-SAMMS, and 2.1 silanes/nm^2 for Prop-Phos-SAMMS.

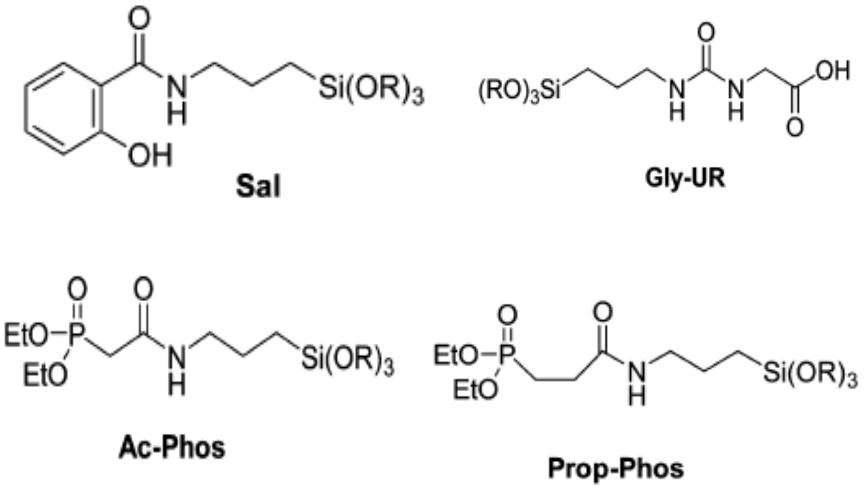

Figure 5.3.Structures of silane ligands used by Fryxell et. Al. to create actinide and lanthanide binding SAMMS.[19]

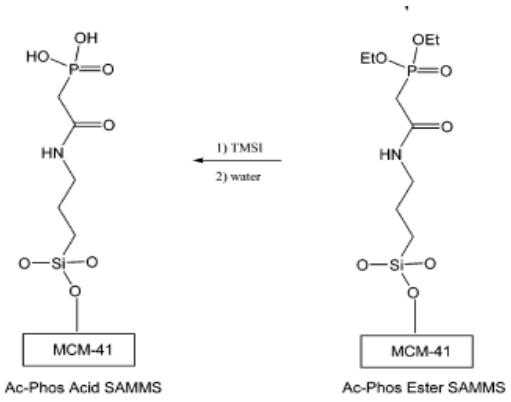

Figure 5.4. Conversion of Ac-Phos ester SAMMS to Ac-Phos acid SAMMS.[16]

Binding of La, Nd, Eu, and Lu was tested in solutions of 2 ppm La, 0.1 M $NaNO_3$ over a pH range of 1 to 6.5. Lanthanide binding occurred within one minute, and a two hour contact time was used for equilibrium studies. All of the complexation was pH-dependent, and none of the materials bound lanthanides in solutions with pH < 2. Sal-SAMMS showed high affinity for Nd and Lu ($K_d > 1* 10^5$) from pH 6.5 solution, and decent affinity for Eu ($K_d \sim 1.7 * 10^4$) from pH 4.5 solution. Gly-UR-SAMMS showed increasing affinity for all of the lanthanides with increasing pH, with K_ds ~ 1.3-1.8 * 10^4 in pH 4.5 solution, and K_ds ~ 4.1-9.4 * 10^4 in pH 6.5 solution. The prop-phos ester SAMMS showed no affinity for lanthanides, while the Ac-Phos ester SAMMS showed affinity in pH 2.5 and above solution, with affinity increasing with solution pH and usually with atomic number (smaller ionic radius) of the cation. In pH 2.5 the Ac-Phos ester K_ds were ~ 1.8 * 10^3-1.5 * 10^4, and in pH 6.5 solution they K_ds were ~ 6.3 * 10^4-2.0 * 10^5. The acid derivatives of Ac-Phos (K_d up to ~ 3.8 * 10^5) and Prop-Phos (K_d up to ~ 4.1 * 10^5) SAMMS turned out to be more effective than the ester versions at binding lanthanides, in solutions of pH ≥ 2. The acid version of Ac-Phos also suffered much less reduction in K_d in tests with excess competing ions, but still showed affinity toward Fe(III), Ni(II), Cu(II), and Zn(II). Only Gly-UR-SAMMS were tested for reuse after removing bound Eu with 0.5 M HCl, with no

decrease in affinity after 10 cycles. A sample of Sal-SAMMS saturated with Eu was subject to EXAFS analysis, which indicated an average Eu-O coordination number of 8 with a bond length of 2.40 Å. They proposed that a 4:1 distorted square antiprism complex was formed by four bidentate salicylamide ligands and Eu^{3+}.[19]

Similar batch sorption experiments were done with Am(III), Pu(IV), Np(V), U(VI), Th(IV) in solutions of pH 0.66 to 5.24 depending on the analyte.[16] In this study the concentration of target species was standardized at 2000 dpm/mL, which gives a range of molar concentrations ranging from 1 nm ^{241}Am to 5 μM ^{237}Np due to the large difference in half-lives for the radionuclides used. The Gly-UR-SAMMS showed increasing affinity for all actinide species with increasing solution pH, the highest K_d being $2.4* 10^5$ for Am(III) in pH 5.24 solution. The Ac-Phos ester SAMMS showed affinity for all of the actinide species tested except Np(V), with the highest being Am(III) (K_d up to ~ $4.6 * 10^5$ at pH 5.24) and then Pu(IV) (K_d ~ $9.4 * 10^4$ at pH 0.66). The Prop-Phos ester SAMMS only bound Pu(IV) (K_d up to~ $6.6 * 10^4$), and took about 3 hours where the Ac-Phos ester SAMMS took about 40 minutes. However, both the Ac-Phos and Prop-Phos acid SAMMS bound Pu(IV) within one minute. Furthermore the ester phosphonates could not compete with EDTA for Pu(IV) complexation, and suffered interference from Fe(III), where the acid versions did not suffer interference from any of the transition metals or complexing agents tested. All of the K_ds in this study decreased when the nitrate concentration increased from 0.1 M to 1 M.

The synthesis of Ac-Phos-SBA-15 was undertaken as a starting point in the present work to see if a similar material from the literature (with a different silica substrate) could be obtained before any novel ligand synthesis would be attempted. The original intention was to also synthesize Prop-Phos-SBA-15, and move on to create novel ligands and materials, but the focus of the project changed over time. Once synthesized, the complexation of Pu(VI) by Ac-Phos-SBA-15 was investigated, and this work constitutes a significant portion of Chapter 5. The PNNL group has published multiple papers with Ac-Phos-MCM-41 (SAMMS).[16-19, 23, 40, 163, 190-193] In the first report of its synthesis it was modeled after carbamoylphosphine oxide (CMPO), and intended for selectivity toward lanthanides and actinides.[163] The acetamide and phosphonate groups in Ac-Phos work together to activate the central enolizable methylene to create the protic portion of the ligand.[19] In Prop-phos the enolization is attenuated, and the chelating ring is larger (7-membered instead of 6-membered). The Ac-Phos acid SAMMS were touted for their selectivity toward lanthanides [19] and actinides,[16] and was used for preconcentration of Pu and Th to collect an alpha spectrum of a dilute solution.[17] The maximum Ce sorption capacity of the Ac-Phos acid SAMMS in 0.01 M HCl was later determined to be 33.0 mg/g, and along with DiPhos SAMMS (Figure 5.5) bound lanthanides effectively in acidic solutions (pH 1.8 to 2.4) and also in natural water and dialysate solutions around pH 8.[23] Although transition metals did not seem to attenuate the affinity of Ac-Phos-acid SAMMS for actinides,[16] the same material in another study showed high uptake of divalent metals ($Pb^{2+} > Cu^{2+} > Mn^{2+} > Cd^{2+} > Zn^{2+} > Co^{2+} > Ni^{2+}$) from solutions of pH 4 and higher, with Langmuir Cd sorption capacity of 0.32 mmol/g in pH 5.5 solution.[190] Therefore the claimed selectivity of the Ac-Phos acid SAMMS for f-elements is questionable. In fact, the same material was incorporated into carbon paste electrodes for detection of Pb^{2+},[191-193] Cu^{2+} and Cd^{2+},[191] and U(VI)[18] via adsorptive stripping voltammetry.

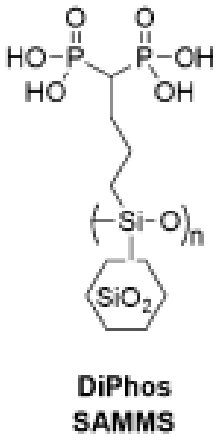

Figure 5.5. Structural reperesentation of DiPhos SAMMS used for lanthanide adsorption.[23]

Another class of ligands that has been modified for functionalization of MCM-41[20, 37] and silica gel[167] for extraction of f-elements are diamides. Figure 5.6 shows the structure of malonamide MCM-41, which extracted over 95% of Am(III) and Eu(III) from 7.5 M $LiNO_3$.[20] A series of template silica gels were also prepared with the malonamide ligand and tested for extraction of Ln(III), Am(III) and Pu(IV) from 0-6 M HNO_3.[167] Figure 5.7 shows the structure of the aminodiacetic amide silane that was grafted to MCM-41 to create IDA-amide-SAMMS, which adsorbed lanthanides from solutions with pH 5-6, with sorption kinetics that improved systematically across the series with decreasing ionic radius.[37] Recently, IDA-amide-SAMMS, 3,4-HOPO-SAMMS, and sulfonic acid SAMMS materials were studied for the sorption of lanthanides and actinides from natural waters, in comparison with conventional Chelex (EDTA) and sulfonic acid resins.[38] No direct conclusion could be made about mesoporous vs. conventional resins, but they generally found HOPO-SAMMS and MnO_2 based materials to be the superior sorbents.

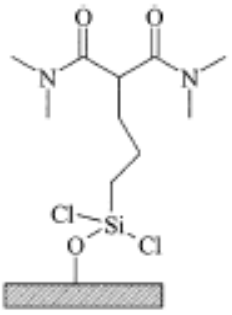

Figure 5.6. Structural representation of malonamide functionalized MCM-41 used for trivalent f-element extraction.[20]

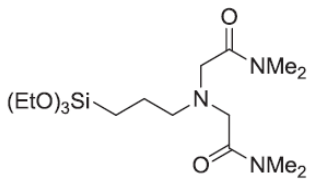

Figure 5.7. Molecular structure of aminodiacetic amide silane that was grafted to MCM-41 to create IDA-amide-SAMMS for lanthanide chelation.[37]

Most of the materials discussed thus far used MCM-41 as the mesoporous substrate, but different mesostructures with larger pore size could be beneficial, especially for extraction of large ions like the actinyl ions. A Canadian group tested phosphonate functionalized SBA-15 and KIT-6 for U(VI) extraction and found improved performance over commercial U-TEVA resin (Figure 5.8).[68] They attributed the enhanced performance of KIT-6 to its higher BET surface area, but also to its cubic structure and larger pore width of around 6 to 7 nm. More recently a group in China reported a series of SBA-15 materials functionalized with alkylphosphine oxides with varying alkyl chains for extraction of U(VI) from HNO_3.[44]

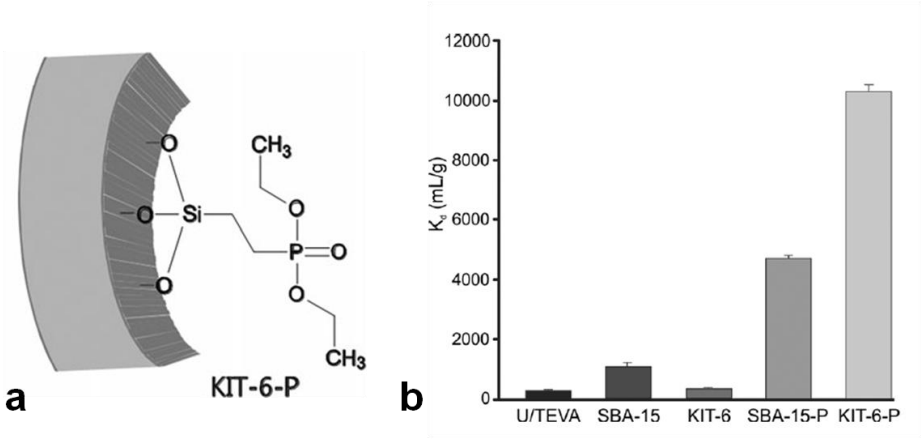

Figure 5.8. Structural representation (a) and extraction results (b) of phosphonate functionalized SBA-15 and KIT-6 mesoporous silica.[68]

In summary, there has been a significant amount of work reported regarding functionalized mesoporous silica for sorption or extraction of lanthanides and actinides, but there is still room for further exploration. Unfortunately, the range of commercially available silanes for grafting is quite limited, and the creation of novel extractant materials will require collaboration with a skilled and well-equipped synthetic chemistry lab. This missing element was the biggest hindrance to our initial efforts in this area. Nevertheless, several new functionalized SBA-15 materials were synthesized with commercially available silanes and tested for plutonium sorption. The Ac-Phos-SBA-15 was synthesized to correlate our work with existing literature, and used for more extensive batch experiments with Pu(VI). One thing notably missing from the literature is the explicit testing of the stability of self-assembled monolayers toward acid hydrolysis. This issue was addressed in a preliminary way with Ac-Phos-SBA-15 (Section 5.3.5), and is being studied systematically for other functionalized mesoporous silica materials by Jennifer Shusterman. In Section 5.4.3 the Pu(VI) uptake capacity of Ac-Phos-SBA-15 was

determined, as the PNNL group generally studied low and variable concentrations of actinides with low liquid-to-solid ratios, which made it difficult to determine the actinide uptake capacities of their materials. Finally, most of the work above describes sorption in aqueous conditions relevant to environmental sequestration, and there have not been any reports of actinide separations using novel extraction chromatography resins based on organically-modified mesoporous silica. Current efforts in the Nitsche group involving organically modified silica are geared toward extraction chromatography.

5.2 SBA-15 synthesis and properties

The label SBA-15 may be given to any mesoporous silica with a 2D-hexagonal mesostructure that was synthesized using non-ionic block copolymers as a structure-directing surfactant.[66, 67] The use of different PEO-PPO-PEO copolymers with different ratios of ethylene oxide (EO) and propylene oxide (PO) causes variation in the SBA-15 pore size, and can lead to other SBA mesoporous silicas with different mesostructures. The synthesis can be done in aqueous solutions of HCl, HBr, HI, HNO_3, H_2SO_4, or H_3PO_4, using tetraethoxysilane (TES), tetramethoxysilane (TMOS) or tetrapropoxysilane (TPOS) as a silica source. The pore size and thickness of the silica wall can be adjusted by varying the heating temperature (35° C to 140° C) or reaction time (11 to 72 hours). The synthetic pathway likely involves both electrostatic and hydrogen-bonding interactions. Under acidic conditions the PPO block is more hydrophobic than the PEO block, and creates mesoscopic order upon heating. In aqueous solution of pH 1, the silicate species is protonated and positively charged, and thus interacts preferentially with the more hydrophilic PEO block. This causes formation of an ordered mesophase that is dense in block polymer and silica, which condensed further into the ordered mesoporous silica gel composite. Calcination at high temperature results in removal of the polymer to yield a rigid ordered mesoporous silica structure.

The synthesis of SBA-15 for this work was completed by an undergraduate assistant of Peidong Yang's group. SBA-15 was prepared in acidic conditions using triblock copolymer poly(ethylene oxide) - poly(propylene oxide) - poly(ethylene oxide) (Pluronic P123, $EO_{20}PO_{70}EO_{20}$, Sigma-Aldrich) as a structure directing agent. First, 27.8 g of P-123 was dissolved in 504 g of distilled water and 15.5 g of HCl (37%). After a clear solution was obtained, TEOS was quickly added into the mixture by stirring at 35 ^{o}C. The mixture was stirred at 35 °C for 24 hours, followed by a hydrothermal treatment at 100 °C for 24 hours. The solid white product was filtered without washing and dried overnight at 100 °C. After that samples were calcined at 550 °C for 6 hours. Three different batches of SBA-15 were prepared for this work, and their properties varied slightly. Unfortunately, the N_2 adsorption porisometry for the second and third batch was not available until much later, after all of the work was completed. Because we were told that the three batches were identical, there is no consistent record of which batch was used in each functionalization reaction.

The particle morphology of SBA-15 was observed in SEM imaging, and example micrographs are shown in Figure 5.9. The particle size and morphology is fairly regular, with rounded cylindrical particles approximately one μm in length. The image quality is poor due to charging effects, but nevertheless the porosity of the particles is evident under high magnification.

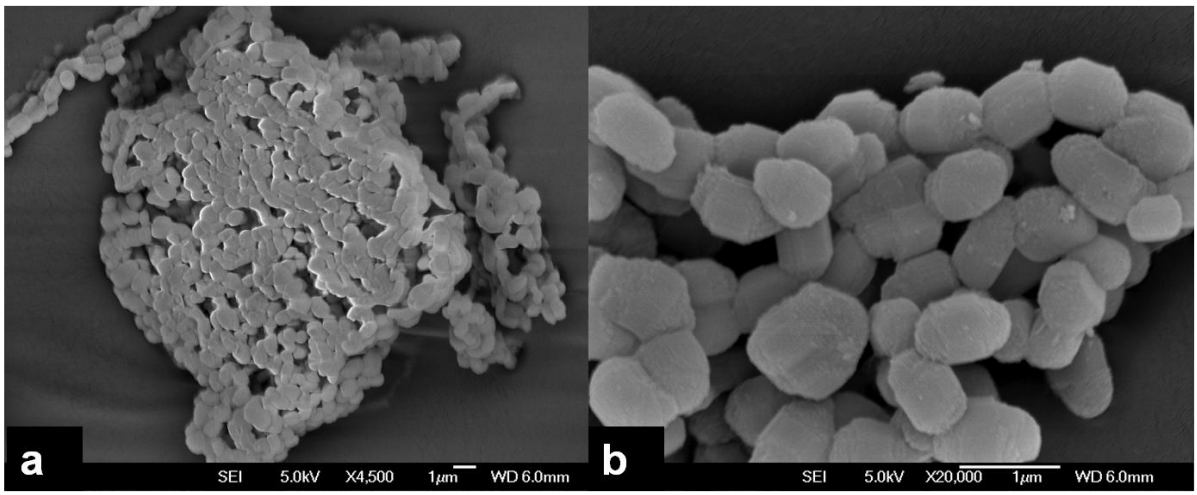

Figure 5.9. SEM images of an aggregate of SBA-15 particles at two different magnifications.

BET surface area, pore size, and total pore volume of SBA-15 were determined by N_2-sorption. The N_2 adsorption-desorption isotherm of one of the SBA-15 samples is depicted in Figure 5.10a. The isotherm is of type IV, according to IUPAC classification. Three well-distinguished regions of the adsorption isotherm are evident for a monolayer multilayer adsorption, capillary condensation, and multilayer adsorption on the outer particle surfaces. The sample has a BET surface area of 727 m^2/g, pore volume of 0.930 cm^3/g, and an average pore size of 7.4 nm (Figure 5.10b). Nitrogen adsorption isotherms of subsequent batches of SBA-15 used in our work showed BET surface areas between 600 and 670 m^2/g, and narrow pore size distributions centered around 7 nm.

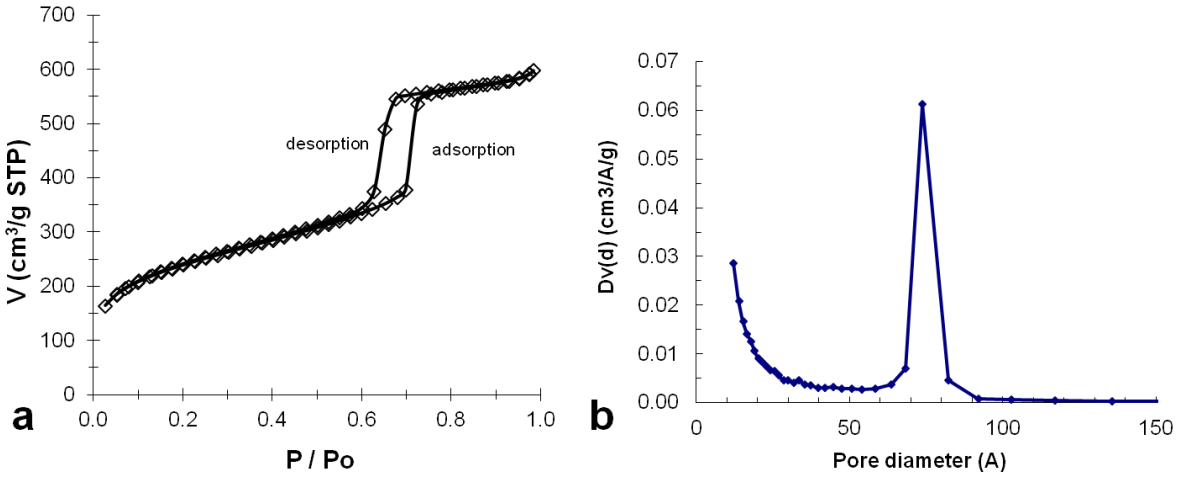

Figure 5.10. Nitrogen adsorption isotherm (a) and BJH pore size distribution plot (b) of an SBA-15 sample.

The ordered structure of the SBA-15 was confirmed with low-angle XRD and further investigated with TEM. Three well resolved XRD peaks were observed corresponding to the 100, 110, and 200 planes of the 2D-hexagonal structure. These are tabulated in table 5.2, but the d-spacings and intensities may be skewed because the system was not optimized for low angles. The TEM image of calcined SBA-15 (Figure 5.11) shows well-ordered hexagonal arrays of

mesopores viewed in both the [110] and [001] directions. The pore sizes observed in all of the TEM micrographs were in agreement with those derived from nitrogen adsorption isotherms.

Table 5.2. Low-angle XRD peaks measured on SBA-15 Sample with Co Kα radiation.

hkl index	2θ	d-spacing (Å)	Rel. intensity (%)
100	1.012	101.4	100.00
110	1.752	58.55	12.57
200	2.012	50.99	8.85

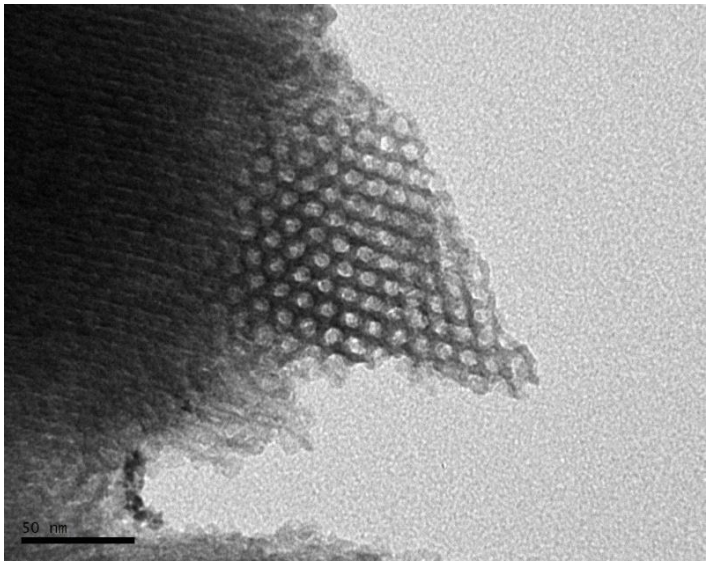

Figure 5.11. Example TEM micrograph of SBA-15 sample.

Efforts were made throughout this project to prepare mesoporous matierials in physical forms that would be more practical for sensing devices than loose powders. Crack-free silica monoliths were prepared by Dr. Harun Tuysüz (former postdoctoral associate of the Yang group) with a highly ordered mesostructure by liquid-paraffin-medium protected solvent evaporation.[73] The synthesis is similar to that of SBA-15, but the reaction occurs in a ceramic vessel that determines the shape of the monolith. Liquid paraffin is added prior to the heating step, and provides protection from the environment and the internal pressure gradient during solvent evaporation. The paraffin is subsequently removed and does not change the chemical composition of the monolith. Figure 5.12 shows two TEM images of monolith pieces, confirming the desired 2-D hexagonal ordered mesostructure. In this case a large monolith was broken into smaller pieces to test them on a small scale, but monoliths can be synthesized in a regular size and shape pattern. The monolith external surface area is negligible, and the internal surface area should theoretically be functionalized similarly to SBA-15. These monoliths were expected to have similar BET surface area, pore-volume, and size distribution to SBA-15, although the pore size appears slightly smaller in the micrograph. Like SBA-15, the monolith pore size is tunable and can easily be doped with metal ions for specific applications. However, attempts to functionalize these monolith pieces using the method employed for SBA-15 powder were unsuccessful (see Section 5.3.1).

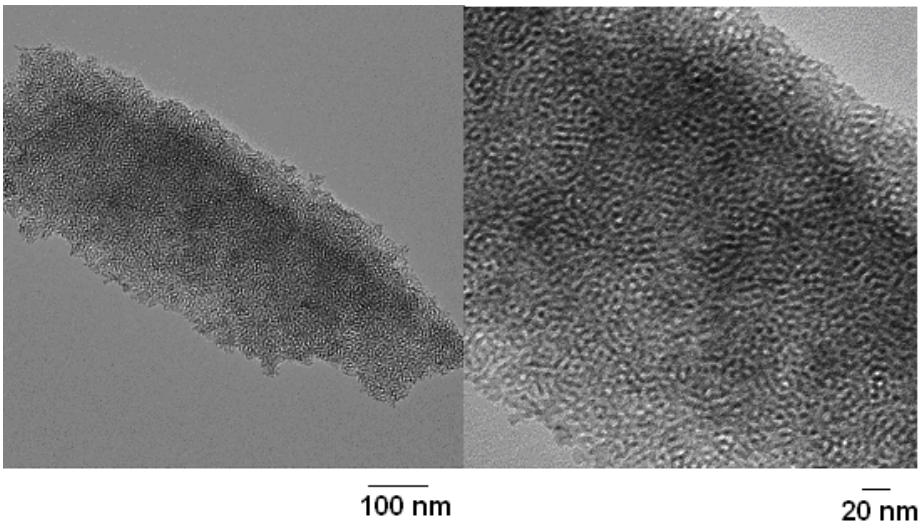

Figure 5.12. Example TEM images of SBA-15-like monolith pieces.

5.3 Functionalization and properties of organically-modified SBA-15

The grafting of a functional organic layer onto mesoporous silica is key to creating materials that are appropriate for actinide binding. The functionalization and subsequent characterization of organically-modified SBA-15 was not trivial, and these efforts are described in the following sections.

5.3.1 Methods of silica functionalization

Organic modification of mesopore surfaces can be executed by co-condensation, surfactant replacement, or post-calcination modification (see Figure 2.5). Post-calcination modification is advantageous because it leaves the mesoporous substrate thermally cross linked and structurally sound, and it also utilizes ligands' ability to self-assemble.[78] The functional chelating ligand is generally preassembled into a hydrolysable organosilane, then covalently attached to the mesopore surface and condensed into a monolayer. For efficient surface coverage, the silica must be pre-hydrated (see Figure 2.6), and two distinct methods of pre-hydration were tested. In one method the mesoporous silica is first hydrated by boiling in water for about four hours and subsequently allowed to dry. The material is then stirred with the ligand under toluene reflux for six hours. One of the hydrolysable groups on the silane reacts with a silanol on the pore surface, leaving the other two available for bonding to neighboring silanes, if proximity allows. The reflux reaction is followed by distillation to 110 °C to remove byproducts (generally methanol, ethanol, or HCl) and the solid is filtered, rinsed, and dried. A similar procedure by Fryxell *et al.*[78] was employed in which interfacial water was added to the toluene and silica mixture, and allowed to stir for 30-60 minutes before the silane is added and reflux begins. Self-assembly is driven by hydrolysis of the ligand, aggregation through hydrogen bonding and Van der Waals forces, followed by condensation. This process (shown in Figure 5.13) creates a covalently grafted monolayer with the functional portion of the silane covering the pore surface and available for interaction with the target species in solution. The distillation step is important for efficient coverage, as excess water can over-polymerize the silane and block surface sites. A comparison test for SBA-15 using aminopropyltriethoxysilane (APS) showed

that the molecular self-assembly method gave much greater surface coverage (determined gravimetrically) than the pre-hydration method. Thus the Fryxell method was adopted as standard and optimized for the SBA-15 substrate as described in Section 5.3.2. However, the polymerization of silanes in the presence of water is difficult to control, and there are some cases where the pre-hydration method would be preferable. The amount of water added was determined stoichiometrically by adding 2-2.5 monolayers,[16] assuming a hydrated monolayer contains 3 H_2O molecules per nm^2. In this work the precise BET surface area of the SBA-15 was unknown until much later, and was estimated at 800 m^2/g for the first batch, and 675 m^2/g for the second and third batches. In some of the reactions too much water may have been added.

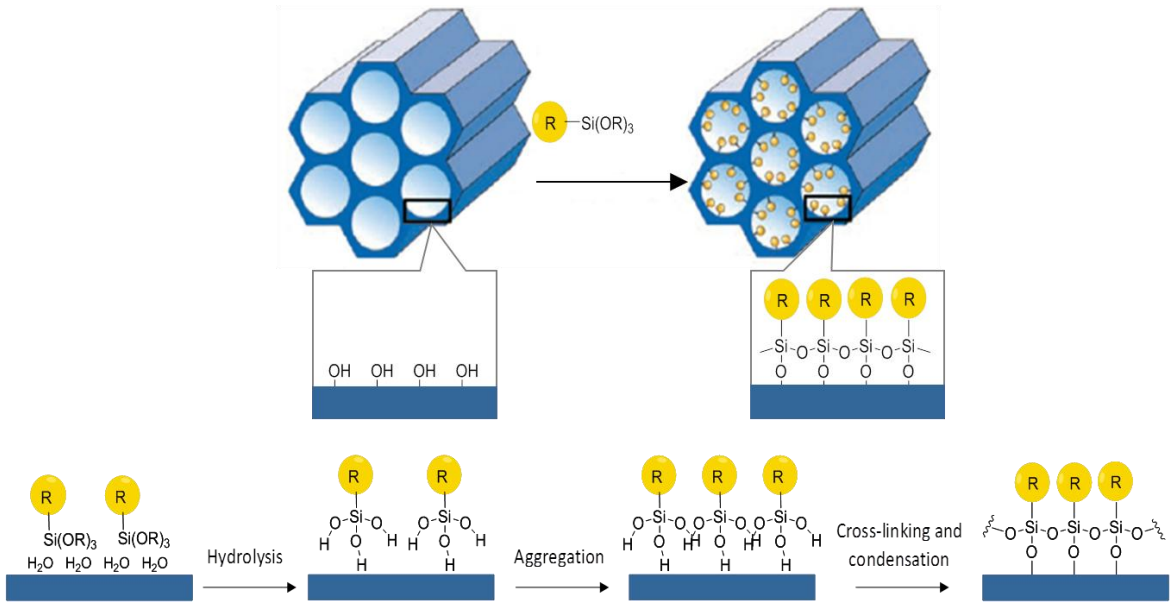

Figure 5.13. A cartoon illustration depicting the formation of a self-assembled silane monolayer on an SBA-15. The image was created by Aude Hubaud.

Vital in designing functionalized mesoporous materials is the design of the ligand in the functional monolayer, which must be matched to both the chemistry of the actinides and the chemistry to graft to the surface. The ligand must exhibit several structural features, diagrammed in Figure 5.14: (i) a binding site with one or more functional groups showing affinity for actinides (ii) a silane anchor necessary to graft the ligand to the silica surface (iii) a carbon chain distancing the binding site from the silane anchor. The ligand also needs to be stable at 110° C and resilient and efficient at low pH. Finally, the commercial availability or synthetic feasibility of the ligand must be considered.

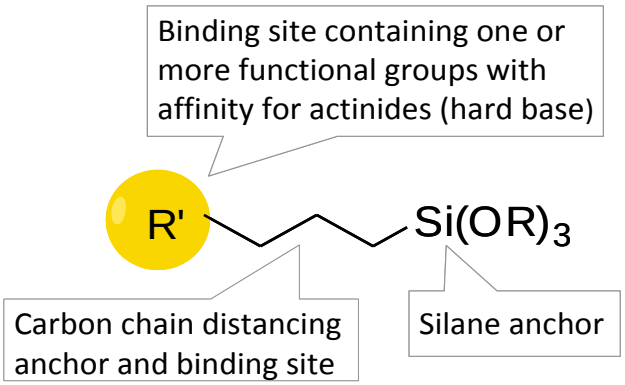

Figure 5.14. Graphical representation of the structural features required of silane ligands to be grafted onto a silica surface.

The silane anchor must have three hydrolysable groups (-OMe, -OEt, -OH, -Cl) for the oligomerization and condensation to occur. Grafting can be achieved with one hydrolysable group, but the other two are necessary for cross linking to neighboring silanes to form a self-assembled monolayer. Alkoxy groups are preferred, since halides and -OH groups are much more reactive, making the silane unstable in the bottle beforehand. Even trialkoxysilanes should be stored in a dessicator or under inert gas to prevent polymerization. Ethoxy groups are preferable to the slightly more reactive methoxy groups mainly because of the toxicity of the methanol by product. The heat of toluene reflux activates the hydrolysis, so if the functional part of the ligand also contains hydrolysable groups, they must be protected prior to the functionalization. Otherwise, oligomerization and polymerization will occur at both ends of the molecule instead of just at the anchor.

The carbon chain is very important for two reasons. Primarily, it separates the functional group from the surface, allowing the conformational freedom needed to adopt the appropriate ligand posture for metal complexation, and providing reach for multiple ligands to come together to coordinate one metal center. The Van der Waals forces between the carbon chains are also essential for molecular organization in the self-assembly process. Liu *et al*. systematically studied the effects of pore size and alkyl chain on the quality of the monolayer using MCM-41 and SBA-15 materials having pore diameters of 3, 10, 17, and 30 nm, and alkyltrialkoxy silanes with chain lengths of 6, 10, and 18 carbons.[80] They found with ^{29}Si NMR that the 10 nm pore size is optimal for silane cross-linking, as the 3 nm pores were easily clogged and the larger pores were subject to disordered multilayer formation due to a rougher surface. Within the 10 nm pore, the 10 carbon chain gave the highest degree of cross-linking due to increased Van der Walls forces, and longer chains are too prone to entanglement. A short alkyl silane may be added to the reaction mixture along with the functional silane having a longer carbon chain, to serve as a spacer.

It is generally preferred to synthesize the silane ligand first, then graft to the surface, but silanes can also be modified after grafting, and there are cases where this approach allows more flexibility in ligand choice. Typically a simple vinyl or amino alkyl silane will be grafted in a monolayer, and additional chemical reactions are used to attach the functional part of the ligand afterward. Self-assembly of silanes is not the only way to graft organic moieties onto silica, but perhaps is the easiest. Direct alkylation of silanols on the surface can be achieved with some molecules, for example perfluoroalkyl sulfones.[78] Of course, silica can also be modified using

non-covalent methods. In one report, a phenyl trialkoxysilane is grafted into a monolayer, and the functional ligand has an aromatic anchor, which sticks to the surface via by non-covalent pi-stacking interactions with the phenyl groups.[194] Another very common technique is incipient wetness impregnation. If the functional molecule can be dissolved in an aqueous phase, then a small volume of the solution is added to a larger volume of an organic phase, and stirred with pre-hydrated silica overnight. The aqueous phase is attracted to the silica, so evaporation of the organic phase leaves an impregnated solid. In this work SBA-15 impregnated humic acid was prepared, and adsorbed Eu(III) and Ce(III) reasonably well. However, during the batch sorption experiment some of the brown humate leached into the aqueous phase, and so this avenue was not pursued further.

Functionalization of the SBA-15-like monolith pieces with APS using the same molecular self-assembly method was attempted, without success. Stirring the monolith pieces directly in the toluene reflux caused them to break into smaller pieces. Aude Hubaud designed a pocket made from Teflon® PFA bags (American Durafilm Inc.) for use in the functionalization and batch complexation studies of the first generation monoliths. The bags have high chemical and thermal stability, high tensile strength, and low permeability. The bags were sealed, with 2 mm holes to allow sufficient contact between the monoliths and the surrounding solutions, and were hung into the solution to hover above the stir bar at the bottom of the roundbottom flask. Unfortunately, the reaction did not work by this method. It is likely that diffusion of water and silane molecules through the Teflon bag and the monolith pieces was hindered. More dedicated experiments need to be done to develop gentle and effective methods of functionalizing thin films and monoliths.

5.3.2 Optimization of SBA-15 functionalization using aminopropyltriethoxysilane

APS was chosen as a simple commercial silane to optimize the silane self-assembly reaction for the SBA-15 substrate, in part because it was a starting product for Ac-Phos and some other silanes that we had planned to synthesize. The reactions and characterization with ^{29}Si MAS NMR and TGA were done by the author and former Junior Specialist Aude Hubaud. The reaction conditions for the APS tests are summarized in Table 5.3. All 5 reactions used 100 mg SBA-15 from the same batch, and 20 mL toluene. For reaction 1, SBA-15 was boiled in water for 4 hours and then filtered by vacuum and allowed to dry in the hood for 65 hours prior to the reflux. In reactions 2-5, the SBA-15 was stirred with variable stoichiometric amounts of water in toluene overnight prior to reflux. The mixture was stirred constantly and refluxed for the designated length of time, followed by distillation to 110° C, about 15-20 minutes. The solid products were filtered by vacuum, washed with copious amounts of isopropanol, and allowed to dry in the hood for at least three days (agitating with a spatula each day) before weighing. The products often seem to have a sticky gooey consistency before they are washed and dried, and should be mixed with the spatula during the washing process. The amounts of water and silane to add per monolayer were calculated assuming that the SBA-15 was 675 m^2/g, and that a monolayer would have 4 silanes per nm^2 or 3 water molecules per nm^2.[79]

Table 5.3. Summary of toluene reflux reaction conditions used for optimization of SBA-15 functionalization with APS.

Reaction	Monolayers* APS added	Monolayers** water added	Reflux duration (hr)	Weight gain (mg)
1	5	N/A	6	20.4
2	5	2	6	65.2
3	5	4	6	88.6
4	2	2	6	34.8
5	5	4	24	95.7

*Assuming 675 m^2/g SBA-15, and 1 monolayer APS = 4 silanes/g SBA-15

*Assuming 675 m^2/g SBA-15, and 1 monolayer H_2O = 3 H_2O/g SBA-15

Based on the mass gained, the pre-hydration method used in reaction 1 was not able to produce a high surface density of ligands like the self-assembly method. Maintaining a 5-fold stoichiometric excess of ligand seemed to be important for maximum surface coverage, and excess water and reflux time seemed to increase the coverage further. However, TGA data (Figure 5.15) showed that after surface dehydration the excess of water and increased reaction time made little difference. The mass loss due to APS for reaction 3 was 18.4 %, which corresponds to a surface density of approximately 3.5 APS molecules per gram SBA-15. Figure 5.16 shows ^{29}Si NMR spectra taken of products from reactions 4 and 5, where there is a large difference in the relative peak intensities. The calculation of surface coverage using TGA data and NMR data are not within agreement, the NMR data gives greater silane concentrations by about a factor of 2 for reaction 4 and a factor of 3 for reaction 5. The ratio of APS per gram SBA-15 in reaction product 4 over that in reaction product 5 is 0.33 by NMR and 0.44 by TGA. As discussed in Section 2.2.5, the surface coverage by NMR may be overestimated due to differences in relaxation times. The TGA data suggests a maximum surface coverage with APS of 4.5 mmol/g (4.0 silanes/nm^2), while NMR analysis gives a maximum surface coverage of 13.6 mmol/g (12.1 silanes/nm^2). For comparison, Liu *et al*. estimated the maximum surface coverage (based on available silanol sites) of a 2d-hexagonal mesoporous silica with 9.3 nm pores and 911 m^2/g surface area to be 7.7 mmol/g (5.1 silanes/nm^2).[80] Based on the results of these optimization tests, the conditions of reaction 2 were adopted as the standard.

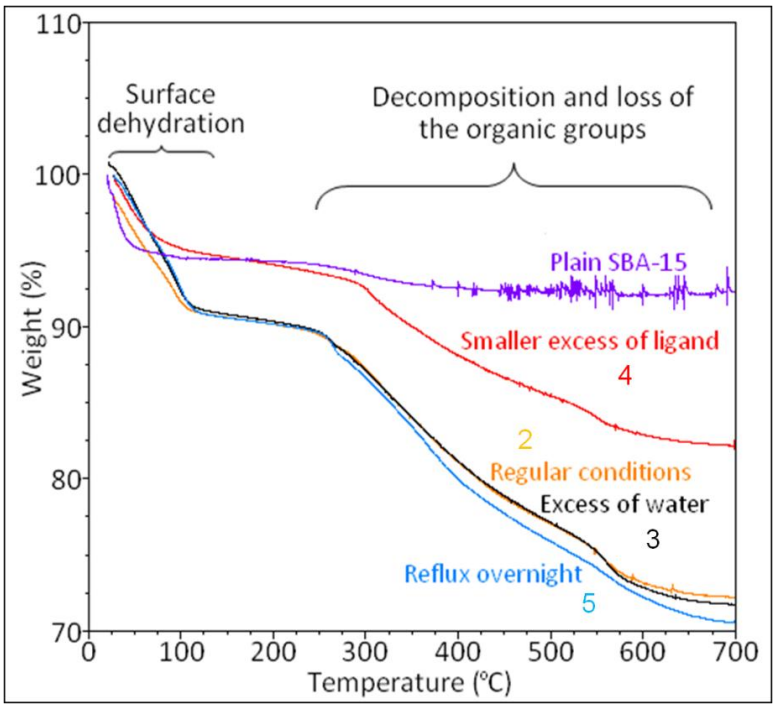

Figure 5.15. TGA results of APS-SBA-15 samples prepared via molecular self-assembly functionalization with varying conditions summarized in Table 5.3.

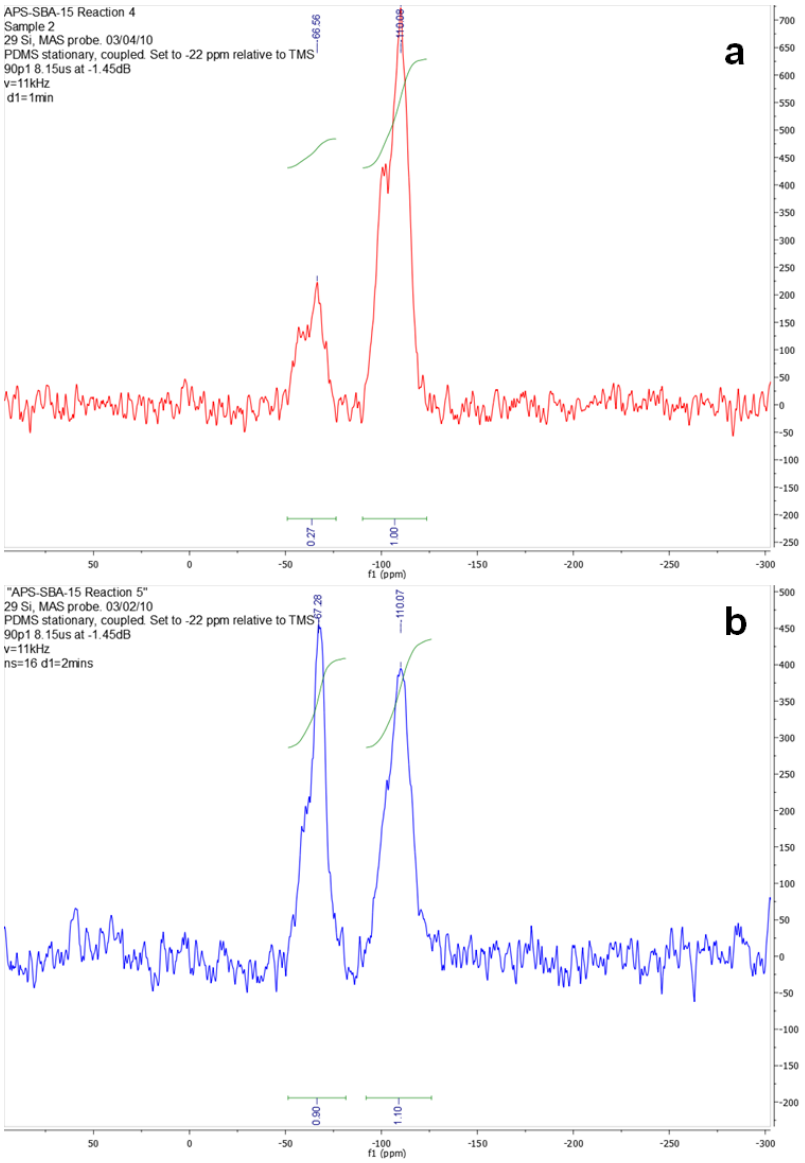

Figure 5.16. ^{29}Si MAS-NMR spectra of APS-SBA-15 products of reactions 4 (a) and 5 (b) described in Table 5.3.

Incidentally, the APS-SBA-15 seems to be an effective material for the capture of carbon dioxide, as amines have a high affinity for CO_2. The highly symmetric peak around 165 ppm in the ^{13}C spectra of the APS-SBA-15 products (example shown in Figure 5.17) may be attributed to CO_2, and characteristic stretches were also observed in the FTIR spectra. Since neither of these spectra can be used for quantitative analysis, it is unknown how the CO_2 capture of the APS-SBA-15 compares to other materials designed for that purpose.

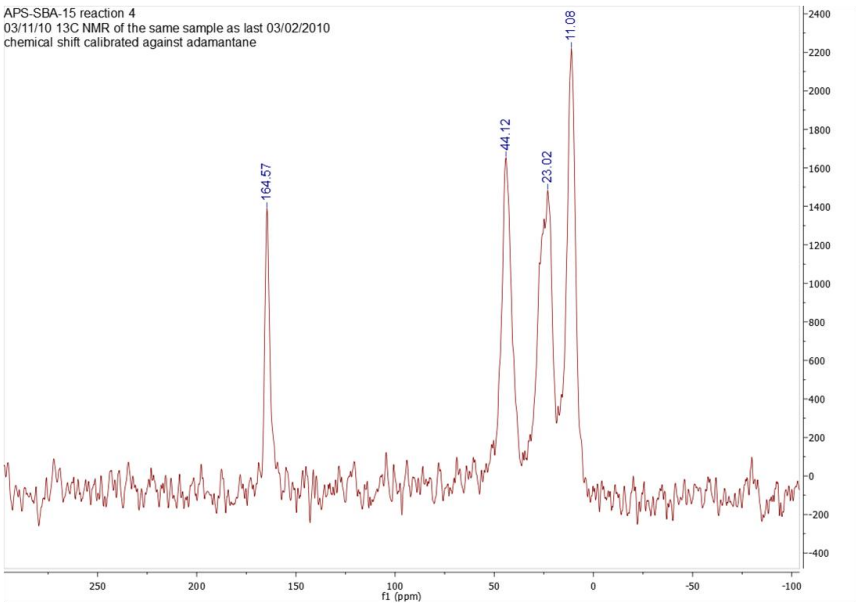

Figure 5.17. ^{13}C CP-MAS-NMR spectrum of APS-SBA-15 product from reaction 4. The 3 peaks between 0 and 50 ppm correspond to the carbons in the APS molecule, and the peak at 164.57 ppm likely corresponds to CO_2 that was captured from the surrounding air.

5.3.3 Summary of functionalized SBA-15 materials synthesized

The structures of the ligands that were grafted to SBA-15 by the procedure described in Section 5.3.2 are depicted in Figure 5.18, as well as the names adopted to represent them. TESPMA (triethoxysilylpropylmaleamic acid), MHAPS (N-(3-methacryloxy-2-hydroxypropyl)-3-aminopropyl-triethoxysilane), and AGAPS (N-(acetylglycyl)-3-aminopropyltrimethoxysilane) were obtained from the Gelest company, while Ac-Phos was synthesized in-house as described in Section 5.3.4. Although the reaction conditions that were optimized for APS were generally applied, the 5-fold excess of silane was not maintained. There were some variations in the silane solvent, and volume of solvent added in order to obtain the 5-fold stoichiometric excess of silane. For example, the functionalization of AGAPS-SBA-15 did not work well because the starting material was only 5% AGAPS in methanol, which led to a large volume of methanol in the reflux. Therefore the 5-fold excess of silane was not possible with this ligand. Table 5.4. describes some variables in the functionalization reactions.

Table 5.4. Summary of functionalized SBA-15 reactions

Reaction	Silane reagent	mmol silane added per g SBA-15	Product	Mass gain (g gained per g SBA-15)
TESPMA-SBA-15	90% TESPMA in ethanol	10.8	Sandy texture, pale yellow	1.58
AGAPS-SBA-15	5% AGAPS in methanol	3.4	Dense yellow powder	N/A
MHAPS-SBA-15	50% MHAPS in ethanol	92.1	Clumpy, plaster-like, white	1.72
Ac-Phos-SBA-15	Reaction mixture described in section 5.3.4	14.0	variable	variable

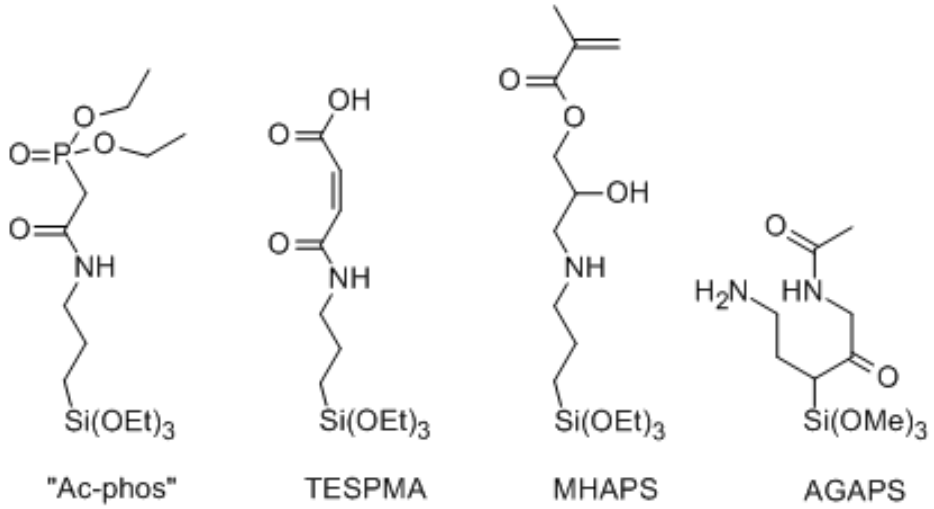

Figure 5.18. molecular structures of several silane ligands that were grafted to SBA-15.

The functionalized SBA-15 products were characterized by ^{29}Si NMR, ^{13}C NMR, FTIR, and TGA. The ligand densities of the products, estimated by TGA, are summarized in Table 5.5. For TESPMA-SBA-15, the TGA and ^{29}Si NMR (Figure 2.13) results indicate successful grafting of a fairly dense monolayer, and the ^{13}C NMR spectrum (Figure 2.11) and FTIR spectrum (Figure 2.16) are consistent with the expected structure. The TGA results also indicated successful grafting of MHAPS to SBA-15. However, the ^{13}C NMR spectrum (Figure 5.19a) is not consistent with the MHAPS structure, which should show 10 distinct carbon species. It seems that the functional end of the MHAPS molecule may have polymerized during the reflux reaction. Figure 5.19b shows that the silane peak in the ^{29}Si NMR spectrum is larger than the silica peak, further indicating polymerization. Because the TESPMA reaction seemed to be the most successful, with only a 2-fold excess of ligand, a 5-fold excess of ligand may not always be beneficial. One may also assume that higher purity silane reagents improve the reaction. It appears from the Ac-Phos syntheses presented in the next section that having a complicated starting mixture is a great detriment to reproducibility.

Table 5.5. Estimated silane densities of functionalized SBA-15 determined by TGA.

Sample	Ac-Phos 2	Ac-Phos 7	TESPMA	AGAPS	MHAPS
mmol ligand grafted per g SBA-15	1.10	1.20	4.13	1.25	3.64
Average ligands grafted per square nm	0.99	1.07	3.71	1.12	3.28

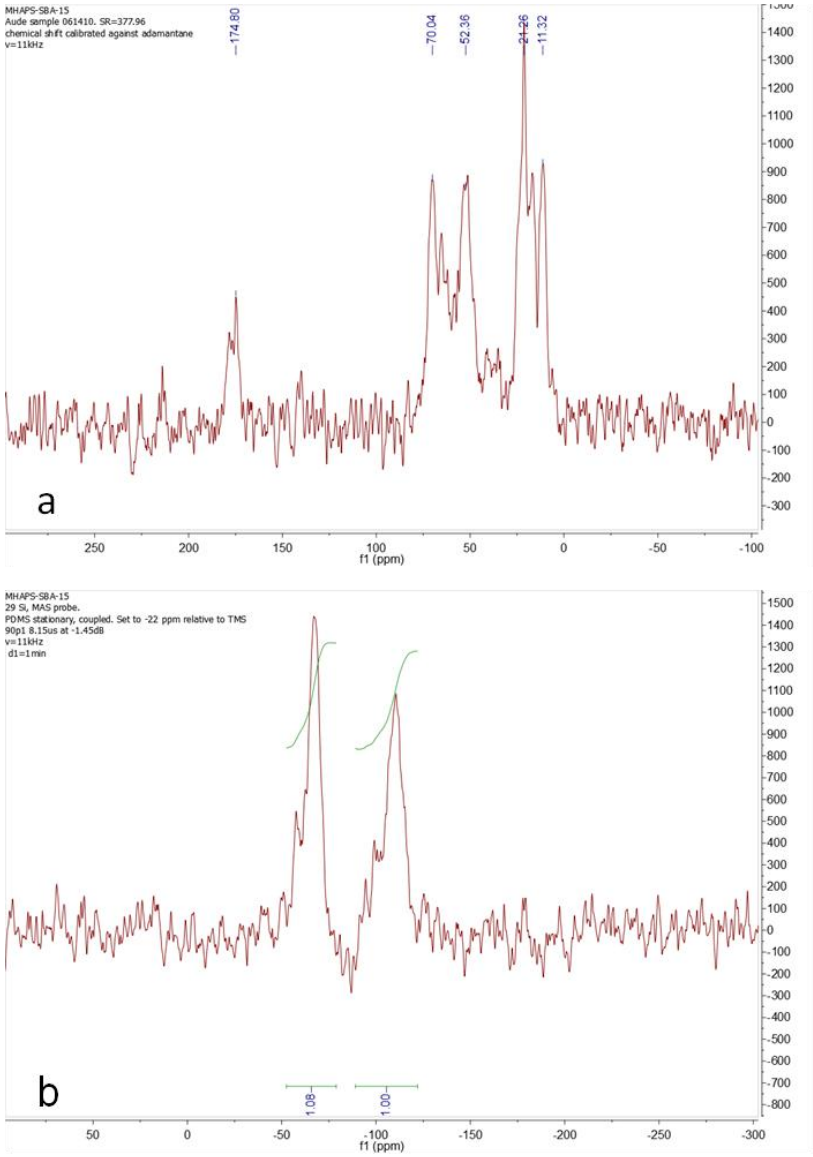

Figure 5.19. ^{13}C CP-MAS NMR spectrum (a) and ^{29}Si MAS-NMR spectrum (b) of product obtained by toluene reflux of MHAPS and SBA-15. The unexpected ^{13}C spectrum and the particularly large silane peak in the ^{29}Si spectrum may indicate that excessive polymerization of the ligand occurred during the reaction.

5.3.4 Synthesis of Ac-Phos SBA-15

The synthesis of Ac-Phos (acetamide phosphonate silane) was inspired by Birnbaum *et al*.,[163] and was chosen to see if we could successfully reproduce a synthesis from the literature before embarking on novel syntheses. The Birnbaum paper[163] did not give a lot of details, so some adjustments were made, and several attempts to optimize and repeat this reaction were made both by the author and former Junior Specialist Aude Hubaud. The synthesis involves an amidation reaction of the corresponding phosphonoacetic acid (PAA) with aminopropylsilane (APS) as shown in Figure 5.20. In this synthesis, the carboxylic acid functionality is activated with carbonyl diimidazole (CDI) before reacting with the aminosilane in a second step. We attempted to optimize this reaction, but the separation of the ligand from the reaction mixture remains problematic. As a result, we used the reaction mixture directly for the subsequent functionalization step according to the literature.[163]

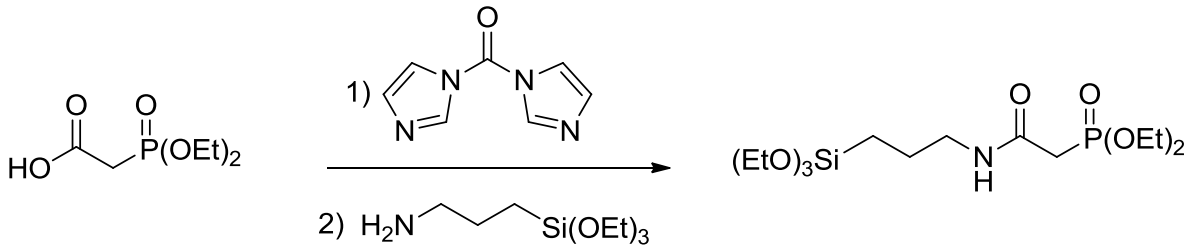

Figure 5.20. Reaction scheme for Ac-Phos silane.

In early attempts at this synthesis, we tried to remove some of the solvent (dimethylacetamide) and by-products by roto-evaporation, but these efforts did not work very well, and this step was abandoned after the third reaction, where the reaction mixture turned into a viscous orange gel. Table 5.6 describes some observations in the 9 attempted Ac-Phos-SBA-15 syntheses. In a typical reaction, 0.5 g SBA-15 stirred overnight in 25 mL toluene with 86 µL Milli-Q water, and the flask was filled with argon the next day. In another flask, under argon, 7 mmol (1.16 g) CDI was dissolved in 7 mL dimethylacetamide (DMA), then stirred with 7 mmol (1.15 mL) phosphonoacetic acid for one hour. Seven mmol (1.66 mL) aminopropyltriethoxysilane (APS) was added and the reaction continued four hours until the entire reaction mixture was added by syringe to the toluene/SBA-15 for overnight reflux with a gentle flow of argon blowing into the top of the condenser. After approximately 17 hours of reflux, distillation to 110° commenced, then the product was filtered by vacuum and washed at least 3 times with toluene, then at least 5 times with isopropanol. These typical conditions were used for reactions 1, 2 and 5. Reactions 6-9 employed the same conditions, except that the reaction times were 30 minutes and 3 hours, instead of 1 and 4 hours. Also in reactions 6-9, 120 µL H_2O was used for the hydration step instead of 86 µL. Liquid proton NMR spectra were taken before adding the reaction mixture of reactions 1 and 2, but the spectra were difficult to interpret.

Table 5.6. Summary of Ac-Phos-SBA-15 reactions.

Synthesis	Departure from standard	Mol ratio PAA:CDI: APS	Description of Product	Mass gained (g) per g SBA-15	Completed by	Notes on success
Ac-Phos 1	none	1:1:1	White powder	0.392	AH	Failed ligand synthesis?
Ac-Phos 2	rotovap	1:1:1	White powder	1.53	AH & TPM	Mixed product?
Ac-Phos 3	Mol ratios, rotovap	1.2:1.5:1	Light orange, clumpy	n/a	AH & TPM	Mixed product?
Ac-Phos 4	Mol ratios and grafted APS first	1.5:1.5: 1	n/a	n/a	AH	Failed ligand synthesis + excessive polymerization
Ac-Phos 5	none	1:1:1	White powder	1.57	AH	Failed ligand synthesis + excessive polymerization
Ac-Phos 6	1.4x H_2O	1:1:1	Hard and clumpy, white	1.47	TPM	Excessive polymerization
Ac-Phos 7	1.4x H_2O	1:1:1	White powder	0.60	TPM	Maybe successful
Ac-Phos 8	1.4x H_2O	1:1:1	Gray gum	n/a	TPM	Failed
Ac-Phos 9	Acetonitrile as solvent, rotovap	1:1:1	Gray gum	n/a	TPM	Failed

The Ac-Phos-SBA-15 products were evaluated based on macroscopic texture, ^{13}C and ^{29}Si NMR spectra, and Pu(VI) sorption. Significant difficulties were encountered in both the silane synthesis step and the grafting step. Figure 5.21 shows the Ac-Phos-MCM-41 structure with the chemical shifts reported by Fryxell *et. al*[37] from their ^{13}C MAS-NMR spectrum. The first attempt at the synthesis produced a product that showed similar chemical shifts in its ^{13}C CP-MAS-NMR spectrum, shown in Figure 5.22a. However, the first product showed no affinity for Pu(VI) (see Figure 5.25), which indicated that the synthesis somehow didn't work. Although the solvent and by-products could not be removed completely, roto-evaporation was used to remove some of the solvent. Proton NMR of the second reaction mixture indicated that the Ac-Phos silane was synthesized, but there was still APS in the mixture. Therefore, it is likely that the resulting SBA-15 has both APS and Ac-Phos grafted, and there could be other side products also. The ^{13}C peaks from APS would likely overlap with those from Ac-Phos. The ^{13}C NMR spectrum of the second product is shown in Figure 5.22b, and there are three extra peaks that indicate the presence of a side product. One possibility for the two peaks around 135 and 121 ppm is the moiety shown in Figure 5.22b, that could have been grafted if the CDI reacted with APS. Despite being a mixed product, Ac-Phos-SBA-15-2 showed good affinity for lanthanides and Pu(VI), and was used for all of the lanthanide experiments and most of the Pu experiments.

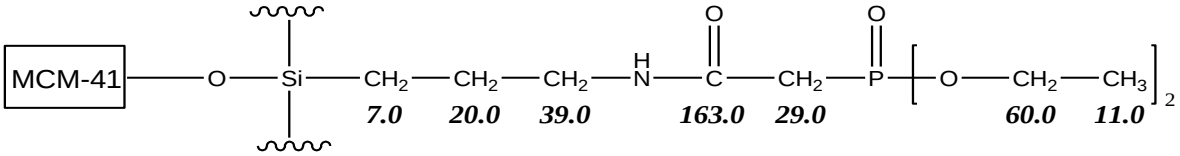

Figure 5.21. Chemical shifts reported by Fryxell *et. al*[37] from their ^{13}C NMR spectrum of Ac-Phos-MCM-41.

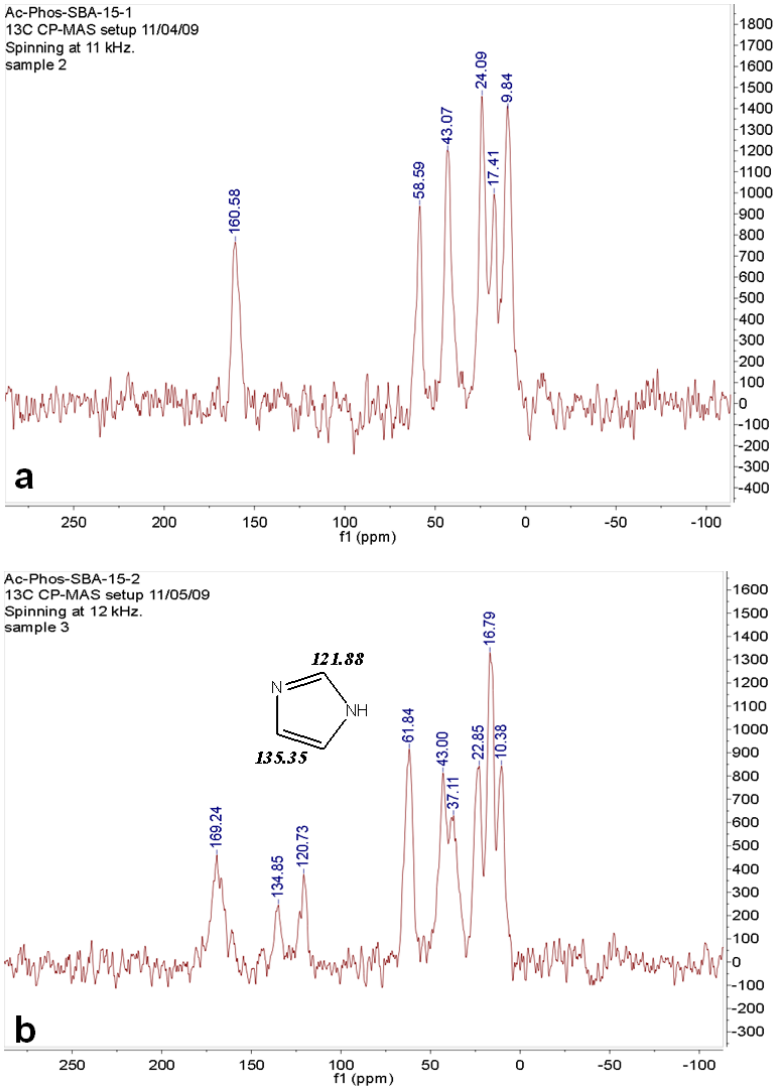

Figure 5.22. ^{13}C CP-MAS-NMR spectra of Ac-Phos-SBA-15-1 (a) and Ac-Phos-SBA-15-2 (b). The second product (b) may contain a mixture of Ac-Phos, APS, and another side product.

In the third and fourth reactions we attempted to prevent APS from grafting to the SBA-15 surface by adding a stoichiometric excess of PAA and CDI. The PAA is viscous and difficult to pipette, which led to less of an excess being added in reaction 3 than originally intended. After roto-evaporation the mixture was orange where the others were yellowish, and more viscous than the others. The ^{13}C spectrum was similar to that of Ac-Phos-SBA-15-2, except that the carbonyl peak was split into two small peaks, one at 170 ppm and one at 164.8 ppm, and without the 37 ppm peak. Based on all of the results it seems that the Ac-Phos amide carbonyl peak in our

system occurs at 169-170 ppm. This peak was observed in products 2, 3, 6 and 7. The peak at 165 ppm was observed in products 3, 4, and 5, and it could possibly be attributed to CO_2 adsorbed onto APS, or the amide side product shown in Figure 5.23. In reaction 4, the APS silane was grafted to SBA-15 first, and the APS-SBA-15 was added to the reaction mixture and stirred for 4 hours. Based on the ^{13}C NMR spectrum of the APS-SBA-15-4 product, this approach yielded only the side products that were in products 2 and 3, and none of the Ac-Phos. Reaction 5 repeated the reaction conditions of reactions 1 and 2, and yielded a product with a similar ^{13}C NMR pattern to product 3, except that instead of the peak around 170 ppm there is one around 176 ppm. Based on this NMR spectrum and the lack of affinity for Pu, it may be assumed that the ligand synthesis failed in reaction 5.

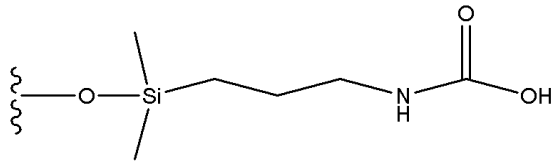

Figure 5.23. A possible side product that could have given rise to the ^{13}C NMR peak around 165 ppm that was observed for Ac-Phos-SBA-15 products 3, 4 and 5.

The increase in water that was used for reactions 6-8 was a bad mistake, and likely caused excessive polymerization of the silane. All of these products were very difficult to wash, and required excessive soaking and stirring with toluene and isopropanol. Product 8 could not even be characterized because no powder could be retrieved. Ac-Phos-SBA-15 products 2 and 7, which were the most successful at binding Pu, showed silane-to-silica peak integration ratios of 0.28 and 0.24, respectively, in their ^{29}Si MAS-NMR spectra, and TGA data (see Table 5.5) that estimated the surface density of Ac-Phos groups to be slightly less than Fryxell's Ac-Phos-MCM-41.[37] On the other hand, the ^{29}Si MAS-NMR spectra of Ac-Phos-SBA-15 products 4, 5 and 6 showed huge silane peaks with integrations larger than the silica peak. No ^{29}Si MAS-NMR spectrum was obtained for product 3. The ^{13}C NMR spectra of products 6 and 7 were very similar to that of product 2, but without the side-product peaks around 135 and 121 ppm. Based on the spectra, and the affinity for Pu(VI) presented below, it is assumed that the Ac-Phos silane was successfully synthesized in both reactions, but excessive polymerization during the grafting step left product 6 with a clumpy texture and clogged pores, greatly reducing its actinide binding capacity. A representative TEM image of Ac-Phos-SBA-15-2 is shown in Figure 5.24, indicating a well-preserved mesostructure with only a slight reduction in average pore size.

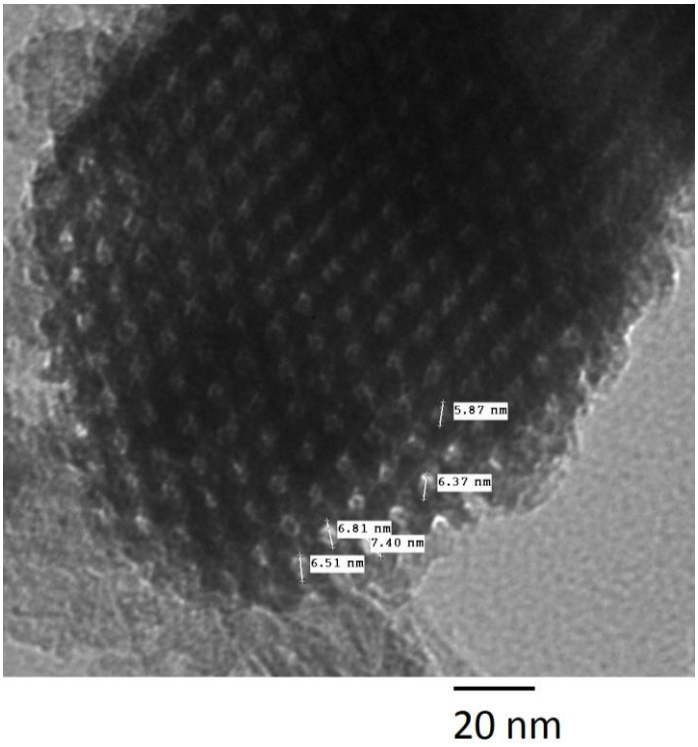

Figure 5.24. TEM image of Ac-Phos-SBA-15-2, showing the well-preserved ordered mesoporous structure.

Another way that the different reaction products were assessed was by their affinity for Pu(VI). Figure 5.25 shows average batch results from duplicate samples of seven different Ac-Phos-SBA-15 products in an approximate 1g to 6700 mL ratio with a pH 1.8, 0.1 M $NaClO_4$, 6.8 ± 0.3 µM Pu(VI) solution. Percent sorption after 20 hours contact time was determined by LSC (see Section 3.3.3) as described in Section 5.4. All of the products that bound plutonium under these conditions showed similar peaks in their ^{13}C CP-MAS-NMR spectra (along with side product peaks in reactions 2 and 3), while those that did not bind plutonium at all had variations in the ^{13}C CP-MAS-NMR spectra indicating that the silane synthesis was not successful. The decreased plutonium sorption of the Ac-Phos 3 and Ac-Phos 6 products seems to correlate with the clumpy texture and an unusually high silane-to-substrate ratio given by ^{29}Si-MAS-NMR spectra. All of the lanthanide batch sorption experiments employed Ac-Phos-SBA-15-2, and the batch experiments with Pu employed both products 2 and 7.

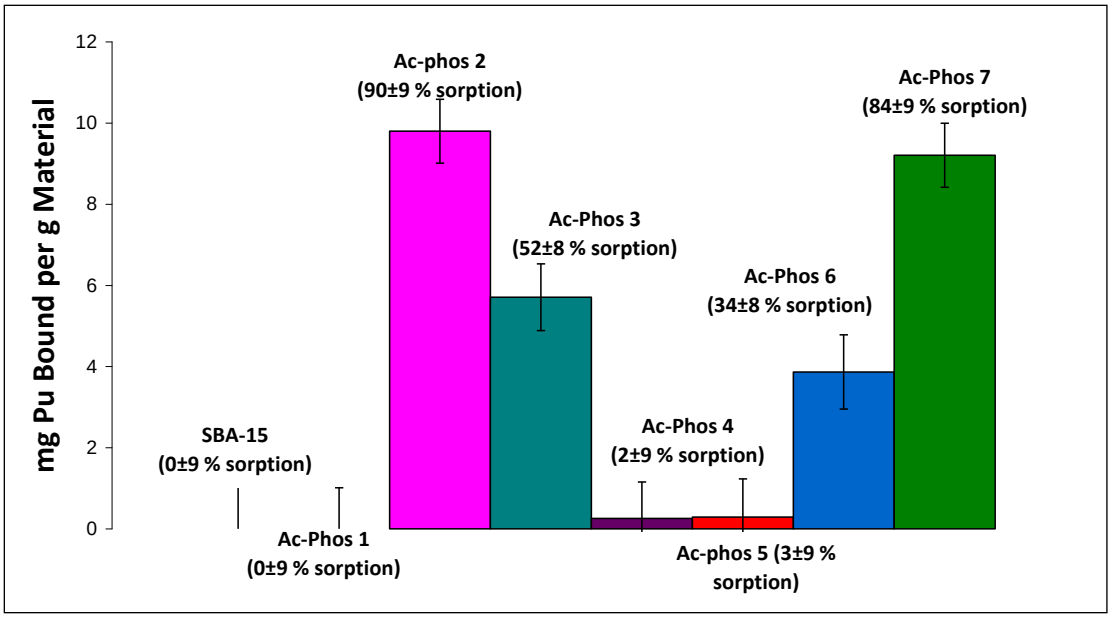

Figure 5.25. Pu(VI) binding capacities of different Ac-Phos-SBA-15 products after 20 hours contact time with 6.4 µM Pu solution in a pH 1.8 perchlorate matrix; liquid-to-solid ratio ≈ 6700 mL/g. Error bars represent 90% confidence. Results of duplicate samples are averaged.

Some important lessons were learned regarding organic modification of mesoporous silica via silane self-assembly. First, the higher purity silane that can be obtained prior to reflux, the more consistent the reaction will be. Second, our optimization using APS may have been misleading, and the reflux reaction may need to be optimized differently depending on the ligand. One should beware of excessive silane polymerization, and never use more than 2 monolayers of water. In some cases it may be better to pre-hydrate the silica by boiling in water and then drying the silica prior to reflux, instead of wetting the toluene mixture. It is possible in the Ac-Phos-SBA-15 reactions that irreproducibility arose from different sized round-bottom flasks or stir bars used for the reflux, therefore, every small detail should be carefully controlled.

5.3.5 Acid resilience tests

An important aspect of actinide binding systems for any application that requires reuse or detection of ions in acidic solutions will be the overall resilience to acid. To see if the properties of the material are changed by contact with acid, 100 mg of Ac-Phos-SBA-15-7 was rocked in a polypropylene tube with 20 mL 1 M $HClO_4$ for 5 days. The solid was then filtered, rinsed thoroughly with Milli-Q water and then isopropanol, and air dried. This product was labeled Ac-Phos-SBA-15-7'. Another sample of Ac-Phos-SBA-15-7 was rocked in 5 M $HClO_4$ for 5 days, and called Ac-Phos-SBA-15-7". The ^{13}C CP-MAS-NMR and ^{31}P MAS-NMR spectra of Ac-Phos-SBA-15-7, 7', and 7" samples were compared to look for structural changes after contact with acid. Figures 5.26-5.28 show the ^{13}C NMR spectra of the three samples. The spectra of the samples after acid contact seem to have a lower signal-to-noise, and splitting of the peak around 43 ppm and its shoulder at 38 ppm into two small peaks. As these peaks likely represent CH_2-N species in the Ac-Phos molecule and the APS side-product, the spectra suggest the cleavage occurs at the amide linkage, which is the part of the molecule most vulnerable to hydrolysis.

Acid resilience is likely dependent on the specific silane structure, but the most important feature is the hydrolysable linkage of the ligand to the surface.

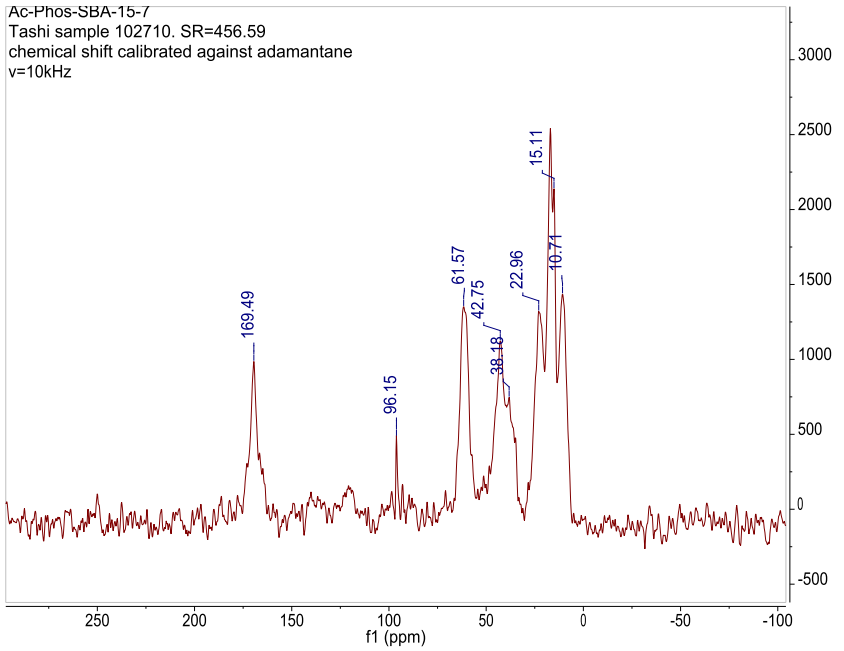

Figure 5.26. ^{13}C CP-MAS-NMR spectrum of Ac-Phos-SBA-15-7.

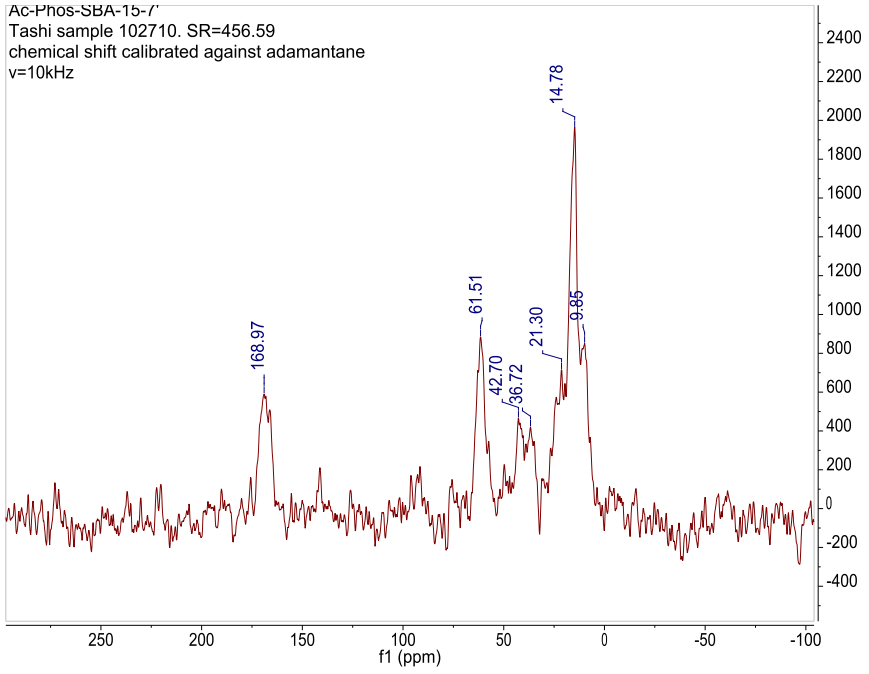

Figure 5.27. ^{13}C CP-MAS-NMR spectrum of Ac-Phos-SBA-15-7'.

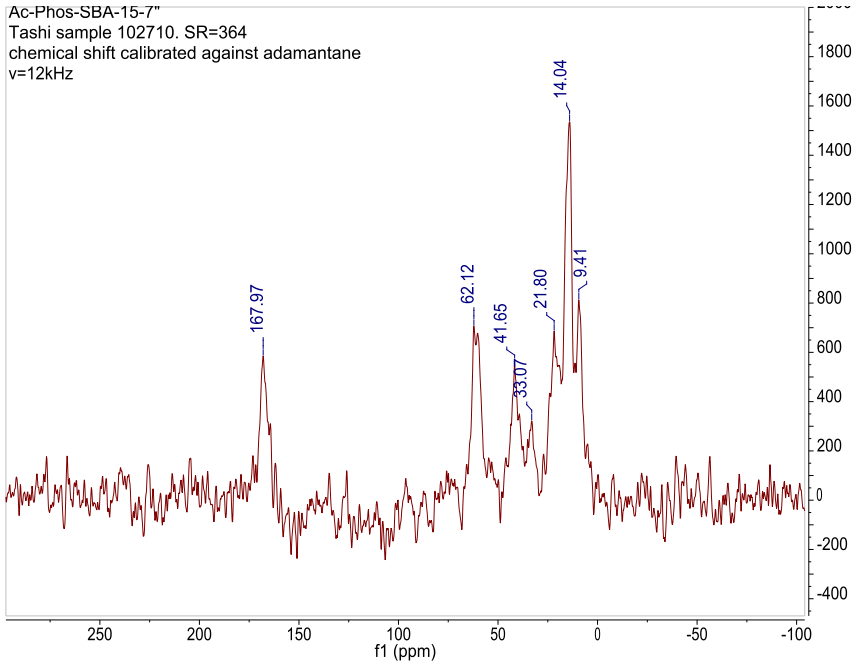

Figure 5.28. ^{13}C CP-MAS-NMR spectrum of Ac-Phos-SBA-15-7".

The ^{31}P MAS-NMR spectrum of Ac-Phos-SBA-15-7 sample is shown in Figure 5.29. The larger peak at ~16 ppm (relative to H_3PO_4 reference set to 0 ppm) is likely from the main phosphonate phosphorous in the Ac-Phos ligand, and the shoulder at ~24 ppm could be due to the starting product phosphonoacetic acid somehow bound to the surface. The ^{31}P spectra of the Ac-Phos-SBA-15-7' and Ac-Phos-SBA-15-7" samples were similar, but the main peak shifted to ~18 ppm, and the relative intensity of the shoulder increased as indicated in Table 5.7. If the increase in the ratio of the shoulder to the main peak corresponds to loss of the Ac-Phos silane, then about 28% was lost in Ac-Phos-SBA-15-7', and 61% was lost in Ac-Phos 7". The Ac-Phos-SBA-15-7 and The Ac-Phos-SBA-15-7' were later analyzed by TGA, which estimated that the 5 days contact with 1 M acid resulted in a 35% loss of surface functionalization (see Table 5.7). However, the TGA analysis assumes the loss of the entire ligand, which could be inaccurate since hydrolysis of the amide linkage would leave APS functional groups grafted. Nonetheless, the apparent reduction in Pu capacity is in fair agreement with the analysis of ^{31}P spectra and TGA results. Samples of Ac-Phos-SBA-15 7' with a liquid-to solid ratio of 6700 ± 100 mL/g at pH 1.8 and 6.8 ± 0.3 µM Pu(VI) showed a 20-hour capacity of 6.3 ± 0.9 mg per gram. This is 32% less than the original Ac-Phos SBA-15-7 samples under similar conditions, which bound 9.2 ± 0.8 mg Pu(VI) per gram after 20 hours. Unfortunately the Ac-Phos-SBA-15-7" sample was very small, and could not be analyzed beyond NMR, but the ^{31}P NMR results suggest that there was more degradation in 5 M acid than in 1 M acid.

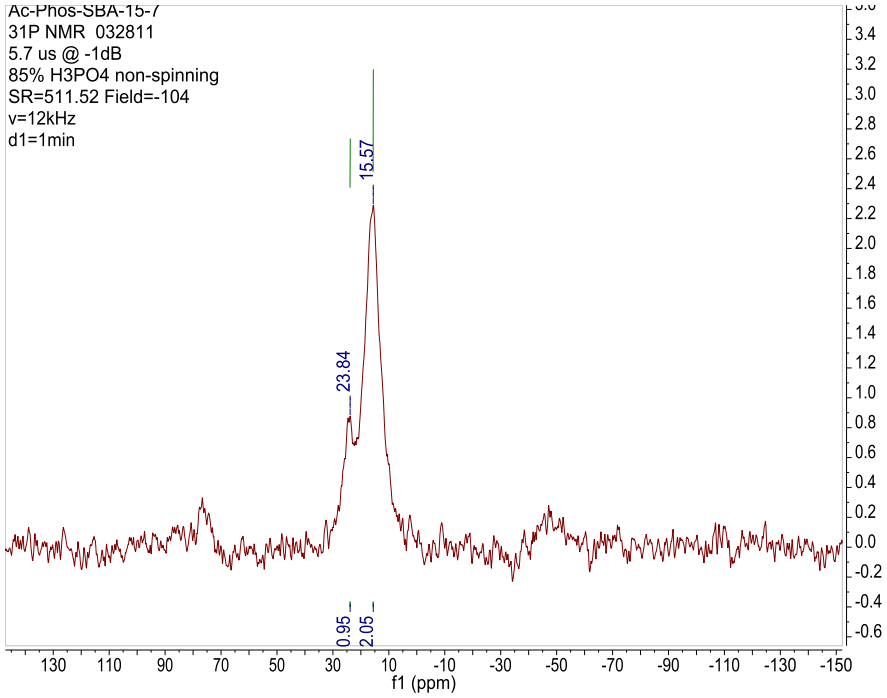

Figure 5.29. ^{31}P MAS-NMR spectrum of Ac-Phos-SBA-15-7 sample.

Table 5.7. A summary of changes in the ^{31}P NMR spectra, TGA results, and Pu binding capabilities of Ac-Phos-SBA-15-7 samples after prolonged acid contact.

Sample	^{31}P Peak integration ratio, ~24 ppm/~16 ppm	mmol Ac-Phos per g SBA-15 by TGA	mg ^{239}Pu(VI) bound per g Ac-Phos-SBA-15*
Ac-Phos-SBA-15-7	0.46	1.20	9.2 ± 0.8
Ac-Phos-SBA-15-7'	0.59	0.78	6.3 ± 0.9
Ac-Phos-SBA-15-7"	0.74	N/A	N/A

* liquid-to solid ratio of 6700 ± 100 mL/g, pH 1.8, 0.1 M $NaClO_4$, 6.8 ± 0.3 µM Pu(VI), 20 hours contact

The hydrolytic instability of organically modified silica could be one of the biggest limitations to the application of these materials to actinide extraction. The resistance to different common acids should be tested for each individual material, and is expected to vary greatly depending on the type of linkage of the ligand to the silane anchor. For example, imine linkages in other functionalized SBA-15 materials were found by Nitsche graduate student Eva Uribe to be highly unstable even in neutral pH aqueous solutions. Materials that contain only C-Si and C-C bonds between the functional group and the silica are expected to be more resistant than those containing amide linkages like in Ac-Phos. Of course, such materials are generally more synthetically challenging.

5.4 Batch sorption experiments

The batch sorption experiments simply quantify the uptake of target species in aqueous solutions by the solid mesoporous powder. We have extensively studied the complexation of Pu(V/VI), added as Pu(VI) (see Section 3.4.4), while a few experiments have also been done

with tetravalent plutonium, as well as Eu^{3+} (fission product, smaller lanthanide), Ce^{3+} (fission product, larger lanthanide), and Zr^{4+} (fission product and model for tetravalent actinides). The solids were weighed carefully into acid-washed polypropylene tubes using an antistatic ionizer. The pH-adjusted 0.1 M $NaClO_4$ or $NaNO_3$ solutions of Eu, Ce, or Zr were prepared ahead of time and directly added to the solid in the desired ratio. Small amounts of Na_2CO_3 and $NaHCO_3$ solutions were added to the 0.1 M $NaClO_4$ solutions with pH greater than 5, in order to obtain the equilibrium concentrations of HCO_3^- and CO_3^{2-} expected from dissolution of CO_2 from the atmosphere. In the Pu experiments, the background ion solution was equilibrated with the solid for one day prior to addition of ^{239}Pu stock solution. In both cases, the solution pH was adjusted immediately following contact of the target analyte with the solid, and the samples were left on a rocking platform, which rocked the sample back-and-forth about once per second for gentle mixing. The pH was checked and adjusted if necessary to maintain a constant value within 0.2 pH units. The samples were usually allowed to stand for a few minutes before aliquots were removed to monitor changes in aqueous concentration of the target species. The aliquots were centrifuged through 30000 molecular weight cut off (MWCO) regenerated cellulose filters for 12-15 minutes at 7000 revolutions per minute (RPM) to remove any solids, and the filtrate was measured using ICP-MS (see Section 4.4.1) or LSC (see Section 3.3.3). The centrifuge filters used for ICP-MS samples were 5 mL capacity Amicon series from Millipore. For Pu, 0.5 mL capacity regenerated cellulose centrifugal filters of the Vivacon 500 series from Sartorius Stedim were used. Control experiments were performed to test the analyte solubility, along with sorption to the sides of the vials and the filters. The control samples were prepared in the same way as batch contact samples, and underwent the same measurement procedures, but without a solid sorbent. For timed batch experiments, the assay time was recorded at the beginning of centrifugation. The percent sorption was calculated using Equation 5.2, where C_i and C_f are the initial and final analyte concentrations, respectively. For samples from which more than one aliquot was removed, such as batch kinetic experiments, the value of C_i was corrected for solution volume and plutonium removed from previous assays.

$$\%\, Sorption = \frac{C_i - C_f}{C_i} \times 100\ \% \qquad (5.2)$$

For many of the experiments, C_i was taken as the measured concentration of the lowest-pH control sample in the series of batch experiments. For some of the Pu experiments, C_i was calculated based on the amount of Pu stock solution pipetted into the sample. The author chose to use percent sorption as the standard measure of affinity of the solid sorbents for the target species instead of K_d, given by Equation 5.1, even though K_d is more commonly used in the literature. The main reason for this is that when there is essentially 100 percent sorption, which was often the case in Ac-Phos-SBA-15 and oxidized mesoporous carbon samples, the K_ds become arbitrarily large. This leads to large differences in K_d between samples even when the actual difference in the final concentration is within the measurement uncertainty. Furthermore, the final measured concentrations were sometimes below background (> 100 % sorption), which skewed the K_ds even more. Also K_ds technically refer to an equilibrium distribution, and in many of the Pu samples no equilibrium could be reached. Ultimately the percent sorption seemed to be more informative, but one must consider the experimental conditions (analyte concentration, liquid-to-solid ratio, etc.) when interpreting the results. The largest uncertainty associated with any of these measurements was pipetting error, which was estimated to be around five percent with 90% confidence. To justify this estimate, 1,300 sets of duplicate LSC samples containing ≥

20 dpm ^{239}Pu that were pipetted by the author in a glovebox were examined, and it was found that 67% of the duplicate vials measured the same within 2σ from counting statistics or within 2.5 %, and near 90% measured within 5%. In the ICP-MS samples, the 5% pipetting uncertainty was propagated with one standard deviation from the measured replicates, and error bars represent ≥ 1σ. For Pu measurements, the pipetting uncertainty was propagated appropriately along with 2σ from counting statistics and the standard error between the two duplicates to give the error bars that represent a 2σ confidence interval.

The use of centrifuge filters in batch experiments is controversial because the wetting volume and sorption to the filters can possibly change the measured analyte concentration. This needs to be tested whenever filters are used. Extensive filter testing experiments were done with by the author and Kestrel Brogan with Pu(VI) and both polyethersulfone and regenerated cellulose filters, and most of these results are summarized in appendix D.3 of L.K. Brogan's thesis.[83] It was found that use of the regenerated cellulose filters is acceptable under most conditions, but significant Pu sorption to polyethersulfone filters was observed. Therefore all data collected using polyethersulfone filters were disregarded. Since then, some more filter testing has been done by this author as needed. For example, it was suggested that the 40 µL aliquots used in many of the Pu experiments were too small, and thus the measured concentration changes due to the wetting volume. This was tested with solutions of 2-7 µM Pu in 1 M $HClO_4$ and 0.1 M $NaClO_4$ solutions of pH 4 and 7. Duplicate 10 µL aliquots were taken directly from about 0.75 cm below the meniscus, and duplicate 40 µL and 200 µL aliquots were removed for filtration by centrifuge. These aliquots were centrifuged through Vivacon 0.5 mL 30K MWCO regenerated cellulose filters for 13 minutes at 7000 RPM, then duplicate 10 µL aliquots of the filtrate were measured by LSC. The results showed no significant difference between any of the measured concentrations of these three solutions. In general, the use of filters is not recommended if the phases can be effectively separated by centrifugation alone. In that case, not using filters can avoid complications and the hassle of filter testing. However, some materials do not centrifuge down well, and filters must be used and tested in all applicable conditions. Here it should be emphasized that all of the batch sorption data presented in this dissertation has been verified as sorption to the solid powders using control samples and/or filter testing. Any effects of ultrafiltration on the results fall within the error bars on the plotted data.

In accordance with literature [16, 19] our first batch complexation studies were performed with an approximate 200:1 solution:solid ratio at two or more separate pH values. Each material was initially tested for affinity toward dilute solutions of a single analyte (preparation of Pu stock described in Section 3.4.3, and of lanthanide solutions in Section 4.3.2) in a 0.1 M $NaClO_4$ matrix. pH balanced solution and solid were placed in an acid washed polypropylene tube, shaken, and left on a rocking platform for one week. During the rocking period the pH of the solution was checked periodically and adjusted as necessary The Ac-Phos and TESPMA systems were further investigated in the perchlorate matrix with Pu to understand the effects of pH, liquid-to-solid ratio, Pu concentration, sorption kinetics, and reversibility.

5.4.1 Pu and lanthanide sorption as a function of pH

Batch complexation measurements of 0.15 µM Pu(VI) were performed in 0.1 M $NaClO_4$ solutions ranging from pH 1 to pH 6. In this pH range, the plutonium is relatively soluble and initially exists primarily as PuO_2^{2+} and PuO_2OH^+ (see Figure 3.13 in Section 3.4.1). Slow self-reduction to PuO_2^+ over time is expected, and at these low concentrations, Pu(V) is kinetically

stable. The initial testing conditions represent a very large excess of ligand molecules to Pu atoms, since the estimated ligand surface coverage is 1-4 mmol of ligand per gram of SBA-15 (see Table 5.5). One hundred percent binding under these conditions is only about 0.007 milligrams Pu per gram of solid (2.9 x 10^{-5} mmol/g), so high sorption is expected for any ligand with affinity toward the plutonyl cation. Figure 5.30 shows batch sorption of oxidized Pu as a function of pH for several of the functionalized SBA-15 materials. From these results, it is clear that there is no sorption to the SBA-15 substrate or the polypropylene sample vial. The SBA-15 functionalized with MHAPS and AGAPS shows little affinity toward oxidized Pu. The Ac-Phos-SBA-15 bound 100% of the plutonium at all tested pH conditions, and the TESPMA-SBA-15 bound 90% at pH 5.7. Relativistic density functional theory computations that employed B3LYP parameterization[195] have shown that the TESPMA ligand is an effective chelator of PuO_2^{2+} and PuO_2OH^+, but only when in its deprotonated form. Therefore effective binding of plutonium by this material is only expected above the predicted pKa of 3.6.

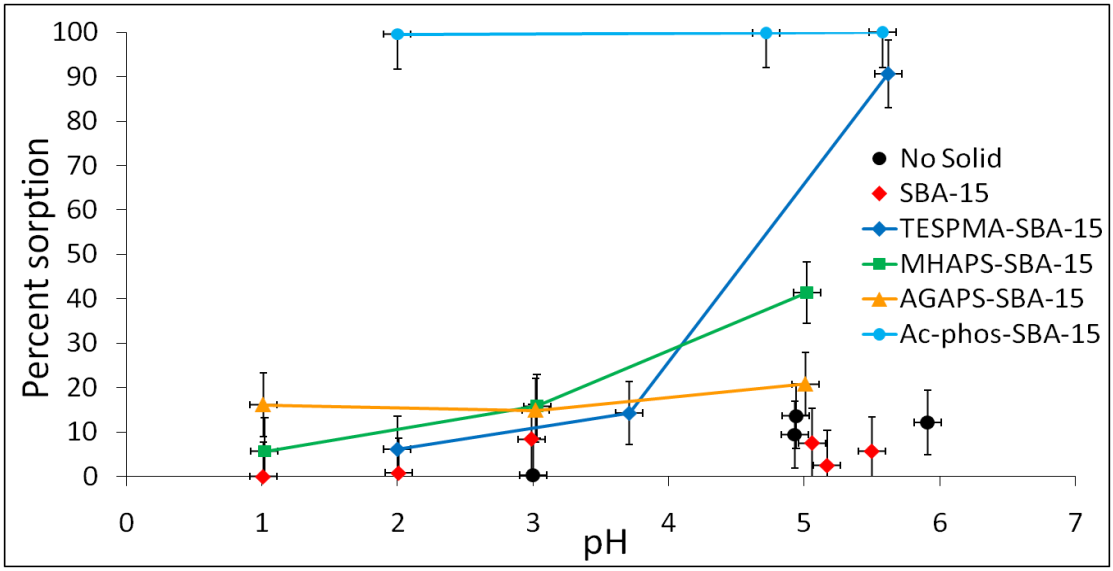

Figure 5.30. Percent Pu(VI) sorption vs. pH for SBA-15 and functionalized SBA-15 in 1:200 ratio with 0.1 M $NaClO_4$ and 0.15 µM Pu solution for 1 week. Lines are added to guide the eye.

Experimental complexation studies of Pu(IV) were limited to acidic solutions due to the very low solubility of Pu(IV) above pH 2. Batch complexation measurements of 0.15 µM Pu(IV) were performed in 0.2 M and 1 M HNO_3. Results of these tests are shown in Figure 5.31. As expected, sorption to the SBA-15 silica substrate is more significant for Pu(IV) than for Pu(VI), and the Ac-Phos-SBA-15-2 bound near 100% of the Pu in 0.2 M HNO_3. All materials showed decreased Pu(IV) binding with increased solution acidity. It is interesting to note that the MHAPS and particularly the AGAPS functionalized SBA-15 showed significant uptake of Pu(IV) in 0.2 M HNO_3, and very little uptake of PuO_2^{2+} in pH 1 $NaClO_4$. This was a promising sign of oxidation state selectivity that could be further explored. The extent of the Pu(IV) affinity of these materials was further investigated by repeating the experiment in 0.2 M HNO_3, and 0.98 ± 0.06 µM Pu(IV). Figure 5.32 shows a plot of percent sorption versus Pu(IV) concentration for these materials, indicating that AGAPS-SBA-15 has a higher capacity to bind Pu(IV) than MHAPS-SBA-15. More experiments at higher plutonium concentrations would be able to determine the true Pu(IV) capacity of these materials.

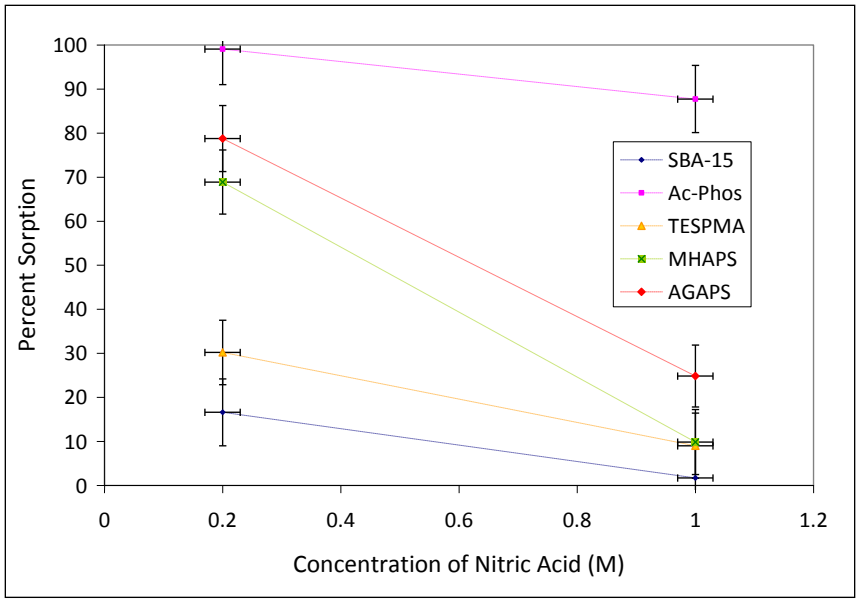

Figure 5.31. Percent Pu(IV) sorption vs. [HNO_3] for SBA-15 and functionalized SBA-15 in 1:200 liquid:solid ratio with 0.15 µM Pu solution. Lines are added to guide the eye.

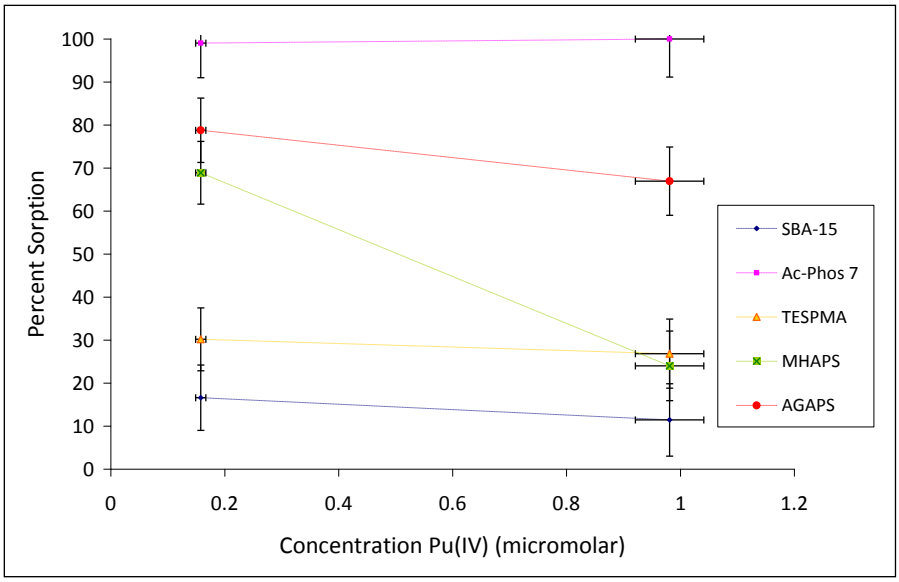

Figure 5.32. Percent Pu(IV) sorption vs. Pu concentration (µM) for SBA-15 and functionalized SBA-15 in 1:200 ratio with 0.2 M HNO_3 solution. Lines are added to guide the eye.

Figure 5.33 shows batch sorption of several species to unmodified SBA-15 type mesoporous silica. The material shows high affinity for Zr(IV) in solutions of pH 0 to 2, and bound approximately 99% of the Zr from the pH 2 solution. The trivalent lanthanides did not adsorb to SBA-15 when in solutions with pH lower than 6. In pH 6 solutions, approximately 100 percent of Eu^{3+} and Ce^{3+} adsorb to the silica surface within one week, giving 0.4 mg Ce or Eu per gram SBA-15. Significant sorption of Pu(VI) to the SBA-15 surface was not observed after one week but did occur over an extended time period. After 9 days, SBA-15 had removed only 14% Pu, initially added as Pu(VI), from a pH 6 solution, but with an additional 3 months 45% was

removed. This was likely a consequence of slow autoreduction of Pu(VI) and Pu(V) to Pu(IV). Table 5.8 summarizes the Pu uptake in aged SBA-15 samples.

Table 5.8. SBA-15 and Pu batch samples with approximately 200 mL 0.1 M $NaClO_4$ per g SBA-15, Pu uptake over time.

Solution pH after 1 week with SBA-15	% Pu removed after 1 week	% Pu removed after 6 months
2.01	1	16
5.17	3	18
5.50	6	100

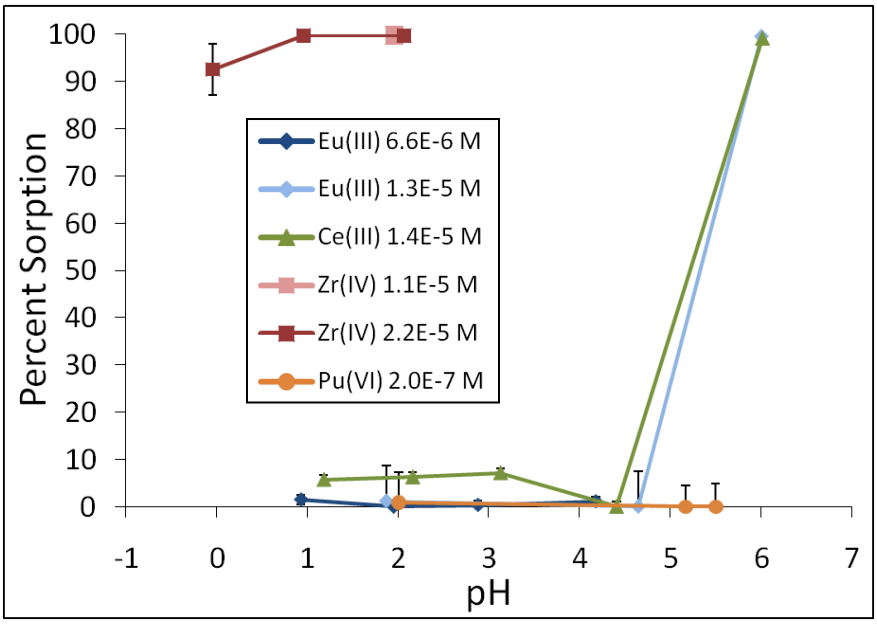

Figure 5.33. Percent sorption vs. pH for SBA-15 in 200:1 liquid:solid ratio with 0.1M $NaClO_4$ solutions containing different metal ions. Lines are added to guide the eye.

Figure 5.34 summarizes batch sorption of different target species to TESPMA-SBA-15. The TESPMA molecule contains a carboxyl group with a pKa of about 3.6, and seems to bind metal cations only when deprotonated, as expected. The apparent differences in binding affinity for Ce(III), Eu(III), and Pu(VI) at pH 3.6-4.0 are interesting considering the goal of selectivity, although the overall capacity of this material may be too low for application in separations. The material bound about 90% of Zr at pH 2, but was outperformed by the bare SBA-15 substrate, which bound approximately 99% of the Zr as described above. Overall, the TESPMA ligand seems to bind actinides and lanthanides too weakly and slowly for most applications. However, the molecule showed selectivity in different conditions, and the results were informative and demonstrated some consistency with theoretical predictions.

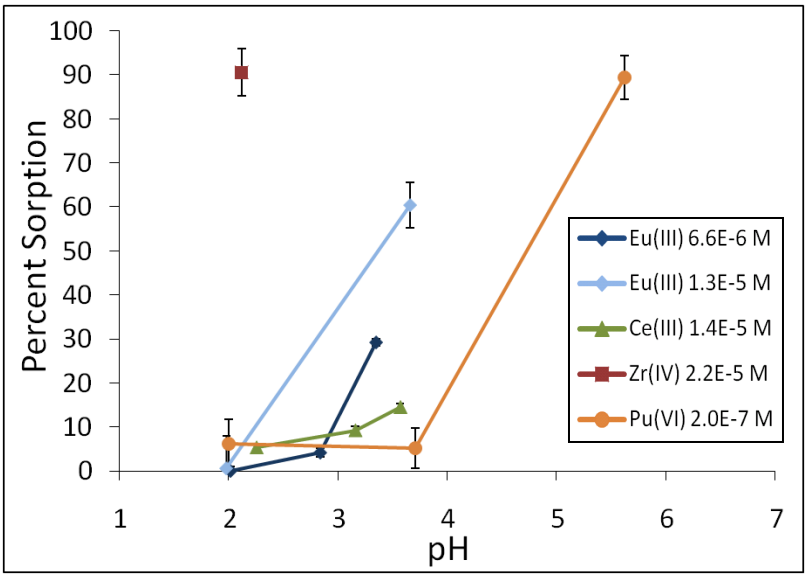

Figure 5.34. Percent sorption vs. pH for TESPMA-SBA-15 in 200:1 liquid:solid ratio with 0.1M $NaClO_4$ solutions containing different metal ions. Lines are added to guide the eye.

The results of batch experiments with Ac-Phos-SBA-15-2 with various cations are shown in Figure 5.35. Indeed this material binds 100% of all target metals in the pH range from 2 to 6. In batch experiments at all pH conditions studied, none of the Pu was released back into solution after six months, indicating good stability of the system in aqueous environments. The Ac-Phos-SBA-15 offers strong and fast binding of actinides and lanthanides as well as long-term stability. Because of the binding success of the Ac-Phos-SBA-15, a more extensive investigation of plutonium sorption with this material was performed, presented in following sections. The Ac-Phos-SBA-15 is an effective all-purpose sorbent material, but unfortunately does not seem to show any selectivity.

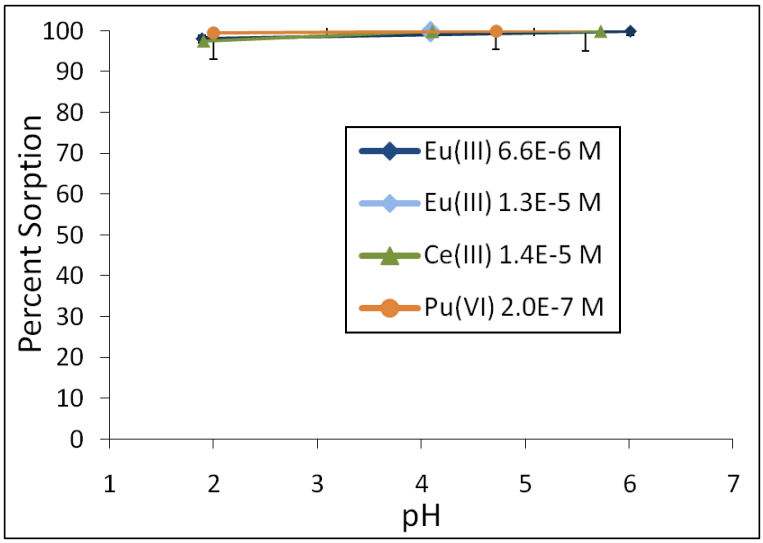

Figure 5.35. Percent sorption vs. pH for Ac-Phos-SBA-15 in 200:1 liquid:solid ratio with 0.1M $NaClO_4$ solutions containing different metal ions. Lines are added to guide the eye.

5.4.2 Pu sorption kinetics

Figure 5.36 shows percent sorption versus time for samples of Ac-Phos-SBA-15-2 and TESPMA-SBA-15 in contact with 0.2 µM Pu(VI) in pH 6 $NaClO_4$ solution with a liquid-to-solid ratio of 200 mL/g. The complexation by Ac-Phos-SBA-15 is fast, PuO_2^{2+} was completely removed from the pH 6 within 15 minutes of contact. On the other hand, TESPMA-SBA-15 seems to react slowly to bind Pu species, as shown in Figure 5.36. About 80% of the Pu in solution was removed within two days, and 98% was bound after nine days. When the solution was assayed again three months later, 99% of the Pu remained on the solid, showing that the Pu was not released back into solution over time. In lower pH environments, the TESPMA-SBA-15 binds more Pu over long periods of time, as indicated by the results shown in Table 5.9. This is also likely because of reduction to Pu(IV) over time.

Table 5.9. Pu uptake over time in batch samples of TESPMA SBA-15 with approximately 200 mL 0.1 M $NaClO_4$ 0.2 µM Pu solution per g TESPMA-SBA-15.

Solution pH after 1 week with TESPMA-SBA-15	% Pu removed after 1 week	% Pu removed after 6 months
2.00	6	67
3.71	14	96
5.62	91	100

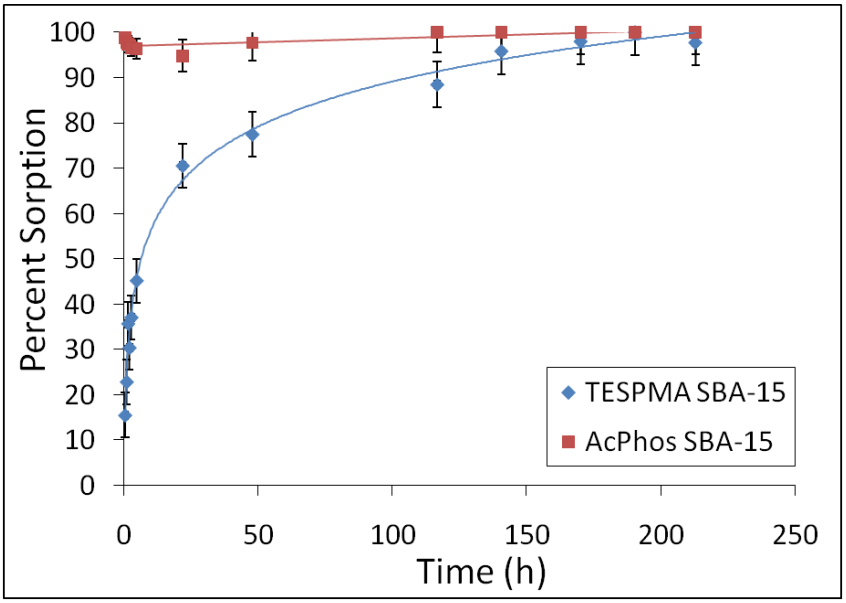

Figure 5.36. Complexation kinetics of AcPhos SBA-15 and TESPMA SBA-15 with 0.2 µM Pu(VI) in pH 6 $NaClO_4$ solution. Lines are added to guide the eye.

In some cases, sorption is very fast when there is a large excess of surface groups, but takes longer when there is more Pu to bind. The kinetics of Pu(VI) uptake to Ac-Phos-SBA-15-2 was later measured in a batch sample with 900 ± 20 mL/g $NaClO_4$ solution with ionic strength of approximately 0.4 M, 53 ± 13 µM Pu, maintained at pH 4.0 ± 0.1. Figure 5.37 is a plot of percent Pu sorbed vs. minutes elapsed since Pu was added to the solution in contact with the Ac-

Phos-SBA-15-2. The first aliquot was taken after 2 minutes when the solution pH was still ~1.5, and already over 98% of the Pu was on the solid phase. An interesting side note is that this experiment was done 3 years after the Ac-Phos-SBA-15-2 synthesis, and the results indicate that the material is stable in air with a long shelf-life.

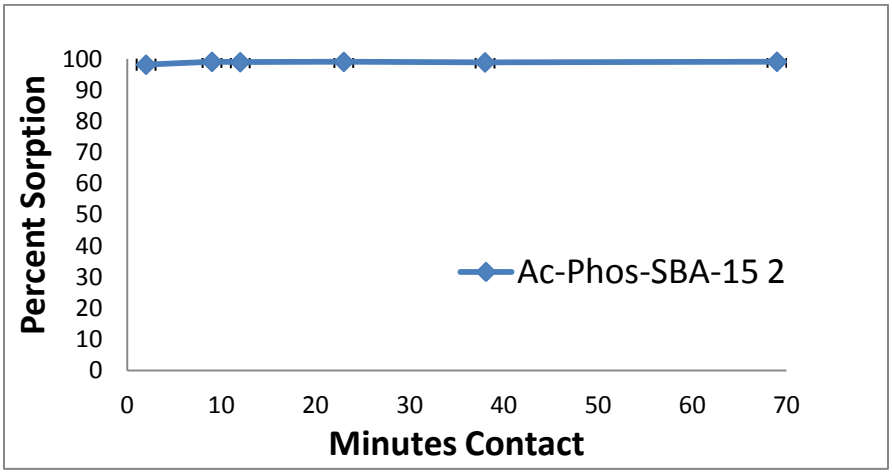

Figure 5.37. Percent Pu(VI) sorption to Ac-Phos-SBA-15 vs. minutes contact in a batch sample with 900 ± 20 mL/g $NaClO_4$ solution with ionic strength of approximately 0.4 M, 53 ± 5 µM Pu(VI), maintained at pH 4.0 ± 0.1 (except the first and second data points, which were taken when the pH was 1.5 and 3.6, respectively).

5.4.3 Pu uptake capacities

Sorption experiments performed at low plutonium concentrations and low liquid-to-solid ratios served to demonstrate the materials' affinity toward plutonium, but gave no information about the plutonium capacity of each material. In an attempt to experimentally determine the limits of Pu uptake of the Ac-Phos functionalized SBA-15, batch experiments were performed with a high liquid-to solid ratio of 6700 ± 100 mL/g at pH 1.8. Fresh Pu(VI) stock solution in 1 M $HClO_4$ was added in 7 increments, each time adjusting the pH and measuring the plutonium concentration in solution after 1-5 days via LSC. The SBA-15 tubes served as control samples to verify the amount of Pu added to each tube and demonstrate the solubility of Pu in the experimental conditions since it was previously shown that Pu(VI) does not sorb to SBA-15 below pH 5. Figure 5.38 shows a plot of the total milligrams of Pu bound per gram of Ac-Phos-SBA-15-2 and Ac-Phos-SBA-15-7 versus the total plutonium concentration. Under these conditions, the experimentally determined Pu(VI) capacity is 30 ± 3 mg ^{239}Pu per gram Ac-Phos-SBA-15. This corresponds to approximately 0.13 mmol sorbed per g Ac-Phos-SBA-15, which indicates either greater than 1:1 complexation between the Ac-Phos molecule and the Pu cation, or that not all of the Ac-Phos molecules are available for binding under these conditions, since TGA analysis estimated a surface coverage of 0.9-1.1 mmol AcPhos per g Ac-Phos-SBA-15. The Ac-Phos-SBA-15-7 seemed to have slightly higher capacity than Ac-Phos-SBA-15-2, although the difference is within the error bars. The irreproducibility of the uptake with larger amounts of Pu is likely due to surface saturation. However, the system may have difficulty reaching equilibrium at such high liquid-to-solid ratios. Another experiment was performed in which duplicate samples of Ac-Phos-SBA-15 product 7 were prepared with liquid-to-solid ratios varying from 200 to 5000 mL/g, all with 0.1 M $NaClO_4$ at pH 1.80 ± 0.04 and 0.18 ± 0.01 µM ^{239}Pu(VI). With a contact time of 20 hours, 100% Pu uptake was expected for samples that had

reached equilibrium since the amount of Pu added was well below capacity. Figure 5.39 shows the results, which indicate that that the batch samples with liquid-to-solid ratios above 2000 mL/g give variable sorption. A standard liquid-to-solid ratio of 1000 mL/g was adopted for subsequent experiments. The experimental capacity of Ac-Phos-SBA-15 is likely greater than or equal to 30 mg ^{239}Pu per gram at lower liquid-to-solid ratios, and may also be pH dependent.

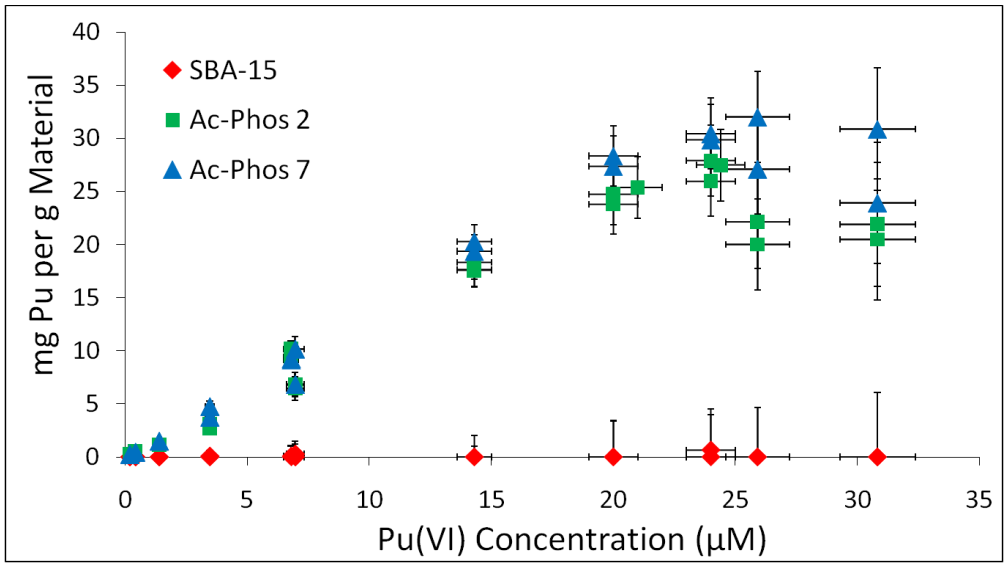

Figure 5.38. Milligrams ^{239}Pu bound per g Ac-Phos-SBA-15 while in contact with pH 1.8 0.1 M $NaClO_4$ samples with a liquid-to-solid ratio of 6700 mL/g.

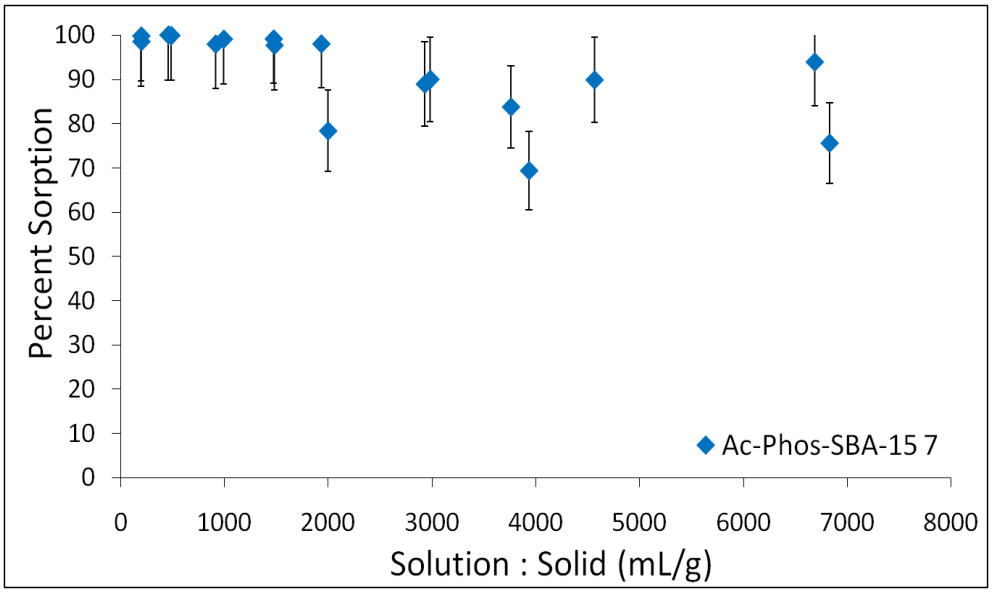

Figure 5.39. Percent Pu sorption vs. liquid-to-solid ratio for samples of Ac-Phos-SBA-15-7, in contact with pH 1.8, 0.1 M $NaClO_4$, 0.18 µM Pu solution for 20 hours.

5.4.4 Reversibility of Pu sorption

One major challenge for this project is to develop binding sites on functional materials that are effective in acidic solutions where actinides are most commonly found due to their solubility, and yet can be reused after binding is reversed. It has been reported with similar materials in the literature[37] that metal ions were removed with 0.5 M HCl for effective reuse of the material. However, attempts to remove small amounts of Pu from Ac-Phos-SBA-15 batch samples with up to 3 M HCl were unsuccessful. This Ac-Phos ester silane is a neutral molecule and a good example of a surface ligand that is effective in low pH conditions. The reversibility of Pu binding was tested in samples with both relatively large amounts of Pu and small amounts of Pu loaded. Concentrated $HClO_4$ was added incrementally to pH 1.8 0.1 M $NaClO_4$ samples with an initial liquid-to-solid ratio of 6700 mL/g and a total Pu concentration of 24 ± 1 μM, and allowed at least 20 hours of equilibration time before assay. The final liquid-to-solid ratio of the samples was 7500 ± 100 mL/g, and the final total Pu concentration was 22 ± 1 μM. Figure 5.40 presents a plot of the milligrams of ^{239}Pu per gram Ac-Phos SBA-15 that remain bound to the solid versus the H^+ activity of the solution. In these samples, approximately 70% of the plutonium was recovered in 1 M $HClO_4$, and little improvement was observed with higher acid concentrations. Ac-Phos-SBA-15 samples of various liquid-to-solid ratios, all in 0.1 M $NaClO_4$ at pH 1.8 and 0.18 ± 0.01 μM $^{239}Pu(VI)$ were subject to the incremental addition of $HClO_4$ and the plutonium concentration was measured after at least one day of equilibration. Figure 5.41 shows a plot of percent sorption versus H^+ activity for these low Pu concentration samples. These results confirm that the Ac-Phos-SBA-15 material does not release small amounts of Pu in equilibrium with up to 3 M acid, especially at low liquid-to-solid ratios. Testing with $HClO_4$ concentrations greater than 3 M was incompatible with the centrifuge filtration method employed for LSC analysis. The sorption of Pu(IV) to Ac-Phos-SBA-15 seems to be irreversible. The acidity of the Ac-Phos-SBA-15 XAS sample containing about 5 mg/g sorbed Pu, which was loaded as Pu(IV) in 0.6 M HNO_3, was increased to 2.5 M HNO_3, with no desorption of Pu. The results of these reversibility experiments suggest that the Ac-Phos-SBA-15 material may be more suitable for vitrification and long-term waste storage applications than for sensor applications. However, it is possible that a dynamic flow of acidic solution could remove all the plutonium bound to Ac-phos-SBA-15. The reversibility of materials that exhibit pH-dependent binding was expected to be easier to achieve, and this was tested with TESPMA-SBA-15. Figure 5.42 shows percent sorption vs. pH for the TESPMA-SBA-15 XAS sample that had about 3 mg/g Pu loaded as Pu(VI) in pH 6 solution. Desorption was incomplete and started at a lower pH than expected based on the sorption curve. However, the different desorption behavior makes sense in light of the XANES analysis of this sample (see Section 5.5.1), which showed that the Pu associated with the solid phase was tetravalent.

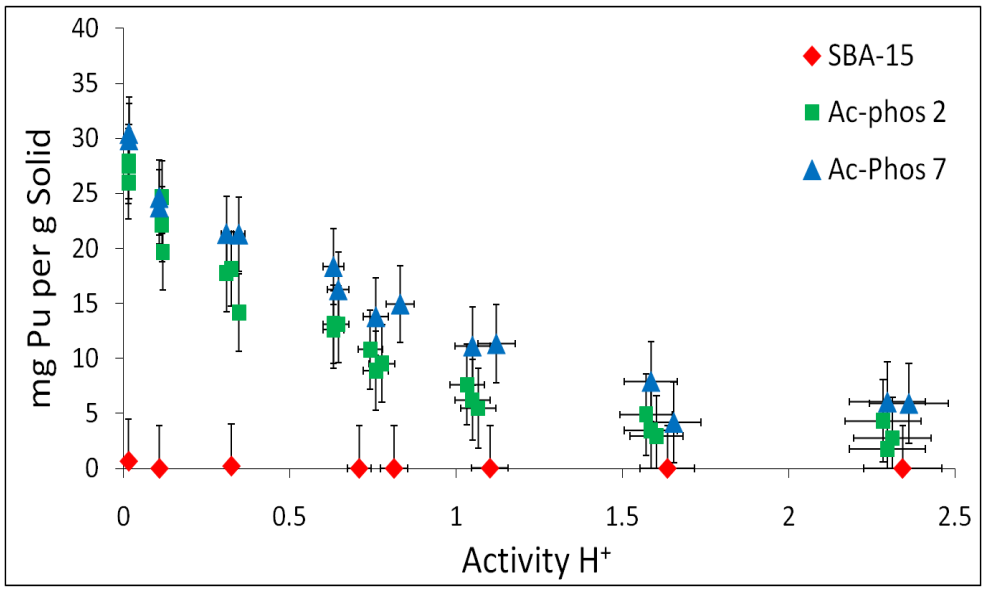

Figure 5.40. Milligrams Pu bound per g Ac-Phos-SBA-15 vs. H^+ activity as $HClO_4$ was incrementally added to samples starting at pH 1.8, in 0.1 M $NaClO_4$ and 24 ± 1 µM Pu, and a liquid-to-solid ratio of 6700 mL/g.

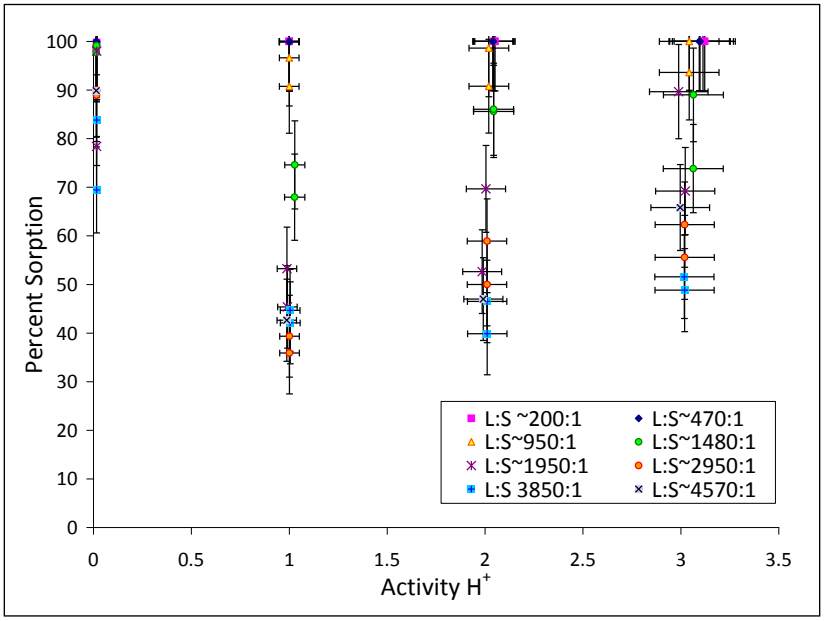

Figure 5.41. Percent sorption vs. H^+ activity as $HClO_4$ was incrementally added to Ac-Phos-SBA-15 samples of various liquid-to-solid ratios, all initially at pH 1.8 with 0.1 M $NaClO_4$ and 0.18 ± 0.01 µM ^{239}Pu(VI).

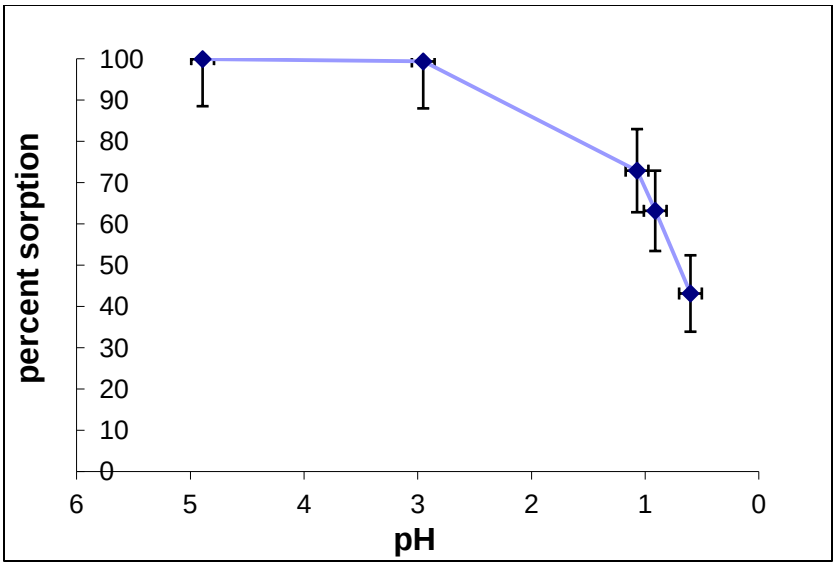

Figure 5.42. Percent sorption vs. pH as $HClO_4$ was incrementally added to a sample of TESPMA-SBA-15 with approximately 3 mg/g Pu sorbed as Pu(VI) from pH 6, 0.1 M $NaClO_4$ solution. Lines are added to guide the eye.

5.5 X-ray absorption spectroscopy (XAS) experiments

Plutonium L_{III}-edge XAS experiments were performed on samples of Pu(VI) bound by both Ac-Phos-SBA-15-2 and TESPMA-SBA-15 in a perchlorate matrix, and on Pu(IV) bound by Ac-Phos-SBA-15-7 in a nitrate matrix. Section 3.3.5 gives an overview of how the XAS experiments work and the methods used for data analysis.

5.5.1 Pu L_{III} XANES analysis of Ac-Phos-SBA-15 and TESPMA-SBA-15 samples

Table 5.10 summarizes the batch conditions of the three samples of functionalized SBA-15 that were prepared for analysis by XAS. The first was a sample of Ac-Phos-SBA-15-2 loaded with Pu(VI) in a pH 4.3-4.6 perchlorate solution. The XANES data collected on this sample were analyzed by Yung-Jin Hu, who carefully considered the beam-induced reduction of Pu in the sample.[61, 196] Figure 5.43 shows the plutonium L_{III}-edge XANES spectra of 20 consecutive scans overlaid. The least-squares fits of these individual spectra are plotted against the time exposed to the X-ray beam in Figure 5.44. The XANES data in the first scan revealed that the plutonium bound to or associated with the solid surface was approximately 68% Pu(VI) and 32% Pu(V), indicating that no redox chemistry occurred during the binding process. Reduction of Pu(VI) to Pu(V) is expected without the presence of any solid, and the control sample described in Section 3.4.4 suggests that without interference from the solid, the sample would have contained between 40% and 50% Pu(VI) at the time of measurement. Complexation by the Ac-Phos molecule would be expected to stabilize Pu(VI) somewhat, relative to Pu(V), so the higher percentage of Pu(VI) in this sample is not surprising. However, Figure 5.44 shows that over the period of 8 hours of beam exposure there was furthur reduction of Pu(VI) to Pu(V). The Nitsche group has previously observed X-ray beam-induced reduction of plutonium in mineral samples at room temperature, but cryogenic temperatures below 50 K had thus far been sufficient to retard such chemistry.[196] Plutonium in organically modified silica samples seems to undergo slight beam-induced reduction even at 30 K.

Table 5.10. Summary of functionalized SBA-15 samples prepared for XAS.

Sample	g solid (± 0.0001)	mL Solution (± 0.1)	Solution	mg Pu per g solid (± 0.3)	% Sorption (± 7%)	Days contact before measurement
Pu(VI)-AcPhos	0.0963	10	0.1 M $NaClO_4$, pH 4.6	6.3	99.8	6
Pu(IV)-AcPhos	0.0924	10	0.1 M HNO_3	5.0	92.7	3
Pu(VI)-TESPMA	0.1100	10	0.1 M $NaClO_4$, pH 5.0	3.0	98.4	12

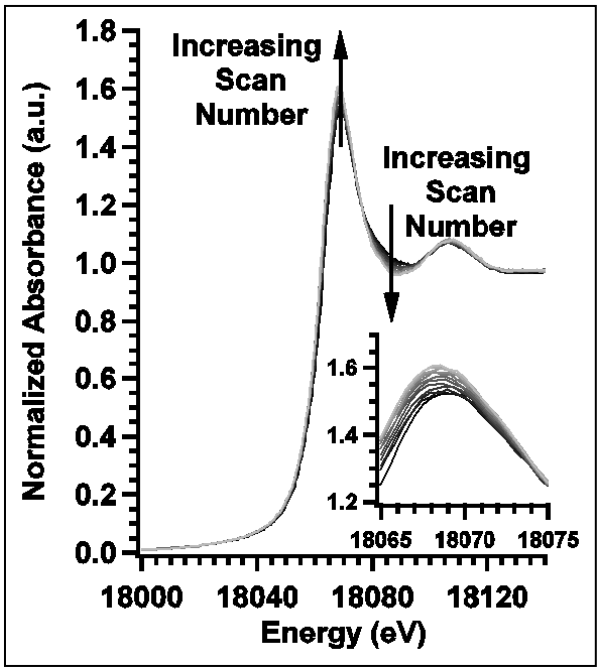

Figure 5.43. L_{III}-edge XANES spectra of plutonium on Ac-Phos-SBA-15 in a pH 4.4 solution at 30 K. 20 scans at approximately 25 minutes per scan are overlaid. (Inset) Enlargement of the XANES peak better displays the spectral changes with increasing beam exposure.[61]

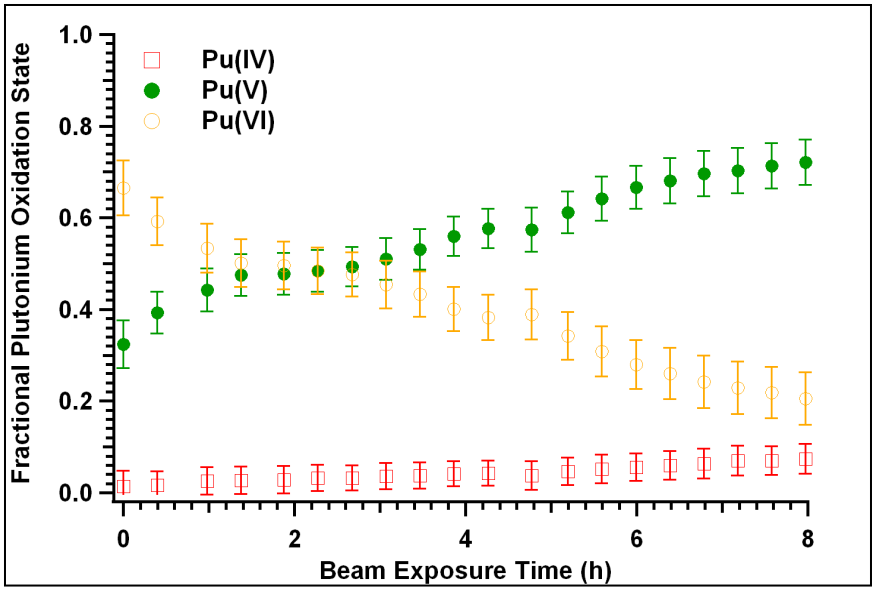

Figure 5.44. Least-squares fit of XANES spectra of plutonium on Ac-Phos-SBA-15 in a pH 4.4 solution at 30 K (Figure 5.43), plotted against the time exposed to the X-ray beam.[61]

All subsequent organically-modified silica XAS experiments were then limited to 5 scans, and data from each individual scan was subject to least-squares fitting to ensure accuracy. Duplicate XAS samples were prepared from each batch sample to gain better statistics, and fortunately the plutonium loading capacity of the functionalized-SBA-15 materials is high, so the quality of data obtained in just a few scans is sufficient. The XANES data was analyzed by Dr. Daniel Olive. Figure 5.45 shows the normalized X-ray absorption spectra in the XANES region, offset for clarity, along with the XANES spectra for the standards used in linear combination analysis (LCA) fitting. The feature in the sample spectra at 18082 eV is from a crystal glitch in the monochromator and did not significantly affect the fits. Visual inspection of the spectra reveals the presence of the plutonyl shoulder in the Pu(VI)-AcPhos sample, and to a lesser extent in the Pu(IV)-AcPhos sample, while the Pu(VI)-TESPMA sample looks closer to Pu(IV).

The data collected on each sample in the first scan were subject to LCA fitting, using a solid state Pu(IV) and aqueous Pu(V) and Pu(VI) standards. No restraints were applied to the fitting. In two of the cases, the addition of a third candidate standard had no impact on the fit, and so they were fit with only two standards. The combinations were selected based on providing the best quality fit with no restraints that still yielded physical (non-negative values) results. Totals of components were between 97.6 and 103.9 % for all cases, and have been rescaled to a total of 100%. The LCA fitting results from the three samples are shown in Figures 5.46-5.48, and tabulated in Table 5.11. The residual component in each plot represents the difference between the actual data and the fit. A slightly different oxidation state composition was obtained for the Pu(VI)-AcPhos sample from the LCA fitting performed by Dr. Olive (Figure 5.46, Table 5.11) than that performed by Dr. Hu, and this is likely due to the slightly different choice of standards for fitting. However, both analyses indicate that all of the Pu in this sample remains in an oxidized state (mostly Pu(VI)), showing that there is no redox reaction between Pu and Ac-Phos-SBA-15. The Pu(IV)-AcPhos sample also underscored this point, as Pu in that sample is largely tetravalent. The Vis-NIR spectrum of the nitric acid solution that was loaded onto this

sample showed Pu(IV) with a very small Pu(VI) component, so the XANES analysis demonstrates that the Pu oxidation state was completely unchanged upon Pu complexation by Ac-Phos. This was the expected result, as the Ac-Phos molecule has no obvious source of electrons to act as a reducing agent. On the other hand, the Pu(VI)-TESPMA sample was loaded with Pu(VI), and XANES analysis (Figure 5.48, Table 5.11) indicate that the Pu is tetravalent. Interpretation of this result is complicated by the fact that the sample equilibrated for 12 days in pH 5 solution before the XAS measurement, so significant auto-reduction of Pu would be expected in this sample (see Section 3.4.4). However, as discussed in Section 3.4.4, the dominant expected reduced species is Pu(V), which was shown in 0.1 M $NaClO_4$ solutions to be kinetically stable for up to 236 days in a concentration of ~ 1 μM.[142] The total Pu concentration in the Pu(VI)-TESPMA sample was approximately 138 μM, so more disproportionation of Pu(V) would be expected. Still, it appears likely that a mixture of Pu oxidation states would be obtained without the presence of the TESPMA-SBA-15, thus the TESPMA molecule acted in some capacity as a reducing agent toward Pu. That result was unexpected, as the oxidation product of maleamic acid is not obvious. A possible electron source for Pu reduction is the C=C double bond in between the carboxyl and amide groups, but the loss of these electrons would form carbocations, which generally only exist as intermediates in alkene addition reactions.

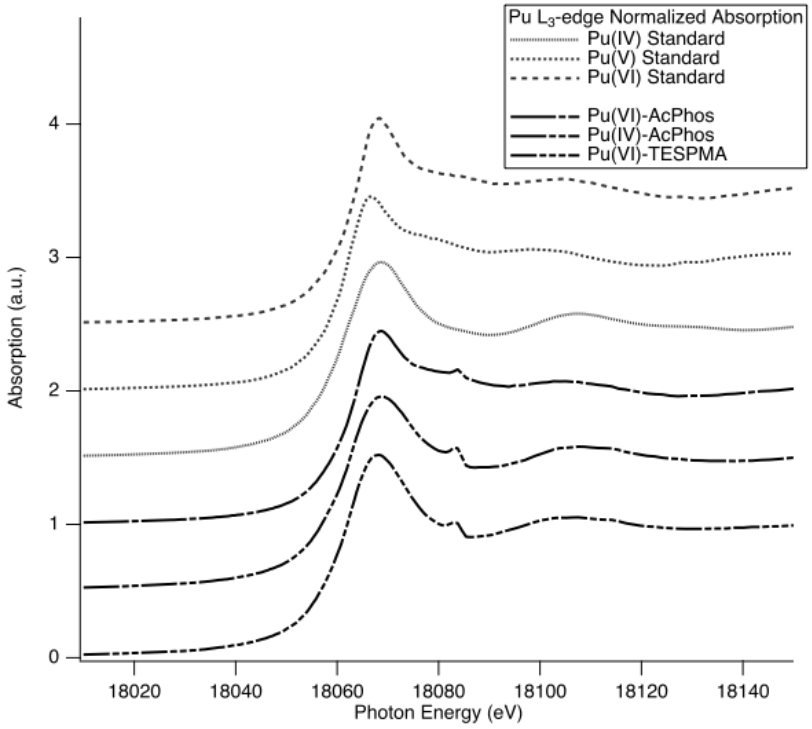

Figure 5.45. Normalized XANES spectra are shown for the XANES standards (used in LCA fitting, Table 5.11) and the functionalized SBA-15 samples, offset for clarity.

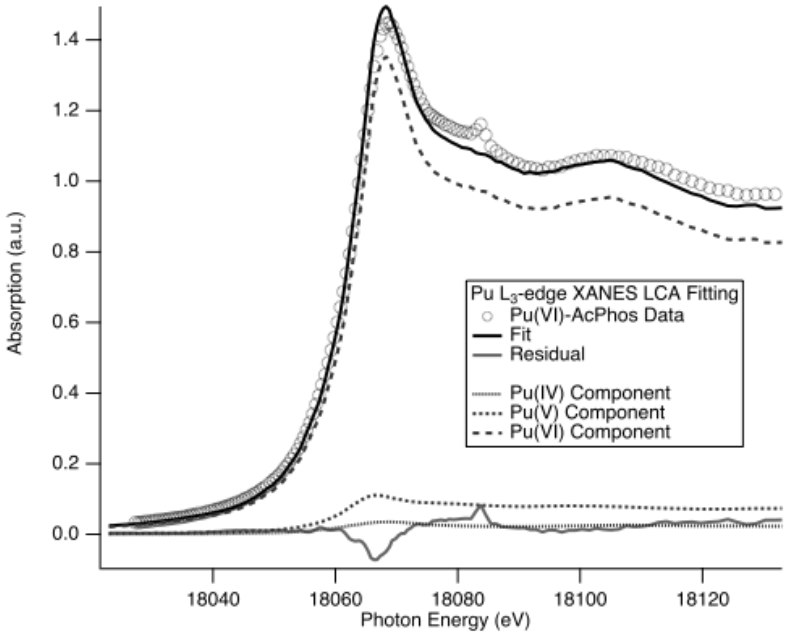

Figure 5.46. Linear combination analysis fitting results for the Pu(VI)-AcPhos sample.

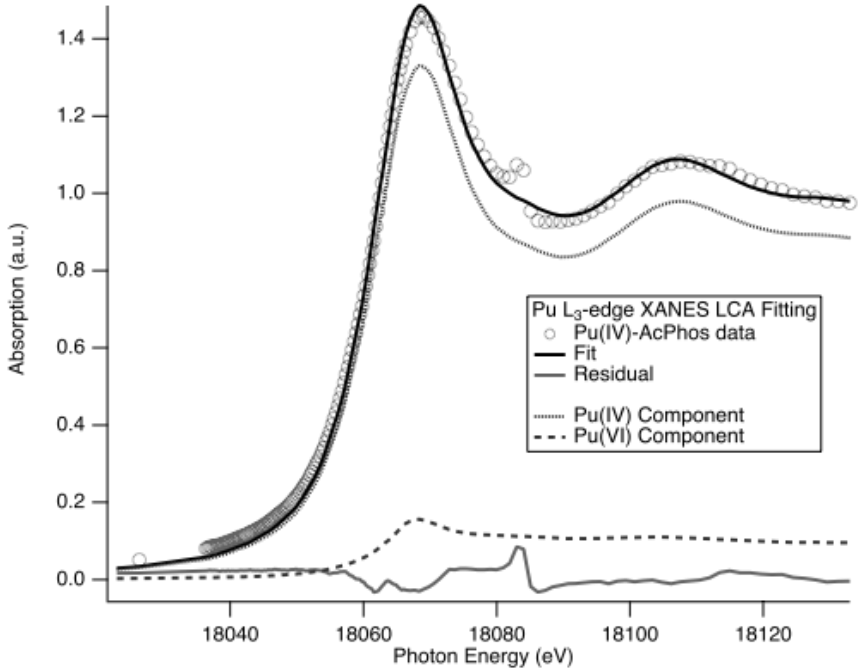

Figure 5.47. Linear combination analysis fitting results for the Pu(IV)-AcPhos sample.

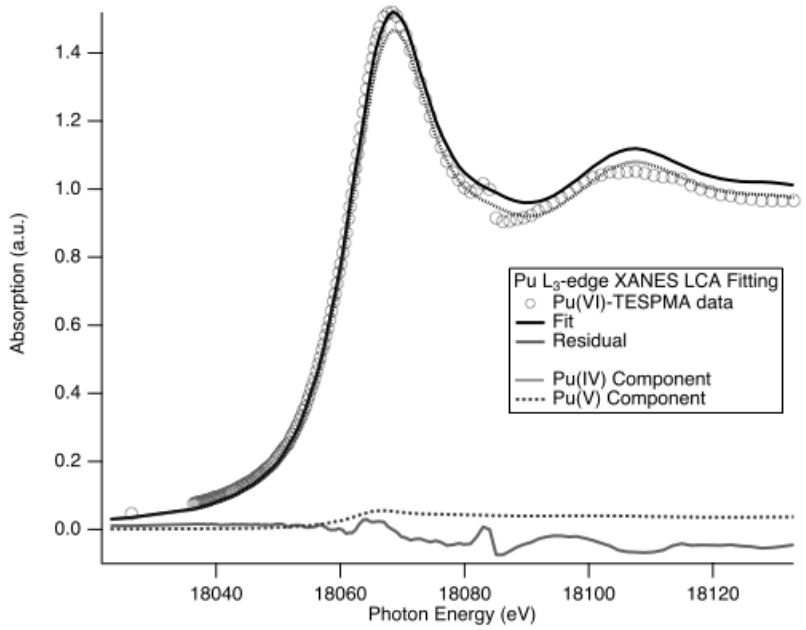

Figure 5.48. Linear combination analysis fitting results for the Pu(VI)-TESPMA sample.

Table 5.11. Summary of results from linear combination analysis of XANES data collected on samples of Pu bound to functionalized SBA-15.

Sample	Edge Position (eV)	Peak Position (eV)	% Pu(IV)	% Pu(V)	% Pu(VI)
Pu(IV)-AcPhos	18062.8 ± 0.3	18068.9 ± 0.3	90.0 ± 10.0	-	10.0 ± 10.2
Pu(VI)-TESPMA	18062.9 ± 0.3	18068.1 ± 0.3	96.3 ±10.3	3.7 ± 10.3	-
Pu(VI)-AcPhos	18064.5 ± 0.3	18068.7 ± 0.3	2.5 ± 13.9	7.8 ± 15.5	89.8 ±13.9

5.5.2 Pu L_{III} EXAFS of Ac-Phos-SBA-15 and TESPMA-SBA-15 samples

As described in Section 3.3.5, analysis of the EXAFS region of XAS spectra can provide information about the coordination environment of Pu in the samples. The project included collaboration with Professor Krishnan Balasubramanian and his group, formerly of California State University, East Bay, and now at the University of Houston, Texas, who did high-level relativistic *ab initio* computational modeling studies on the Pu(VI) complexes expected on the functionalized SBA-15 materials. Only the EXAFS data collected on the Pu(VI)-AcPhos-SBA-15 sample could be fit to the calculated model, because no models were calculated for Pu(IV) complexes. The Pu(IV)-AcPhos and Pu(VI)-TESPMA samples contained only tetravalent Pu, and the Fourier transforms of their EXAFS spectra are shown in Figure 5.49. Inspection of the Fourier transforms indicates a lack of Pu-Pu scattering in the samples, which manifests as a peak at 3.7 Å in the Fourier transform of the PuO_2 EXAFS data. It has been demonstrated with the carbon samples (see Section 6.4) that this Pu-Pu scattering feature would be observed if there were PuO_2 precipitates or colloids in the samples.[63, 119] Thus, the Pu in the functionalized SBA-15 samples appears to be complexed rather than precipitated. This result was completely

expected in the Pu(IV)-AcPhos sample, as the solution was acidic, and the Ac-Phos molecule is established as an effective Pu complexing ligand.[16] The lack of PuO_2 precipitates or colloids in the Pu(VI)-TESPMA sample is remarkable considering the relatively high solution pH, and slow rate of sorption of Pu to TESPMA-SBA-15 (see Figure 5.36). The reduction of Pu(V/VI) to Pu(IV) must have occurred just as slowly as the Pu complexation by TESPMA, otherwise the Pu(IV) would have precipitated in pH 5 solution.

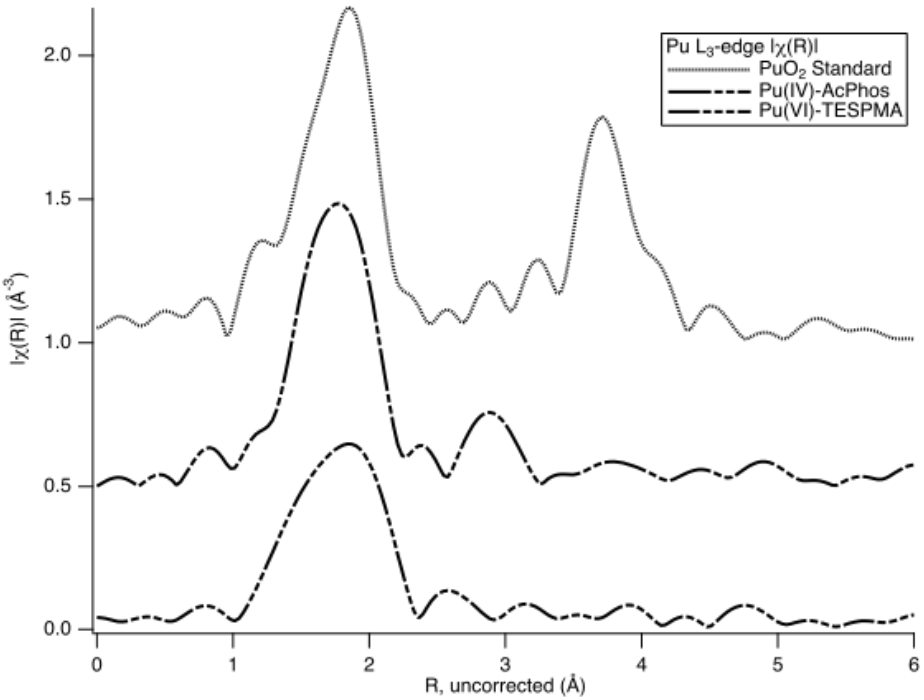

Figure 5.49. EXAFS Fourier transform magnitude of the Pu(IV)-AcPhos and Pu(VI)-TESPMA samples, showing a lack of Pu-Pu scattering (the peak at 3.7 Å in the PuO_2 sample).

The high-level relativistic *ab initio* computational modeling studies included density functional theory computations that employed B3LYP parameterization, and were intended to inform experiments and guide our choice of ligands. However, consistent agreement between experimental and computational results must be demonstrated before modeling can be used predictively. Based on the experimental and computational results for PuO_2^{2+} complexation by Ac-Phos, TESPMA, AGAPS and MHAPS, the calculations were not predictive. The DFT calculations could accurately predict when a ligand has no affinity for a target species, but when high thermodynamic stability is predicted, experimental results varied because of kinetic hindrances and other factors. Because there are no crystallographic data available with Pu complexes by these ligands, the calculated optimized geometries served as models for fitting the EXAFS data. Figure 5.50 shows geometry optimizations of the plutonyl complexes that were performed with initial *trans*- orientation of the *di*-oxo group on the plutonium. The axial and equatorial Pu-O bond lengths in the complexes $[(TESPMA)_2\text{-}PuO_2]$ and $[(Ac\text{-}Phos)_2\text{-}PuO_2]^{2+}$ are pictorially shown in Figure 5.50 for gas-phase calculations using simplified truncated versions of the Ac-Phos and TESPMA ligands. Both Ac-Phos and TESPMA form 2:1 bidentate octahedral complexes with the plutonyl cation, and the equatorial Pu-O bond lengths are notably shorter in the Ac-Phos complex. Table 5.12 gives a comparative tabulation of the metric parameters (bond lengths and bond angles) around the Pu center for the full anchored ligands in the gas phase, and

the truncated ligands in gas and solution phase. The geometry optimization of the complexes showed very little change in the axial O=Pu=O bond lengths, whereas the equatorial Pu-O bond length showed more variations for the complexes. The equatorial bond lengths were similar for the trunctated and full anchored complexes, and only the truncated version was modeled in solution phase. The solution phase data were used as models for EXAFS fitting, because the experimental systems were always in aqueous media, and solvation effects can be significant.

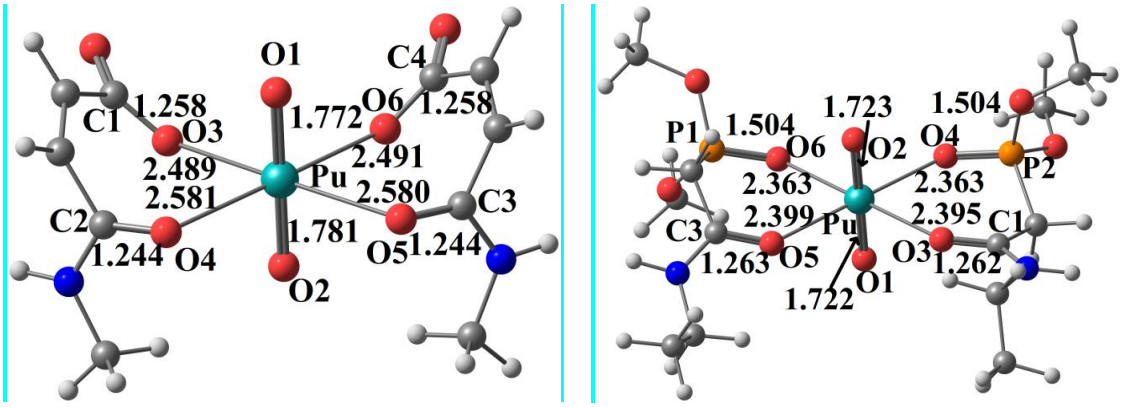

(a) (b)

Figure 5.50. DFT optimized gas phase structures of the complexes formed by (a) TESPMA and (b) Ac-Phos.

Table 5.12. Calculated gas phase structural parameters for the SBA-15 anchored system and both gas and solution phase parameters for the free model complexes TESPMA-PuO_2 and Ac-Phos-PuO_2^{2+}.

Label	Anchored TESPMA PuO_2	Anchored Ac-Phos PuO_2^{2+}	Free Model TESPMA-PuO_2		Free Model Ac-Phos-PuO_2^{2+}	
			Gas	Solution	Gas	Solution
			Bond Lengths (Å)			
Pu-O1	1.769	1.736	1.772	1.756	1.722	1.746
Pu-O2	1.783	1.738	1.781	1.751	1.723	1.746
Pu-O3	2.574	2.385	2.581	2.431	2.395	2.409
Pu-O4	2.501	2.374	2.489	2.354	2.363	2.436
Pu-O5	2.574	2.387	2.580	2.431	2.399	2.428
Pu-O6	2.500	2.379	2.491	2.355	2.363	2.446
C1-O3	1.242	1.261	1.244	1.271	1.262	1.266
C2-O4	1.245	-	1.258	1.292	-	-
C3-O5	1.242	1.260	1.244	1.271	1.263	1.268
C4-O6	1.245	-	1.258	1.293	-	-
P1-O4	-	1.504	-		1.504	1.501
P2-O6	-	1.505	-		1.504	1.501
N1-H1	1.010	1.013	1.010	1.059	1.013	1.064
			Bond Angles			
Pu-O3-C1	134.6	142.1	116.9	132.4	143.8	144.2
Pu-O4-C2	133.4		138.2	135.2	-	-
Pu-O4-P1	-	135.5	-	-	134.7	132.9

Figure 5.51 shows the Fourier transformed EXAFS data and fit of Pu(VI)-AcPhos to two oxygen and one carbon single scattering path. The fit was performed with 27 independent points fit with 19 variables, over an R-space range of 1.2 to 4 Å, using data from 1.322 – 12.134 $Å^{-1}$ in

k-space. The background was minimized with respect to contributions below 1.2 Å. This was likely necessary due to interference by the monochromator glitch in the initial background removal step. An F-test[197] indicated the resulting fit is justifiably better at the 98% confidence level. Compared to leaving the background unfit, the best fit values of the amplitudes changed by less than 10%, no worse than the systematic uncertainty of EXAFS, and the distances were essentially unchanged. The amplitude reduction factor, S02, and EXAFS scattering paths used in the fit, were determined using FEFF9[198] calculations. The EXAFS fitting parameters are summarized in Table 5.13. Overall, the fit demonstrates reasonable agreement between the experimental EXAFS data and the computational results. The 2:1 bidentate octahedral complex shown in Figure 5.50b may describe the system quite well. The experimental equatorial Pu-O bond lengths match the bond lengths calculated in solution phase fairly well, and the amplitudes of the Fourier transform give the appropriate number of atoms in each scattering path from the expected structure, within statistical uncertainty. However, a good fit could not be obtained when the single scattering path from the phosphorous atom was included. Considering the Ac-Phos molecular structure, it is unlikely to complex Pu without the phosphoric oxygen. There are likely multiple scattering path interferences at the distances of the carbon and phosphorous, so it is possible that a fit could be achieved with more extensive analysis using single and multiple scattering paths from all four atoms.

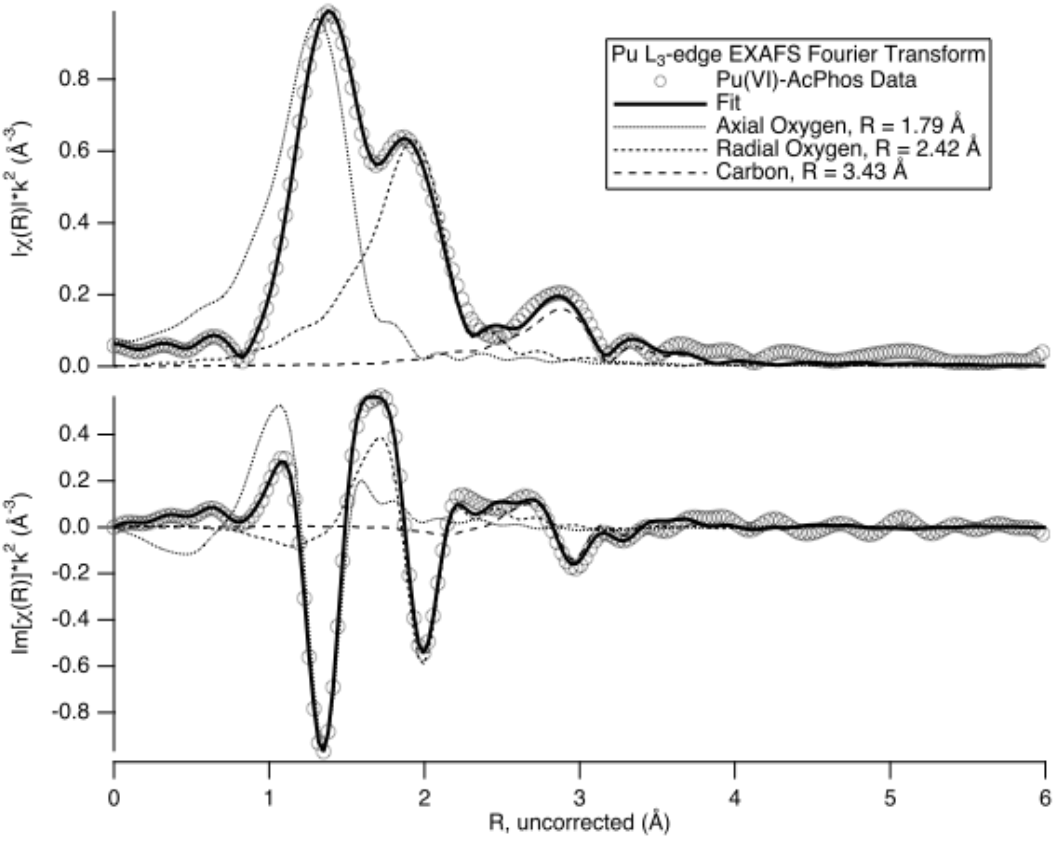

Figure 5.51. Fourier transformed EXAFS data and fit of Pu(VI)-AcPhos to two oxygen and one carbon single scattering path. The magnitude of the Fourier transform is shown in the top panel, the imaginary component is shown in the bottom.

Table 5.13. Summary of EXAFS fitting parameters. The same E_0 was applied to all paths and was 3.79 ± 0.61 eV, and S02 was set to 0.9. The R-factor (goodness of fit) was 0.0062. Uncertainties listed are from inversion of the covariance matrix, as reported by IFEFFIT.

Path	Number of atoms (N)	Distance (Å)	EXAFS Debye-Waller Factor, σ^2 (Å^2)
Pu – O – Pu	2.3 ± 0.2	1.79 ± 0.01	0.0063 ± 0.0009
Pu – O – Pu	3.7 ± 0.3	2.42 ± 0.01	0.0060 ± 0.0012
Pu – C – Pu	2.9 ±0.9	3.43 ±0.02	0.0037 ± 0.0031

6 Carbon

Ordered mesoporous carbon substrates were first introduced to the project by Dr. Harun Tüysüz when he worked as a postdoctoral researcher in Professor Peidong Yang's group at UC Berkeley. The adoption of carbon substrates was of interest for several reasons. First, the electrical conductivity of solid carbon materials renders them ideal platforms for the development of electrochemical actinide sensors, or for electrochemical separations of the actinides. Furthermore, activated carbons are well established as inexpensive, high surface-area sorbent materials,[199, 200] but relatively little exploration of the fundamental interactions of actinides with solid carbon materials has been published. Ordered mesoporous carbons (OMCs) have extremely high surface area, high thermal and chemical stability, well-defined pore size, flexible framework composition, and electrical conductivity. Such desirable properties make OMC attractive in the areas of adsorption, catalysis, energy storage, and electrochemical sensing.

Carbon-paste and screen-printed carbon electrodes have been widely applicable as robust and versatile electrochemical sensors.[201] Their simplicity and portability make this type of electrochemical sensor ideal for in-the-field determinations of inorganic analytes, where rapid information regarding sample components is required rapidly. Zhu *et al.*[202] compared the electrochemical behavior of an OMC paste electrode to that of a conventional graphite paste electrode and carbon nanotube electrode using cyclic voltammetry. They found that the OMC paste electrode showed improved electron transfer kinetics, smaller background current, and increased sensitivity, particularly in the determination of heavy metals. Another potential application of OMCs is in electrochemical separations of actinides. A group at PNNL used carbon-based electrodes for electrochemically modulated separations of uranium and plutonium, and coupled the separation with ICP-MS for isotopic analysis.[203-206] The high surface areas and large pore volumes of OMCs may prove to be advantageous for such applications.

Before extensive functionalization of OMCs, or their application toward actinide sensing can be effectively implemented, the fundamental sorption and redox reactions of actinides with OMCs must be understood. The work presented in chapter 6 represents a significant contribution to such an understanding. When the author first began sorption experiments with mesoporous carbon, there were almost no publications concerning actinide interactions with OMCs. Since then interest in this area has grown. Section 6.1 gives a brief summary of existing literature that discusses actinide and lanthanide sorption to carbon-based materials. In this work, a total of seven different porous carbon materials were tested in batch experiments with plutonium. Their synthesis and properties are described in Section 6.2. The results of batch experiments with all seven of the carbons are described in Section 6.3, and are organized by subtopic rather than

chronologically. Only samples of CMK type and C-CS type OMCs were prepared for XAS experiments and those results are presented in Section 6.4.

The author's work with mesoporous carbons began with a plutonium sorption study of nanocast (CMK) type mesoporous carbon both before and after chemical oxidation with HNO_3. A commercially available activated carbon with high surface area was used for comparison to the CMK. This study highlights the high plutonium capacity and fast kinetics of OMC compared to commercial activated carbon, but also showed that the structure of the CMK samples was not as stable and uniform as desired. Additionally, the nanocasting process for synthesis of CMK type carbons is quite arduous and sensitive, and gives only small batches of OMC. For those reasons, a collaboration was established with the Zhao group of Fudan University, who are world-renowned experts in the area of OMC synthesis. The plan was to continue actinide and lanthanide sorption studies using FDU-16-type OMC, which have a more reproducible synthesis, a more robust structure and more pristine carbon surface than CMK-type OMCs. The plutonium sorption studies with CMK left some ambiguity about the role of oxidized surface groups in the Pu sorption mechanism, as the difference between the oxidized and untreated surface was subtle. Dr. Jinxiu Wang, who was a graduate student of Professor Zhao and handling the synthesis, suggested that we oxidize the FDU-16 surface using acidic ammonium persulfate (AAPS) to generate more carboxyl groups.[90] The oxidation decreased the surface area of FDU-16 so much that Professor Zhao suggested we include the C-CS type OMC in our study, because it has much higher surface area and two networks of mesopores. The batch sorption of Pu with both OMCs as synthesized, and after chemical oxidation, was investigated. The C-CS type OMC proved most effective for plutonium uptake, so further experiments with plutonium and europium focused on C-CS and oxidized C-CS in an effort to better understand the mechanism by which plutonium and lanthanides sorb to pristine and oxidized OMCs.

Section 6.5 describes the redox reactions that were observed between actinides and porous carbons in acidic solutions. The reduction of Pu to the trivalent state by carbon was first observed when the author measured an optical absorbance spectrum of a Pu solution that was desorbed from an oxidized CMK sample in 1 M $HClO_4$. The redox chemistry of plutonium with solid carbon materials has not, to the author's knowledge, been reported in the literature, and so this interesting result was further explored. Exploratory experiments were done to test the redox activity of different carbon materials toward Pu in different acidic solutions. The results indicate that porous carbons are strong reducing agents for Pu. This might be useful for a variety of applications.

6.1 Background and previous work

Porous carbon materials have been used for centuries and can be applied for catalysis, purification of water and air, gas separation, energy storage, and electrochemical applications.[207] Examples of amorphous carbon powders include activated carbon (AC), carbon fibers, and carbon blacks. In 1991, a new allotrope of carbon, carbon nanotubes (CNTs), was discovered by Iijima[208], and much research into the properties and applications of CNTs followed. Investigations of the properties of graphene sheets, CNTs, fullerenes and carbon nanowires have contributed greatly to understanding how dimensionality affects the physical and chemical behavior of materials. The first ordered mesoporous carbons were synthesized in 1999 by Ryoo *et al.*[72] via the nanocasting technique with an MCM-48 silica template, and were called CMK-1 (**c**arbons **m**esostructured by **K**orea Advanced Institute of Science and Technology).[71] Variation

of the carbon precursor solution and the hard template in the nanocasting approach led to CMK-2 through CMK-9,[68, 207, 209] OMCs of various structures that are precise inverse replicas of their parent silica. Depending upon the concentration of carbon precursor, the CMK type OMC will be an ordered array of carbon nanorods or hollow nanotubes. More recently, a variety of soft-template methods for OMC synthesis have been developed by Zhao *et al*. of Fudan University.[74, 76, 77, 210-218] The soft template methods can be used to create highly ordered mesoporous carbons on a large scale, with a wide range of properties, and have led to easier synthesis of OMC thin films[76] and monoliths[218, 219]. These advances have greatly increased the utility of OMCs in a wide range of applications.

In early 2011 when the author first began batch experiments with mesoporous carbon and plutonium there was only one published study of an OMC-based material being explored for actinide sorption, from Jung *et al*., who incorporated carboxymethylated polyethyleneimine (CMPEI) into CMK-3 for the confinement of uranium[7] and europium[220]. There has been more work published on uranium[200, 221-229] and europium[230-232] sorption to activated carbon, and also reports of actinide and lanthanide sorption to multi walled carbon nanotubes (MWCNTs)[233-246] and nanofibers[247, 248]. Since then, a number of publications have appeared concerning functionalized OMCs for adsorption of U(VI) from seawater[32-34, 45, 48-50, 249] and other aqueous solutions[7, 27, 35, 41-43, 250, 251]. Very high U(VI) sorption capacities have been reported for functionalized and oxidized OMCs, but there seems to be some disagreement regarding the affinity of pristine OMCs for U(VI). Recently, graphene oxide has been studied for sorption of Eu(III)[252, 253] and other radionuclides,[253] showing improved uptake kinetics and sorption capacities compared to nanotubes and activated carbons. To the author's knowledge, the work presented in this chapter constitutes the first published investigation of ordered mesoporous carbons with a transuranic element.[63, 119] Table 6.1 gives an overview of other groups who have published literature concerning actinide and lanthanide sorption to solid carbon materials, although the list may not be exhaustive, and is certainly growing with interest in this area of research. The names listed in Table 6.1 may or may not be of the principal investigators, a name common to the literature published by each group was listed.

Table 6.1. Overview of literature reporting actinide and lanthanide sorption to solid carbon materials.

Group	Type of carbon	Functionalization	Target species	References
Sichuan University, China, Li *et al.*	AC CMK-5 Hydrothermal carbon	Benzoylthiourea grafted Oxime grafted	U(VI)	27, 228, 250, 254
Oak Ridge National Laboratory, USA, Mayes, *et al.*	Soft templated hierarchical OMCs and polymers	Amidoxime grafted & polymer infiltrated	U(VI)	32, 48-50, 249
East China Institute of Technology, Zhang *et al.*	CMK-3 Hydrothermal carbon	Polyanaline coated APS oxidation	U(VI)	35, 41-43, 251, 255
University of Chicago, USA, Lin *et al.*	Commercial mesoporous carbon and silica	Grafted amidoxime, phosphoryl, and carboxly groups	U(VI)	45, 46

Group	Type of carbon	Functionalization	Target species	References
Korea Atomic Energy Research Institute, Jung *et al.*	CMK-3	Incorporation of CMPEI	Eu(III) and U(VI)	7, 220
Russian Academy of Science, Myasoedov *et al.*	MWCNTs "Taunit"	HNO_3 oxidation, impregnation with CMPO, TOPO, TBP, DMOOHEMA , ionic liquids	U(VI), Pu(III)-(VI), Eu(III), Am(III), Np(V) Tc(VII)	233-236, 246
Japan Atomic Energy Agency, Arisaka *et al.*	Activated carbon, carbon black, graphite, carbon nanotubes	Untreated	Am(III) selectivity over Eu(III)	230, 239, 256
Chinese Academy of Sciences: Wang, *et al.*	MWCNTs Graphene oxide	HNO_3 oxidation, carboxymethyl cellulose grafting	Am(III), U(VI), Eu(III), Sr(II)	237, 240, 241, 244, 245, 252
Anhui Medical University: China, Wang *et al.*	MWCNTs	HNO_3 oxidation	Th(IV)	238
Chemnano Materials, Ltd., USA: Wang *et al.*	MWCNTs	Phosphonates, crown ethers, malonamides, diglycolamides, ect.	Actinides and REE	257
Università di Pavia, Italy, Maggi *et al.*	Activated charcoal	Incorporated phosphate salts	U(VI), Np(VI) Pa(V), Th(IV), Eu(III)	222, 223
Atomic Energy Authority, Egypt, Someda & Sheha, several others	Activated charcoal AC from rice straw AC	Impregnated oxalic and succinic acids untreated	U(VI), Th(IV) Eu(III), Zn(II)	224, 227, 229, 231, 232
Lomonosov Moscow State University, Russia w/ Rice University, USA, Kosynkin *et al.*	Graphene oxide compared to bentonite and activated carbon	Graphene oxidized w/ H_2SO_4, H_3PO_4 and $KMnO_4$	Am(III), Th(IV), Pu(IV), Np(V), U(VI), Sr(II), Eu(III), Tc(VII)	253
Centre de Reserche Nucléaire, Algeria, Melleh, *et al.*	Activated carbon	Untreated	U(VI)	200
West Virginia University, USA, Zondlo *et al*	Carbon fibers	electrosorption	U(VI)	248
Forschungszentrum Dresden-Rossendorf, Germany, Schierz and Zänker	MWCNTs	HNO_3/H_2SO_4 oxidation	U(VI)	242
Lawrence Livermore National Laboratory, USA, Reynolds *et al.*	Granular activated carbon	Phosphonate silica aerogel composites	U(VI)	225

Group	Type of carbon	Functionalization	Target species	References
Savannah River National Laboratory, USA, Hobbs *et al.*	Granular activated carbon	None	U(VI), Np(V), Pu(IV)	221
Harbin Engineering University, China, Zhang *et al.*	Carbon microspheres	Heat treatment	U(VI)	258
Hashemite University, Jordan, Fasfous and Dawoud	MWCNTs	none	U(VI)	243

As one can see in Table 6.1, the most common actinide species investigated for its sorption interactions with solid carbon materials is U(VI). Uranium is generally the most studied actinide because it is the most abundant, and many more laboratories have access to U than Pu, for example. Interest in high-capacity uranium sorbents stems from its importance as a nuclear fuel source, and its abundance in the environment. It has been estimated that sufficient U remains in terrestrial ores for 70 more years of nuclear power generation at the current consumption rate, although demand will certainly increase.[45] A lot of research is being directed toward new technologies for extraction of U from seawater, because there is an estimated 4.5 billion tons of U in the ocean, over 1000 times the terrestrial amount.[45] Extraction of U from seawater is challenging because it is in low concentration, and forms very stable and soluble carbonate complexes. Other studies of U sorption from a variety of aqueous conditions could aid in recovery of U from industrial wastewaters or contaminated groundwater. A brief survey of the literature concerning U(VI) sorption to carbon-based materials can provide some context for the author's work investigating hexavalent Pu sorption to OMCs.

Despite the fact that activated carbons have been known for centuries, their utility for U sorption has only been investigated in the last 10-15 years.[200, 221-226] Mellah *et al.*[200] studied batch sorption of U(VI) onto untreated granular activated carbon, and found maximum U sorption occured at pH 3 after 4 hours, with an uptake capacity of 28.3 mg/g. They attributed the sharp decrease in sorption above pH 4 to the inability of activated carbon to adsorb hydrolyzed U precipitates. They concluded that U sorption to AC is physical in nature, spontaneous, and exothermic. Oji *et al.*[221] investigated the loading capacity of granular activated carbon for U(VI), Np(V), and Pu(IV) from caustic salt solutions. They found no uptake of U(VI) under those conditions, and small uptake capacities for Pu and Np. Other groups have tested the uptake of U(VI) and other species by activated carbons modified with chelating salts[222, 223, 226], oxalic and succinic acids[224, 227], and silica aerogels[225]. Those materials generally showed lower U sorption capacities, although may react by specific chemical adsorption (chemisorption) rather than physisorption. The most effective method of AC functionalization for U sorption or extraction seems to be chemical grafting. Zhao *et al.* found that the U sorption capacity of AC functionalized with benzoylthiourea (shown in Figure 6.1) tripled to 82.0 mg/g in pH 4.5 solution, and maintained high U sorption in the presence of competing ions.[228]

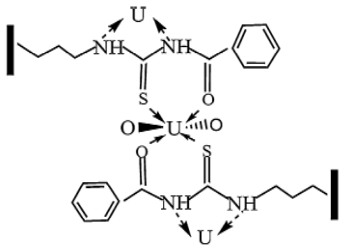

Figure 6.1. Structural representation and proposed U sorption mechanism for benzoylthiourea-grafted activated carbon.

Although activated carbons have large pore volumes and surface areas, they tend to be very disordered, and mostly microporous. More ordered and controlled forms of carbon, such as carbon nanotubes have also been explored as sorbents for uranium and other actinides. Fasfous and Dawoud found that maximum U sorption to multi-walled carbon nanotubes (MWCNTs) occurred from pH 5 solution, with a Langmuir sorption capacity of 24.9 mg/g at room temperature. They concluded that the sorption was physical, spontaneous, and exothermic, although the maximum U capacity increased with temperature. Schierz and Zänker found that acid oxidation of MWCNTs increased their colloidal stability, and increased the uranium sorption capacity from 18 mmol/g to 193 mmol/g in pH 5 solution. These reported U capacity values based on the Langmuir sorption model seem impossibly large, causing the author to wonder if there was a typing or calculation error. These numbers would be in accordance with other reports if the units were mg/g. The oxidation also expanded the pH range of high U uptake on both ends, to approximately pH 2-9 [242]. Scientists at the Chinese Academy of Sciences have studied sorption of U and several other actinides on oxidized MWCNTs. They found that equilibrium was reached after 4 hours, the sorption increased sharply between pH 4 and 6, and that sorption was only affected by ionic strength below pH 5 [244]. It was proposed that sorption in solutions below pH 6 was caused by outer-sphere complexation and cation exchange, while the sorption in higher pH environments was due to surface precipitation. They found a maximum sorption capacity at pH 5 of 140 μmol/g, compared to 80 μmol/g for pristine MWCNTs. The presence of humic and fulvic acids increased U sorption to oxidized MWCNTs slightly at low pH, but caused a significant decrease in sorption from near-neutral or basic solutions. This finding agrees with another study done by Yakout *et al.* with an activated carbon in pH 5.5 solution, where the presence of humic acid drastically decreased the U sorption capacity of AC [229].

Ordered mesoporous carbons have been studied for U extraction, usually after additional functionalization of the surface, with very high U uptake capacities resulting from the large surface areas and pore volumes. The first OMC utilized was CMK-3, which is a nanocast 2D-hexagonal OMC with a nanorod structure. On the atomic scale, CMK and other OMCs are usually amorphous (although graphitic OMCs can be prepared) and thus more akin to activated carbon than to CNTs. The BET surface areas of CMK-3 ranges from approximately 800 to 1400 m^2/g, much higher than those of CNTs, which are typically 80-180 m^2/g. Jung *et al.* coated CMK-3 with the chelating polymer CMPEI, creating a material with a U sorption capacity of 151.5 mg U per g sorbent in pH 4 solution [7]. However, 30% of the U leached back into the pH 4 solution after one day, and another 5 % over 20 days. Those results indicate that polymer coated OMCs may not be completely stable in aqueous solutions, thus several other researchers turned

to chemical grafting. Tian et al. grafted CMK-5 with 4-acetophenone oxime, depicted in Figure 6.2 [27]. CMK-5 is also a nanocast 2d-hexagonal OMC, but has a tubular structure instead of the rod structure, giving it a secondary pore network and generally higher surface area. The oxime grafted CMK-5 proved to be a fast (< 30 min) and reusable sorbent of U, with a maximum sorption capacity of 65.18 mg/g in pH 4 solution, compared to approximately 32 mg/g for raw CMK-5. Unlike the pristine CMK-5, the oxime-CMK-5 was selective for U in the presence of other ions, and U sorption to the oxime-CMK-5 decreased with acid concentration or NaCl concentration [27]. A materials chemistry group at Oak Ridge National Laboratory also used the amidoxime functionality, along with novel synthetic strategies to design mesoporous polymers [48] and carbons [49] tailored for extraction of U from seawater. Their OMCs are synthesized by the soft-template method, similar to FDU-type OMCs, with a bimodal pore size distribution around 2 and 9 nm. They studied the effects of varying pretreatment parameters and reaction conditions for the polymerization of acrylonitrile in the OMC under ultrasound, and subsequent conversion to amidoxime [49]. The best U sorption capacity they achieved in simulated seawater was close to 4 mg U per g sorbent, an improvement over standard commercial adsorbents in similar conditions.

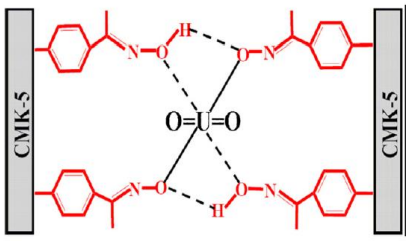

Figure 6.2. Structure and proposed U complexation of oxime-CMK-5 [27].

Carboni *et al*. employed traditional grafting techniques with a commercial mesoporous carbon having a relatively low BET surface area of 189 m^2/g, to prepare 15 different materials functionalized with variations of amidoxime, phosphoryl, and carboxyl groups.[45] The functionalized carbon with the highest U sorption capacity was the simple phosphoric acid grafted material, with a Langmuir U sorption capacity of 97 mg/g in pH 4 solution, and 67 mg/g in artificial seawater. This paper stated that without functionalization, background sorption to the carbon would be negligible, although it did not seem to be explicitly tested. Nie *et al.* studied uranium sorption to unfunctionalized CMK-3 as a function of solution pH, contact time, ionic strength, and temperature.[41] Their CMK-3 was prepared against an SBA-15 silica template using sucralose as a carbon precursor, and NaOH for removal of the template. They determined that maximum U sorption to CMK-3 occurred in pH 6 solution after 35 minutes, and that sorption was spontaneous and endothermic. The U uptake capacity of CMK-3 was 112 mg/g in 0.01 KNO_3 solution, and decreased to 84 mg/g in 0.1 M KNO_3, indicating that physisorption was involved. Another paper by the same group compared U sorption to CMK-3 and CMK-3 that was oxidized by APS, CMK-3-COOH.[35] The oxidation shifted the optimal solution pH to 5.5, and increased the Langmuir sorption capacity from 178 mg/g to 250 mg/g. Little difference was observed in the contact time necessary, but the CMK-3-COOH showed much better selectivity for U(VI) over various divalent cations than did the CMK-3.

Overall the literature pertaining to U sorption to carbon materials demonstrates that sorption capacities of OMC-based materials tend to be much higher than those of activated

carbons or CNTs. The improvement over CNTs may be largely explained by the much higher surface areas and pore volumes of OMCs, although subtle differences in surface chemistry may also contribute. All carbon materials may have different chemical and physical properties depending on various conditions of their synthesis, post-treatments, and activation. Activated carbons can have surface areas as high as OMCs, and in this case the improved sorption properties likely stem from the greater volume of mesopores, facilitating diffusion of aqueous species into the pores to allow easier access to the surface. Generally it seems that unfunctionalized carbons do show some affinity for U(VI), although the sorption is not specific to U and is generally considered to be physisorption, and/or surface precipitation. The actual U uptake capacities of untreated carbons vary widely with the properties of the individual carbon substrates and solution conditions tested, but it is faulty to assume that only negligible U sorption occurs to pristine carbon surfaces. Specific U sorption is usually achieved by functionalization of the carbon surface with polymers or grafted ligands based on amidoxime, phosphoric acid, or carboxyl functional groups.

In this work, batch sorption of Eu(III) to C-CS type OMCs was investigated, thus a survey of literature pertaining to Eu sorption to other carbonaceous materials is appropriate. Gad and Awwad studied the batch sorption of Eu(III) to carbonized apricot stone, chemically activated with H_3PO_4 or KOH.[231] The H_3PO_4 activation yielded an AC with much greater surface area, pore volume, and Eu sorption capacity. They found that maximum Eu sorption without precipitation occurred in pH 5 solutions, and equilibrium was reached in 60 minutes. By grinding and separating the AC particles into size fractions, the Eu sorption amount and rate increased slightly in the smaller sized fractions. Their thermodynamic studies indicated that the sorption process was spontaneous and endothermic, with a Eu capacity of 46.5 mg/g. The presence of phosphate, carbonate, oxalate and acetate increased the affinity of Eu for AC, while sorption was decreased with addition of nitrate or chloride. Omar and Moloukhia oxidized a commercial activated carbon with HNO_3, and found that maximum Eu sorption occurred in pH 4 solution, and equilibrium was reached in 90 minutes.[232] They reported a relatively low sorption capacity of 18.4 mg/g, but did not discuss the surface area or other textural properties of the AC. A similar Eu capacity of 17.6 mg Eu per g carbon was calculated from the breakthrough curve in a study that used carbon fibers for preconcentration of lanthanides.[247]

Fan et al. studied the sorption of Eu and humic acid to MWCNTs oxidized with nitric acid, as a function of pH and ionic strength.[240] They found that Eu sorption increased with pH, decreased with ionic strength, and increased in the presence of humic acid. The highest Langmuir sorption capacity obtained at pH 4.3 without humic acid was 9.2 μg Eu per g CNTs. Using batch results and X-ray photoelectron spectroscopy (XPS) analysis, they concluded that sorbed Eu was either bound by humic acid, or by deprotonated hydroxyl groups at the CNT surface. In another paper, the same group used both XPS and computational modeling to conclude that Eu complexation at the oxidized MWCNT surface occurs by both carboxylic and hydroxy groups.[241] More recently this group studied Eu(III) interactions with graphene oxide nanosheets (GONS) using batch, EXAFS, and modeling techniques.[252] This material has a BET surface area of 120 m^2/g, similar to that of MWCNTs, but has approximately 3 times greater density of acidic surface sites. Unlike the Eu sorption to CNTs, sorption to GONS was unaffected by ionic strength, indicating along with EXAFS data that inner-sphere complexation occurred. The maximum sorption capacity for Eu to GONS was calculated from the Langmuir isotherms to be 161 mg/g in pH 4.5 solution and 175 mg/g in pH 6 solution, which is higher than

any other sorbent reported. It was proposed that it is the Lewis-base nature of the delocalized π electron system in a graphene layer that enhances the surface complexation of Eu(III) to graphene oxide. Interpretation of the EXAFS data indicated monodentate, mononuclear complexes were formed at the GONS surface in solutions with pH 6 and below.

Graphene oxide has recently attracted attention as an effective sorbent material of other radionuclides as well. Romanchuk *et al*. surveyed batch sorption to graphene oxide (GO) of Th(IV), Pu(IV), Am(III), Eu(III), U(VI), Sr(II), Tc(VII), and Np(V) of various concentrations ranging from ~10^{-14} M to ~10^{-7} M depending on the radionuclide.[253] Little sorption of Tc(VII) or Np(V) was observed, and appreciable sorption of Sr(II) only occurred at high pH values. Quantitative sorption of both tetravalent species occurred in solutions of pH ~1.5-11, and of the trivalent species above pH 2.3. The pH window of high U(VI) sorption was narrower, and peaked around pH 6. In pH 3.5 solution, steady-state conditions were achieved within 5 minutes, even with < 0.1 g/L GO, indicating GO has faster sorption kinetics than porous carbon materials due to the lack of internal surface. In pH 5 solutions, GO demonstrated Langmuir sorption capacities for U(VI) and Eu(III) of 0.116 mmol/g and 0.760 mmol/g, respectively. The material was also much more effective than AC or bentonite at extracting U(VI) and Pu(IV) from simulated nuclear waste solutions containing various complexing substance.

Several studies have previously been published concerning the sorption of transuranic actinides to porous carbon or MWCNT based materials. Wang *et al.* found strong but slow (85% after 4 days, 95% after 1 month) sorption of Am(III) to nitric-acid oxidized MTCNTS [237]. Chemisorption was proposed as the mechanism, as Am uptake increased with solution pH, and was essentially independent of ionic strength, in contrast to Eu(III) on the same material.[240, 241] Interestingly, Arisaka and Watanabe *et al*. discovered that untreated activated carbons[230] and carbon nanotubes[239] show selectivity for sorption of Am(III) over Eu(III) from aqueous solutions of pH 1-4, regardless of the AC source material or activation method. Extensive work has been done at the V. I. Vernadsky Institute of Geochemistry and Analytical Chemistry, Russian Academy of Sciences to develop actinide extractants based on "Taunit" MWCNTs.[233-236] Myasoedova *et al.* found unmodified Taunit to be an effective sorbent of Am(III), Eu(III), Pu(IV), U(VI), and Tc(VII) from pH 3 and pH 7 aqueous solutions. Impregnation of the MWCNTs with extractant molecules and ionic liquids prepared effective solid extractants for preconcentration of Am(III), Eu(III), Pu(IV), and U(VI) from 3 M HNO_3.[235, 246] Perevalov and Molochnikova[236] studied sorption of various oxidation states of Pu from 0.1 M $NaClO_4$ onto nitric acid-treated MWCNTs as a function of solution pH, time, and Pu concentration. The batch studies had a very high liquid-to-solid ratio of 80,000 mL solution per g carbon, and were carried out in 0.1 M $NaClO_4$ solutions with ~50 μM Pu. The sorption of polymeric Pu(IV) was nearly quantitative over a solution pH range of 2-10, and was faster than sorption of ionic species. It was suggested that sorption of polymeric Pu occurs through an intermolecular interaction involving H-bonding between the CNT surface and the oxygens in the Pu colloid. They proposed that sorption of Pu ions occurred by chemisorption, and found Pu(VI) had the strongest binding and highest sorption rate of all the ionic species. They found that over 90% of uptake occured within 3 hours, and reported a Pu(VI) monolayer sorption capacity of 37.9 μmol/g.

The above literature survey reveals that carbonaceous materials have been demonstrated as effective sorbents for U and other actinides. Generally ordered mesoporous substrates and graphene oxides seem to show better sorption kinetics and uptake capacities than activated

carbons and nanotubes. However, little work has been published thus far with carbon materials for sorption of actinide species besides U. Extensive study of Pu sorption was only done for oxidized MWCNTs, which showed high affinity for Pu, especially in polymeric or hexavalent form.[236] Thus the investigation of Pu sorption to OMCs is promising because OMCs have different structures and about 10 times the specific surface area of MWCNTs. The published papers on U sorption to OMCs are interesting for comparison because UO_2^{2+} and PuO_2^{2+} are generally considered to be chemically analogous. However, there are fundamental differences in the redox behavior and coordination chemistry of the actinyl ions,[53] thus the investigation of OMC interactions with Pu presents an opportunity for new discoveries.

6.2 Synthesis and properties

Generally solid carbon can be produced by heating organic matter to very high temperatures, called carbonization. When this process occurs around an ordered mesoporous template, OMC can be formed. There are many different forms of carbon, with a wide variety of physicochemical properties. The individual properties of carbon solids depend on the allotrope, synthetic method and starting material, carbonization temperature, and any chemical or physical activation treatments following carbonization. Section 6.2.1 introduces the different allotropes of carbon and some of their general properties. In this work, four different porous carbons were either purchased or synthesized by collaborators, and were characterized by various combinations of N_2 adsorption, SAXS, SEM, TEM, TGA, FTIR, elemental analysis and determination of the PZC via powder addition (see Chapter 2 for details about these techniques) Sections 6.2.2-6.2.5 describe the syntheses and properties of the different carbon materials used in this work. The methods and results of the two different liquid oxidation treatments are described in Section 6.2.6, and the physicochemical properties of all seven carbon materials are summarized and tabulated in Section 6.2.7.

6.2.1 General properties of carbon

There are several stable and metastable allotropes of carbon, each with remarkably unique properties. Figure 6.3 illustrates the molecular structures of eight different allotropes, which give rise to the observed properties. The most commonly known sp^3 and sp^2 hybridized carbon structures are diamond (Figure 6.3a) and graphite (Figure 6.3b), and their physical properties are opposite in many ways. Both diamond and lonsdaleite (Figure 6.3c) consist of carbons with four sp^3 bonds in a nearly perfect tetrahedral lattice, with a C-C distance of ~1.54 Å, and these are the hardest known substances.[259] The difference between the two is the stacking of the tetrahedral layers, where diamond has the 3-layer stacking sequence "…ABCABC…" along the (111) cubic direction, lonsdaleite exhibits a 2-layer stacking "…ABAB…" along the (001) hexagonal direction. Diamond is formed naturally at high pressures, and is thermodynamically unstable at ambient conditions but kinetically stable due to the very high activation energy required for the conversion of diamond to graphite. Synthesis of diamonds can be achieved from graphite at high pressures with a catalyst, by shock treatment, or by chemical vapor deposition. Diamond is highly conductive of heat, but an electrical insulator, and is commonly used for its hardness in many different industries. In contrast, graphite (Figure 6.3b) is among the softest of materials, can be used for heat insulation, and is electrically conductive

due to the extended π system across the layer of sp^2 bonded carbons. The C-C bond length within the hexagonal graphite layer is ~1.42 Å, and the layers are held together by weak Van der Waals forces at a distance of 3.41 Å.[259] The softness of graphite comes from the ease of removing layers, making this material useful in lubricants and pencils. A free-standing single atomic layer of graphite is called graphene, and can be synthesized or isolated from graphite in a variety of ways. Graphene has attracted a lot of attention in the past 10 years because its unique electronic and mechanical properties make it suitable for a variety of applications and fundamental research. Graphene is the thinnest known material, and the strongest ever measured. It is extremely conductive of heat and electricity, and can sustain extremely high current densities.[260] The charge carriers in graphene have zero effective mass and high intrinsic mobility, and its electronic properties are widely studied.[260] Other allotropes of carbon derived from variations of graphene layers are fullerenes (Figure 6.3d,e,f) and carbon nanotubes (Figure 6.3h). A single walled carbon nanotube (SWCNT) is pictured, but MWCNTs are better able to withstand wet oxidation treatments and so were more commonly encountered as sorbents or extractant supports (see Section 6.1). Amorphous carbon (Figure 6.3g) refers to any carbon without a long-range crystalline structure and includes materials such as charcoal or activated carbon, carbon blacks, carbon fibers, glassy or vitreous carbon, and most OMCs. Amorphous carbons generally consist of disordered arrays of graphitic microstructures, but can contain a mixture of sp^2 and sp^3 hybridized carbons. All of the carbons studied in this work are amorphous, and the ratios of sp^2 to sp^3 hybridized carbons in these materials are unknown, but are likely much higher in sp^2 bonded carbons. Amorphous carbons are electrically conductive, and the physical properties vary widely with the macrostructure. The main difference between carbon blacks and activated carbons is in the agglomeration of the particles. Carbon blacks are formed by thermal decomposition or partial oxidation of hydrocarbons, leading to aromatic macromolecules in the vapor phase that nucleate into droplets, which become the carbon black particles.[89] On the other hand charcoal or activated carbon particles are formed from mechanical grinding of larger pieces of carbonized organic matter such as wood, nutshells and fruit-pits. Glassy carbon or vitreous carbon is a hard solid material with a glass-like appearance and fracture behavior. Glassy carbon is produced by thermal degradation of selected polymers, such as resins of furfuryl alcohol and phenol formaldehyde.

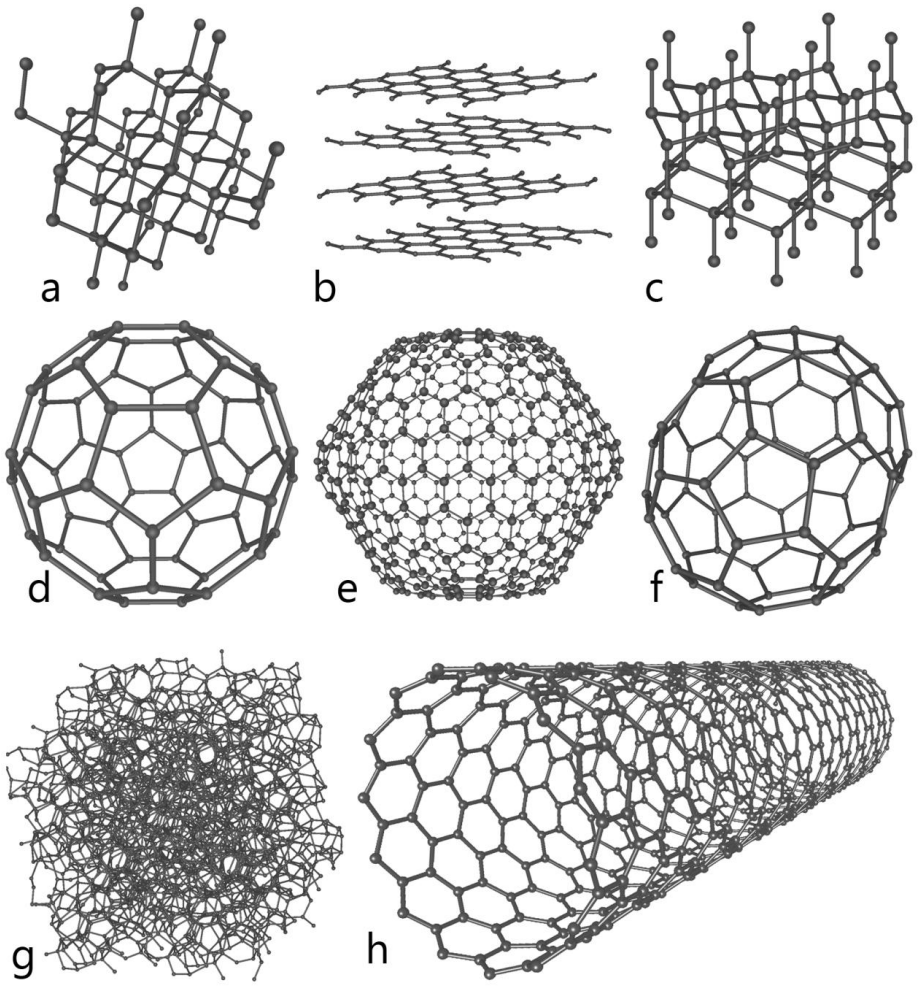

Figure 6.3. Eight different allotropes of carbon: a) Diamond, b) Graphite, c) Lonsdaleite, d) C_{60} (Buckminsterfullerene or buckyball), e) C_{540}, f) C_{70}, g) Amorphous carbon, and h) single-walled carbon nanotube or buckytube. Image from http://en.wikipedia.org/wiki/Allotropes_of_carbon.

Graphitic and amorphous carbons are electrically conductive and selected for many electrochemical applications because of good conductivities, low density, adequate resistance to corrosion, low cost, low thermal expansion and low elasticity.[89] Even among conductive carbons, the specific resistivities vary by three orders of magnitude from that of a semimetal (graphite, parallel to planes, 3.9 x 10^{-5} Ω-cm) to semiconductor (graphite, perpendicular to planes, 1 x 10^{-2} Ω-cm). The effect of carbonization temperature on the conductivity of a carbon material is understood by the electronic band model. When an aromatic hydrocarbon is heated to about 600° C, the band gap is ~0.3 eV, and this gap decreases with increasing temperature until about 1300° C, when the two bands begin to merge. The overall electrical resistance of a packed bed of carbon particles is a function of intra-particle resistance and the contact resistance between particles, which usually dominates. The contact resistance depends on particle size, aggregate structure, porosity, and oxygen content.[89]

Even the crystalline allotropes of carbon such as graphite contain defect sites that become saturated with hydrogen, or oxygen-containing functional groups. Carbon materials can have a variety of surface functional groups including carboxyl, carboxylic anhydrides, carbonyl groups,

lactones, lactols, phenols, quinones, ethers, and γ-pyrone-like structures[96, 97] shown in Figure 6.4. The type and density of functional groups at the carbon surface greatly affect the chemical and electrochemical properties of carbon. Usually, defect sites are capped by hydrogens, and the bulk carbon material is relatively hydrophobic. However, the more oxygen-containing surface groups there are, the more hydrophilic the material will be. Carbons that are low in oxygen-containing groups are effective sorbents of organic aromatic molecules due to the interactions of the π electrons. The carbon basal planes (C_π) can also behave as a Brønsted base according to Reaction 6.1, giving the slurry of a pure carbon powder a slightly basic pH.[89]

$$C_\pi + H_2O \rightarrow C_\pi H_3O^+ + OH^- \quad (6.1)$$

Oxygen-containing surface groups exhibit anion or cation exchange properties, and generally carbons are oxidized to increase the concentration of surface groups (see section 6.2.6), if the carbon is to be used for sorption of metal ions or other polar species. The pH of a slurry of oxidized carbon is lowered by Reactions 6.2 and 6.3, where >-OH and >-COOH are surface groups with active hydrogen. More oxidized carbons generally have lower PZCs (see section 2.2.7) and thus show cationic exchange behavior in mildly acidic conditions.

$$>\text{-OH} + H_2O \rightarrow >\text{-}O^- + H_3O^+ \quad (6.2)$$

$$>\text{-COOH} + H_2O \rightarrow >\text{-}COO^- + H_3O^+ \quad (6.3)$$

Carbon materials are known for their electrocatalytic properties, and can be used as ion-specific electrodes.[89] The potentiometric response of carbons is important for the development of ion-selective electrodes based on carbon or graphite, and is dependent on the type and concentration of functional groups at the surface. The potentiometric response of carbon to ionic species arises from the adsorption behavior of surface oxides. For example, a potential-pH response has been observed for many carbon electrodes, and is thought to arise from the electrochemical reaction of quinone (Q) (see Figure 6.4g) and hydroquinone (H_2Q) groups on the surface, shown in Reaction 6.4.[89]

$$Q + 2H^+ + 2e^- \rightarrow H_2Q \quad (6.4)$$

Much of the electrochemical activity of carbons is attributed to the quinone/hydroquinone redox couple, Reaction 6.4. This is of great interest here because throughout this work carbons were found to reduce plutonium species. The redox potential of Reaction 6.4 is pH dependent and also varies with the type of carbon and solution matrix, and a wide range of values has been reported. Several investigators attributed cyclic voltammetry peaks to this reaction, measured in 1 M H_2SO_4 on various carbon surfaces the peaks occurred between between 525 and 700 mV vs. a normal hydrogen electrode (NHE) (this corresponds to 303-498 mV vs. Ag/AgCl electrode).[89] Other surface groups can also be oxidized, and carbon itself can be electrochemically oxidized in aqueous solutions according to Reactions 6.5-6.7, depending on solution pH. The standard electrode potentials vs. a standard hydrogen electrode (SHE) at 25° C for Reactions 6.5 and 6.7 are 207 mV and 518 mV, respectively. Although the reactions suggest that carbon is unstable in aqueous solutions, they are highly reversible, which makes carbon solids relatively corrosion resistant in practice. These reactions can occur to make gaseous products, as written, but electrochemical oxidation of carbon is also known to create surface oxides.[89]

$$C + 2H_2O \rightarrow CO_2 + 4H^+ + 4e^- \quad (6.5)$$

$$C + H_2O \rightarrow CO + 2H^+ + 2e^- \quad (6.6)$$

$$C + 6OH^- \rightarrow CO_3^{2-} + 3H_2O + 4e^- \quad (6.7)$$

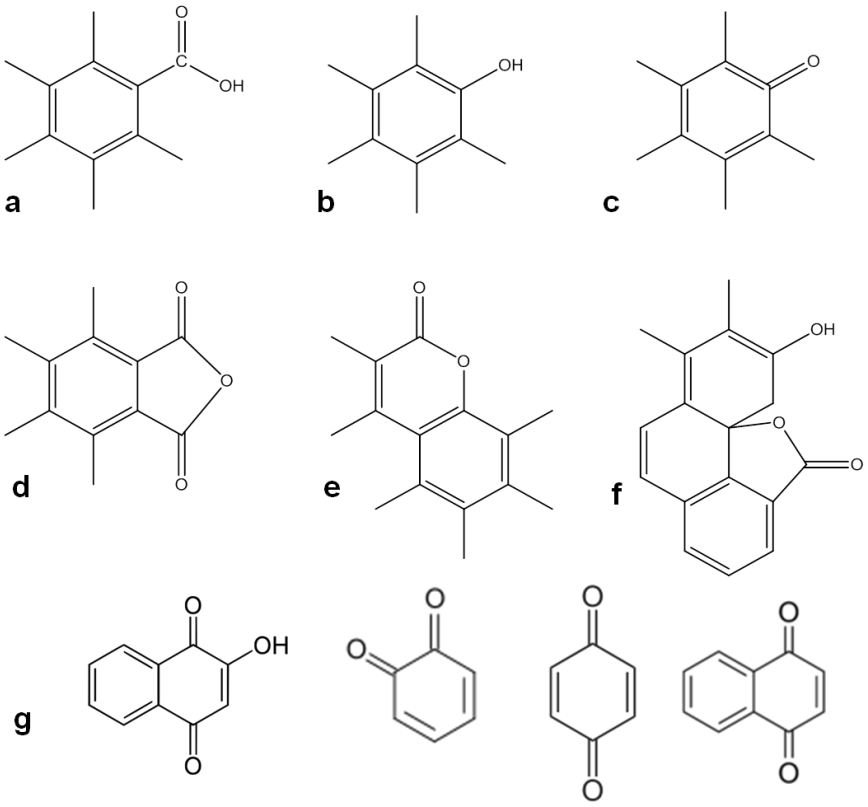

Figure 6.4. Common functional groups on carbon surfaces, including (a) carboxylic acid, (b) phenolic, (c) carboxyl, (d) acid anhydride, (e) lactone, (f) complex lactone (g) quinones

6.2.2 Activated carbon

Activated carbons (ACs) are amorphous, porous carbon materials that are prepared by carbonization of organic material, followed by thermal or chemical activation to increase the porosity and surface area. The resulting particles contain a disordered mixture of macropores, mesopores, and micropores, as illustrated in Figure 6.5. The surface area and porosity of activated carbons vary with the source material and the method of activation, as does the surface chemistry. Activated carbons with very high surface areas tend to be mostly microporous. Various source materials can be used, commonly including sawdust, coconut shells, black ash charcoal, lignite, bituminous coal, and petroleum coke.[89, 207] Thermal activation involves heating the previously charred material to 800-1000° C in the presence of an oxidizing gas, such as steam or CO_2. In chemical activation, a dehydrating agent is mixed into the raw material prior to carbonization at 200-650° C. Common dehydrating agents for chemical activation are H_3PO_4, $ZnCl_2$, and H_2SO_4, which are leached out for reuse following the reaction. Generally carbons activated by chemical methods are more porous and have higher specific surface areas than thermally activated AC. In some cases, both properties may be employed to get ACs with the

desired properties. Selection of the source materials and control of the activation conditions allows some control over the physical properties of AC, but never to the extent that can be achieved with template-directed porous carbons. Usually, AC materials with the highest specific surface areas were prepared by chemical activation of a wood source. The ash content of ACs varies with source material, from 0-1.2% (wood) up to 15-20% (coals). Ash content refers to the weight percent of inorganic elements in the AC, and these contaminants are usually washed out with water or hot alkaline solutions. Activated carbon is most commonly used for its excellent properties as an adsorbant. Common uses include water and air purification, solvent or solute recovery, gas refining, exhaust desulfurization, deodorization, gas separation, and as a catalyst or catalyst support.[89]

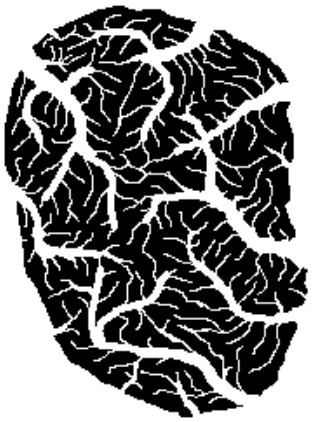

Figure 6.5. Illustration of a section through an activated carbon particle, showing a conceptual representation of the pore structure. Image taken from http://www.roplex.co.uk/carbon_adsorption_vru.htm

In this work, a commercially-available activated carbon powder (CAS# 7440-44-0) was purchased from Strem Chemicals Inc. (LOT#A4301040), for comparison of its plutonium sorption properties to those of the OMCs. Little information was provided about the AC prior to purchase, but the catalog indicated it was prepared by $ZnCl_2$ activation of sawdust. It was chosen because it was expected to have a higher specific surface area than the other AC materials available. The AC was used as received, and characterized by SEM, N_2 adsorption, ATR-FTIR, and powder addition (PZC determination). Other desired characterizations such as TEM, TGA, and elemental analysis were not available to the author at the time this work was done.

A representative SEM image of the AC powder is shown in Figure 6.6. A rough and irregular morphology is observed with a wide range of particle sizes. Although the samples were sonicated prior to analysis to break up large aggregates, particles as large as 500 μM were observed. The particle morphology is not likely to exert a large influence on the sorption properties of these powders, since most of the surface area in inside the particles on the pore walls. However, the particle size may be a factor in determining sorption kinetics, especially for a microporous material such as AC, where the rate is expected to be partially controlled by diffusion. The SEM images confirmed that the solid particulates can be effectively filtered out of solution aliquots using the 30,000 MWCO filters.

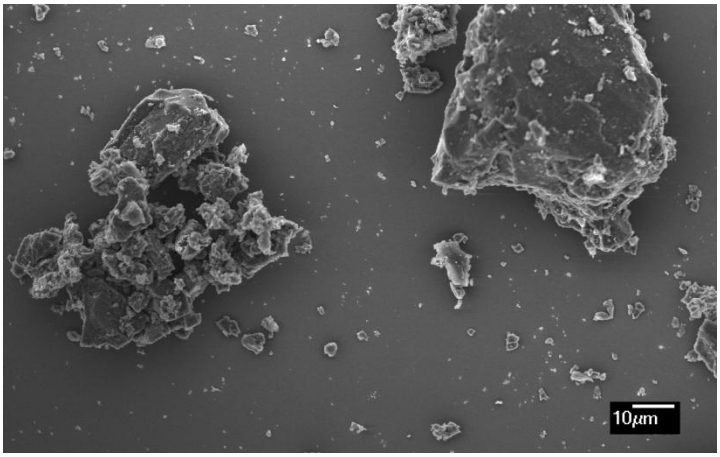

Figure 6.6. Representative SEM image of activated carbon particles.

A representative N_2 adsorption isotherm collected on an activated carbon sample is shown in Figure 6.7. The BET plots from duplicate samples outgassed at 110° C were linear, and gave an average BET surface area of 1150 ± 30 m^2/g. The presence of the hysteresis loop suggests some mesoporosity in the sample, and the shape indicates a heterogenous distribution of pore dimensions. The t-plot analysis showed that approximately 62% of the pore volume and 80% of the surface area is in micropores (< 2 nm width) (see Table 6.2). As discussed in section 2.2.3, BJH analysis is not meaningful for such microporous samples[87] and is omitted from this discussion. Furthermore, the Autosorb software seemed to have a problem with the algorithm for BJH pore size distribution, and meaningful values could not be obtained for the CMK mesoporous carbons either. Collecting the N_2 adsorption isotherm after outgassing 20 hours at 250° C had little effect on the BET surface area or pore volume compared to the samples outgassed at 120° C, indicating that there were few surface groups and that micropores were sufficiently evacuated at 120° C.

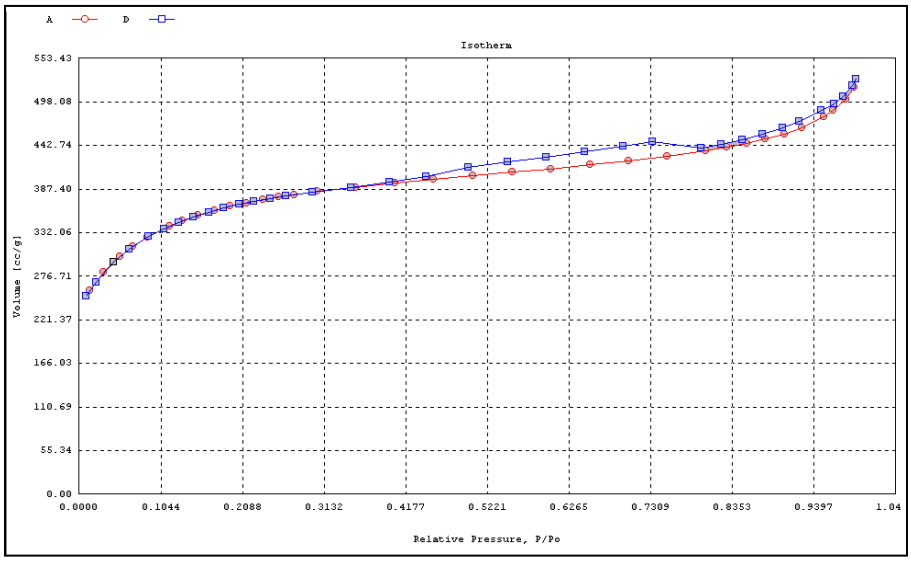

Figure 6.7. Nitrogen adsorption isotherm collected on AC sample after outgassing 20 hours at 120°C.

The baseline-corrected ATR-FTIR spectra (see Section 2.2.6) of AC, UN CMK, and OX CMK carbon samples are shown in Figure 6.8. That the spectra are noisy and have large baseline absorbance is expected for solid carbon samples because there is considerable scattering of IR photons by the carbon. The spectral noise between 1850 and 2300 cm^{-1} occurred in all spectra and seemed to come from the instrument. The ATR-FTIR spectrum of AC indicates there is a relatively low concentration of surface groups. The broad bands between 1000 and 1300 cm^{-1} may be attributed to stretching of C-O single bonds.[96, 261, 262] The CMK spectra show greater intensity in this region than the activated carbon. A strong band at 1590 cm^{-1} also occurs, which can be ascribed to symmetric COO- vibration and/or aromatic ring stretching coupled to highly conjugated keto groups.[90]

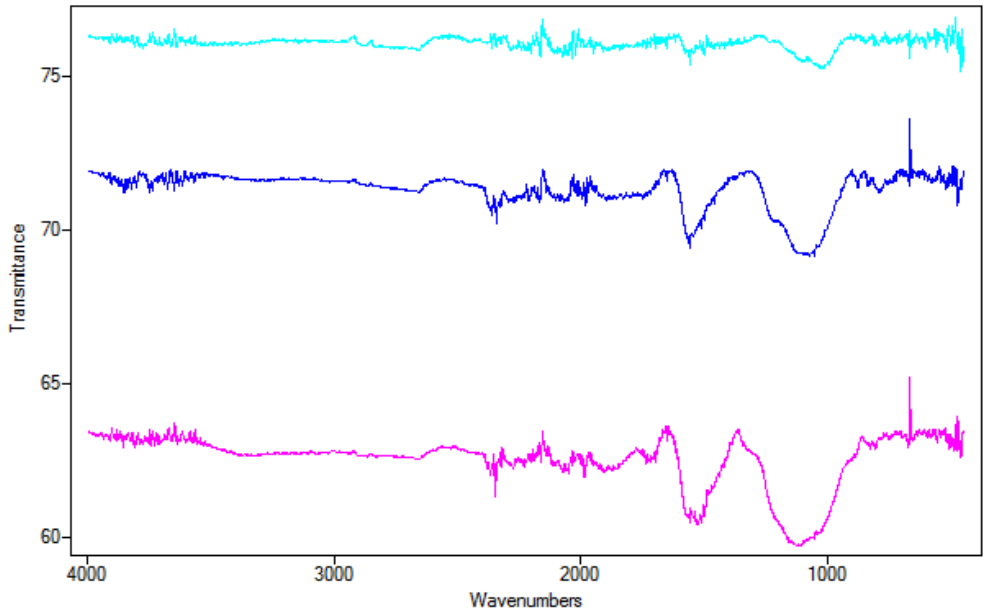

Figure 6.8. Baseline corrected ATR-FTIR spectra of activated carbon (turquoise), UN CMK (blue) and OX CMK (pink).

The PZC of AC was measured by powder addition with 1.4 g AC per L, and pH measurements were taken after 24 hours and after one week (see Section 2.2.7 for details). Figure 6.9 shows that the plot of ΔpH vs. $pH_{initial}$ was linear only in the initial pH range 6-9. Unlike with the CMK materials, the PZC calculated from the one week measurement (7.85) differed significantly from the 24-hour PZC (9.83). This could be due to slow diffusion of hydroxides or protons through the micropores of the activated carbon, but could also be attributed to formation of carbonate from CO_2 contamination. The powder addition method was developed for minerals and accurate PZCs depend on maintaining carbonate-free samples. However, this is likely not possible in solid carbon samples because of Reactions 6.5 and 6.7. Ultimately it was decided to use PZCs measured after 22-24 hours for all of the carbon materials. A lower solid-to-liquid ratio was used than was previously used for mineral samples [94], because the OMCs were in limited supply and needed to be conserved. This was justified by the very high specific surface area of the materials, but AC was used to test the difference between the PZC measured with 4 g/L and 1.4 g/L carbon. In this case, a higher PZC of 10.70 ± 0.22 was measured for the AC. Thus the PZC values tabulated in Table 6.3 for all of the carbon materials

should not be considered absolute, thermodynamic quantities, but are useful for comparing the overall surface properties of the carbon powders. The high PZC of the activated carbon suggests that it has low oxygen content and is expected to exhibit anionic exchange behavior.[261]

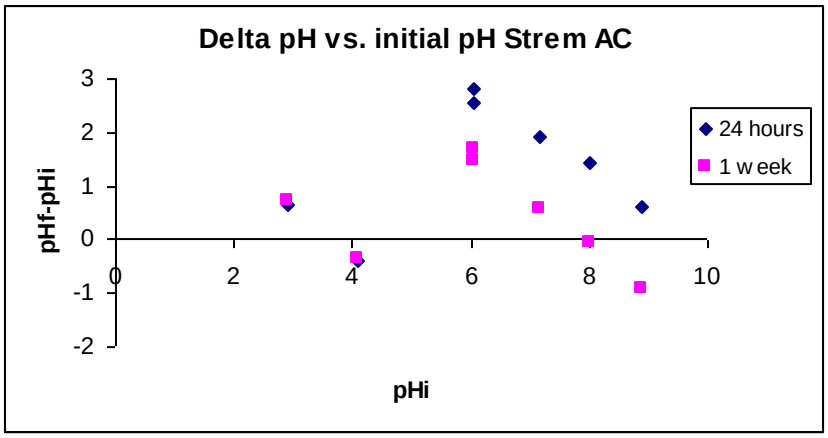

Figure 6.9. Plot of ΔpH vs. initial pH for powder addition samples containing 1.4 g/L AC, measured after 24 hours (blue diamonds) and one week (pink squares).

6.2.3 Synthesis and properties of CMK-9

An illustration of the hard-template (also known as nanocasting) technique for carbon (CMK-type) synthesis is shown in Figure 6.10, using a 2D-hexagonal structure as an example. In this approach, an inverse replica is formed of a rigid, thermally stable and removable ordered mesoporous silica scaffold. This is only possible if there is 3-D pore connectivity in the silica template, and the success of this technique actually showed that SBA-15 has a secondary network of micropores interconnecting the primary mesopores.[263] The three steps of nanocasting are template formation, casting, and template removal. Suitable templates include KIT-6, SBA-15 and MCM-48 mesoporous silicas [207]. In the casting step, a carbon precursor and acid polymerization catalyst are introduced into the channels of the template, allowed to react, and then pyrolyzed at high temperatures (> 700° C). Suitable carbon precursors are monomers such as furfuryl alcohol, phenol resins, sucrose or acetylene, which polymerize at moderate temperatures in an acid-catalyzed condensation reaction. The acid catalyst can be solid Al incorporated into the scaffold, or oxalic or sulfuric acid dissolved in the carbon source. If the concentration of carbon precursor is high enough, and the template is interconnected, a continuous mesoporous carbon framework is formed. The concentration of precursor can be controlled to obtain either the carbon rod or "nanopipe" structure (CMK-3, CMK-8) shown in Figure 6.10, or a tubular structure (CMK-5, CMK-9) from lower concentration solutions. The silica template can be removed either with HF or NaOH, but generally more traces of silica are left behind when NaOH is used.

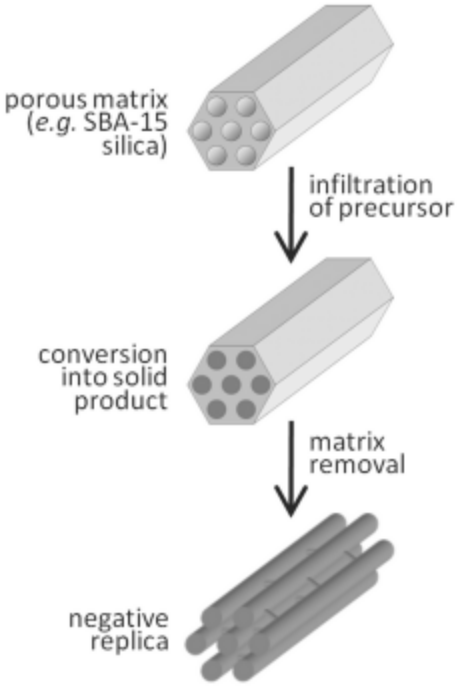

Figure 6.10. Schematic representation of the nanocasting process shown with a 2D-hexagonal structure. Image taken from https://chemie.uni-paderborn.de/en/research/ac/tiemann-group/nanoporous-materials/.

Nanostructured *Ia*3*d* 3D-bicontinuous ordered mesoporous carbons with the nanopipe (CMK-8) or nanotube (CMK-9) structure are prepared using KIT-6 as a hard silica template.[68] The synthetic procedure rigorously followed those first employed with SBA-15 to make CMK-3 and CMK-5.[264] Lu *et al*. published an easier nanocasting procedure for synthesis of CMK-5,[265] in which oxalic acid instead of solid Al was used as a polymerization catalyst, and carbonization occurs under argon, instead of under vacuum. For the work described here, Dr. Harun Tüysüz employed the procedure of Lu *et al*.[265] with a KIT-6 template, for the synthesis of CMK-9. The resulting OMC should demonstrate a well-interconnected framework and a bimodal pore system with cubic *Ia3d* symmetry. However, the ordered mesostructure of the carbon product could not be verified with low-angle XRD or the N_2 adsorption isotherms. Because the numbering system implies a specific mesostructure, the terms UN CMK and OX-CMK are used throughout this dissertation to refer to the the as-synthesized and chemically oxidized (see Section 6.2.6) products respectively. All of the plutonium work was done with the second synthesized batch of CMK, unless specifically stated otherwise. The first batch was oxidized without keeping any of the as-synthesized product for comparison. This material will be called OX CMK', and is discussed only because it showed different properties than the second batch. This highlights the sensitivity of the nanocasting technique, which makes the synthesis less reproducible than soft-template methods. The CMKs were characterized with SEM, TEM, N_2 adsorption, FTIR, and powder addition.

The synthesis of KIT-6 was done according to Kleitz, *et al.*[68] A triblock copolymer-butanol mixture was used as the structure-directing agent. 13.5 g of surfactant (Pluronic 123, $EO_{20}PO_{70}EO_{20}$) was dissolved in a solution of 487.5 g distilled water and 26.1 g concentrated HCl (37%). 13.5 g n-butanol was added to the homogenous solution at 35 °C. After one hour of

stirring, 29 g of triethoxyorthosilicate (TEOS) was quickly added to the solution, followed by stirring at this temperature for 24 hours. After that, the mixture was heated at 100 °C for another 24 hours under static conditions. The solid product was filtered without washing, dried at 90 °C overnight, and then calcined at 550 °C for six hours.

The synthesis of CMK-9 used a similar technique of surface-templating to that reported for CMK-5,[265] but with the KIT-6 hard template instead of the SBA-15 template. Furfuryl alcohol (FA) dissolved in trimethylbenzene (TMB) in a 50% volume proportion was used as the carbon precursor, and oxalic acid was added as the polymerization catalyst. Incipient wetness impregnation was used at room temperature to infiltrate the KIT-6 template with the FA solution, and then polymerization occurred at 60° and 80°, each for 16 hours under air. The PolyFA-silica composite was carbonized under argon by first heating for 3 hours at 150 °C, then heating to 300 °C at a rate of 1 °C/min, and up to 850 °C at a rate of 5 °C/min. The sample was held under argon at 850 °C for 4 hours, yielding a black powder composite. The etching of the silica template was achieved using 2 M NaOH aqueous solution.

A representative SEM image of the CMK product is shown in Figure 6.11. The particle morphology is similar to that of the AC, but with a slightly smaller range of particle sizes, generally up to about 100 μM.

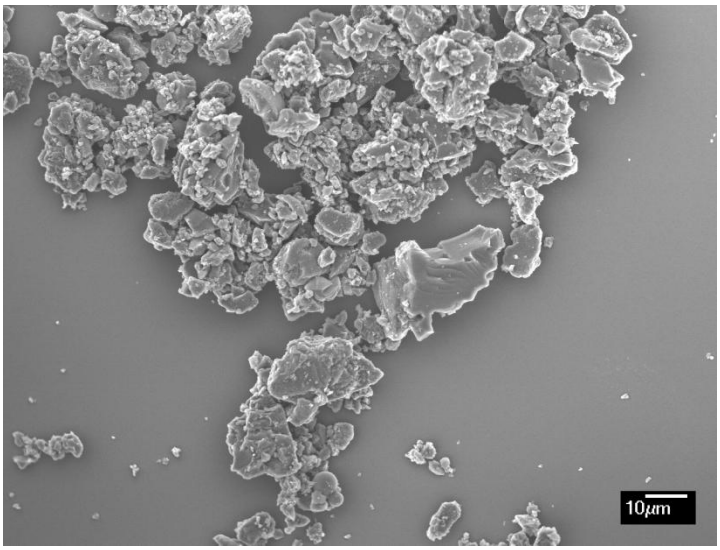

Figure 6.11. Representative SEM image of CMK mesoporous carbon particles.

The UN CMK N_2 adsorption isotherm shows a type IV curve (Figure 6.12), indicative of a mesoporous solid. Also the BET surface area is quite high (see Table 6.2), which suggests that at least part of the product has the nanotube structure of CMK-9. However, the hysteresis loop is much wider than expected, indicating a poorly defined pore size distribution. The BJH analysis of the isotherm could not produce any meaningful pore size distribution, as already discussed above. From TEM (Figure 6.13) and knowledge of the KIT-6 template, the mesopores seem to be approximately 6-8 nm in diameter. Although the TEM images show large domains of ordered mesostructure, the product may contain structural defects and some disordered mesopores. In the nanocasting synthesis, any carbon precursor that is not properly infiltrated into the pore network becomes disordered microporous carbon, which could lower the sample quality. However, the micropore volume and surface area in micropores are relatively low in the CMK sample, 4.6%

and 9.9 % of the total pore volume and BET surface area, respectively. Another possibility is that the precursor mixture was somehow not evenly distributed throughout the template. The shape of the N_2 adsorption isotherm of OX CMK'(Figure 6.14), as well as the lower BET surface area, is consistent with that reported for the nanorod CMK-8 structure,[68] even though the 50% FA mixture should have yielded the tubular CMK-9 structure with a bimodal pore size distribution. The oxidation treatment is not what caused the structural difference, and the N_2 adsorption isotherm of OX CMK (2^{nd} batch) was very similar to that of the untreated material shown in Figure 6.12. Nanocasting is known to be fastidious, and the irreproducibility and lower sample quality of the CMKs inspired the author to seek soft-templated OMCs.

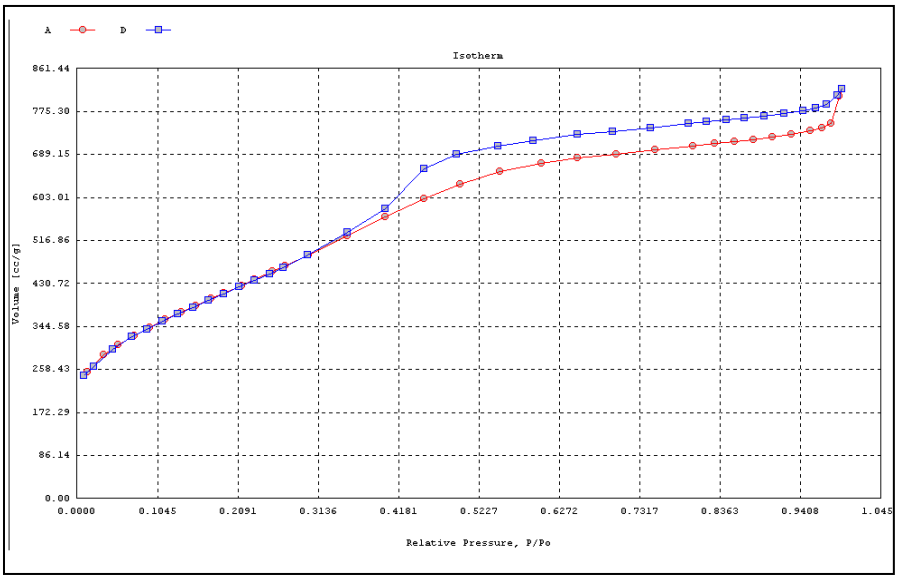

Figure 6.12. N_2 adsorption isotherm of an untreated CMK sample, showing a wide hysteresis loop, characteristic of a poorly defined mesopore size distribution.

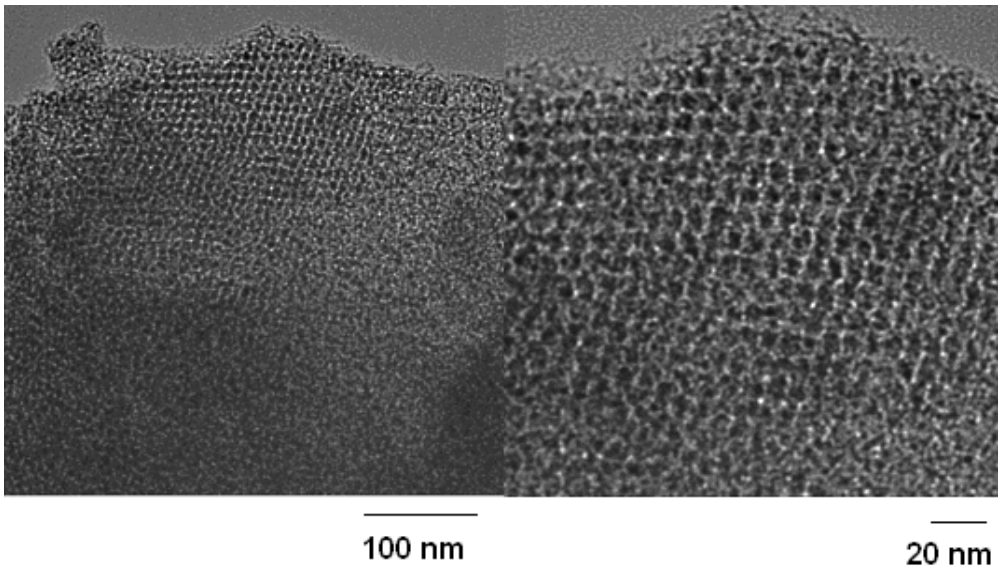

Figure 6.13. Representative TEM images of untreated CMK, 40,000x magnified (left), and 80,000x magnified (right).

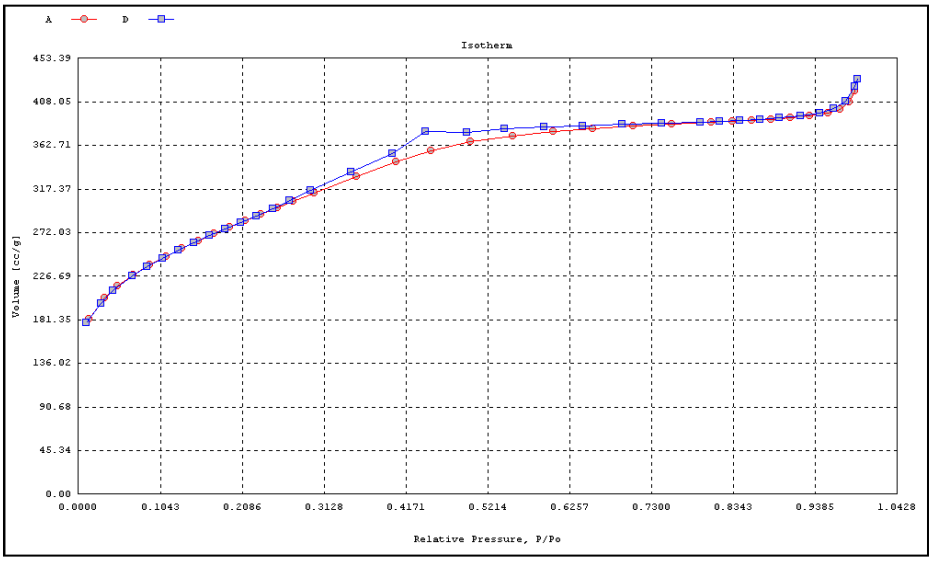

Figure 6.14. N_2 adsorption isotherm of an OX CMK' sample, which has a similar hysteresis loop to reported isotherms from the cubic nanorod OMC CMK-8.[207]

From the powder addition experiments with CMK and OX CMK, the plots of ΔpH (pH_f - pH_i) vs. pH_i were linear within the initial pH range 4 to 10 ($R^2 \geq 0.99$). The data were more linear and consistent than that of AC, with much smaller change after one week. The slightly basic PZC of the untreated CMK (8.1 ± 0.4) is characteristic of pure carbon surfaces, such as graphite.[104] However, the ATR-FTIR spectrum (Figure 6.8) of untreated CMK shows absorbance bands in the region 1000 cm^{-1} to 1300 cm^{-1} as well as around 1600 cm^{-1}, with significantly greater intensity than the AC. This implies that there is a significant concentration of ester and conjugated keto groups on the CMK surface. The N_2 adsorption isotherm that was measured after outgassing at 250° C gave a BET surface area approximately 13% greater than those

outgased at 120° C, further indicating that the CMK surface is decorated with functional groups. It is likely that removal of the silica template using NaOH also activated the surface with reactions such as reaction 6.7, but formed surface oxides instead of aqueous carbonate.

6.2.4 Synthesis and properties of FDU-16

As noted in the last section, nanocasting is a fastidious process that can only create small batches of mesoporous carbon, and the sample quality varies from batch to batch. The Zhao group at Fudan University has greatly advanced the soft template approach to OMC synthesis with the evaporation induced self assembly (EISA) method.[211, 213] The use of triblock copolymers to form the mesoporous template makes this method easier than casting against a hard template, and highly reproducible. OMCs synthesized by this technique are highly ordered and have very thick pore walls, which makes them exceptionally hydrothermally stable. The EISA synthetic process is outlined in Figure 6.15, and involves five steps. In the first step, a low molecular-weight phenolic resin called resol is prepared by polymerization of phenol and formaldehyde under basic conditions. The selection of resol as the carbon precursor is key to the EISA approach, as it contains a high concentration of –OH groups, which hydrogen-bond with the PEO blocks of the copolymer template during the second step. The second step is organic-organic self assembly, which is called evaporation-induced because the ratio of resol to template changes as the solvent evaporates, and this induces self assemply of the template into ordered mesophases. The mesostructure can be altered by selection of the triblock copolymer and control of the resol/copolymer ratio. Step three is thermopolymerization of the resol precursor, and the template is removed in step 4. If an ordered mesoporous polymer is desired, the template can be removed by calcination below 600° C, and temperatures above 600° C yield ordered mesoporous carbon.

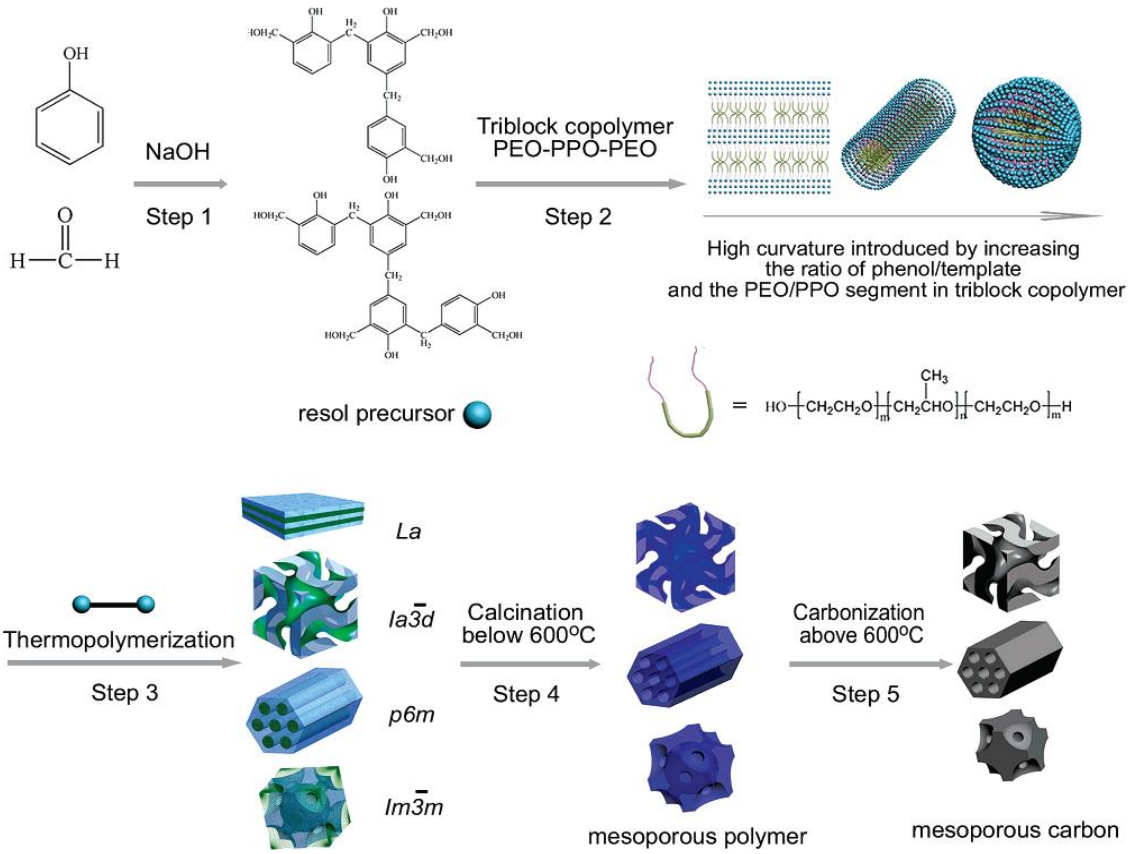

Figure 6.15. Schematic diagram indicating the 5 major steps for OMC synthesis with the EISA method: 1) resol precursor preparation, 2) the formation of an ordered hybrid mesophase by organic-organic self assembly during solvent evaporation, 3) thermopolymerization of the resols around the template to solidify the ordered mesophase, 4) template removal, 5) carbonization.[213]

The *Im3m* body-centered cubic ordered mesoporous carbon denoted FDU-16 was synthesized by Dr. Jinxiu Wang of the Zhao group at Fudan University, using evaporation-induced organic-organic self assembly as previously reported by Meng *et al.*[213] Triblock copolymer F127 was dissolved in ethanol, and then an ethanol solution of resol precursors phenol and formaldehyde was added and stirred for 10 minutes. The molar ratio of reagents used was phenol/formaldehyde/NaOH/F127 = 1:2:0.1:0.003-0.008. The homogenous mixture was poured into dishes and allowed to evaporate for 5-8 hours at room temperature, then placed in a 100° oven for 24 hours. The resulting film was scraped from the dish and ground into fine powder, then calcined in a tubular furnace under argon. The sample was heated to 600° C at the rate of 1° C/min, then to 900° C at the rate of 5° C/min, and held for two hours at 900° C. The carbons synthesized at Fudan (FDU-16, C-CS and their oxidized counterparts) were characterized by Dr. Wang using SAXS, TEM, N_2 adsorption, transmission FTIR, elemental analysis, and TGA. SEM images were collected at UC Berkeley by Dr. Anthony Bruchet. Powder addition and ATR-FTIR characterizations were done at UC Berkeley by the author and Stephen Jones.

Representative SEM micrographs of FDU-16 particles are shown in Figure 6.16. The FDU-16 has different particle morphology than the rough surfaces observed on AC and CMK particles, with relatively smooth planes that seem to be layered into rectangular structures. The

particle size is large, up to approximately 800 μm long. The porosity inside the FDU-16 particles can be viewed by increasing magnification on the SEM (Figure 6.17). It appears that the particles have a smooth, glassy surface with holes and defects that allow entry into the porous inside of the particle.

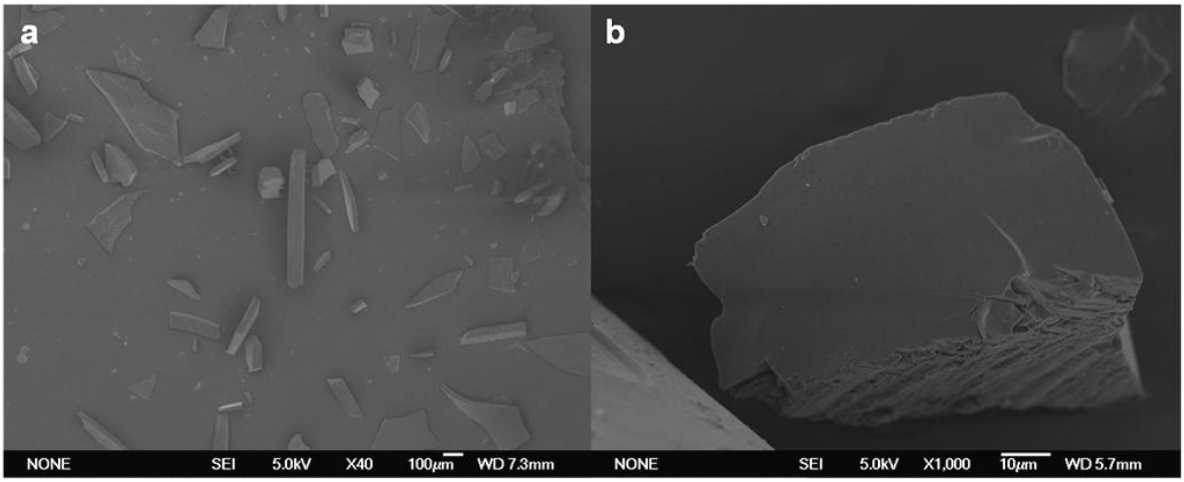

Figure 6.16. Representative SEM images of FDU-16 particles magnified 40 times (a) and 1000 times (b).

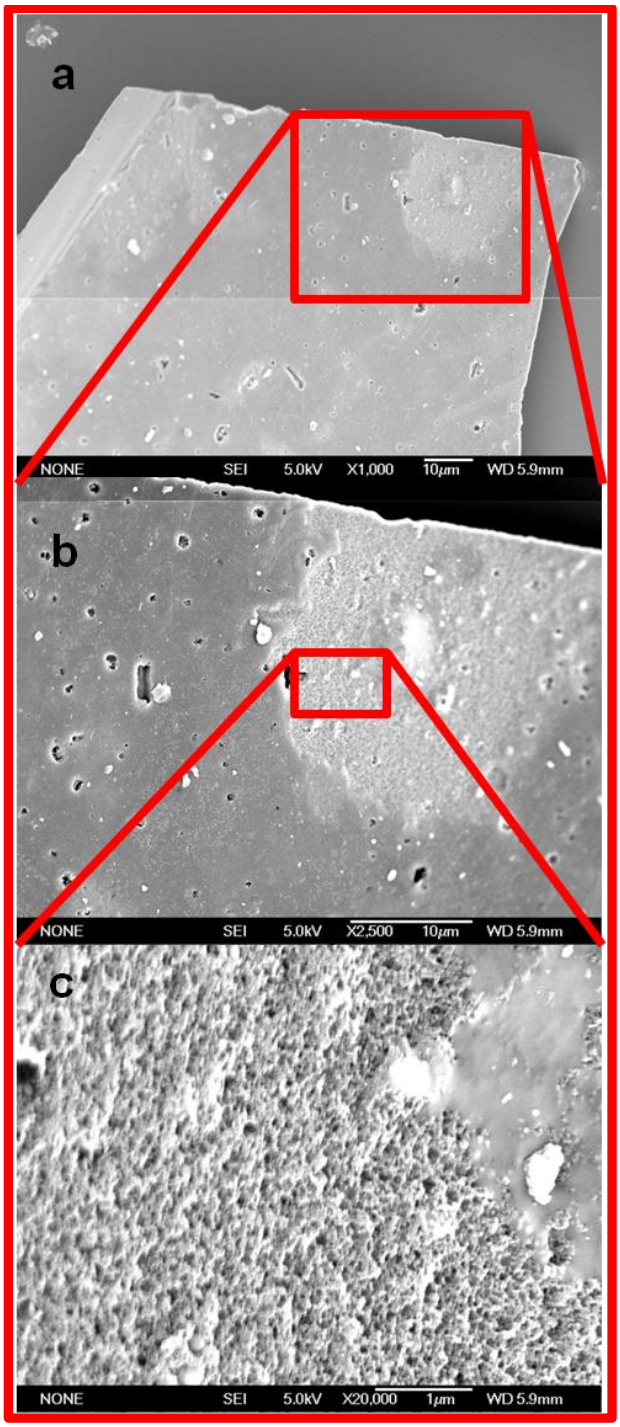

Figure 6.17. SEM image of an FDU-16 particle magnified 1000 times (a), 2500 times (b), and 20,000 times (c), showing the high porosity of the particle.

The successful synthesis of FDU-16 with high sample quality was confirmed by SAXS, TEM, and N_2 adsorption. The SAXS pattern (Figure 6.18) shows three well-resolved scattering peaks that can be indexed to the 110, 200 and 211 diffractions of a highly ordered three-dimensional (3D) cubic *Im3m* mesostructure. This is further confirmed by TEM images that show the 3D cubic mesostructure in large domains of FDU-16 (Figure 6.19a,b,c) and FDU-16-COOH (Figure 6.19d,e,f), viewed along the [100] (a, d), [110] (b, e), and [111] (c, f) directions. The N_2 adsorption isotherm of FDU-16 is shown along with the other Fudan carbons in Figure 6.21a, but the hysteresis loop is difficult to see on this scale, so the isotherm for FDU-16 is plotted alone in Figure 6.20, with a shorter Y-scale. The pore size distribution (Figure 6.21b) is centered around 2.7 nm, on the smaller end of the meso-range. The material has a moderate BET surface area and pore volume of 564 m^2/g, and 0.27 cm^3/g, respectively. Analysis of the isotherm by the t-plot method showed that approximately 62% of the pore volume and 75% of the surface area is in micropores (see Table 6.2).

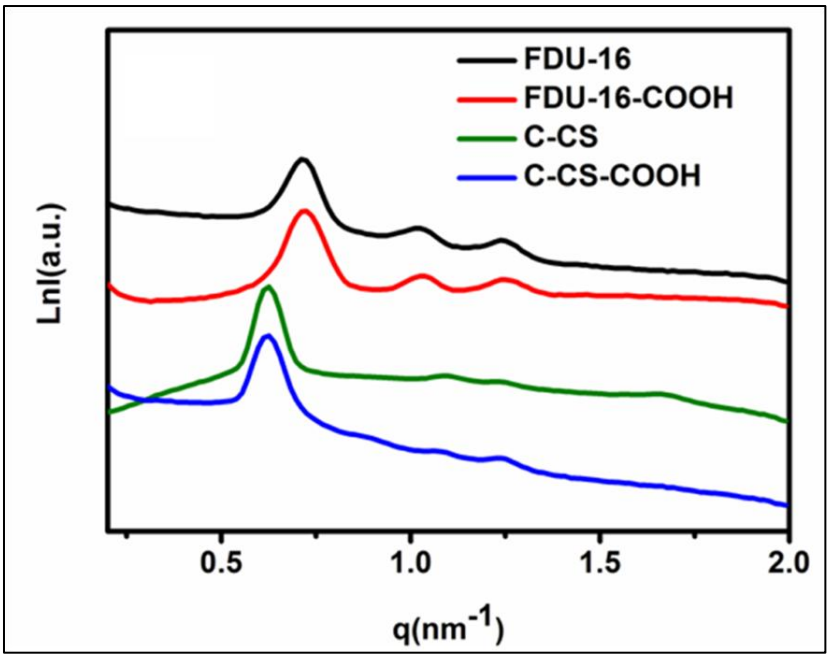

Figure 6.18. SAXS patterns collected on samples of FDU-16 (black), FDU-16-COOH (red), C-CS (green), and C-CS-COOH (blue) ordered mesoporous carbon powders.

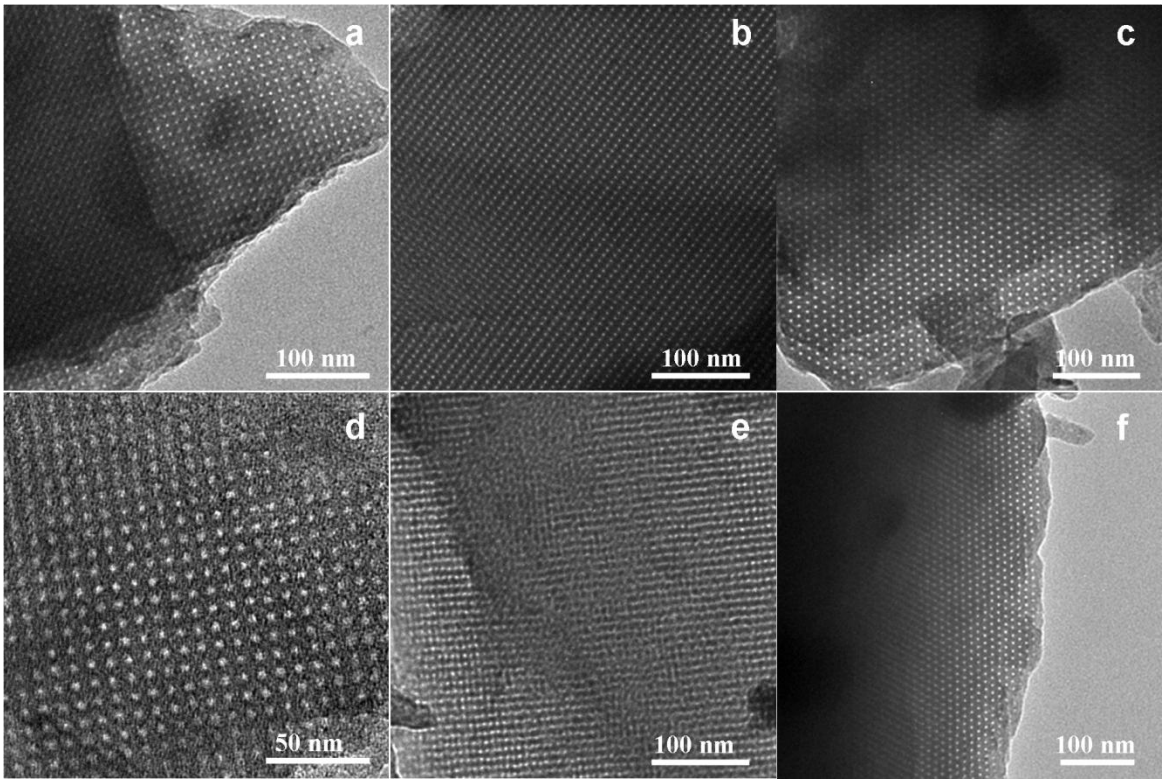

Figure 6.19. TEM images of FDU-16 (a,b,c) and FDU-16-COOH (d,e,f), viewed along the [100] (a, d), [110] (b, e), and [111] (c, f) directions; and C-CS (g) and C-CS-COOH (h) viewed along the [110] directions, showing the highly ordered 3D cubic *Im3m* mesostructure.

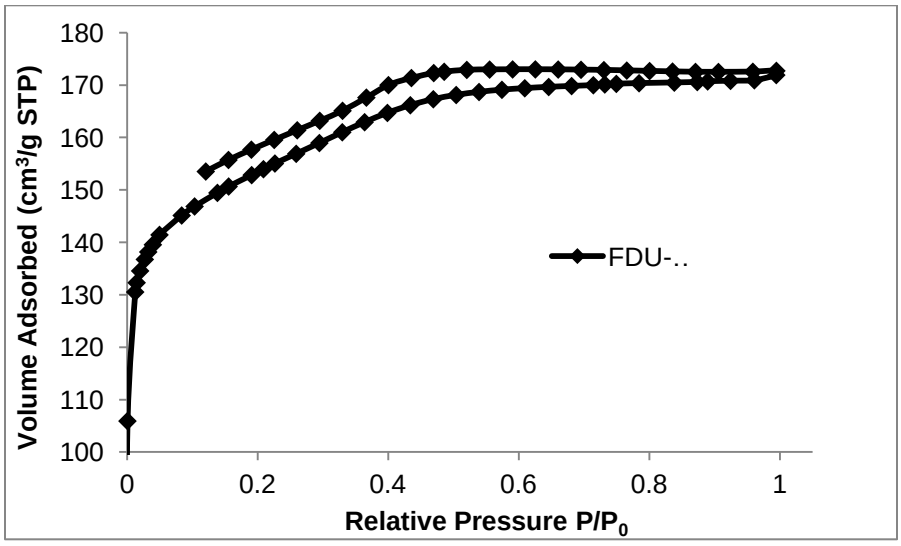

Figure 6.20. N_2 adsorption isotherm of FDU-16.

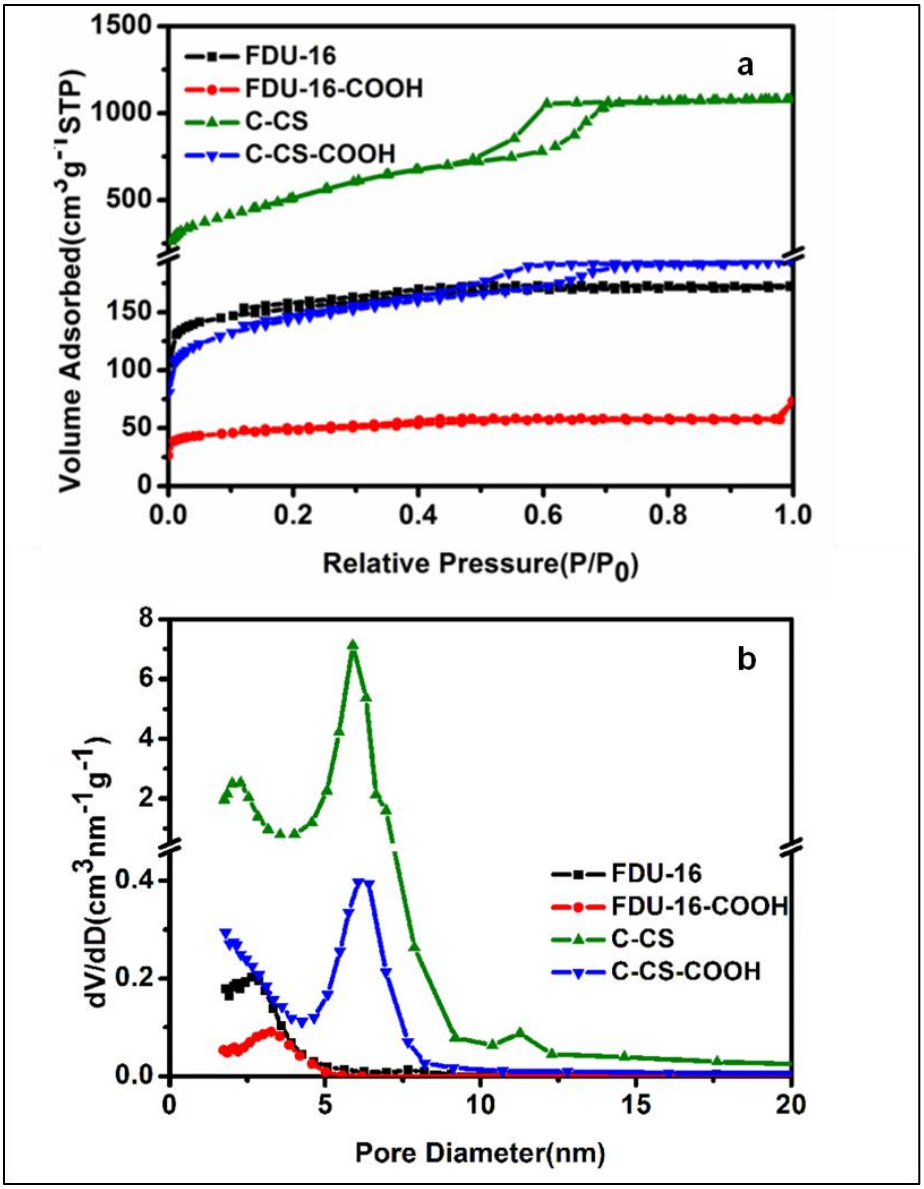

Figure 6.21. N_2 adsorption isotherms (a) and pore size distribution derived from the adsorption branch by the BJH method (b) collected on samples of FDU-16 (black), FDU-16-COOH (red), C-CS (green), and C-CS-COOH (blue) ordered mesoporous carbon powders.

The TGA curve (Figure 6.22), FTIR (Figure 6.23), elemental analysis (Table 6.3), and PZC measured by powder addition (7.1 ± 0.1) all indicate that FDU-16 has a low concentration of surface groups. From the TGA data, the sample contains an estimated 0.28 mmol carboxyl groups and 0.26 mmol phenol groups per g FDU-16, and elemental analysis showed only 2.7 % O by weight.

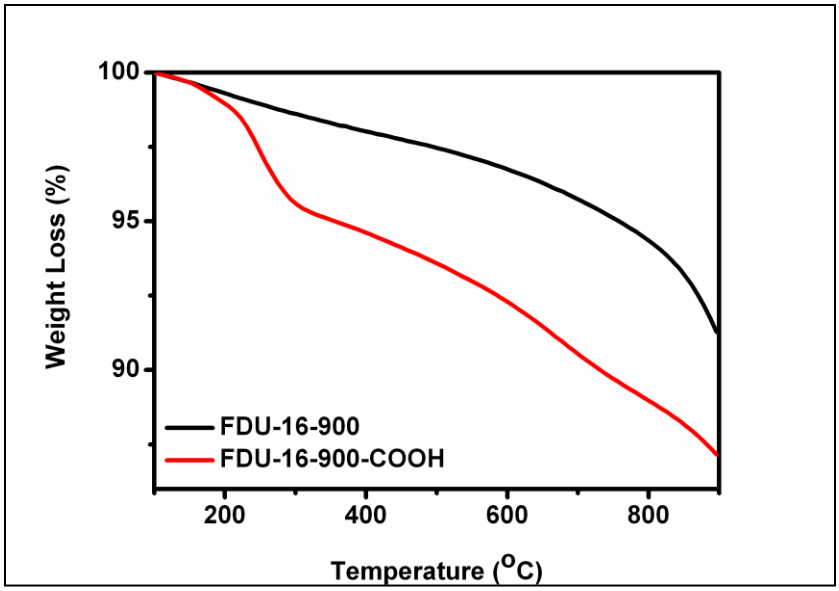

Figure 6.22. TGA data collected on FDU-16 (black) and FDU-16-COOH (red) OMC powders.

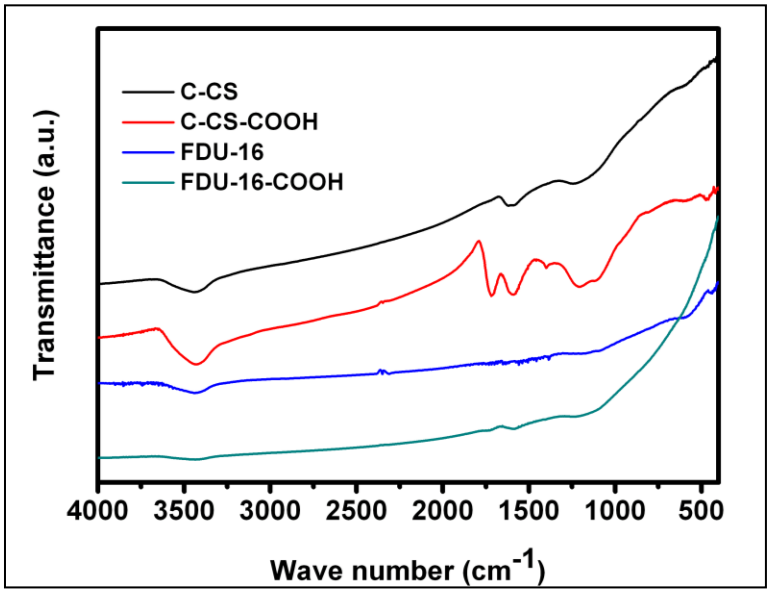

Figure 6.23. FTIR spectra of FDU-16 (blue), FDU-16-COOH (teal), C-CS (black), and C-CS-COOH (red) OMC powders.

6.2.5 Synthesis and properties of C-CS

Although the FDU-16 is much more ordered than the CMK, the surface area and pore volume are significantly smaller, and largely composed of micropores. OMCs with large pores and very high surface areas can be synthesized by etching away the silica component of carbon-silica nanocomposites formed by triconstituent self-assembly.[212] The synthetic method is diagrammed in Figure 6.24. Mesostructured carbon-silica nanocomposites are prepared by co-assembly of preformed resols, silica oligomers from acid-catalyzed hydrolysis of TEOS, and triblock copolymer F127 using the EISA approach. Weak interactions between the silica

oligomers and the phenol groups in the carbon precursor create a composite within the mesopore wall, which is described in an analogy as concrete (resol) reinforced with steel bars (silica oligimers). Calcination at 300° C removes the polymer template, giving an ordered mesoporous nanocomposite with large pores. Ordered mesoporous resol polymer frameworks normally shrink during carbonization, but here the "reinforcing steel bar" silicates greatly inhibit shrinkage, allowing a large-pore OMC to be formed. After carbonization, removal of the silica component with HF leaves an additional network of pores within the walls of the primary mesostructure, which yields an OMC with extremely high surface area. The crosslinking of the silicate component can be increased by prolonging the acid-catalyzed hydrolysis of the TEOS silica precursor in the first step. In this case, the secondary pore network inside the walls of the primary carbon mesostructure is composed of smaller mesopores with a narrow size distribution. This is a 2D-hexagonal OMC with a bimodal pore size distribution, similar to CMK-5.

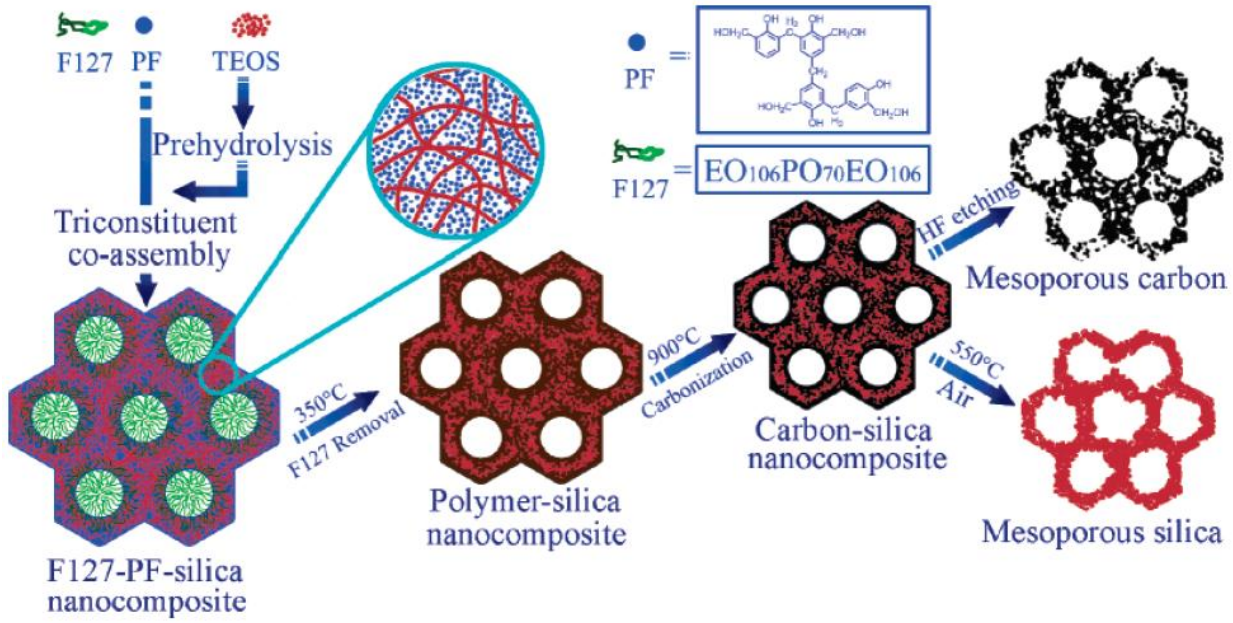

Figure 6.24. Schematic diagram illustrating triconstituent co-assembly of polymer-silica nanocomposites and the corresponding ordered mesoporous silica or carbon.[212]

The ordered mesoporous carbon denoted C-CS was synthesized from a carbon-silica nanocomposite produced by the evaporation-induced triconstituent co-assembly method [212]. Briefly, the triblock copolymer F127 was dissolved in ethanol with 0.2 M HCl and stirred for one hour at 40° C. Tetraethyl orthosilicate (TEOS) and 20% resol ethanolic solution were added, and stirred at 40° C for five hours. The initial mixture composition was F127/resol/TEOS/EtOH/HCl/H_2O = 1 : 0.5 : 2.08 : 12 : 7.3 x 10^{-3} : 1 in mass ratio. The mixture was then transferred to a dish, and the ethanol was evaporated at room temperature (5-8 hours) before thermopolymerization at 100° C for 24 hours. The resulting film was scraped from the dish and ground into fine powder, then calcined in a tubular furnace under N_2 flow. The sample was heated to 600° C at the rate of 1° C/min, then to 900° C at the rate of 5° C/min, and held for two hours at 900° C. The nanocomposite was immersed in 10% HF solution for 24 hours, which removed all of the silica to yield the 2-D hexagonal ordered mesoporous carbon C-CS.

The C-CS was rinsed thoroughly, but the first time the PZC was measured, a value around pH 4 was obtained, which was lower than expected (see Figure 6.25a). Therefore the remaining C-CS powder was put in dialysis tubing and rocked gently with Milli-Q water that was changed at least twice daily until constant conductivity of the water was measured. After dialysis, the C-CS powder was dried in an oven at 130° C. The PZC measured after dialysis was significantly higher, 7.3 ± 0.4. The experiments with Pu and Eu used the dialyzed C-CS. The other three Fudan carbons underwent dialysis later, after experiments had already been done, due to concern about possible trace contaminants. No significant change in PZC was observed for C-CS-COOH, FDU-16, or FDU-16-COOH before and after dialysis.

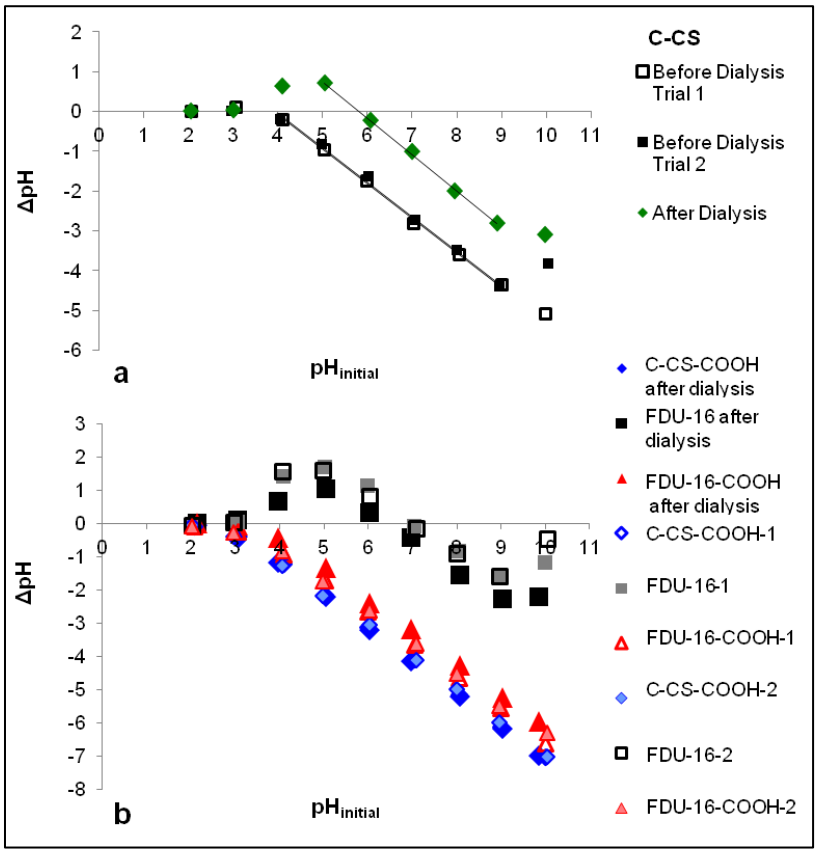

Figure 6.25. Plots of change in pH vs. initial pH from powder addition experiments with C-CS (a) and C-CS-COOH, FDU-16, FDU-16-COOH (b) before and after dialysis of the OMC powders. The PZC of C-CS after dialysis was considerably higher than the PZC measured before dialysis, perhaps due to the removal of trace HF and/or silica left from the synthesis. Dialysis of the other three OMC powders did not significantly alter their PZCs.

Figure 6.26 is a representative SEM image of C-CS particles, showing that the morphology is more similar to that of FDU-16 than to CMK. The size distribution of particles was smaller, ranging from approximately 3 to 100 μm. The ordered mesostructure was observed by TEM along the [110] direction, shown in Figure 6.27. The SAXS pattern of C-CS (Figure 6.18) shows four diffraction peaks, which can be indexed to 10, 11, 20 and 21 planes of a 2-D hexagonal mesostructure (space group *p6m*). The N_2 adsorption isotherm (Figure 6.21) shows that the C-CS has very high surface area and large pore volume (see Table 6.3). The C-CS has a much higher surface area and pore volume than the FDU-16 due to the secondary pore network

inside the walls of the primary mesostructure. The bimodal pore size distribution was observed with BJH analysis of the adsorption branch (Figure 6.21b). Like the untreated CMK, the micropore volume and surface area in C-CS are low, only about 4.8% and 11% of the total pore volume and surface area, respectively.

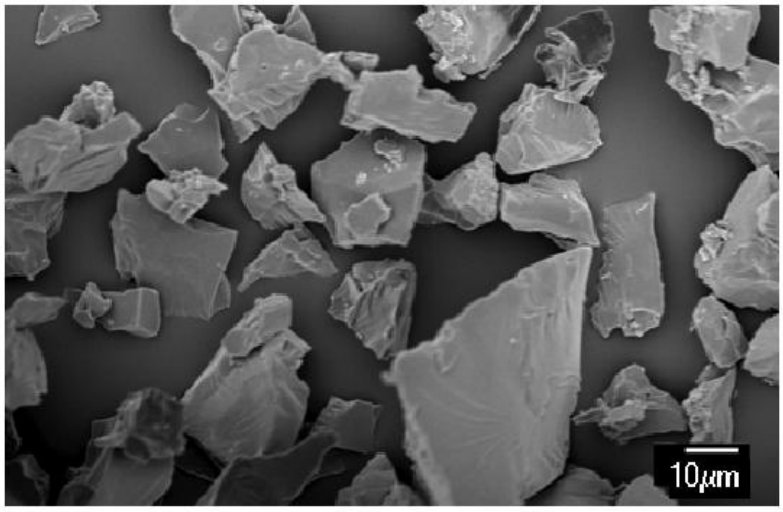

Figure 6.26. Representative SEM image of C-CS particles.

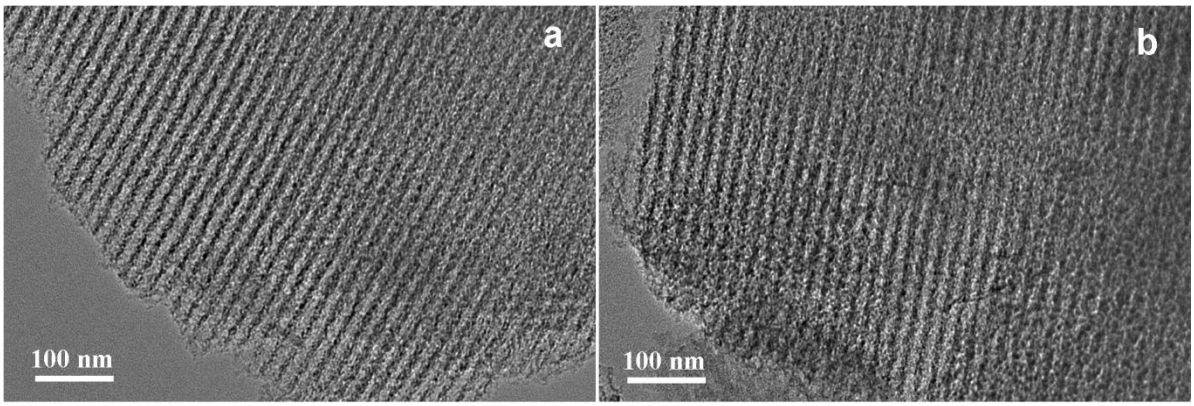

Figure 6.27. Representative TEM images of C-CS (a) and C-CS-COOH (b) viewed along the [110] direction.

The TGA data from C-CS and C-CS-COOH powders is shown in Figure 6.28. The C-CS has estimated carboxyl and phenol concentrations of 0.17 mmol/g and 0.19 mmol/g, respectively. The O-H stretching band around 3400 cm^{-1} can be seen in the FTIR spectrum (Figure 6.23), but the peak around 1720 cm^{-1} associated with the carbonyl stretch of non-aromatic COOH groups is not observed in the C-CS spectrum. Bands are observed around 1250 cm^{-1} and 1590 cm^{-1}, suggesting instead the presence of esters and highly conjugated keto groups. Elemental analysis indicates the C-CS is 9.1 % O by weight. The greater concentration of surface groups compared to FDU-16 is only due to the much larger specific surface area of C-CS. From comparison of their ATR-FTIR spectra (C-CS shown in Figure 2.17, UN CMK in Figure 6.8), it is clear that the C-CS has fewer functional groups than the untreated CMK. The use of HF to etch away silica leaves a more pristine carbon surface than NaOH.

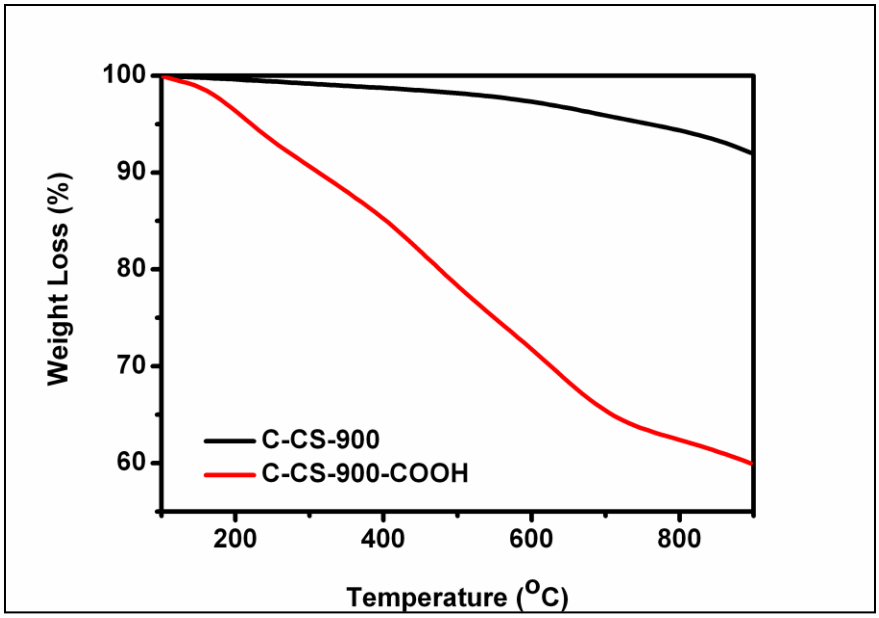

Figure 6.28. TGA data collected on C-CS (black) and C-CS-COOH (red) OMC powders.

6.2.6 Liquid oxidation treatments

For many applications, and especially sorption of metal ions, carbon surfaces are first functionalized by polymer coating, ligand impregnation, ligand grafting, chemical vapor deposition, or oxidation. Oxidation is the most common surface treatment of porous carbons, making them more hydrophilic with greater ion exchange capacity.[207] Chemical grafting techniques are available that functionalize carbon directly, while others use oxidation as the first step and graft molecules to the oxidized functional groups with an esterification reaction.[45] Oxidation can be achieved electrochemically, or chemically under dry or wet conditions. Dry oxidation involves heating the sample in the presence of an oxidizing gas with a catalyst, and wet oxidation uses acids like HNO_3 and H_2SO_4, with or without other oxidizing agents. In any case carbon oxidation involves the degradation of carbon layers, so the conditions must be optimized to preserve the ordered mesostructure of OMC. Bazula *et al*. studied nitric acid oxidation of CMK-3 and CMK-5 to optimize the oxidation reaction without structural damage.[266] They determined that for thin-walled OMC such as CMK-5, the nitric acid concentration should be limited to 1 M so that the ordered mesostructure would not be destroyed. A comprehensive study of the structural stability and surface oxidation of FDU-15 with several wet oxidation techniques[90] determined that acidic ammonium persulfate (AAPS) is a powerful and gentle oxidant, which created more carboxyl groups on the OMC surface than nitric acid. FDU-15 is far more robust and resistant to mesostructural damage than CMK-3, because of their different structural frameworks. FDU-15 has thick walls, while the mesostructure of CMK-3 arises from small random pillars connecting the nanorods, which are easily attacked for structural collapse.

Before venturing into chemically grafted OMCs, the interactions of actinides and lanthanides with pristine and oxidized OMCs should be better understood. The CMK was oxidized by nitric acid according to Bazula *et al*.[266] A portion of the second batch of CMK was treated for 3 hours at 80 °C with 1 M HNO_3 (150 mL/g), then washed thoroughly with distilled water and dried overnight at 90 °C. The resulting carbon powder is denoted OX CMK. The first

batch of CMK underwent the same procedure, and is called OX CMK'. A portion of both the FDU-16 and the C-CS mesoporous carbons were oxidized with acidic ammonium persulfate (APS, $(NH_4)_2S_2O_8$) according to the reported procedure,[90] and will be called FDU-16-COOH, and C-CS-COOH, respectively. The carbon was added to 1.0 M AAPS solution, prepared in 2 M H_2SO_4, in the ratio of 1 g carbon per 60 mL APS solution. The mixture was stirred and refluxed in an air-proof round-bottom flask at 60° C for 12 hours. The OMCs were filtered, washed thoroughly with water and ethanol, then dried under vacuum overnight at 60° C.

The textural parameters of UN CMK and OX CMK can be compared by their electron micrographs and N_2 adsorption isotherms. No differences in particle size or morphology were observed by SEM after oxidation treatment of all the carbons. Figure 6.29 shows representative TEM images of OX CMK, which still show domains of ordered mesostructure like those of UN CMK given in Figure 6.13. The shape of the N_2 adsorption isotherm of CMK was the same before and after oxidation treatment. The nitric acid oxidation treatment decreased the BET surface area of CMK by 11.7%, but increased the micropore surface area by 183%. The resulting OX CMK has 31.7 % of its surface area and 20.2 % of its pore volume in micropores. The chemical properties of OX CMK and UN CMK can only be compared by their FTIR spectra (Figures 6.8) and their relative PZCs (Table 6.3), as TGA and elemental analysis were not available. The intensity of the broad C-O stretching band in the ATR-FTIR spectrum of OX CMK is increased compared to the UN CMK spectrum, particularly around 1200 cm^{-1}. The oxidized CMK shows a small new feature around 1340 cm^{-1}, which was also observed by Bazula *et al.* on the spectra of HNO_3 treated CMK-5,[266] and could possibly be assigned to nitroso groups.[103] The increased absorbance in the OX CMK spectrum around 1400 cm^{-1} and 1560 cm^{-1} are likely due to symmetric and asymetric -COO- stretches of carboxylic acids,[103] and the peak around 1720 cm^{-1} is characteristic of C=O stretching in carboxyl or ketone groups.[50, 103, 261, 262, 266] The PZC of OX CMK was lowered to 3.3 ± 0.2, consistent with higher concentrations of oxygen-containing surface groups.[96, 98, 99, 101, 103, 105, 107] However, the changes in the FTIR specrum of OX CMK compared to UN CMK were rather subtle, because UN CMK seemed to have significant concentrations of surface groups already. Bazula *et al*. found with X-ray photoelectron spectroscopy (XPS) that treatment of CMK-5 with 1 M HNO_3 increased the atomic percentage of O from 3% to 4%.[266]

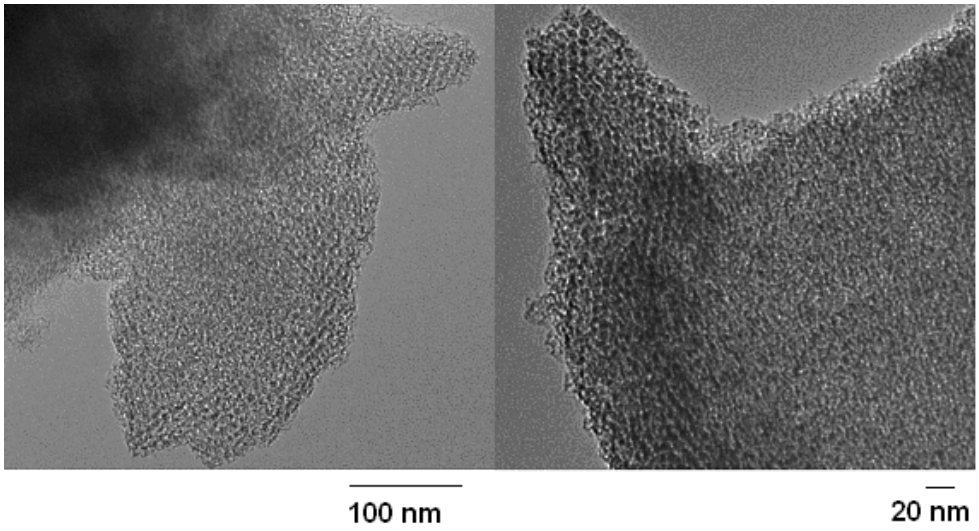

Figure 6.29. TEM images of OX CMK 40,000x magnified (left) and 80,000x magnified (right).

The SAXS patterns collected on FDU-16 and C-CS-COOH samples (Figure 6.18) show that the ordered mesostructures were retained after wet oxidation with AAPS, and this is further confirmed by the TEM micrographs (Figures 6.19 and 6.27). The BET surface areas and total pore volumes of both the AAPS treated samples are significantly lower than the untreated samples (see Table 6.2). It is interesting to note that the BET surface areas and total pore volumes of the oxidized C-CS-COOH and the pristine FDU-16 are very similar. The relative amount of microporosity in the samples did not increase as much as those treated with nitric acid, and the BJH pore size increased slightly with AAPS oxidation (see Figure 6.21b and Table 6.2). Pristine FDU-16 has high micropore content, and the oxidation blocked many of the micropores, causing a dramatic decrease in both the micropore surface area and total BET surface area. The micropore surface area of C-CS increased with oxidation, and the total BET surface area decreased significantly, indicating many of the smaller mesopores were blocked. This is because the oxidation occurs preferentially in the smallest pores, leaving the micropores blocked, while degradation of carbon layers give mesopores that are slightly larger than those of the pristine carbons.[90] Figure 6.30 shows possible models of FDU-15 surface structure proposed by Wu *et al*.,[90] and illustrates the proposed mechanism of oxidation. At first the small mesopores and micropores are blocked by functional groups, then they open with increasing reaction time and temperature. After the reaction is complete, many of the smallest pores are either blocked or have been enlarged.

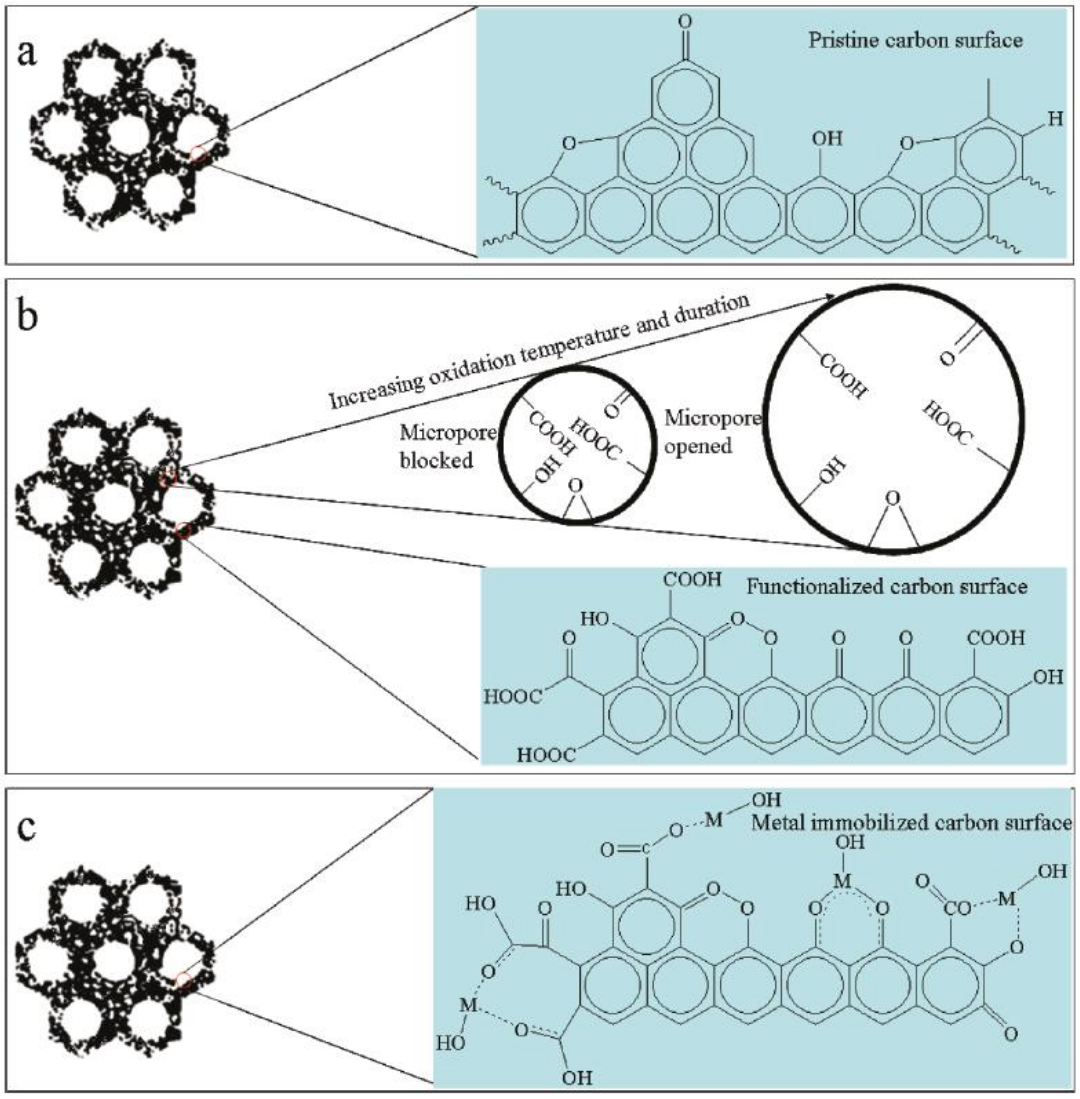

Figure 6.30. Possible surface structure models of pristine FDU-15 (a), oxidized FDU-15 with an illustration of how micropores are blocked, then opened with increasing oxidizing temperature and duration (b) and the oxidized FDU-15 complexing metal ions (c) [90].

FTIR spectral changes in the FDU-16 upon oxidation with AAPS are difficult to see (Figures 6.23 and 2.17) because of the lower surface areas, lower content of functional groups, and increased baseline absorbance due to thicker walls in the FDU-16 type OMCs. A new intense band at 1721 cm^{-1} attributed to the carbonyl stretch of non-aromatic carboxyl groups appears for C-CS-COOH with treatment by AAPS. A strong band at 1590 cm^{-1} also occurs, which can be ascribed to symmetric COO- vibration and/or aromatic ring stretching coupled to highly conjugated keto groups, and there are also increased absorbances in the O-H and C-O stretching regions. The sharp band near 670 cm^{-1} that is characteristic of $S_2O_8^{2-}$ is absent from all spectra, indicating that these anions were thoroughly removed after the oxidation treatment.[90] Table 6.3 summarizes some chemical properties of the OMC surfaces, as determined by elemental analysis, TGA and powder addition. The carbon content decreased while the H and O content increased dramatically after the treatment with AAPS (up to 39.5% O in C-CS-COOH),

indicating successful functionalization. The densities of surface oxides were determined by TGA measurement according to a previous report,[90] as described in Section 2.2.4. The density of carboxylic groups is 0.89 and 1.89 mmol/g for FDU-16-COOH and C-CS-COOH, respectively. This is much higher than that of the untreated FDU-16 and C-CS. A similar phenomenon is also observed for the density of phenolic groups. Furthermore, the high concentration of carboxyl groups on the oxidized materials leads to much lower PZCs in these materials, compared to the near-neutral PZCs of the pristine C-CS and FDU-16 carbons.[98, 103] The most successful oxidation reaction was the acidic AAPS treatment of C-CS to yield C-CS-COOH. It appears that the high surface area, relatively low micropore content, and bimodal pore size distribution of C-CS make it an ideal OMC substrate for functionalization under this wet oxidation condition.

6.2.7 Summary of the properties of carbons studied

The seven different porous carbons studied represent wide variations in properties that may affect their interactions with lanthanides and actinides, including particle size and morphology, ordered mesostructure, BET surface area, total pore volume, mesopore size distribution, microporosity, PZC, and elemental and functional group composition. Table 6.2 summarizes the textural parameters measured for all of the carbons, and Table 6.3 summarizes some of their chemical properties. What they all have in common is that they are porous, amorphous carbons with surface areas higher than typical mineral adsorbants and carbon nanotubes. Also, the carbonization temperature was similar for all of them (850° C for CMKs, 900° C for Fudan carbons), although this parameter is unknown for AC. Therefore, the electrical conductivity of these carbon powders is expected to be similar.[89] Large variations in their affinity for actinide and lanthanide sorption may be expected based on the wide variation of physicochemical properties. Although the effect of these properties were not systematically studied, the Pu sorption behaviors of all seven carbons were surveyed under the same conditions (see Section 6.3.1), allowing comparison between materials having different properties. The extensive characterization of these carbons helped lead to more informed hypotheses regarding sorption mechanisms and which properties are most important to optimize the sorption reactions.

The FTIR spectra (Figures 2.17, 6.8, and 6.23) show that the difference in surface chemistry between UN CMK and OX CMK is much less pronounced than that of C-CS and oxidized C-CS-COOH. This is both because the C-CS is more pristine than the CMK, and because the AAPS treatment is more oxidizing than the nitric acid treatment. The larger difference in surface chemistry of C-CS and C-CS-COOH was very important for the efforts to understand how plutonium interacts with pristine and highly oxidized OMC surfaces.

Table 6.2. Summary of textural parameters of porous carbons, derived from N_2 adsorption, SAXS, or TEM.

Carbon Sample	Unit Cell Parameter (nm)	BET Surface Area (m^2/g)	Micropore area (m^2/g)	BJH Pore Diameter (nm)	Pore Volume (cm^3/g)	Micropore Volume (cm^3/g)	Meso-structure
AC	N/A	1133 ± 17	908 ± 8	N/A	0.76 ± 0.02	0.470 ± 0.006	N/A
UN CMK	N/A	1530 ± 11	151 ± 2	~ 6-8	1.169 ± 0.009	0.0543 ± 0.009	*Ia3d* domains
OX CMK	N/A	1351 ± 28	428 ± 9	~ 5-7	0.98 ± 0.03	0.198 ± 0.004	*Ia3d* domains
OX CMK'	N/A	948 ± 22	416 ± 29	~ 5-7	0.64 ± 0.01	0.21 ± 0.01	*Ia3d* domains
C-CS	11.6	1817	199	2.1/6.0	1.67	0.08	*p6m*
C-CS-COOH	11.6	521	310	2.1/6.2	0.30	0.13	*p6m*
FDU-16	12.4	564	424	2.7	0.27	0.17	*Im3m*
FDU-16-COOH	12.4	176	122	3.3	0.11	0.05	*Im3m*

Table 6.3. Chemical properties of OMCs derived from elemental analysis, powder addition and TG data.

Sample	PZC (pH)	Carboxyl (mmol/g)	Phenol (mmol/g)	C/H/N/O wt %
AC	9.8 ± 0.4	N/A	N/A	N/A
UN CMK	8.1 ± 0.4	N/A	N/A	N/A
OX CMK	3.3 ± 0.2	N/A	N/A	N/A
C-CS	7.3 ± 0.4	0.17	0.19	86.9/3.6/0.1/9.1
C-CS-COOH	2.8 ± 0.1	1.89	2.13	56.2/4.1/0.2/39.5
FDU-16	7.1± 0.1	0.28	0.26	91.7/4.3/0.4/2.7
FDU-16-COOH	3.1 ± 0.1	0.89	0.57	84.6/3.6/0.4/11.4

6.3 Batch sorption experiments

All seven carbon powders were tested in batch sorption and desorption experiments with plutonium, added as Pu(VI). The first body of work with Pu compared the sorption interactions with AC, CMK and OX CMK, which all have fairly high surface areas but different

concentrations of surface functional groups, and different porosity in AC. Batch experiments investigated pH dependence, sorption kinetics, Pu uptake capacity, competition with aqueous chelating agent, Pu desorption and reusability. The results left some ambiguity regarding the effects of OMC surface oxidation on the Pu sorption interaction. The pH-dependent batch sorption experiment was repeated with FDU-16, FDU-16-COOH, C-CS, and C-CS-COOH for initial assessment of their potential for Pu sorption. Based on the results, subsequent experiments focused on the comparison of C-CS and C-CS-COOH. These experiments were aimed at better understanding the different sorption interactions that occur with Pu and pristine or oxidized carbon surfaces, by examining the kinetics and effects of ionic strength on sorption. The batch sorption interactions of Eu(III) as a representative lanthanide with C-CS and oxidized C-CS-COOH were investigated for comparison with the plutonium results.

Batch sorption experiments performed with ^{239}Pu and carbon powders were similar to those described in Section 5.4. A liquid-to-solid ratio of 1000 ± 100 mL/g was adopted as standard because of the results obtained with Ac-Phos-SBA-15 displayed in Figure 5.39, and was always used except where otherwise specified. Samples of pH-adjusted 0.1 M (except where stated otherwise) $NaClO_4$ or NaCl with carbon powders were generally prepared one day before addition of Pu or Eu. In the CMK and AC experiments, small amounts of HCO_3^- and CO_3^{2-} were added to solutions of pH ≥ 6 to reach the equilibrium concentrations expected due to dissolution of CO_2 from the atmosphere.[61] This was not done in the work with the Fudan carbons, but has little relevance to most of the experiments, which were conducted at pH 4. LSC measurements of plutonium solutions after contact with the OMCs were taken after the solids were allowed to settle for at least 20 minutes, or after centrifuge filtration as described in Section 5.4.

The Eu batch sorption experiments with carbon were designed by the author to compliment the Pu studies, and executed by Erin May of the Nitsche group, using the ^{152}Eu radiotracer method described in section 4.4.2. Samples of C-CS or C-CS-COOH with 1000 ± 50 mL/g of pH-adjusted 0.1 M NaCl were prepared in acid-washed polypropylene centrifuge tubes 1 day before the addition of Eu stock. After the Eu stock addition, the pH was adjusted with small volumes of HCl and NaOH, and the samples were allowed to rock for the desired length of time. Phase separation was achieved by centrifuging the samples for 2 minutes at 6000 rpm, and then duplicate 100 µL aliquots were pipetted from the liquid phase into small conical vials for gamma counting with a high-purity Ge detector.

The percent sorption was calculated using Equation 5.2. The error bars on percent sorption in plots of data from experiments with AC, UN CMK, and OX CMK represent 90% confidence, and were generated as described in Section 5.4. In Pu and Eu batch experiments with the Fudan carbons, uncertainties at the 1σ confidence level of measured concentrations incorporate an estimated 2.5% pipetting uncertainty (5% in Eu experiments), the standard error between duplicate measurements, and 1σ from counting statistics. The error bars on percent sorption represent 2σ by using a worst-case method with upper limits for initial and final concentrations (c) of c + 2σ, and lower limits of c - 2σ. Values from duplicate aliquots were averaged, but data from duplicate samples were not averaged and are displayed together.

6.3.1 Pu and Eu sorption and desorption as a function of pH

Batch experiments were performed with 10 or 11 ± 1 µM Pu(VI) in a 0.1 M $NaClO_4$ matrix at various pH values between 1-10 and each carbon powder in the ratio of 1000 ± 50

mL/g. The Pu concentration of the solution was measured after 3 hours, 23 hours, and again after 1 week in some cases. Figure 6.31 shows the percent Pu sorption to the vial and/or filter vs. pH in the control samples without a solid sorbent. The solutions in Figure 6.31a with pH ≥ 6 had sufficient HCO_3^- and CO_3^{2-} added to reach equilibrium concentrations expected due to dissolution of CO_2 from the atmosphere, as did samples of AC, UN CMK, and OX CMK. A small amount of Pu was lost (≤ 20 %) to precipitation and sample vials from solutions of pH 6-8, where the neutral carbonate complex of Pu(VI) is expected to prevail (see Figure 3.13). Figure 6.31b shows the same data from solutions without HCO_3^- or CO_3^{2-} added, where up to 25 % of the Pu seemed to have precipitated in the higher pH solutions within 3 hours. After 23 hours, some of the initially precipitated Pu may have redissolved due to auto-reduction and/or introduction of carbonate to the system from atmospheric CO_2. Generally, no sorption or precipitation of Pu occurred in solutions below pH 6. Therefore any loss of Pu from the solution phase greater than 10% in carbon samples with pH ≤ 5, or greater than 25% in samples with pH ≥ 6, can be attributed to sorption to the carbons.

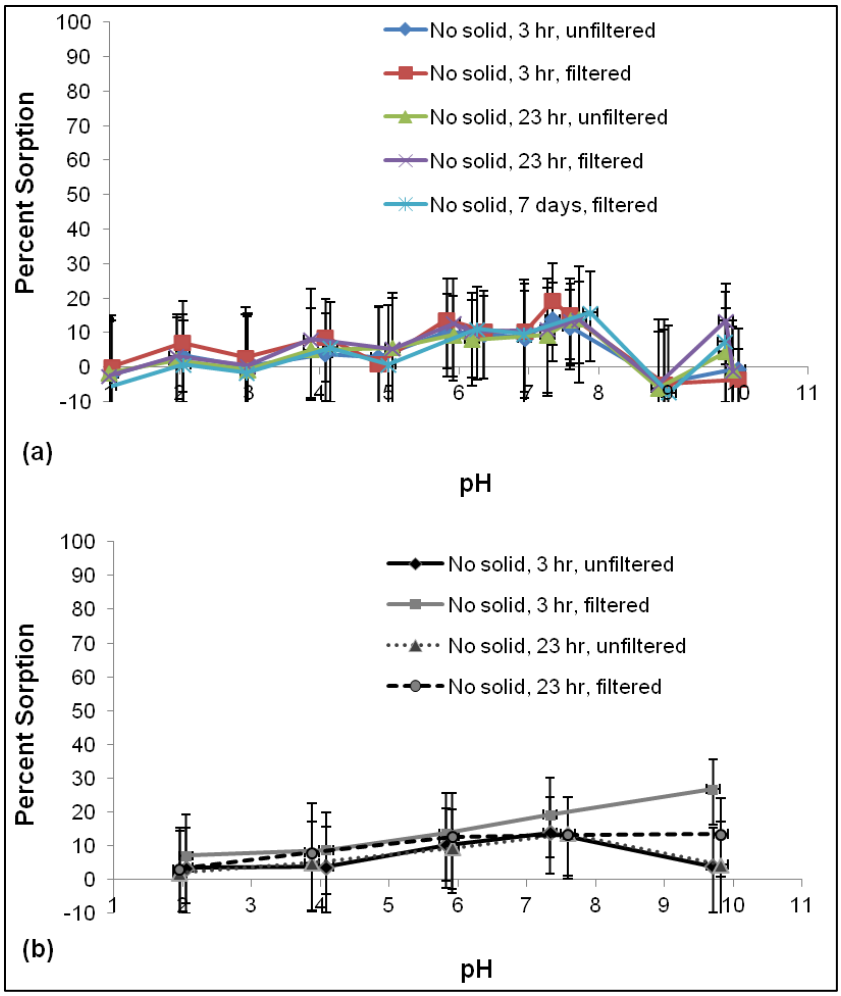

Figure 6.31. Percent Pu sorption vs. pH for control samples of 0.1 M $NaClO_4$ and 10 ± 1 µM Pu solution, measured after different times, with expected equilibrium concentrations of of HCO_3^- and CO_3^{2-} added to solutions of pH ≥ 6 (a), and with no HCO_3^- and CO_3^{2-} added (b). Unfiltered aliquots were pipetted directly from the solution phase after allowing the solid to settle, and filtered aliquots were centrifuged through Vivacon 30K MWCO regenerated cellulose filters as described in Section 5.4. Lines are only to guide the eye.

Figures 6.32-6.35 show plots of percent sorption versus pH for activated carbon, CMK carbons, FDU-16, and C-CS-type OMCs, respectively. Generally the higher surface area OMCs show high Pu uptake from solutions over a wide pH range. Quantitative sorption is observed over the widest pH range (pH 2-10) for C-CS-COOH, within 3 hours of contact time (see Figure 6.35). High uptake to the pristine C-CS OMC occurred more slowly, and only at pH values 4 and above. These same trends are observed when comparing the Pu sorption curves of CMK and OX CMK (Figure 6.33). The slower plutonium sorption to FDU-16-COOH is likely associated with the much lower surface area, and possibly slow diffusion into the larger particles (Figure 6.34). The pristine FDU-16 is not an effective sorbent material for plutonium, as only 20-40% sorption is observed, and this seems relatively independent of pH. The activated carbon showed fairly high uptake from solutions with pH values between 3 and 10, but only after a week of contact (Figure 6.32). The plutonium sorption to AC may be hindered by slow diffusion through the micropores. Given the various speciation of Pu(VI) over this wide pH range, and the high Pu uptake of the untreated OMCs, it seems likely that more than one type of binding site is employed. The wide pH range of high uptake would be unusual for chemisorption of ions to amphoteric solids. The speciation of Pu(VI) in aqueous solutions open to air varies with solution pH from the positively charged plutonyl cation to neutral, and negatively charged carbonate complexes at higher pH values (see Figure 3.13 in Section 4.3.2), while oxygen groups at the carbon surface are expected to be deprotonated in pH environments above the PZC. Acidic carbons always have some basic sites, and vice-versa, so for carbon powders with such high surface areas the PZC cannot necessarily be used to predict the solution conditions in which sorption will be observed. XANES data later showed that the Pu on the OMC surfaces had been reduced to Pu(IV) (see Section 6.4), which would be expected to hydrolyze and precipitate in solutions less acidic than pH 1-2, unless complexation by surface groups is more favorable. Therefore, the observed sorption may be a mixture of surface ion complexation, precipitation, and adsorption of intrinsic Pu colloids formed upon reduction to Pu(IV). Although the binding mechanism is unclear, the extent of Pu uptake clearly depends on the carbon sorbent material, and is not simply bulk precipitation of self-reduced Pu in solution. This is evidenced by the control samples, as well as the lower and slower uptake of Pu in the activated carbon and FDU-16 samples. All subsequent batch experiments with carbons and plutonium in the perchlorate medium were conducted at pH 4 to observe maximum Pu uptake, while maintaining solubility of oxidized Pu.

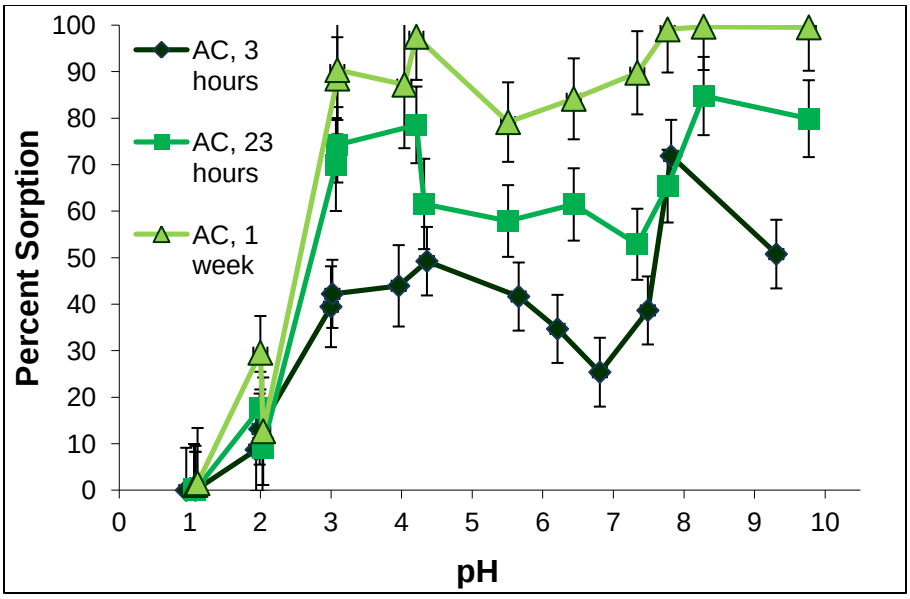

Figure 6.32. Percent Pu sorption vs. pH after different contact times for samples of 0.1 M $NaClO_4$ and 11 ± 1 µM Pu(VI) at pH 1-10 and activated carbon powder. Lines are added to guide the eye.

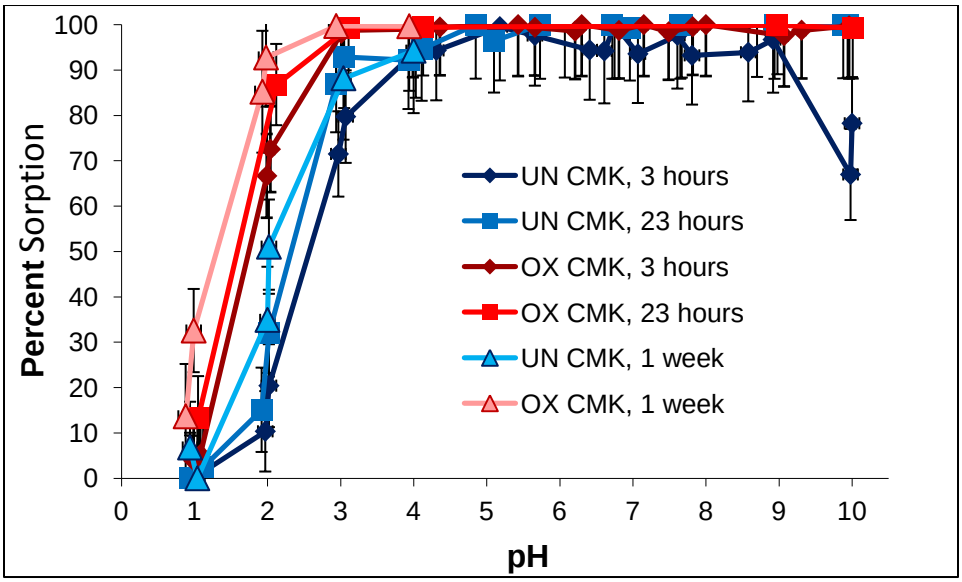

Figure 6.33. Percent Pu sorption vs. pH after different contact times for samples of 0.1 M $NaClO_4$ and 11 ± 1 µM Pu(VI) at pH 1-10 and CMK powders. Lines are added only to guide the eye.

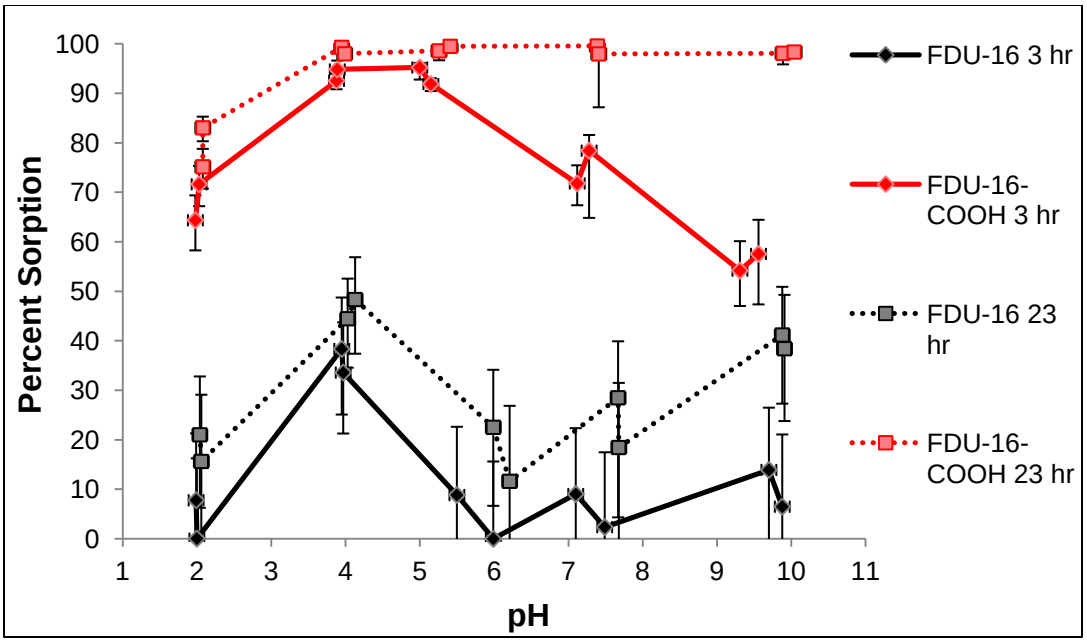

Figure 6.34. Percent Pu sorption vs. pH after 3 hours and 23 hours for samples of 0.1 M $NaClO_4$ and 10 ± 1 µM Pu(VI) at different pH values and FDU-16 OMC powders. Lines are added only to guide the eye.

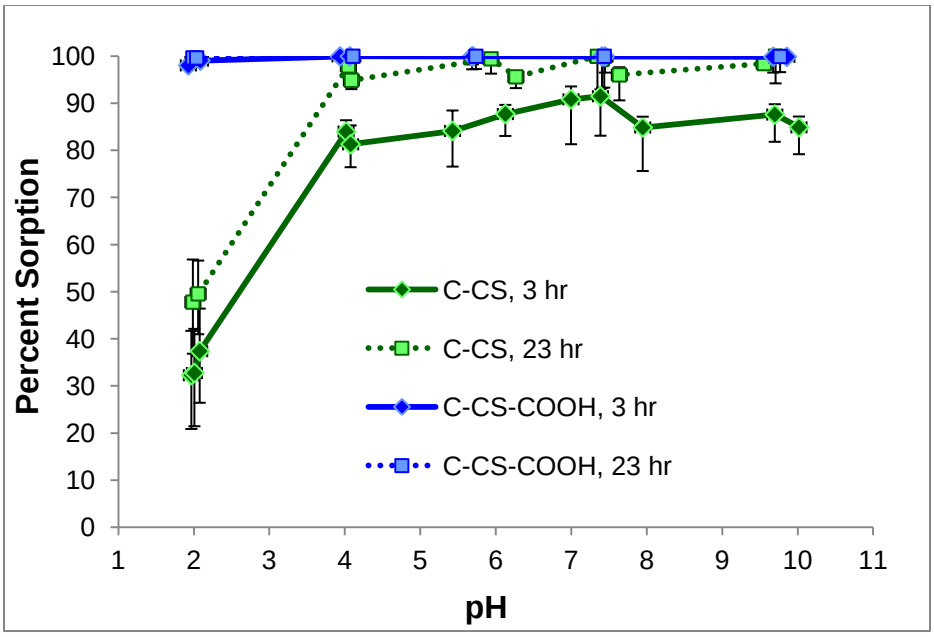

Figure 6.35. Percent Pu sorption vs. pH after 3 hours and 23 hours for samples of 0.1 M $NaClO_4$ and 10 ± 1 µM Pu(VI) at different pH values and C-CS OMC powders. Lines are added only to guide the eye.

It is important for most applications that target species could be removed after binding to the surface, as it would be both convenient and economical if the materials could be reused. Desorption studies were done by adding small volumes of concentrated $HClO_4$ to the batch sorption samples after sorption occurred, rocking for an allotted amount of time, then remeasuring the Pu concentration in the liquid phase. All of the Pu could usually be removed from untreated CMK and activated carbon in 11 µM Pu batch samples by lowering the sample

pH to pH 1, but 1 M $HClO_4$ was required for complete removal of Pu from oxidized CMK samples (intermediate acidities were not tested with AC and CMK samples). The equilibration time at each acidity was 1 week, so desorption kinetics in 1 M $HClO_4$ were tested for UN CMK and OX CMK samples, initially at pH 4, ranging from 10 to 250 µM Pu. Generally, contact with 1 M $HClO_4$ for one day was sufficient for Pu removal, but desorption was not always consistent, and sometimes longer times were needed for 100% of Pu to return to the solution phase. This could be due to slow dissolution of precipitated PuO_2 crystals in some samples, as EXAFS analysis of samples with pH 6 and above showed that a portion of the Pu associated with the CMK was PuO_2 (see Section 6.4.1).

Figure 6.36 shows the results of stripping Pu from Fudan carbons by adding $HClO_4$ to the 10 µM Pu, 0.1 M $NaClO_4$ samples, plotted as percent sorption, which is the total percentage of Pu remaining in the solid phase, vs. total acid concentration in the samples. The contact time at each acidity was 24 ± 1 hours. Most of the sorbed plutonium could be removed from C-CS and FDU-16-COOH by acidifying the samples to pH 1, but about 80-90% of the plutonium in C-CS-COOH samples remained on the solid phase. This is likely due to the very high concentration of functional groups on the C-CS-COOH, as even at pH 1 there are enough negatively charged groups to attract Pu cations. Plutonium in these samples returned to the solution phase when enough $HClO_4$ was added to give a total concentration of about 0.5 M. Only the FDU-16, and the FDU-16-COOH in the pH 10 sample, retained over 30 % of the Pu even in 1 M acid. It could be that plutonium in those samples precipitated, and perhaps the dissolution and diffusion out of the large particles was slow. In order to reduce the volume of high activity waste, a different method of desorption was adopted, in which the bulk liquid phase was removed and a small volume of 1 M HCl was added to the Pu-containing solid carbon. After about 1 day of contact, this method was effective at removing at least 70% of the plutonium from the solid phase in all samples, including those with more Pu loaded.

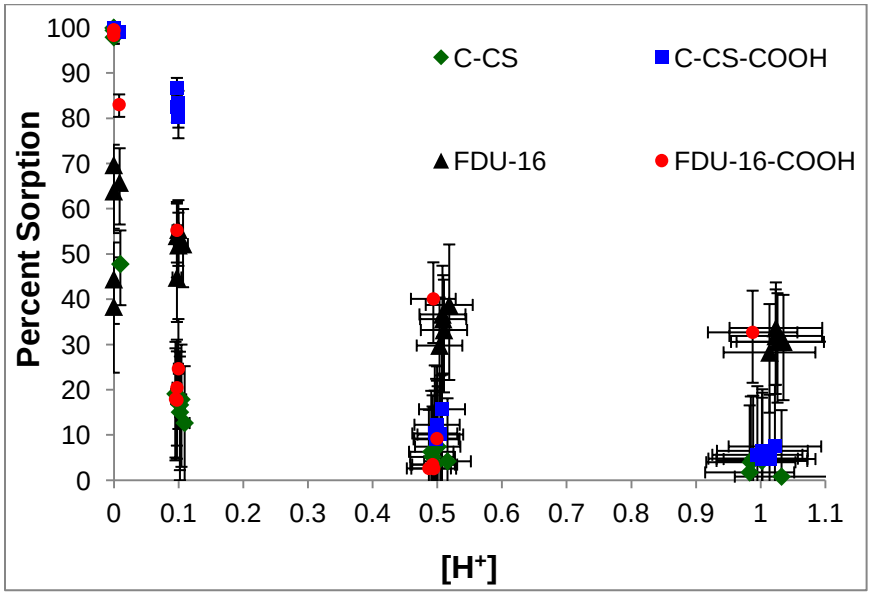

Figure 6.36. Percent sorption (total percentage of Pu remaining in the solid phase) vs. total acid concentration as $HClO_4$ was incrementally added to samples of Fudan OMC powders with 10 µM Pu in 0.1 M $NaClO_4$ of various pH between 2 and 10. The contact time at each acidity was 24 ± 1 hours.

Because C-CS OMCs were the most effectively oxidized, and showed the highest affinity for Pu, sorption studies with FDU-16 and FDU-16-COOH were not further pursued. The interactions of Pu(VI) and Eu(III) with pristine C-CS and oxidized C-CS-COOH were investigated. Because Eu(III) is expected to only interact electrostatically with deprotonated surface groups, Eu sorption to unoxidized OMCs should be pH-dependent and may be less favorable overall than sorption of Pu. Most Pu sorption experiments were performed using $NaClO_4$ as a non-complexing background electrolyte, so as to probe the fundamental interactions between Pu and OMCs without interference from solution anions. However, Eu sorption curves for C-CS and C-CS-COOH were measured with 0.1 M NaCl solutions, because the stock ^{152}Eu solution was received in 0.1 M HCl and a matrix change would have compromised the known specific activity. For comparison of Pu sorption to Eu sorption experiments, the Pu pH-dependent sorption curves for C-CS and C-CS-COOH were measured again in 0.1 M NaCl solutions. The results displayed in Figure 6.37 show that the plutonium sorption trends of the C-CS type OMCs are the same from 0.1 M NaCl and $NaClO_4$ solutions. The only difference is that there is slightly higher Pu sorption to pristine C-CS from pH 2 perchlorate solutions than from pH 2 chloride solutions.

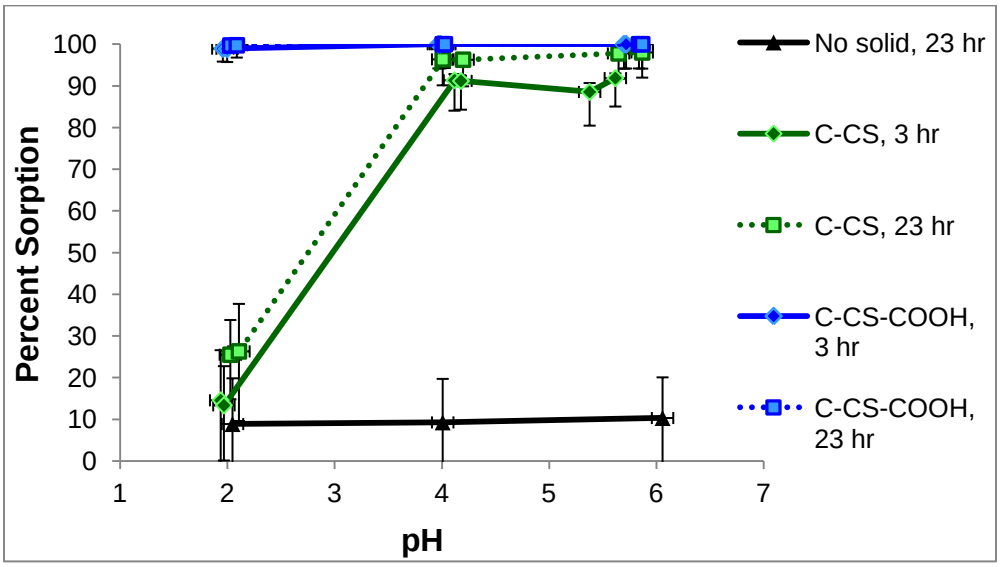

Figure 6.37. Percent Pu sorption vs. pH after 3 hours and 23 hours for samples of 0.1 M NaCl and 10 ± 1 µM Pu(VI) at different pH values and C-CS OMC powders. Lines are added only to guide the eye.

Uptake of Eu by the C-CS carbons was measured from 0.1 M NaCl, 10 ± 1 µM Eu solutions with pH values 2, 4 and 6. Solutions with higher pH values were not investigated to avoid insoluble Eu hydrolysis products in solution. Figure 6.38 shows percent Eu sorption vs. pH for C-CS and control (no solid) samples. At all of the pH values, less than 20% loss of Eu to the vial was observed. For both materials, no significant difference in Eu sorption was observed after 23 hours contact compared to 3 hours contact. In pH 4 solution, 70 ± 7 % Eu sorption to C-CS was observed (Figure 6.38), compared to 96 ± 6 % Pu (Figure 6.37). This suggests that the untreated C-CS surface has more affinity for Pu than for Eu.

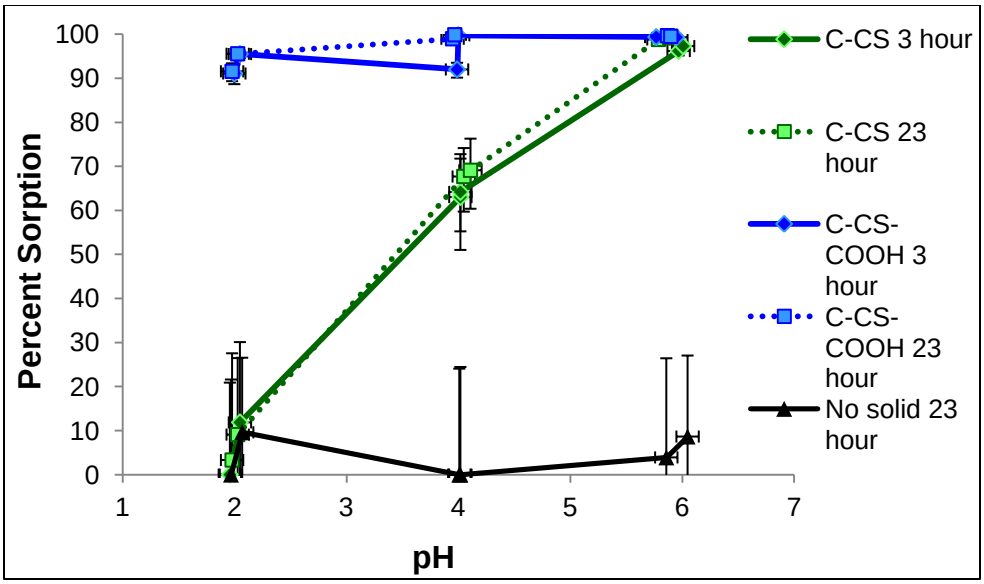

Figure 6.38. Percent Eu sorption vs. pH after 3 hours and 23 hours for samples of 0.1 M NaCl and 10 ± 1 µM Eu(III) at different pH values and C-CS OMC powders. Lines are added only to guide the eye.

The reversibility of sorption upon incremental addition of HCl to Pu and Eu C-CS and C-CS-COOH samples on 0.1 M NaCl is demonstrated in Figure 6.39a and b. The Pu desorption trends in HCl (Figure 6.39a) are similar to what was observed with $HClO_4$ (Figure 6.36), with slightly less Pu being retained by the C-CS and C-CS-COOH in 0.1 M HCl than in 0.1 M $HClO_4$. As with Pu sorption, Eu sorption to C-CS is reversible in 0.1 M HCl (Figure 6.39b). Approximately 30% of the total Eu was retained by C-CS-COOH in 0.1 M HCl, but was removed by increasing the acidity to 0.5 M. Figure 6.39a shows that 60-70% of the total Pu was retained by C-CS-COOH in 0.1 M HCl, indicating that the Pu is more strongly bound to the oxidized surface than Eu.

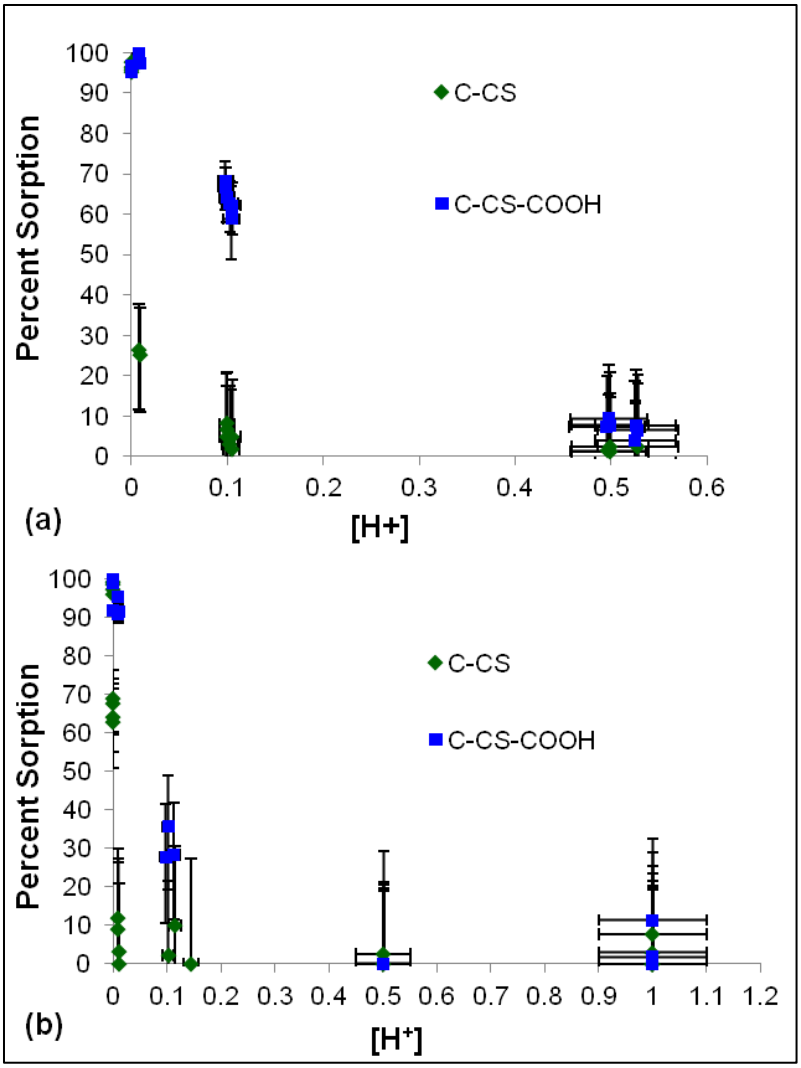

Figure 6.39. Percent sorption (total percentage of Pu or Eu remaining in the solid phase) vs. total acid concentration as HCl was incrementally added to samples of C-CS OMC powders with 10 ± 1 µM Pu (a) and Eu (b) in 0.1 M NaCl of various pH between 2 and 6. The contact time at each acidity was 24 ± 1 hours.

6.3.2 Pu and Eu sorption kinetics

The pH-dependency batch experiments demonstrated that Pu and Eu sorption to high-surface area OMCs was generally achieved within 3 hours. The sorption kinetics for the CMK and C-CS materials were more closely examined in batch experiments with pH 4 solutions at several different concentrations of Pu and Eu. An important aspect to these experiments is to adjust the sample pH as quickly as possible after adding the target species, without allowing the pH to exceed pH 4. The samples must approach pH 4 from the acidic side, and often the first one or two data points from samples are taken when the solution pH is still between 1.5 and 3.5. If too much base is added, and the solution pH is elevated beyond pH 5, even for 10 seconds, the kinetic data will not be reliable. Figure 6.40 illustrates this point by showing kinetic data from 11 ± 1 Pu samples of CMK that were adjusted to pH 4 from the acidic side overlaid with data from samples that were accidentally brought to pH ~8 or greater for 10-30 seconds before being adjusted back to pH 4 (called bad equil.).

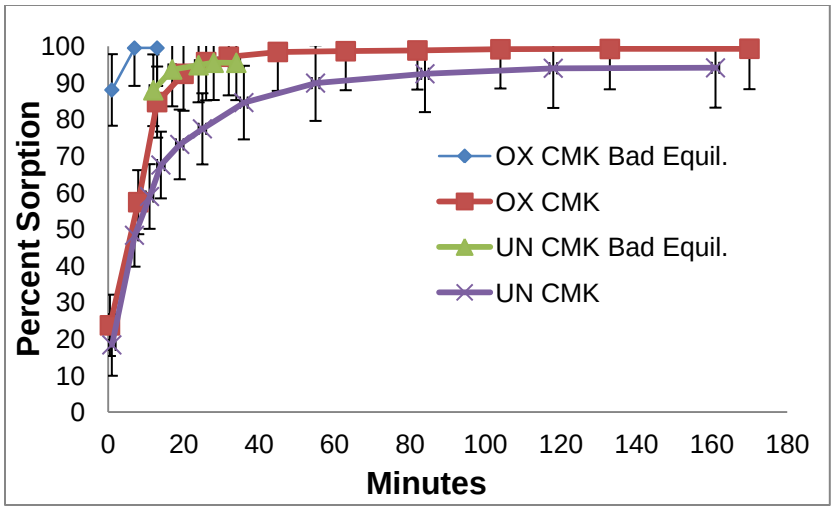

Figure 6.40. Percent sorption vs. contact time for batch experiments with Pu(VI) on CMK carbons with pH 4 0.1 M $NaClO_4$ 11 ± 1 µM Pu solution. The effect of momentary basic conditions during equilibration is illustrated by the "bad equilibration" samples.

Batch sorption kinetic experiments were done with CMK and C-CS materials in pH 4 0.1 M $NaClO_4$ 10-11 ± 1 µM Pu(VI) solution, and C-CS materials with 10 ± 1 µM Eu in 0.1 M NaCl. Figure 6.41 shows percent sorption to CMK vs. minutes elapsed. The data shows that not only is equilibrium uptake greater for oxidized CMK at pH 4, but the time to reach equilibrium is approximately 45 minutes, in contrast to approximately 90 minutes required for the untreated CMK. There seems to be a slower intermediate step in the uptake to untreated CMK. Figure 6.42 shows similar data for the C-CS materials. In this case, quantitative Pu sorption to C-CS-COOH occurred immediately upon adjustment of the solution to pH 4 (the first two data points in each set were taken while the solution pH was still about 1.5-2.8). The pristine C-CS carbon takes at least 180 minutes to reach maximum sorption, even longer than the untreated CMK. The trends observed in these four OMCs show that the sorption rate increases with the concentration of oxygen-containing functional groups in the sample, and the sorption mechanism in 10 µM Pu samples appears to be controlled by surface chemistry. Figure 6.43 shows that quantitative sorption of Eu to C-CS-COOH was also achieved immediately upon pH adjustment, and that a steady-state condition in samples of C-CS and Eu was reached within approximately 100 minutes. There were no significant changes in Eu solution concentration in these samples measured after 23 hours contact.

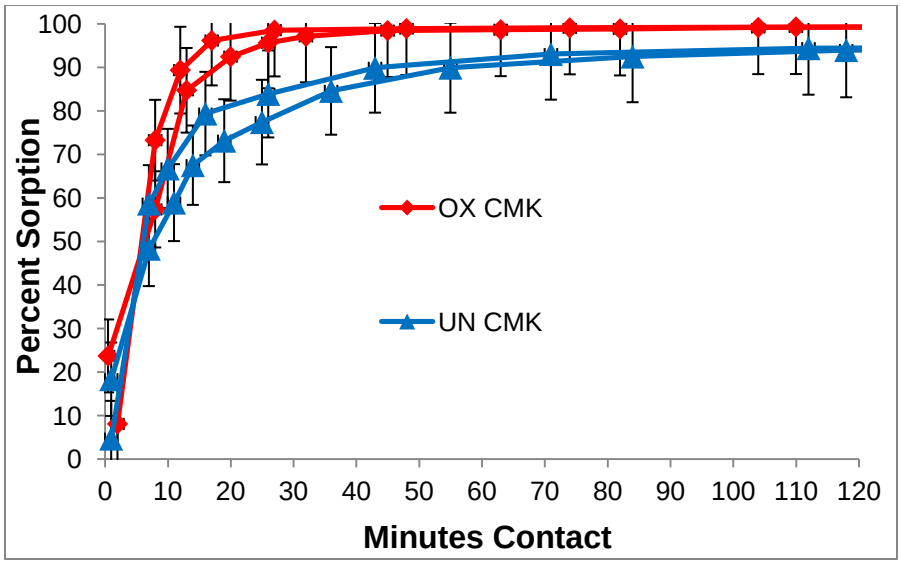

Figure 6.41. Percent sorption vs. minutes contact for batch CMK samples with approximately 900 mL/g of pH 4 0.1 M $NaClO_4$ 11 ± 1 µM Pu(VI) solution. Lines are added only to guide the eye along data collected from the same sample.

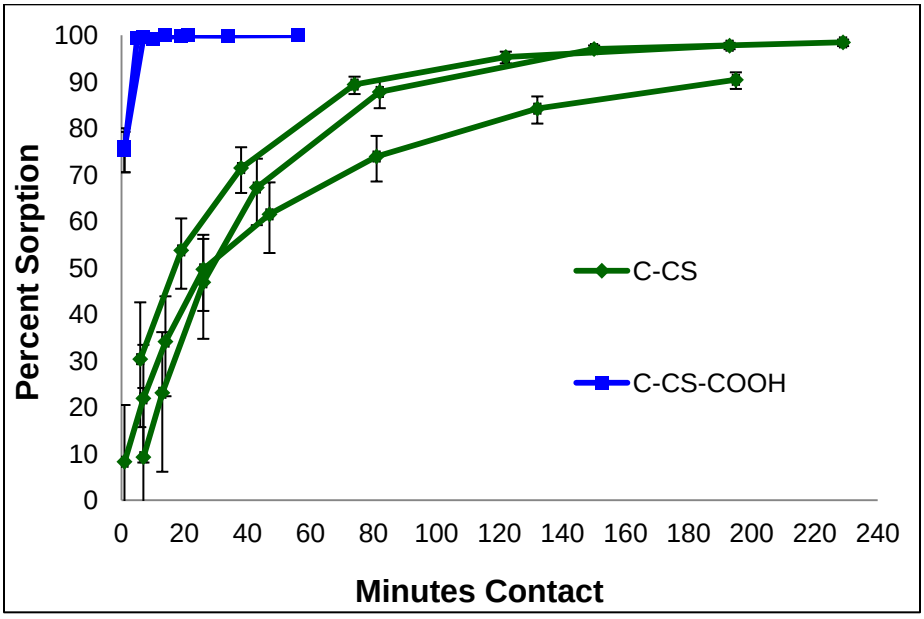

Figure 6.42. Percent sorption vs. minutes contact for batch C-CS samples with approximately 1000 mL/g of pH 4 0.1 M $NaClO_4$ 10 ± 1 µM Pu(VI) solution. Lines are added only to guide the eye along data collected from the same sample.

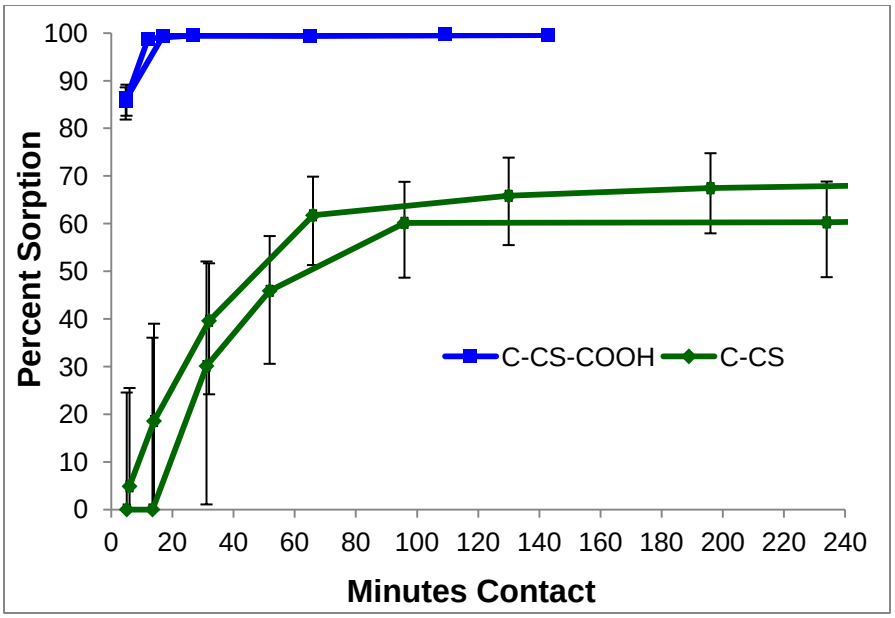

Figure 6.43. Percent sorption vs. minutes contact for batch C-CS samples with approximately 1000 mL/g of pH 4 0.1 M NaCl 10 ± 1 µM Eu(III) solution. Lines are added to guide the eye along data from the same sample.

It is common in the literature[27, 45, 236, 267] to fit batch kinetic data to pseudo-first-order, pseudo-second-order, and intra-particle diffusion model equations, and to extract rate constants from the models. Kinetic data sets from 10-11 µM Pu or Eu samples with UN CMK, OX CMK, C-CS, and C-CS-COOH fit very well to the pseudo-second-order rate model. The model is described in its linear form by Equation 6.8, where q_e is mg/g sorbed at equilibrium, q_t is mg/g sorbed at time t, k_2 is the second-order rate constant, and the term $k_2 q_e^2$ from describes the initial sorption rate as t approaches 0.

$$\frac{t}{q_t} = \frac{1}{k_2 q_e^2} + \frac{t}{q_e} \qquad (6.8)$$

The satisfactory fit to this model suggests that the sorption mechanism is second order with respect to the carbon, and allows quantitative comparison between samples with the same experimental conditions. It has also been suggested that sorption processes that follow pseudo-second-order kinetics involve both physical and chemical adsorption.[41] Attempted fits of kinetic data to pseudo-first-order and intra-particle diffusion models gave poor R^2 values, showing that the sorption kinetics are not only diffusion controlled, but depend heavily on the concentration of binding sites in the samples. This assessment agrees with the fact that the Pu sorption rate decreases with concentration of functional groups in the order C-CS-COOH > OX CMK > UN CMK > C-CS. Many of the studies found in the literature also found that Eu[231] or U[35, 41, 45, 200] sorption to carbonaceous materials fit best to the pseudo-second-order kinetic model. However, Perevalov and Molochnikova reported that the sorption of Pu to oxidized MWCNTs follows pseudo-first-order kinetics.[236] Example fits of Pu and Eu batch kinetic data to the pseudo-second-order model are shown for C-CS samples in Figure 6.44, and Table 6.4 summarizes the derived constants for the data presented in Figures 6.41-6.43.

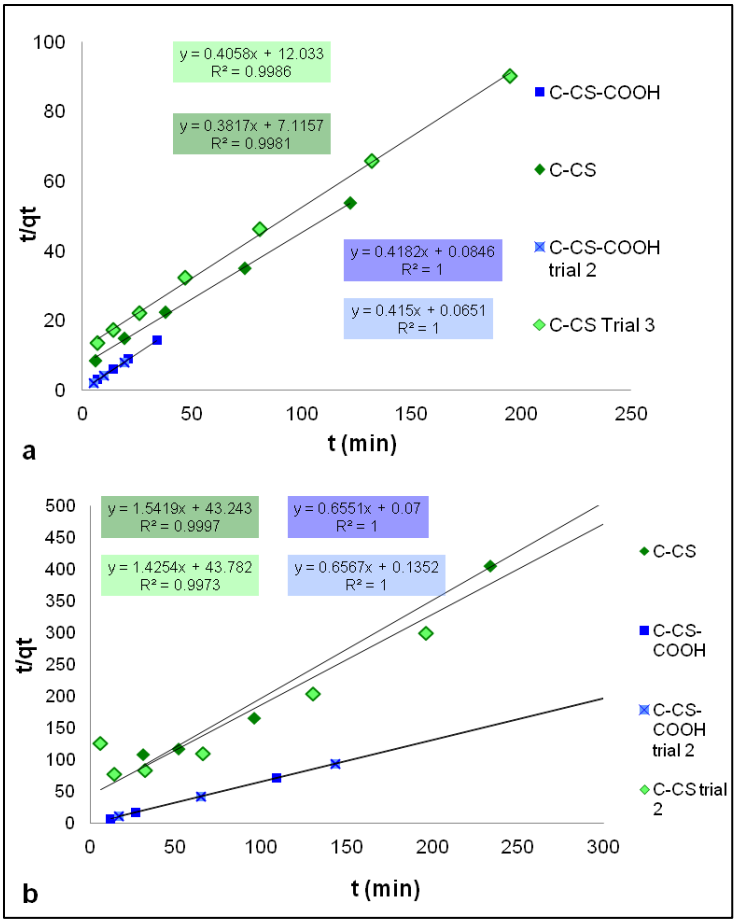

Figure 6.44. Pseudo-second-order kinetic model plots of data from batch C-CS samples with approximately 1000 mL/g of pH 4 0.1 M $NaClO_4$ 10 ± 1 µM Pu solution (a) and pH 4 0.1 M NaCl 10 ± 1 µM Eu solution (b).

Table 6.4. Pseudo-second-order kinetic constants for batch carbon samples with approximately 900-1000 mL/g of pH 4 0.1 M $NaClO_4$ 10-11±1 µM Pu(VI) solution.

Sample	$k_2 q_e^2$ (mg $g^{-1}min^{-1}$)	k_2 (g $mg^{-1}min^{-1}$)	q_e (mg/g)	R^2
UN CMK 11 µM Pu	0.46 ± 0.08	0.07 ± 0.01	2.58 ± 0.03	0.9998
OX CMK 11 µM Pu	1.1 ± 0.2	0.15 ± 0.01	2.7 ± 0.1	0.9994
C-CS 10 µM Pu	0.11 ±0.04	0.017 ± 0.004	2.5±0.1	.9981
C-CS-COOH 10 µM Pu	13.6±2.5	2.4 ± 0.4	2.40±0.01	1
C-CS 10 µM Eu	0.0230 ± 0.0002	0.051 ± 0.006	0.68± 0.04	0.9973
C-CS-COOH 10 µM Eu	10.8 ± 4.9	4.7 ± 2.0	1.526 ± 0.001	1

Sensing or preconcentration applications would require relatively fast interaction with target species at very low concentration, so the Pu(VI) sorption kinetics in pH 4, 1.3 x 10^{-8} M Pu, 0.1 M $NaClO_4$ solutions were tested with 1000 ± 100 mL per g carbon. The results are plotted in Figure 6.45 for the CMK materials. Both CMK materials sorbed 100% of the Pu, but again the oxidized CMK proved kinetically advantageous, with complete Pu uptake occurring within 20 minutes. To further test the preconcentration capability, samples were prepared with solution-to-solid ratios of 5000 ± 200 mL per g. Figure 6.46 shows that at such low solid carbon concentrations, the sorption time increased dramatically, especially for the untreated CMK. The results are remarkably not reproducible with low Pu concentration, so these experiments were not continued with the other OMCs. However, given the results of C-CS-COOH kinetic tests with 10 µM Pu, it is assumed that quantitative sorption of smaller amounts of Pu would also occur immediately.

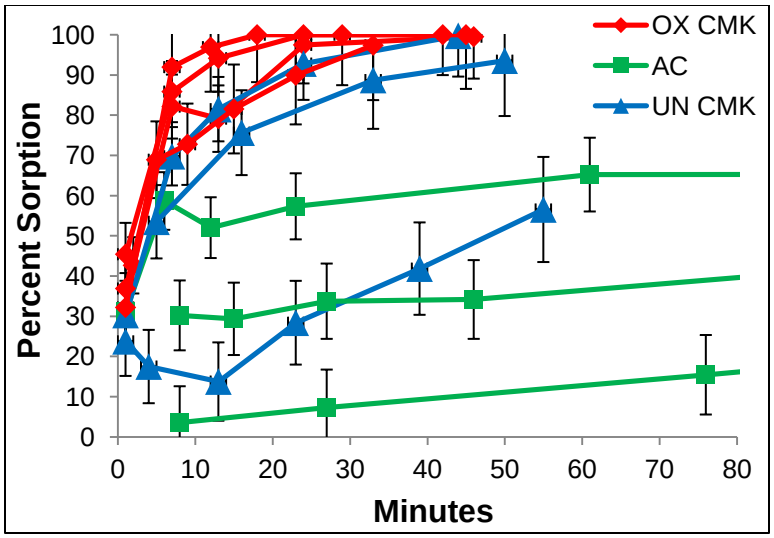

Figure 6.45. Percent sorption vs. minutes contact for carbon powders with 0.01 µM Pu, pH 4, 0.1 M $NaClO_4$ solution, approximately 1000 mL/g. Lines are added to guide the eye along data collected from the same sample.

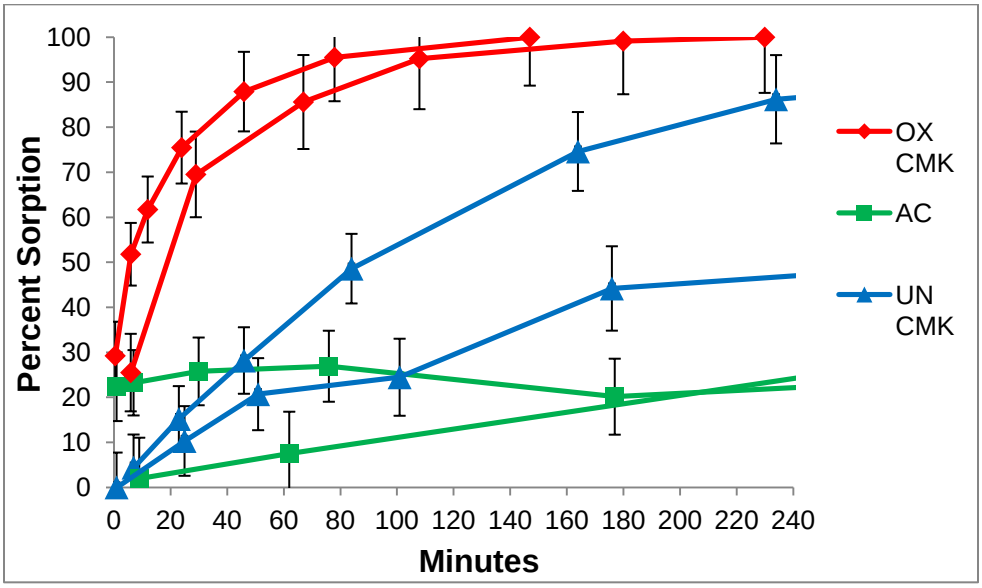

Figure 6.46. Percent sorption vs. minutes contact for carbon powders with 0.01 µM Pu, pH 4, 0.1 M $NaClO_4$ solution, approximately 5000 mL/g. Lines are added to guide the eye along data collected from the same sample.

The Pu sorption kinetics for the carbon materials were measured in batch experiments with approximately 900-1000 mL/g of pH 4, 0.1 M $NaClO_4$, 250 ± 17 µM Pu(VI) solutions, to see if equilibrium can be established with high concentrations of Pu. It is important to have control samples to test the stability and solubility of Pu at this relatively high concentration. These are discussed in Section 3.4.4, and showed the Pu to be soluble for at least 4 days. Figure 6.47 plots percent sorption vs. hours elapsed since plutonium was added to CMK and AC samples. Although 95-97 percent sorption was achieved by the CMK materials within 1 day, the samples did not reach equilibrium, but rather the solution concentrations kept gradually decreasing over the following weeks, as shown in Figure 6.48. It was concluded that equilibrium

cannot be established in samples of Pu with porous carbons in any reasonable length of time. This is not surprising, considering the known oxidation state instability of Pu that is discussed in Section 3.4.4. The CMK data from the 250 μM samples also fit best to the pseudo-second order kinetic model. The AC data fit best to the intra-particle diffusion model, shown in Figure 6.49, although the fit is not satisfactory enough to conclude that diffusion is the only controlling process. The intraparticle diffusion model is described by equation 6.9, and predicts that if adsorption is controlled by intraparticle diffusion, then a plot of q_t vs. $t^{0.5}$ will be linear and pass through the origin.

$$q_t = k_{id} t^{0.5} \tag{6.9}$$

The intraparticle diffusion model plots shown in Figure 6.49 could be divided into two or three straight lines, correlating to the number of different processes controlling the sorption kinetics.[27] The first linear portion is generally considered to represent intraparticle diffusion, and the initial slope taken as the intraparticle diffusion rate constant k_{id}. The low initial slope in the AC data in Figure 6.49 supports the idea that Pu sorption to AC is hindered by slow diffusion due to the large particles and small pores (high percentage of micropore surface area and pore volume).

The oxidized CMK is no longer a more efficient Pu scavenger than the untreated CMK at high Pu concentrations. This could be partially explained by the greater specific surface area and slightly larger pore size and pore volume of the UN CMK. It also suggests that the bulk of the Pu uptake is not due to complexation by carboxyl groups, but a different process dictates sorption in conditions of high Pu loading. In light of the XAS data, which shows that the Pu associated with the carbon is tetravalent, surface precipitation is likely significant in the observed Pu uptake. However, bulk precipitation was not observed in the activated carbon or the control samples. The results presented in Figure 6.47 were unexpected and created uncertainty about the importance of OMC surface oxidation for the Pu sorption reaction. However, the results are difficult to interpret as both UN CMK and OX CMK show significant surface groups in their FTIR spectra, but quantitative data about their surface groups were not available. This ambiguity could later be resolved by studying the Pu sorption reaction to C-CS and C-CS-COOH by batch, XAS, and TEM methods.

It is interesting to compare the Pu sorption kinetics of the two different batches of OX CMK (OX CMK' and OX CMK) because the first batch had a significantly lower BET surface area and pore volume, but seemed to be more ordered with a narrower pore size distribution (see Figures 6.12, 6.14 and Table 6.2). The micropore surface area and pore volume were similar in the two samples, as well as the surface chemistry. It is generally believed that the extent of order or disorder in the mesostructure is not important for sorption applications, only the surface area, pore volume, and surface chemistry are important. Comparison of the batch kinetic data of OX CMK' and OX CMK in samples with pH 4, 0.1 M $NaClO_4$, 11 ± 1 μM Pu(VI) solution showed no difference, which was expected because the two samples should have the same surface chemistry. However, in samples with relatively large amounts of Pu (900-1000 mL/g of pH 4, 0.1 M $NaClO_4$, 250 ± 17 μM Pu), the sorption kinetics of OX CMK' are significantly improved over the OX CMK samples, despite the larger BET surface area and pore volume in the OX CMK sample (Figure 6.50). The most likely explanation of this is that the wide pore size distribution in the OX CMK sample favors smaller mesopores, which slows the diffusion of

solution species into the pores. This effect would be particularly important if the samples contained intrinsic Pu colloids (as later shown for C-CS, see Section 6.42) because any surface area within pores that are smaller than the colloidal Pu particle size would be inaccessible for Pu adsorption.

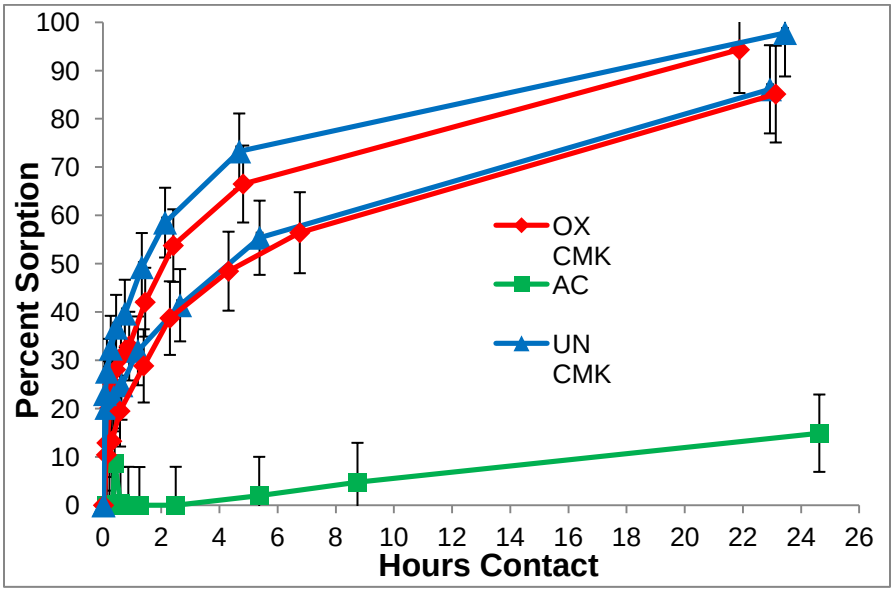

Figure 6.47. Percent sorption vs. hours contact for carbon powders with 250 µM Pu, pH 4, ~0.2 M perchlorate solution, approximately 900-1000 mL/g. Lines are added to guide the eye along data from the same sample.

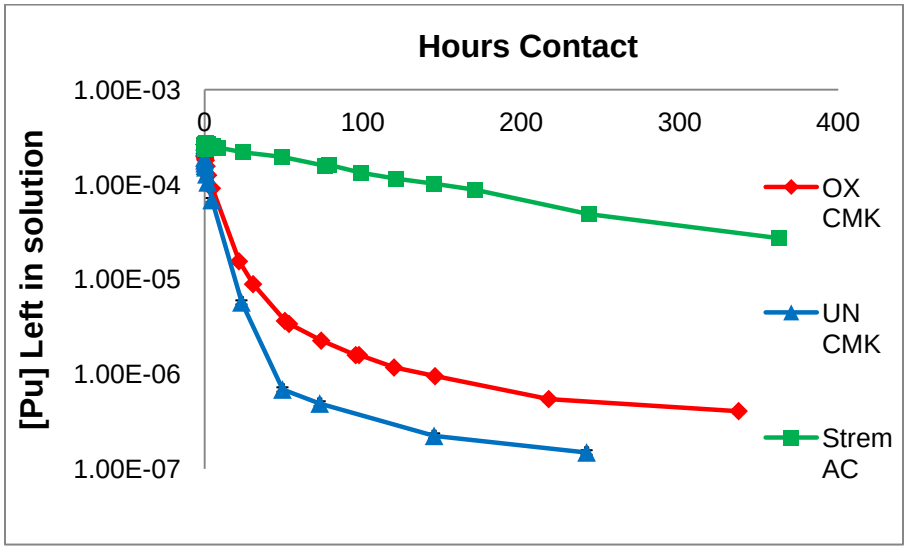

Figure 6.48. Molarity Pu left in solution (Log scale) vs. hours contact for carbon powders with initially 250 µM Pu, pH 4, ~0.2 M perchlorate solution, approximately 900-1000 mL/g. Lines are added only to guide the eye. The samples demonstrate that Pu and porous carbons do not reach equilibrium within 300 hours (over 12 days).

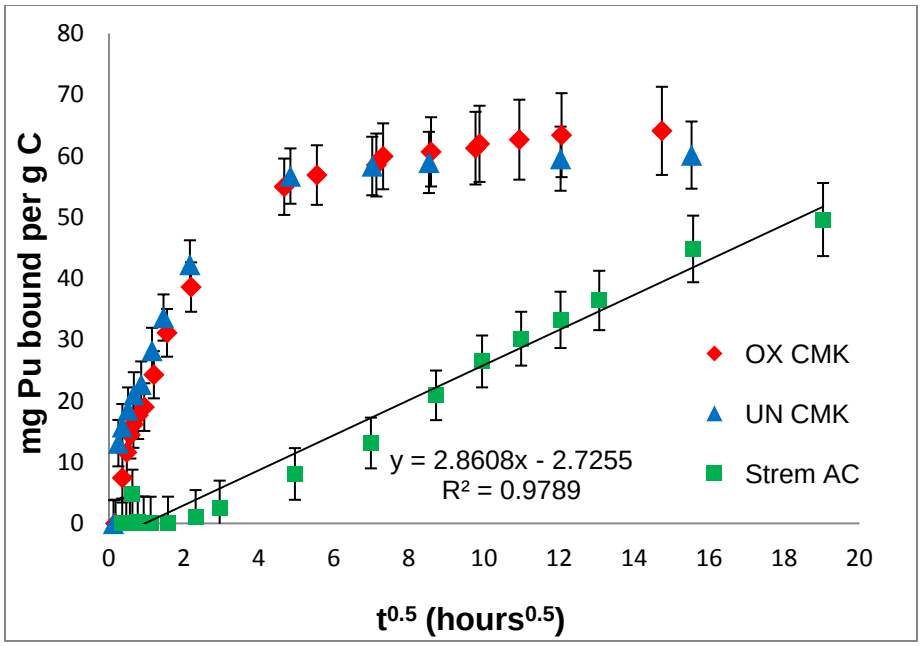

Figure 6.49. Intraparticle diffusion kinetic model plot of batch sorption data from samples of carbon powders with 250 µM Pu, pH 4, ~0.2 M perchlorate solution, approximately 900-1000 mL/g.

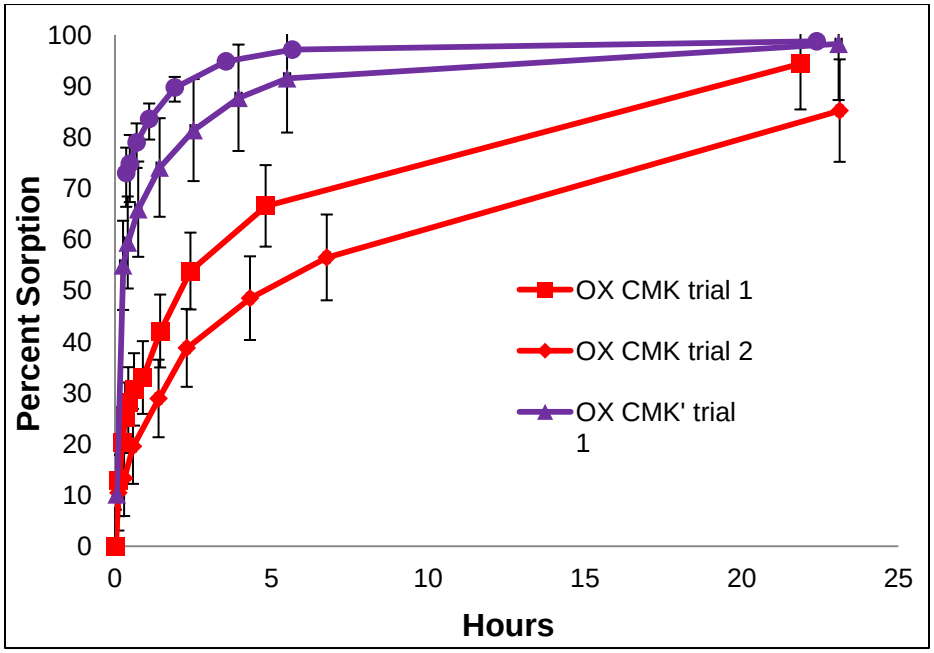

Figure 6.50. Percent sorption vs. hours contact for OX CMK' (first batch) and OX CMK with 250 µM Pu, pH 4, ~0.2 M perchlorate solution, approximately 900-1000 mL/g. Lines are added to guide the eye along data from the same sample. OX CMK' displays much better Pu sorption kinetics than OX CMK, even though OX CMK' has lower surface area.

The results of high Pu loading kinetic experiments with UN CMK and OX CMK (Figure 6.47) suggested that the carboxyl and other surface groups in both samples were saturated, and further sorption occurred by a different mechanism. Because the concentration of carboxyl

groups in the C-CS-COOH is far greater than in those CMK materials, samples of C-CS and C-CS-COOH with high Pu concentrations were expected to yield very different results. Figure 6.51 shows that untreated C-CS samples took over 23 hours to reach maximum sorption, like the CMK samples. However, complete Pu sorption to C-CS-COOH occurs within 30-40 minutes under these conditions. Approximately 0.25 mmol Pu per g carbon was loaded in these samples, so the surface carboxyl and phenol groups in the C-CS are saturated, and in the C-CS-COOH there is still an excess of surface groups. These results show further evidence that sorption occurs preferably via complexation by deprotonated carboxyl groups, and when no surface groups are available an alternate binding mechanism is employed for increased Pu uptake. The batch kinetic results from C-CS and C-CS-COOH samples of 250 ± 15 µM Eu in pH 4 0.1 M NaCl are plotted in Figure 6.52. As with Pu, quantitative Eu uptake to C-CS-COOH occurred within 1 hour, and the data fit very well to the pseudo-second-order kinetic model. No significant Eu uptake from 250 µM Eu samples was observed to C-CS, indicating that the secondary binding mechanism employed for high Pu uptake does not work for Eu. There were no further changes in Eu concentration in these samples over the course of 3 days. Hence, C-CS-COOH is a fast and effective scavenger of both actinide and lanthanide cations, while the high sorption on C-CS is unique to Pu.

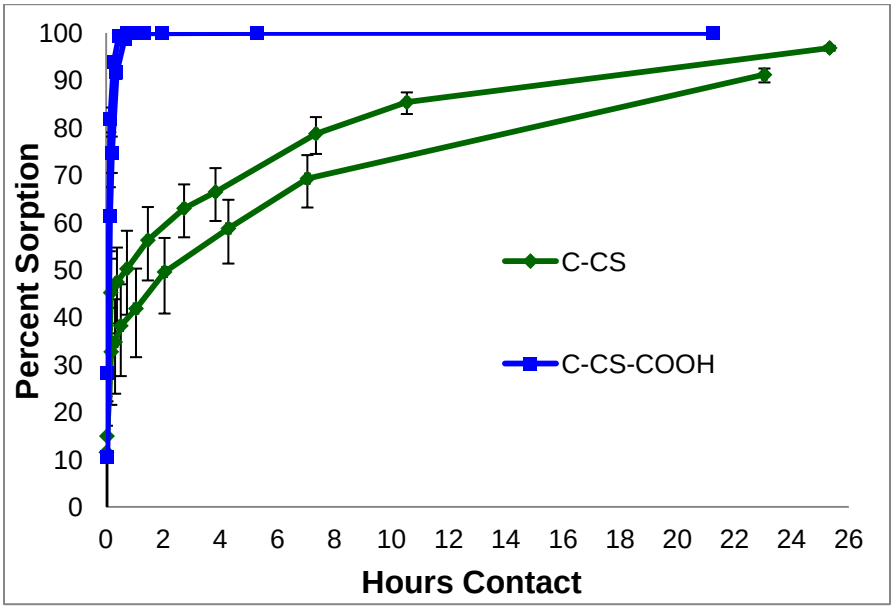

Figure 6.51. Percent sorption vs. hours contact for carbon powders with 250 µM Pu, pH 4, ~0.15 M perchlorate solution, approximately 1000 mL/g. Lines are added to guide the eye along data from the same sample.

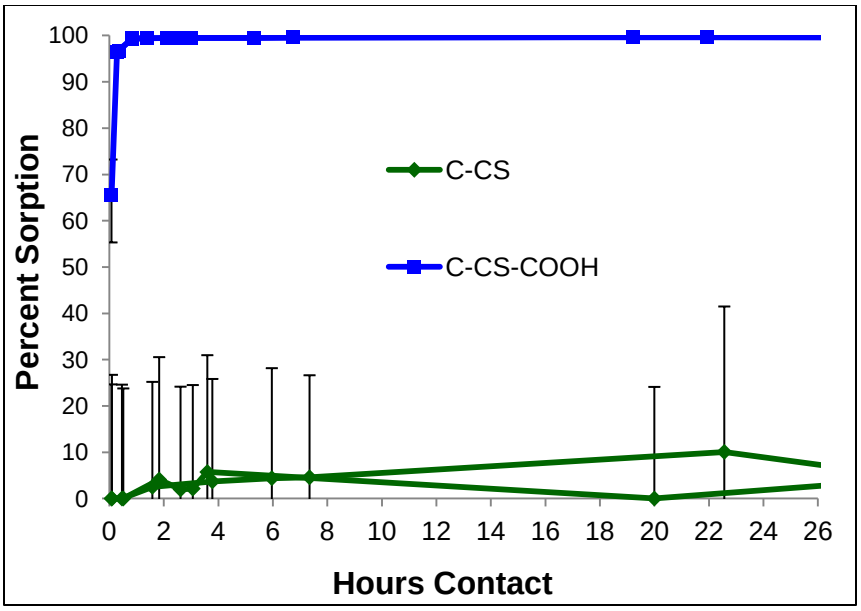

Figure 6.52. Percent sorption vs. minutes contact for batch C-CS samples with approximately 1000 mL/g of pH 4 0.1 M NaCl 250±15 µM Eu(III) solution. Lines are added to guide the eye along data from the same sample.

The detection of Si, Al, and Fe in TEM samples of Pu with C-CS-COOH (see Section 6.4.2) induced concern about trace contaminants in the samples. The bulk samples were checked by elemental analysis, and only trace silica was detected in the C-CS and C-CS-COOH samples. It is the author's belief that the trace Fe and Al in the TEM samples may have been introduced to the grids during transfer of the sample onto the grids, perhaps in a workspace that was contaminated with those elements. Only the bulk C-CS OMC powder was put through dialysis before the experiments with Pu and Eu were done, but the FDU-16, FDU-16-COOH and C-CS-COOH underwent dialysis after experiments were already done, due to concern about possible contaminants. Therefore, the batch kinetic experiment with 1000 mL/g of pH 4, 0.1 M $NaClO_4$, 250 ± 17 µM Pu(VI) solution was repeated with the dialyzed C-CS-COOH. The results shown in Figure 6.53 show that there is no significant difference in the Pu sorption behavior to C-CS-COOH before and after the powder was dialyzed. Therefore it seems unlikely that the trace Si interfered with the Pu sorption interaction.

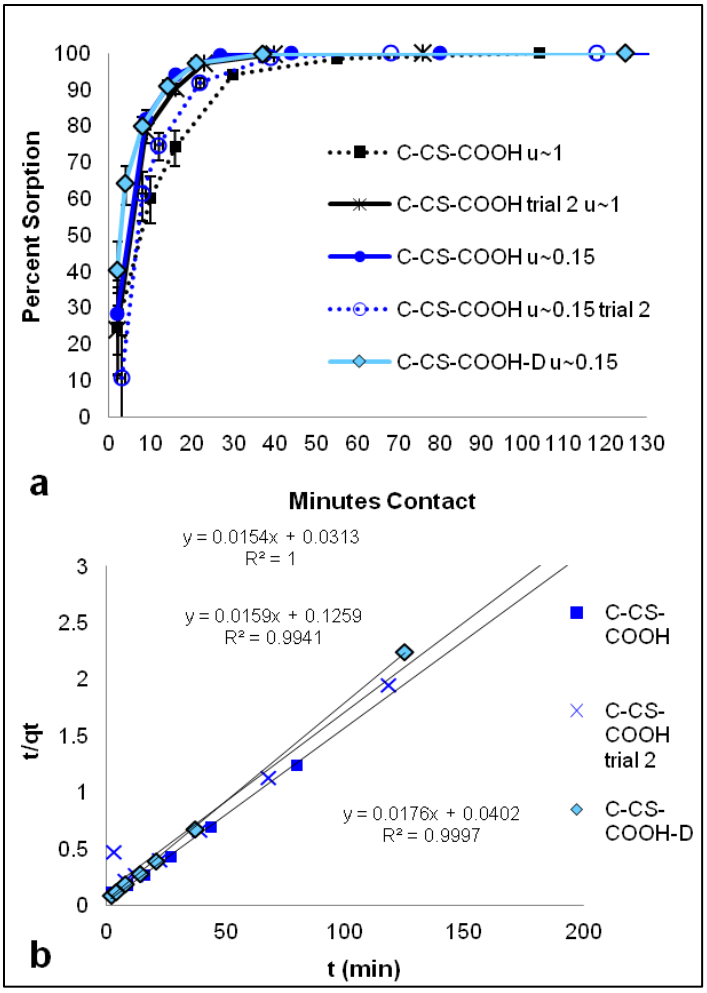

Figure 6.53. Percent Pu Sorption vs. minutes contact (a) and pseudo-second-order kinetic model plot (b) for batch C-CS-COOH samples with 250 ± 15 µM Pu(VI), 0.1 M or 1 M $NaClO_4$, pH 4.0 ± 0.1 (except first and second data points, which were always lower pH). Lines in (a) are only to guide the eye along data collected from the same sample. C-CS-COOH-D is the material after dialysis, and shows similar sorption behavior to the samples before dialysis.

6.3.3 Pu and Eu uptake capacities

It is common in the literature to estimate the batch sorption capacity for adsorbents by measuring a sorption isotherm, which is a set of data describing the equilibrium distribution of the target species between the solid and liquid phases in samples covering a range of total target species concentration.[27, 35, 41, 45, 200, 231, 236] Fitting the isotherm data to common sorption models can give an idea of how well the system follows the assumptions made by the models. The kinetic studies showed that the carbon-Eu samples could reach equilibrium, so Eu sorption isotherms were measured in 0.1 M NaCl solutions adjusted to pH 4, to estimate the Eu uptake capacities of C-CS and C-CS-COOH. Duplicate samples were prepared with 1 g/L C-CS or C-CS-COOH and solutions with total Eu concentrations 10 µM, 50 µM, 100 µM, 250 µM, 500 µM, and 1 mM, and the solution concentration of Eu was measured after 2 days contact. The isotherm data are plotted in Figure 6.54 as µmol Eu bound per g carbon vs. µM Eu per mL left in solution at equilibrium. Visually one can see that the Eu sorption capacity of C-CS-COOH is

very high, and the Eu capacity of C-CS is limited to under 100 µmol/g. The isotherm data were fit to two common sorption models, the Langmuir and Freundlich isotherm models (Figure 6.55). The Langmuir model is given by Equation 6.10, and assumes homogenous sorption of the target species in a monolayer fashion at specific binding sites in the sorbent.[231]

$$\frac{C_e}{q_e} = \frac{1}{bq_m} + \frac{C_e}{q_m} \tag{6.10}$$

In Equation 6.10, C_e is the equilibrium concentration of Eu in solution (µmol/mL), q_e is the corresponding amount of Eu bound to the solid (µmol/g), q_m is the monolayer sorption capacity (µmol/g), and b (mL/µmol) is the Langmuir adsorption constant related to the energy of adsorption. The Freundlich isotherm model is given by Equation 6.11, and assumes a heterogeneous surface with a non-uniform distribution of heat-of-adsorption over the surface.[231]

$$lnq_e = lnK_F + \frac{1}{n} lnC_e \tag{6.11}$$

In Equation 6.11, C_e and q_e have the same significance as in Equation 6.10, and K_F and n are Freundlich constants related to the uptake capacity and energy of adsorption, respectively. In this model, values of n between 1 and 10 indicate a favorable sorption process. The parameters derived from fitting the Eu isotherm data to these models are given in Table 6.5. The C-CS-COOH Eu sorption isotherm data fit very well to the Langmuir model, indicating that the sorption process is homogenous. The most likely binding site is deprotonated carboxyl groups. The monolayer sorption capacity derived is 0.91 mmol/g (138 mg/g), which is far greater than previously reported Eu capacities for activated carbons[231], and comparable to Eu uptake capacities reported for graphene oxide [252, 253]. The data from the C-CS isotherm did not fit well to either of these models, as the C-CS has low affinity for Eu. The irreproducibility of Eu uptake by C-CS in 1 mM Eu samples likely occurred due to fluctuations in the amount of precipitated Eu without a favorable sorbent. Removing these data point improved the fits only somewhat. Based on the results with C-CS and Eu, pristine OMCs are expected to have a very low sorption capacity for soluble metal cations. The plutonium uptake capacities cannot be measured with sorption isotherms, because the samples do not reach equilibrium (see Section 6.3.2). Both C-CS and C-CS-COOH removed 60 ± 3 mg Pu from pH 4 solutions (Figure 6.51), and the true uptake capacities are likely much greater. Wang et al. studied uranyl sorption to untreated and oxidized CMK-3-type OMCs, and found Langmuir sorption capacities from pH 6 solutions of 178.6 mg/g and 250.0 mg/g, respectively.[35] The relatively high capacity of the untreated CMK for uranium, compared to our results with Eu, could suggest interactions of the axial oxygens in the actinyl moiety with carbon surfaces. For true comparison, however, the uptake of U and other actinides should be studied on the same OMCs under the same conditions, as the surface chemistry of OMCs can vary depending on the synthetic method, and certainly with solution pH.

Table 6.5. Parameters derived from fitting C-CS and C-CS-COOH Eu sorption isotherm data to Langmuir and Freundlich sorption models.

Sample	Langmuir q_m (µmol/g)	Langmuir b (mL/µmol)	Langmuir R^2	Freundlich K_F (mL/µmol)	Freundlich n	Freundlich R^2
C-CS-COOH	909.09	550	0.9993	5686	1.946	0.9151
C-CS	96.15	2.889	0.298	66.55	2.29	0.7903
C-CS omitting 1 mM samples	28.74	49.707	0.931	41.5	3.117	0.9071

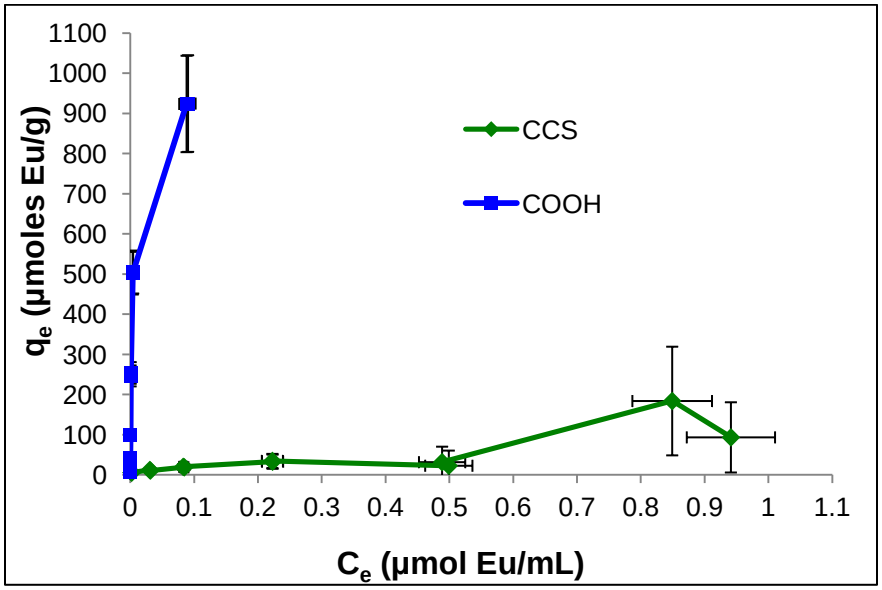

Figure 6.54. Eu(III) sorption isotherms for C-CS samples with pH 4, 0.1 M NaCl solutions of Eu concentrations ranging from 10 µM to 1 mM. Lines are added to guide the eye.

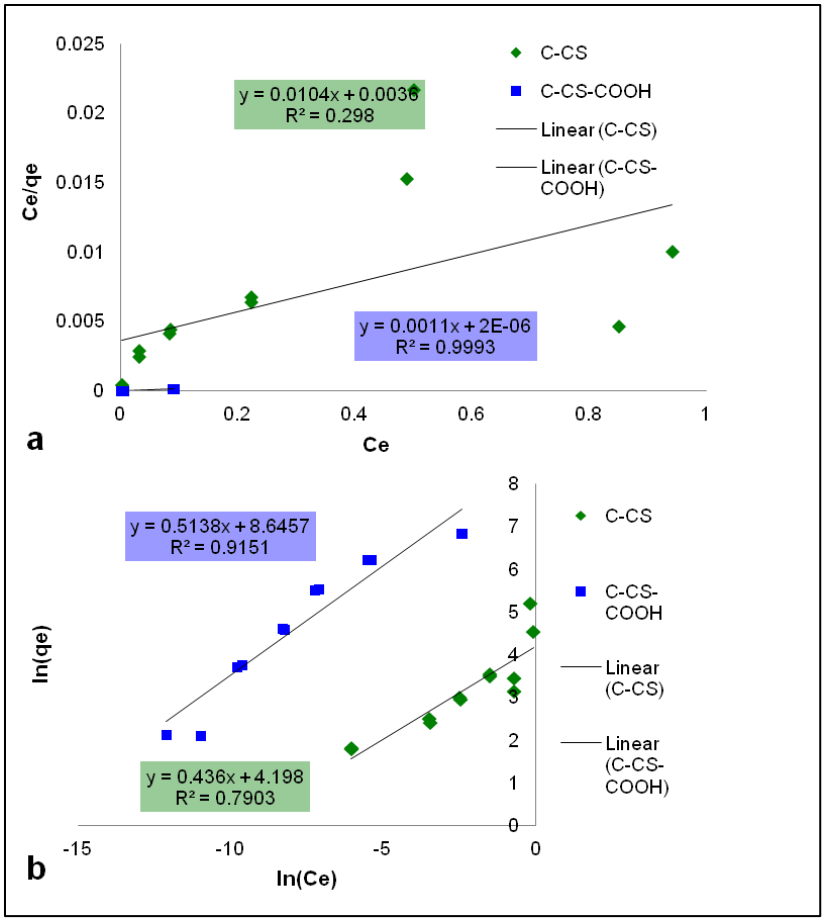

Figure 6.55. Langmuir (a) and Freundlich (b) sorption isotherm model plots of data from C-CS samples with approximately 1000 mL/g of pH 4 0.1 M NaCl solutions with Eu concentrations ranging from 10 µM to 1 mM.

Batch experiments with the CMK carbons and initial Pu concentrations ranging from 10 to 270 µM were prepared in pH 4 perchlorate solution, and sorption was measured after 23 hours. Results of these measurements are plotted in Figure 6.56, as mg Pu bound per g carbon vs. initial Pu concentration in µM. The 23-hour capacity of activated carbon is clearly limited to approximately 12 mg/g, while the linear trends observed for the CMK materials indicate that the true capacity has not been reached, but sorption up to 58 ± 5 mg Pu per g has been observed. The actual Pu uptake capacity of the OMCs cannot be measured, as the solubility of Pu is questionable at higher concentrations, and large liquid-to-solid ratios tend to give results that are not reproducible (see Figure 5.39 in Section 5.43). The observed Pu uptake by OMCs far exceeds that to activated carbon, and the Pu uptake capacities of oxidized MWCNTs reported by Perevalov and Molochnikova.[236] The XAS data (see Section 6.4) suggest that all of the Pu in these samples has been reduced to Pu(IV), so much of the Pu uptake observed in pH 4 samples is likely due to surface precipitation of hydrolyzed Pu, and the uptake capacity may be limited by the capacity for redox reactions at the surface. It should be emphasized that only about 5% of the Pu in the control samples was lost to precipitation or sorption to filters and vials. Although the sorption mechanism is undetermined, the data show clearly that mesoporous carbons are much more effective than activated carbon at removing Pu from solution. The redox chemistry at the

carbon surface would be expected for the activated carbon as well, because all three powders consist of amorphous carbon, and activated carbons have demonstrated spontaneous reduction of other metal ions.[268-270] The large difference in sorption rate and capacity observed between the OMCs and activated carbon powders could be due to increased availability of the carbon surface in the OMC materials.

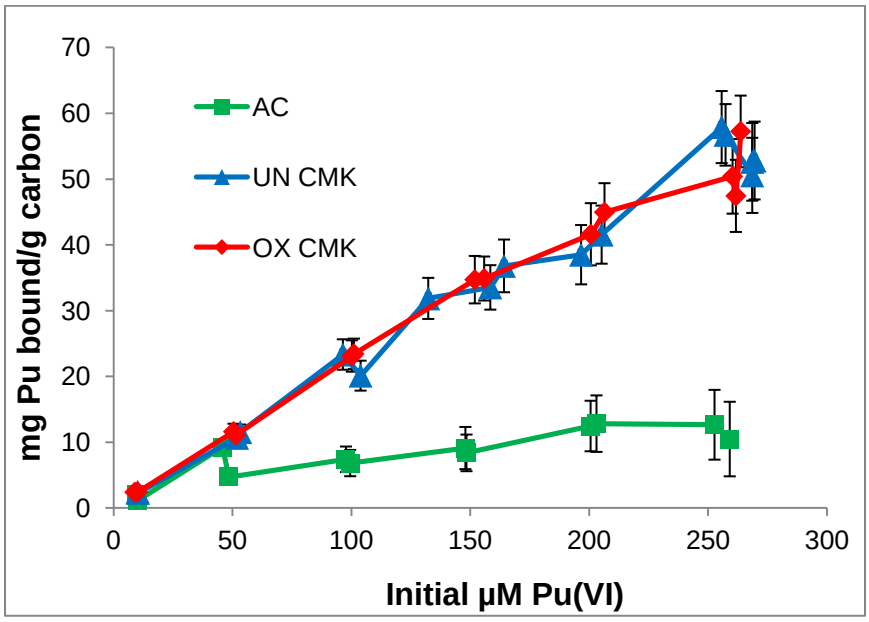

Figure 6.56. Milligrams Pu bound per gram carbon vs. initial µM Pu, after 23 hour contact of carbon powders with pH 4 perchlorate Pu solutions.

6.3.4 Competition with EDTA

To see if surface complexation could compete with the common carboxyl chelating agent ethylendiaminetetraacetic acid (EDTA), Pu uptake was measured from 0.02 M, .002 M, and .0002 M EDTA solutions, all adjusted to pH 4.0 ± 0.1 and 100 ± 8 µM Pu(VI). The EDTA is expected to be doubly deprotonated in pH 4 solution, and $NaClO_4$ was used to adjust the ionic strength to approximately 0.1. Several formation constants for PuO_2 have been documented for the 1:1 EDTA-PuO_2 complex, ranging from $10^{14.6}$ to $10^{16.4}$.[271, 272] Therefore, without interference from the carbon surface over 99% of the Pu would be complexed at all three EDTA concentrations studied. Experimental evidence of this came from the UV-Vis spectra of 200 µM Pu(VI) pH 4 solutions at each EDTA concentration. At such a low plutonium concentration, only the 830 nm peak was observed, and this peak disappeared in the EDTA solutions. This is consistant with the spectrum documented by Foreman and Smith,[112] which they attributed to the 1:1 plutonyl-EDTA chelate, where the characteristic plutonyl peak at 830 nm disappeared and a new peak at 570 nm appeared with much lower extinction coefficient. Of course, this spectrum could also be attributed to Pu(V), but the spectral changes were only observed with EDTA.

Figure 6.57 shows the percent Pu sorption to the three carbon materials (measured after 23.0 ± 0.1 hours) plotted against [EDTA] on a log scale, and symbols to the right of the y-axis show the percent sorption in similar samples without EDTA. It appears that the presence of 0.0002 M EDTA enhances the affinity of Pu to the activated carbon, but Pu sorption decreases

with higher EDTA concentrations. Pu uptake to the CMK and oxidized CMK continuously decreases with increasing EDTA concentration, which may indicate competition between the oxidized surface and the EDTA in solution. Overall it seems that the carbon surface is unable to compete with excess EDTA for Pu complexation.

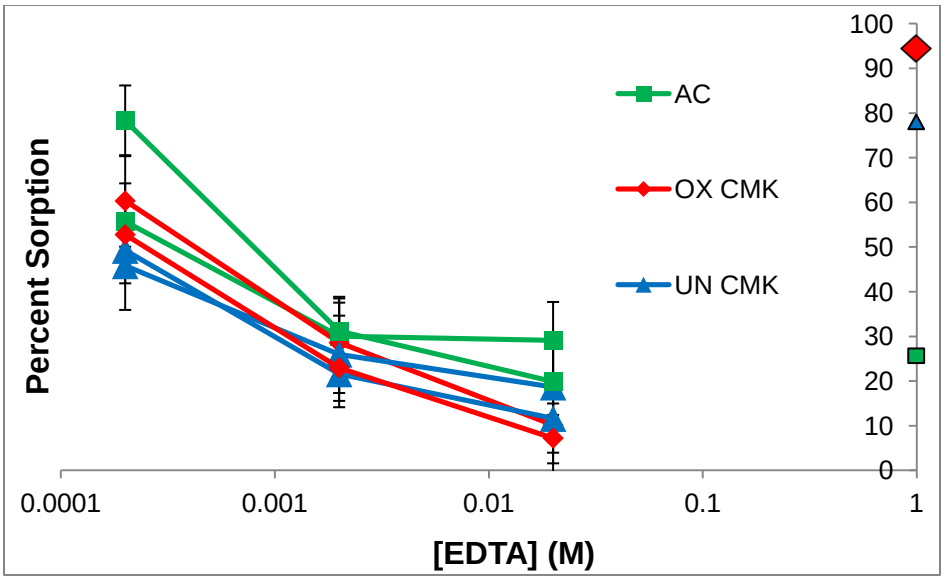

Figure 6.57. Percent Pu sorption to carbon powders after 23.0 ± 0.1 hours contact with EDTA solutions adjusted to pH 4.0 ± 0.1 and 100 ± 8 µM Pu(VI), plotted against [EDTA] on a log scale. Symbols to the right of the y-axis show the percent sorption in similar samples without EDTA. Lines are only to guide the eye.

6.3.5 Reuse of CMK as Pu sorbent

Duplicate batch regeneration experiments were performed with the used CMK materials, which had undergone at least 1 week contact with 1 M $HClO_4$ and up to four months contact with pH 2-3 solution. The conditions for testing reuse were pH 4.0 ± 0.1, 900 ± 150 mL/g, and 100 ± 10 µM Pu, with a 23 hour equilibration time. The Pu was then stripped by adding acid and allowing 23 ± 1 hours equilibration with 1 M $HClO_4$, after which the majority of the solution was removed, and fresh solution was added and equilibrated to pH 4 for the next sorption cycle. Three cycles of reuse (use 2-4) were tested on the same samples, and the mg Pu bound per g carbon are compared to similar samples containing unused CMK (Use 1) in Figure 6.58. Overall the data show that the CMK materials are reusable as Pu adsorbents, with only a small decrease in Pu affinity. This suggests that the CMK is reasonably stable in aqueous, mildly acidic environments, but there is currently no structural data to verify this. The propagated uncertainty in mass CMK, volume solution, and total Pu added results in very large error bars (representing 90% confidence) after several cycles, so the samples were not tested beyond 4 uses.

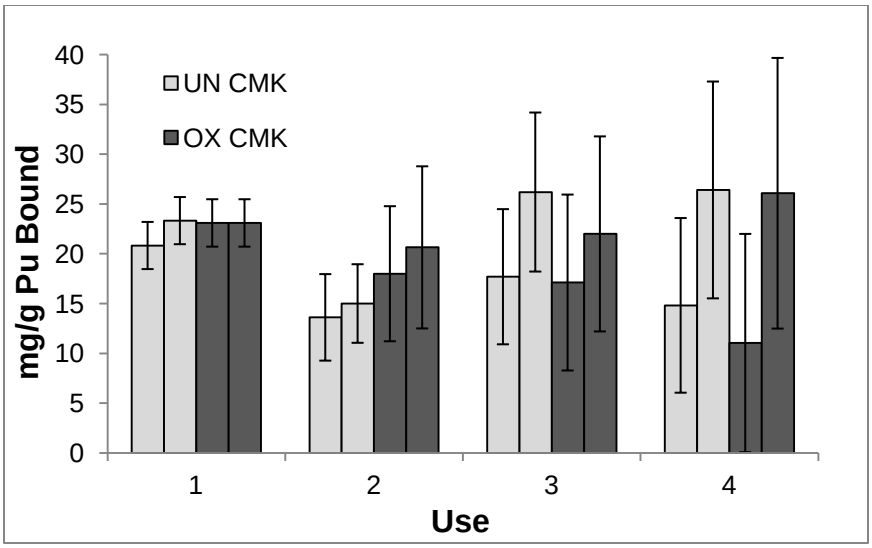

Figure 6.58. Milligrams Pu bound per gram carbon measured after 23 hours contact with 900 ± 150 mL/g solution (pH 4.0 ± 0.1, 100 ± 10 µM Pu), for CMK and oxidized CMK before (use 1) and after (use 2-4) removal of Pu by 1 M $HClO_4$ and several months stored in pH 2 solution.

6.3.6 Effect of ionic strength on Pu sorption

The ionic strength (I) of the CMK samples was not controlled, but this effect needed to be tested, as ionic strength can strongly influence uptake if outer-sphere complexation or physisorption is involved. If the binding mechanism is due to chemisorption, or inner-sphere complexation, then the uptake should be independent of ionic strength.[273] The effect of ionic strength on Pu sorption to C-CS and C-CS-COOH was tested in the non-complexing $NaClO_4$ medium at pH 4 with 10-15 µM Pu (Figure 6.59). The ionic strength in this range did not seem to significantly affect the Pu uptake to either C-CS or C-CS-COOH, but the percent sorption to C-CS was slightly more variable at the higher ionic strength. These results suggest that the C-CS-COOH binds Pu via chemisorption, as was expected.

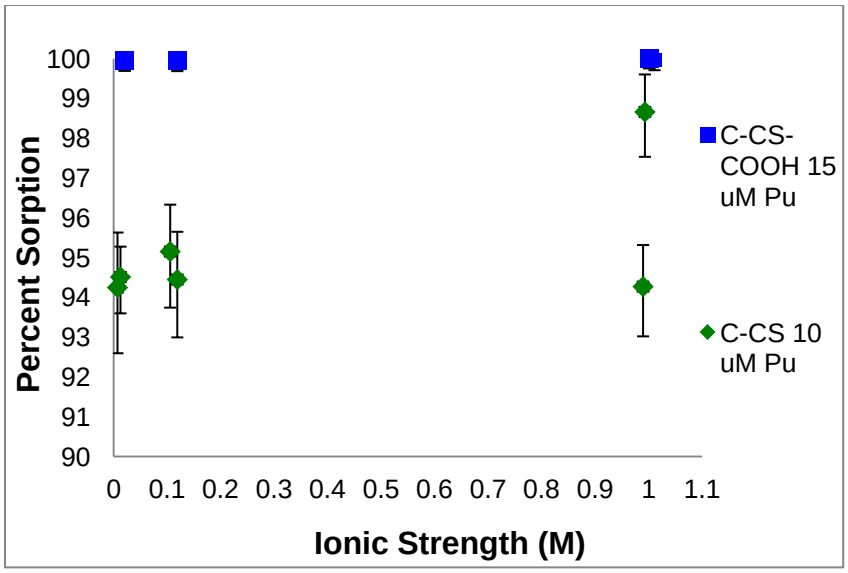

Figure 6.59. Percent Pu sorption vs. ionic strength for 10 µM Pu C-CS samples, and 15 µM Pu C-CS-COOH samples in pH 4 $NaClO_4$ solutions.

The effect of ionic strength on the Pu sorption kinetics of these two materials was tested at two Pu concentrations, and proved to be negligible in samples of 10 µM Pu (Figure 6.60), further indicating that ionic strength does not affect the sorption mechanism. Figure 6.61 shows percent Pu sorption vs. minutes contact with pH 4 perchlorate solutions with 250 µM Pu and ionic strength of approximately 1, and can be compared to Figure 6.51 in Section 6.3.2, which shows the data from similar experiments with the ionic strength around 0.13. The Pu sorption kinetics were the same for C-CS-COOH, but there was a dramatic difference in the time required for complete Pu uptake by C-CS. Almost quantitative sorption of Pu to C-CS from the solutions with ionic strength near 1 occurred within 20 minutes of contact, as opposed to uptake from solutions of lower ionic strength, which took over 23 hours. This unexpected result again suggests that Pu sorption to C-CS at high Pu concentrations occurs by an alternate mechanism. Considering that Pu(VI) and Pu(V) in CMK samples were reduced to Pu (IV) at the carbon surfaces (see Section 6.4.1), lead to the hypothesis that the high Pu sorption to unoxidized C-CS is either surface precipitation or adsorption of Pu(IV) intrinsic colloids. The increased rate of Pu sorption to C-CS that was observed at higher ionic strength could actually be an increase in the rate of Pu colloid formation. Thus the high Pu uptake capacity of pristine C-CS is very much dependent on the reduction to Pu(IV), and is unique to Pu. This hypothesis inspired further analysis of the Pu associated with C-CS and C-CS-COOH via TEM and XAS, and these results are presented is Section 6.4.2. The batch kinetic experiment was repeated at several intermediate ionic strengths (Figure 6.62), but no clear trend was observed. Only the Pu uptake from solutions with the ionic strength near 1 was rapid, and the uptake from all of the lower ionic strength solutions took at least 23 hours. The reasons for this discrepancy are unclear. Little Eu sorption was observed in a sample of 250 ± 15 µM Eu in 1 M $NaClO_4$ that was adjusted to pH 4 (Figure 6.63), indicating that the increased rate of Pu sorption rate at high ionic strength was not a result of oxidation or any other modification of the C-CS surface by perchlorate.

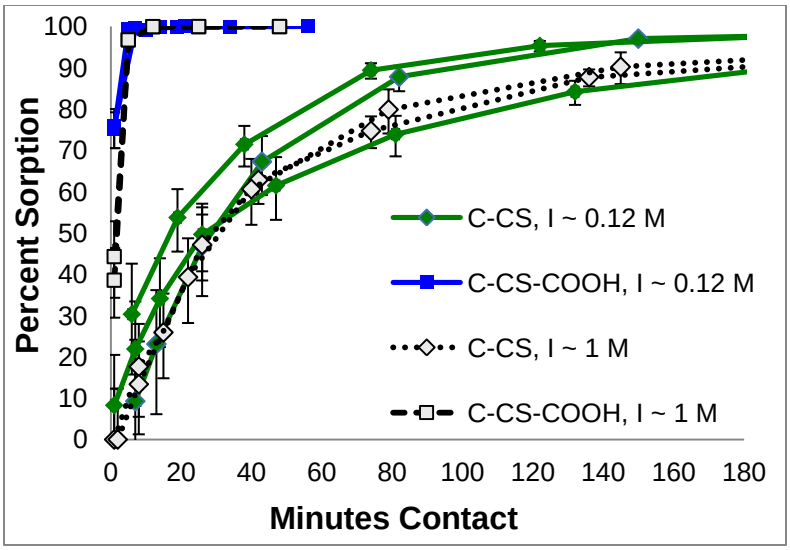

Figure 6.60. Percent sorption vs. minutes contact for C-CS carbon powders with 10 µM Pu, pH 4 $NaClO_4$ solutions of different ionic strengths. Lines are added only to guide the eye along data from the same sample.

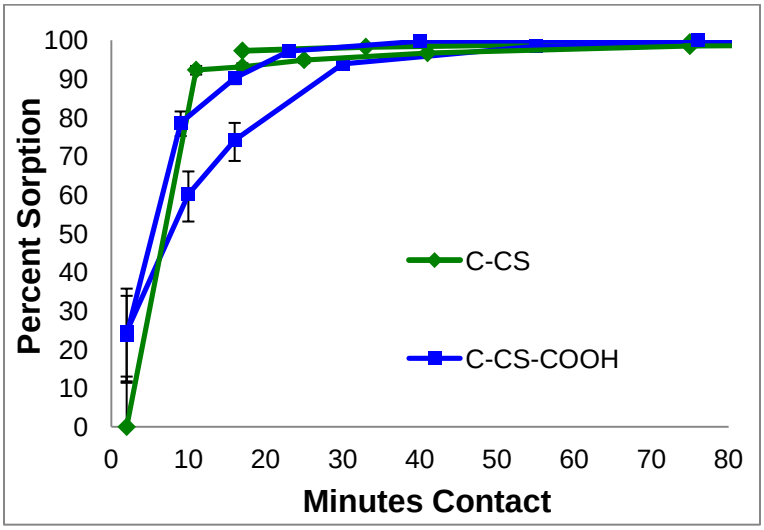

Figure 6.61. Percent sorption vs. minutes contact for C-CS carbon powders with 250 µM Pu, pH 4 $NaClO_4$ solutions with ionic strength of approximately 1 M. Lines are added only to guide the eye along data from the same sample.

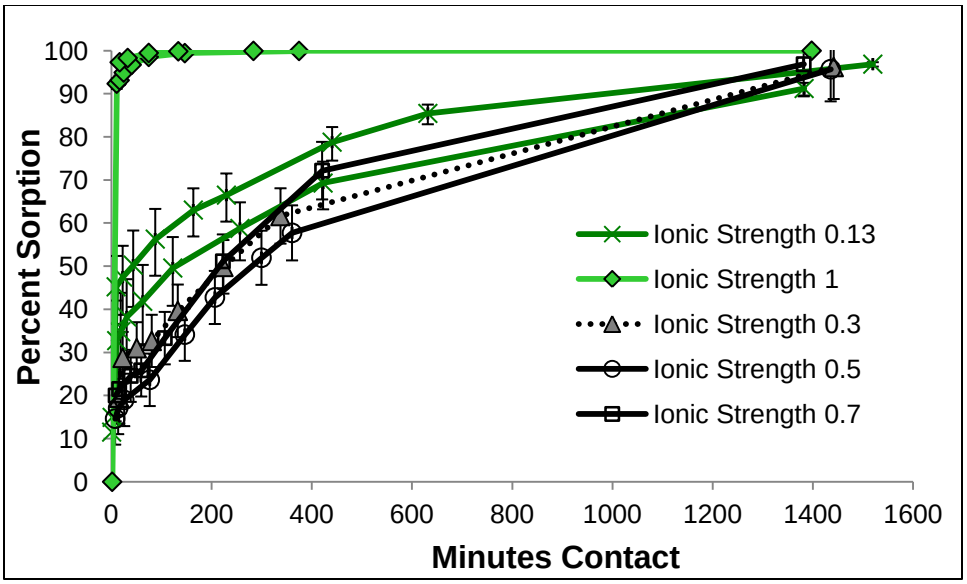

Figure 6.62. Percent sorption vs. minutes contact for C-CS carbon powder with 250 µM Pu, pH 4 $NaClO_4$ solutions of different ionic strengths. Lines are added to guide the eye along data from the same sample.

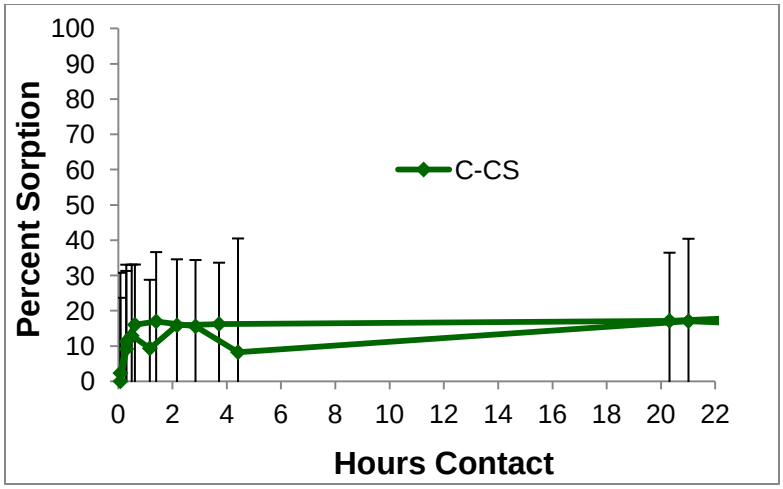

Figure 6.63. Percent sorption vs. minutes contact for batch C-CS samples with approximately 1000 mL/g of pH 4 1 M $NaClO_4$ 250 ± 15 µM Eu(III) solution. Lines are added to guide the eye along data from the same sample.

6.4 XAS and TEM experiments

Pu XANES measurements provided direct assignment of the Pu oxidation state at the carbon surface, *in situ*. Interpretation of the EXAFS region of spectra from carbon samples is difficult both because of the heterogeneous nature of Pu species in the samples and the limited R-space resolution afforded by our k-range. In this work, the EXAFS region was used to estimate the percentage of plutonium that precipitated as PuO_2. Near the beginning of investigation of Pu sorption interactions with porous carbons, samples of UN CMK and OX CMK were prepared for XAS measurements in perchlorate solutions with pH both below and above the PZC of each material. Analysis of the XANES data was done by Deborah Wang, and Dr. Daniel Olive

analyzed the EXAFS data. These results are presented in Section 6.4.1. Later, samples of C-CS and C-CS-COOH were prepared with the same conditions as many of the batch experiments (250 μM Pu, 0.1 M $NaClO_4$, pH 4) for analysis by TEM and XAS. These experiments were designed to test the hypothesis that Pu was complexed at the oxidized C-CS-COOH surface, while surface precipitation or sorption of Pu colloids occurred at the untreated C-CS surface. The TEM analysis was carried out by the author and Dr. Zurong Dai, Dr. Marvrik Zavarin, and Dr. Annie B. Kersting at the Glenn T. Seaborg Institute, Lawrence Livermore National Laboratory (LLNL). The XAS data on the C-CS samples were collected by Stephen Jones, Dr. Daniel Olive, and Deborah Wang of the Nitsche group, and analyzed by Dr. Daniel Olive. The results of these experiments are presented in Section 6.4.2. An introduction to XAS is given in Section 3.3.5, along with the sample packaging and measurement parameters, and the methods used for data analysis.

6.4.1 Pu L_{III} XAS of CMK samples

Samples of both CMK materials were prepared for XAS measurements in perchlorate solutions with pH both below and above the PZC of each material. The XAS samples were prepared in a similar manner to the batch sorption samples described above. Approximately 9.6 mg ^{239}Pu(VI) per g carbon (only 4.8 mg/g on pH 2.3 sample) was loaded on to CMK samples with approximately 200 mL 0.1 M $NaClO_4$ solution (200 ± 10 μM Pu) per g carbon. After 1 day of contact, over 99% of the Pu was determined by LSC to be associated with the solid phase.

The results of XANES analysis show that the Pu associated with UN CMK and OX CMK surfaces is tetravalent. A representative fit of the Pu L_{III} edge XANES data collected from an oxidized CMK sample containing only Pu(IV) to known oxidation state standards is shown in Figure 6.64. The standards used for LCA of the XANES data included aqueous Pu(IV), Pu(V), and Pu(VI) standards.[124] Figure 6.65 shows a representative fit of the Pu L_{III} edge on an untreated CMK sample containing mostly Pu(IV) and some Pu(V). Table 6.6 summarizes the results obtained by the Pu XANES spectral fits of all CMK samples measured. None of the samples contained significant amounts of Pu(VI) at the time of measurement, and most of the Pu present was identified as Pu(IV).

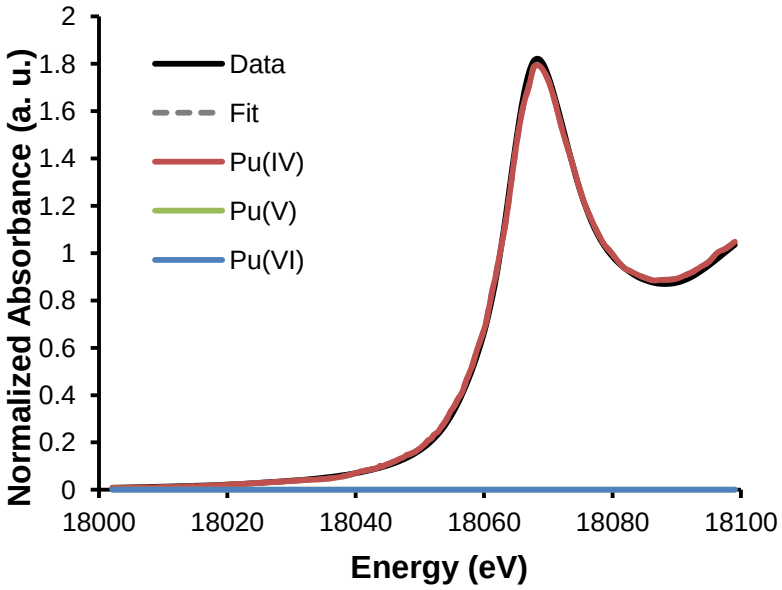

Figure 6.64. Pu L_{III} edge XANES spectral fit of data collected on sample of OX CMK in pH 2.3 solution to standards of known oxidation state. The fits show that all Pu in the sample has been reduced to the tetravalent state. The Pu(V) component lies under the Pu(VI) component, as neither contributed to the fit.

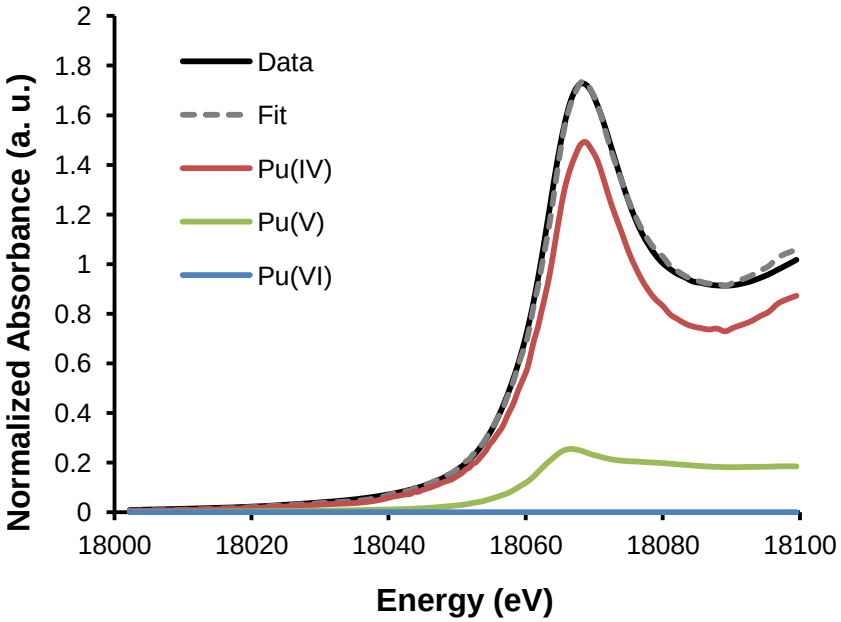

Figure 6.65. Pu L_{III} edge XANES spectral fit of data collected on UN CMK pH 7 sample to standards of known oxidation state. The fits show that most Pu in the sample has been reduced to the tetravalent state, but a portion of the Pu was reduced only to the pentavalent state.

Table 6.6. Results of spectral fits of XAS spectra measured for CMK samples

Sample	mg Pu per g C	Solution pH	Days contact before measurement	Percent Pu(IV)	Percent Pu(V)	Percent PuO_2
UN CMK pH 6	9.0 ± 0.5	6.03 ± 0.05	2.3	88 ± 5	13 ± 5	42 ± 10
UN CMK pH 7*	9.4 ± 0.5	7.05 ± 0.05	2.5	84 ± 5	17 ± 5	27 ± 10
OX CMK pH 2.3	4.9 ± 0.3	2.25 ± 0.05	3.0	101 ± 5	0 ± 5	6 ± 10
OX CMK pH 4.7	9.1 ± 0.5	4.70 ± 0.05	3.4	97 ± 5	2 ± 5	9 ± 10
OX CMK pH 6	9.6 ± 0.7	6.14 ± 0.05	6.0	84 ± 5	19 ± 5	48 ± 10

*Solution pH started at 8.76 and drifted to 7.05 during 23 hours of sorption time

Results of the XAS measurements clearly show that Pu at the surfaces of both untreated and oxidized CMK carbon has been reduced to Pu(IV). The samples were loaded with freshly oxidized Pu(VI) stock solutions in perchloric acid, which were verified by Vis-NIR spectroscopy, and no other reducing agents were present in the samples. Visible spectroscopy of the pH 4 control sample (see Figure 3.15 in Section 3.4.4) showed that without the presence of carbon, over 50% of the Pu in such solutions remains as PuO_2^{2+} after 5 days, and most of the XAS samples were measured between 2 and 3 days after initial batch sample preparation. Therefore it appears that the CMK carbon powders in these samples are contributing to the reduction of Pu(VI) and Pu(V) to Pu(IV), and the reduced Pu is strongly associated with the carbon surface. The data show no evidence that the extent of Pu reduction depends on the extent of oxidation of the carbon surface. There seems to be a subtle dependence of the extent of reduction on solution pH, where more of the Pu is reduced in the lower pH samples.

The redox chemistry on the CMK surface could help explain why the Pu uptake capacity and kinetics in samples with high Pu concentrations are about equal for oxidized and untreated CMK. Tetravalent Pu is expected to either adsorb to surfaces or precipitate in any solution with pH ≥ 2. The similarity in Pu uptake kinetics likely occurs because the UN CMK and OX CMK have similar concentrations of surface groups, based on the FTIR spectra. The kinetic experiments with C-CS and C-CS-COOH (Section 6.3.2) show that the sorption kinetics are very different for pristine carbon surfaces and highly oxidized carbon surfaces, at all concentrations. The comparison between UN CMK and OX CMK leaves a lot of ambiguity as to which surface groups are responsible for reduction and/or complexation of Pu. The most likely source of electrons for Pu reduction is the oxidation of surface functional groups such as C-H, C-OH, and C=O to form C-OH, C=O, and COOH groups, respectively. The oxidation of hydroquinones in the reverse of Reaction 6.4 is a strong possibility, as the redox properties of humic acids are generally attributed to reversible redox conversions of quinonoid moieties inherent within humic structures.[274-276] Marquardt *et. al*[277] found that Pu(VI) and Pu(V) were rapidly reduced to Pu(IV)

in humic-rich groundwater of pH 4.9-6.8. They showed that the humic substances were responsible for the reduction, and some of the Pu(IV) slowly reduced to Pu(III) over several weeks. Nash *et. al*[278] also reported complexation of Pu(VI) and reduction to Pu(IV) by humic acid under various pH conditions ranging from 3.2 to 10.1. Choppin and coworkers have also shown humic acid to reduce Pu(VI) and Pu(V) to the tetravalent state under various environmental conditions.[279-281] However, the redox potentials of these groups are highly pH-dependent, and increase with increasing acidity,[275, 282] which would make them less reducing in more acidic solutions. Given the apparent increase in Pu reduction with solution acidity, it is likely that other groups are also involved. This could include the direct oxidation of aliphatic carbon atoms (like in Reactions 6.5 and 6.6) by the plutonium. The oxidation of aromatic carbons in humic acid by Np(VI) and Pu(VI) was postulated by Nash *et al*. when it was observed that a stoichiometric excess of actinide species were reduced by humic acid compared to the functional groups present.[278]

The spontaneous reduction of other metal ions, such as Ag^{+}, Pt^{4+}, Pd^{2+}, and Au^{3+}, has previously been observed on activated carbon fibers,[268-270, 283] and the spontaneous reduction of Ag^{+} was also observed on glassy carbon[284] and of Pt^{4+} on graphite surfaces[285]. In all cases, X-ray photoelectron spectroscopy (XPS), temperature-programmed desorption (TPD) and/or imaging techniques were used to conclude that it is the oxidation of functional groups on these carbon surfaces that is responsible for the reduction of metal ions. Unfortunately, there are no facilities that allow radioactive samples for XPS or TPD measurements, and it was not analytically determined which groups are responsible.

The redox chemistry at mesoporous carbon surfaces is noteworthy because it could mean that they have higher uptake capacities for redox active species than for metal ions that are less redox active, and could possibly be exploited for separations under certain conditions. The apparent preference of pristine OMCs for Pu sorption was demonstrated by the low affinity of C-CS for Eu(III), and its high affinity for Pu (see Section 6.3). In the case of Pu, the reduction of Pu(VI) and Pu(V) to the less soluble tetravalent state can be useful for remediation efforts.

Attempts to fit Pu-Pu scattering paths to the EXAFS region of the spectra from UN CMK and OX CMK samples indicate that most of the Pu(IV) is not in the form of crystalline PuO_2, but Pu(IV) species with no long range order. The amount of PuO_2 precipitated, as estimated by comparing the amount of Pu-Pu scattering to the amount of Pu-O scattering, varied between 6% and 48%. Figure 6.66 displays an example fit of the Pu-Pu scattering in the untreated pH 7 sample, showing that not all of the Pu-O scattering in the first shell can be explained by precipitated PuO_2 alone. This contribution is attributed to Pu(IV) sorbed to the surface and lacking any long-range Pu-Pu coordination, as EXAFS has been shown to be able to differentiate between chemisorbed Pu(IV) and ordered PuO_2 colloids.[142] The fitting results indicating percent contribution from crystalline PuO_2 are included in Table 6.6. The samples with significant amounts of precipitated PuO_2 were pH 6 or higher, for both oxidized and untreated CMK. The oxidized and untreated CMK samples of the same pH (pH 6) were very similar in both the extent of reduction to Pu(IV), and the amount of Pu(IV) associated with crystalline PuO_2. The Pu in the samples without near Pu neighbors may be complexed by oxygen-containing surface groups, some of which could have been created on the untreated CMK surface upon reduction of PuO_2^{2+} or PuO_2^{+}. The Pu-Pu scattering observed in the EXAFS spectra of the CMK samples could possibly be attributed to PuO_2 nanocrystals that grow or deposit onto the carbon surface as excess

Pu is reduced to the tetravalent state, which was shown for C-CS by TEM (see Section 6.4.2). The untreated CMK samples with pH 6 and 7 also contained similar amounts of Pu(IV), and the higher pH sample contained slightly less precipitated PuO_2. The amount precipitated is very close, considering experimental uncertainty, but this result is still unexpected. It is possible that the greater concentration of CO_3^{2-} and HCO_3^- from dissolved atmospheric CO_2, along with a more negative surface charge on the carbon allowed for more slightly more complexation of monomeric Pu species in the higher pH sample.

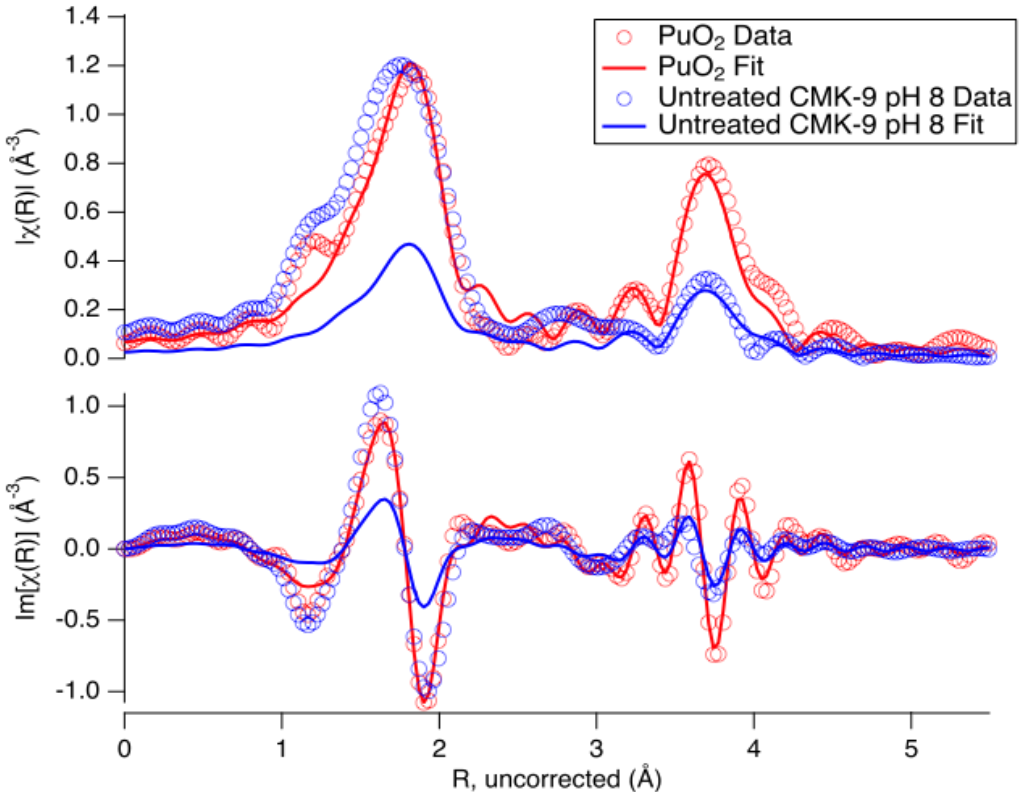

Figure 6.66. EXAFS fitting results, the second coordination shell in the UN CMK pH 7 sample was fit simultaneously using the data from the PuO_2 standard. The fit is satisfactory in the region of the second shell, but the amount of Pu-Pu scattering is insufficient to account for all of the oxygen scattering in the first shell, assuming the Pu-Pu scattering comes from PuO_2.

6.4.2 Pu L_{III} XAS and HRTEM of C-CS samples

Considering the XAS results obtained with the CMK carbons, and the results of 250 µM batch experiments with the C-CS and C-CS-COOH, led to the hypothesis that Pu adsorbs to unoxidized OMCs in the form of intrinsic colloids. C-CS and C-CS-COOH samples with the same conditions as the batch experiments were analyzed by TEM and XAS, in order to characterize the Pu associated with the carbon surfaces. 60 ± 3 mg ^{239}Pu(VI) per gram carbon was loaded on to C-CS and C-CS-COOH samples with 1020 ± 10 mL 0.1 M $NaClO_4$ solution (245 ± 13 µM Pu) per gram carbon. The sorption samples for TEM were prepared in exactly the same way as the XAS samples, except that the carbon powders were ground with a mortar and pestle prior to the TEM experiment. After 1 day of contact, LSC measurements determined that 99.7 ± 0.3 % of the Pu was with the C-CS-COOH solid phase, and 95.0 ± 1.2 % of the Pu was associated with the C-CS solid phase. Therefore, the Pu loading was 60 ± 3 mg/g, which is far

more than was loaded onto the CMK materials for XAS analysis. After sorption occurred, the solid phase was allowed to settle, and the bulk liquid phase was removed. The carbon was washed by adding 10^{-4} M HCl, shaking for 1 minute, centrifuging for 10 minutes at 7000 rpm, and then removing the liquid phase. The washing process was repeated ten times, and LSC analysis of the supernatants determined that over 98% of the total Pu added remained on the solid phase in the C-CS-COOH sample, and over 88% remained associated with the C-CS. The samples were shipped as approximately 0.3 g/L slurries in 10^{-4} M HCl to Lawrence Livermore National Laboratory (LLNL), where 10 µL aliquots were drop-cast onto lacey formvar/carbon coated Cu TEM grids. The micrographs were collected with a Philips CM300 FEG TEM operating at 300 kV. The *in-situ* elemental analysis was performed by X-ray energy dispersive spectroscopy (EDS) with an Oxford detector under the TEM. Several grids were prepared and analyzed with each sample to ensure that micrographs were representative of the bulk sample.

Figure 6.67 shows a low-magnification TEM image of a C-CS particle loaded with Pu, and a magnified image of the edge of the particle, with the corresponding X-ray EDS spectrum. All of X-ray EDS spectra measured on Pu-loaded C-CS particles identified only carbon, oxygen and plutonium in the samples. The 2d-hexagonal ordered mesostructure seems to be preserved but was only observed along the [110] direction. Figure 6.68 shows HRTEM images from the same particle. There is a high concentration of crystalline nanoparticles on the surface, about 3 nm in diameter. The Fourier transforms (FFTs) shown in the insets correspond with the face centered cubic (fcc) structure of crystalline PuO_2. These nanocrystals were observed on all of the Pu-loaded C-CS particles imaged, and another example is shown in Figure 6.69. The size of the crystals is about the same as the secondary mesopore network in C-CS, but there is no evidence that this is more than coincidence. The size of these particles is similar to those observed by Romanchuk *et al.*[142] via HRTEM on hematite that had Pu(VI) added to it. Plutonium oxide nanoparticles with a similar size were also prepared by Powell *et al.*[136] both by neutralizing a 1 µM Pu(IV) solution, and by adding Pu(IV) incrementally to quartz and goethite. In that work, the nanocolloids formed on quartz and in solution were fcc PuO_2, but the crystals formed on the goethite surface epitaxially adopted the body centered cubic (bcc) Pu_4O_7 crystal structure. In the present work, no such epitaxial distortion was expected due to the amorphous nature of the carbon, and it is not clear whether these PuO_2 nanocrystals grew on the surface of C-CS, or were formed in solution and then adsorbed strongly to the surface. In either case, the carbon must have first reduced Pu(VI) and Pu(V) to Pu(IV). The PuO_2 nanocrystals are strongly associated with the C-CS particles, as the 10 cycles of rinsing did not remove them, and they were not observed on the TEM grids apart from the C-CS particles. The TEM results on C-CS samples are interesting in that they add to the growing body of evidence suggesting that Pu(IV) Eigencolloids are actually crystalline nanostructures.[135, 136]

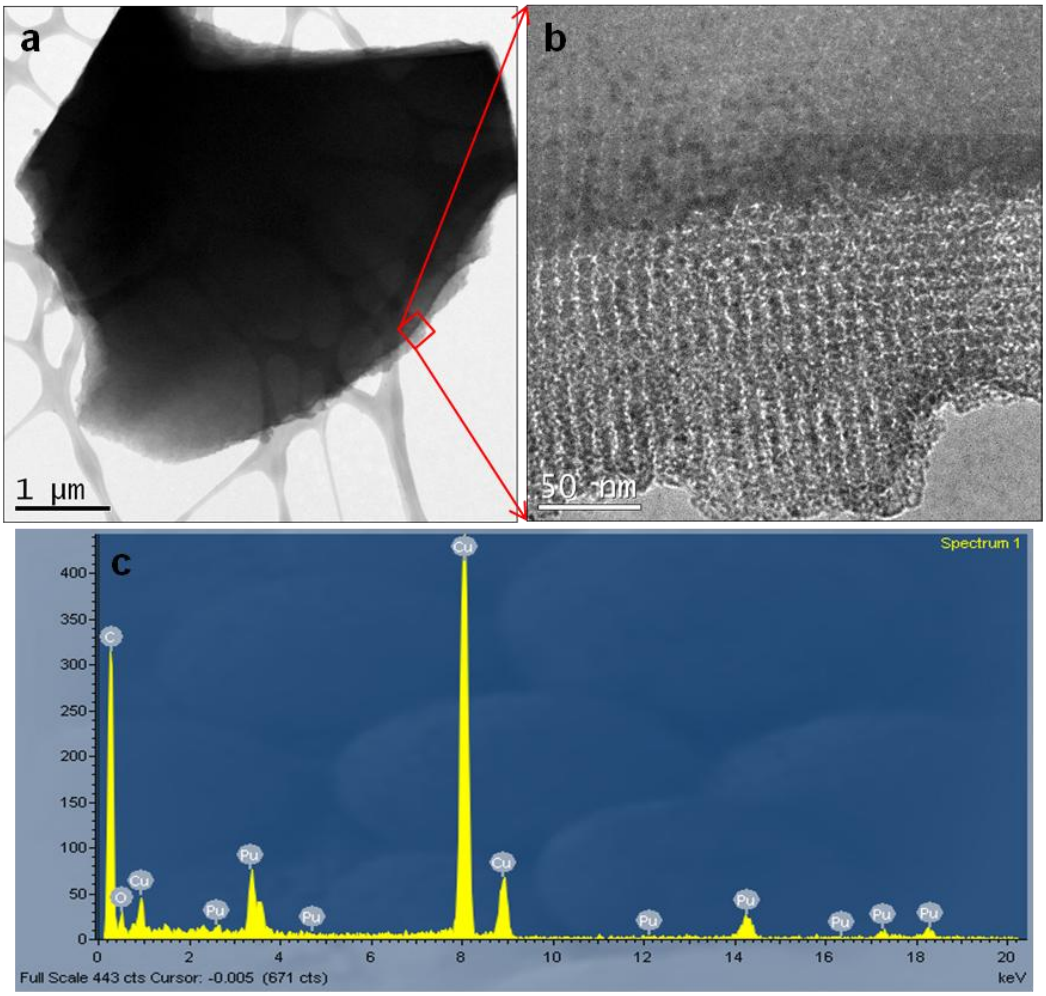

Figure 6.67. A low magnification bright-field TEM image of a C-CS mesoporous carbon particle (a), a magnified TEM image from the edge of the C-CS particle (b), and an X-ray EDS spectrum collected from the particle showing strong Pu peaks (c). The copper signal comes from the TEM grid, and Pu, O and C were detected in the sample.

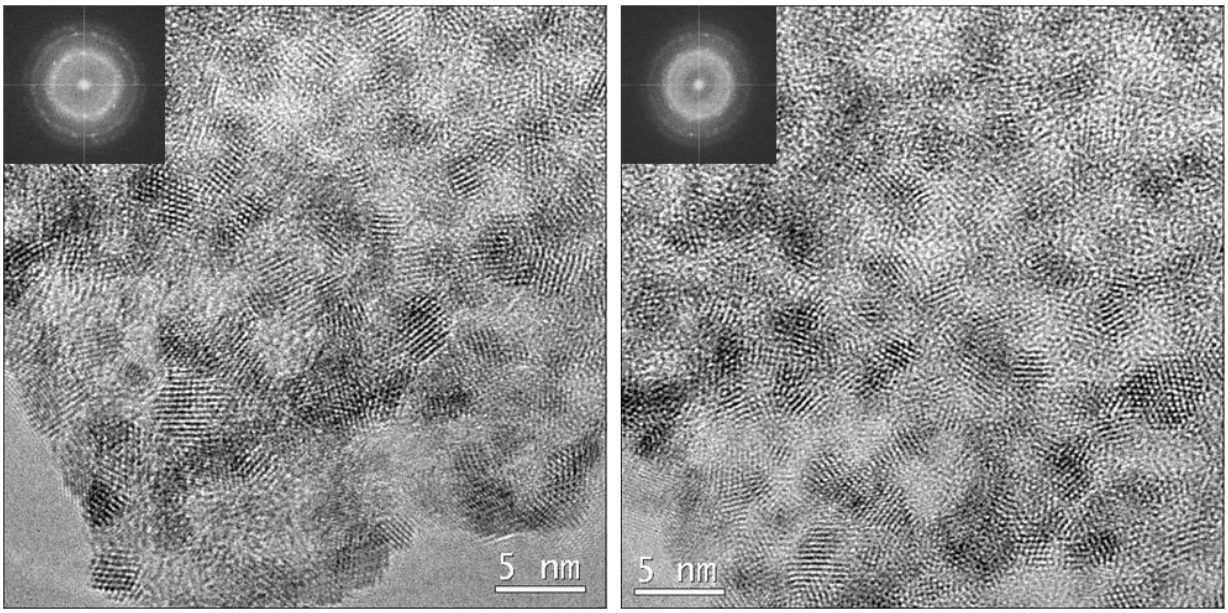

Figure 6.68. High resolution TEM (HRTEM) images taken from edge of the C-CS particle shown in Figure 6.67. Crystalline nano-particles with a primary size of ~3 nm in diameter can be identified. Insets are corresponding FFTs, with patterns that match the structure of fcc PuO_2.

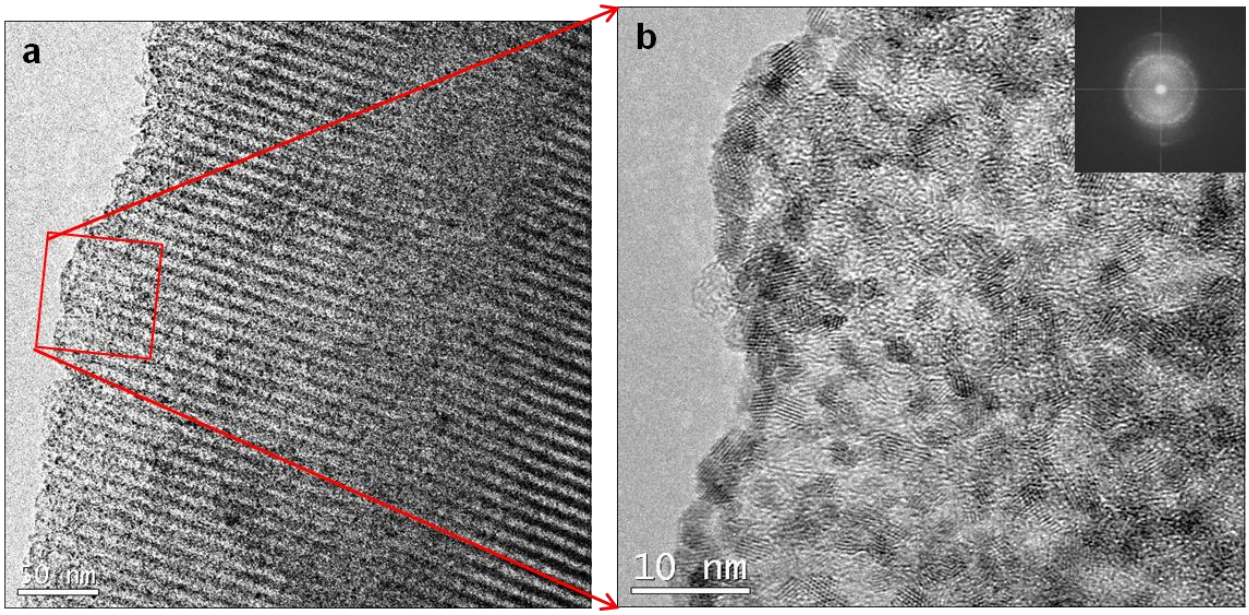

Figure 6.69. Bright-field TEM image of C-CS loaded with Pu (left), HRTEM image (right) and FFT (inset). Crystalline nano-particles approximately 3 nm in diameter can be identified, matching fcc PuO_2.

Figure 6.70 is a bright-field TEM image of C-CS-COOH, with the FFT inset, showing the 2d-hexagonal ordered mesostructure along the [001] direction. In all HRTEM images of C-CS-COOH (examples presented in Figures 6.71 and 6.72), no crystalline PuO_2 particles were observed, even though strong Pu peaks were identified in the corresponding X-ray EDS spectra. In HRTEM images of some of the C-CS-COOH particles, a few tiny clusters of local order were

observed, like those circled in Figure 6.71. These small clusters could be related to some form of Pu, but there was no way to ascertain that. The majority of the Pu associated with the C-CS-COOH is amorphous, and presumably complexed by carboxyl and other surface groups. This TEM experiment confirmed that the sorption mechanism of Pu to pristine carbon is quite different than that to highly oxidized carbon. It should be noted that the X-ray EDS spectra from the C-CS particles indicated the presence of only C, O, and Pu, but the spectra from C-CS-COOH particles showed various amounts of Al, Fe, and Si as well. The trace Si seems to be left over from the synthesis, but the Fe and Al were not detected by elemental analysis of the bulk C-CS-COOH sample, and may have been introduced during the preparation of the grids. None of the contaminants seemed to be associated with the Pu on the grids. The bulk C-CS-COOH powder underwent dialysis following the TEM experiment, and although it did seem to excrete some ions, the PZC measured by powder addition was the same before and after dialysis (see Figure 6.25 in Section 6.2.5). The batch sorption of Pu from a pH 4, 0.1 M $NaClO_4$ Pu(VI) solution was tested again, and the results after dialysis were the same as those from before (see Figure 6.53 in section 6.3.2). Therefore it seems unlikely that any trace elements present in previous samples interfered greatly with the interactions between Pu and C-CS-COOH.

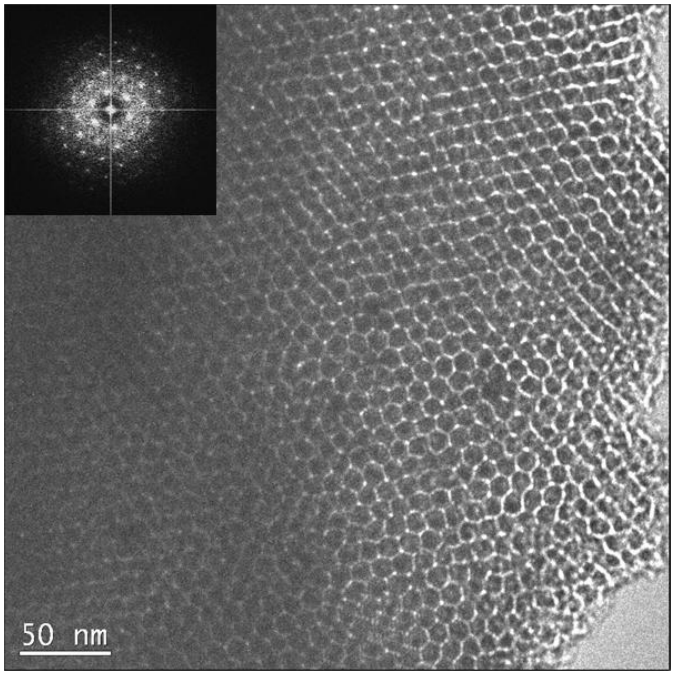

Figure 6.70. Bright-field TEM image of C-CS-COOH loaded with Pu, and corresponding FFT inset, showing 2d-hexagonal ordered structure along the [001] direction.

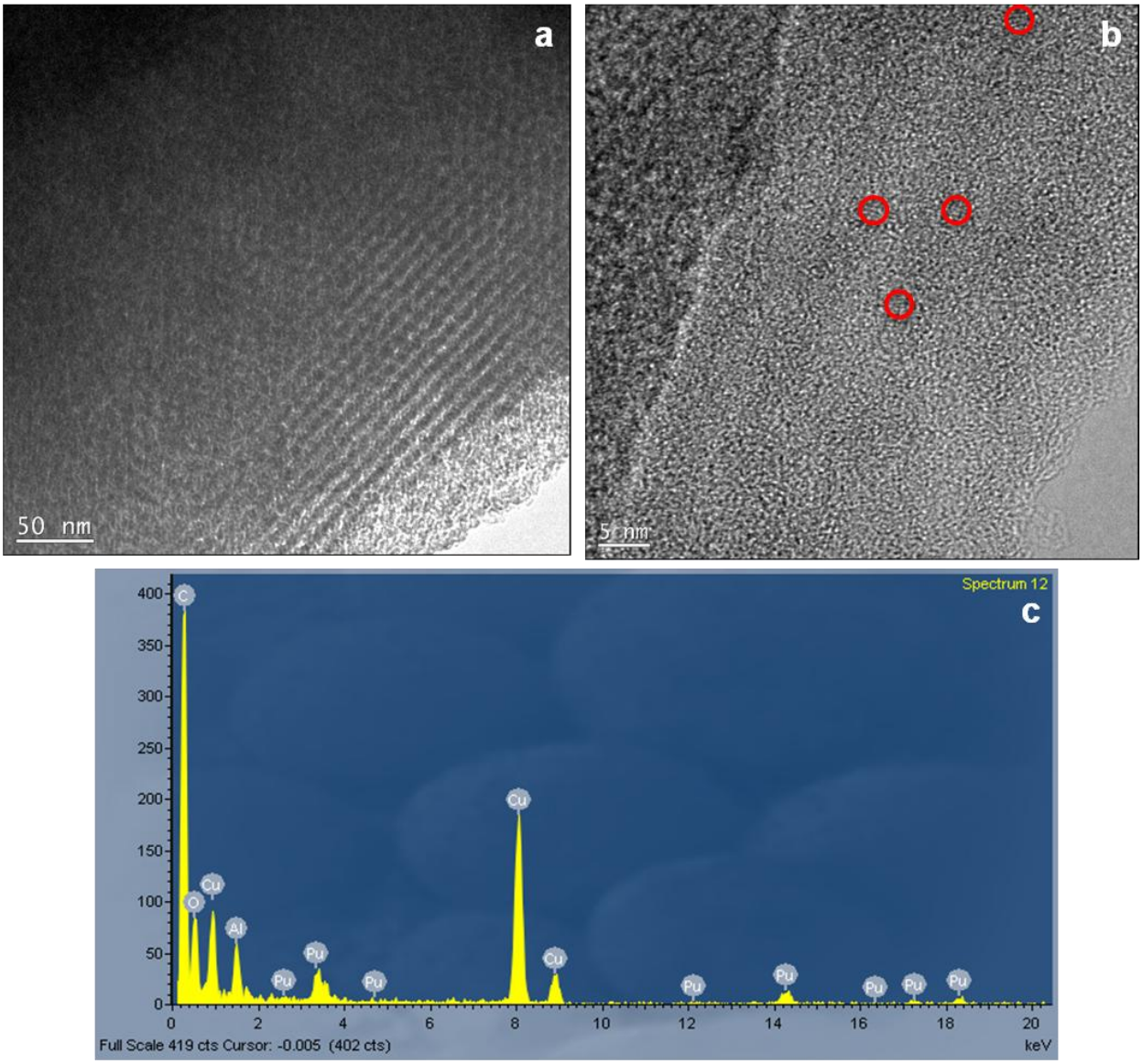

Figure 6.71. TEM image (a), HRTEM image (b) and X-ray EDS spectrum (c) of C-CS-COOH particle loaded with Pu. No crystalline PuO_2 particles were identified, but some local ordered clusters can be identified, as marked by circles. Al was detected along with C, O and Pu.

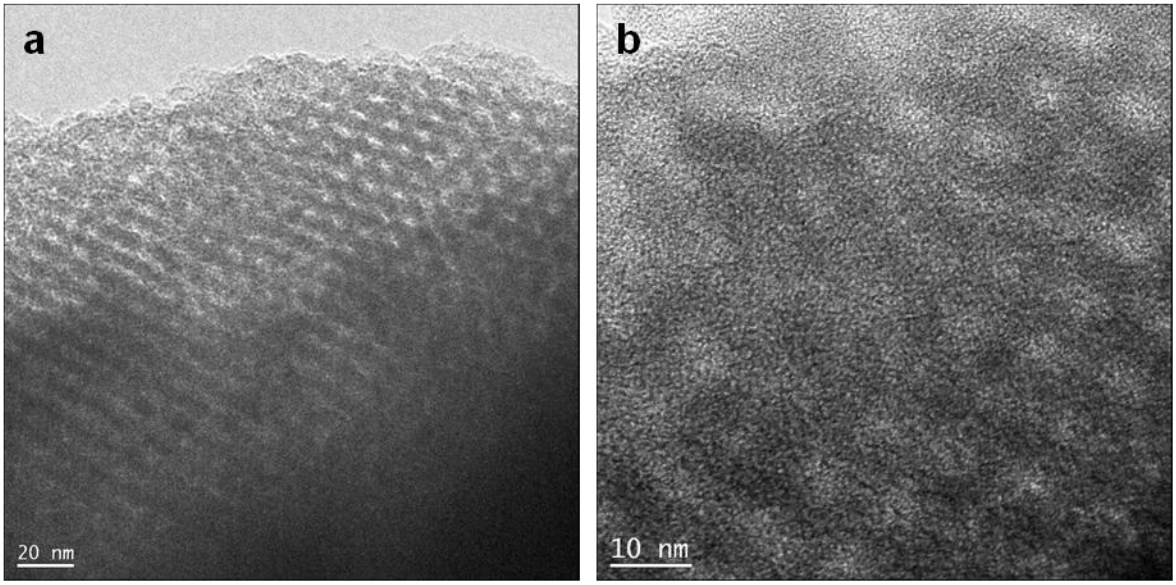

Figure 6.72. TEM image (a) and HRTEM image (b) of C-CS-COOH particle loaded with Pu. No crystalline PuO_2 particles were identified. A strong Si peak was detected in the EDS spectrum along with C, O, Al and Pu.

Pu L_{III}-edge XANES spectra (Figure 6.73) collected from C-CS and C-CS-COOH samples show little of the characteristic plutonyl shoulder that would be expected if significant amounts of Pu(V) or Pu(VI) were present in the samples. LCA results of the XANES spectra vary slightly depending on the choice of standards for comparison. If the possible standards were limited to aqueous Pu(IV)/Pu(V)/Pu(VI) only, then the fitting results indicate around 75% Pu(IV) and 25% Pu(V) for both samples. However, principal component analysis indicated the need for at least three components to reproduce the experimental spectra, and target transformation indicated that PuO_2 was a valid component, while $Pu(VI)_{(aq)}$ was not. The use of PuO_2 for a fitting standard in the C-CS sample was justified, as TEM and EXAFS analysis confirmed the presence of PuO_2 in that sample. Its inclusion as the third standard for the C-CS-COOH sample can be understood considering that the Pu present in the sample, being reduced to Pu(IV), and in the solid state, would necessarily have different XANES features than Pu(IV) in an aqueous state [286]. The XANES LCA fitting results with Pu(IV), Pu(V), and PuO_2 as the standards indicate that essentially all the Pu in both has been reduced to the tetravalent state, and the local atomic environment around the Pu atoms is consistent with a mixture of $Pu(IV)_{(aq)}$ and PuO_2. Considering that all four mesoporous carbons reduce Pu(V/VI) to Pu(V), regardless of surface oxidation, it seems likely that more than one kind of surface site is redox active with Pu. Figure 6.22 shows that in TGA the C-CS and C-CS-COOH samples lost approximately 5% and 4% of their weight, respectively, between 650° C and 900° C, which shows that they both have lactone, quinine, and anhydride groups on their surface.[90] Therefore the oxidation of hydroquinoid species may play a role, and the other possibilities discussed in Section 6.4.1 cannot be discounted either.

Analysis of XANES data can unambiguously determine the Pu oxidation state, but in order to elucidate the Pu coordination environment (i.e. the presence or absence of PuO_2) the EXAFS data must be examined. Figure 6.74 shows that there is little to no contribution from the first Pu-Pu scattering shell at 3.82 Å in the EXAFS of the C-CS-COOH sample, in contrast with

the C-CS sample, which shows a strong scattering feature consistent with that seen in bulk PuO_2. The EXAFS data sets from samples were fit simultaneously with the PuO_2 data set to a model based on PuO_2 (Figure 6.75 shows the C-CS fit). This technique applied to the C-CS-COOH data indicated little change in the first oxygen shell, consistent with Pu(IV), but essentially no Pu-Pu scattering that would be expected if there were any bulk PuO_2 precipitates. Table 6.7 summarizes the fitting parameters for the XAS data. The XAS data shows that although both C-CS and C-CS-COOH reduce Pu(V/VI) to Pu(IV), PuO_2 is only formed in C-CS samples. These results corroborate very well the TEM results presented above.

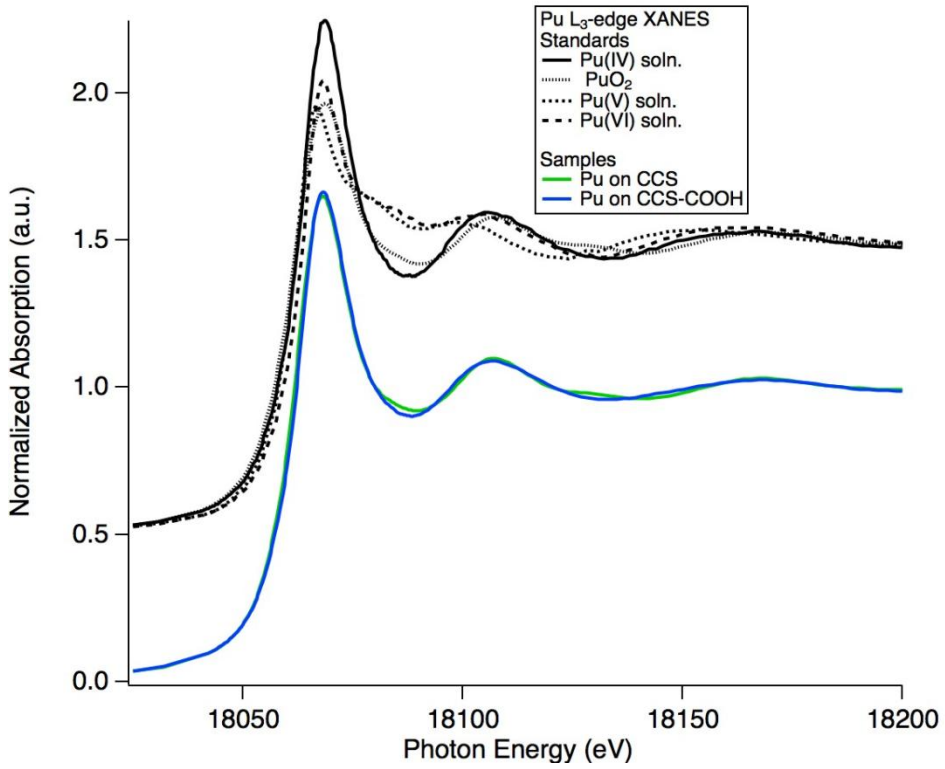

Figure 6.73. XANES spectra of the Pu on C-CS and C-CS-COOH samples, and associated Pu reference spectra (offset for clarity) used in XANES fitting. The spectra of both samples lack the plutonyl shoulder seen in Pu(V) and Pu(VI) spectra.

Table 6.7. Summary of EXAFS path fitting results, where fitting a total of 12 paths each for the PuO_2 standard and the sample were refined simultaneously using 10 variables over approximately 70 independent points. The E_0 shift for the C-CS sample was 2.6 ± 0.3 eV, and 2.6 ± 0.6 eV for the C-CS-COOH sample.

Sample	Scattering Shell	R (Å)	No. of Atoms	Debye-Waller Factor ($Å^2$)
Pu-C-CS	Oxygen	2.31 ± 0.03	7.8 ± 1.0	0.0086 ± 0.0009
	Plutonium	3.81 ± 0.01	6.2 ± 1.0	0.0036 ± 0.0003
	Plutonium	5.39 ± 0.01	1.7 ± 0.9	0.0036 ± 0.0003
Pu-C-CS-COOH	Oxygen	2.33 ± 0.01	9.1 ± 2.0	0.011 ± 0.0017
	Plutonium	3.81 ± 0.02	0.3 ± 0.3	0.0016 ± 0.0014
	Plutonium	5.39 ± 0.02	0.1 ± 0.1	0.0016 ± 0.0014

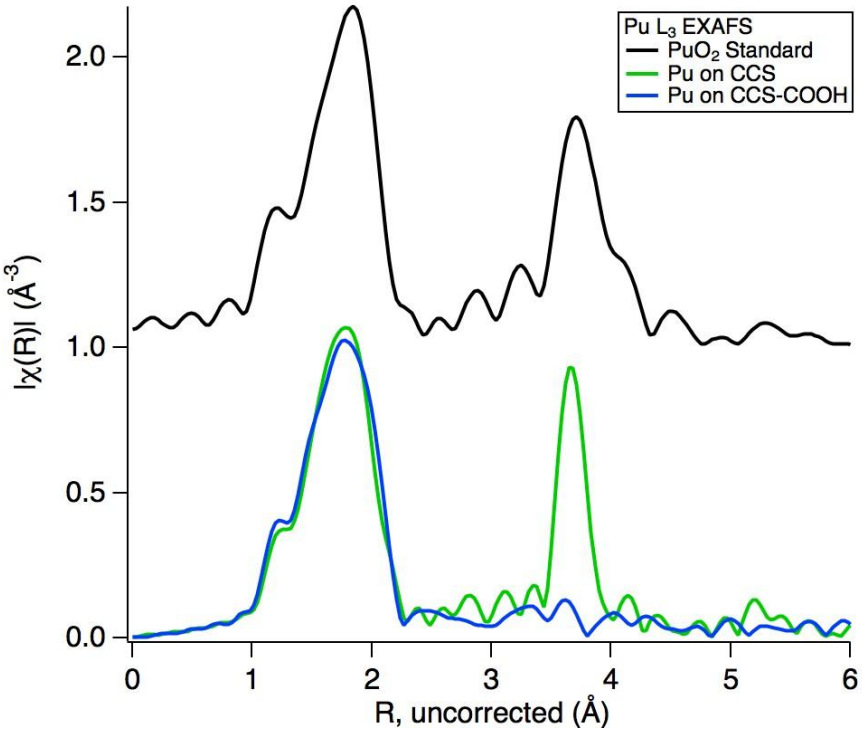

Figure 6.74. Fourier transform magnitude of the EXAFS from C-CS and C-CS-COOH samples, and PuO_2 (offset) for comparison. The difference in widths of the Pu-Pu scattering peak between the PuO_2 and the untreated C-CS sample is an artifact of the shorter k-space range available for the Fourier transform of the PuO_2 standard.

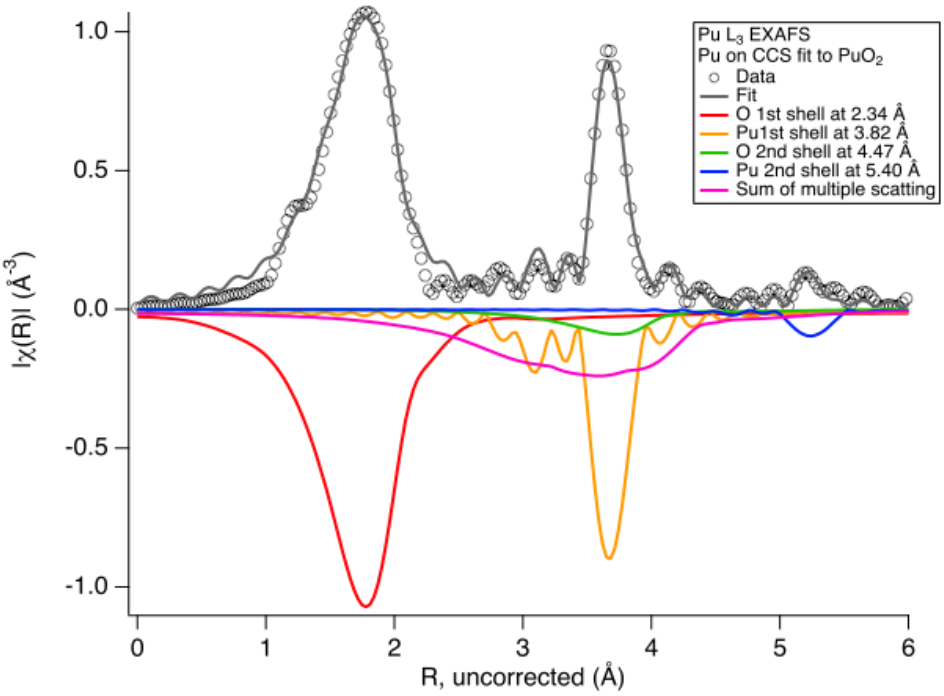

Figure 6.75. Fitting of the Pu EXAFS in the C-CS sample to the PuO_2 crystal structure. Scattering shells have been reflected about the x-axis for clarity, and the 8 weak multiple scattering paths used in the fit have been summed as well. The first 11 scattering paths, as well as the 2nd shell Pu path have been used in the fit. The R-factor of the fit to the C-CS sample was 0.0297, and for the C-CS-COOH sample it was 0.0995.

The batch sorption, XAS, and TEM experiments with oxidized Pu on unmodified and highly oxidized C-CS have illustrated how Pu interacts with OMCs. Both oxidized and pristine OMCs show high sorption capacities for Pu in aqueous pH 4 solutions, at least 60 mg Pu per g carbon, and both reduce Pu(V/VI) to Pu(IV). Chemisorption to carboxyl and possibly other functional groups on the surface occurs rapidly, and this prevents Pu(IV) from forming colloids in pH 4 solutions with C-CS-COOH. Once those surface binding sites are saturated, any remaining Pu(IV) forms PuO_2 nanocrystals that strongly associate with the carbon surface. Kinetic data suggest that the formation of PuO_2 nanocolloids is the rate-limiting step for Pu sorption to pristine OMCs. The batch sorption data with Eu indicate that oxidized OMCs make an effective general sorbent material for other actinide and lanthanide cations, while the high sorption to pristine OMCs may be unique to Pu, due to the reduction and subsequent formation and sorption of PuO_2 nanocrystals. Along with high surface area, the pore size distribution may be important for effective sorption of Pu nanocolloids. This is illustrated by the much lower Pu uptake in batch experiments with 250 μM Pu solutions by commercial AC (see Figure 6.47 in Section 6.3.2 and Figure 6.56 in Section 6.3.3), which is mostly microporous. The larger pores and high surface areas of mesoporous materials are ideal for sorption of large molecules and colloids. For example, C-CS type OMC recently proved to be an excellent adsorbent material for the large toxic bio-molecule microcystin-LR.[287]

The sorption interactions of Pu(IV) colloids with OMCs will be further explored. The current data are insufficient to explain whether the nanocrystals grew onto the C-CS surface, or formed in solution after the redox reaction, then adsorbed to the surface. Perevalov and Molochnikova found polymeric Pu(IV) had a high affinity for oxidized MWCNTs, and suggested the intermolecular interaction occurred through hydrogen bonding between the

oxygens in the Pu polymer and the functional groups at the CNT surface.[236] There could also be a weak electrostatic interaction between the Pu colloids and the π electrons in the carbon basal planes. If oxidation of aliphatic carbon (like in Reactions 6.5 and 6.6) is partially responsible for the reduction of Pu(VI/V) to Pu(IV), then the redox interaction would create more oxygen-containing surface groups for interaction with Pu. Therefore, it will be interesting to compare the sorption interactions of PuO_2 colloids that are formed by adding Pu(VI) to pristine OMCs, to interactions that occur when Pu(IV) colloids are added directly to samples of OMCs.

6.5 Application for facile reduction of plutonium in acidic solutions

An interesting phenomenon was observed in the desorption tests of batch samples of OX CMK', where the Vis-NIR absorbance spectra showed that it was Pu(III) that desorbed in the 1.5 M $HClO_4$. This was unexpected, and follows the trend suggested by the CMK XANES data, in which the Pu was further reduced in more acidic solutions. The spontaneous reduction of Pu in acidic solutions by porous carbons was further explored, as to the author's knowledge there are no previous reports of spontaneous actinide reduction at a carbon surface. Manipulation and control of the oxidation state of plutonium is applicable to almost all processes involving remediation, separation and chemical purification of plutonium, both in industrial and academic laboratory settings. Electrochemical methods using a potentiostat are generally preferred for preparation of the different Pu oxidation states in chemistry laboratories.[117] Reduction of Pu in any oxidation state at a platinum cathode will yield Pu(III), but if the starting oxidation state is Pu(V) or Pu(VI), the reduction is quite slow due to the large overvoltage required for the Pu(V)-Pu(IV) reduction.[117] Reduction by this method is time-consuming and not feasible if there is a large volume of solution to be reduced. Alternative methods generally involve the addition of chemical reducing agents, such as Fe(II),[288] or NO_2^-.[289] However, the addition of chemicals can further complicate the solution chemistry, leading to more purification steps. Thus, the idea of Pu(VI) reduction to a lower oxidation state by simple contact with a solid surface is appealing. Furthermore, the ability to concentrate Pu(VI) from large solutions onto a solid, and then strip the Pu in a lower oxidation state with a small volume of acid for reprocessing would help the laboratory avoid expensive transuranic waste requisitions, with very little time commitment.

Vis-NIR analysis of acidic solutions of plutonium desorbed from C-CS and C-CS-COOH samples is discussed in Section 6.5.1. Initial exploratory investigations of Pu reduction by porous carbon materials were done to see whether or not the sorption of Pu would be necessary for reduction to occur, to test porous carbons having different properties as Pu reductants, and to scope which solution conditions would support the redox chemistry. Batch contact experiments were done with a liquid-to-solid ratio of 200 ± 10 mL/g, by preparing the actinide solutions in the appropriate solution matrix and concentration, and pipetting the solution directly into samples of pre-weighed solid powders. After rocking gently for a given amount of time, the samples were allowed to settle, and then the solution was removed and centrifuged at 7000 rpm for at least 7 minutes before most of the solution was transferred to the cuvette for optical spectroscopy. Aliquots were also measured by LSC to see if any sorption occurred. After measurement the solution was returned to the original polypropylene vial and rocked until the next measurement. The Vis-NIR absorbencies of Pu and Np solution species were monitored for up to 30 days using an OceanOptics S2000 fiber-optic spectrometer, as described in Section 3.3.4. Spectra were collected in absorbance mode by averaging 100,000 scans with an integration time of 6-8 msec, using OceanOptics Spectrasuite software. Reference spectra were stored and

subtracted each time by scanning acid solutions of the same composition, and prepared the same day as the actinide solutions being examined. Quartz cuvettes with a 1 cm path length were used to collect Pu spectra, and were rinsed three times with the appropriate acid in between measurement of different solutions. Disposable plastic cuvettes with a 1 cm path length were used for Np spectra collection. The absorbance spectra were used to identify the oxidation states of Pu present in solution,[109, 116] and control solutions were monitored to ensure that contact with the carbons was responsible for redox activity. All experiments were performed at least twice to ensure reproducibility. Batch contact experiments of various carbon powders, and SBA-15 for comparison, were performed with 1.25 ± 0.05 mM Pu solutions in 1.2-1.3 M $HClO_4$. These results are discussed in Section 6.5.2, along with demonstration of Pu reduction using a column packed with AC. The reaction of Pu with C-CS and oxidized C-CS-COOH were also tested in HCl and HNO_3, presented in Section 6.5.3. Batch contact experiments were also performed with Np(V) and U(VI) in 1.2 M $HClO_4$, and these results are presented in Section 6.5.4.

6.5.1 Vis-NIR spectroscopy of Pu desorbed from carbon samples

Vis-NIR spectroscopy was first used to determine the oxidation state of Pu desorbed from samples of OX CMK' that had 55 ± 5 mg/g ^{239}Pu loaded as Pu(VI) via 1 day of contact with a pH 4, 220 ± 20 µM Pu perchlorate solution. The samples were stripped of Pu by adding 800 µL 1.5 M $HClO_4$ after removal of the bulk liquid phase. Within 1 day, approximately 80% of the Pu returned to the liquid phase. The desorbed Pu showed spectral features of Pu(III), and the experiment was repeated with C-CS and C-CS-COOH, using batch sorption and XAS samples described in Sections 6.3 and 6.4. The results of the sorption and desorption experiments with C-CS and C-CS-COOH OMC were in agreement with what had previously been observed with OX CMK'. Over 99% sorption to both C-CS and C-CS-COOH was observed from 250 ± 13 µM Pu, pH 4 perchlorate samples with ionic strengths of approximately 1 M, after 23 hours contact. From similar samples with lower ionic strengths of 0.13-0.15, over 99% sorption to C-CS-COOH, and 91-97% sorption to C-CS occurred. Under both conditions, the Pu was added as Pu(VI) in concentrated $HClO_4$, and XAS and TEM data showed that the Pu was reduced to the tetravalent state at the carbon surface (see Section 6.4.3). After removal of the bulk liquid phase and 24 hours contact with either 1 M $HClO_4$ or 1 M HCl, the amount of Pu remaining on the solid phase ranged from 14% to 34%. The Vis-NIR absorbance spectra of the Pu desorbed from both materials showed distinct features of Pu(III), whether HCl or $HClO_4$ was used for desorption. Figure 6.76 shows examples of these spectra, along with the spectrum of the Pu(VI) stock solution that was added to the carbon samples.

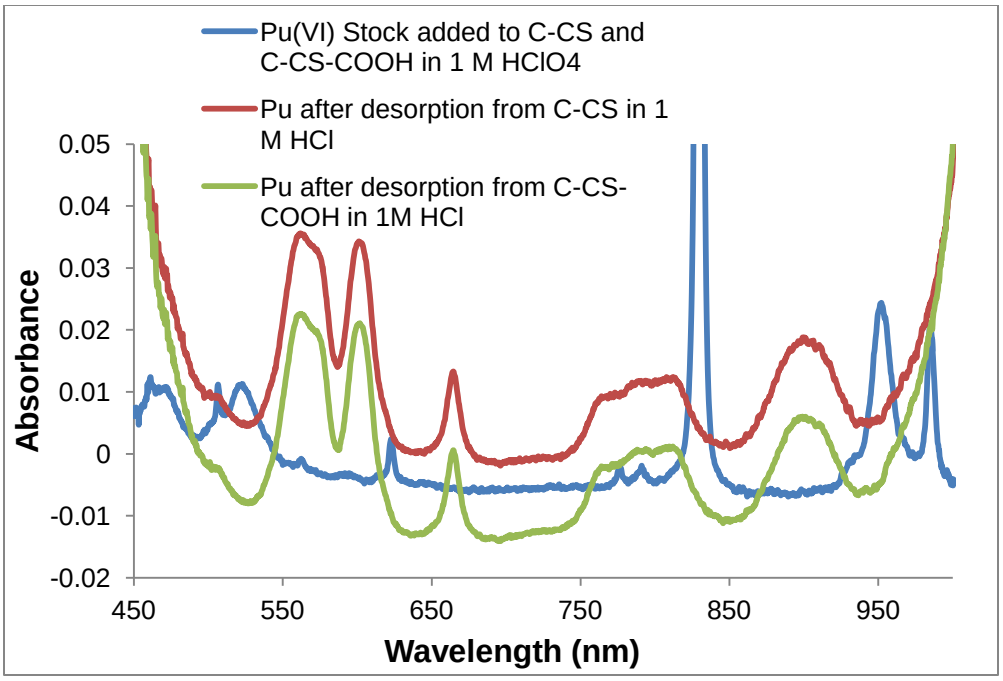

Figure 6.76. Visible-NIR absorbance spectrum of Pu stock (blue), and Pu after 1 day of sorption to C-CS (red) and C-CS-COOH (green) in a pH 4, 250 ± 13 µM Pu perchlorate solution, followed by 1 day of desorption in 1 M HCl. Although the Pu was added to the samples as Pu(VI), the Pu that desorbed from the samples clearly shows spectral features of Pu(III).

The upward sloping absorbance below 500 nm could indicate the presence of some Pu(IV) colloids in the solution along with the Pu(III). However, the spectrometer used does not give reliable absorbance values below 450 nm, so it is difficult to separate instrumental noise from the observation of colloidal species. The features observed below 500 nm and above 950 nm were not always consistent, and could also have contributions from small carbon particles due to incomplete phase separation. Nevertheless, in all spectra of desorbed Pu, only spectral features associated with Pu(III) were observed between 500 and 950 nm, with absorbance values that were consistent with solution concentrations measured by LSC.

The XAS and TEM experiments showed that the Pu sorbed to both C-CS and C-CS-COOH surfaces in pH 4 solution was tetravalent. The Pu that was left on the solid after 24 hours in 1 M acid is likely PuO_2 that did not dissolve completely. The bulk of the Pu did dissolve and/or desorb from the carbon, and was further reduced to Pu(III), indicating that the reduction potentials of the redox-active surface sites decrease with increasing $[H^+]$. This trend was indicated by the XANES data on CMK samples (see Section 6.4.1), but the differences between the Pu oxidation state distributions in different pH samples were too small to draw any conclusions. The further reduction of Pu(IV) to Pu(III) in acidic conditions must be a function of the carbon surface, because the Pu(III/IV) redox couple does not involve H^+ and is thought to be independent of pH.[290] However, it is also possible that Pu(IV) is stabilized in samples with pH ≥ 2 by complexation with surface groups or by crystallization into PuO_2, and the Pu is reduced to Pu(III) in acidic solutions where the crystals dissolve and the surface groups are deprotonated. It may be that different surface sites are involved in redox reactions depending on the solution conditions. In acidic solutions, it is unlikely that oxidation of hydroquinoid moieties is responsible for Pu reduction, because the reduction potentials of these groups increase with

increasing acid concentration,[275, 282] and the reverse of Reaction 6.4 would be unfavorable in acidic solutions according to Le Chatelier's principle.

The fact that the carbon surfaces seem to reduce Pu(VI) only to Pu(IV) could be advantageous for environmental remediation efforts. Because Pu(IV) is far less soluble in aqueous media than Pu(V) or Pu(VI), there is interest in studying minerals, microbes, or other natural organic matter that create reducing conditions. The migration of PuO_2 colloids is a major mode of Pu mobility through the environment,[291] therefore stable, solid materials that reduce the higher, more soluble oxidation states to Pu(IV) and also strongly sorb PuO_2 colloids might be desirable for creating barricades around contaminated sites or waste repositories. Ordered mesoporous carbon shows great potential for such applications, as they are notoriously stable in a wide pH range and can be synthesized into large bricks on the kilogram scale.[217] In a laboratory setting, OMC monoliths that can adsorb and concentrate Pu from waste solutions would prove useful for recovering valuable isotopes, and for reducing the specific activity of transuranic waste, thereby making it less expensive to process. The dissolution of Pu(IV) colloids using porous carbon solids will be further explored. The polymerization of Pu(IV) is generally considered irreversible because of the difficulty in dissolving the colloids.[111] Therefore, if dissolution of colloids can be catalyzed by simple contact with a solid surface, that would be very useful in laboratory settings.

6.5.2 Reduction of Pu(VI) by various carbon substrates in $HClO_4$

Samples of 1.25 ± 0.05 mM Pu in 1.2-1.3 M $HClO_4$ were examined by optical spectroscopy after contact with solid powders (liquid-to-solid ratio of 200 ± 10 mL/g), to see if the sorption step was actually necessary in order for the redox interaction between OMC and Pu(VI). The physical and chemical properties of the carbon powders are tabulated in Tables 6.2 and 6.3, respectively. C-CS and C-CS-COOH represent pristine and highly oxidized OMCs with high surface areas, and oxidized and untreated FDU-16 were tested as highly ordered mesoporous carbons with lower surface areas. Activated carbon has high surface area, but is mostly microporous and has even fewer functional groups on its surface than C-CS. The SBA-15 mesoporous silica was not expected to participate in redox chemistry, and was tested as a secondary control. The oxidized OMCs have a high density of carboxyl surface groups, but also have more incompletely oxidized oxygen-containing groups than their untreated counterparts. Thus, the oxidized materials might be expected to be stronger reductants if oxygen-containing groups are the primary electron source. The Pu concentration of these samples was monitored by LSC, and no significant sorption to these materials was observed under the acidic conditions.

The absorbance spectra collected from a control sample of 1.25 ± 0.05 mM Pu(VI) in 1.2 M $HClO_4$, measured periodically over 30 days are shown in Figure 6.77. The Y-axis is scaled such that the Pu(VI) peak at 830 nm is cut off, which is necessary to observe spectral features of other oxidation states because their extinction coefficients are one order of magnitude lower (see Section 3.3.4). Initially the spectrum is completely consistent with that of pure Pu(VI). On the 12^{th} day a very slight increase in absorbance can be observed around 570 nm, corresponding to the introduction of Pu(V) in solution. This absorbance peak became more prominent on the 20^{th} and 30^{th} day, as did the 470 nm and 650 nm peaks, which indicate the presence of Pu(IV). The upward slope toward the UV region could indicate the presence of Pu(IV) colloids in solution. The majority of the Pu remains in the hexavalent state over the 30 day period, and the slow

introduction of Pu(V) and Pu(IV) is consistent with the expected pattern of radiation-induced auto-reduction.[292] The appearance of these features is very similar in the spectra of solution after contact with the SBA-15. As expected, no redox reaction between the Pu and the silica was observed.

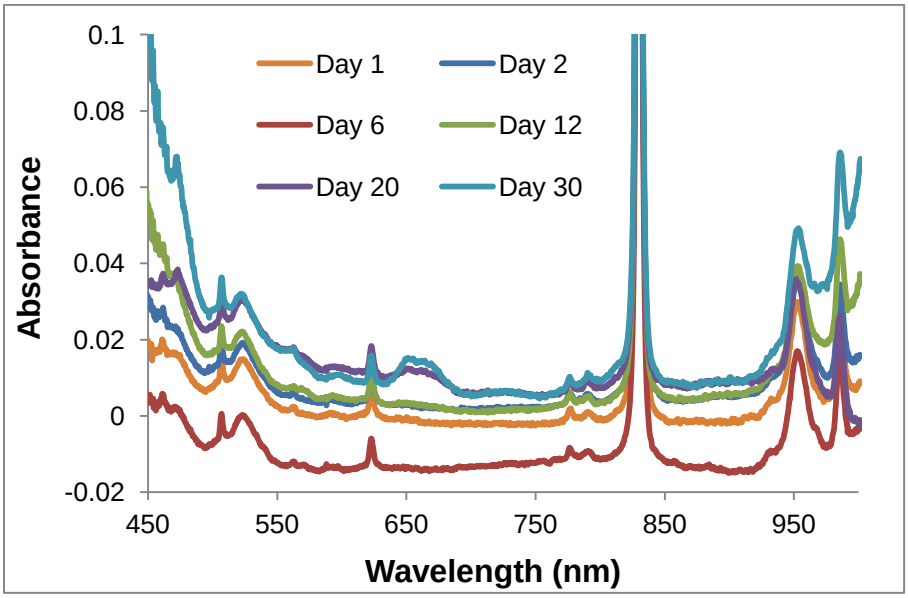

Figure 6.77. Vis-NIR absorbance spectra of 1.25 mM Pu(VI) solution in 1.2 M $HClO_4$. Th slow indroduction of Pu(V) and Pu(IV) solution species is attributed to radiation-induced autoreduction of Pu(VI).

The absorbance spectra of solutions of 1.25 ± 0.05 mM Pu(VI) in 1.2 M $HClO_4$, measured after various amounts of time in contact with C-CS or C-CS-COOH are shown in Figures 6.78 and 6.79, respectively. In both samples the Pu(VI) is completely reduced to Pu(III), which is clearly due to contact with the carbons. The rate of reduction is faster with the unoxidized C-CS, where only the first spectrum, taken after 22 minutes mixing and 57 minutes total contact time, shows a small Pu(VI) absorbance peak at 830 nm. By the time the second absorbance spectrum was measured, after only 42 minutes of mixing, the only oxidation state clearly detected was Pu(III), and the absorbance spectrum did not change over the following days. In the spectra of the solution in contact with C-CS-COOH, the 830 nm Pu(VI) peak decreased over several hours, and the first spectrum that showed only Pu(III) was measured after 1 day of contact. The faster reaction with the unoxidized surface could indicate that the oxidation of aliphatic carbon as in Reactions 6.5 and 6.6 is partially responsible for Pu reduction, because the C-CS initially has few functional groups, but has a much higher surface area than C-CS-COOH. Whatever the electron source may be, both the C-CS and its highly oxidized counterpart reduce Pu(VI) to Pu(III) completely within one day. Under these conditions, this represents 0.75 meq electrons donated per g carbon, although the full capacity for reduction has not been determined.

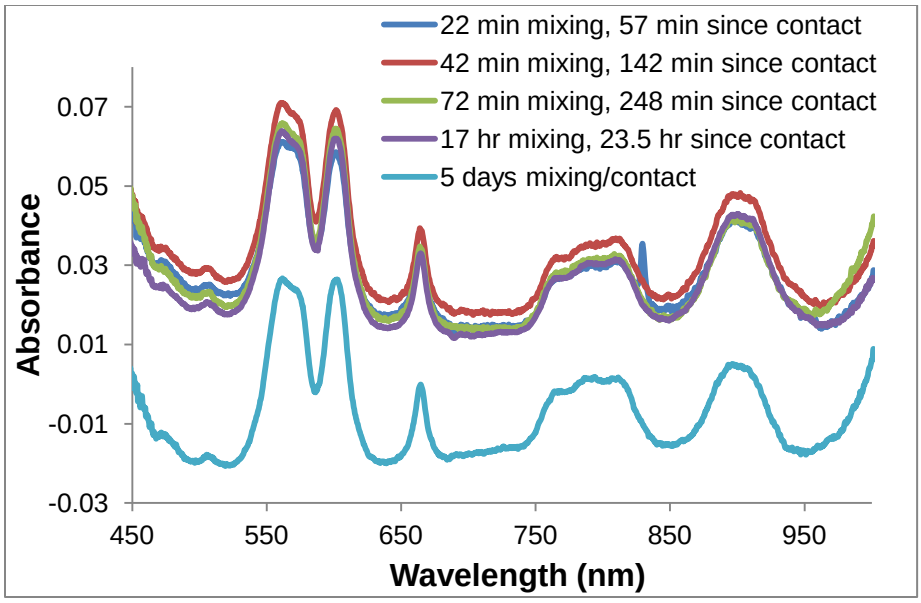

Figure 6.78. Vis-NIR absorbance spectra of 1.25 mM Pu(VI) solution in 1.2 M $HClO_4$, after contact with C-CS mesoporous carbon. Most of the Pu(VI) is reduced to Pu(III) within the first hour after contact, and after 42 minutes mixing only Pu(III) is detected in solution.

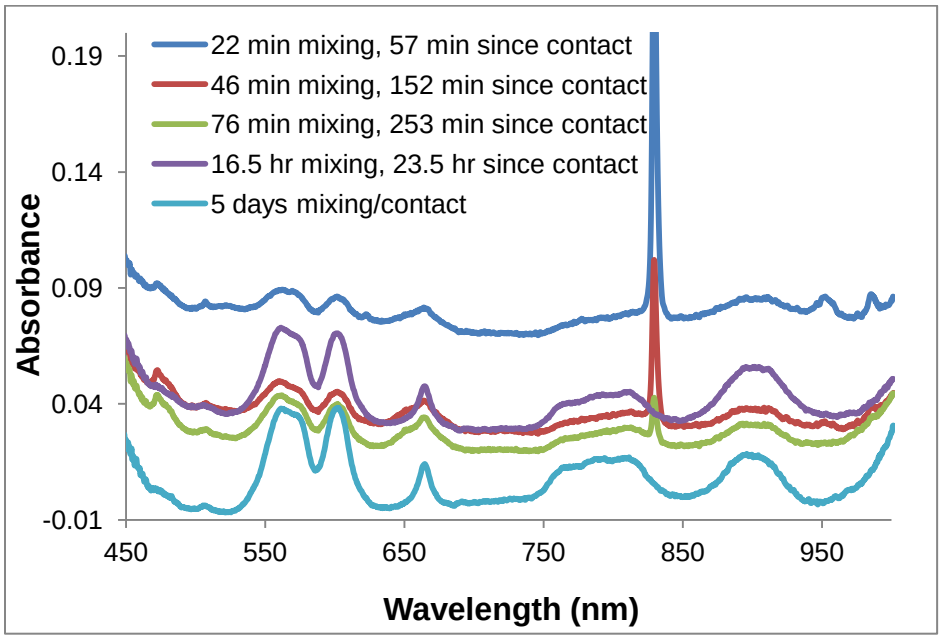

Figure 6.79. Vis-NIR absorbance spectra of 1.25 mM Pu(VI) solution in 1.2 M $HClO_4$, after contact with C-CS-COOH mesoporous carbon. It appears to take several hours of contact for the Pu(VI) to be completely reduced to Pu(III).

The absorbance spectra of solutions of 1.25 ± 0.05 mM Pu(VI) in 1.2 M $HClO_4$ were measured after various amounts of time in contact with FDU-16, FDU-16-COOH, and activated carbon. All of the spectra are not shown, for brevity, but the results are summarized in Table 6.8. Eventually all of the Pu(VI) in the FDU-16 and FDU-16-COOH samples was reduced, mostly to Pu(III), but the reduction was significantly slower than with the C-CS carbons. The absorbance

spectrum of the Pu sample after one day of contact with FDU-16 still shows trace Pu(VI) in solution, but after 5 days contact the Pu(VI) was completely reduced to Pu(III), and possibly a small amount of Pu(IV). After 5 days contact with FDU-16-COOH there was still a trace of Pu(VI) in solution, and the spectrum after 11 days contact showed features of Pu(III) and Pu(IV). As with C-CS and oxidized C-CS-COOH, the oxidized FDU-16-COOH is slower to reduce Pu than the as-synthesized FDU-16. It is still unclear whether this is only due to the reduced surface area after the oxidation treatment, or if the carboxyl groups are also slowing the overall rate of reduction by re-oxidizing reduced Pu ions. The most likely reason for the dramatic difference in rate between the C-CS and FDU-16 is that the former has a much larger surface area. However, the oxidized C-CS-COOH completely reduced the Pu(VI) faster than the FDU-16, even though the BET surface areas are similar. Therefore, surface chemistry and/or pore structure must also be considered.

Table 6.8. Summary of Pu oxidation state changes in 1.25 mM Pu, 1.2-1.3 M $HClO_4$ solutions after batch contact with porous solids.

Solid	Initial ox. state	Final ox. state	Time required for reduction
None	(VI)	Mostly (VI), some (IV)/(V)	12-30 d
SBA-15	(VI)	Mostly (VI), some (IV)/(V)	12-30 d
FDU-16	(VI)	Mostly (III), some (IV)	1-5 d
FDU-16-COOH	(VI)	Mostly(III), some (IV)	$\geq$ 5 d
C-CS	(VI)	(III)	$\leq$ 1 hr
C-CS-COOH	(VI)	(III)	4 hr
Activated carbon	(VI)	(III)	1 hr

The first spectrum measured after 22 minutes mixing with AC was very similar to the corresponding spectrum measured after contact with C-CS mesoporous carbon. These results indicate that the ordered mesostructure does not contribute to improving the redox reaction with Pu in acidic solutions. Both C-CS and AC have high surface areas, which seems to be important for a rapid redox reaction to occur. The results with AC suggest that a microporous carbon may be just as effective as a mesoporous carbon for reducing Pu. The AC has very few functional groups on its surface (see FTIR spectrum in Figure 6.8), so the rapid reduction of Pu by AC indicates that the direct oxidation of carbon, and/or oxidation of C-H groups are primarily responsible for the reducing power of carbons in acidic solutions. In summary, the contact time required for complete reduction of Pu appears to decrease with higher surface area, and increase with carbon surface oxidation. The pore size and ordered structure of the carbon have little to no impact on the redox reaction if the surface area is high.

A proof-of-principle experiment with AC was done to see if oxidized Pu solutions could be reduced by passing through a column packed with porous carbon particles. The column has the advantage of simplicity and complete phase separation. Approximately 30 mg of activated carbon was packed into a glass column (2 cm x 2.5 mm) as a slurry in 1 M $HClO_4$, and solutions

of Pu (both 1.3 ± 0.05 mM Pu(VI) in 1.24 ± 0.05 M $HClO_4$ and 1.10 ± 0.05 mM Pu(VI) in 1.20 ± 0.05 M $HClO_4$) were reduced by passing through the column. Figure 6.80 shows the Vis-NIR absorbance spectra of the 1.3 ± 0.05 mM Pu in 1.24 ± 0.05 M $HClO_4$ both before and after passing through the AC column, and clearly illustrates that Pu(VI) was reduced to Pu(III) by passing through the column of AC particles. No preconditioning or changes of solution matrix were necessary. With gas pressure the elution rate was ~10 seconds per drop, and it took 13 minutes to pass 800 µL of solution through the column. Thus, it was demonstrated with AC that a column packed with porous carbon is a quick, clean and convenient way to reduce oxidized Pu to Pu(III) in acidic solutions.

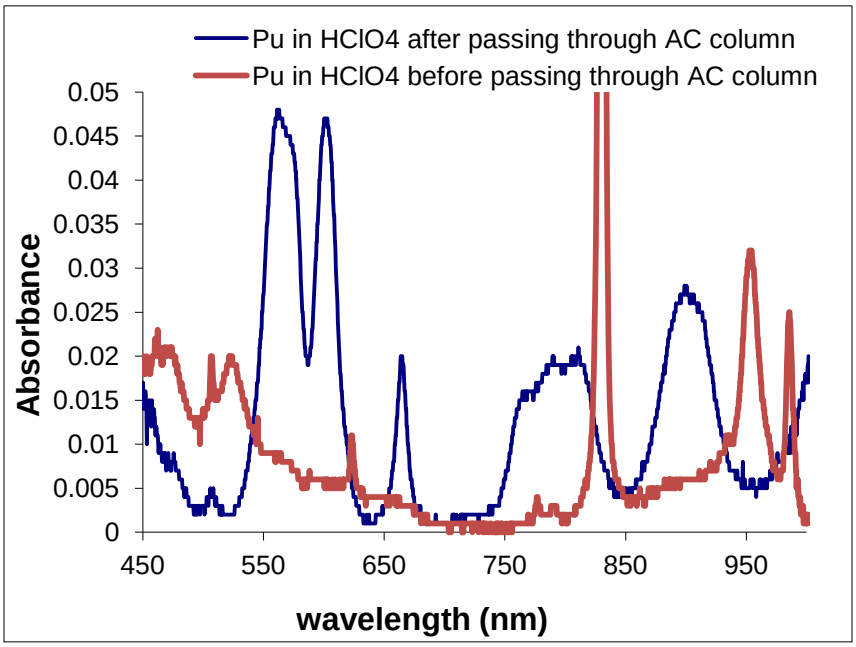

Figure 6.80. Vis-NIR absorbance spectra of a 1.3 ± 0.05 mM Pu, 1.24 ± 0.05 M $HClO_4$ solution, both before and after passing through the AC column. Pu(VI) was reduced to Pu(III) by passing through the AC column.

6.5.3 Reduction of Pu by C-CS carbons in HCl and HNO_3

Samples of C-CS and C-CS-COOH were prepared with 1.25 ± 0.05 mM Pu in other acidic matrices, to test the versatility of the redox reaction. For brevity, example absorbance spectra are only shown from the control and C-CS samples, and the results of the solution matrix tests are summarized in Table 6.9. Figure 6.81 shows optical absorbance spectra of a solution of Pu(VI) in 1.00 ± 0.05 M HCl, and 0.30 ± 0.05 M $HClO_4$, monitored over time with no solid (a), and after contact with C-CS (b). This solution was prepared by adding Pu(VI) stock solution in concentrated $HClO_4$ to 1 M HCl. The shoulder on the 830 nm peak in Figure 6.81a may be attributed to a Pu(VI) chloride complex. Without contact with any solid, the spectrum did not change significantly over the course of 30 days. This is consistent with previous observations that the presence of chloride greatly slows the rate of auto-reduction in Pu solutions.[292] Within one day of contact with either C-CS or C-CS-COOH, the Pu(VI) in this solution was reduced to Pu(III). This result suggests that the presence of chloride has little to no effect on the redox reaction between Pu and the carbon surface, and that if ClO_4^- is involved, high concentrations are not necessary.

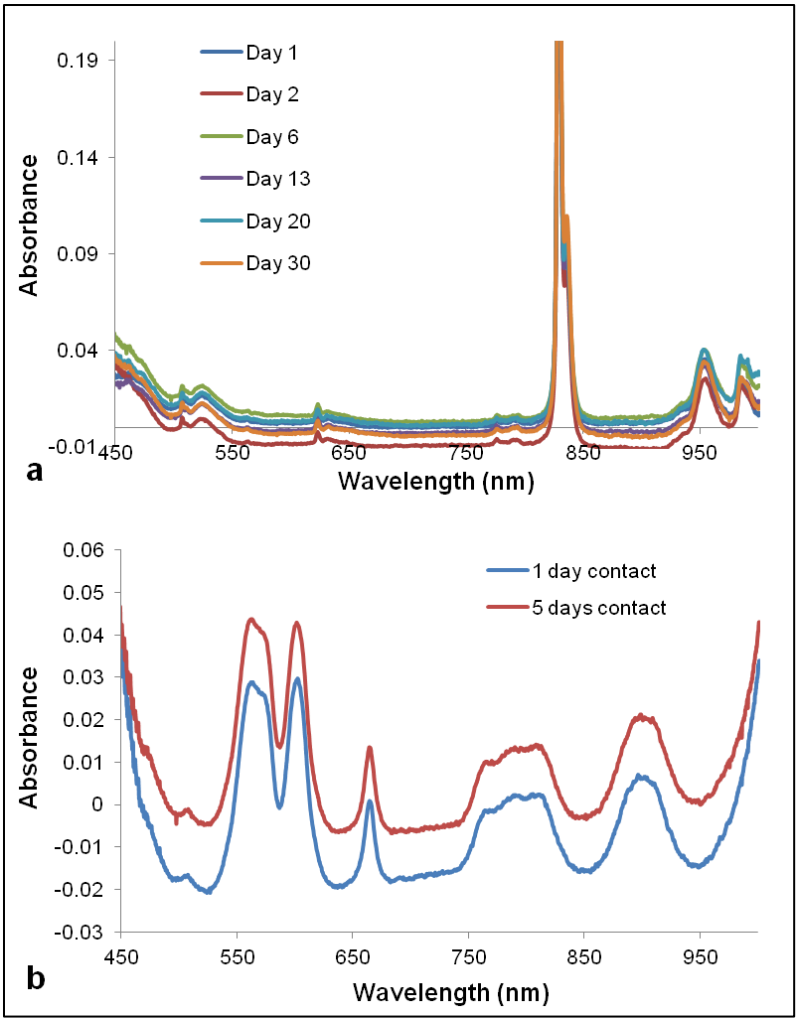

Figure 6.81. Vis-NIR absorbance spectra of 1.25 mM Pu(VI) solution in 1 M HCl, 0.3 M $HClO_4$ with no solid (a) and in batch contact with C-CS OMC powder (b). The Pu(VI) in solution is stable over the course of 30 days, but is reduced to Pu(III) within one day of contact with C-CS.

Spectra of a solution of Pu in 1.45 ± 0.05 M HCl monitored over time with no solid (a), and after contact with C-CS (b) are shown in Figure 6.82. The spectra shown in Figure 6.82a indicate that the solution contained a mixture of Pu(III) and Pu(IV), and the features of this spectrum did not change over the course of 30 days. Within one day of contact with C-CS or C-CS-COOH, all the Pu(IV) in solution was reduced to Pu(III) (Figure 6.82b). This reduction is easier to achieve than that of Pu(VI), but these results still confirm that the presence of perchloric acid is not necessary in order for Pu to be reduced by carbon surfaces.

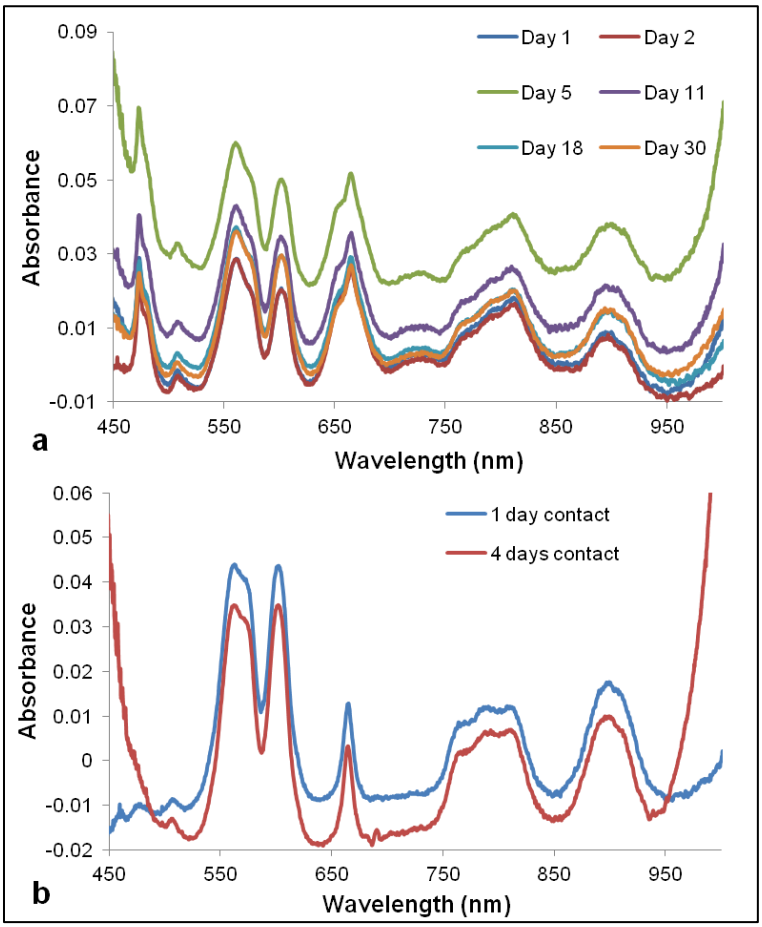

Figure 6.82. Vis-NIR absorbance spectra of 1.25 mM Pu solution in 1.45 M HCl with no solid (a) and after contact with C-CS OMC powder (b). The Pu in solution appears to be a mixture of Pu(III) and Pu(IV), and the spectral features do not change significantly over the course of 30 days. The Pu(IV) that was present in the original solution was reduced to Pu(III) within one day of contact with C-CS.

Figure 6.83 shows Vis-NIR absorbance spectra from a solution of Pu in 1.3 M HNO_3, monitored over time with no solid (a) and after contact with C-CS (b). Nitric acid is an oxidizing solution, and slowed the reduction of Pu dramatically compared to the $HClO_4$ matrix. Pu redox chemistry is complicated by the reduction of NO_3^- to NO_2^-. In the absence of any solid, the solution is a mixture of Pu(VI) and Pu(IV), and the composition did not appear to change over the course of 30 days (Figure 6.83a). In the presence of C-CS or CS-COOH, the Pu(VI) was slowly reduced over time, and after 29 days contact, Pu(IV) dominates the solution, although a very small amount of Pu(VI) remains (Figure 6.83b). The reduction was initially faster when in contact with the C-CS compared to the C-CS-COOH, but after 29 days the compositions of the

two Pu solutions were similar. It appears that with prolonged contact with a high-surface area carbon material, all the Pu in the nitric acid solution would go to Pu(IV), although this has not been experimentally verified. Plutonium probably cannot be reduced to Pu(III) by this method in nitric acid because both NO_3^- and NO_2^- behave as oxidizing agents toward Pu(III), and the Pu(IV) is also stabilized by nitrate complexation.

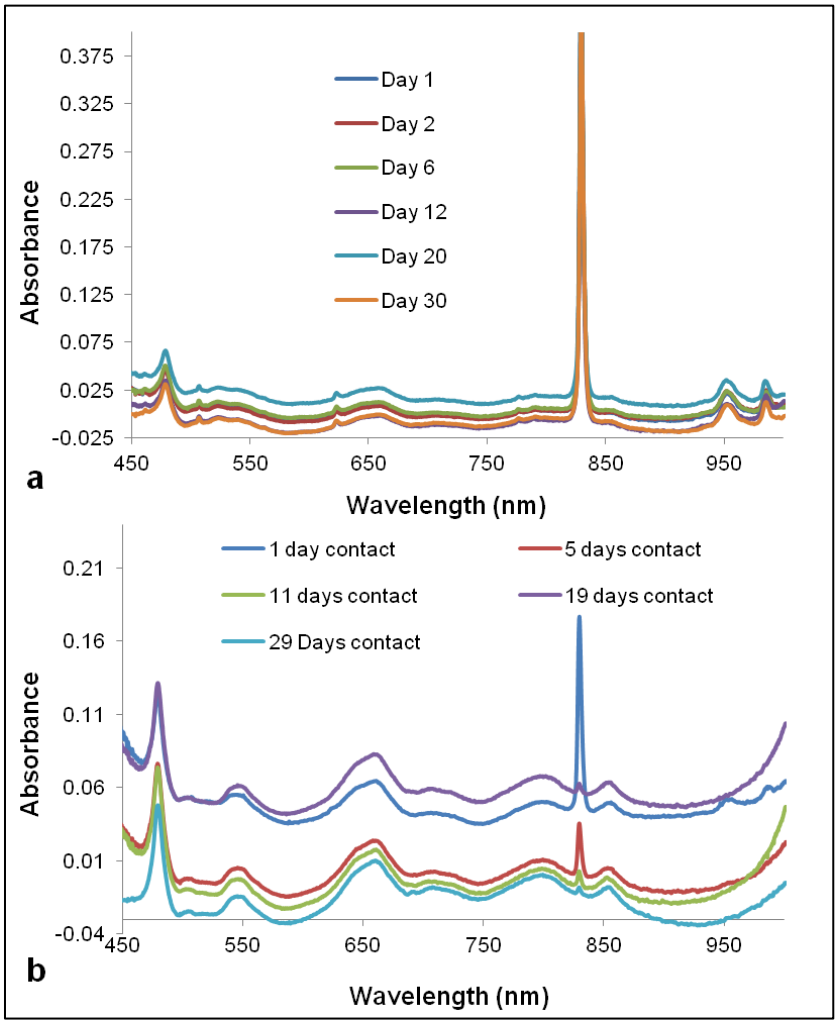

Figure 6.83. Vis-NIR absorbance spectra of 1.25 mM Pu solution in 1.3 M HNO_3 with no solid (a), and in contact with C-CS OMC powder (b). The Pu in solution appears to be a mixture of Pu(VI) and Pu(IV), and the spectral features do not change significantly over the course of 30 days without the carbon. The composition of the mixture shifts toward Pu(IV) as the Pu(VI) is slowly reduced over 29 days of contact with C-CS OMC.

The results presented above are summarized in Table 6.9, and show that the extent and rate of Pu reduction by porous carbon materials depends on the solution matrix. The most important features of the carbon material for this spontaneous reaction seem to be surface area and the surface chemistry. The carbonization temperature is likely important too, as it affects the conductivity of carbon solids, but these effects were not tested here. The solid carbon materials seem to be stronger reducing agents toward Pu than humic acids, which have been found to reduce Pu(VI) in 1 M $HClO_4$ to Pu(IV) with a half-life of 10 days.[278]

6.5.4 Reduction of Np(V) and U(VI) by carbon substrates in $HClO_4$

Preliminary experiments with neptunium were performed by contacting C-CS and C-CS-COOH with 1.25 ± 0.05 mM $^{237}Np(V)$ in 1.3 M $HClO_4$. The Np was purified from its daughter products by Deborah Wang, via anion exchange, and refluxed in $HClO_4$ to obtain the pure Np(V) stock solution. Figure 6.84 shows the absorbance spectrum of the control solution monitored over time with no solid material (a) and after contact with C-CS (b). The large absorbance peak at 980 nm corresponds to Np(V),[293] which appears to be stable in the solution over the 30 day time span, as shown in Figure 6.84a. Contact with C-CS or C-CS-COOH reduces much of the Np(V) to Np(IV), as indicated by suppression of the 980 nm peak, and in-growth of peaks at 723 nm and 960 nm.[293] In both samples of C-CS and C-CS-COOH, a steady-state condition was reached and the mixture of Np(V) and Np(IV) did not change further in composition. As was observed with Pu reduction, the reduction of Np by C-CS (within one day) was faster than that by C-CS-COOH (within 10 days), but the final composition of Np oxidation states was the same for both samples.

Table 6.9. Summary of oxidation state changes of 1.25 mM Pu or Np solutions upon batch contact with C-CS and C-CS-COOH.

Solution	Initial actinide ox. state	Ox. State after C-CS, (rxn time)	Ox. State after C-CS-COOH, (rxn time)
Pu in 1M HCl, 0.3 M $HClO_4$	VI	III (≤ 1 d)	III (≤ 1 d)
Pu in 1.5 M HCl	III/IV	III (≤ 1 d)	III (≤ 1 d)
Pu in 1.3 M HNO_3	IV/VI	IV (29 d)	IV (≥ 29 d)
Pu in 1-1.3 M $HClO_4$	IV and IV colloid	III (≤ 24 h TBD)	III (≤ 24 h TBD)
Pu in 1 M HCl	IV and IV colloid	III (≤ 24 h TBD)	III (≤ 24 h TBD)
Np in 1.3 M $HClO_4$	V	IV > V (≤ 26 hr)	IV > V (4-10 d)

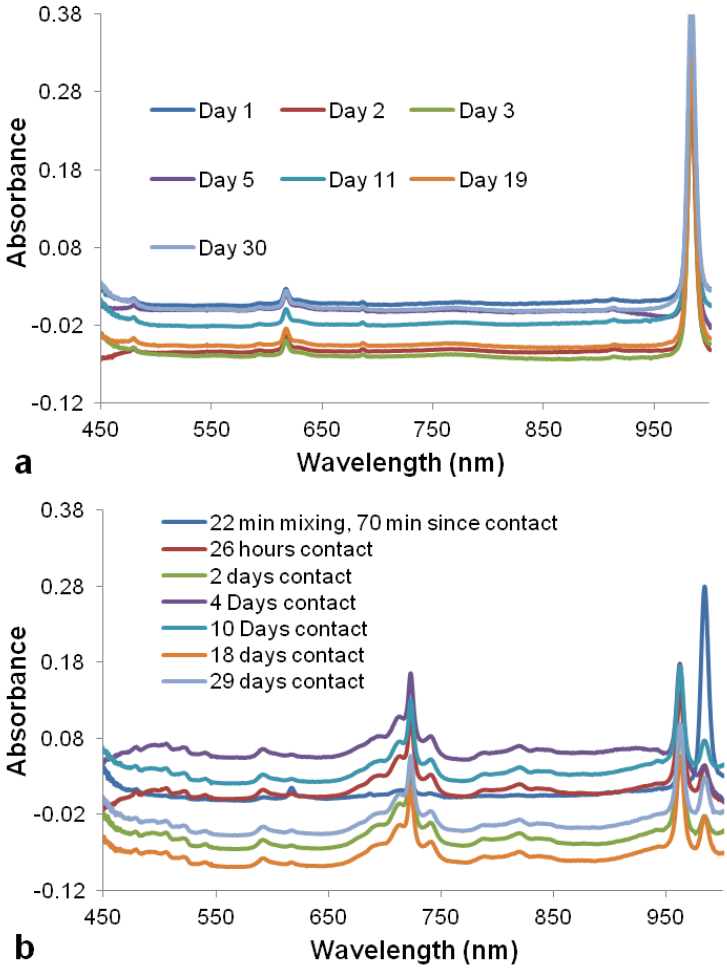

Figure 6.84. Vis-NIR absorbance spectra of 1.25 mM Np(V) in 1.3 M $HClO_4$ monitored over time with no solid (a), and in contact with C-CS OMC powder (b). The Np(V) is stable in solution over the 30 day time period alone in solution. Much of the Np(V) is reduced to Np(IV) within the first day of contact with C-CS, after which the mixture of Np(IV) and Np(V) does not change in composition.

The standard reduction potential for NpO_2^+ is lower than that of PuO_2^{2+},[290, 294] and previous work studying actinide reduction by humic substances generally report more reduction of Pu than of Np. The reduction of Np in environmentally relevant conditions is of great interest due to the mobility of Np(V) and the very long half-life of ^{237}Np. Nash *et al.* showed that solid humic acid reduced Np(VI) to Np(V) in solutions ranging from pH 7 to 11, where Pu(VI) was reduced to Pu(IV).[278] A study of Np(V) reduction and complexation by "designer" quinonoid-enriched humic derivatives in anaerobic pH 4.7 solutions found that the Np(V) was slowly reduced to Np(IV) until a steady mixture of both oxidation states was reached.[274]

Preliminary experiments contacting AC, C-CS, and C-CS-COOH powders with a solution of approximately 1.2 mM U(VI) in 1.2 M $HClO_4$ were attempted by Eva Uribe. The results were inconclusive because the solution concentration of U was too low to observe distinctive spectral features of the different oxidation states. Considering the results with Np, it was expected that the porous carbons were not able to reduce U(VI) to lower oxidation states. Standard reduction potentials in 1 M acidic solutions for the NpO_2^+/Np^{4+} redox couple between

0.57 and 0.75 V vs. NHE have been reported, and the standard redox potential for the PuO_2^{2+}/Pu^{3+} couple is between 1.002 and 1.022 V vs. NHE.[294] Uranium is much harder to reduce, with a standard redox potential between 0.163 and 0.05 V vs. NHE for the UO_2^{2+}/UO_2^{+} couple. Based on the results with Np(V) and Pu(VI), the standard reduction potentials of the redox active sites on ordered mesoporous carbon surfaces may be around 0.5 V in 1.2-1.3 M $HClO_4$. However, the carbon surfaces can remarkably overcome the large overvoltage that is usually required for reduction of PuO_2^{+} or NpO_2^{+} to the tetravalent state. This may be attributed to the electrocatalytic property of solid carbon, and has not been reported previously. The electrocatalytic activity of platinum electrodes modified with single-walled carbon nanotubes toward the Pu(IV)/Pu(III) redox couple was recently observed,[295] and this might be explored with OMCs as well. Solid porous carbons appear to be stronger reducing agents toward Pu than humic acids, and offer a convenient way to reduce oxidized Pu in acidic solutions, which might be useful in a variety of applications. Unfortunately, this method is not likely to be applicable in many industrial processes, such as PUREX, because these processes occur in nitric acid, which hinders the reduction of Pu by carbon.

7 Conclusions

7.1 Closing remarks

The experimental results presented in Chapters 5 and 6 of this dissertation increased our understanding of the interactions of plutonium and lanthanides with ordered mesoporous materials, and laid a foundation for more experiments with ordered mesoporous materials and actinides that are ongoing in the Nitsche group. From the investigation of organically modified SBA-15, much was learned about the optimal conditions for synthesis and batch sorption experiments with mesoporous materials. The complexation of PuO_2^{2+} by Ac-Phos-SBA-15 was investigated for the first time, and the material showed high Pu capacity in acidic solutions. Other new functionalized SBA-15 materials indicated potential for oxidation state selectivity. The fundamental redox and sorption interactions between oxidized Pu and both pristine and oxidized porous carbon powders were extensively investigated for the first time. The results indicate that all porous carbon materials behave as reducing agents toward Pu, but ordered mesoporous carbons are much better than amorphous activated carbon for sorption of Pu. High Pu sorption capacities are achieved by both pristine and oxidized OMCs, but by different mechanisms.

The functionalization of SBA-15 ordered mesoporous silica via self-assembly of small organosilane ligands under toluene reflux was optimized, but the best reaction conditions may depend on the size and hydrolytic stability of the individual silane. Four different organically modified SBA-15 materials were prepared, with silane densities ranging from 1.1 to 4.1 mmol silane per g SBA-15. The challenges associated with functional silane synthesis were demonstrated with the Ac-Phos silane molecule, but ultimately successful synthesis was achieved. Batch sorption experiments with functionalized SBA-15 samples in contact with solutions of Eu(III), Zr(IV), Ce(III), Pu(IV) and Pu(VI) demonstrated their relative affinity for these target species. It was determined that little to no sorption of Eu(III), Ce(III), and Pu(VI) to SBA-15 occurred in solutions with pH $\leq$ 5, but very high Zr(IV) sorption to unfunctionalized SBA-15 was observed in solutions with pH 0-2. The maleamic acid derived TESPMA-SBA-15

showed high sorption of Pu(VI) and Eu(III) in solutions with pH greater than 4, but the sorption of Pu(VI) was kinetically hindered and took 9 days to achieve. XANES data indicated that the TESPMA-SBA-15 reduces oxidized Pu to the tetravalent state, and EXAFS data showed that the Pu(IV) was sorbed, not precipitated. MHAPS-SBA-15 and AGAPS-SBA-15 may show selectivity for Pu(IV) over Pu(VI), but further studies are needed to verify this. Ac-Phos-SBA-15 bound 100% of all target species under the studied conditions, demonstrating little to no selectivity. Sorption of Pu by Ac-Phos-SBA-15 was rapid, and complete within two minutes. The Pu(VI) uptake capacity of Ac-Phos-SBA-15 was determined in batch experiments with a high liquid-to-solid ratio of pH 1.8 perchlorate solution to be 30 ± 3 mg Pu per g Ac-Phos-SBA-15. However, it was established that the liquid-to-solid ratio in batch experiments with mesoporous materials should be kept below 2000 mL/g for reproducible results. The complexation of Pu by Ac-Phos-SBA-15 was only partially reversible, and it was also established that prolonged contact with acid partially degrades the functionalized SBA-15 material. XANES data showed that there are no redox reactions between Ac-Phos-SBA-15 and Pu. Relativistic DFT modeling studies by collaborators postulated a 2:1 bidentate octahedral complex of PuO_2^{2+} by Ac-Phos-SBA-15. Careful fitting of EXAFS data to this model indicated that this is a reasonable structure to describe the experimental system.

Three different mesoporous carbon materials, and their oxidized counterparts were characterized by a variety of techniques, and their Pu sorption capabilities were compared to that of a commercial activated carbon. Batch studies with initially Pu(VI) solutions in a 0.1 M $NaClO_4$ matrix were performed to investigate pH dependence, sorption kinetics, Pu uptake capacities, competition with EDTA in solution, Pu desorption, and effects of ionic strength. The carbon powders showed affinity for Pu in solutions across a wide pH range, and the oxidized carbons C-CS-COOH followed by OX CMK were most effective in acidic solutions. The mesoporous carbons greatly outperformed the activated carbon in terms of Pu sorption kinetics and uptake capacity. The 23-hour Pu uptake capacity of the OMC materials was measured in pH 4 solution to be at least 60 ± 5 mg ^{239}Pu per g CMK carbon, compared to 12 ± 5 mg ^{239}Pu per g activated carbon. Desorption and/or dissolution of Pu from all carbon powders was achieved by further acidifying the samples. Batch kinetic data suggests that complexation of Pu cations by oxygen-containing surface groups is the preferred binding mechanism, and occurs within 20-60 minutes, depending on the excess of surface sites. After functional groups are saturated, additional Pu sorption occurs by surface precipitation or sorption of Pu(IV) colloids, and the formation of colloids may be the rate-limiting step for Pu sortion to pristine OMCs.

Spectral fits of the Pu L_{III} XANES data from XAS measurements to known oxidation state standards show that Pu associated with the OMC surfaces is tetravalent, and both untreated and oxidized OMCs reduce Pu(VI) and Pu(V) to Pu(IV) in solutions with pH 2-7. Samples with pH 6 and above still had 10-20 % Pu(V) present, while in the lower pH samples 100% of the Pu was reduced to Pu(IV). Fitting of EXAFS data suggests that in oxidized OMC samples most of the Pu(IV) is sorbed to the surface rather than precipitated. TEM analysis of pristine C-CS samples loaded with Pu showed PuO_2 nanocrystals sorbed to the surface, and these were further evidenced by strong Pu-Pu scattering features in the EXAFS data.

Oxidized C-CS-COOH mesoporous carbon is a fast and effective scavenger of Pu and Eu. This material removes cations from aqueous solutions via chemisorption, and the monolayer sorption capacity for Eu(III) in pH 4 solution (0.91 mmol Eu per g C) is higher than those reported previously for most other carbon-based materials.[231, 240, 241] Pristine C-CS showed a low

affinity for Eu, but a large capacity for Pu sorption. XAS and TEM data showed that Pu(VI/V) was reduced to the tetravalent state by both oxidized and untreated C-CS. The oxidized C-CS-COOH complexed monomeric Pu(IV) and/or small amorphous Pu oxide clusters, preventing the formation of crystalline PuO_2 in pH 4 solution. Pristine C-CS shows high sorption affinity for PuO_2 nanocrystals (~3 nm diameter) formed at or near the carbon surface. The larger pore sizes of OMCs compared to AC make the former ideal for sorption of colloidal Pu. This apparent selectivity for Pu uptake is a novel finding of pristine carbon surfaces, and could be valuable for a variety of applications involving separation or sequestration of actinides.

The redox activity of porous carbon powders was also investigated with batch contact experiments in a variety of acidic solutions. Plutonium associated with OMC surfaces can be desorbed as Pu(III) in 1 M HCl or $HClO_4$. Solutions of Pu(IV) or Pu(VI) in 1-1.5 M HCl or $HClO_4$ are reduced to Pu(III) when put in contact with AC or OMCs, both untreated and oxidized. The contact time required for complete reduction of Pu decreases with higher surface area, and generally increases with carbon surface oxidation. The pore size and ordered structure of the carbon do not appear to influence the reaction if the surface area is high. It was demonstrated with AC that acidic solutions of oxidized Pu can easily be reduced to Pu(III) by being passed through a column packed with porous carbon particles. This is a fast (~ 16 min per mL solution) and convenient way to reduce oxidized forms of Pu without changing the solution matrix, adding chemical reagents, or using a potentiostat.

7.2 Future work

There are several possible avenues for continuation of the work presented in this dissertation, and here a few ideas are presented. Some of these experiments will be completed soon within the Nitsche group.

Because there is negligible background sorption of many species to mesoporous silica, it may be a good substrate for the development of novel resins for extraction chromatography. This is where the current focus of work in this area by other graduate students within the Nitsche group lies. The utility of functionalized mesoporous materials for actinide extraction will be limited by two major factors: the synthetic feasibility of functionalized materials that will show high selectivity for actinides of interest, and the hydrolytic stability of these materials. Both of these issues are currently being investigated in the Nitsche group, with particular interest in the extraction of trivalent actinides. With regards to the specific materials discussed in chapter 5, there are a few experiments that may be of interest. The possible selectivity of AGAPS-SBA-15 and MHAPS-SBA-15 for Pu(IV) may be further explored, but first their syntheses should be repeated until the products can be truly verified. Batch sorption experiments with Pu(IV) and other actinide species should be done under identical conditions for valid comparison. Also the batch uptake of target species in solutions containing competing ions must be performed to see if the materials demonstrate selectivity. If so, the materials may be packed into a glass column to test their application for actinide separations. Analysis of functionalized SBA-15 samples loaded with target actinides using XAS, NMR and FTIR spectroscopies may help to better characterize the complexes involved with actinide binding.

The conductivity and electrocatalytic activity of mesoporous carbons may render them suitable substrates for the development of electrochemical actinide sensors. However, further

characterization of their fundamental interactions with actinides should be done first. Exploratory batch sorption experiments may be done with Np(V), Am(III), Th(IV), U(VI) and Pu(IV) solutions in contact with pristine and oxidized OMCs to look for different sorption behavior among actinides of different oxidation states. Batch sorption should be tested in solutions other than 0.1 M $NaClO_4$, and in the presence of competing ions and complexing agents. After the interactions of actinides with untreated and oxidized OMCs are established, the OMC surfaces may be functionalized with oxidation state specific complexing ligands. The unique combination of the carbon redox activity and ligand chemistry could lead to interesting extractant and sensing materials.

Most immediately, the sorption and redox interactions of Pu(IV) colloids with oxidized and untreated porous carbons will be further explored. In Section 6.4.2 it was shown that untreated C-CS strongly adsorbs PuO_2 nanocrystals, while the highly oxidized C-CS-COOH prevents their formation in pH 4 solutions. These nanocolloids were formed at or near the C-CS surface upon reduction of Pu(V) and Pu(VI) to Pu(IV). It will be interesting to investigate the sorption of Pu(IV) colloids that are formed in solution prior to contact with OMCs, and those formed by addition of aqueous Pu(IV) to OMC samples. TEM studies could determine how the PuO_2 nanoparticle size distribution on C-CS changes depending on how the colloids were produced. A combination of batch sorption and XAS experiments can help establish the affinity of Pu(IV) colloids for oxidized C-CS-COOH, and whether they are changed or dissolved by the oxidized surface. Batch sorption experiments with larger liquid-to-solid ratios may be done to compare Pu uptake capacities of OMCs with colloidal and aqueous Pu of different oxidation states.

The reduction of Pu by porous carbons will be further explored. Data discussed in Section 6.5.1 showed that PuO_2 nanoparticles sorbed to carbon surfaces are dissolved within 24 hours of contact with 1 M HCl or $HClO_4$ solution, yielding aqueous Pu(III). Batch contact experiments will be done with Pu(IV) colloids to see if porous carbons can catalyze their dissolution in 1 M acid. If so, a porous carbon column will be tested as a way to quickly dissolve Pu colloids, which would be remarkably useful. The reduction of Pu(VI) to Pu(III) by porous carbons will also be investigated further with AC columns, and OMC thin films and monoliths. These monoliths can serve as Pu-reducing dip-sticks or stir bars. The redox activity of graphene toward Pu will also be tested. The capacity and reusability of each material as a reducing agent will be experimentally determined. The FTIR spectra of pristine porous carbons before and after the redox reactions may give some evidence as to which groups are oxidized on the carbon surface.

Implementation of OMC substrates into electrochemical sensing applications is also possible. The first experiments should study the detection of actinides using differential pulse anodic stripping voltammetry with OMC paste electrodes. The detection limits should be compared to those obtained using graphite-paste or CNT-paste electrodes. From there, OMC thin film and monolith based electrodes may be explored, and functionalization of the carbon could be implemented to create ion-specific electrodes. A deeper understanding of plutonium and other actinides' interactions with ordered mesoporous carbons could also lead to their application for separations or sequestration of actinides.

Bibliography

1. Beck, J. S.; Vartuli, J. C.; Roth, W. J.; Leonowicz, M. E.; Kresge, C. T.; Schmitt, K. D.; Chu, C. T. W.; Olson, D. H.; Sheppard, E. W.; McCullen, S. B.; Higgins, J. B.; Schlenker, J. L., A New Family of Mesoporous Molecular-Sieves Prepared with Liquid-Crystal Templates. *Journal of the American Chemical Society* **1992,** 114, (27), 10834-10843.
2. Kresge, C. T.; Leonowicz, M. E.; Roth, W. J.; Vartuli, J. C.; Beck, J. S., Ordered Mesoporous Molecular-Sieves Synthesized by A Liquid-Crystal Template Mechanism. *Nature* **1992,** 359, (6397), 710-712.
3. Bruzzoniti, M. C.; De Carlo, R. M.; Fiorilli, S.; Onida, B.; Sarzanini, C., Functionalized SBA-15 Mesoporous Silica in Ion Chromatography of Alkali, Alkaline Earths, Ammonium and Transition Metal Ions. *Journal of Chromatography A* **2009,** 1216, (29), 5540-5547.
4. Antonietti, M.; Ozin, G. A., Promises and Problems of Mesoscale Materials Chemistry or Why Meso? *Chemistry-a European Journal* **2004,** 10, (1), 28-41.
5. Makowski, P.; Deschanels, X.; Grandjean, A.; Meyer, D.; Toquer, G.; Goettmann, F., Mesoporous Materials in the Field of Nuclear Industry: Applications and Perspectives. *New Journal of Chemistry* **2012,** 36, (3), 531-541.
6. Goettmann, F.; Sanchez, C., How Does Confinement Affect the Catalytic Activity of Mesoporous Materials? *Journal of Materials Chemistry* **2007,** 17, (1), 24-30.
7. Jung, Y.; Kim, S.; Park, S.-J.; Kim, J. M., Preparation of Functionalized Nanoporous Carbons for Uranium Loading. *Colloids and Surfaces A: Physicochemical and Engineering Aspects* **2008,** 313–314, (0), 292-295.
8. Bruno, S. M.; Coelho, A. C.; Ferreira, R. A. S.; Carlos, L. D.; Pillinger, M.; Valente, A. A.; Ribeiro-Claro, P.; Goncalves, I. S., MCM-41 Derivatised with Pyridyl Groups and its Use as a Support for Luminescent Europium(III) Complexes. *European Journal of Inorganic Chemistry* **2008**, (24), 3786-3795.
9. Wiacek, R. J.; O'Hara, M. J.; Egorov, O.; Fryxell, G. E.; Addleman, R. S., Synthesis and Evaluation of Diphosphonic Acid Functionalized Mesoporous Silica for Actinide Sorption. *Abstracts of Papers, 233rd ACS National Meeting, Chicago, IL, United States, March 25-29,* **2007**, IEC-161.
10. Yantasee, W.; Fryxell Glen, E.; Lin, Y., Voltammetric Analysis of Europium at Screen-Printed Electrodes Modified with Salicylamide Self-Assembled on Mesoporous Silica. *Analyst* **2006,** 131, (12), 1342-6.
11. Wiacek, R. J.; O'Hara, M. J.; Egorov, O. B.; Fryxell, G. E.; Addleman, R. S., Synthesis and Evaluation of Diphosphonic Acid Functionalized Mesoporous Silica for Actinide Sorption. *Abstracts of Papers, 232nd ACS National Meeting, San Francisco, CA, United States, Sept. 10-14,* **2006**, IEC-169.
12. Mattigod, S. V.; Fryxell, G. E.; Parker, K. E.; Lin, Y., Application of Novel Nanoporous Sorbents for the Removal of Heavy Metals, Metalloids, and Radionuclides. *Trace Elem. Environ.* **2006**, 369-380.
13. Li, X. S.; Courtney, A. R.; Yantasee, W.; Mattigod, S. V.; Fryxell, G. E., Templated Synthesis of Mesoporous Titanium Phosphates for the Sequestration of Radionuclides. *Inorg. Chem. Commun.* **2006,** 9, (3), 293-295.
14. Jamali, M. R.; Assadi, Y.; Shemirani, F.; Hosseini, M. R. M.; Kozani, R. R.; Masteri-Farahani, M.; Salavati-Niasari, M., Synthesis of Salicylaldehyde-Modified Mesoporous Silica and its Application as a New Sorbent for Separation, Preconcentration and Determination of

Uranium by Inductively Coupled Plasma Atomic Emission Spectrometry. *Analytica Chimica Acta* **2006,** 579, (1), 68-73.
15. Lin, Y.; Fiskum, S. K.; Yantasee, W.; Wu, H.; Mattigod, S. V.; Vorpagel, E.; Fryxell, G. E.; Raymond, K. N.; Xu, J., Incorporation of Hydroxypyridinone Ligands into Self-Assembled Monolayers on Mesoporous Supports for Selective Actinide Sequestration. *Environ. Sci. Technol.* **2005,** 39, (5), 1332-1337.
16. Fryxell, G.; Lin, Y.; Fiskum, S.; Birnbaum, J.; Wu, H., Actinide Sequestration Using Self-Assembled Monolayers on Mesoporous Supports. *Environ. Sci. Technol.* **2005,** 39, 1324-1331.
17. Addleman, R. S.; Egorov, O. B.; O'Hara, M. J.; Busche, B.; Zemanian, T. S.; Fryxell, G., Preconcentration and Assay of Radionuclides with Self Assembled Monolayers on Mesoporous Supports. *Journal of Radioanalytical and Nuclear Chemistry* **2005,** 263, (1), 59-64.
18. Yantasee, W.; Lin, Y.; Fryxell, G. E.; Wang, Z., Carbon Paste Electrode Modified with Carbamoylphosphonic Acid Functionalized Mesoporous Silica: A New Mercury-Free Sensor for Uranium Detection. *Electroanalysis* **2004,** 16, (10), 870-873.
19. Glen E. Fryxell, H. W., Yuehe Lin, Wendy J. Shaw, Jerome C. Birnbaum, John C. Linehan, Zimin Nie, Ken Kemner and Shelly Kelly, Lanthanide Selective Sorbents: Self-Assembled Monolayers on Mesoporous Supports (SAMMS). *Journal of Materials Chemistry* **2004,** 14, (22), 3356-3363.
20. Trens, P.; Russell, M. L.; Spjuth, L.; Hudson, M. J.; Liljenzin, J. O., Preparation of Malonamide-MCM-41 Materials for the Heterogeneous Extraction of Radionuclides. *Industrial & Engineering Chemistry Research* **2002,** 41, (21), 5220-5225.
21. Feng, X.; Rao, L.; Mohs, T. R.; Xu, J.; Xia, Y.; Fryxell, G. E.; Liu, J.; Raymond, K. N., Self-Assembled Monolayers on Mesoporous Silica, a Super Sponge for Actinides. *Ceram. Trans.* **1999,** 93, 35-42.
22. Yantasee, W.; Fryxell, G. E.; Lin, Y. H.; Wu, H.; Raymond, K. N.; Xu, J. D., Hydroxypyridinone Functionalized Self-Assembled Monolayers on Nanoporous Silica for Sequestering Lanthanide Cations. *Journal of Nanoscience and Nanotechnology* **2005,** 5, (4), 527-529.
23. Yantasee, W.; Fryxell, G. E.; Addleman, R. S.; Wiacek, R. J.; Koonsiripaiboon, V.; Pattamakomsan, K.; Sukwarotwat, V.; Xu, J.; Raymond, K. N., Selective Removal of Lanthanides from Natural Waters, Acidic Streams and Dialysate. *Journal of Hazardous Materials* **2009,** 168, (2-3), 1233-1238.
24. Yousefi, S. R.; Ahmadi, S. J.; Shemirani, F.; Jamali, M. R.; Salavati-Niasari, M., Simultaneous Extraction and Preconcentration of Uranium and Thorium in Aqueous Samples by New Modified Mesoporous Silica Prior to Inductively Coupled Plasma Optical Emission Spectrometry Determination. *Talanta* **2009,** 80, (1), 212-217.
25. Kim, J.; Lee, H.; Yeon, J.-W.; Jung, Y.; Kim, J., Removal of Uranium(VI) From Aqueous Solutions by Nanoporous Carbon and its Chelating Polymer Composite. *Journal of Radioanalytical and Nuclear Chemistry* **2010,** 286, (1), 129-133.
26. Lebed, P. J.; de Souza, K.; Bilodeau, F.; Lariviere, D.; Kleitz, F., Phosphonate-Functionalized Large Pore 3-D Cubic Mesoporous (KIT-6) Hybrid as Highly Efficient Actinide Extracting Agent. *Chemical Communications* **2011,** 47, (41), 11525-11527.
27. Tian, G.; Geng, J.; Jin, Y.; Wang, C.; Li, S.; Chen, Z.; Wang, H.; Zhao, Y.; Li, S., Sorption of Uranium(VI) Using Oxime-Grafted Ordered Mesoporous Carbon CMK-5. *Journal of Hazardous Materials* **2011,** 190, (1-3), 442-450.

28. Yuan, L.-Y.; Liu, Y.-L.; Shi, W.-Q.; Lv, Y.-L.; Lan, J.-H.; Zhao, Y.-L.; Chai, Z.-F., High Performance of Phosphonate-Functionalized Mesoporous Silica for U(VI) Sorption From Aqueous Solution. *Dalton Transactions* **2011,** 40, (28), 7446-7453.
29. Yun, M. H.; Yeon, J. W.; Kim, J. H.; Lee, H. I.; Kim, J. M.; Kim, S.; Jung, Y., Preparation and Application of Chelating Polymer-Mesoporous Silica Composite for Europium-Ion Adsorption. *Macromolecular Research* **2011,** 19, (5), 421-426.
30. Zuo, L. M.; Yu, S. M.; Zhou, H.; Jiang, J.; Tian, X., Adsorption of Eu(III) From Aqueous Solution Using Mesoporous Molecular Sieve. *Journal of Radioanalytical and Nuclear Chemistry* **2011,** 288, (2), 579-586.
31. Brown, S.; Gorka, J.; Mayes, R. T.; Dai, S., Amidoxime-Grafted Mesoporous Carbon and Porous Organic Gel Sorbents for Extraction of Uranium From Seawater. *Abstracts of Papers, 244th ACS National Meeting & Exposition, Philadelphia, PA, United States, August 19-23, 2012* **2012**, I+EC-101.
32. Gorka, J.; Mayes, R. T.; Dai, S., Synergistic Effect of Sonochemical Grafting and Hierarchical Porosity of Carbons on Uranium Adsorption from Seawater. *Abstracts of Papers, 244th ACS National Meeting & Exposition, Philadelphia, PA, United States, August 19-23, 2012* **2012**, I+EC-102.
33. Lin, W.; Carboni, M.; Vivero-Escoto, J.; de Krafft, K. E., Nanoporous Sorbents for Selective Extraction of Actinides. *Abstracts of Papers, 244th ACS National Meeting & Exposition, Philadelphia, PA, United States, August 19-23, 2012* **2012**, I+EC-56.
34. Mayes, R.; Gorka, J.; Brown, S.; Oyola, Y.; Janke, C.; Kang, S. O.; Hay, B.; Dai, S., Funcitonalized Carbon Materials as Uranium Adsorbents. *Abstracts of Papers, 244th ACS National Meeting & Exposition, Philadelphia, PA, United States, August 19-23, 2012* **2012**, I+EC-57.
35. Wang, Y. Q.; Zhang, Z. B.; Liu, Y. H.; Cao, X. H.; Liu, Y. T.; Li, Q., Adsorption of U(VI) From Aqueous Solution by the Carboxyl-Mesoporous Carbon. *Chemical Engineering Journal* **2012,** 198, 246-253.
36. Davidson, J. D.; Wiacek, R. J.; Burton, S.; Li, X. H. S.; Fryxell, G. E.; Addleman, R. S.; Yantasee, W.; Sangvanich, T.; Pattamakomsan, K., Improved Deposition and Deprotection of Silane Tethered 3,4 Hydroxypyridinone (HOPO) Ligands on Functionalized Nanoporous Silica. *Inorganic Chemistry Communications* **2012,** 18, 92-96.
37. Fryxell, G. E.; Chouyyok, W.; Rutledge, R. D., Design and Synthesis of Chelating Diamide Sorbents for the Separation of Lanthanides. *Inorganic Chemistry Communications* **2011,** 14, (6), 971-974.
38. Johnson, B. E.; Santschi, P. H.; Chuang, C. Y.; Otosaka, S.; Addleman, R. S.; Douglas, M.; Rutledge, R. D.; Chouyyok, W.; Davidson, J. D.; Fryxell, G. E.; Schwantes, J. M., Collection of Lanthanides and Actinides from Natural Waters with Conventional and Nanoporous Sorbents. *Environmental Science & Technology* **2012,** 46, (20), 11251-11258.
39. Johnson, B. E.; Santschi, P. H.; Addleman, R. S.; Douglas, M.; Davidson, J.; Fryxell, G. E.; Schwantes, J. M., Optimization and Evaluation of Mixed-Bed Chemisorbents for Extracting Fission and Activation Products From Marine and Fresh Waters. *Analytica Chimica Acta* **2011,** 708, (1-2), 52-60.
40. Yantasee, W.; Sangvanich, T.; Creim, J. A.; Pattamakomsan, K.; Wiacek, R. J.; Fryxell, G. E.; Addleman, R. S.; Timchalk, C., Functional Sorbents for Selective Capture of Plutonium, Americium, Uranium, and Thorium in Blood. *Health Physics* **2010,** 99, (3), 413-419.

41. Nie, B. W.; Zhang, Z. B.; Cao, X. H.; Liu, Y. H.; Liang, P., Sorption Study of Uranium From Aqueous Solution on Ordered Mesoporous Carbon CMK-3. *Journal of Radioanalytical and Nuclear Chemistry* **2013,** 295, (1), 663-670.
42. Liu, Y. H.; Wang, Y. Q.; Zhang, Z. B.; Cao, X. H.; Nie, W. B.; Li, Q.; Hua, R., Removal of Uranium From Aqueous Solution by a Low Cost and High-Efficient Adsorbent. *Applied Surface Science* **2013,** 273, 68-74.
43. Liu, Y. H.; Li, Q.; Cao, X. H.; Wang, Y. Q.; Jiang, X. H.; Li, M.; Hua, M.; Zhang, Z. B., Removal of Uranium(VI) From Aqueous Solutions by CMK-3 and its Polymer Composite. *Applied Surface Science* **2013,** 285, 258-266.
44. Zhang, W.; Ye, G.; Chen, J., Novel Mesoporous Silicas Bearing Phosphine Oxide Ligands with Different Alkyl Chains for the Binding of Uranium in Strong HNO_3 Media. *Journal of Materials Chemistry A* **2013,** 1, (41), 12706-12709.
45. Carboni, M.; Abney, C. W.; Taylor-Pashow, K. M. L.; Vivero-Escoto, J. L.; Lin, W., Uranium Sorption with Functionalized Mesoporous Carbon Materials. *Industrial & Engineering Chemistry Research* **2013,** 52, (43), 15187-15197.
46. Vivero-Escoto, J. L.; Carboni, M.; Abney, C. W.; deKrafft, K. E.; Lin, W. B., Organo-Functionalized Mesoporous Silicas for Efficient Uranium Extraction. *Microporous and Mesoporous Materials* **2013,** 180, 22-31.
47. Dyer, A.; Harjula, R.; Newton, J.; Pillinger, M., Synthesis and Characterisation of Mesoporous Silica Phases Containing Heteroatoms, and Their Cation Exchange Properties. Part 4. Measurement of Distribution Coefficients for ^{241}Am, ^{51}Cr, ^{59}Fe, ^{54}Mn, ^{63}Ni, ^{236}Pu and ^{65}Zn. *Microporous and Mesoporous Materials* **2010,** 130, (1-3), 63-66.
48. Yue, Y. F.; Mayes, R. T.; Kim, J.; Fulvio, P. F.; Sun, X. G.; Tsouris, C.; Chen, J. H.; Brown, S.; Dai, S., Seawater Uranium Sorbents: Preparation from a Mesoporous Copolymer Initiator by Atom-Transfer Radical Polymerization. *Angewandte Chemie-International Edition* **2013,** 52, (50), 13458-13462.
49. Gorka, J.; Mayes, R. T.; Baggetto, L.; Veith, G. M.; Dai, S., Sonochemical Functionalization of Mesoporous Carbon for Uranium Extraction From Seawater. *Journal of Materials Chemistry A* **2013,** 1, (9), 3016-3026.
50. Yue, Y.; Fulvio, P. F.; Brown, S.; Mayes, R. T.; Sun, X.-G.; Dai, S., Isolating Trace Seawater Uranium With Polymer Functionalized Porous Carbon. *Abstracts of Papers, 244th ACS National Meeting & Exposition, Philadelphia, PA, United States, August 19-23, 2012* **2012**, I+EC-103.
51. Jin Kwon, B.; Yun Ku, J.; Hyun Yu, K.; Eun Ko, J.; Jung, H., Preparation and Characterization of Carbamoylphosphonate(CMPO) Silane Grafted on Various Mesoporous Silicas. *Journal of Physics and Chemistry of Solids* **2010,** 71, (4), 663-668.
52. Runde, W., Chemical Interactions of Actinides in the Environment. *Los Alamos Science* **2000,** 26, 392-411.
53. Clark, D. L., The Chemical Complexities of Plutonium. *Los Alamos Science* **2000,** 26, 364-381.
54. Hu, Y.-J.; Kestrel Schwaiger, L.; Booth, C. H.; Kukkadapu, R. K.; Cristiano, E.; Kaplan, D.; Nitsche, H., Molecular Interactions of Plutonium(VI) with Synthetic Manganese-Substituted Goethite. *Radiochimica Acta* **2010,** 98, (9-11), 655-663.
55. Shaughnessy, D. A.; Nitsche, H.; Booth, C. H.; Shuh, D. K.; Waychunas, G. A.; Wilson, R. E.; Gill, H.; Cantrell, K. J.; Serne, R. J., Molecular Interfacial Reactions Between Pu(VI) and

Manganese Oxide Minerals Manganite and Hausmannite. *Environmental Science & Technology* **2003,** 37, (15), 3367-3374.
56. Hu, Y. J.; Schwaiger, L. K.; Cristiano, E.; Nitsche, H., Reaction of Plutonium(VI) with the Manganese-Substituted Iron Oxide Mineral Goethite. *Abstracts of Papers of the American Chemical Society* **2009,** 238.
57. Hixon, A. E.; Hu, Y. J.; Kaplan, D. I.; Kukkadapu, R. K.; Nitsche, H.; Qafoku, O.; Powell, B. A., Influence of Iron Redox Transformations on Plutonium Sorption to Sediments. *Radiochimica Acta* **2010,** 98, (9-11), 685-692.
58. Wang, D. L.; Hu, Y. J.; Schwaiger, L. K.; Nitsche, H., Determination of Plutonium Interactions with Aluminum-Substituted Goethite Using X-ray Absorption Spectroscopy. *Abstracts of Papers of the American Chemical Society* **2010,** 240.
59. Shaughnessy, D. A.; Nitsche, H.; Serne, R. J.; Shuh, D. K.; Waychunas, G. A.; Booth, C. H.; Gill, H. S., Molecular Studies of Interfacial Plutonium-Mineral Interactions on Manganese Oxide Hydroxide Mineral Surfaces. *Abstracts of Papers of the American Chemical Society* **2001,** 221, U85-U85.
60. Shaughnessy, D. A.; Nitsche, H.; Serne, R. J.; Booth, C. H.; Shuh, D. K.; Waychunas, G. A.; Gill, H. S., Interfacial Reaction Studies of Plutonium on Manganese Oxide Hydroxide Mineral Surfaces. *Abstracts of Papers of the American Chemical Society* **2000,** 220, U352-U352.
61. Hu, Y.-J. Reaction of Plutonium(VI) with the Manganese-Substituted Iron Oxide Mineral Goethite. Doctoral Dissertation, University of California, Berkeley, Berkeley, 2011.
62. Wilson, R. E. Reactions of Plutonium(VI) with the Iron Oxide Goethite. Doctoral Dissertation, University of California, Berkeley, Berkeley, 2005.
63. Parsons-Moss, T.; Tüysüz, H.; Wang, D.; Jones, S.; Olive, D.; Nitsche, H., Plutonium Sorption to Nanocast Mesoporous Carbon. *Radiochimica Acta* **2014**, 102, (4)
64. Kresge, C.; Leonowicz, M.; Roth, W.; Vartuli, J.; Beck, J., Ordered Mesoporous Molecular Sieves Synthesized by a Liquid-Crystal Template Mechanism. *Nature* **1992,** 359, (6397), 710-712.
65. Huo, Q.; Margolese, D. I.; Ciesla, U.; Feng, P.; Gier, T. E.; Sieger, P.; Leon, R.; Petroff, P. M.; Schuth, F.; Stucky, G. D., Generalized Synthesis of Periodic Surfactant/Inorganic Composite Materials. *Nature* **1994,** 368, (6469), 317-321.
66. Zhao, D. Y.; Huo, Q. S.; Feng, J. L.; Chmelka, B. F.; Stucky, G. D., Nonionic Triblock and Star Diblock Copolymer and Oligomeric Surfactant Syntheses of Highly Ordered, Hydrothermally Stable, Mesoporous Silica Structures. *Journal of the American Chemical Society* **1998,** 120, (24), 6024-6036.
67. Dongyuan Zhao, J. F., Qisheng Huo, Nicholas Melosh, Glenn H. Fredrickson, Bradley F. Chmelka, Galen D. Stucky, Triblock Copolymer Syntheses of Mesoporous Silica with Periodic 50 to 300 Angstrom Pores. *Science* **1998,** 279, (5350), 548-552.
68. Kleitz, F.; Hei Choi, S.; Ryoo, R., Cubic Ia3d Large Mesoporous Silica: Synthesis and Replication to Platinum Nanowires, Carbon Nanorods and Carbon Nanotubes. *Chemical Communications* **2003**, (17), 2136-2137.
69. Shen, S. D.; Li, Y. Q.; Zhang, Z. D.; Fan, J.; Tu, B.; Zhou, W. Z.; Zhao, D. Y., A Novel Ordered Cubic Mesoporous Silica Templated With Tri-Head Group Quaternary Ammonium Surfactant. *Chemical Communications* **2002**, (19), 2212-2213.
70. Schuth, F., Non-Siliceous Mesostructured and Mesoporous Materials. *Chemistry of Materials* **2001,** 13, (10), 3184-3195.

71. Joo, S. H.; Jun, S.; Ryoo, R., Synthesis of Ordered Mesoporous Carbon Molecular Sieves CMK-1. *Microporous and Mesoporous Materials* **2001,** 44-45, 153-158.
72. Ryoo, R.; Joo, S. H.; Jun, S., Synthesis of Highly Ordered Carbon Molecular Sieves via Template-Mediated Structural Transformation. *Journal of Physical Chemistry B* **1999,** 103, (37), 7743-7746.
73. Yang, H. F.; Shi, Q. H.; Tian, B. Z.; Xie, S. H.; Zhang, F. Q.; Yan, Y.; Tu, B.; Zhao, D. Y., A Fast Way for Preparing Crack-Free Mesostructured Silica Monolith. *Chemistry of Materials* **2003,** 15, (2), 536-541.
74. Xue, C. F.; Tu, B.; Zhao, D. Y., Facile Fabrication of Hierarchically Porous Carbonaceous Monoliths with Ordered Mesostructure via an Organic-Organic Self-Assembly. *Nano Research* **2009,** 2, (3), 242-253.
75. Zhao, D.; Yang, P.; Melosh, N.; Feng, J.; Chmelka, B. F.; Stucky, G. D., Continuous Mesoporous Silica Films with Highly Ordered Large Pore Structures. *Advanced Materials* **1998,** 10, (16), 1380.
76. Feng, D.; Lv, Y. Y.; Wu, Z. X.; Dou, Y. Q.; Han, L.; Sun, Z. K.; Xia, Y. Y.; Zheng, G. F.; Zhao, D. Y., Free-Standing Mesoporous Carbon Thin Films with Highly Ordered Pore Architectures for Nanodevices. *Journal of the American Chemical Society* **2011,** 133, (38), 15148-15156.
77. Wan, Y.; Zhao, D. Y., On the Controllable Soft-Templating Approach to Mesoporous Silicates. *Chemical Reviews* **2007,** 107, (7), 2821-2860.
78. Fryxell, G. E., The Synthesis of Functional Mesoporous Materials. *Inorganic Chemistry Communications* **2006,** 9, (11), 1141-1150.
79. Feng, X.; Fryxell, G. E.; Wang, L. Q.; Kim, A. Y.; Liu, J.; Kemner, K. M., Functionalized Monolayers on Ordered Mesoporous Supports. *Science* **1997,** 276, (5314), 923-926.
80. Liu, J.; Shin, Y.; Nie, Z.; Chang, J.; Wang, L.-Q.; Fryxell, G.; Samuels, W.; Exarhos, G., Molecular Assembly in Ordered Mesoporosity: A New Class of Highly Functional Nanoscale Materials. *J. Phys. Chem. A* **2000,** 104, (36), 8328-8339.
81. Fryxell, G. E.; Lin, Y.; Wu, H.; Kemner, K. M., Environmental applications of Self-Assembled Monolayers on Mesoporous Supports (SAMMS). *Studies in Surface Science and Catalysis* **2002,** 141, (Nanoporous Materials III), 583-590.
82. Goodhew, P. J. H., John; Beanland, Richard, Electron Microscopy and Analysis. In [Online] Third ed.; Taylor and Francis: London and New York, 2001.
83. Brogan, L. K. S. Structural Characterization of and Plutonium Sorption on Mesoporous and Nanoparticulate Ferrihydrite. Doctoral Dissertation, University of California at Berkeley, Berkeley, 2012.
84. Sing, K. S. W., Physisorption of Nitrogen by Porous Materials. *Journal of Porous Materials* **1995,** 2, (1), 5-8.
85. Sing, K. S. W.; Everett, D. H.; Haul, R. A. W.; Moscou, L.; Pierotti, R. A.; Rouquerol, J.; Siemieniewska, T., Reporting Physisorption Data for Gas/Solid Systems With Special Reference to the Determination of Surface Area and Porosity (Recommendations 1984). *Pure and Applied Chemistry* **1985,** 57, (4), 603-19.
86. Brunauer, S.; Emmett, P. H.; Teller, E., Adsorption of Gases in Multimolecular Layers. *Journal of the American Chemical Society* **1938,** 60, 309-319.

87. Groen, J. C.; Peffer, L. A. A.; Peréz-Ramírez, J., Pore Size Determination in Modified Micro- and Mesoporous Materials. Pitfalls and Limitations in Gas Adsorption Data Analysis. *Microporous and Mesoporous Materials* **2003,** 60, (1-3), 1-17.
88. Barrett, E. P.; Joyner, L. G.; Halenda, P. P., The Determination of Pore Volume and Area Distributions in Porous Substances.1. Computations From Nitrogen Isotherms. *Journal of the American Chemical Society* **1951,** 73, (1), 373-380.
89. Kinoshita, K., *CARBON Electrochemical and Physicochemical Properties*. John Wiley & Sons: New York, 1988; p 533.
90. Wu, Z.; Webley, P. A.; Zhao, D., Comprehensive Study of Pore Evolution, Mesostructural Stability, and Simultaneous Surface Functionalization of Ordered Mesoporous Carbon (FDU-15) by Wet Oxidation as a Promising Adsorbent. *Langmuir* **2010,** 26, (12), 10277-10286.
91. Laws, D. D.; Bitter, H. M. L.; Jerschow, A., Solid-State NMR Spectroscopic Methods in Chemistry. *Angewandte Chemie-International Edition* **2002,** 41, (17), 3096-3129.
92. Duer, M. J., *Solid-State NMR Spectroscopy Principles and Applications*. Blackwell Science: Oxford, 2002; p 562.
93. Smith, B. C., Fundamentals of Fourier Transform Infrared Spectroscopy. In [Online] Second Edition ed.; CRC Press, Taylor & Francis: Boca Raton, FL, 2011.
94. Cristiano, E.; Hu, Y.-J.; Siegfried, M.; Kaplan, D.; Nitsche, H., A Comparison of Point of Zero Charge Measurement Methodology. *Clays and Clay Minerals* **2011,** 59, (2), 107-116.
95. Kokunesoski, M.; Gulicovski, J.; Matovic, B.; Logar, M.; Milonjic, S. K.; Babic, B., Synthesis and Surface Characterization of Ordered Mesoporous Silica SBA-15. *Materials Chemistry and Physics* **2010,** 124, (2-3), 1248-1252.
96. Figueiredo, J. L.; Pereira, M. F. R.; Freitas, M. M. A.; Órfão, J. J. M., Modification of the Surface Chemistry of Activated Carbons. *Carbon* **1999,** 37, (9), 1379-1389.
97. H.P, B., Some Aspects of the Surface Chemistry of Carbon Blacks and Other Carbons. *Carbon* **1994,** 32, (5), 759-769.
98. Noh, J. S.; Schwarz, J. A., Effect of HNO_3 Treatment on the Surface Acidity of Activated Carbons. *Carbon* **1990,** 28, (5), 675-682.
99. Fraga, M. A.; Jordão, E.; Mendes, M. J.; Freitas, M. M. A.; Faria, J. L.; Figueiredo, J. L., Properties of Carbon-Supported Platinum Catalysts: Role of Carbon Surface Sites. *Journal of Catalysis* **2002,** 209, (2), 355-364.
100. Leon y Leon, C. A.; Solar, J. M.; Calemma, V.; Radovic, L. R., Evidence for the Protonation of Basal Plane Sites on Carbon. *Carbon* **1992,** 30, (5), 797-811.
101. Stafiej, A.; Pyrzynska, K., Adsorption of Heavy Metal Ions With Carbon Nanotubes. *Separation and Purification Technology* **2007,** 58, (1), 49-52.
102. H.P, B., Surface Oxides on Carbon and Their Analysis: a Critical Assessment. *Carbon* **2002,** 40, (2), 145-149.
103. McPhail, M. R.; Sells, J. A.; He, Z.; Chusuei, C. C., Charging Nanowalls: Adjusting the Carbon Nanotube Isoelectric Point via Surface Functionalization. *The Journal of Physical Chemistry C* **2009,** 113, (32), 14102-14109.
104. Hao, X.; Quach, L.; Korah, J.; Spieker, W. A.; Regalbuto, J. R., The Control of Platinum Impregnation by PZC Alteration of Oxides and Carbon. *Journal of Molecular Catalysis A: Chemical* **2004,** 219, (1), 97-107.
105. Lambert, S.; Job, N.; D'Souza, L.; Pereira, M. F. R.; Pirard, R.; Heinrichs, B.; Figueiredo, J. L.; Pirard, J.-P.; Regalbuto, J. R., Synthesis of Very Highly Dispersed Platinum Catalysts

Supported on Carbon Xerogels by the Strong Electrostatic Adsorption Method. *Journal of Catalysis* **2009,** 261, (1), 23-33.
106. Mustafa, S.; Dilara, B.; Nargis, K.; Naeem, A.; Shahida, P., Surface Properties of the Mixed Oxides of Iron and Silica. *Colloids and Surfaces A: Physicochemical and Engineering Aspects* **2002,** 205, (3), 273-282.
107. Park, J.; Regalbuto, J. R., A Simple, Accurate Determination of Oxide PZC and the Strong Buffering Effect of Oxide Surfaces at Incipient Wetness. *Journal of Colloid and Interface Science* **1995,** 175, (1), 239-252.
108. Choppin, G., Actinide Speciation in the Environment. *Journal of Radioanalytical and Nuclear Chemistry* **2007,** 273, (3), 695-703.
109. Silva, R. J.; Nitsche, H., Environmental Chemistry. In *Advances in Plutonium Chemistry 1967-2000*, Hoffman, D. C., Ed. American Nuclear Society: La Grange Park, IL, 2002; pp 89-111.
110. Choppin, G. R.; Rao, L. F., Complexation of Pentavalent and Hexavalent Actinides by Fluoride. *Radiochimica Acta* **1984,** 37, (3), 143-146.
111. Cleveland, J. M., *The Chemistry of Plutonium*. 2nd ed.; American Nuclear Society: La Grange Park, IL, 1979.
112. Foreman, J. K.; Smith, T. D., The Nature and Stability of the Complex Ions Formed by Ter-, Quadri-, and Sexa-Valent Plutonium Ions With Ethylenediaminetetracetic acid (EDTA). Part II. Spectrophotometric Studies. *Journal of the Chemical Society* **1957**, 1758-1762.
113. Gorden, A.; Xu, J.; Raymond, K., Rational Design of Sequestering Agents for Plutonium and Other Actinides. *chem. Rev.* **2003,** 103, (11), 4207-4282.
114. Tsoulfanidis, N., *Measurement and Detection of Radiation*. 2nd ed.; Taylor and Francis: Washington DC, 1995.
115. OceanOptics *USB2000 Fiber Optic Spectrometer Installation and Operation Manual*; Dunedin, FL, USA, 2001-2005.
116. Cohen, D., The Absorption Spectra of Plutonium Ions in Perchloric Acid Solutions. *Journal of Inorganic & Nuclear Chemistry* **1961,** 18, 211-218.
117. Cohen, D., Electrochemical Studies of Plutonium Ions in Perchloric Acid Solution. *Journal of Inorganic & Nuclear Chemistry* **1961,** 18, 207-210.
118. Nitsche, H.; Silva, R. J., Investigation of the Carbonate Complexation of Pu(IV) in Aqueous Solution. *Radiochimica Acta* **1996,** 72, (2), 65-72.
119. Parsons-Moss, T. W., Jinxiu; Jones, Stephen; May, Erin; Olive, Daniel; Dai, Zurong; Zavarin, Mavrik; Kersting, Annie; Zhao, Dongyuan; and Nitsche, Heino, Interactions of Plutonium and Europium with Ordered Mesoporous Carbon
Journal of Materials Chemistry A **2014,** In submission.
120. Conradson, S. D.; Abney, K. D.; Begg, B. D.; Brady, E. D.; Clark, D. L.; den Auwer, C.; Ding, M.; Dorhout, P. K.; Espinosa-Faller, F. J.; Gordon, P. L.; Haire, R. G.; Hess, N. J.; Hess, R. F.; Keogh, D. W.; Lander, G. H.; Lupinetti, A. J.; Morales, L. A.; Neu, M. P.; Palmer, P. D.; Paviet-Hartmann, P.; Reilly, S. D.; Runde, W. H.; Tait, C. D.; Veirs, D. K.; Wastin, F., Higher Order Speciation Effects on Plutonium L_3 X-ray Absorption Near Edge Spectra. *Inorganic Chemistry* **2003,** 43, (1), 116-131.
121. Webb, S. M., SIXpack: a Graphical User Interface for XAS Analysis Using IFEFFIT. *Physica Scripta* **2005,** T115, 1011-1014.
122. Li, G. G.; Bridges, F.; Booth, C. H., X-Ray-Absorption Fine-Structure Standards - a Comparison of Experiment and Theory. *Physical Review B* **1995,** 52, (9), 6332-6348.

123. Ravel, B.; Newville, M., ATHENA, ARTEMIS, HEPHAESTUS: Data Analysis for X-ray Absorption Spectroscopy Using IFEFFIT. *Journal of Synchrotron Radiation* **2005,** 12, (4), 537–541.
124. Panak, P. J.; Booth, C. H.; Caulder, D. L.; Bucher, J. J.; Shuh, D. K.; Nitsche, H., X-ray Absorption Fine Structure Spectroscopy of Plutonium Complexes With Bacillus Sphaericus. *Radiochimica Acta* **2002,** 90, (6), 315-321.
125. Rehr, J. J.; Deleon, J. M.; Zabinsky, S. I.; Albers, R. C., Theoretical X-ray Absorption Fine-Structure Standards. *Journal of the American Chemical Society* **1991,** 113, (14), 5135-5140.
126. Rehr, J. J.; Albers, R. C.; Zabinsky, S. I., High-Order Multiple-Scattering Calculations of X-ray-Absorption Fine-Structure. *Physical Review Letters* **1992,** 69, (23), 3397-3400.
127. Rehr, J. J.; Albers, R. C., Scattering-Matrix Formulation of Curved-Wave Multiple-Scattering Theory - Application to X-ray-Absorption Fine-Structure. *Physical Review B* **1990,** 41, (12), 8139-8149.
128. Deleon, J. M.; Rehr, J. J.; Zabinsky, S. I.; Albers, R. C., Abinitio Curved-Wave X-ray-Absorption Fine-Structure. *Physical Review B* **1991,** 44, (9), 4146-4156.
129. Stern, E. A., Number of Relevant Independent Points in X-ray-Absorption Fine-Structure Spectra. *Physical Review B* **1993,** 48, (13), 9825-9827.
130. Allen, P. G.; Bucher, J. J.; Shuh, D. K.; Edelstein, N. M.; Reich, T., Investigation of Aquo and Chloro Complexes of UO_2^{2+}, NpO_2^{+}, Np^{4+}, and Pu^{3+} by X-ray Absorption Fine Structure Spectroscopy. *Inorganic Chemistry* **1997,** 36, (21), 4676-4683.
131. Allen, P. G.; Veirs, D. K.; Conradson, S. D.; Smith, C. A.; Marsh, S. F., Characterization of Aqueous Plutonium(IV) Nitrate Complexes by Extended X-ray Absorption Fine Structure Spectroscopy. *Inorganic Chemistry* **1996,** 35, (10), 2841-5.
132. Newton, T. W.; Hobart, D. E.; Palmer, P. D., The Formation of Pu(IV)-Colliod by the Alpha-Reduction of Pu(V) or Pu(VI) in Aqueous-Solutions. *Radiochimica Acta* **1986,** 39, (3), 139-147.
133. Neck, V.; Altmaier, M.; Fanghänel, T., Solubility of Plutonium Hydroxides/Hydrous Oxides Under Reducing Conditions and in the Presence of Oxygen. *Comptes Rendus Chimie* **2007,** 10, (10–11), 959-977.
134. Knopp, R.; Neck, V.; Kim, J. I., Solubility, Hydrolysis and Colloid Formation of Plutonium(IV). *Radiochimica Acta* **1999,** 86, (3-4), 101-108.
135. Soderholm, L.; Almond, P. M.; Skanthakumar, S.; Wilson, R. E.; Burns, P. C., The Structure of the Plutonium Oxide Nanocluster $Pu_{38}O_{56}Cl_{54}(H_2O)_8^{14-}$. *Angewandte Chemie-International Edition* **2008,** 47, (2), 298-302.
136. Powell, B. A.; Dai, Z. R.; Zavarin, M.; Zhao, P. H.; Kersting, A. B., Stabilization of Plutonium Nano-Colloids by Epitaxial Distortion on Mineral Surfaces. *Environmental Science & Technology* **2011,** 45, (7), 2698-2703.
137. Choppin, G. R.; Bond, A. H.; Hromadka, P. M., Redox Speciation of Plutonium. *Journal of Radioanalytical and Nuclear Chemistry* **1997,** 219, (2), 203-210.
138. Chen, Y.; Pearson, F. J., Modeling Plutonium Solubility for Yucca Mountain Performance Assessment. *Radiochimica Acta* **2008,** 96, (9-11), 521-526.
139. Icker, M.; Walther, C.; Neck, V.; Geckeis, H., The Redox Potential of Pu Containing Acidic Solutions and the Fate of "Pu(IV)-Colloids": Direct Measurement Versus Optical Absorption Spectroscopy. *IOP Conf. Ser. Mater. Sci. Eng.* **2010,** 9, 012060/1-012060/9.
140. Cho, H.-R.; Jung, E. C.; Park, K. K.; Song, K.; Yun, J.-I., Effect of Reduction on the Stability of Pu(VI) Hydrolysis Species. *Radiochimica Acta*, **2010**, 98, 555.

141. Nitsche, H.; Lee, S. C.; Gatti, R. C., Determination of Plutonium Oxidation-States at Trace Levels Pertinent to Nuclear Waste-Disposal. *Journal of Radioanalytical and Nuclear Chemistry* **1988,** 124, (1), 171-185.
142. Romanchuk, A. Y.; Kalmykov, S. N.; Egorov, A. V.; Zubavichus, Y. V.; Shiryaev, A. A.; Batuk, O. N.; Conradson, S. D.; Pankratov, D. A.; Presnyakov, I. A., Formation of Crystalline $PuO_{2+x}\cdot nH_2O$ Nanoparticles Upon Sorption of Pu(V,VI) Onto Hematite. *Geochimica et Cosmochimica Acta* **2013,** 121, (0), 29-40.
143. Rabideau, S. W., The Kinetics of the Disproportionation of Plutonium(V). *Journal of the American Chemical Society* **1957,** 79, (24), 6350-6353.
144. Milonjic, S. K.; Cokesa, D. M.; Stevanovic, R. V., Dynamic Adsorption of Uranium(VI) and Zirconium(IV) on Silica-Gel. *Journal of Radioanalytical and Nuclear Chemistry* **1992,** 158, (1), 79-90.
145. Kobashi, A.; Tominaga, T.; Hoshi, M.; Yonezawa, C.; Saeki, M., Separation of Actinoid(III) and Actinoid(IV) by Solvent Extraction and Adsorption. *Journal of Alloys and Compounds* **1993,** 193, (1-2), 107-9.
146. Denecke, M. A.; Geckeis, H.; Pohlmann, C.; Rothe, J.; Degering, D., Extended X-ray Absorption Fine Structure and Time Differential Perturbed Angular Correlation Study of Hafnium(IV) Sorbed Onto Amorphous Silica. *Radiochimica Acta* **2000,** 88, (9-11), 639-643.
147. Pius, I. C.; Charyulu, M. M.; Venkataramani, B.; Sivaramakrishnan, C. K.; Patil, S. K., Studies on Sorption of Plutonium on Inorganic-Ion Exchangers from Sodium-Carbonate Medium. *Journal of Radioanalytical and Nuclear Chemistry* **1995,** 199, (1), 1-7.
148. Moeller, T., *The Chemistry of the Lanthanides*. Reinhold: New York, 1963; p 117.
149. Kaltsoyannis, N. a. S., Peter, *The f elements*. Oxford University Press: Oxford, U.K., 1999; Vol. 85.
150. Smith, H. L.; Hoffman, D. C., Ion-Exchange Separations of the Lanthanides and Actinides by Elution with Ammonium Alpha-Hydroxy-Isobutyrate. *Journal of Inorganic & Nuclear Chemistry* **1956,** 3, (3-4), 243-247.
151. Smith, R. M. a. M., Arthur E., *Critical Stability Constants*. Plenum Publishing Corporation: New York, 1976; Vol. 4: Inorganic Complexes.
152. Choppin, G. R., Inner Versus Outer Sphere Complexation of F-Elements. *Journal of Alloys and Compounds* **1997,** 249, (1-2), 9-13.
153. Ahrland, S.; Grenthe, I.; Noren, B., The Ion Exchange Properties of Silica Gel .2. Separation of Plutonium and Fission Products from Irradiated Uranium. *Acta Chemica Scandinavica* **1960,** 14, (5), 1077-1090.
154. Hultgren, A., Reextraction Concentration and Decontamination on a Silica Gel Column of Plutonium Extracted by Trilaurylamine. *Atomic Energy Review* **1966,** 4, (1), 154.
155. Laser, M., Protactinium, Zirconium and Niobium Sorption on Silica Gels and Vycor-Glass from Hydrochloric Acid Solution. *Chemie Ingenieur Technik* **1969,** 41, (23), 1283.
156. Souka, N.; Farah, K.; Shabana, R., Sorption Behavior of Some Actinides on Silica Gel from Mineral Acids and Alcoholic Solutions. *Journal of Radioanalytical Chemistry* **1976,** 34, (2), 277-84.
157. Rozzell, T. C.; Andelman, J. B., Plutonium in Water Environment 2. Sorption of Aqueous Plutonium on Silica Surfaces. *Advances in Chemistry Series* **1971**, (106), 280.
158. Hafez, M. B.; Hafez, N., Separation of Cerium, Uranium and Plutonium Using Silica-Gel. *Isotopenpraxis* **1990,** 26, (7), 346-347.

159. Pietrelli, L.; Salluzzo, A.; Troiani, F., Sorption of Europium and Actinides by Means of Octyl(phenyl)-N,N -Diisobutylcarbamoylmethyl Phosphine Oxide (CMPO) Loaded on Silica. *Journal of Radioanalytical and Nuclear Chemistry* **1990,** 141, (1), 107-15.
160. Pietrelli, L.; Salluzzo, A.; Troiani, F., Actinide Removal by Means of Octyl(phenyl)-N,N-diisobutyl Carbamoyl Methyl Phosphine Oxide (CMPO) Sorbed on Silica. *New Sep. Chem. Tech. Radioact. Waste Other Specific Appl. [Proc. Tech. Semin.]* **1991**, 87-94.
161. Chiarizia, R.; Horwitz, E. P.; D'Arcy, K. A.; Alexandratos, S. D.; Trochimczuk, A. W., Uptake of Metal Ions by a New Chelating Ion Exchange Resin. Part 9: Silica Grafted Diphosphonic Acid. *Solvent Extraction and Ion Exchange* **1996,** 14, (6), 1077-1100.
162. Chiarizia, R.; Horwitz, E. P.; D'Arcy, K. A.; Alexandratos, S. D.; Trochimczuk, A. W., Uptake of Actinides and Other Ions by Diphosil, a New Silica-Based Chelating Ion Exchange Resin. *Special Publication - Royal Society of Chemistry* **1996,** 182, (Ion Exchange Developments and Applications), 321-328.
163. Birnbaum, J.; Busche, B.; Lin, Y.; Shaw, W.; Fryxell, G., Synthesis of Carbamoylphosphonate Silanes for the Selective Sequestration of Actinides. *chem. Commun.* **2002**, 1374-1375.
164. Fryxell, G.; Mattigoda, S.; Lina, Y.; Wua, H.; Fiskuma, S.; Parkera, K.; Zhenga, F.; Yantaseea, W.; Zemaniana, T.; Addlemana, R.; Liua, J.; Kemnerb, K.; Kellyb, S.; Fengc, X., Design and Synthesis of Self-Assembled Monolayers on Mesoporous Supports (SAMMS): The Importance of Ligand Posture in Functional Nanomaterials. *Journal of Materials Chemistry* **2007,** 17, 2863-2874.
165. Meyer, D.; Conocar, O.; Moreau, J.; Wong Chi Man, M. Inorganic-Organic Hybrid Gels for Extracting Species Such as Lanthanides and Actinides From Aqueous Solutions, and Their Preparation. 98-FR2309 9921654, 19981028., 1999.
166. Broudic, J. C.; Conocar, O.; Moreau, J. J. E.; Meyer, D.; Man, M. W. C., New Hybrid Silica Based Materials for the Solid-Liquid Extraction of Actinides. *Journal of Materials Chemistry* **1999,** 9, (10), 2283-2285.
167. Bourg, S.; Broudic, J. C.; Conocar, O.; Moreau, J. J. E.; Meyer, D.; Man, M. W. C., Tailoring of Organically Modified Silicas for the Solid-Liquid Extraction of Actinides. *Chemistry of Materials* **2001,** 13, (2), 491-499.
168. Bourg, S.; Broudic, J.-C.; Conocar, O.; Moreau, J. J. E.; Meyer, D.; Man, M. W. C., Hybrid Silica Based Materials as New Solid Phase Extractants. *Materials Research Society Symposium Proceedings* **2001,** 628, (Organic/Inorganic Hybrid Materials), CC1 6 1-CC1 6 11.
169. Brandes, S.; Denat, F.; Meyer, M.; Guilard, R., Organic-Inorganic Hybrid Materials in Separation Chemistry: a Molecular Approach Towards the Design of Purification Processes. *Actualite Chimique* **2005**, 108-117.
170. Meyer, D. J. M.; Bourg, S.; Conocar, O.; Broudic, J. C.; Moreau, J. J. E.; Man, M. W. C., Extraction of Plutonium and Americium Using Silica Hybrid Materials. *Comptes Rendus Chimie* **2007,** 10, (10-11), 1001-1009.
171. Shkrob, I. A.; Tisch, A. R.; Marin, T. W.; Muntean, J. V.; Kaminski, M. D.; Kropf, A. J., Surface Modified, Collapsible Controlled Pore Glass Materials for Sequestration and Immobilization of Trivalent Metal Ions. *Industrial & Engineering Chemistry Research* **2011,** 50, (8), 4686-4696.
172. Zhang, A.; Wei, Y.; Kumagai, M., Bleeding Evaluation of the Stationary Phase From a Few Novel Macroporous Silica-Substrate Polymeric Materials Used for Radionuclide

Partitioning From HLLW in MAREC Process. *Journal of Radioanalytical and Nuclear Chemistry* **2005,** 265, (3), 409-417.
173. Zhang, A.; Wei, Y.; Kumagai, M.; Koma, Y., Synthesis and Application of a Macroporous Silica-Based Polymeric Octyl(phenyl)-N,N-Diisobutylcarbamoylmethylphoshine Oxide Composite for the Chromatographic Separation of High Level Liquid Waste. *Journal of Radioanalytical and Nuclear Chemistry* **2006,** 269, (1), 119-128.
174. Zhang, A.; Wei, Y.; Kumagai, M.; Koma, Y., A New Partitioning Process for High-Level Liquid Waste by Extraction Chromatography Using Silica-Substrate Chelating Agent Impregnated Adsorbents. *Journal of Alloys and Compounds* **2005,** 390, (1-2), 275-281.
175. Zhang, A.; Wei, Y.; Kumagai, M., Separation of Minor Actinides and Rare Earths from a Simulated High Activity Liquid Waste by Two Macroporous Silica-based Polymeric Composites. *Separation Science and Technology* **2007,** 42, (10), 2235-2253.
176. Zhang, A.; Wei, Y.; Hoshi, H.; Kumagai, M.; Koma, Y., Leakage of Octyl(phenyl)-N,N-di-isobutylcarbamoylmethylphosphine Oxide from a Macroporous Silica-Based Chelating Polymeric Adsorption Material and its Recovery by Some Selected Porous Adsorbents. *Adsorption Science & Technology* **2005,** 23, (9), 721-737.
177. Zhang, A.; Wei, Y.; Hoshi, H.; Kumagai, M.; Kamiya, M.; Koyama, T., Resistance Properties of a Macroporous Silica-Based N,N,N',N'-tetraoctyl-3-oxapentane-1,5-diamide-Impregnated Polymeric Adsorption Material Against Nitric Acid, Temperature and Gamma - Irradiation. *Radiation Physics and Chemistry* **2005,** 72, (6), 669-678.
178. Zhang, A.; Wei, Y.; Hoshi, H.; Kumagai, M., Chromatographic Separation of Strontium (II) From a Nitric Acid Solution Containing Some Typically Simulated Elements by a Novel Silica-Based TODGA Impregnated Polymeric Composite in the MAREC Process. *Solvent Extraction and Ion Exchange* **2005,** 23, (2), 231-247.
179. Zhang, A.; Wang, W.; Chai, Z.; Kuraoka, E., Modification of a Novel Macroporous Silica-Based Crown Ether Impregnated Polymeric Composite with 1-Dodecanol and its Adsorption for Some Fission and Non-Fission Products Contained in High Level Liquid Waste. *European Polymer Journal* **2008,** 44, (11), 3899-3907.
180. Zhang, A.; Mei, C.; Wei, Y.; Kumagai, M., Preparation of a Novel Macroporous Silica-Based Diglycolamide Derivative-Impregnated Polymeric Composite and its Adsorption Mechanism for Rare Earth Metal Ions. *Adsorption Science & Technology* **2007,** 25, (5), 257-272.
181. Zhang, A.; Kuraoka, E.; Kumagai, M., Impregnation Synthesis of a Novel Macroporous Silica-Based TODGA Polymeric Composite and its Application in the Adsorption of Rare Earths in Nitric Acid Solution Containing Diethylenetriaminepentaacetic acid. *European Polymer Journal* **2007,** 43, (2), 529-539.
182. Zhang, A.; Kuraoka, E.; Kumagai, M., Group Partitioning of Minor Actinides and Rare Earths from Highly Active Liquid Waste by Extraction Chromatography Utilizing Two Macroporous Silica-Based Impregnated Polymeric Composites. *Separation and Purification Technology* **2007,** 54, (3), 363-372.
183. Zhang, A.; Kuraoka, E.; Kumagai, M., Preparation of a Novel Macroporous Silica-Based 2,6-bis(5,6-diisobutyl-1,2,4-triazine-3-yl)pyridine Impregnated Polymeric Composite and its Application in the Adsorption for Trivalent Rare Earths. *Journal of Radioanalytical and Nuclear Chemistry* **2007,** 274, (3), 455-464.
184. Zhang, A.; Kuraoka, E.; Hoshi, H.; Kumagai, M., Synthesis of Two Novel Macroporous Silica-Based Impregnated Polymeric Composites and Their Application in Highly Active Liquid

Waste Partitioning by Extraction Chromatography. *Journal of Chromatography, A* **2004,** 1061, (2), 175-182.
185. Zhang, A.; Hu, Q.; Wang, W.; Kuraoka, E., Application of a Macroporous Silica-Based CMPO-Impregnated Polymeric Composite in Group Partitioning of Long-Lived Minor Actinides from Highly Active Liquid by Extraction Chromatography. *Industrial & Engineering Chemistry Research* **2008,** 47, (16), 6158-6165.
186. Zhang, A. Method for Separating Minor Actinides (MA) and Rare Earth (RE) From High-Level Liquid Waste (HLLW) by Selective Adsorption. 2009-10096094
101483079, 20090209., 2009.
187. Bhanushali, R. D.; Pius, I. C.; Mukherjee, S. K.; Vaidya, V. N., Sorption of Pu(IV) on Aliquat-336 Impregnated Silica-Gel From Nitric Acid-Oxalic Acid Medium. *Journal of Radioanalytical and Nuclear Chemistry* **2002,** 254, (2), 299-303.
188. Naik, P. W.; Dhami, P. S.; Misra, S. K.; Jambunathan, U.; Mathur, J. N., Use of Organophosphorus Extractants Impregnated on Silica Gel for the Extraction Chromatographic Separation of Minor Actinides from High Level Waste Solutions. *Journal of Radioanalytical and Nuclear Chemistry* **2003,** 257, (2), 327-332.
189. Ayata, S.; Aydinci, S.; Merdivan, M.; Binzet, G.; Külcü, N., Sorption of Uranium Using Silica Gel With Benzoylthiourea Derivatives. *Journal of Radioanalytical and Nuclear Chemistry* **2010,** 285, (3), 525-529.
190. Yantasee, W.; Lin, Y.; Fryxell, G. E.; Busche, B. J.; Birnbaum, J. C., Removal of Heavy Metals from Aqueous Solution Using Novel Nanoengineered Sorbents: Self-Assembled Carbamoylphosphonic Acids on Mesoporous Silica. *Separation Science and Technology* **2003,** 38, (15), 3809-3825.
191. Yantasee, W.; Lin, Y. H.; Fryxell, G. E.; Busche, B. J., Simultaneous Detection of Cadmium, Copper, and Lead Using a Carbon Paste Electrode Modified With Carbamoylphosphonic Acid Self-Assembled Monolayer on Mesoporous Silica (SAMMS). *Analytica Chimica Acta* **2004,** 502, (2), 207-212.
192. Yantasee, W.; Timchalk, C.; Fryxell, G. E.; Dockendorff, B. P.; Lin, Y. H., Automated Portable Analyzer for Lead(II) Based on Sequential Flow Injection and Nanostructured Electrochemical Sensors. *Talanta* **2005,** 68, (2), 256-261.
193. Yantasee, W.; Deibler, L. A.; Fryxell, G. E.; Timchalk, C.; Lin, Y. H., Screen-Printed Electrodes Modified With Functionalized Mesoporous Silica for Voltammetric Analysis of Toxic Metal Ions. *Electrochemistry Communications* **2005,** 7, (11), 1170-1176.
194. Carter, T. G.; Yantasee, W.; Sangvanich, T.; Fryxell, G. E.; Johnson, D. W.; Addleman, R. S., New Functional Materials for Heavy Metal Sorption: "Supramolecular" Attachment of Thiols to Mesoporous Silica Substrates. *Chemical Communications* **2008**, (43), 5583-5585.
195. Krishnan Balasubramanian, B. R., N. S. Venkataramanan, L.K. Brogan, T. Parsons-Moss, and H. Nitsche, Computational Modeling of Functionalized Mesoporous Materials for Plutonyl Complexation. Unpublished work completed in 2011.
196. Hu, Y.-J.; Wilson, R. E.; Booth, C. H.; Parsons-Moss, T.; Schwaiger, L. K.; Nitsche, H., Synchrotron X-ray Beam-Induced Chemistry on Plutonium(VI) Sorbed to Various Substrates. **2011**, In preparation.
197. Downward, L. B., C.H.; Lukens, W.W.; Bridges, F. A Variation of the F-Test for Determining Statistical Relevance of Particular Parameters in EXAFS Fits, *X-ray Absorption Fine Structure-XAFS13: 13th International Conference, 2007*; AIP: **2007**; pp 129-131.

198. Rehr, J. J.; Kas, J. J.; Vila, F. D.; Prange, M. P.; Jorissen, K., Parameter-Free Calculations of X-ray Spectra With FEFF9. *Physical Chemistry Chemical Physics* **2010,** 12, (21), 5503-5513.
199. Pyrzynska, K., Application of Carbon Sorbents for the Concentration and Separation of Metal Ions. *Analytical Sciences* **2007,** 23, (6), 631-637.
200. Mellah, A.; Chegrouche, S.; Barkat, M., The Removal of Uranium(VI) From Aqueous Solutions Onto Activated Carbon: Kinetic and Thermodynamic Investigations. *Journal of Colloid and Interface Science* **2006,** 296, (2), 434-441.
201. Kalcher, K.; Svancara, I.; Buzuk, M.; Vytras, K.; Walcarius, A., Electrochemical Sensors and Biosensors Based on Heterogeneous Carbon Materials. *Monatshefte fuer Chemie* **2009,** 140, (8), 861-889.
202. Zhu, L.; Tian, C.; Zhu, D.; Yang, R., Ordered Mesoporous Carbon Paste Electrodes for Electrochemical Sensing and Biosensing. *Electroanalysis* **2008,** 20, (10), 1128-1134.
203. Pretty, J. R.; Duckworth, D. C.; Van Berkel, G. J., Electrochemical Sample Pretreatment Coupled On-Line with ICP-MS: Analysis of Uranium Using an Anodically Conditioned Glassy Carbon Working Electrode. *Analytical Chemistry* **1998,** 70, (6), 1141-1148.
204. Clark, W. J.; Park, S. H.; Bostick, D. A.; Duckworth, D. C.; Van Berkel, G. J., Electrochemically Modulated Separation, Concentration, and Detection of Plutonium Using an Anodized Glassy Carbon Electrode and Inductively Coupled Plasma Mass Spectrometry. *Analytical Chemistry* **2006,** 78, (24), 8535-8542.
205. Liezers, M.; Lehn, S.; Olsen, K.; Farmer, O.; Duckworth, D., Determination of Plutonium Isotope Ratios at Very Low Levels by ICP-MS Using On-Line Electrochemically Modulated separations. *Journal of Radioanalytical and Nuclear Chemistry* **2009,** 282, (1), 299-304.
206. Liezers, M.; Pratt, S. H.; Hart, G. L.; Duckworth, D. C., Electrochemically modulated Separations for Rapid and Sensitive Isotopic Analysis. *Journal of Radioanalytical and Nuclear Chemistry* **2013,** 296, (2), 1037-1043.
207. Nitz, J.-J. Synthesis and Functionalization of Ordered Mesoporous Carbons for Catalytic Applications. Ph.D. Thesis, Ruhr Universität Bochum, Bochum, 2009.
208. Iijima, S., Helical Microtubules of Graphitic Carbon. *Nature* **1991,** 354, (6348), 56-58.
209. Ryoo, R.; Joo, S. H.; Jun, S.; Tsubakiyama, T.; Terasaki, O., Ordered Mesoporous Carbon Molecular Sieves by Templated Synthesis: the Structural Varieties. *Stud. Surf. Sci. Catal.* **2001,** 135, 1121-1128.
210. Zhang, F. Q.; Meng, Y.; Gu, D.; Yan, Y.; Yu, C. Z.; Tu, B.; Zhao, D. Y., A Facile Aqueous Route to Synthesize Highly Ordered Mesoporous Polymers and Carbon Frameworks with Ia3d Bicontinuous Cubic Structure. *Journal of the American Chemical Society* **2005,** 127, (39), 13508-13509.
211. Meng, Y.; Gu, D.; Zhang, F. Q.; Shi, Y. F.; Yang, H. F.; Li, Z.; Yu, C. Z.; Tu, B.; Zhao, D. Y., Ordered Mesoporous Polymers and Homologous Carbon Frameworks: Amphiphilic Surfactant Templating and Direct Transformation. *Angewandte Chemie-International Edition* **2005,** 44, (43), 7053-7059.
212. Liu, R. L.; Shi, Y. F.; Wan, Y.; Meng, Y.; Zhang, F. Q.; Gu, D.; Chen, Z. X.; Tu, B.; Zhao, D. Y., Triconstituent Co-assembly to Ordered Mesostructured Polymer-Silica and Carbon-Silica Nanocomposites and Large-Pore Mesoporous Carbons with High Surface Areas. *Journal of the American Chemical Society* **2006,** 128, (35), 11652-11662.
213. Meng, Y.; Gu, D.; Zhang, F. Q.; Shi, Y. F.; Cheng, L.; Feng, D.; Wu, Z. X.; Chen, Z. X.; Wan, Y.; Stein, A.; Zhao, D. Y., A Family of Highly Ordered Mesoporous Polymer Resin and

Carbon Structures From Organic-Organic Self-Assembly. *Chemistry of Materials* **2006,** 18, (18), 4447-4464.
214. Deng, Y. H.; Cai, Y.; Sun, Z. K.; Gu, D.; Wei, J.; Li, W.; Guo, X. H.; Yang, J. P.; Zhao, D. Y., Controlled Synthesis and Functionalization of Ordered Large-Pore Mesoporous Carbons. *Advanced Functional Materials* **2010,** 20, (21), 3658-3665.
215. Li, W.; Zhang, F.; Dou, Y. Q.; Wu, Z. X.; Liu, H. J.; Qian, X. F.; Gu, D.; Xia, Y. Y.; Tu, B.; Zhao, D. Y., A Self-Template Strategy for the Synthesis of Mesoporous Carbon Nanofibers as Advanced Supercapacitor Electrodes. *Advanced Energy Materials* **2011,** 1, (3), 382-386.
216. Gao, W. J.; Wan, Y.; Dou, Y. Q.; Zhao, D. Y., Synthesis of Partially Graphitic Ordered Mesoporous Carbons with High Surface Areas. *Advanced Energy Materials* **2011,** 1, (1), 115-123.
217. Wang, J. X.; Xue, C. F.; Lv, Y. Y.; Zhang, F.; Tu, B.; Zhao, D. Y., Kilogram-Scale Synthesis of Ordered Mesoporous Carbons and Their Electrochemical Performance. *Carbon* **2011,** 49, (13), 4580-4588.
218. Florent, M.; Xue, C. F.; Zhao, D. Y.; Goldfarb, D., Formation Mechanism of Cubic Mesoporous Carbon Monolith Synthesized by Evaporation-Induced Self-assembly. *Chemistry of Materials* **2012,** 24, (2), 383-392.
219. Wei, H.; Lv, Y. Y.; Han, L.; Tu, B.; Zhao, D. Y., Facile Synthesis of Transparent Mesostructured Composites and Corresponding Crack-free Mesoporous Carbon/Silica Monoliths. *Chemistry of Materials* **2011,** 23, (9), 2353-2360.
220. Jung, Y.; Lee, H. I.; Kim, J. H.; Yun, M.-H.; Hwang, J.; Ahn, D.-H.; Park, J.-N.; Boo, J.-H.; Choi, K.-S.; Kim, J. M., Preparation of Polypyrrole-Incorporated Mesoporous Carbon-Based Composites for Confinement of Eu(III) Within Mesopores. *Journal of Materials Chemistry*, **2010,** 20, (22), 4663-4668.
221. Oji, L. N.; Wilmarth, W. R.; Hobbs, D. T., Loading Capacities for Uranium, Plutonium, and Neptunium in High Caustic Nuclear Waste Storage Tanks Containing Selected Sorbents. *Nuclear Technology* **2010,** 169, (2), 143-149.
222. Ganzerli, M. T. V.; Crespi Caramella, V.; Maggi, L., Adsorption of Actinides by Chelating Agents Containing Benzene Rings, Fixed on Charcoal. *Journal of Radioanalytical and Nuclear Chemistry* **2002,** 254, (1), 3-7.
223. Ganzerli, M. T. V.; Crespi Caramella, V.; Maggi, L., The Role of Salts Derived From Benzilic Acid and Quinolines in the Adsorption of Some Actinides, Part I: Characterization of the Adsorbers. *Journal of Radioanalytical and Nuclear Chemistry* **2004,** 260, (3), 579-583.
224. Someda, H. H.; Sheha, R. R., Solid Phase Extractive Preconcentration of Some Actinide Elements Using Impregnated Carbon. *Radiochemistry* **2008,** 50, (1), 56-63.
225. Coleman, S. J.; Coronado, P. R.; Maxwell, R. S.; Reynolds, J. G., Granulated Activated Carbon Modified with Hydrophobic Silica Aerogel-Potential Composite Materials for the Removal of Uranium from Aqueous Solutions. *Environmental Science & Technology* **2003,** 37, (10), 2286-2290.
226. Starvin, A. M.; Rao, T. P., Solid Phase Extractive Preconcentration of Uranium(VI) Onto Diarylazobisphenol Modified Activated Carbon. *Talanta* **2004,** 63, (2), 225-232.
227. Someda, H. H.; Sheha, R. R., Solid Phase Extractive Preconcentration of Some Actinide Elements Using Impregnated Carbon. *Journal of Nuclear and Radiochemical Sciences* **2006,** 7, (2), 37-43.

228. Zhao, Y.; Liu, C.; Feng, M.; Chen, Z.; Li, S.; Tian, G.; Wang, L.; Huang, J.; Li, S., Solid Phase Extraction of Uranium(VI) Onto Benzoylthiourea-Anchored Activated Carbon. *Journal of Hazardous Materials,* **2010,** 176, (1-3), 119-124.
229. Yakout, S. M.; Metwally, S. S.; El-Zakla, T., Uranium Sorption Onto Activated Carbon Prepared From Rice Straw: Competition with Humic Acids. *Applied Surface Science* **2013,** 280, (0), 745-750.
230. Arisaka, M.; Watanabe, M.; Kimura, T., Selective Adsorption of Trivalent Actinides From Lanthanides Onto Activated Carbons in Acidic Aqueous Solution. *Journal of Nuclear Materials* **2010,** 407, (2), 116-118.
231. Gad, H. M. H.; Awwad, N. S., Factors Affecting the Sorption/Desorption of Eu (III) using Activated Carbon. *Separation Science and Technology* **2007,** 42, (16), 3657-3680.
232. Omar, H. A.; Moloukhia, H., Use of Activated Carbon in Removal of Some Radioisotopes From Their Waste Solutions. *Journal of Hazardous Materials* **2008,** 157, (2-3), 242-246.
233. Myasoedova, G. V.; Molochnikova, N. P.; Tkachev, A. G.; Tugolukov, E. N.; Mishchenko, S. V.; Myasoedov, B. F., Sorption Preconcentration of Radionuclides on Taunit Carbon Nanostructural Material. *Radiochemistry (Moscow, Russian Federation)* **2009,** 51, (2), 156-158.
234. Mokhodoeva, O. B.; Malikov, D. A.; Molochnikova, N. P.; Zakharchenko, E. A.; Perevalov, S. A.; Myasoedova, G. V.; Kulyako, Y. M.; Tkachev, A. G.; Mishchenko, S. V.; Myasoedov, B. F., Carbon Nanotubes: Potential Application for Radionuclide Preconcentration. *Russian Journal of General Chemistry* **2011,** 54, (3), 61-68.
235. Zakharchenko, E. A.; Malikov, D. A.; Myasoedova, G. V.; Mokhodoeva, O. B.; Molochnikova, N. P.; Kulyako, Y. M., Solid-Phase Extractants Based on Taunit Carbon Nanotubes for Actinide and REE Preconcentration From Nitric Acid Solutions. *Radiochemistry* **2012,** 54, (2), 159-163.
236. Perevalov, S. A.; Molochnikova, N. P., Sorption of Pu in Various Oxidation States Onto Multiwalled Carbon Nanotubes. *Journal of Radioanalytical and Nuclear Chemistry* **2009,** 281, (3), 603-608.
237. Wang, X.; Chen, C.; Hu, W.; Ding, A.; Xu, D.; Zhou, X., Sorption of ^{243}Am(III) to Multiwall Carbon Nanotubes. *Environmental Science & Technology* **2005,** 39, (8), 2856-60.
238. Wang, M.; Tao, X.; Song, X., Effect of pH, Ionic Strength and Temperature on Sorption Characteristics of Th(IV) on Oxidized Multiwalled Carbon Nanotubes. *Journal of Radioanalytical and Nuclear Chemistry* 288, (3), 859-865.
239. Watanabe, M.; Arisaka, M.; Kimura, T., Adsorption of Trivalent Actinides and Lanthanides to Carbon Materials. *Abstracts of Papers, 239th ACS National Meeting, San Francisco, CA, United States, March 21-25, 2010* **2010**, NUCL-46.
240. Fan, Q. H.; Shao, D. D.; Hu, J.; Chen, C. L.; Wu, W. S.; Wang, X. K., Adsorption of Humic Acid and Eu(III) to Multi-Walled Carbon Nanotubes: Effect of pH, Ionic Strength and Counterion Effect. *Radiochimica Acta* **2009,** 97, (3), 141-148.
241. Chen, C. L.; Hu, J.; Xu, D.; Tan, X. L.; Meng, Y. D.; Wang, X. K., Surface Complexation Modeling of Sr(II) and Eu(III) Adsorption Onto Oxidized Multiwall Carbon Nanotubes. *Journal of Colloid and Interface Science* **2008,** 323, (1), 33-41.
242. Schierz, A.; Zanker, H., Aqueous Suspensions of Carbon Nanotubes: Surface Oxidation, Colloidal Stability and Uranium Sorption. *Environmental Pollution* **2009,** 157, (4), 1088-1094.

243. Fasfous, II; Dawoud, J. N., Uranium (VI) Sorption by Multiwalled Carbon Nanotubes From Aqueous Solution. *Applied Surface Science* **2012,** 259, 433-440.
244. Sun, Y.; Yang, S.; Sheng, G.; Guo, Z.; Wang, X., The Removal of U(VI) From Aqueous Solution by Oxidized Multiwalled Carbon Nanotubes. *Journal of Environmental Radioactivity* **2012,** 105, (0), 40-47.
245. Shao, D.; Jiang, Z.; Wang, X.; Li, J.; Meng, Y., Plasma Induced Grafting Carboxymethyl Cellulose on Multiwalled Carbon Nanotubes for the Removal of UO_2^{2+} from Aqueous Solution. *Journal of Physical Chemistry B* **2009,** 113, (4), 860-864.
246. Mokhodoeva, O. B.; Myasoedova, G. V.; Zakharchenko, E. A., Solid-Phase Extractants for Radionuclide Preconcentration and Separation. New Possibilities. *Radiochemistry* **2011,** 53, (1), 35-43.
247. Chen, S. Z.; Xiao, M. F.; Lu, D. B.; Zhan, X. L., Carbon Nanofibers as Solid-Phase Extraction Adsorbent for the Preconcentration of Trace Rare Earth Elements and Their Determination by Inductively Coupled Plasma Mass Spectrometry. *Analytical Letters* **2007,** 40, (11), 2105-2115.
248. Xu, Y.; Zondlo, J. W.; Finklea, H. O.; Brennsteiner, A., Electrosorption of Uranium on Carbon Fibers as a Means of Environmental Remediation. *Fuel Processing Technology* **2000,** 68, (3), 189-208.
249. Kim, J.; Tsouris, C.; Mayes, R. T.; Oyola, Y.; Saito, T.; Janke, C. J.; Dai, S.; Schneider, E.; Sachde, D., Recovery of Uranium from Seawater: A Review of Current Status and Future Research Needs. *Separation Science and Technology* **2013,** 48, (3), 367-387.
250. Yang, X. D.; Li, J.; Liu, J.; Tian, Y.; Li, B.; Cao, K. C.; Liu, S. B.; Hou, M.; Li, S. J.; Ma, L. J., Simple Small Molecule Carbon Source Strategy for Synthesis of Functional Hydrothermal Carbon: Preparation of Highly Efficient Uranium Selective Solid Phase Extractant. *Journal of Materials Chemistry A* **2014,** 2, (5), 1550-1559.
251. Zhang, Z. B.; Cao, X. H.; Liang, P.; Liu, Y. H., Adsorption of Uranium From Aqueous Solution Using Biochar Produced by Hydrothermal Carbonization. *Journal of Radioanalytical and Nuclear Chemistry* **2013,** 295, (2), 1201-1208.
252. Sun, Y. B.; Wang, Q.; Chen, C. L.; Tan, X. L.; Wang, X. K., Interaction Between Eu(III) and Graphene Oxide Nanosheets Investigated by Batch and Extended X-ray Absorption Fine Structure Spectroscopy and by Modeling Techniques. *Environmental Science & Technology* **2012,** 46, (11), 6020-6027.
253. Romanchuk, A. Y.; Slesarev, A. S.; Kalmykov, S. N.; Kosynkin, D. V.; Tour, J. M., Graphene Oxide for Effective Radionuclide Removal. *Physical Chemistry Chemical Physics* **2013,** 15, (7), 2321.
254. Li, X. L.; Song, Q.; Liu, B. J.; Liu, C. X.; Wang, H.; Geng, J. X.; Chen, Z.; Liu, N.; Li, S. J., Adsorption of Uranium by Carbon Materials from Aqueous Solutions. *Progress in Chemistry* **2011,** 23, (7), 1446-1453.
255. Zhang, Z. B.; Nie, W. B.; Li, Q.; Xiong, G. X.; Cao, X. H.; Liu, Y. H., Removal of Uranium(VI) From Aqueous Solutions by Carboxyl-Rich Hydrothermal Carbon Spheres Through Low-Temperature Heat Treatment in Air. *Journal of Radioanalytical and Nuclear Chemistry* **2013,** 298, (1), 361-368.
256. Arisaka, M.; Watanabe, M. Process for Trivalent Actinide and Trivalent Lanthanide Separation. 2009-56415 2937562, 20090918.
257. Wang, P. Carbon Nanotubes Using for Recovery of Radionuclides and Separation of Actinides and Lanthanides. 2008-US11623 2009048596, 20081009., 2009.

258. Zhang, X. F.; Wang, J.; Li, R. M.; Liu, Q.; Li, L.; Yu, J.; Zhang, M. L.; Liu, L. H., Efficient Removal of Uranium(VI) From Aqueous Systems by Heat-Treated Carbon Microspheres. *Environmental Science and Pollution Research* **2013,** 20, (11), 8202-8209.
259. Hazen, R. M.; Downs, R. T.; Jones, A. P.; Kah, L., Carbon Mineralogy and Crystal Chemistry. In *Carbon in Earth*, Hazen, R. M.; Jones, A. P.; Baross, J. A., Eds. Mineralogical Soc Amer: Chantilly, 2013; Vol. 75, pp 7-46.
260. Geim, A. K., Graphene: Status and Prospects. *Science* **2009,** 324, (5934), 1530-1534.
261. Boehm, H. P., Some Aspects Of The Surface Chemistry of Carbon Blacks and Other Carbons. *Carbon* **1994,** 32, (5), 759-769.
262. Boehm, H. P., Surface Oxides on Carbon and Their Analysis: A Critical Assessment. *Carbon* **2002,** 40, (2), 145-149.
263. Shin, H. J.; Ryoo, R.; Kruk, M.; Jaroniec, M., Modification of SBA-15 Pore Connectivity by High-Temperature Calcination Investigated by Carbon Inverse Replication. *Chemical Communications* **2001**, (4), 349-350.
264. Joo, S. H.; Choi, S. J.; Oh, I.; Kwak, J.; Liu, Z.; Terasaki, O.; Ryoo, R., Ordered Nanoporous Arrays of Carbon Supporting High Dispersions of Platinum Nanoparticles. *Nature* **2001,** 412, (6843), 169-172.
265. Lu, A. H.; Li, W. C.; Schmidt, W.; Kiefer, W.; Schuth, F., Easy Synthesis of an Ordered Mesoporous Carbon With a Hexagonally Packed Tubular Structure. *Carbon* **2004,** 42, (14), 2939-2948.
266. Bazula, P. A.; Lu, A. H.; Nitz, J. J.; Schuth, F., Surface and Pore Structure Modification of Ordered Mesoporous Carbons via a Chemical Oxidation Approach. *Microporous and Mesoporous Materials* **2008,** 108, (1-3), 266-275.
267. Yuan, L. Y.; Liu, Y. L.; Shi, W. Q.; Lv, Y. L.; Lan, J. H.; Zhao, Y. L.; Chai, Z. F., High Performance of Phosphonate-Functionalized Mesoporous Silica for U(VI) Sorption From Aqueous Solution. *Dalton Transactions* **2011,** 40, (28), 7446-7453.
268. Chen, S.; Zeng, H., Improvement of the Reduction Capacity of Activated Carbon Fiber. *Carbon* **2003,** 41, (6), 1265-1271.
269. Fu, R.; Zeng, H.; Lu, Y., The Reducing Property of Activated Carbon Fibre and its Application in the Recovery of Gold. *Minerals Engineering* **1993,** 6, (7), 721-729.
270. Fu, R.; Zeng, H.; Lu, Y.; Lai, S. Y.; Chan, W. H.; Ng, C. F., The Reduction of Pt(IV) With Activated Carbon Fibers—An XPS study. *Carbon* **1995,** 33, (5), 657-661.
271. Nitsche, H.; Becraft, K., The Complexation Behavior of Neptunium and Plutonium With Nnitrilotriacetic Acid. *Abstracts of Papers of the American Chemical Society* **1990,** 200, 57-NUCL.
272. Foreman, J. K.; Smith, T. D., 331. The Nature and Stability of the Complex Ions Formed by Ter-, Quadri-, and Sexa-Valent Plutonium Ions With Ethylenediaminetetraacetic Acid. Part I. pH Titrations and Ion-Exchange Studies. *Journal of the Chemical Society* **1957**, 1752-1758.
273. Parks, G. A., Surface Energy and Adsorption at Mineral/Water Interfaces: An Introduction. In *Mineral-Water Interface Geochemistry*, Hochella, M. F. J. W., Art F., Ed. Mineralogical Society of America: Washington, D.C., 1990; Vol. 23, p 603.
274. Shcherbina, N. S.; Perminova, I. V.; Kalmykov, S. N.; Kovalenko, A. N.; Haire, R. G.; Novikov, A. P., Redox and Complexation Interactions of Neptunium(V) with Quinonoid-Enriched Humic Derivatives. *Environmental Science & Technology* **2007,** 41, (20), 7010-7015.
275. Osterberg, R.; Shirshova, L., Oscillating, Nonequilibrium Redox Properties of Humic Acids. *Geochimica et Cosmochimica Acta* **1997,** 61, (21), 4599-4604.

276. Nurmi, J. T.; Tratnyek, P. G., Electrochemical Properties of Natural Organic Matter (NOM), Fractions of NOM, and Model Biogeochemical Electron Shuttles. *Environmental Science & Technology* **2002,** 36, (4), 617-624.
277. Marquardt, C. M.; Seibert, A.; Artinger, R.; Denecke, M. A.; Kuczewski, B.; Schild, D.; Fanghanel, T., The Redox Behaviour of Plutonium in Humic Rich Groundwater. *Radiochimica Acta* **2004,** 92, (9-11), 617-623.
278. Nash, K.; Fried, S.; Friedman, A. M.; Sullivan, J. C., Redox Behavior, Complexing, and Adsorption of Hexavalent Actinides by Humic Acid and Selected Clays. *Environmental Science & Technology* **1981,** 15, (7), 834-837.
279. Choppin, G. R.; Roberts, R. A.; Morse, J. W., Effects of Humic Substances on Plutonium Speciation in Marine Systems. *ACS Symposium Series* **1986,** 305, 382-388.
280. Choppin, G. R., Actinide Speciation in Aquatic Systems. *Marine Chemistry* **2006,** 99, (1–4), 83-92.
281. Andre, C.; Choppin, G. R., Reduction of Pu(V) by Humic Acid. *Radiochimica Acta* **2000,** 88, (9-11), 613-616.
282. Petrova, S. A.; Kolodyazhny, M. V.; Ksenzhek, O. S., Electrochemical Properties of Some Naturally Occurring Quinones. *Journal of Electroanalytical Chemistry and Interfacial Electrochemistry* **1990,** 277, (1–2), 189-196.
283. Chen, L.; Ma, D.; Pietruszka, B.; Bao, X., Carbon-Supported Silver Catalysts for CO Selective Oxidation in Excess Hydrogen. *Journal of Natural Gas Chemistry* **2006,** 15, (3), 181-190.
284. Dekanski, A.; Stevanović, J.; Stevanović, R.; Jovanović, V. M., Glassy Carbon Electrodes: II. Modification by Immersion in $AgNO_3$. *Carbon* **2001,** 39, (8), 1207-1216.
285. Zoval, J. V.; Lee, J.; Gorer, S.; Penner, R. M., Electrochemical Preparation of Platinum Nanocrystallites With Size Selectivity on Basal Plane Oriented Graphite Surfaces. *Journal of Physical Chemistry B* **1998,** 102, (7), 1166-1175.
286. Conradson, S. D.; Abney, K. D.; Begg, B. D.; Brady, E. D.; Clark, D. L.; den Auwer, C.; Ding, M.; Dorhout, P. K.; Espinosa-Faller, F. J.; Gordon, P. L.; Haire, R. G.; Hess, N. J.; Hess, R. F.; Keogh, D. W.; Lander, G. H.; Lupinetti, A. J.; Morales, L. A.; Neu, M. P.; Palmer, P. D.; Paviet-Hartmann, P.; Reilly, S. D.; Runde, W. H.; Tait, C. D.; Veirs, D. K.; Wastin, F., Higher Order Speciation Effects on Plutonium L-3 X-ray Absorption Near Edge Spectra. *Inorganic Chemistry* **2004,** 43, (1), 116-131.
287. Teng, W.; Wu, Z. X.; Fan, J. W.; Chen, H.; Feng, D.; Lv, Y. Y.; Wang, J. X.; Asiri, A. M.; Zhao, D. Y., Ordered Mesoporous Carbons and Their Corresponding Column for Highly Efficient Removal of Microcystin-LR. *Energy & Environmental Science* **2013,** 6, (9), 2765-2776.
288. Seils, C. A.; Meyer, R. J.; Larsen, R. P., Amperometric Titration of Plutonium(VI) with Iron(II). *Analytical Chemistry* **1963,** 35, (11), 1673-1675.
289. Colvin, C. A., Reduction of Plutonium(VI) to Plutonium(III) and (IV) by Sodium Nitrite. In GE, Ed. Hanford Declassified Document Retrieval System: 1963.
290. Silva, R. J.; Nitsche, H., Actinide Environmental Chemistry. *Radiochimica Acta* **1995,** 70-1, 377-396.
291. Kersting, A. B., Plutonium Transport in the Environment. *Inorganic Chemistry* **2013,** 52, (7), 3533-3546.

292. Newton, T. W. *The Kinetics of the Oxidation-Reduction Reactions of Uranium, Neptunium, Plutonium, and Americium in Aqueous Solutions*; TID-26506; Los Alamos Scientific Laboratory, University of California: Oak Ridge, Tennessee, 1975.
293. Hagan, P. G.; Cleveland, J. M., Absorption Spectra of Neptunium Ions in Perchloric Acid Solution. *Journal of Inorganic & Nuclear Chemistry* **1966,** 28, (12), 2905.
294. Kihara, S.; Yoshida, Z.; Aoyagi, H.; Maeda, K.; Shirai, O.; Kitatsuji, Y.; Yoshida, Y., A Critical Evaluation of the Redox Properties of Uranium, Neptunium and Plutonium Ions in Acidic Aqueous Solutions - (Technical report). *Pure and Applied Chemistry* **1999,** 71, (9), 1771-1807.
295. Gupta, R.; Guin, S. K.; Aggarwal, S. K., A Mechanistic Study on the Electrocatalysis of the Pu(IV)/Pu(III) Redox Reaction at a Platinum Electrode Modified With Single-Walled Carbon Nanotubes (SWCNTs) and Polyaniline (PANI). *RSC Advances* **2012,** 2, (5), 1810-1819.